UNIVERSITY OF COPENHAGEN
FACULTY OF SCIENCE

Software for simulation and design of neutron scattering instrumentation

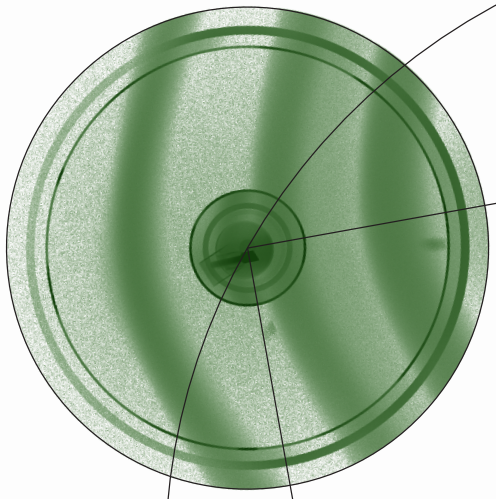

PhD Thesis

June 20, 2017

Mads Bertelsen
Nano-Science Center
Niels Bohr Institute
University of Copenhagen

Supervisor:
Kim Lefmann, Niels Bohr Institute

This thesis has been submitted to the PhD School of
The Faculty of Science, University of Copenhagen

Abstract

This thesis revolves around the simulation of neutron scattering instrumentation using the Monte Carlo ray-tracing package McStas. McStas and similar tools are used extensively in the design of instrumentation at the European Spallation Source currently under construction in Sweden, and has played a similar role in the construction of most modern neutron scattering facilities. McStas allows the user to build an instrument from building blocks called components, such as guide sections, samples and detectors. The modular nature of McStas facilitates international collaboration, as such components are contributed by super users to be used by others, and thus the capabilities of the package is continuously expanded.

The contents of this thesis includes work on neutron guide optimization, including development of analytical constraints that minimize thermal neutron background. These constraints originate from the limit on guide performance given by the Liouville theorem when the desired beam is specified with both a limited spatial extend, divergence and wavelength range. Given such a beam description, the constraints will limit the optimization to guides with minimal thermal background that can still potentially reach the Liouville performance limit. For this reason the constraints are nicknamed "the Minimalist Principle". Guides optimized with and without the Minimalist Principle are compared, showing the expected advantage in terms of the fraction of neutrons delivered by the guide included in the desired beam description. A tool called "guide_bot" is presented which reduces the effort required to program neutron guide optimizations. This is achieved by generating the required McStas files, iFit optimization code and scripts from simple user input describing the desired beam and overall guide geometry. The optimized guides are thoroughly characterised in a consistent manner, empowering instrument teams to compare large numbers of guide alternatives with limited effort. The features of guide_bot are presented along with examples of complex guides optimized using the software. The software was further used for optimizing guides for the majority of the proposed instruments for the European Spallation Source for a range of moderator heights, which resulted in a data set partly used to select the final moderator height of the facility.

The thesis also presents a contribution to the McStas package called the "Union components" that circumvents basic McStas restrictions to include multiple scattering throughout complicated sample environments and the like. Within the Union components the task of a typical McStas sample component is separated into multiple components. Materials are defined from a description of absorption together with an arbitrary number of physical processes such as incoherent scattering, powder scattering and single crystal scattering. When defining the geometry to be simulated, volumes such as boxes, spheres and cylinders are used to build the overall geometry, and each are assigned the appropriate material definition. These volumes can overlap, allowing the construction of windows in sample environments, complicated sample holders including shielding and the like. The simulation performed using Union components are not done in a linear fashion, but rather using an optimized logical network that reduces the computational requirements. The developed algorithm for propagation and the generation of the optimized networks are presented. The Union components are used to simulate the triple axis spectrometer MACS and time of flight powder spectrometer MARI. Both instrument simulation are used to recreate recent measurements. Each recreation have details that deviate, but are mostly in agreement with measurements.

Resume

Denne afhandlings omdrejningspunkt er simulation af neutronsprednings instrumentering ved hjælp af Monte Carlo strålings-sporings pakken McStas. McStas og lignende redskaber bruges i høj grad til design af instrumentering til den Europæiske Spallations Kilde, der er under opførsel i Sverige, og har spillet lignende roller under opførslen af de fleste moderne neutronsprednings faciliteter. McStas tillader brugeren at bygge instrumenter med byggeklodser kaldet komponenter, det kan være guidesektioner, prøver og detektorer. Den modulære opbygning af McStas muliggøre internationalt samarbejde, da disse komponenter biddrages af superbrugere så de derefter kan bruges af andre, og på denne måde bliver pakkens muligheder udvidet.

Denne afhandling indeholder optimering af neutronguides, inklusive udvikling af analytiske randbetingelser som minimerer termisk neutron baggrund. Disse randbetingelser stammer fra grænsen for en guides ydeevne sat af Liouvilles teorem, når den ønskede stråle er specificeret både med begrænset rumlig udstrækning, divergens og bølgelængde interval. Givet sådan en stråle beskrivelse vil randbetingelserne begrænse optimeringen til guides med minimal termisk baggrund, som stadig potentielt kan opnå Liouville grænsen for ydeevne. Af denne grund har randbetingelserne fået navnet "Minimalist Princippet". Guides optimeret med og uden Minimalist Princippet er sammenlignet, hvilket viser den forventede fordel i form af brøkdelen af neutroner afleveret af guiden indenfor de opgivne stråle specifikationer. Et værktøj kaldet "guide_bot" som reducerer den nødvendige arbejdsmængde påkrævet for at programmere en neutronguideoptimering er præsenteret. Dette er opnået ved at generer de påkrævede McStas filer, iFit optimerings kode og scripts ud fra simpelt bruger input der beskriver den ønskede stråle og den overordnede guide geometri. De optimerede guides er grundigt karakteriseret på en konsistent måde, hvilket tillader et instrumenthold at sammenligne et stort antal guide alternativer med begrænset indsats. Funktionerne indeholdt i guide_bot er præsenteret sammen med eksempler af komplicerede guides, der er optimeret ved brug af programmet. Programmet er endvidere brugt til optimering af guides for størstedelen af foreslåede instrumenter til den Europæiske Spallations Kilde for et interval af moderator højder, hvilket resulterede i data som biddrog til at beslutte facilitetens endelige moderator højde.

Denne afhandling præsentere også et biddrag til McStas pakken kaldet "Union komponenterne" som omgår basale McStas restriktioner så gentagene spredning kan inkluderes i komplicerede prøve milijøer. Indenfor Union komponenterne er en typisk McStas komponents opgaver blevet opdelt i flere komponenter. Materialer er defineret ud fra en beskrivelse af absorption sammen med et arbitrært antal af fysiske processer såsom inkoherent spredning, pulver spredning og enkelt krystal spredning. Når geometrier der skal simuleres defineres bruges volumener såsom bokse, kugler og cylindere til at bygge den overordnede geometri, og hver af disse tilknyttes en passende materiale-definition. Disse volumener kan overlappe, hvilket tillader konstruktion af vinduer i prøve milijøer, komplicerede prøveholdere inklusive afskærmning og lignende. Simulationerne udført med Union komponenterne er ikke lineære, men i stedet bruges et optimeret logisk netværk, der reducerer computermæssige krav. De udviklede algoritmer til propagation og generationen af de optimerede netværk er præsenteret. Union komponenterne er brugt til at simulere tre-akse-spektrometeret MACS og flyvetids-pulver-spektrometeret MARI. Begge instrument simulationer er blevet brugt til at genskabe målinger. Hver simulation har nogle detaljer der afviger, men er overvejende i overensstemmelse med målingerne.

Contents

Preface

This document is the PhD thesis by Mads Bertelsen employed at the Niels Bohr Institute X-ray and Neutron Science group March 2012 to June 2017. The position was financed by the Niels Bohr Institute itself, and supervised by Kim Lefmann. The PhD position was of the 4+4 type, meaning a 60 ECTS point master thesis was to be submitted after 2 years of study. The subject of the master thesis was neutron guide design, introducing analytical constraints for guide optimizations and an early version of the software package guide_bot. Due to discoveries in the field of neutron moderation, the European Spallation Source needed a large amount of guide optimization work to determine if drastic changes in the moderator dimensions would be worthwhile. The investigation had to be performed with urgency as a delayed decision would delay the entire project. A years leave of absence was taken from the PhD programme in 2014-2015 during which I reported to Ken Andersen, the head of the instrumentation group. Guides were optimized for a range of proposed moderators for the majority of the instrument suite, and guide_bot was developed further to lift the task.

When returning to the PhD position, the focus was shifted to the original problem of advancing McStas sample simulation. The mandatory stay abroad was at Johns Hopkins University, USA, in the group of Collin Broholm. Here the developed McStas code was used to simulate the triple axis spectrometer MACS.

The contents of this thesis is thus split between the neutron guide design work and work on McStas sample simulation. The thesis includes 3 papers of which I am the first author, 1 which is published (A.1), 1 which is accepted (A.2) and 1 draft that is almost ready for publication (A.3). I was first author on the paper A.4, it is included here for completeness, but is not to be considered in the assessment of the PhD thesis as it was submitted as part of the master thesis. In addition, I have co authored 9 papers in the period, primarily in the field of neutron guide design, A.5, A.6, A.7, A.8, A.9, A.10, A.11, A.12 and A.13.

A.1: **Constraining neutron guide optimizations with phase-space considerations** M. Bertelsen, K. Lefmann. Nuclear Instruments and Methods in Physics Research Section A: Accelerators, Spectrometers, Detectors and Associated Equipment, Vol. 830, (2016), DOI: 10.1016/j.nima.2016.06.003

A.2: **The automatic neutron guide optimizer guide_bot** (accepted) M. Bertelsen. Nuclear Instruments and Methods in Physics Research Section A: Accelerators, Spectrometers, Detectors and Associated Equipment, (2017), DOI: 10.1016/j.nima.2017.06.012

A.3: **Expanding the McStas sample simulation logic with McStas Union components** (in preparation), M. Bertelsen, K. Lefmann. Review of Scientific Instruments.

A.4: **Exploring performance of neutron guide systems using pinhole beam extraction** M. Bertelsen, H. Jacobsen, U.B. Hansen, H.H. Carlsen, K. Lefmann. Nuclear Instruments and Methods in Physics Research Section A: Accelerators, Spectrometers, Detectors and Associated Equipment, Vol. 729, (2013) DOI: 10.1016/j.nima.2013.07.062

A.5: **Neutron guide-split: A high performance guide bundle concept for elliptical guides** S. L. Holm, N. Rasmussen, L. Høpfner, M. Bertelsen, J. Voigt, K. H. Andersen, K. Lefmann. Nuclear Instruments and Methods in Physics Research Section A: Accelerators, Spectrometers, Detectors and Associated Equipment, Vol. 782, (2015), DOI: 10.1016/j.nima.2015.01.045

A.6: **Simulation of waviness in neutron guides** U.B. Hansen, M. Bertelsen, E.B. Knudsen, K. Lefmann. Journal of Neutron Research, Vol. 18, (2016) DOI: 10.3233/JNR-150023

A.7: **CAMEA ESS - The Continuous Angle Multi-Energy Analysis Indirect Geometry Spectrometer for the European Spallation Source** P. G. Freeman, J. O. Birk, M. Mark, M. Bertelsen, J. Larsen, N. B. Christensen, K. Lefmann, J. Jacobsen, Ch. Niedermayer, F. Juranyi, H. M. Ronnow. European Physical Journal Web of Conferences, Vol. 83, (2015), DOI: 10.1051/epjconf/20158303005

A.8: **HEIMDAL: A thermal neutron powder diffractometer with high and flexible resolution combined with SANS and neutron imaging - Designed for materials science studies at the European Spallation Source** S.L. Holm, K. Lefmann, P.F. Henry, M. Bertelsen, J Schefer, M. Christensen. Nuclear Instruments and Methods in Physics Research Section A: Accelerators, Spectrometers, Detectors and Associated Equipment, Vol. 828, (2016), DOI: 10.1016/j.nima.2016.05.046

A.9: **VESPA: The vibrational spectrometer for the European Spallation Source** A. Fedrigo, D. Colognesi, M. Bertelsen, M. Hartl, K. Lefmann, P. Deen, M. Strobl, F. Grazzi, M. Zoppi. Review of Scientific Instruments, Vol. 87(6), (2016), DOI: 10.1063/1.4952430

A.10: **Neutron guide shielding for the bifrost spectrometer at ESS** K. Mantulnikovs, M. Bertelsen, C.P. Cooper-Jensen, K. Lefmann and E.B. Klinkby. Journal of Physics: Conference Series, Vol. 746, (2016), DOI: 10.1088/1742-6596/746/1/012027

A.11: **An optional focusing SELENE extension to conventional neutron guides: A case study for the ESS instrument BIFROST** U. B. Hansen, M. Bertelsen, J. Stahn, K. Lefmann. Nuclear Instruments and Methods in Physics Research Section A: Accelerators, Spectrometers, Detectors and Associated Equipment, Vol. 852, (2017), DOI: 10.1016/j.nima.2017.01.075

A.12: **On the nature of magnetic stripes in cuprate superconductors** (submitted), H. Jacobsen, S.L. Holm, M.-E. Lăcătuşu, M. Bertelsen, M. Boehm, R. Toft-Petersen, J.-C. Grivel, S. B. Emery, L. Udby, B.O. Wells, K. Lefmann. Physical Review Letters, (2017)

A.13: **Field-induced inter-planar correlations in the high-temperature superconductor La1.88Sr0.12CuO4** A. T. Roemer, P. Jensen, H. Jacobsen, L. Udby, B. M. Andersen, M. Bertelsen, S. L. Holm, N. B. Christensen, R. Toft-Petersen, M. Skoulatos, M. Laver, A. Schneidewind, P. Link, M. Oda, M. Ido, N. Momono, K. Lefmann. Phys. Rev. B 91, (2015)

Acknowledgements

I thank the Niels Bohr Institute for funding part of the PhD position, and the European Spallation source for providing a 1 year position on guide design.

This PhD thesis would not have been possible without the assistance a number of people, who are thanked here.

First and foremost I would like to thank my supervisor Kim Lefmann who has been my mentor for the last 7 years, and provided a very open work environment where I could tackle the issues at hand in my own ways. Ken Andersen deserves special thanks for guidance and discussions during my year at the ESS and on many other occasions.

The stay abroad was at Johns Hopkins University, Baltimore, USA in the group of Collin Broholm. I am very thankful for the opportunity, and had a fruitful 6 months stay where I met many friendly scientists such as Allen Scheie and Kemp Plumb.

A large part of the work performed have been technical in nature and connected to the McStas Monte Carlo ray-tracing package. Peter Willendrup and Erik Bech Knudsen have been instrumental in introducing me to the development side of the software.

A large amount of CPU time have been used for simulations, which have primarily been provided by the cluster of The ESS Data Management and Software Centre but also from the cluster available at the Neutron Optics and Scientific Computing Group at PSI. I am very grateful for the access to these clusters and the work performed by the administrators to keep all required software functioning and up to date.

I would like to thank Linn Johanna Ellström for proof reading part of the thesis and support through the writing phase.

I have shared office with a number of students whom have always been up for discussion and never hesitated to help whenever issues arose. All of these people deserves thanks, but a few deserves a special mention, Jonas O. Birk, Henrik Jacobsen, Pia Jensen and Sonja L. Holm.

Lastly, a number of people have used the software written as a part of this PhD thesis and given valuable feedback as well as bug reports: Niko Tsapatsaris, Jonas O. Birk, Martin Olsen, Manuel Morgano, Emmanouela Rantsiou, Leland Harriger, Britt R. Hansen, Esben B. Klinkby, Sándor Tóth and Kaspar H. Klenø.

Chapter 1

Introduction

The understanding of materials is fundamental to societies' technological progress, as the available materials is the basis of what can be achieved. Progress in pharmaceuticals, information storage, superconductivity, magnetic systems, chemistry and many other are all dependent on information about the atomic structure of molecules and crystals. Scattering techniques provide the bulk of this information, and the two most important scattering probes are X-rays and neutrons.

X-ray scattering is by far the most common of the two, because the production of X-rays is simpler and can be easily controlled, which results in tight powerful beams that yield precise results. However, there are issues, as the energy scale for X-rays are in keV, while interesting crystal excitations can be in the meV range. In addition, the photon interacts so strongly with typical materials, that studying samples in extreme environments becomes difficult.

Neutron scattering is an alternative technique that can be used to compliment the information gathered from X-ray experiments. The energy scale for thermal neutrons is meV, similar to the energy scale of basic excitations of molecules and crystals. The neutron interacts with the nucleus and has a lower probability for scattering, allowing even illumination of samples and more straightforward construction of sample environments. However, intense neutron beams are much more difficult to produce and control.

Neutron scattering has primarily been performed using dedicated reactor sources producing constant beams; yet the newest generation of high performance sources are predominantly using the spallation process [1]. Spallation yields more neutrons for the same amount of heat, and the neutron production can be performed in short bursts. The time of flight for neutrons can be used to deduce their energy and using this information allows for entirely different instrument design. Time of flight instrumentation has always been possible on continuous sources, but the related loss of intensity have been prohibitively high for most use cases.

The European Spallation Source (ESS) [2] currently under construction in Lund, Sweeden, employs a novel long-pulse time structure. The new time structure provides new possibilities and limitations, which once again have challenged instrument designers to abandon conventional wisdom.

Numerical simulations are currently playing a central role in the design of new neutron scattering instrumentation and sources, hence the quality of these simulations sets the bar for the certainty of each decision made. The range of capabilities provided by this software also dictates the limits for what can be investigated and optimized; meaning all aspects outside of these capabilities are dealt with using potentially outdated conventional wisdom.

The use of numerical simulation of instrumentation in data analysis is a long standing ambition of the simulation community. Simulations have not been widely used, since the capabilities of the simulations have not yet reached the ever changing frontier of the science being performed.

For these reasons, the importance of the accuracy, quality and capabilities of numerical simulations used in neutron scattering is greater than ever.

The numerical simulations used to design the neutron scattering experiments at ESS can be split into two categories, the general packages primarily for high energy particles, and the specialised thermal neutron packages. The general packages such as MCNPX [3] and GEANT4 [4] are used for high energy neutrons and other particles, such as describing the spallation target and neutron moderation [5], but also detectors [6]. A range of packages specialised in thermal neutron scattering exists, which focuses on instrumentation and sample physics. These simulate the path of neutrons from the source to the detector, and are thus used extensively for design of the all important instrumentation [7–15].

The most widely used packages of this kind are called McStas [16–20], RESTRAX / SIMRES [21, 22] and VITESS [23–25]. They are all modular, meaning that the user can build an instrument simulation using smaller building blocks here referred to as components. Rays are propagated through a linear succession of components, for example from a source, through a guide, to a sample and finally to a detector.

This software structure is excellent for simulating neutron guides, as the necessary guide sections are placed in the desired order and virtual neutrons are propagated through the system. Subtle effects from the exact geometry, gravity and even mirror imperfections are easily simulated and optimized. Many publications focus on these aspects [26–44]. The sheer amount of studied alternatives is, however, becoming overwhelming when instrument designers are looking for the best possible guide for their instrument. Considerable effort is needed to evaluate the possibilities for the specific needs of the instrument.

Instrument simulation packages are also well suited to simulate the intended beampath of the instrument backend. Such simulations can provide valuable information on expected count rates, resolution functions and secondary extinction effects.

As the level of detail required from these packages increase, problems have started to arise from the simple structure of the software. One issue originates in the linear succession of components when instruments are becoming increasingly parallel. This is also problematic in areas of the instrument where the path of the simulated neutrons are not clear, for example when simulating a sample in sample holder. If the sample and sample holder are simulated using two components, the user must specify the order in which the neutrons can interact with these, or allow just one of them to scatter. This can be circumvented by programming additional logic, yet this can hardly be expected of every user. These limitations are mostly prevalent when studying background from multiple scattering as opposed to the intended beampath producing the desired signal. Some less used simulation packages have overcome some of these issues, the earliest of which is named MSCAT [45] and was published in 1986. A package called NISP [46–49] can handle arbitrary beam paths, but is not kept updated for modern operating systems. Recently the MCViNE package [50] demonstrated multiple scattering for arbitrary component orders in a tree like scattering logic structure.

This thesis will focus on contributions made to the McStas simulation package and work performed using these. A large part of the work performed is connected to neutron guide design and the numerical optimization of guide geometry. A set of constraints for the geometrical parameters describing a guide is derived for the case of known beam requirements. The constraints are named the "Minimalist Principle" as they minimize the thermal neutron background while maintaining the potential for the best possible performance. Using the Minimalist Principle prevents the optimizer from selecting solutions with horrible efficiency in terms of the ratio of neutrons extracted from the source to neutrons delivered to the sample. Furthermore a software tool named "guide_bot" was produced with the purpose of reducing the time spent programming when performing numerical optimizations of guide geometry. A simple description of the desired beam and facility constraints is given to guide_bot along with a one line description of each guide geometry to be optimized. The output consists of the necessary McStas files, iFit optimization files and scripts that together will perform the required numerical optimization and evaluate the performance of the optimal guide. The guide_bot tool allows the user to compare a large number of different guide solutions for the specific needs of an instrument. Here guide_bot was used to perform guide optimizations for the majority of the proposed ESS instrumentation suite for a range of moderators heights. The decision on the final moderator height of the ESS was taken partly on the basis of the provided data.

A separate contribution is made to McStas in the form of a set of components named the "Union components". These takes a new approach to the use of the McStas component structure, and have the main goal of allowing all beampaths in complicated geometries composed of multiple materials. Instead of single sample components describing both the geometry and all physics, the Union components describe materials and geometry separately. Materials are defined using an absorption description and a number of physical processes such as incoherent scattering, powder scattering and single crystal scattering. When placing geometries in the simulation, such a material definition is used to describe the physics of that geometry. As the geometries are allowed to overlap, complicated shapes can be created using large numbers of geometries. One can for example create a sample of the relevant material, kept in place by a aluminium sample holder, inside an intricate sample environment, and have multiple scattering between all these simulated. With this addition to McStas, not only the intended beampath can be investigated, but also background from unintended beampaths, providing a much richer instrument background. The Union components are demonstrated by simulating the triple axis spectrometer MACS and the time of flight powder spectrometer MARI. Simulations recreating elastic parts of recent experiments on both instruments are compared to the measured data.

Chapter 2

Theory

This chapter introduces the field of neutron scattering through basic scattering theory and a description of the experimental technique. In addition, the Monte Carlo ray-tracing package McStas is introduced because it is widely used for the design of neutron scattering instrumentation and plays a central role in the thesis.

2.1 Neutron scattering

This section outlines basic neutron scattering theory, with emphasis on elastic scattering. The contents is inspired by [51] and [52].

2.1.1 Meet the neutron

The neutron is a charge neutral particle with mass $m = 1.675 \cdot 10^{-27}$ kg and spin 1/2. Neutrons used for scattering purposes have a low speed and can be treated classically. The kinetic energy of the neutron, E, is a function of the neutron mass m and speed v,

$$E = \frac{1}{2}mv^2. \tag{2.1.1}$$

As a massive particle, the neutron can be ascribed a de-Broglie wavelength λ,

$$\lambda = \frac{h}{mv}. \tag{2.1.2}$$

The wavevector of a neutron has the same direction as the velocity, with the magnitude,

$$k = \frac{2\pi}{\lambda}. \tag{2.1.3}$$

The energy of a neutron can be calculated from the wavevector or wavelength,

$$E = \frac{\hbar^2 k^2}{2m} = \frac{h^2}{2m\lambda}. \tag{2.1.4}$$

2.1.2 Cross section

A beam of neutrons can be described by the flux Ψ, which is the number of neutrons passing through a unit area A per second.

Letting a beam with flux Ψ hit a sample will scatter some fraction of the beam depending on the scattering strength of the sample. The number of scattered neutrons can be described with a quantity known as the cross section,

$$\sigma = \frac{\text{neutrons scattered per second}}{\Psi}. \tag{2.1.5}$$

By only counting neutrons emitted in a certain solid angle, the differential cross section can be measured,

$$\frac{\mathrm{d}\sigma}{\mathrm{d}\Omega} = \frac{\text{neutron scattered into solid angle } \mathrm{d}\Omega \text{ per second}}{\Psi \mathrm{d}\Omega}. \tag{2.1.6}$$

Measuring the neutrons scattered into a small final energy range yields the partial differential scattering cross section,

$$\frac{\mathrm{d}^2\sigma}{\mathrm{d}\Omega \mathrm{d}E_f} = \frac{\text{neutrons scattered into solid angle } \mathrm{d}\Omega \text{ with energy between } E_f \text{ and } E_f + \mathrm{d}E_f}{\Psi \mathrm{d}\Omega \mathrm{d}E_f}. \tag{2.1.7}$$

When a beam interacts with a physical system, some neutrons are absorbed by nuclei in the sample, which can be described by the absorption cross section,

$$\sigma_{abs} = \frac{\text{neutrons absorbed per second}}{\Psi}. \tag{2.1.8}$$

For most nuclei, the wavelength dependence of the absorption cross section is inversely proportional to the speed. The absorption cross section is often given for a reference speed, from which the cross section for a desired speed can be calculated,

$$\sigma_{abs} = \sigma_{abs\,th}\frac{v_0}{v} = \sigma_{abs\,th}\frac{\lambda}{\lambda_0}. \tag{2.1.9}$$

Consider a system consisting of a single fixed nucleus at the origin of the coordinate system illuminated by a neutron beam. The beam before interaction with the nuclei can be described by a plane wave,

$$\psi_i = e^{ikz}. \tag{2.1.10}$$

The neutron scatters from the nucleus itself through the strong force, the scatterer is therefore much smaller than the wavelength of the neutrons scattering from it. Hence the resulting scattering can be described by a spherical wave and can be written in terms of the distance from the nucleus r,

$$\psi_s = -\frac{b}{r}e^{-ikr}. \tag{2.1.11}$$

A nuclei dependent constant b named the scattering length is introduced. The overall sign in (2.1.11) is arbitrary, but chosen so that most scattering lengths are positive. The scattering length can be a complex quantity, where the complex part describes absorption partially in the form of resonance phenomena where drastic changes in the absorption cross section occurs when the total system energy is close to an excited nuclei state. Here the discussion is limited to systems with real scattering lengths.

The number of neutrons passing through an area $\mathrm{d}\mathbf{S}$ a distance r from the nuclei can be calculated,

$$v\mathrm{d}\mathbf{S}|\psi_s|^2 = v\mathrm{d}\mathbf{S}\frac{b^2}{r^2} = vb^2\mathrm{d}\Omega. \tag{2.1.12}$$

The initial beam corresponds to a flux of $\Psi = v|\psi_i|^2 = v$, therefore the differential cross section can be written,

$$\frac{\mathrm{d}\sigma}{\mathrm{d}\Omega} = \frac{vb^2\mathrm{d}\Omega}{\Psi\mathrm{d}\Omega} = b^2. \tag{2.1.13}$$

Integrating over all directions yields,

$$\sigma = 4\pi b^2. \tag{2.1.14}$$

Scattering from a single nuclei thus produces homogeneous scattering proportional to the scattering length squared.

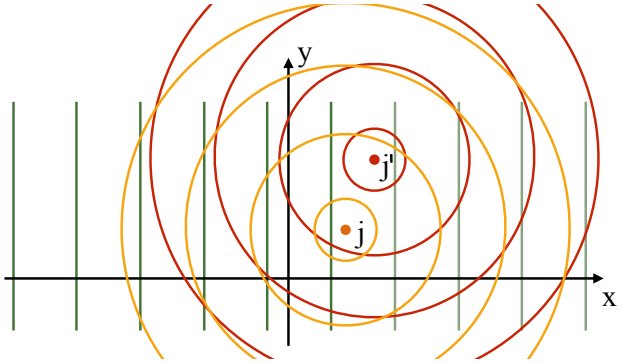

Figure 2.1: Illustration of the two nuclei system illuminated by a wave with incoming wavevector.

2.1.3 Scattering from a system of fixed nuclei

Here the scattering from two fixed nuclei labelled j and j' is calculated. The system is illustrated in figure 2.1. Their positions are denoted $\mathbf{r}_j$ and $\mathbf{r}_{j'}$, and they have scattering lengths b_j and $b_{j'}$. The scattered wave is now a sum of two spherical waves each emitted from one of the nuclei with a phase determined by the incoming beam,

$$\psi_s(\mathbf{r}) = -\left(\frac{b_j\psi_i(\mathbf{r}_j)}{|\mathbf{r}-\mathbf{r}_j|}e^{ik_f|\mathbf{r}-\mathbf{r}_j|} + \frac{b_{j'}\psi_i(\mathbf{r}_{j'})}{|\mathbf{r}-\mathbf{r}_{j'}|}e^{ik_f|\mathbf{r}-\mathbf{r}_{j'}|}\right), \tag{2.1.15}$$

where Y is a necessary normalization constant. Since the nuclei are much closer than the position where the neutron is to be measured, $|\mathbf{r}_j - \mathbf{r}_{j'}| \ll r$, origo can be placed close to the nuclei and we approximate both denominators to r. The expression for the scattered wave can be rewritten,

$$\psi_s(\mathbf{r}) = -\frac{1}{\sqrt{Y}}\frac{1}{r}\left(b_j e^{i\mathbf{k}_i\cdot\mathbf{r}_j}e^{ik_f|\mathbf{r}-\mathbf{r}_j|} + b_{j'}e^{i\mathbf{k}_i\cdot\mathbf{r}_{j'}}e^{ik_f|\mathbf{r}-\mathbf{r}_{j'}|}.\right) \tag{2.1.16}$$

The distance from nuclei to detector is rewritten using the parallel and perpendicular components of $\mathbf{r}_j$,

$$|\mathbf{r}-\mathbf{r}_j| = |\mathbf{r}-\mathbf{r}_{j,\parallel}-\mathbf{r}_{j,\perp}| = \sqrt{|\mathbf{r}-\mathbf{r}_{j,\parallel}|^2 + |\mathbf{r}_{j,\perp}|^2} \tag{2.1.17}$$

With origo close to the nuclei, the perpendicular distance is much smaller than the parallel, and the last term can be neglected, and thus, $|\mathbf{r}-\mathbf{r}_j| \approx |\mathbf{r}-\mathbf{r}_{j,\parallel}|$. With this result, $k_f|\mathbf{r}-\mathbf{r}_j|$ can be written $\mathbf{k}_f\cdot(\mathbf{r}-\mathbf{r}_{j,\parallel})$. Since $\mathbf{k}_f\cdot\mathbf{r}_{j,\perp} = 0$, it can be added, therefore $\mathbf{k}_f\cdot(\mathbf{r}-\mathbf{r}_{j,\parallel}) = \mathbf{k}_f\cdot(\mathbf{r}-\mathbf{r}_j)$. The approximation is, $k_f|\mathbf{r}-\mathbf{r}_j| \approx \mathbf{k}_f\cdot(\mathbf{r}-\mathbf{r}_j)$, and the expression for the final wave can be rewritten,

$$\psi_s(\mathbf{r}) = -\frac{1}{\sqrt{Y}}\frac{1}{r}\left(b_j e^{i\mathbf{k}_i\cdot\mathbf{r}_j}e^{i\mathbf{k}_f\cdot(\mathbf{r}-\mathbf{r}_j)} + b_{j'}e^{i\mathbf{k}_i\cdot\mathbf{r}_{j'}}e^{i\mathbf{k}_f\cdot(\mathbf{r}-\mathbf{r}_{j'})}\right) \tag{2.1.18}$$

$$= -\frac{1}{\sqrt{Y}}\frac{1}{r}\left(b_j e^{i\mathbf{k}_i\cdot\mathbf{r}_j}e^{i\mathbf{k}_f\cdot\mathbf{r}}e^{-i\mathbf{k}_f\cdot\mathbf{r}_j} + b_{j'}e^{i\mathbf{k}_i\cdot\mathbf{r}_{j'}}e^{i\mathbf{k}_f\cdot\mathbf{r}}e^{-i\mathbf{k}_f\cdot\mathbf{r}_{j'}}\right) \tag{2.1.19}$$

$$= -\frac{1}{\sqrt{Y}}\frac{1}{r}\left(b_j e^{i\mathbf{k}_i\cdot\mathbf{r}_j}e^{-i\mathbf{k}_f\cdot\mathbf{r}_j} + b_{j'}e^{i\mathbf{k}_i\cdot\mathbf{r}_{j'}}e^{-i\mathbf{k}_f\cdot\mathbf{r}_{j'}}\right)e^{i\mathbf{k}_f\cdot\mathbf{r}} \tag{2.1.20}$$

$$= -\frac{1}{\sqrt{Y}}\frac{1}{r}\left(b_j e^{i(\mathbf{k}_i-\mathbf{k}_f)\cdot\mathbf{r}_j} + b_{j'}e^{i(\mathbf{k}_i-\mathbf{k}_f)\cdot\mathbf{r}_{j'}}\right)e^{i\mathbf{k}_f\cdot\mathbf{r}}. \tag{2.1.21}$$

Using this expression, the number of neutrons expected in an area $\mathrm{d}\mathbf{S}$ can be calculated,

$$v\mathrm{d}\mathbf{S}|\psi_s|^2 = \frac{1}{Y}v|b_j e^{i(\mathbf{k}_i-\mathbf{k}_f)\cdot\mathbf{r}_j} + b_{j'}e^{i(\mathbf{k}_i-\mathbf{k}_f)\cdot\mathbf{r}_{j'}}|^2\frac{\mathrm{d}\mathbf{S}}{r^2} \tag{2.1.22}$$

$$= \frac{1}{Y}v|b_j e^{i\mathbf{q}\cdot\mathbf{r}_j} + b_{j'}e^{i\mathbf{q}\cdot\mathbf{r}_{j'}}|^2\mathrm{d}\Omega. \tag{2.1.23}$$

The scattering vector $\mathbf{q} = \mathbf{k}_i - \mathbf{k}_f$ is introduced for convenience. The differential cross section can now be calculated,

$$\frac{\mathrm{d}\sigma}{\mathrm{d}\Omega} = \frac{1}{Y} v |b_j e^{i\mathbf{q}\cdot\mathbf{r}_j} + b_{j'} e^{i\mathbf{q}\cdot\mathbf{r}_{j'}}|^2 \frac{\mathrm{d}\Omega}{\Psi \mathrm{d}\Omega} = |b_j e^{i\mathbf{q}\cdot\mathbf{r}_j} + b_{j'} e^{i\mathbf{q}\cdot\mathbf{r}_{j'}}|^2. \tag{2.1.24}$$

If the two scattering lengths are equal, $b_j = b_{j'}$, the expression can be reduced to,

$$\frac{\mathrm{d}\sigma}{\mathrm{d}\Omega} = b^2 |e^{i\mathbf{q}\cdot\mathbf{r}_j} + e^{i\mathbf{q}\cdot\mathbf{r}_{j'}}|^2 = 2b^2 \left(1 + \cos[\mathbf{q}\cdot(\mathbf{r}_j - \mathbf{r}_{j'})]\right). \tag{2.1.25}$$

This expression demonstrates the interference effects arising from the spherical waves originating from the two nuclei. There are scattering vectors with no expected scattering and scattering vectors that result in greater intensity than the two-atoms individually. Given the importance of the scattering vector $\mathbf{q}$ it is considered how it relates to the experimental setting. In the case of elastic scattering, $k_i = k_f = k$, the magnitude of the scattering vector is,

$$q = 2k \sin(\theta), \tag{2.1.26}$$

where 2θ is known as the scattering angle, shown in figure 2.2. A hypothetical sample consisting of two fixed nuclei can be investigated with elastic scattering by measuring the intensity as a function of θ, or by rotating the sample. The result from the two-nuclei sample

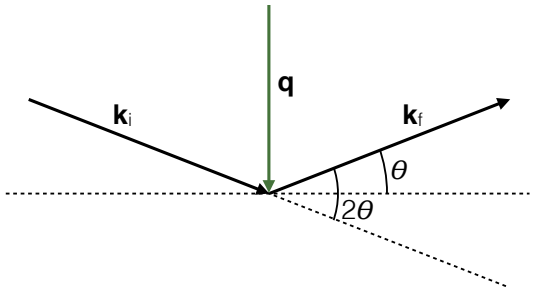

Figure 2.2: Elastic scattering with a scattering angle of 2θ and resulting scattering vector $\mathbf{q}$.

can be generalized to an arbitrary number of fixed nuclei,

$$\frac{\mathrm{d}\sigma}{\mathrm{d}\Omega} = \left| \sum_j b_j e^{i\mathbf{q}\cdot\mathbf{r}_j} \right|^2. \tag{2.1.27}$$

2.1.4 Generalization to macroscopic systems

The cross section is often given per atom, and hence not directly applicable for macroscopic systems. The inverse penetration distance μ is defined for a system with a N atoms per volume V or number density $n = N/V$,

$$\mu = \frac{N\sigma}{V} = n\sigma. \tag{2.1.28}$$

For a material with a number of different elements with a number density n_i and inverse penetration depth μ_i, the total inverse penetration depth is,

$$\mu = \sum_i n_i \sigma_i. \tag{2.1.29}$$

As with the cross section, the inverse penetration depth is also separated into scattering and absorption $\mu_{tot} = \mu_{abs} + \mu_{scat.}$. Since the probability for scattering per length is constant, the beam attenuation can be written,

$$I/I_0 = e^{-\mu z}, \tag{2.1.30}$$

where I_0 is the initial beam intensity and I is the intensity after a distance of z.

2.1.5 Scattering cross section contributions

When generalizing to larger systems, it is important to consider the variation in the scattering length of the scatterers. The scattering length depend on the isotope and nuclear spin direction, and is as a consequence almost never constant throughout a system. Consider the distribution of scattering lengths for a system large enough to be described as an ensemble average. In this case the scattering length of an individual scatterer j can be written in terms of the average scattering length $\langle b_j \rangle$ and the local deviation δb_j,

$$b_j = \langle b_j \rangle + \delta b_j. \tag{2.1.31}$$

The average of the local deviation is zero, $\langle \delta b_j \rangle = 0$, and it is assumed that there is no correlation between sites, $\langle \delta b_j \delta b_{j'} \rangle = 0$. These assumptions are applied to the two-atom system,

$$\left\langle \frac{\mathrm{d}\sigma}{\mathrm{d}\Omega} \right\rangle = \left\langle |b_j e^{i\mathbf{q}\cdot\mathbf{r}_j} + b_{j'} e^{i\mathbf{q}\cdot\mathbf{r}_{j'}}|^2 \right\rangle \tag{2.1.32}$$

$$= \left\langle b_j^2 + b_j e^{i\mathbf{q}\cdot\mathbf{r}_j} b_{j'} e^{-i\mathbf{q}\cdot\mathbf{r}_{j'}} + b_{j'} e^{i\mathbf{q}\cdot\mathbf{r}_{j'}} b_j e^{-i\mathbf{q}\cdot\mathbf{r}_j} + b_{j'}^2 \right\rangle \tag{2.1.33}$$

$$= \left\langle b_j^2 \right\rangle + \left\langle b_j b_{j'} \right\rangle e^{i\mathbf{q}\cdot\mathbf{r}_j} e^{-i\mathbf{q}\cdot\mathbf{r}_{j'}} + \left\langle b_{j'} b_j \right\rangle e^{i\mathbf{q}\cdot\mathbf{r}_{j'}} e^{-i\mathbf{q}\cdot\mathbf{r}_j} + \left\langle b_{j'}^2 \right\rangle. \tag{2.1.34}$$

Here all terms squaring the same index get the form, $\langle b_j^2 \rangle = \langle b_j \rangle^2 + \langle \delta b_j^2 \rangle$ while cross terms yields, $\langle b_j b_{j'} \rangle = \langle b_j \rangle \langle b_{j'} \rangle$. Using this one obtains,

$$\left\langle \frac{\mathrm{d}\sigma}{\mathrm{d}\Omega} \right\rangle = \left\langle b_j \right\rangle^2 + \langle \delta b_j^2 \rangle + \left\langle b_j \right\rangle \left\langle b_{j'} \right\rangle e^{i\mathbf{q}\cdot\mathbf{r}_j} e^{-i\mathbf{q}\cdot\mathbf{r}_{j'}} + \left\langle b_{j'} \right\rangle \left\langle b_j \right\rangle e^{i\mathbf{q}\cdot\mathbf{r}_{j'}} e^{-i\mathbf{q}\cdot\mathbf{r}_j} + \left\langle b_{j'} \right\rangle^2 + \langle \delta b_{j'}^2 \rangle \tag{2.1.35}$$

$$= \langle \delta b_j^2 \rangle + \langle \delta b_{j'}^2 \rangle + \left\langle b_j \right\rangle^2 + \left\langle b_{j'} \right\rangle^2 + \left\langle b_j \right\rangle \left\langle b_{j'} \right\rangle e^{i\mathbf{q}\cdot\mathbf{r}_j} e^{-i\mathbf{q}\cdot\mathbf{r}_{j'}} + \left\langle b_{j'} \right\rangle \left\langle b_j \right\rangle e^{i\mathbf{q}\cdot\mathbf{r}_{j'}} e^{-i\mathbf{q}\cdot\mathbf{r}_j} \tag{2.1.36}$$

$$= \langle \delta b_j^2 \rangle + \langle \delta b_{j'}^2 \rangle + \left| \langle b_j \rangle e^{i\mathbf{q}\cdot\mathbf{r}_j} + \langle b_{j'} \rangle e^{i\mathbf{q}\cdot\mathbf{r}_{j'}} \right|^2. \tag{2.1.37}$$

It is evident that the average over local deviations from the average scattering length gives rise to constant scattering terms. Since these do not contain any $\mathbf{q}$ dependence, they correspond to scattering in all directions. The total cross section $\sigma = 4\pi b^2$ is divided into two parts, the coherent $\sigma_{coh} = 4\pi \langle b \rangle^2$ and the incoherent $\sigma_{inc} = 4\pi \langle (\delta b)^2 \rangle$. With this definition the differential cross section can be written,

$$\left\langle \frac{\mathrm{d}\sigma}{\mathrm{d}\Omega} \right\rangle = \frac{\sigma_{inc,j}}{4\pi} + \frac{\sigma_{inc,j'}}{4\pi} + \left| \langle b_j \rangle e^{i\mathbf{q}\cdot\mathbf{r}_j} + \langle b_{j'} \rangle e^{i\mathbf{q}\cdot\mathbf{r}_{j'}} \right|^2. \tag{2.1.38}$$

The quantity $\langle b \rangle$ that controls the interference part of the differential cross section is named the coherent scattering length. The expression can be generalized to a general number of nuclei,

$$\left\langle \frac{\mathrm{d}\sigma}{\mathrm{d}\Omega} \right\rangle = \sum_j \frac{\sigma_{inc,j}}{4\pi} + \left| \langle b_j \rangle e^{i\mathbf{q}\cdot\mathbf{r}_j} \right|^2. \tag{2.1.39}$$

2.1.6 Scattering from crystals

Describing scattering from single crystals requires a description of the positions of atoms in a repeating lattice. Such a structure can be built by repeating unit cells and their positions $\mathbf{r}$ can be described by,

$$\mathbf{r} = n_a \mathbf{a} + n_b \mathbf{b} + n_c \mathbf{c}. \tag{2.1.40}$$

Here $\mathbf{a}, \mathbf{b}, \mathbf{c}$ are lattice vectors describing the sides of the unit cell, and n_a, n_b, n_c are integers. The lattice vectors are selected to be right handed, so the volume of the unit cell can be calculated,

$$V_0 = \mathbf{a} \cdot \mathbf{b} \times \mathbf{c}. \tag{2.1.41}$$

The result describing scattering from an arbitrary number of fixed nuclei,

$$\frac{\mathrm{d}\sigma}{\mathrm{d}\Omega} = \left| \sum_j b_j e^{i\mathbf{q}\cdot\mathbf{r}_j} \right|^2, \tag{2.1.42}$$

is considered for an infinite lattice. In order for the exponential to give a finite result, the phase needs to be a multiple of 2π, which motivates the definition of the reciprocal unit cell $\mathbf{a}^*, \mathbf{b}^*, \mathbf{c}^*$ that satisfies,

$$\mathbf{a}^* \cdot \mathbf{b} = \mathbf{a}^* \cdot \mathbf{c} = 0, \quad \mathbf{b}^* \cdot \mathbf{a} = \mathbf{b}^* \cdot \mathbf{c} = 0, \quad \mathbf{c}^* \cdot \mathbf{a} = \mathbf{c}^* \cdot \mathbf{b} = 0, \tag{2.1.43}$$

$$\mathbf{a}^* \cdot \mathbf{a} = 2\pi, \quad \mathbf{b}^* \cdot \mathbf{b} = 2\pi, \quad \mathbf{c}^* \cdot \mathbf{c} = 2\pi. \tag{2.1.44}$$

With this construction, only points in reciprocal space that satisfy,

$$\boldsymbol{\tau}_{hkl} = h\mathbf{a}^* + k\mathbf{b}^* + l\mathbf{c}^*, \tag{2.1.45}$$

for integers h, k, l, will contribute to the differential cross section. All other points will not contribute as the phases will vary over the whole unit circle for large enough systems. The integers h, k, l are named Miller indices. Such reciprocal lattice vectors can be constructed with the form,

$$\mathbf{a}^* = \frac{2\pi}{V_0}\mathbf{b} \times \mathbf{c}, \quad \mathbf{b}^* = \frac{2\pi}{V_0}\mathbf{c} \times \mathbf{a}, \quad \mathbf{c}^* = \frac{2\pi}{V_0}\mathbf{a} \times \mathbf{b}. \tag{2.1.46}$$

The condition for scattering is therefore that the scattering vector is equal to the reciprocal lattice vector, $\mathbf{q} = \boldsymbol{\tau}$, called the Laue condition. The scattering condition can be written,

$$|\boldsymbol{\tau}| = 2k\sin(\theta) = \frac{4\pi\sin(\theta)}{\lambda}. \tag{2.1.47}$$

The possible final wavevectors for a given crystal orientation and initial wavevector can be found by setting up an Ewalds sphere as depicted in figure 2.3.

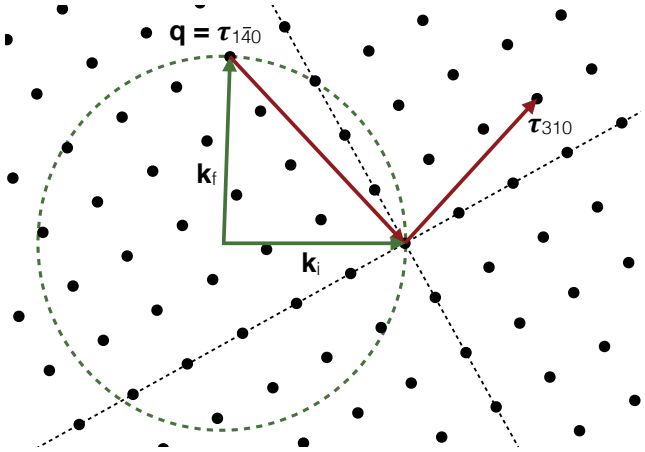

Figure 2.3: Illustration of initial and final wavevector both confined to a plane and k_i ending in origo. The reciprocal lattice is shown, and all reciprocal lattice points on the surface of the included Ewalds sphere satisfy the scattering condition, while all others do not.

The lattice spacing corresponding to a given set of Miller indices can be calculated [51],

$$d_{hkl} = \frac{2\pi}{|\boldsymbol{\tau}_{hkl}|}, \tag{2.1.48}$$

which combined with equation (2.1.47) yields the well known Bragg scattering condition,

$$\lambda = 2d_{hkl}\sin(\theta). \tag{2.1.49}$$

The more common equation, $n\lambda = 2d\sin(\theta)$, has the order n explicit, yet here the orders are described by different sets of Miller indices.

2.1.7 Debye Waller

In physical crystals the nuclei are not fixed, they have some thermal motion. A full quantum mechanical description of this yields the interaction between neutrons and lattice vibrations named phonons. Here a classical approach is used to show the more basic consequences of thermal motion on elastic scattering.

The position of each nucleus $\mathbf{R}_j(t)$ is described by a fixed position in the lattice $\mathbf{r}_j$, and the time dependent deviation from this position $\mathbf{u}_j(t)$,

$$\mathbf{R}_j(t) = \mathbf{r}_j + \mathbf{u}_j(t). \tag{2.1.50}$$

The fixed position $\mathbf{r}_j$ in equation (2.1.27) is substituted with the free position $\mathbf{R}_j(t)$,

$$\frac{\mathrm{d}\sigma}{\mathrm{d}\Omega} = \left\langle \left| \sum_j b_j e^{i\mathbf{q}\cdot\mathbf{R}_j(t)} \right|^2 \right\rangle, \tag{2.1.51}$$

where the time average is taken on the right side as the cross section is measured over a time scale much larger than that of thermal atom movement. Evaluating this expression yields,

$$\frac{\mathrm{d}\sigma}{\mathrm{d}\Omega} = \left\langle \left| \sum_j b_j e^{i\mathbf{q}\cdot\mathbf{R}_j(t)} \right|^2 \right\rangle = \left\langle \sum_{jj'} b_j b_{j'} e^{i\mathbf{q}\cdot\mathbf{R}_j(t)} e^{-i\mathbf{q}\cdot\mathbf{R}_{j'}(t)} \right\rangle \tag{2.1.52}$$

$$= \sum_{jj'} b_j b_{j'} e^{i\mathbf{q}\cdot\mathbf{r}_j} e^{-i\mathbf{q}\cdot\mathbf{r}_{j'}} \left\langle e^{i\mathbf{q}\cdot\mathbf{u}_j(t)} e^{-i\mathbf{q}\cdot\mathbf{u}_{j'}(t)} \right\rangle. \tag{2.1.53}$$

The contribution from the thermal movement of the nuclei results in a random phase. It was previously identified that Bragg peaks occur because all contributions are in phase, hence this random deviation will smear the Bragg peaks and reduce their intensity. The random phase contribution is Taylor expanded to second order,

$$\left\langle e^{i\mathbf{q}\cdot\mathbf{u}_j(t)} e^{-i\mathbf{q}\cdot\mathbf{u}_{j'}(t)} \right\rangle \approx \left\langle \left(1 - i\mathbf{q}\cdot\mathbf{u}_j(t) - (\mathbf{q}\cdot\mathbf{u}_j(t))^2/2\right) \left(1 + i\mathbf{q}\cdot\mathbf{u}_{j'}(t) - (\mathbf{q}\cdot\mathbf{u}_{j'}(t))^2/2\right) \right\rangle. \tag{2.1.54}$$

It is assumed that there is no correlation between the thermal motions of atoms, so the cross terms can be assumed not to contribute, $\langle \mathbf{u}_j(t)\mathbf{u}_{j'}(t)\rangle = 0$. In addition it is assumed that the amplitudes are isotropic and equal so that $\langle \mathbf{u}_j(t)^2\rangle = \langle \mathbf{u}_{j'}(t)^2\rangle$. With these assumptions, the previous expression can be reduced to,

$$\left\langle e^{i\mathbf{q}\cdot\mathbf{u}_j(t)} e^{-i\mathbf{q}\cdot\mathbf{u}_{j'}(t)} \right\rangle \approx \left\langle 1 - (\mathbf{q}\cdot\mathbf{u})^2 \right\rangle \approx e^{\langle -(\mathbf{q}\cdot\mathbf{u})^2 \rangle}. \tag{2.1.55}$$

This correction term is named the Debye-Waller factor and often written as, e^{-2W}. The expression for scattering from a system of nuclei with limited thermal motion can be written,

$$\frac{\mathrm{d}\sigma}{\mathrm{d}\Omega} = e^{-2W} \left| \sum_j b_j e^{i\mathbf{q}\cdot\mathbf{r}_j} \right|^2. \tag{2.1.56}$$

For q close to zero, the Debye-Waller factor is close to one, and in this case not an important consideration, but for large q the term approaches zero and reduces the scattering from the system.

2.1.8 The form factor

When describing all but the simplest of crystals the concept of a unit cell is necessary. The crystal lattice can be built from repeating unit cells, where each unit cell have a small number of atoms. The position of a nuclei in the crystal lattice can then be described as

a sum of the position of the lattice, $\mathbf{r}_j$, and the position of the nuclei within the unit cell, $\mathbf{\Delta}_i$. With this terminology, the differential cross section for coherent scattering from a single crystal is,

$$\frac{\mathrm{d}\sigma}{\mathrm{d}\Omega} = e^{-2W}\left|\sum_{ij} b_i e^{i\mathbf{q}\cdot(\mathbf{r}_j+\mathbf{\Delta}_i)}\right|^2 = e^{-2W}\left|\sum_i b_i e^{i\mathbf{q}\cdot\mathbf{\Delta}_i}\right|^2\left|\sum_j e^{i\mathbf{q}\cdot\mathbf{r}_j}\right|^2. \tag{2.1.57}$$

The sum only concerned with the unit cell is named the nuclear form factor $F_N(\mathbf{q})$,

$$\frac{\mathrm{d}\sigma}{\mathrm{d}\Omega} = e^{-2W}\left|F_N(\mathbf{q})\right|^2\left|\sum_j e^{i\mathbf{q}\cdot\mathbf{r}_j}\right|^2. \tag{2.1.58}$$

The scattering signal is as a result contingent on both the Bragg condition being fulfilled and the form factor being non-zero.

The lattice sum can be evaluated [51], and one obtains,

$$\frac{\mathrm{d}\sigma}{\mathrm{d}\Omega} = N\frac{(2\pi)^3}{V_0}e^{-2W}|F_N(\mathbf{q})|^2\sum_{\boldsymbol{\tau}}\delta(\mathbf{q}-\boldsymbol{\tau}), \tag{2.1.59}$$

where N is the number of unit cells. As expected, the total cross section is proportional to the number of scatterers, and scattering only occurs when a lattice vector is equal to the scattering vector.

2.1.9 Cross section from a single Bragg peak

The total cross section from a single Bragg peak can be obtained by integrating the differential cross section,

$$\sigma_{\boldsymbol{\tau}} = \int\left(\frac{\mathrm{d}\sigma}{\mathrm{d}\Omega}\right)_{\boldsymbol{\tau}}\mathrm{d}\Omega. \tag{2.1.60}$$

The initial wavevector $\mathbf{k}_i$ is assumed constant and as a single Bragg peak is investigated, the reciprocal lattice vector $\boldsymbol{\tau}$ is constant as well. The integral is over the remaining variable, final wavevector $\mathbf{k}_f$. The integral over the delta function in 2.1.59 is considered,

$$\int\delta(\mathbf{q}-\boldsymbol{\tau})\mathrm{d}\Omega. \tag{2.1.61}$$

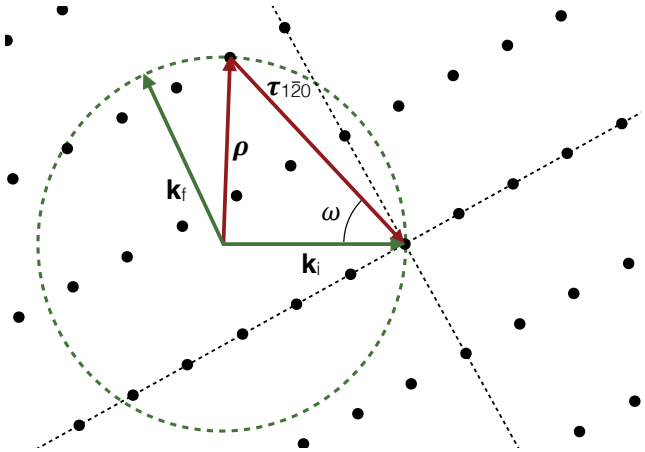

Figure 2.4: Definition of $\boldsymbol{\rho} = \mathbf{k}_i - \boldsymbol{\tau}$ and the angle ω between $\mathbf{k}_i$ and $\boldsymbol{\tau}$ in scattering plane.

It is convenient to transform the contents of the delta function so that the integrated variable is explicit, this is achieved by introducing $\boldsymbol{\rho} = \mathbf{k}_i - \boldsymbol{\tau}$ as shown in figure 2.4. The delta function will be non-zero when $\rho = k_f$, which is used to rewrite the integral,

$$\int \delta(\mathbf{q} - \boldsymbol{\tau})\mathrm{d}\Omega = \int \delta(\boldsymbol{\rho} - \mathbf{k}_f)\mathrm{d}\Omega = c\delta(\rho^2 - k_f^2). \tag{2.1.62}$$

For the last step it was chosen to square both terms, which is allowed because the difference is still zero only when they are equal, yet the following calculations are simplified considerably. The introduced constant, c, is found by performing the integral over $\mathbf{k}_f$ in spherical coordinates,

$$1 = \int \delta(\boldsymbol{\rho} - \mathbf{k}_f)\mathrm{d}\mathbf{k}_f = \int \left(\int \delta(\boldsymbol{\rho} - \mathbf{k}_f)\mathrm{d}\Omega \right) k_f^2 \mathrm{d}k_f = \int c\delta(\rho^2 - k_f^2)k_f^2 \mathrm{d}k_f. \tag{2.1.63}$$

This integral is solved using substitution of variables, $u = k_f^2$ is introduced and hence, $\mathrm{d}u = 2k_f \mathrm{d}k_f$,

$$1 = \int c\delta(\rho^2 - k_f^2)k_f^2 \mathrm{d}k_f = \frac{c}{2}\int \delta(\rho^2 - u)\frac{u}{k_f}\mathrm{d}u = \frac{c}{2}\int \delta(\rho^2 - k_f^2)k_f \mathrm{d}k_f^2 \tag{2.1.64}$$

$$= \frac{c}{2}\int \delta(\rho - k_f)k_f \mathrm{d}k_f^2 = \frac{c\rho}{2}. \tag{2.1.65}$$

Accordingly $c = 2/\rho = 2/k_i$, and the considered integral can be written,

$$\int \delta(\mathbf{q} - \boldsymbol{\tau})\mathrm{d}\Omega = \frac{2}{\rho}\delta(\rho^2 - k_f^2) = \frac{2}{\rho}\delta(\rho^2 - k_i^2) = \frac{2}{\rho}\delta(\tau^2 - 2k_i\tau\cos(\omega)). \tag{2.1.66}$$

The elastic scattering condition of $k_i = k_f$ was used. Therefore the cross section for a single Bragg peak integrated over possible final wavevectors is,

$$\sigma_{\boldsymbol{\tau}} = N\frac{(2\pi)^3}{V_0}\frac{2}{k_i}e^{-2W}|F_N(\boldsymbol{\tau})|^2\delta(\tau^2 - 2k_i\tau\cos(\omega)). \tag{2.1.67}$$

In the case of a single crystal in a monochromatic beam of flux Ψ, the scattering power is found by integrating the crystal orientation over the so called rocking curve. This corresponds to an integral over ω defined in figure 2.4 close to the angle corresponding to $\mathbf{q} = \boldsymbol{\tau}$,

$$P \equiv \Psi \int \sigma_\tau \mathrm{d}\omega = \Psi N\frac{2(2\pi)^3}{V_0}e^{-2W}|F_N(\boldsymbol{\tau})|^2 \int \frac{1}{k_i}\delta(\tau^2 - 2k_i\tau\cos(\omega))\mathrm{d}\omega \tag{2.1.68}$$

$$= \Psi N\frac{(2\pi)^3}{V_0}e^{-2W}|F_N(\boldsymbol{\tau})|^2\frac{1}{k_i^3\sin(\theta)}. \tag{2.1.69}$$

The integral was solved using substitution, $u = 2k_i\tau\cos(\omega)$, where it was assumed that $\tau = 2k\sin(\theta)$, meaning that the scattering condition was fulfilled. Through measuring a number of Bragg peaks, the relative intensities and known initial wavevectors can be used to determine the form factor, from which the atom positions in the unit cell can be deduced.

2.1.10 Scattering from powder of single crystals

In many cases it is not possible to grow single crystals of sufficient size for neutron scattering experiments, however it may possible to produce a powder consisting of small single crystals. In order to calculate the expected scattering, it is assumed that all crystal orientations are equally probable and that all are represented. The problem is considered in spherical coordinates with the azimuth angle ω between $\mathbf{k}_i$ and $\boldsymbol{\tau}$, and the polar angle denoted ϕ. With all crystal orientations represented and the scattering condition depending only on ω,

the resulting scattering will appear in cones of constant ω. The cross section for such a cone is found by averaging the total cross section for a Bragg peak over all crystal orientations,

$$\sigma_\tau = \frac{1}{4\pi}\int \sigma_\tau \mathrm{d}\Omega = \frac{1}{4\pi}\int \sigma_\tau \mathrm{d}\phi \sin(\omega)\mathrm{d}\omega \tag{2.1.70}$$

$$= N\frac{(2\pi)^3}{V_0}\frac{2}{k_i}e^{-2W}|F_N(\boldsymbol{\tau})|^2\frac{1}{4\pi}\int 2\pi\sin(\omega)\delta(\tau^2 - 2k_i\tau\cos(\omega))\mathrm{d}\omega \tag{2.1.71}$$

$$= Ne^{-2W}\frac{1}{V_0}\frac{\lambda^3}{4\sin(\theta)}\sum_{\boldsymbol{\tau}}|F_N(\boldsymbol{\tau})|^2. \tag{2.1.72}$$

The final sum is over all reciprocal lattice vectors with the same length, as these can not be distinguished. It was assumed that the scattering condition is fulfilled $\tau = 2k_i\sin(\theta)$.

From an experiment on a powder sample it remains possible to obtaining information about the form factor, however, the ambiguity from the inability to distinguishing between lattice vectors with the same magnitude is a drawback. Despite this drawback, powder scattering is a very popular and fast method of obtain sufficient information for refining the form factor and determining the nuclear positions in the unit cell.

2.1.11 Scattering functions $S(\mathbf{q},\omega)$ and $S_i(\mathbf{q},\omega)$

Using a more thorough theoretical approach [52] than chosen here, the scattering from a general system can be described by the thermal average of operators relevant to the system of scatterers. The partial differential coherent scattering cross section for a Bravis lattice can be written in terms of the scattering function $S(\mathbf{q},\omega)$,

$$\left(\frac{\mathrm{d}^2\sigma}{\mathrm{d}\Omega\mathrm{d}E_f}\right)_{coh} = \frac{\sigma_{coh}}{4\pi}\frac{k_f}{k_i}NS(\mathbf{q},\omega). \tag{2.1.73}$$

The scattering function depends on the momentum transfer, energy transfer and the position of the scatterers in the system at all times. It is defined,

$$S(\mathbf{q},\omega)_{coh} = \frac{1}{2\pi\hbar}\int \frac{1}{N}\sum_{jj'}\left\langle e^{-i\mathbf{q}\cdot\mathbf{R}_{j'}(0)}e^{-i\mathbf{q}\cdot\mathbf{R}_j(t)}\right\rangle e^{-i\omega t}\mathrm{d}t. \tag{2.1.74}$$

This can be interpreted as coherent scattering emerging from correlations between different scatterers in the system at different times.

In a similar fashion, incoherent scattering can be described using the incoherent scattering function $S_i(\mathbf{q},\omega)$,

$$\left(\frac{\mathrm{d}^2\sigma}{\mathrm{d}\Omega\mathrm{d}E_f}\right)_{inc} = \frac{\sigma_{inc}}{4\pi}\frac{k_f}{k_i}NS_i(\mathbf{q},\omega). \tag{2.1.75}$$

The incoherent scattering function is similar to the coherent version,

$$S_i(\mathbf{q},\omega)_{inc} = \frac{1}{2\pi\hbar}\int \frac{1}{N}\sum_{j}\left\langle e^{-i\mathbf{q}\cdot\mathbf{R}_j(0)}e^{-i\mathbf{q}\cdot\mathbf{R}_j(t)}\right\rangle e^{-i\omega t}\mathrm{d}t. \tag{2.1.76}$$

The important difference is that incoherent scattering depends on self correlations, the correlation between the position of the same scatterer at different times.

Because the scattering functions depend directly on operators connected to the scattering system, they can be calculated theoretically without knowledge of the experimental technique of neutron scattering. These functions can be utilized as a natural handover point from theorists to experimentalists.

2.1.12 Multiple scattering

The differential cross sections derived for crystal structures assume the system is small and the scattering is measured far away, hence there is an implicit assumption of single scattering. A neutron that fulfils the Bragg condition can have a very high probability to scatter, making more than one scattering event a likely occurrence. However, the distance between the two scattering positions may not be sufficient to allow the far field approximation used here. A single crystal is assumed to be composed of many small single crystal grains, each of which large enough to fulfil the approximations on system size leading to Bragg scattering, yet small enough that only single scattering is likely. A macroscopic single crystal can then have multiple scattering events, each of which follow the theory described. The orientation of the grains can have some small distribution, normally described as a mosaicity.

2.1.13 Reflectivity

The behaviour of a neutron in a medium is similar to that of light, and can be described using the refractive index for the medium n_m,

$$n_m = \frac{\lambda_0}{\lambda_m} = \frac{k_m}{k_0}. \tag{2.1.77}$$

Here λ_0 and k_0 are the wavelength and wavevector in vacuum respectively, while λ_m and k_m are the wavelength and wavevector in the medium respectively.

As with light, Snell's law describes the change of direction for a neutron propagating from one medium to another as shown in figure 2.5,

$$n_1 \cos(\theta_1) = n_2 \cos(\theta_2). \tag{2.1.78}$$

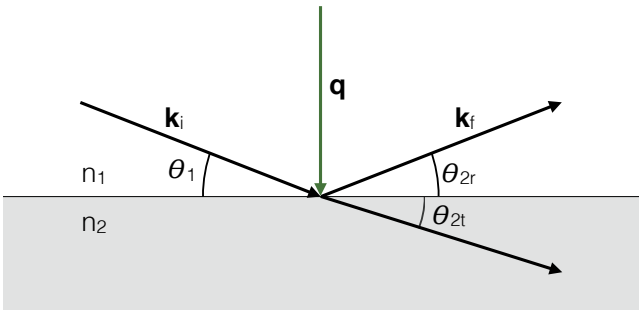

Figure 2.5: Sketch of neutron propagating from one media with refractive index n_1 to a media with refractive index n_2.

The reflected and transmitted waves are described by the reflectivity coefficient r and transmission coefficient t given by Fresnel's equations,

$$r = \frac{n_1 \sin(\theta_1) - n_2 \sin(\theta_2)}{n_1 \sin(\theta_1) + n_2 \sin(\theta_2)} = \frac{k_{1z} - k_{2z}}{k_{1z} + k_{2z}} \tag{2.1.79}$$

$$t = \frac{2n_1 \sin(\theta_1)}{n_1 \sin(\theta_1) + n_2 \sin(\theta_2)} = \frac{2k_{1z}}{k_{1z} + k_{2z}}, \tag{2.1.80}$$

where the z component of the wavevector is denoted $k_{jz} = k_j \sin(\theta_j)$. The measured quantity in a reflectivity experiment is the reflected intensity I_r as a function of q_z, and when compared to the beam intensity I_0, the reflectivity $\mathcal{R}$ can be calculated,

$$\mathcal{R} = \frac{I_r}{I_0} \tag{2.1.81}$$

The reflectivity is related to the reflectivity coefficient through $\mathcal{R} = |r|^2$. In the case of $n_1 > n_2$, Snell's law results in a complex value for θ_2 when $n_2 < n_1 \cos(\theta_1)$. It can be shown that this value inserted into the Fresnel equation for the reflectivity coefficient yields a case where $|r|^2 = \mathcal{R} = 1$. Therefore, the reflected beam intensity is identical to the initial beam intensity and the beam is said to have undergone total reflection. This happens for the critical angle $\cos(\theta_1) = n_2/n_1$ and below.

Nickel is often used in applications where a large critical scattering vector is required, as the vacuum nickel interface has $q_{c\,Ni} = 0.0217$ Å^{-1} [53, chap 3.2-9], which corresponds to approximately $\sim 0.1°\lambda$ with the wavelength measured in Å.

2.1.14 Supermirror

Using stratified layers of material with large contrast between refractive index and varying thickness, it is possible to create a so-called neutron supermirror. Below the critical scattering vector of the substrate material, total reflection occurs as described in 2.1.13, and at scattering vectors in a region between q_c and $mq_{c\,Ni}$, there will be a section of layers with a spacing so that the neutron is scattered. The constant m is named the m-value of the supermirror. The concept is shown in figure 2.6.

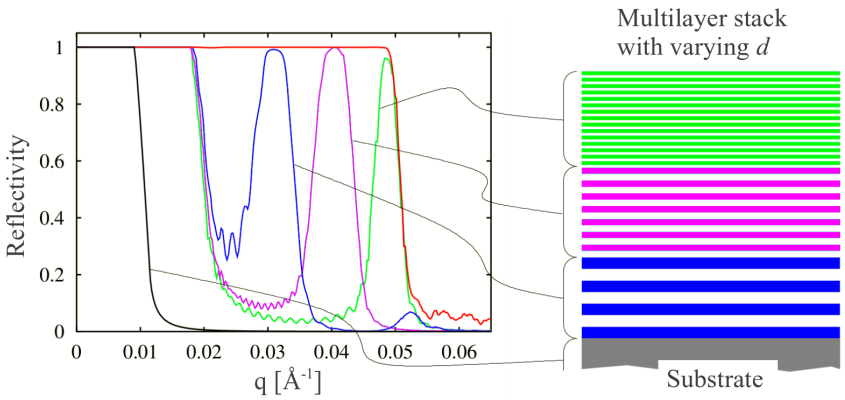

Figure 2.6: Illustration of supermirror with varying layer thickness and associated reflectivity curve. Figure from[54].

The reflectivity for $q_c < q < mq_{c\,Ni}$ is less than unity, partly because of roughness of the layers, but also from absorption due to the length travelled by the neutron before the layers with the appropriate separation are encountered. Reflectivity measurements and common reflectivity models for supermirrors are shown on figure 2.7. Equation (2.1.82) is a simple analytical model of supermirror reflectivity $R(q)$, and includes parametrisation of the slope, α, and cut-off width, W as well as the reflectivity below the critical angle, R_0.

$$R(q) = \begin{cases} R_0 & \text{if } q < q_c \\ R_0(1 - \tanh((q - mq_c)/W))(1 - \alpha(q - q_c))/2 & \text{otherwise} \end{cases} \tag{2.1.82}$$

Using supermirrors, a neutron beam can be channelled through a neutron guide, provided the necessary scattering vectors are within the reflectivity edge of the used supermirrors. A neutron with wavelength λ can be transported through a guide if the angle of incidence θ_i satisfy,

$$q_z = \frac{4\pi}{\lambda} \sin(\theta_i) < mq_{c\,Ni}, \tag{2.1.83}$$

for all reflections. A single neutron may be reflected a large number of times, yet if the reflectivity is close to unity, the probability for transport can still be high. The divergence of a neutron, η, is defined as the angular deviation from the optical axis. In a guide with parallel mirrors, the angle of incidence is equal to the component of the divergence orthogonal

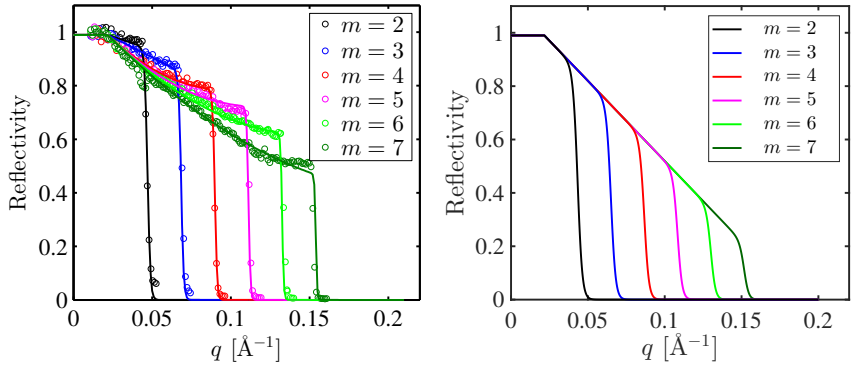

Figure 2.7: (Left) Reflectivity data from supermirror manufacturer Swiss Neutronics and fits to the reflectivity curves depending only on the m-value, from [43]. (Right) Simple reflectivity model described by equation (2.1.82).

to the mirror. The largest divergence expected from a long straight guide, η_s, can then be written,

$$\eta_s = \sin^{-1}\left(\frac{\lambda m q_{c\,Ni}}{4\pi}\right). \tag{2.1.84}$$

Therefore the transport of beams with large divergence and low wavelength requires supermirrors with large m values.

2.1.15 phase-space

When describing the performance of a guide, it is convenient to do so in a phase-space. A phase-space is spanned by a set of independent variables that describe all possible states of a system. For a system of classical point particles the position and velocity is commonly used. With the equations of motion for the system known, the trajectory through phase-space can be calculated for any point in phase-space. Since each point is a full description of the particle state, trajectories for two different initial points can not cross, since the trajectory for the cross point would correspond to two different initial conditions.

In the context of neutron guides a slightly different phase-space is used to describe the neutron beam. Since the velocity can be transformed into the divergence from some axis and the wavelength of the neutron, these are equivalent descriptions of the momentum. If the z axis of the coordinate system is chosen as the beam direction, this can be written, $(v_x, v_y, v_z) \leftrightarrow (\eta_x\eta_y, \lambda)$, where the divergence from the z axis in the x and y direction are denoted η_x and η_y. Since the wavelength of the neutron does not change under reflection in a supermirror, the wavelength is often omitted. The phase-space is relevant at certain points along the z axis, and thus the full phase-space is taken at a specific z value with the remaining dimensions, $(x, y, \eta_x\eta_y, \lambda)$. When describing a beam, v_z is assumed to be positive so that increasing time corresponds to increasing z coordinate.

A neutron beam can be described as a swarm of points in phase-space. Mathematically this is described as a phase-space volume with a boundary. The entire phase-space volume can be propagated as a whole by propagating the boundary, as no points from the inside can have a trajectory that escapes the boundary of the volume.

Here such a phase-space volume describing a beam is denoted with Greek letters as α, while the size of the geometrical volume inside the boundary is denoted $V(\alpha)$. The density of points within a phase-space volume is denoted $\rho(\alpha)$.

An idealized example of the phase-space delivered by a over-illuminated long straight guide is shown on figure 2.8.

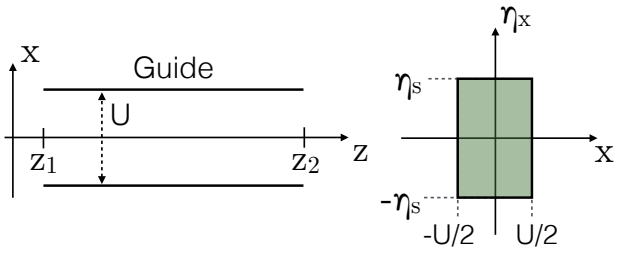

Figure 2.8: Illustration of phase-space volume leaving a guide with parallel mirrors. The phase-space volume shown is at the position denoted z_2, and assumes the phase-space volume that enters the guide at z_1 is larger and homogeneous.

2.1.16 Liouvilles theorem

Liouvilles theorem states that the size of any phase-space volume is constant along its trajectory,

$$\frac{dV(\alpha)}{dt} = 0. \tag{2.1.85}$$

It follows immediately that the phase-space density of a volume can not be increased, as the size can not be decreased and no trajectories can cross the boundary of the phase-space volume. The phase-space density of a volume can however be decreased, for example through reflectivity losses, and thus,

$$\frac{d\rho(\alpha)}{dt} \leq 0. \tag{2.1.86}$$

2.1.17 Brilliance transfer

The brilliance transfer expresses how large a fraction of the phase-space density of a certain phase-space volume is preserved when propagating a neutron beam from one position to another. If we define two phase-space volumes, α and β identical in terms of phase-space dimensions $(x, y, \eta_x, \eta_y, \lambda)$, but place α at the source and β at the sample, then the brilliance transfer is given by,

$$\mathcal{B} = \frac{\rho(\beta)}{\rho(\alpha)}. \tag{2.1.87}$$

The brilliance transfer itself is thus a scalar between zero and one. It is, however, possible to calculate the brilliance as a function of variables that make up the used phase-space, by slicing the relevant phase-space volume into a range of volumes that varies the desired variable. This could for example be done for the wavelength or divergence.

2.2 Experiments

This section provides an overview of how neutron scattering experiments are conducted. The different types of neutron sources are introduced along with the necessary step of neutron moderation. The most successful neutron scattering facilities are mentioned and the upcoming European Spallation Source (ESS) is outlined. An overview of neutron scattering instrumentation is given as well as the most common technical solutions to the various problems faced by experimentalists.

2.2.1 Neutron sources

Producing a beam of neutrons requires nuclear processes, as the neutron is bound in some mother nuclei. Currently, three different nuclear processes are used to produce neutron beams, most common among them is nuclear fission.

Controlled critical fission reaction maintained in a nuclear reactor produces a steady output of high energy neutrons. There are rare cases where super critical fission is being used to create pulsed reactors. Approximately three neutrons are emitted in each nuclear process, and of these one is needed to maintain the chain reaction, and as a result the fission process has limited neutron yield per process. Nuclear fission also generates a large heat load and needs considerable cooling.

Alternatively, several fusion processes produce free neutrons, but these are only used for compact and small-scale sources that do not produce beams of the necessary brightness for neutron scattering purposes.

The last process is called spallation, which is achieved by letting a beam of high energy particles collide with a target consisting of heavy nuclei. The nuclei are excited and undergo nuclear evaporation, releasing a large number of neutrons, depending on the target nuclei and beam energy [1]. The energy deposited to the target per produced neutron is less than for nuclear fission. Spallation sources are commonly pulsed because the process depends on an easily controllable beam, and pulsed neutrons are advantageous as will be shown below.

Regardless of the method of neutron production, the energy of the released neutrons are in the order relevant for nuclear reactions, MeV, that corresponds to a wavelength of the order 10^{-4} Å. The energy of the released neutrons are far greater than excitations in condensed matter at relevant temperatures, and the wavelength is far smaller than the distance between atoms, making scattering experiments impossible. Scattering experiments can be conducted with a neutron wavelength in the order 1 Å and a corresponding energy in the order of meV, and as a consequence the energy of the produced neutrons need to be reduced to this level.

Inelastic collisions between the produced fast neutrons and slow lightweight nuclei leave the neutron with less energy while the slow nuclei gains energy. This process is used in neutron moderators, which are materials with a low absorption cross section and a large inelastic scattering cross section, kept at a fixed temperature. Given enough collisions, the produced neutrons will reach a speed comparable to the moderator nuclei, which is given by a Maxwell distribution depending on the moderator temperature. A neutron beam can therefore be attributed a temperature corresponding to that of the used moderator. In this way moderators provides beams of a desired energy range, yet the neutrons are emitted in a near isotropic direction. Furthermore the time spent for each neutron in a moderator can vary significantly, increasing the pulse width of pulsed sources.

2.2.2 Facilities

Due to the technical complexity of creating a neutron beam with sufficient brightness for scattering experiments, the sources are primarily situated at dedicated neutron scattering facilities. The most common source is the research reactor that produces a constant neutron flux, and often has a number of moderators kept at different temperatures. The most successful of these, and arguably the most successful source overall, is Institute Laue-Langevin (ILL) in France [55]. A single pulsed reactor source exists [56].

A small number of short pulsed Spallation sources have been built [57–59]. All of these use a storage ring to increase the beam current to obtain high beam power in short pulses. The time scale of neutron moderation is in many cases the limiting factor for energy resolution, leading to so called poisoned moderators with larger absorption cross sections that limit the resulting pulse width. Several moderators can be used for a single source, as they need to be suited to the instrument in terms of temperature and pulse width. One continuous spallation source, SINQ at the Paul Scherrer Institute (PSI) [60], deserves special mention as it has been operating like a reactor through using a constant beam current.

All these sources have extensive user programs, meaning that experiment proposals are sent from small research teams. The proposals are rated and beamtime is allocated to the best proposals free of charge. This system makes neutron scattering an accessible technique for universities and industry despite of the high cost of building and maintaining the necessary facilities.

The European Spallation Source [2, 61] currently under construction in Sweden will be a long pulsed spallation source, and thus forego the storage ring of the short pulse sources. The pulse length will be similar or larger than the time scale of moderation, which results in another set of constraints for instrument design. One limiting factor for short pulsed sources is the maximal beam current on the target, which is a lesser concern for a long pulsed source, as the beam can be delivered over a much longer time, allowing a larger amount of energy to be delivered in each pulse. The ESS design only allows for two moderator positions, these are however situated very close to the spallation target.

2.2.3 Instruments

Neutron scattering instruments use the produced neutron beam to investigate the scattering and in some cases transmission from a sample. There is a large number of different types of instruments, each with a different purpose. Most can be described by their coverage of possible scattering vectors, coverage of energy transfer and a description of the instrument resolution.

Obtaining the scattering vector requires knowledge of the initial and final wavevector, and hence the direction and energy of the neutron before and after scattering in the sample. The initial direction is given by the neutron beam, yet the divergence of the beam introduces a random error that can be reduced with slits and collimation at the cost of flux. The final direction is deduced by the detector placement, and its uncertainty arise from the size of the sample and detector.

The energy of the neutron can be determined either by deduction of its speed or by using Bragg scattering from a known crystal. Either method can be used before or after interaction with the sample, or both.

The class of instruments that determine both the initial and final energy is named spectrometers, and they can thus measure $S(\mathbf{q}, \omega)$ within some $\mathbf{q}$ volume and ω range defined by the spectrum of the source and attainable scattering angles. The uncertainty in $\mathbf{q}$ and ω is described by the resolution function, and the measured signal is the scattering function folded with the resolution function.

Instruments only concerned with elastic scattering neglect measuring the final neutron energy, assuming it is unchanged. This class of instruments is called diffractometers. Such instruments effectively measure all accessible energy transfers in addition to the elastic signal, but these contributions are in general much smaller.

Determining energy using Bragg scattering

The classic three axis spectrometer as shown in figure 2.9 uses Bragg scattering both for selecting the initial and final energy. The crystal used for selecting the initial energy is suitably named the monochromator while the crystal selecting the investigated final energy is called the analyzer. Scattering from crystals have the inherent problem that in addition to the desired wavelength λ, the higher orders are scattered as well with wavelength $\lambda/2, \lambda/3, ...$ Filter are used to suppress unwanted orders, these are composed of powders that strongly

scatter certain wavelength ranges, with weak scattering in the desired wavelength range. This can be achieved by using the Bragg edges of a material. Using Bragg scattering to select energies imposes no restrictions on the instrument length, but requires that the relevant angles can be achieved. An important property of crystals used for this purpose is the mosaicity, since it introduces an error in the scattering angle, but also allow a larger flux to be reflected. An additional uncertainty in the scattering angle is introduced by the beam divergence. An estimate of the uncertainty of the wavelength, $\delta\lambda$ can be obtained from Braggs law,

$$\lambda = \frac{2d}{n}\sin(\theta) \Rightarrow \delta\lambda = \frac{2d}{n}\cos(\theta)\delta\theta \Rightarrow \frac{\delta\lambda}{\lambda} = \cot(\theta)\delta\theta. \tag{2.2.1}$$

Thus the uncertainty in energy can be minimized by selecting a monochromator crystal with a lattice spacing that results in scattering angles close to $2\theta = 180°$ for the desired wavelengths. Reducing beam divergence and mosaicity results in lower energy uncertainty too, but at the cost of intensity as a smaller fraction of the beam can satisfy the scattering condition.

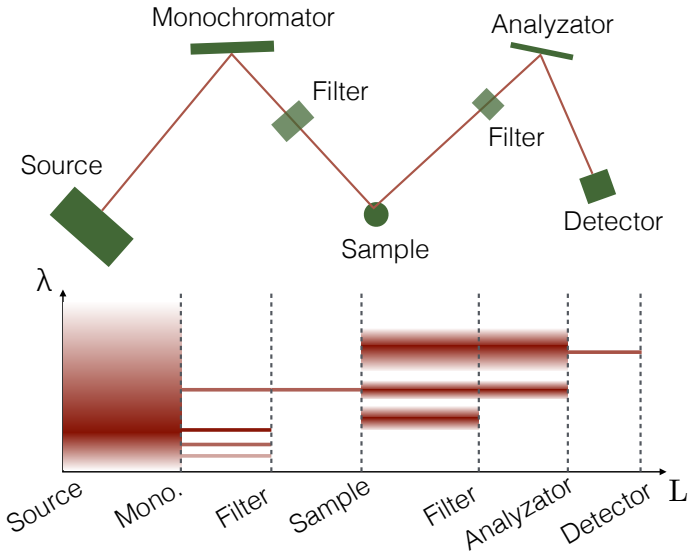

Figure 2.9: Illustration of a triple-axis spectrometer and the wavelength spectrum through the flight path of the instrument, where Bragg scattering and filters are used to select a desired wavelength range.

Determining energy using time of flight

Deducing the speed of the neutron requires knowing the position at two different times. If a distance L is travelled in time t, the neutron wavelength is,

$$v = \frac{h}{m\lambda} = \frac{L}{t} \Rightarrow \lambda = \frac{h}{m}\frac{t}{L}. \tag{2.2.2}$$

The travel time is often deduced using the inherent time distribution from the source or choppers. Choppers are rotating absorbers that allow the beam to pass only at certain angles, and hence the time structure of the beam can be controlled by the rotational speed and phase of the choppers. The uncertainty on the wavelength determined by time of flight is dominated by the uncertainty in the time measurement, δt,

$$\delta\lambda = \frac{h}{mL}\delta t \Rightarrow \frac{\delta\lambda}{\lambda} = \frac{h}{mL\lambda}\delta t = \frac{\delta t}{t}. \tag{2.2.3}$$

A long instrument is thus beneficial for the energy resolution, as is limiting the unavoidable uncertainty in the time measurement. On pulsed sources, the pulse width would be the primary contribution to the time uncertainty, yet it can be modified by the use of choppers. A long instrument length compared to the pulse frequency does however lead to the problem of frame overlap, where the neutrons with low energy arrives at the instrument after the high energy neutrons of the previous pulse. Choppers are thus used to select a wavelength band $\Delta\lambda$, and to avoid frame overlap, it must satisfy,

$$T > \frac{mL\Delta\lambda}{h}, \tag{2.2.4}$$

where T is the time between pulses. Thus longer instruments will naturally have narrower wavelength bands and better energy resolution. An illustration of a time of flight spectrometer is shown in figure 2.10. Here the wavelength of the neutron before and after interaction with the sample is determined from the detection time and the chopper settings.

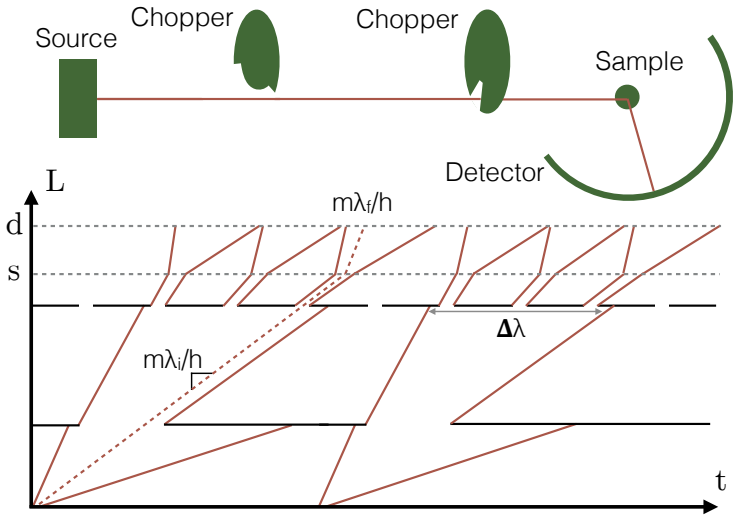

Figure 2.10: Illustration of a time of flight spectrometer and time of flight diagram of two pulses with the distance to sample and detector denoted s and d respectively. A frame overlap chopper and a monochromating chopper is used. The wavelength of the neutron before and after the sample is calculated from the known slope of the trajectory in the time of flight diagram.

Sample environment

In material science it is of utmost importance to investigate the sample under different conditions, for example temperature, magnetic field, and pressure. One of the great advantages of using the neutron as a scattering probe is the low scattering and absorption cross section of aluminium which can be used to create elaborate sample environments such as cryostats, furnaces and large magnets. The scattering from aluminium is however still problematic and can lead to background that can be mistaken for sample signal.

Background and spurious signals

Neutron scattering instrumentation aims to measure the scattering cross section, yet the measured intensity can arise in other ways than the assumed single scattering event in the sample. This risk should be considered both during analysis of the data and planning of the measurement.

The intensity measured in excess of the sample scattering is considered background, and is often estimated by performing the same measurement without the sample. This

background estimate will contain general neutron background and scattering from the sample environment, air and other components. Subtracting such a background measurement from the full signal is a significant improvement, but strong scattering from the sample can significantly change the background from, for example, the cryostat. Such signals that appear after background subtraction, but are not the desired single scattering, are named spurious signals - or just spurions. They most often originate from multiple scattering, yet can also be caused by absorption from a sample which in turn reduce scattering from sample environment included in the background measurement.

Time of flight instruments are especially prone to spurions from multiple scattering, as the distance travelled is increased, and therefore produces systematic errors in the calculated energy. Triple axis instruments are not affected by the additional distance travelled, yet multiple scattering is still an issue as signals can appear at unexpected scattering angles or energy transfers.

2.2.4 Neutron guides

Most neutron scattering instruments use a neutron guide, as it allows more instruments to use the same source and separates the instrument backend from the high background environment near the neutron source. The brilliance at the moderator can be transported to the backend with only small losses provided the supermirror can reflect the neutrons at the desired wavelength and divergence. In addition to the background reduction from separating the source and instrument backend, it is possible to further limit the background from the source by breaking line of sight through the guide. A generic guide is illustrated on figure 2.11, and the different aspects depicted will be described.

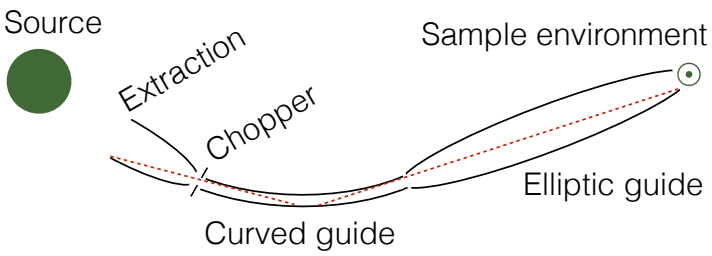

Figure 2.11: Generic guide from source to sample environment, including a narrower section for a chopper, a curved guide breaking line of sight and an elliptical section.

Beam extraction

The environment close to a neutron source will usually have a very high heat load due to the high energy radiation released in connection with neutron production. The most common substrates for supermirror production can not tolerate the high temperatures, and thus some distance between the source and guide is needed. Recently supermirrors with aluminium substrates have been shown to have higher tolerance, and could potentially allow guides to extend closer to the source. When several guides use the same source, they are constrained to start at a certain distance in order to avoid collision.

Accommodating choppers

On time of flight instruments a number of choppers placed at strategic places along the guide are often used to control the wavelength band and pulse length. Mechanical choppers are limited to certain ranges of diameters and rotational frequencies, and thus the width of the guide impacts the possible opening and closing times of the chopper, adding to the time uncertainty. For this reason, guides the guide should be as narrow as possible at the positions

of the choppers. Some choppers that does not directly influence the time uncertainty but prevent frame overlap are however not as sensitive to this issue.

Breaking line of sight

Due to the high radiation environment near the neutron source, it is in most cases preferable to introduce shielding between the instrument backend and source. This can be done by bending the guide so that there is no line of sight through it. Estimates of the resulting background does however require simulation software that can handle high energy particles and contains the relevant cross sections. In appendix A.10, a link between the McStas simulation describing the guide and MCNPX describing the shielding was used to produce a complete simulation including the background. The procedure is described in Ref [62]. Such work have later been simplified by the MCPL [63].

Room for sample environment

The guide delivers a beam to the backend of the instrument, but there are usually practical concerns that limit how close the guide can extend towards the delivery point, be it a monochromator or the sample position.

Providing a high flux

The time required to do a measurement depend on the flux delivered to the instrument. The phase-space density is however limited by Liouvilles theorem as discussed in section 2.1.16, so the main influence by the guide on the flux is the divergence that can be delivered. As mentioned the divergence of the beam influences the resolution of the instrument, and hence the divergence requirements of instruments differ greatly depending on their design and purpose. Providing the highest flux within these constraints amounts to providing the largest possible brilliance transfer.

Providing a large brilliance transfer means the losses from supermirror reflectivity less than unity should be minimized. This can be achieved by minimizing reflection angles and the number of reflections. Increasing the dimensions of the guides over some distance results in two important effects that help achieve this. One part is the increased distance between the mirrors that results in fewer reflections given the same divergence. The other is that increasing the distance between the mirrors provides sloped mirrors that decrease the divergence under reflections, reducing both angles of incidence and the number of reflections. Ballistic guide is a term for guides that increase their cross section to transform the initial beam into a large low divergent beam that can be easily be transported, and then subsequently narrows the guide near the end to provide a small high divergent beam. Such ballistic guides can provide a large brilliance transfer even at larger divergences.

2.3 McStas Simulation

Computer simulation of neutron scattering instrumentation is a widespread technique used primarily for the design and understanding of instrumentation, yet has the potential to be used in data reduction and analysis. The most popular simulation scheme is Monte Carlo ray-tracing, where virtual neutrons are propagated through a simulated instrument using random numbers. One of the most prominent Monte Carlo ray-tracing packages is called McStas, and this section is dedicated to introducing this piece of software. The modular nature of the McStas package is an important aspect, as it relies primarily on its user base to expand its capabilities through code contributions in the form of *components*. A component is a simulation of a small part of an instrument, such as a guide section, sample or detector. Instrument simulations are then built from a number of components specified in an *instrument file*. The name McStas originates from the earliest use of the simulation package where triple-axis (TAS) instruments were simulated, but the package has later evolved to cover all major instrumentation types.

2.3.1 Monte Carlo ray-tracing technique

Monte Carlo ray-tracing is performed by selecting an initial position and velocity for a ray and propagating it through the simulated system using random numbers drawn from appropriate probability distributions. A large number of rays is simulated to obtain the necessary statistical accuracy on the final results. A single ray does not in general correspond to a single neutron, as the intensity of the source, I, is split into a number of rays each with a so called initial weight p_0 so that,

$$I = \sum_i p_{0\,i}. \tag{2.3.1}$$

When simulating an event such as absorption or scattering, the weight of a ray can be manipulated using a weight factor π, and so the final weight of a ray after a number of interactions labeled j can be written,

$$p = p_0 \prod_i \pi_i. \tag{2.3.2}$$

The sampling probability f for a event can be manipulated along with the weight factor, as long as the real probability P is preserved [64, 65],

$$P = \pi f. \tag{2.3.3}$$

When describing for example absorption or reflectivity, this relationship can be used to avoid discarding rays and instead decrease the weight accordingly.

The expected intensity, I, in a detector is the sum of the N final weights of the rays that reached the detector,

$$I = \sum_i^N p_i = N\bar{p}, \tag{2.3.4}$$

where $\bar{p}$ is used to designate the average weight. Assuming N and p are independent and follow Gaussian distributions, it can be shown the variance on the recorded intensity is [65],

$$\sigma^2(I) = \frac{N}{N-1}\left(\sum_i p_i^2 - \bar{p}^2\right) \approx \sum_i p_i^2. \tag{2.3.5}$$

The relative intensity uncertainty can thus be expressed,

$$\frac{\sigma(I)}{I} = \frac{\sqrt{\sum_i p_i^2}}{\sum_i p_i}. \tag{2.3.6}$$

Imagine that the number of simulated rays is increased by a factor of K, thus splitting the intensity over a larger number of rays with smaller weight. Assume the number of rays that arrive at the same detector is now NK, yet with weight p_i/K. The relative uncertainty on the intensity can then be written,

$$\frac{\sigma(I_{NK})}{I_{NK}} = \frac{\sqrt{K\sum_i (p_i/K)^2}}{K\sum_i p_i/K} = \frac{\sqrt{\frac{1}{K}\sum_i p_i^2}}{\sum_i p_i} = \frac{1}{\sqrt{K}}\frac{\sqrt{\sum_i p_i^2}}{\sum_i p_i} = \frac{1}{\sqrt{K}}\frac{\sigma(I_N)}{I_N}. \tag{2.3.7}$$

This is an oversimplification, yet it indicates a problem with the Monte Carlo technique, namely the large increase in the number of simulated rays needed to increase the accuracy.

2.3.2 Instrument file

A McStas simulation is performed by compiling a instrument file into a c program. The instrument file is written in a meta language built on the c programming language. The c program is then compiled and executed with appropriate input parameters which in turn writes the results to disk. A basic user can work almost entirely in the McStas meta language used in instrument files, using components and appropriate input to describe the desired instrument. All instrument files are composed of a number of sections, each of which is described here.

Instrument definition

In the instrument definition a number of input parameters can be defined. These are declared automatically and can be used in all remaining sections. It is possible to select a default value for these parameters.

Declare section

Necessary parameters in addition to those in the instrument definition are declared here using normal c syntax.

Initialize section

The initialize section can contain a piece of c code to be executed before the ray-tracing simulation is performed.

Trace section

The trace section describes the ray-tracing simulation in the meta language. A linear succession of components are used to describe the simulated system. Each component is placed in space with a position and rotation. The task of a component is to propagates the ray through this part of the instrument and update the position, velocity, weight and spin state accordingly.

It is possible to do some changes in the linear succession of components by using the GROUP statement which will effectively set two components or more in parallel, making each ray interact with at most one of the components. This is useful for a monochromator where rays would not normally interact with two different crystals, but less effective for sample and sample environment where the ray should be able to interact with both in any arbitrary order.

It is possible to expand the code of a used component by using an EXTEND section after the component. Here c syntax can be used to for example tag rays that scattered in a component, or do additional calculations not included in the component.

Finally section

The finally section can contain a piece of c code to be executed after the ray-tracing simulation is performed.

2.3.3 Components

The McStas component library is designed to be expandable by the user community through the contribution of components. Components usually describe a spatially seperated part of an instrument and are almost stand alone simulations. As the components are written in the plain c language, their modification is reserved for more experienced users. The code contained in a component is segregated into a number of sections, each of which is executed at a different point in the overall simulation.

Component definition

In the component definition the name of the component is selected and the input parameters are specified. Default values can be selected.

Share section

The share section contains code shared only included once in the generated c program, regardless of the number of times this component appears in a instrument. This section is appropriate for defining functions to be used in the component.

Declare section

Here additional parameters can be declared.

Initialize section

The initialize section is executed before the ray-tracing occurs, and can thus contain calculations only needed once, which can reduce computational requirements. Input sanitation is often done by reporting errors when unreasonable input is detected. The initialize section of the instrument file is executed first, after which the initialize sections of the specified components are executed in turn.

Trace section

The trace section propagates a ray through the component, and is thus potentially executed for every ray simulated. A number of functions for common ray-tracing tasks are provided by the McStas core.

Finally section

Contains a piece of c code to be executed after all rays have been simulated. Here diagnostics can be reported.

Mcdisplay section

In order for McStas to draw the simulated instrument, it calls upon each component to draw their simulated part. This task is performed in the mcdisplay section using provided draw functions.

2.3.4 McStas core

The McStas core handles logistics around the simulation while the simulation itself is primarily performed by the components. The McStas core is however responsible for transforming between the coordinate systems of the individual components in an instrument file as shown in figure 2.12. The figure also provides an example of a component GROUP as mentioned in section 2.3.2, and how that deviates from the linear sucession of components. It is also possible to use the JUMP keyword to manipulate the path of a ray through the list of components, yet this is reserved for super users that understand the consequences of doing so.

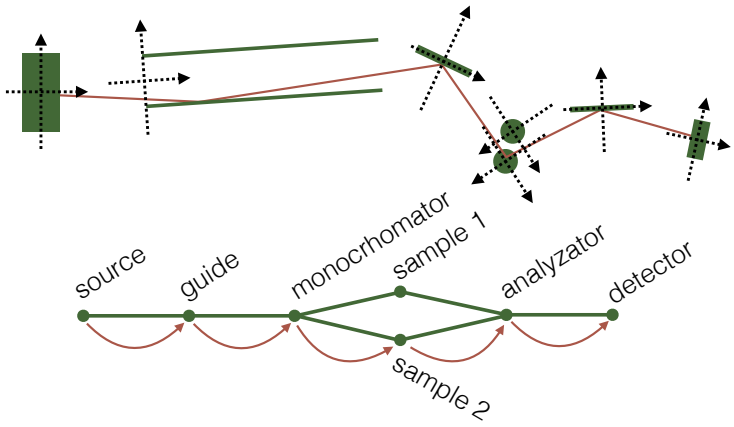

Figure 2.12: Illustration of McStas instrument file composed of a number of components each with their own place in the component chain and coordinate system provided by the McStas core. The components named sample 1 and sample 2 are in a GROUP, and thus the ray can interact with one of them, but not both.

2.3.5 McStas sample component features

McStas includes a number of sample components that describe various combinations of scattering processes and have different features. The Single_crystal component simulates a crystal with coherent Bragg scattering, incoherent scattering and absorption. The component simulates multiple scattering within the crystal. Using sutable settings, the component can take a number of different shapes such as a box, cylinder or sphere, or even a closed non-convex polyhedra using a 3D model file [66].

Some component such the powder sample powderN allow so called concentric mode, which allow it to contain another component. This is done by having an instance of powderN before and after the contained component, and the ray can thus scatter on this concentric container both before and after interacting with the contained component. This concentric mode does not support scattering back and forth between the two sides, and the ray can not be scattered back into the contained component. The system can be used to provide limited multiple scattering between a sample and the sample environment, and several layers can be made. It is however not possible to use the 3D model geometries for concentric components.

2.3.6 McStas uses

Here some of the popular use cases of the McStas simulation package and similar Monte Carlo ray-tracing simulations are outlined.

Instrument design

The primary use case for McStas is the design and understanding of neutron scattering instrumentation. Analytical calculations are often used in X-ray scattering for this purpose, but the large divergences and sources used in neutron scattering makes such calculations more difficult. McStas excels at tasks such as selecting the appropriate mosaicity for a monochromator or investigating the effect of chopper frequency on the instrument resolutions. Design of instrumentation includes a number of compromises, each of which can be investigated without building prototypes. See appendix A.7, A.8 and A.9 for examples included in this thesis.

Guide design and optimization

The Monte Carlo ray-tracing method is inherently suited for simulations of guides, as gravity is an important consideration. A guide is required to deliver a homogeneous phase-space

to the instrument backend, which can easily be disturbed when breaking line of sight or introducing gaps for choppers. The simulation of imperfections in the used supermirrors are also well suited for ray-tracing methods. Examples of guide simulation studies are available in appendix A.6 and A.11.

Most modern guides are designed using numerical optimizers, as the underlying ray-tracing simulations have a sufficiently low execution time. Here a number of free parameters are varied to maximize a certain figure of merit produced by the simulation. Most often such figure of merit would be the brilliance transfer in a phase-space volume carefully chosen to correspond to the requirements of the instrument backend.

The McStas simulation package can be controlled by the MATLAB expansion iFit [67] that includes a number of numerical optimization algorithms. It has been shown that swarm algorithms are the most successful for problems with noise, like the results from Monte Carlo simulations. All guide optimizations included in this thesis is performed using iFit and swarm optimizers. An example of a guide system optimized in this way can be seen in appendix A.4 and A.5.

Virtual experiments

The term virtual experiment was proposed in Ref [68], and describes simulations that are used as real instruments. To qualify for the term, the instrument must be simulated from source to detector, absolute intensities must be used, and the simulation should be controlled as a real instrument. Data from the simulation should be written in such a way that data analysis can be performed using the same tools as for a real experiment. It is proposed that such virtual experiment could be performed directly by the instrument computer, allowing the scientists running an experiment to estimate required counting time and similar.

Potentially data analysis

The accuracy attainable by Monte Carlo ray-tracing simulations makes it viable to use instrument simulations to assist in data analysis. The work required to obtain an instrument model of sufficient quality is however prohibitive, and currently the effort is rarely made. In cases where the measured signal is close to the instrument limitations, a simulation can help distinguish the measured features from instrument effects [69]. One example of such a case is presented in appendix A.12.

With a sufficiently accurate instrument model, simulation results may in the future be used for basic data reduction for all experiments on an instrument. On a spectrometer, the well understood elastic scattering contributes to background through multiple scattering, partly with the sample environment, and such contributions could be identified and subtracted. As the single scattering cross section is the desired quantity, creating software that from the total scattering can identify the single scattering contribution, is a long term goal [70].

Chapter 3

Contributions to field of neutron guide design

In this chapter, my work on neutron guide design is presented and discussed. My contributions consist of analytical considerations, software development, and the application of these in the survey of performance dependence of moderator height for proposed ESS instruments. The analytical work use phase-space propagation to derive constraints appropriate for numerical optimization of neutron guides with predefined phase-space requirements. The constraints limit the guide intake of phase-space to the minimal value while preserving the possibility for a brilliance transfer of unity, and the method is thus named the "Minimalist Principle" (MP). The contribution of software is the widely used guide_bot automatic guide designer that generates the McStas code necessary for a guide optimization from limited user input. The constraints from the MP is included in guide_bot, but can be disabled if desired. The developed software was finally used to simulate the majority of guides for proposed ESS instruments for a range of moderator heights in order to provide the necessary data for selecting the moderator best suited for the instruments. In addition to the guide work presented here, I have designed the guides for several instrument proposed for construction at ESS: CAMEA A.7, Heimdal A.8, VESPA A.9 and ESPRESSO [71].

3.1 Minimalist principle

Neutron guide design is often performed either with brute force numerical optimizations, or analytical considerations. Optimizing a guide using simulations and numerical optimizations allow for complex guide systems that can not be described analytically, yet the analytical approach can tailor the needed phase-space exactly to the requirements. In this section, constraints on the parameter space used for guide optimization are derived from analytical considerations of minimal possible illumination, effectively providing a more balanced approach. The constraints reduces the intake phase-space volume to the minimal possible that can obtain a brilliance transfer of close to unity.

This section is based directly on the published paper A.1 and has been adapted to fit into the context of the thesis.

3.1.1 Reasoning behind the Minimalist Principle

It follows from Liouville's theorem 2.1.16 that the phase-space density at the sample can not exceed that of the phase-space density near the moderator. If one requires a neutron beam described by a closed phase-space volume, it follows that there is a maximum possible neutron flux in this phase-space volume. This limit is the foundation of the MP, as there is a point where additional neutron intake can not possibly contribute to the brilliance transfer.

When optimizing a guide system with the FOM chosen as the number of neutrons in such a phase-space volume, there is a corresponding maximum FOM. It is of interest to find

a guide, which delivers a FOM close to this maximum, but it is also important to limit the potential background from the neutron source. The background can be split into high energy particles that should be absorbed by shielding, and unwanted cold and thermal neutrons able to be reflected by the neutron mirrors. The high energy background is not taken into account in this paper, but is expected to be handled by choosing a guide geometry that allows sufficient shielding between moderator and sample.

In the MP, geometrical constraints on the guide geometry are designed to minimize the background from unnecessary cold and thermal neutrons. This is done by only transporting the neutrons necessary to fully illuminate the FOM phase-space volume. In order to calculate which neutrons are necessary, the phase-space volume corresponding to the FOM is propagated from the sample back to the end of the guide by acceptance diagrams. This yields the phase-space volume the guide should be able to deliver, and as this volume has a certain spatial width, the dimensions of the end of the guide can be determined, which is the first important constraint.

As it is theoretically possible for a guide to transport a phase-space volume without increasing its size or decreasing its phase-space density, the size of the phase-space volume that enters the guide should be at least equal to the size of the phase-space volume that the guide must deliver. If the size of the incoming phase-space volume is smaller than needed, it is not possible to reach the maximum FOM. By providing the guide with a phase-space volume of the same size as the one it has to deliver, the optimal brilliance transfer should be achievable. Increasing the incoming phase-space volume at this point would only increase the background if a perfect brilliance transfer is already achieved. As the size of the incoming phase-space volume depends on the size of the guide entrance, the distance to the source and the source dimensions, this requirement results in a constraint on these parameters.

A guide that only delivers the exact phase-space volume needed to evenly illuminate the sample is considered truly focusing. Such guides exist, for example the Selene guide system as described in [28]. A truly focusing guide will work through single reflections per guide element, because multiple reflections will in general destroy the necessary perfect correlations in phase-space.

Most guide designs rely on multiple reflections. Even a perfect elliptical guide will have large amounts of the intensity from this process for anything but point sources [35]. An ideal multiple reflecting guide is assumed to have a divergence distribution that is independent of position, or at least a weaker correlation than that of a truly focusing guide. Without the focusing ability, the delivered phase-space needs to be larger than for a focusing guide in order to cover the FOM. The exact size of this larger phase-space volume is again derived using acceptance diagrams.

Guides designed using the MP constraints have a more direct control over the outgoing divergence, which will be limited to the divergence limits of the FOM in the case of a perfect guide. In practice, there will be unwanted neutrons at higher divergences than requested on some parts of the sample, but very limited in comparison to a guide optimized without any constraints. In addition, the amount of neutrons entering the guide is as low as possible, under the condition that the guide is still theoretically able to achieve the maximum possible FOM. This causes lower neutron losses along the guide than traditional geometries, yielding a guide which is highly efficient in terms of neutrons delivered in relation to background generated from absorbing these neutrons either in the guide or near the sample. It will also reduce radiation damage on the supermirrors and necessary shielding along the guide.

3.1.2 Derivation of the Minimalist Principle

In this section appropriate terminology and notation is introduced, followed by a derivation of the MP using acceptance diagrams.

Notation

The MP considers the beam propagation before and after the guide, and thus assumes a generic guide setup as seen in figure 3.1, where the shape and length of the guide is

arbitrary, but the dimensions at both ends are known. For now it is assumed the guide is closed meaning without gaps, but the appropriate corrections are described later in the section. All parts of the source, guide and sample are assumed rectangular, meaning the horizontal and vertical component of the neutron trajectory can be calculated independently. All calculations are done for a single direction, but is valid for both if gravity is neglected.

The width of the moderator in the relevant direction is denoted M, and the distance between the moderator and guide is denoted L_M. The width of the start and end of the guide is denoted W and U. The distance between the end of the guide and the sample is L_S, and is often small. The width of the sample is denoted S and together with the divergence requirement, ϕ, describes the FOM. It is assumed the guide is placed with the center of the guide entrance aligned with the center of the moderator, and the center of the end of the guide is aligned with the center of the sample.

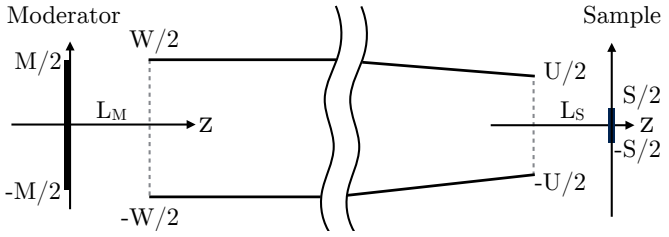

Figure 3.1: A sketch of the generic guide system investigated when using the MP, and the variables used to describe it.

The phase-space volume that enters the guide is called α and the phase-space volume leaving the guide is called β. The FOM phase-space volume at the sample is called Ω, and is assumed to be a rectangle in space with a position independent symmetric divergence requirement. The brilliance transfer can be written as $\rho(\Omega)/\rho(\Omega_M)$ with Ω_M being the FOM phase-space volume, but translated to the moderator surface.

Beam propagation without guide

A neutron beam with a given width and divergence distribution will propagate under simple rules from classical mechanics. The divergent beam can be easily visualized by acceptance diagrams [72], as shown for the x direction in figure 3.2. The wavelength range is ignored as it does not influence the trajectories when gravity is neglected. Under these conditions the ideal spatial and divergence distributions are tophat functions. When the beam propagates, the diagram shears as shown. When propagating a neutron a distance L, the divergence η_x is unchanged while the transverse distance travelled can be calculated from,

$$\Delta x = L \tan(\eta_x). \tag{3.1.1}$$

Thus a beam where the highest divergence is ϕ and the lowest is $-\phi$ will be $2L\tan(\phi)$ wider when propagated a distance L, as shown in figure 3.2.

Propagation between sample and guide

When considering propagation from the end of the guide to the sample with the objective to reach a brilliance transfer of unity, the entire FOM must be covered, and since the neutrons at the extremes of the divergence interval are translated by (3.1.1), the guide should be $2\Delta x$ wider than the sample,

$$U = S + 2L_s \tan(\phi). \tag{3.1.2}$$

Any neutrons outside the FOM phase-space volume are considered background, so it is important to find the smallest possible phase-space volume that will still cover the FOM. Here a phase-space volume with the dimension U and entire divergence range $[-\phi : \phi]$ is

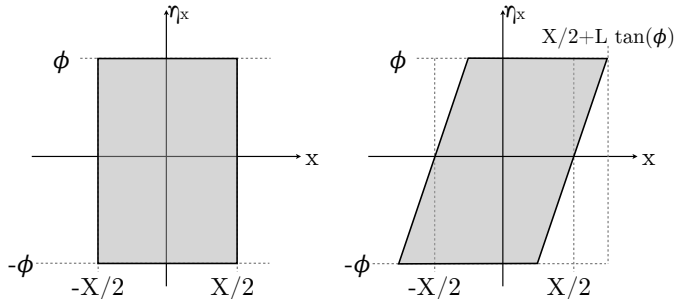

Figure 3.2: Acceptance diagrams showing propagation without guide. The left side shows a beam at $z = z_0$ with width X and a uniform divergence distribution between $-\phi$ and ϕ . The phase-space at $z = z_0 + L$ is shown on the right side, where the propagation of the beam has caused a shearing of the phase-space volume, which can be calculated from (3.1.1).

denoted β_M and is propagated from the end of the guide to the sample, which can be seen in figure 3.3. When using a rectangular phase-space volume at the end of the guide, it is clear that the FOM is covered, but that some of the propagated phase-space is outside the FOM area. By propagating the FOM volume back to the end of the guide, the smallest possible phase-space volume is found, here denoted β_F.

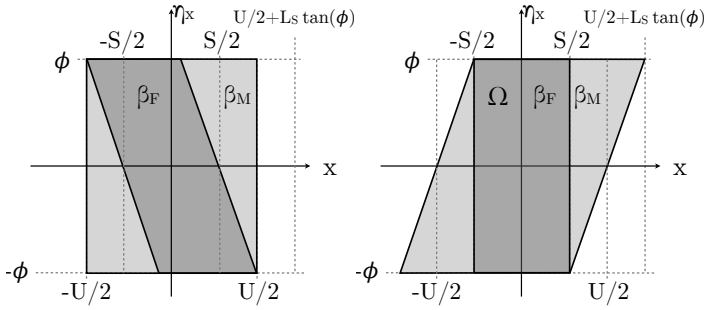

Figure 3.3: Acceptance diagram for a guide of width U illuminating a sample of width of S from a distance of L_S. The left part is at the end of the guide, while the right side is at the sample position. The light grey area is the phase-space volume designated β_M while the dark grey is the phase-space volume designated β_F, and the latter corresponds perfectly to the FOM phase-space volume at the sample position, Ω.

The volumes β_M and β_F correspond to two extremes in terms of focusing ability. The β_F volume corresponds to perfectly focusing, as the entire phase-space volume exactly covers the FOM volume when propagated to the sample. The β_M volume corresponds to the case of a guide relying on multiple reflections, as the correlations between position and divergence are smeared out. In order to generalize this we introduce the focusing parameter, Y, that describes a linear transition from the focusing case to the multiple reflecting case, so that the size of the needed phase-space volume at the end of the guide can be written,

$$V(\beta_F) = 2S\phi \tag{3.1.3}$$
$$V(\beta_M) = 2U\phi = 2(S + 2L_S \tan(\phi))\phi \tag{3.1.4}$$
$$V(\beta) = 2(S + 2YL_S \tan(\phi))\phi. \tag{3.1.5}$$

Thus $Y = 0$ corresponds to perfectly focusing, while $Y = 1$ corresponds to a guide completely dominated by multiple reflections. The appropriate value of Y will depend on the geometry of the entire moderator, guide, sample system including the selected FOM, and

is not known. It is intended that a reasonable value of Y should be found from experience with similar cases. The highest possible value of $Y = 1$ will still be an aggressive reduction of unwanted neutrons.

Supplying the needed phase-space volume size

As the phase-space volume size $V(\beta)$ is known at the end of the guide, it is of interest to determine the minimal phase-space size needed at the start of the guide $V(\alpha)$ in order to illuminate the FOM phase-space volume.

From Liouville's theorem it is known that phase-space density can not be increased, and thus the best case is no reduction in phase-space density under transport. If one assumes a perfect guide, it should only be necessary to supply a phase-space volume with a size identical to the needed phase-space volume.

$$V(\alpha) = V(\beta) \tag{3.1.6}$$

$$\rho(\alpha) = \rho(\beta) \tag{3.1.7}$$

This is a very ambitious requirement, and will only result in guides with a high brilliance transfer if a suitable geometry is within the specified parameter space, and the mirror quality is sufficient. One can relax the requirement by introducing a illumination factor k, so that,

$$V(\alpha) = kV(\beta). \tag{3.1.8}$$

Here a guide optimized using the constraint with $k < 1$ should not be able to reach a brilliance transfer of unity, unless the focusing parameter Y have been set too high for the selected guide geometry. Setting $k = 1$ corresponds to the case discussed so far. Using $k > 1$, will introduce additional background but may also increase the FOM.

We have experienced that adjusting the parameter k for a range of guide optimizations is superior to adjusting the guide opening manually, as one is always aware of the balance between FOM and background when using k-adjustments.

Propagating from moderator to guide

In order to calculate the size of the phase-space volume received by the guide, the known phase-space volume at the moderator is propagated to the start of the guide. It is assumed that the moderator emits neutrons in every direction with equal probability, and thus the phase-space volume emitted is not closed in the divergence direction. There is thus effectively no top or bottom in the acceptance diagram. For the small divergence values needed here, we assume that the sides are straight lines. The acceptance diagram is propagated forward a distance of L_M. From figure 3.2, the slope can be calculated as,

$$a = \frac{\Delta\eta_x}{\Delta x} = \frac{\phi}{L_M \tan(\phi)} \approx \frac{1}{L_M}, \tag{3.1.9}$$

with divergence measured in radians. The size of the phase-space volume α which enters the guide is calculated using the appropriate acceptance diagram on figure 3.4. The area of the parallelogram is,

$$V(\alpha) = aMW = MW/L_M. \tag{3.1.10}$$

Applying the Minimalist Principle

The preceding calculations are sufficient to use the MP, as one uses the derived equations as constraints in the parameter space describing the guide geometry. Assuming that a truly focusing guide can use the entire incoming phase-space volume size, a combination of (3.1.5), (3.1.8) and (3.1.10) yields,

$$V(\alpha) = kV(\beta_F) \Rightarrow WM/L_M = 2kS\phi. \tag{3.1.11}$$

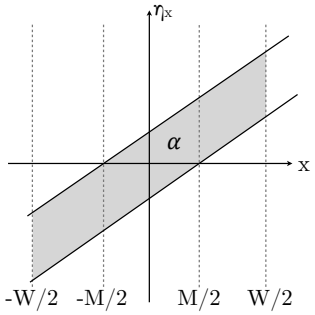

Figure 3.4: Acceptance diagram a distance L_M after a moderator of width M. A guide with width W starts here, and the phase-space volume which enters the guide is denoted α.

In addition (3.1.2) should also be used, to ensure not to waste phase-space volume size by illuminating an area larger than the sample,

$$U = S + 2L_S \tan(\phi). \tag{3.1.12}$$

By applying both equations (for both x and y directions) the number of free parameters to be optimized is reduced by 4, which can in many cases be essential. In addition only the guides which can potentially reach the best possible FOM without over-illuminating the guide entrance are investigated. The 4 free parameters are effectively replaced by 4 tunable parameters that should not be selected by the optimizer, an illumination factor for each direction, and a focusing factor for each direction.

Gaps in the guide

If the guide is not closed, but contains gaps for choppers or similar, it is not a reasonable assumption that phase-space volume is conserved along the guide. This situation can be handled by applying the MP on the closed guide on each side of the gap, starting from the sample. The guide piece between the sample and the gap will have a constraint to determine the end of the guide, but will not have any constraints for selecting the size of the guide opening after the gap, which can be chosen by the optimizer. This guide piece will need a phase-space volume of a certain size which can be calculated from (3.1.5). The guide piece between the moderator and gap will consider the guide opening after the gap as the sample, and from the dimensions chosen, a divergence requirement can be calculated from the necessary phase-space volume size, and the MP can thus be applied to the first guide piece. There is, however, the issue of selecting a reasonable value of the focusing parameter Y, in this work $Y = 1$ (non-focusing) have been used for gaps.

Kink in the guide

A surprisingly efficient way of escaping line of sight is to simply have a kink in the guide instead of a long bending section. Here a kink is defined as a gap between two guides, where the second guide has a new direction. After using the MP on the guide after the kink, the needed divergence can be calculated from its phase-space volume size requirement and start width. It is then of interest to calculate the width and needed divergence from the first guide so that this requirement is met. This is achieved by the appropriate phase-space diagram in figure 3.5, where a guide with divergence requirement ϕ is kinked an angle of χ. The guide before the kink have the width X_1, while the width of the guide after the kink is denoted X_2. The second guide is translated a distance t in order to minimize the needed phase-space volume from the first guide. The derivation is done only for the case of multiple scattering guides, meaning a focusing parameter of $Y = 1$, and is a generalization of the case discussed in section 3.1.2.

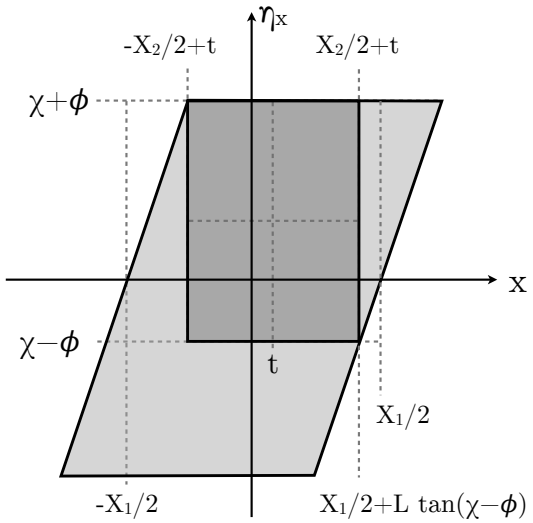

Figure 3.5: The acceptance diagram after a kink with length L and angular change χ. The guide before the kink ends with dimension X_1 just large enough to evenly illuminate a guide with width X_2 and divergence requirement ϕ angled χ relative to the first guide. The light grey box is the output of the first guide, while the dark grey box is needed phase-space volume for the second.

The beam needed at the guide after the kink will have an increased width when propagated back to the guide before the kink of $2L\tan(\phi)$ from (3.1.1), and thus $X_1 = X_2 + 2L\tan(\phi)$. The necessary translation is found from figure 3.5, as it must satisfy,

$$t + X_2/2 = X_1/2 + L\tan(\chi - \phi) \Rightarrow t = L\tan(\phi) + L\tan(\chi - \phi) \approx L\chi. \tag{3.1.13}$$

The needed phase-space volume size for the guide before the kink is $2X_1(\phi + \chi)$. In this derivation it is implicitly assumed that the second guide will need a symmetric phase-space volume, as the area directly under the dark grey box in figure 3.5 would also be received by the second guide, but is assumed to be absorbed due to the high divergence relative to the second guide. This can however give some asymmetry at higher wavelengths in kinked guides.

3.1.3 The Minimalist Principle in practice

We now present examples of guides optimized with the MP, both to show how they differ from guides optimized without these constraints, and to explore the parameters used to adjust the optimization within the MP.

Effect of the Minimalist Principle

In order to demonstrate the MP, a guide is optimized with and without the constraint in (3.1.8). This will show how the amount of unnecessary neutrons are limited, as there will not be a limit on neutron intake in the reference case. In order to illustrate how the illumination factor affects the results, the optimization using the MP is done with both $k = 1$ and $k = 1.25$.

The guide geometry to be optimized consists of a focusing piece (a "feeder" [36, 43]) before a gap at 5.9 m followed by an elliptic section, a curved guide, and an elliptic section. The gap length is 20 cm, and the following elliptic guide section has a starting width of 3 cm. The guide ends 50 cm before the sample, and is not allowed to start closer than 2 m from the moderator. The guides are curved so that line of sight through the guide is eliminated 5 m before the end. The remaining geometrical parameters are controlled by the optimizer. The

FOM is a 1.5×1.5 cm^2 area with a divergence requirement of $0.75°$ horizontally and $1.0°$ vertically. The FOM wavelength range is 1.5 Å to 4 Å. The moderator is a 12×12 cm^2 square, and the sample is situated 150 m from the moderator. The supermirror coating of the guide is $m = 3$ everywhere with $q_c = 0.0217$ Å^{-1} [53, chap 3.2-9], being the critical scattering vector for the Ni Vacuum interface. The guide is assumed multiple reflecting, and uses $Y = 1$ when the MP is applied. These requirements are similar to a large amount of guides optimized for ESS instruments using the TDR [2] moderator description. The optimizations was done using McStas [16–18, 20] and iFit [67], the resulting guide geometries are shown in figure 3.6.

The brilliance transfer as a function of wavelength for the optimized guides are shown in figure 3.7. The brilliance transfer for the guides optimized with the MP normalized to the guide optimized without is seen in figure 3.8. Here the amount of useful neutrons the three guides delivers to the sample are compared, as only neutrons which are within the spatial and divergence requirement are considered.

It is clear that the guide optimized without the MP has the highest brilliance transfer at all wavelengths, but the difference down to the guide with $k = 1.25$ is quite small. The guide with $k = 1$ has an integrated brilliance transfer of 80% of the guide optimized without the MP. The small decrease in brilliance transfer at larger wavelengths for the guide with $k = 1$ is caused by gravity and not punished by the optimizer as the FOM wavelength range is 1.5 Å to 4 Å.

Figure 3.9 shows the horizontal acceptance diagrams used to compare the guides performance in terms of homogeneity of divergence and spatial distributions. As the acceptance diagram shows a larger phase-space volume than the FOM, they also show neutrons transported that did not enter the FOM. The guide optimized without the MP has the most homogeneous phase-space volume inside the FOM box, as the guides designed with the MP have some structure in the form of thin lines with lower brilliance transfer. However, for many applications these small features are of little importance as they are much smaller than the instrument resolution.

The guides optimized with the MP have far fewer neutrons transported outside the FOM box. At low wavelengths where the transported divergence is limited by the coating of the supermirrors, the solutions are very similar. At higher wavelengths, the guide optimized without the MP starts to expand the divergence distribution beyond what was requested, while the guide optimized with $k = 1$ does not have any additional phase-space volume size to allow for that, and thus has a divergence which matches the requested even at larger wavelengths. The guide optimized with $k = 1.25$ does go to higher divergence than requested, but still reaches a limit where the divergence is not increased further (not shown).

Note the corners of the FOM box are just covered by the transported phase-space volume because (3.1.2) was used, even when optimizing without the MP.

The behaviour shown in the acceptance diagrams signifies that the guides designed with the MP would have an advantage in terms of signal to noise. This is explored as a function of wavelength in figure 3.10 where the neutrons within the FOM volume is counted as signal, and noise is counted as all other neutrons in a 10×10 cm^2 area centred at the sample position. This area corresponds to typical sample environment sizes where slits are commonly used to reduce the background from the unnecessary neutrons, and here we explore how much this task can be reduced by using the MP. As with the acceptance diagrams we see similar performance in the low wavelength region where the performance is limited by the supermirrors, but at higher wavelengths the unwanted high divergence neutrons in the reference case results in a large advantage for the guides optimized with the MP. When comparing the two guides optimized with the MP, we see the highest signal to noise for the guide optimized with $k = 1$ as expected from the derivation, but the guide with $k = 1.25$ is close. This indicates that illumination factors slightly above 1 are very interesting, as the performance is improved with only a small loss in signal to noise.

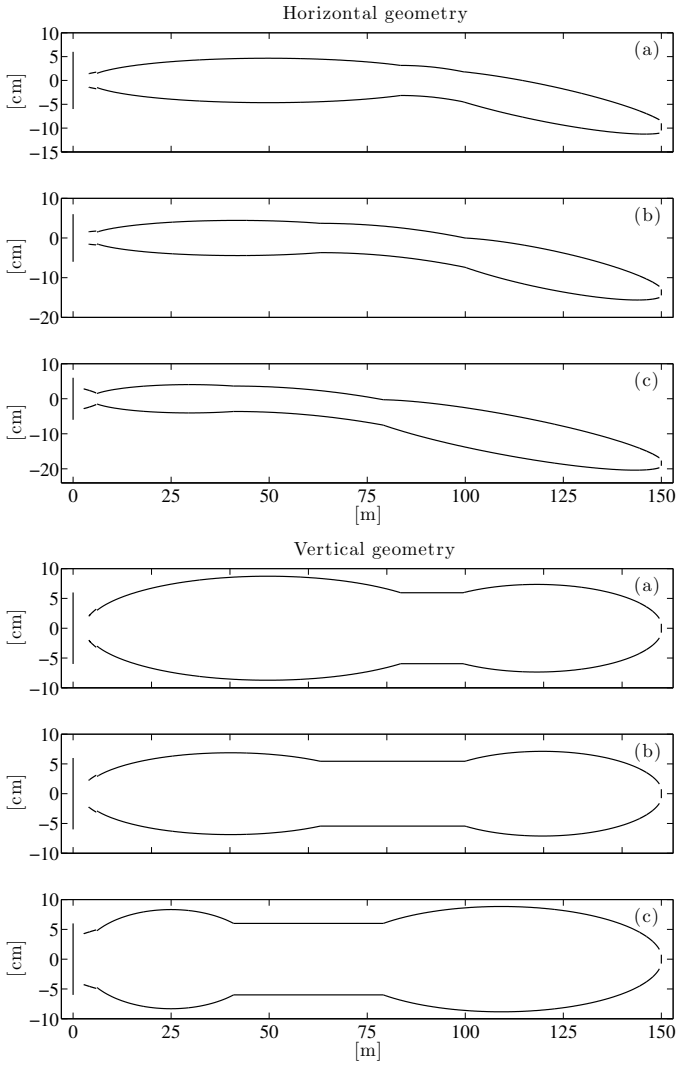

Figure 3.6: Geometry of the three guides to be compared, (a) is with the MP and $k = 1$ where (b) is with $k = 1.25$ and (c) is without the MP.

The effect of the illumination factor

We now investigate how guides optimized by using the MP perform as a function of the illumination factor, k. The FOM is a 2×2 cm^2 area with a divergence requirement of 0.75° for both directions and a wavelength range of $1 - 4$ Å. The source is 12×12 cm^2, and the sample is located 160 m from the source. A coating of $m = 3.5$ was used in the entire guide. Four different guide geometries are optimized using the MP for a range of k values.

- Elliptic guide
- Parabolic defocusing to curved guide followed by parabolic focusing.
- Parabolic feeder ending at 6.5 m from the source connected to a 1 m straight 3 cm wide guide followed by an elliptic guide
- Guide composed of three sections with flat mirrors

Figure 3.11 shows the resulting brilliance transfer for these guides optimized over a range of illumination factor values with the focusing factor $Y = 0$, meaning the guides are assumed truly focusing. Examples of the optimized geometries are shown in figure 3.12. It

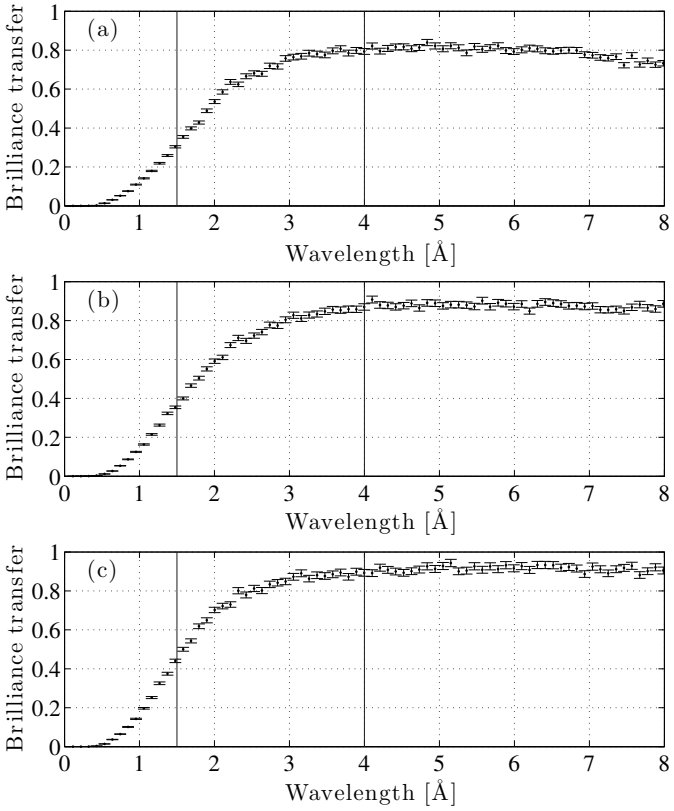

Figure 3.7: Brilliance transfer as a function of wavelength for the three guides optimized under different conditions. Graph (a) is with the MP and $k = 1$ where (b) is with $k = 1.25$ and (c) is without the MP. All guides were optimized for the wavelength band 1.5-4 Å.

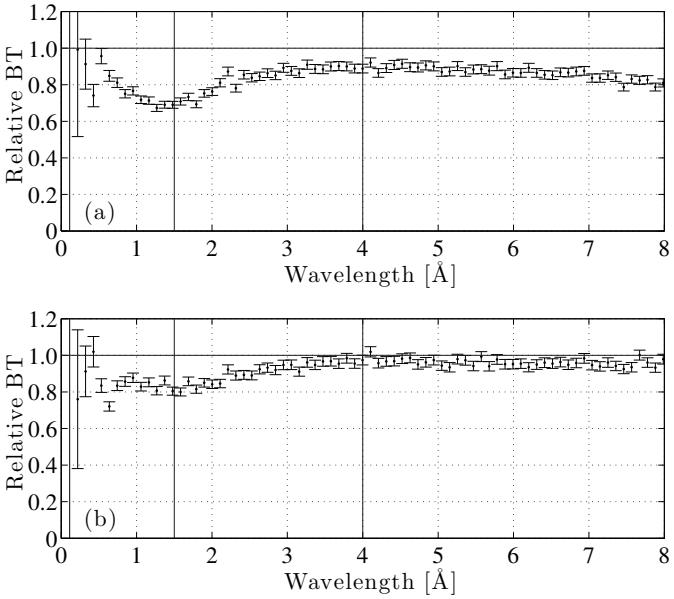

Figure 3.8: Brilliance transfer as a function of wavelength for the two guides optimized with the MP normalized to the brilliance transfer of the guide optimized without. Graph (a) is for $k = 1$ while (b) was optimized using $k = 1.25$.

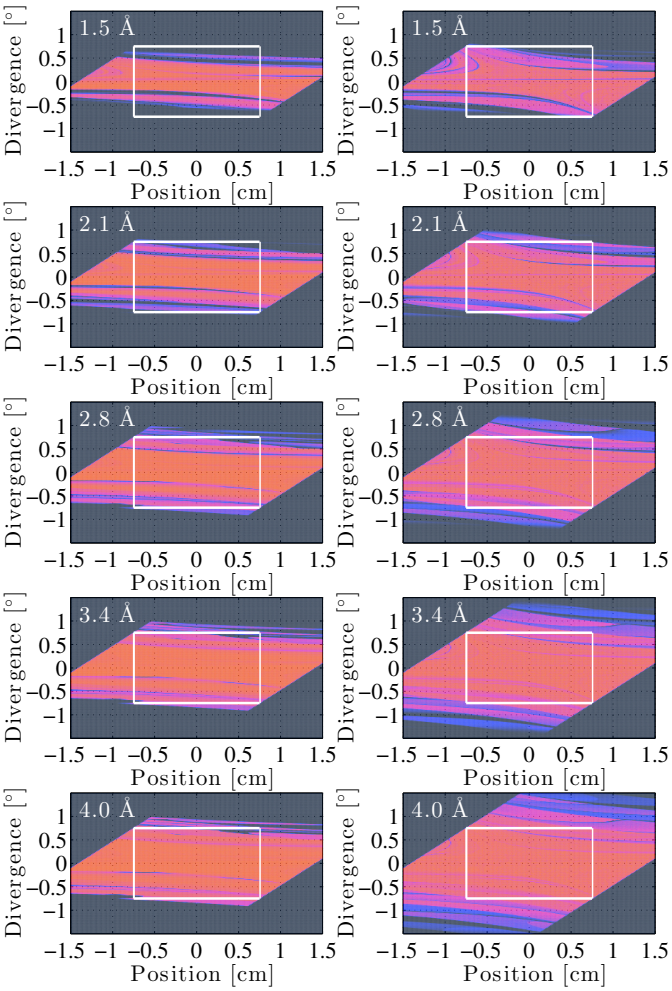

Figure 3.9: Horizontal acceptance diagrams for the sample position for two different guides shown for five different wavelengths (rows). The left column is for a guide optimized with the MP and $k = 1$, while the column to the right is for a guide optimized without any restrictions on the incoming phase-space volume.

is expected that the brilliance transfer should asymptotically reach a saturation value at high illumination factors where additional incoming neutrons simply does not add to the brilliance transfer.

In figure 3.13 a similar scan has been made, but with a focusing factor of $Y = 1$, assuming the guides are not able to focus on the sample. The optimal geometries are similar to the results for the truly focusing case shown in figure 3.12, but their entrances have a slightly larger solid angle as seen from the moderator. In this case the brilliance transfer of all guides levels off at higher illumination factors as they approach a saturation brilliance transfer. The tapered guide clearly reaches a limit earlier than the remaining guides in this comparison. At low illumination factors, the elliptic guides perform better than expected, as the brilliance transfer exceed the minimalist factor, which means it must have some focusing capability. The important prediction of the MP is that the start of the flat part of the brilliance transfer curve should be at or close to $k = 1$, after which there should be diminishing returns of accepting more neutrons into the guide. For the tested guides this seems to happen somewhere in the range $k = [1 : 1.25]$, which is close to the prediction.

The brilliance transfer saturates well below the actual performance limit of unity from Liouville's theorem. This can be explained by the high requirements for the guide compared to the used mirror quality. A brilliance transfer above 80% (70% without line of sight

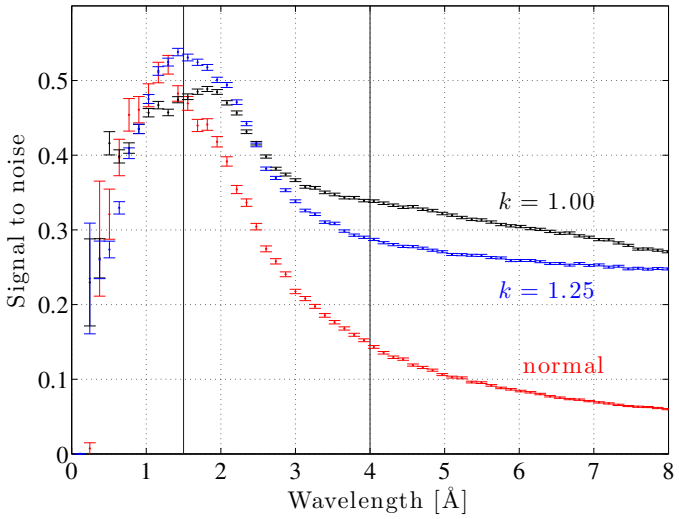

Figure 3.10: Signal to noise for a guide designed without the use of the MP compared to two guides designed using the MP, but with illumination factors of $k = 1$ and $k = 1.25$ respectively.

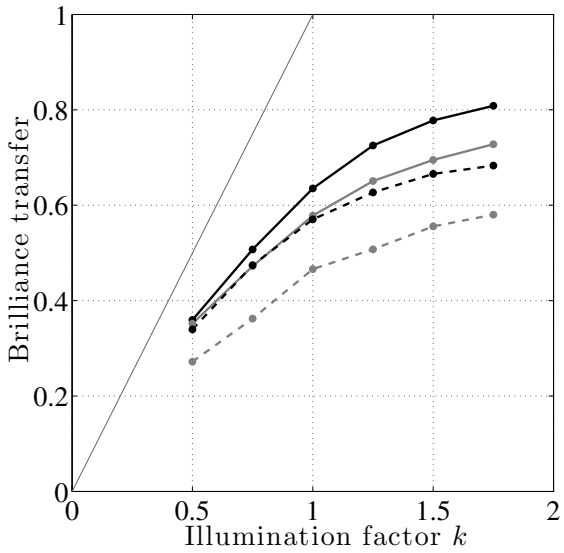

Figure 3.11: Scans of the illumination factor k for four different guide geometries which are all assumed truly focusing, $Y = 0$. From highest performance to lowest there is the elliptic guide (black), the curved with parabolic focusing (grey), the elliptic guide with feeder (black dashed) and the straight tapered (grey dashed). All brilliance transfers are for the entire wavelength range, of $1 - 4$ Å. Examples of the geometry of each guide are displayed in figure 3.12.

through guide) is, however, a respectable performance in this case, and is achieved with an over-illumination of 25% this corresponds to $1.25^2 \approx 1.56$ times more neutrons than with $k = 1$, a factor of k for each direction.

As the brilliance transfer values in both figure 3.11 and 3.13 are averages over the wavelength band, they do conceal some complexity. Over the wavelength range the brilliance transfer of the guides changes from being limited by the supermirror quality to being limited by neutron intake, and both contribute to the values shown in the figures. We have, however, selected not to show brilliance transfer for smaller wavelength ranges as they are

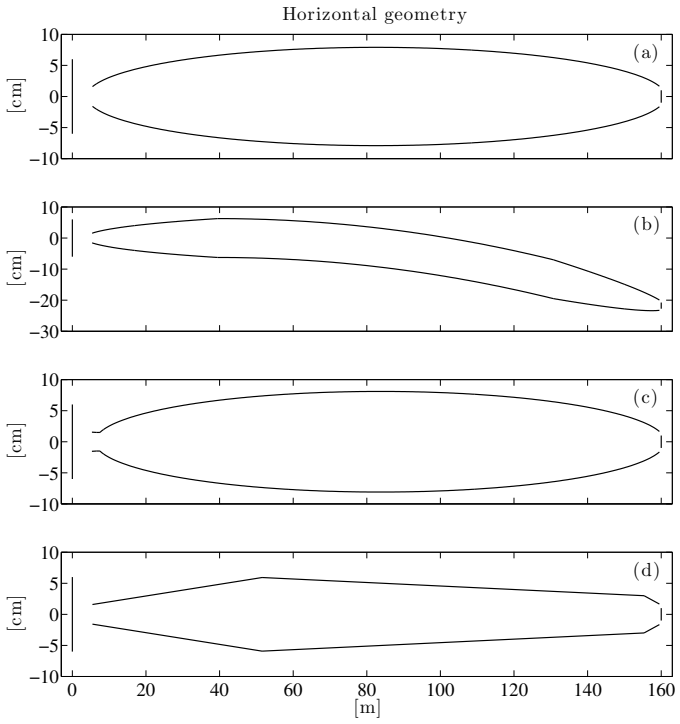

Figure 3.12: Examples of the geometry of the four investigated guides with the focusing parameter $Y = 0$ and all with illumination factor $k = 1$. The elliptic guide (a), the curved with parabolic focusing (b), the elliptic guide with feeder (c) and the straight tapered (d).

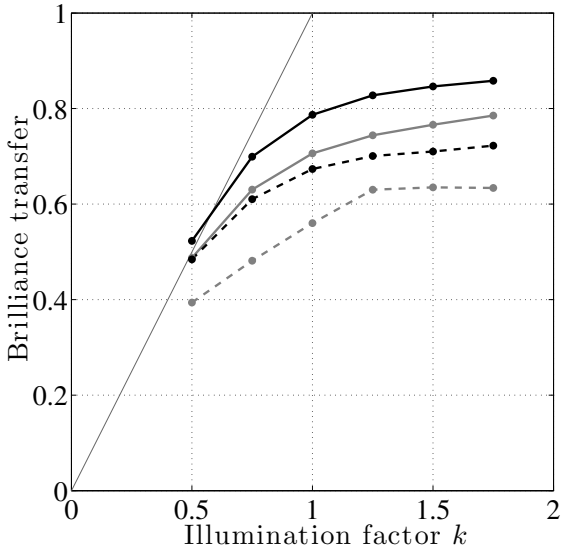

Figure 3.13: Scans of the illumination factor k for four different guide geometries which are all assumed multiple scattering, $Y = 1$. From highest performance to lowest there is the elliptic guide (black), the curved with parabolic focusing (grey), the elliptic guide with feeder (black dashed) and the straight tapered (grey dashed). All brilliance transfers are for the entire wavelength range, of $1 - 4$ Å. The geometries are similar to the truly focusing case shown in figure 3.12. Here we see the brilliance transfer reaching a plateau just above $k = 1$.

similar to the averaged case.

Analysing guide data using the Minimalist Principle

Here we investigate the relation between the phase-space intake recommended by the MP, and those selected by an optimizer without the derived constraints. Data from a previous publication A.4 is analysed, as it contains a large amount of guides optimized for different FOM's without use of the MP. The optimized guides all have a pinhole at 6.0 m from the moderator, and an elliptic guide to transport from pinhole to sample. The performance increase gained by inserting a parabolic feeder before this pinhole was investigated. The phase-space volume size received by each guide will be compared to the phase-space volume size recommended by the MP under different assumptions.

Even though there is a small gap between the pinhole and the start of the elliptical guide, this is not taken into account when applying the MP because the relation between pinhole size and opening of the elliptic guide behind can be chosen by the optimizer such that no neutrons are lost.

With this assumption, the MP will recommend the required phase-space at the start of the guide to be equal to the phase-space volume size required at the end of the guide. This phase-space volume size is calculated using (3.1.5). Here we investigate the data for the extreme cases of no focusing, $Y = 1$, and perfect focusing $Y = 0$.

Since the minimalist concept was not used to optimize the guides appendix A.4, the phase-space volume size which enters the guide is not in general equal to the minimalist requirements. In the following the size of the recieved phase-space volume is calculated using (3.1.10).

For guides optimized without using the minimalist concept, a unitless scalar, P, is defined, that describes the ratio between the phase-space volume size received by the guide and the size recommended by the MP with $k = 1$. It is clear that the value of P will depend upon the focusing parameter, Y, the FOM and the geometry of the guide and moderator.

Since the guides investigated in appendix A.4 are identical in the horizontal and vertical directions, the phase-space volume sizes for one of these is calculated and squared in order to get the full phase-space volume size. The value is calculated using (3.1.10) and (3.1.5),

$$P = \frac{\text{recieved PS size}}{\text{needed PS size}} = \left(\frac{WM}{2\phi L_M (S + 2Y L_S \tan(\phi))} \right)^2 . \tag{3.1.14}$$

The value of P will be compared to the brilliance transfer obtained for each individual guide, here denoted B. When calculating the brilliance transfer, the FOM phase-space volume is used, here with a sample area of 1×1 cm^2, a wavelength interval of $2 - 10$ Å and the specified divergence requirement.

If the assumptions are fulfilled for guides optimized using the MP, the relation $P \geq B$ should be true, as any non ideal guide would lose some phase-space density under reflections. Since $B \leq 1$, it is expected the data will be close to but below $B = P$ for $P \leq 1$, and $B = 1$ for $P > 1$. This prediction is referred to as the theory line. When the assumptions used are not fulfilled, it is possible for data points to lie above the $B = P$ line, for example by using a focusing factor larger than appropriate. The value of B will however never exceed the Liouville limit ($B = 1$).

For guides optimized without the MP, the situation is not as clear because they can have a guide end which is narrower than the minimalist constraint, and thus gain some efficiency at the cost of inhomogeneous sample illumination. Because of this, guides with $Y > 0$ can have $B > P$ when $P < 1$, even when delivering a rectangular shaped phase-space volume at the end of the guide, but the divergence distribution will be dependent on position. When assuming a guide is truly focusing ($Y = 0$), the minimalist limit reduces to the Liouville limit, and thus every data point must be below or at the theory line, regardless of using the MP or not.

In figure 3.14, the brilliance transfer is plotted against the ratio of received to needed phase-space size, P when using $Y = 0$ in (3.1.14). Here two groups of guides separated in P are clearly visible, and correspond to guides with and without feeder. The guides without feeder are much closer to fulfilling the assumptions, as they are closer to the theory line. It is clear that an assumption of a perfectly focusing guide is better for a single ellipse than a

Property	Marker description			
Guide	No feeder Large		Feeder Small	
Divergence	±0.5° Green	±1.0° Blue	±2.0° Red	
Length	24 m Star	75 m Square	150 m Circle	300 m Triangle

Table 3.1: The markers used in figure 3.14-3.15 to indicate which guide from appendix A.4 each point corresponds to. Each marker appears 5 times, reflecting 5 pinhole settings.

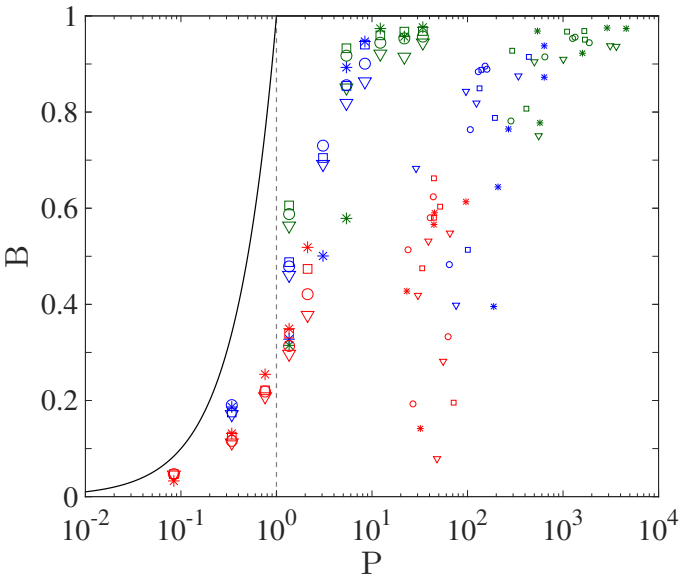

Figure 3.14: Comparison of optimized brilliance transfer obtained, B, and ratio P between incoming and required phase-space volume size, for the guides in appendix A.4. Here the guides are assumed truly focusing and the entire incoming phase-space size volume is expected to be useful. The solid black line is the maximal performance achievable according to the MP under the stated assumptions. The marker symbols are explained in table 3.1.

feeder followed by an ellipse, but it is still surprising that most feeder guides received phase-space volume sizes more than a factor of hundred over the theoretically needed. It can be argued that a higher coating m-value would cause the guides without feeder to approach the theory line, but it is hardly relevant as expensive $m = 6$ coatings are used.

In figure 3.15 a similar plot is made, but using $Y = 1$ in (3.1.14), corresponding to guides without any focusing ability, which thus need a larger phase-space volume, decreasing the value of P for each guide. Under these assumptions P will also depend on the distance between the end of the guide and the sample L_S, which is 50 cm in all cases shown here. It is worth noting that the difference between the needed phase-space volume in the focusing and multiple reflecting case is proportional to this distance.

The guides without feeder have brilliance transfer which surpass the theory for lower values of P, either because of focusing or higher efficiency from inhomogeneous illumination of the sample.

The brilliance transfer for the guides without feeder saturates close to $P = 1$. This is the most important prediction of the theory. Had a guide of this geometry been designed to be at $P = 1$, it would be able to achieve a brilliance transfer of approximately 95%, where solutions with $P = 10$ are only a few percent better. To obtain these last few percent in brilliance transfer one would have to accept a 10 times increase in neutrons that enters the guide, and thus almost 90% of these would have to be absorbed along the guide or in slits

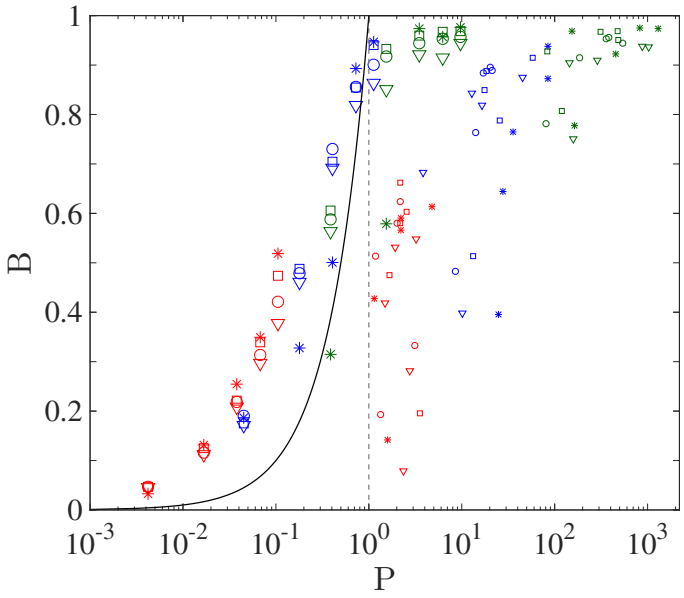

Figure 3.15: Comparison of optimized brilliance transfer obtained, B, and ratio P between incoming and required phase-space volume size, for the guides in appendix A.4. Here the guide is assumed multiple reflecting and the entire incoming phase-space size volume is expected to be useful. The solid black line is the maximal performance achievable according to the MP under the stated assumptions. The marker symbols are explained in table 3.1.

near the instrument which will only contribute to unwanted background.

The guides that use a feeder are not close to the theory line. This implies that they are not particularly efficient in terms of the amount of neutrons accepted by the guide to reach a certain brilliance transfer. If the optimizer system is not punished for the over intake, it is clear that very large intake values can be obtained. If the minimalist concept was used to optimize such a guide, the constraints would force the guide to be more conservative with the phase-space intake, and most likely find solutions closer to the theory line, but probably with lower brilliance transfer.

3.1.4 Discussion

Using the MP changes the way a guide is designed. There are several new choices to be made and consequences which should be understood. This section will discuss the problems it solves as well as the problems it generates.

Performance

Guides optimized without the MP have every geometrical parameter available to the optimizer. Thus the minimalist optimization will happen in a subspace of the parameter space and should therefore not be able to surpass this method in terms of brilliance transfer on sample. The success of the MP depends on its ability to select a parameter space which ensures minimal background while still allowing for performance close to the global optimum.

From the comparison between a guide optimized with the MP and without, we clearly see the expected increase of signal to noise, mostly for higher wavelengths as it becomes possible to transport neutrons with divergence beyond the requested. This excess divergence is however avoided when using the MP. The increase in signal to noise from the MP thus starts at the wavelength where the typical reflections for reaching a divergence higher than FOM are within the critical scattering vector of the supermirrors, making the relevance of the MP highly dependent on the FOM, mirror choice and wavelength band.

From the acceptance diagrams we see behaviour close to the theoretical prediction for $Y = 1$, meaning the guides are not focusing. The loss in performance when using the most aggressive background suppression, $k = 1$ was only 20% when averaging over the relevant wavelength band, and with the slight increase to $k = 1.25$, we see a performance loss of less than 10%.

The scan of the illumination factor k showed the expected results when using $Y = 1$, as a plateau occurred where additional incoming neutrons did not add significantly to the brilliance transfer. Furthermore, the point at which this happens was close to the theoretically predicted from the MP. The scan with $Y = 0$ did not correspond well to the theory, which can be explained either by the used guides not being focusing, or a failure of the theory to accurately describe the data in this limit.

The MP was used to view data from a previous publication A.4 in a different way, and showed that while the addition of a a parabolic focusing element before the pulse-shaping chopper does increase brilliance transfer, it is also very inefficient in terms of the ratio between neutrons entering the guide, and arriving at the sample. The guides without a focusing element were much closer to the theory, but again only when they were considered multiple scattering ($Y = 1$), and in this case the MP accurately predicted the optimal neutron intake. The brilliance transfer as a function of intake was surprisingly sharp, as just a small decrease from the optimal value would lower performance drastically, while a small increase would have little effect.

Advantages and disadvantages

The MP as presented here is per construction used to find the limit where only an ideal guide would be able to deliver the perfect result, here being a brilliance transfer of unity. It is the task of the optimizer to find such a solution, and it may not even be in the given parameter space.

Since the brilliance transfer is limited to be less than unity, it is very clear from the optimization results if the guide is close to the optimal. In the case where the brilliance transfer is not satisfactory, it is possible to increase the size of the incoming phase-space volume with the illumination factor, k. If the FOM increases when the guide is supplied a larger phase-space volume ($k > 1$), this may be necessary. If the FOM does not increase, the limitation could be insufficient coating quality. This makes it imperative to calculate the brilliance transfer and not just the intensity on sample, as the brilliance transfer indirectly shows the losses in the guide, when $k = 1$.

Working in units of the illumination factor will make it easy to balance between efficient low background guide (k close to unity) and over-illumination of the guide entrance which give higher performance and background (larger k). Without this information, the optimizer will search among guides with vastly different efficiencies, or a needlessly restricted parameter space.

Using the MP will stop the optimizer searching among guides which do not receive sufficient phase-space ($k < 1$) to obtain the maximal FOM. Experience with very small moderators does, however, show that $k < 1$ can be beneficial, as $k = 1$ can lead to unreasonably large guide entrances that results in high angles of incidence, meaning the goal of a brilliance transfer at unity is unrealistic in any case.

Selecting a reasonable value for the focusing parameter Y before an optimization is necessary, as letting this parameter be determined by the optimizer will almost certainly result in the uncorrelated value $Y = 1$, because this will allow both higher signal and background, where the FOM only considers the signal. When using a FOM that punishes background intensity, it may be reasonable to let the focusing parameter be a free parameter. A classical straight guide with parallel mirrors will not focus in any way, and thus needs $Y = 1$, where the Selene type guide system [28] is truly focusing and can still perform perfectly with $Y = 0$. In addition this consideration should include the size of the moderator, which e.g. in the case of a single ellipse will determine the correlation between position and divergence necessary for fully exploiting the focusing abilities.

In addition there are real-world problems to consider when recommending building a

guide on the limit of what is possible in terms of efficiency. Misalignment of guide segments in a guide designed without the MP is not problematic with todays precision [73]. When designing a guide with the MP and a minimalist factor of $k = 1$, the guide will not be over-illuminated, and thus any amount of phase-space lost will decrease performance. Because of this it is advised to check guides designed using k close to 1 for sensitivity to alignment, which may be improved by increasing the value of k.

In any case the simple equations derived for the MP will help understanding the consequences of pre-selected parameters. For example how the distance between the sample and guide will affect the signal to noise ratio for a multiple reflecting guide. Reducing this distance improves the efficiency of such guides, especially for small samples, as it lowers the required phase-space volume size. This fact may be missed in usual optimizations.

3.1.5 Conclusion on Minimalist Principle

Basic constraints on the geometrical parameters describing a neutron guide to be optimized was derived under the assumption of a FOM at the sample position which have limits in both position and divergence. These constraints ensure that only a minimal amount of neutrons are allowed to enter the guide while still allowing for a performance close to the theoretical limit. It was shown to be practically applicable in realistic examples using Monte Carlo ray-tracing simulation, where it was demonstrated that the resulting guides clearly limit excessive divergence, even at higher wavelengths, while suffering very little performance loss.

3.2 guide_bot

Here, the automatic guide optimizer guide_bot is presented. The purpose of the software is to reduce the time spent programming when setting up neutron guide optimizations, as this allows for investigation of a much wider array of guides in the same time frame. The resulting guides are all analyzed and can be easily compared. The software is used by scientists at the European Spallation Source, the Paul Scherrer Institute, and National Institute for Standards and Technology.

This section is based on the paper in appendix A.2, which is accepted for publication in Nuclear Instruments and Methods A, and have been adapted to fit the context of the thesis.

3.2.1 guide_bot overview

The main task of guide_bot is to quickly optimize the geometrical part of neutron guides and a specified overall geometry and FOM. This is accomplished by having the program read a simple input file describing the problem and generate the code needed to complete that task; which will in turn solve the original problem when the generated code is compiled and executed. guide_bot itself runs in MATLAB, but the generated code is in multiple programming languages linked together by scripts that are easily executed. The required ray-tracing simulation is performed using the generated McStas instrument file that describe the desired guide system. Generated iFit scripts control both the guide optimization and visualization of results.

MATLAB was selected because it has the necessary plotting functionality, and is widely used in the community. The add-on iFit [67] enable control of McStas through MATLAB, and has comprehensive optimization libraries. The clusters available at the ESS Data Management and Software Centre and Paul Scherrer Institute Scientific Computing group both use the queue management system SLURM [74] which is supported by guide_bot.

The following sections will describe the important parts of the code and the use of guide_bot.

guide_bot input file

The input file is a short MATLAB script the contents of which the user will edit to correspond to the desired guide geometry and optimization. The mandatory input consists of describing a FOM, which here refers to a closed phase-space volume, meaning a fixed area, divergence range and wavelength range. The average brilliance transfer 2.1.16 is calculated by normalizing the density of one phase-space volume with the density of the same same phase-space volume placed at the source.

The total length between source and sample is fixed as is the distance between guide-end and sample. The distance between source and guide start is optimized, however the user must define the interval of allowed starting distances.

A homogeneous rectangular source is always used for calculation of brilliance transfer, and the dimensions of this source are given as input. In addition, a more realistic source is chosen which is used for calculation of the absolute intensities. In most cases the optimization is performed on the rectangular source. However the optimization can be performed on the ESS TDR and Butterfly sources [2, 16] including optimizing the angle at which the guide views the moderator. Optionally, the optimization can be performed on the rectangular source, and the optimized guide is then placed on the realistic source where only this angle is optimized.

The guide geometry is described using a character string, which corresponds to a linear succession of guide elements. The following input string will generate an optimization of a guide consisting of a straight section using flat mirrors, a curved guide section and finally an elliptic guide section.

```
S C E
```

A single part of such an input string (separated by spaces) is referred to as a module, and the currently available modules in guide_bot are listed in table 3.2.

Module	Explanation	McStas component
S	Straight guide	guide_gravity
E	Elliptic guide	Elliptic_guide_gravity
P	Parabolic guide	Elliptic_guide_gravity
G	Gap	Arm
K	Kink	Arm
C	Curved guide	Bender
Slit	Slit	Slit
Selene	Selene guide	Elliptic_guide_gravity / Arm / Slit

Table 3.2: The available modules of which an input string describing a guide can be assembled.

In the example, no details other than selecting the sequence of guide elements are given. Hence, the resulting guide optimization will have all possible geometrical parameters for the 3 modules as free parameters in the numerical optimization. This may not be appropriate for a particular application, as certain constraints could be needed. These are incorporated for each module by adding options. In the following input string, such options are used to constrain the optimization, both by adjusting the optimization limits and by locking certain parameters.

```
S(maxStartHeight=0.1) C(maxlength=20,start=6.5,StartWidth=0.03) E
```

This input string adds a height limit to the start of the first straight section of 10 cm and locks the starting position of the curved section to 6.5 m from the source. Furthermore, the width of the curved guide at its starting position is locked to 3 cm, while its length is limited to a maximum of 20 m. The full list of available options is described in the manual distributed with the software [16].

If an input string contains a curved section or a kink, both commonly used to break line of sight through a guide, guide_bot will assume breaking line of sight is the intention and dynamically select a curvature or angle deviation just sufficient to break line of sight between the start and end of the full guide. The guide curvature or angle deviation will thus depend on, for example, the guide width and where in the guide the curved section is placed. It is possible to adjust this behaviour by selecting, e.g., a smaller section of the guide line of sight should be broken over or to break line of sight multiple times in different sections. This system can be disabled by selecting suitable options.

McStas instrument file

The McStas instrument file contains the necessary input parameters in the basis appropriate for the numerical optimizer, and the code for transforming these parameters to the type needed for the individual McStas components. The instrument file also contains a piece of ray-tracing code that will control how line of sight is broken for this particular user input.

Each of the modules used in the geometry input string will typically correspond to a single instance of a McStas component in the instrument file, and the components used for each module are listed in table 3.2.

Most of the written McStas instrument file is intended to be human readable, especially the trace section containing the McStas components. The initialize section containing the transformation of the parameter space and the added ray-tracer is, however, not meant to be changed by the user.

When optimizing a guide that eliminates line of sight, many geometrical parameters influence whether line of sight can be drawn or not. A short algorithm written to the McStas initialize file is used to check if the guide blocks line of sight. Instead of providing the curvature as a free parameter in the optimization, the McStas file will find the smallest curvature that will eliminate line of sight. This is achieved by starting with a nearly straight guide and increasing the curvature until line of sight is blocked. By default line of sight is broken between the start of the guide at the moderator and exit at the sample, but line of

sight can be broken between two points specified in the options for the relevant modules. In addition, line of sight can be broken several times, as long as the sections do not overlap. Line of sight can be broken over multiple curved sections, in this case the ratio between their curvatures is optimized as a free parameter. The importance of this is that all guides compared by the optimizer will have similar background characteristics, which is chosen by the user, instead of a large variation in background suppression.

Reflectivity curves

Since the neutron ray-tracing is performed by McStas, the reflectivity models available in guide_bot are those implemented in most McStas components. There are two models available, a fully adjustable first order model, and a second order model with only the m-value as a free parameter. These are briefly described in 2.1.14.

In order to show the robustness of optimized guides, the performance is evaluated both with the selected mirror quality and an artificially degraded description, where the m-value is reduced by 20%, and the reflectivity slope is increased by 40%. When using the second order reflectivity model there is however no parameter describing the slope, so only the m-value is reduced and in most cases this actually decreases the reflectivity slope which should be kept in mind.

iFit optimization

The iFit files control the generated McStas files by setting up a numerical optimization using the appropriate parameter space and a particle swarm optimization algorithm. All variables to be optimized are specified with their constant limits, meaning that the limits do not depend on values of other parameters. A numerical optimization takes place in a parameter space, and it is an important choice which parameter space is used. As the optimizer will take a range for each parameter to be optimized, and these are considered independent, it is necessary that every possible value in these ranges corresponds to a valid guide geometry, regardless of all other selected values. This is no problem for the width and height of all guides, but for example the horizontal(vertical) small axis of an elliptic guide can be problematic, as it can not be lower than both the start and end width(height). In the same way the lengths of the modules have an overall constraint of keeping a total guide length fixed.

The parameter space including all geometrical variables to be entered into the McStas components is referred to as the full parameter space, here with N dimensions. A number of constraints, k, is taken into account. These originate from the basic guide problem, but can also be given by the user through options in the input string. A space with dimensionality $N - k$ is created where all points adhere to these constraints, and this is called the reduced parameter space. In this reduced parameter space, the limits on each parameter may depend on the value selected by another, which as discussed is not allowed. The solution used in guide_bot is to transform this reduced parameter space to a box parameter space of the same dimensionality where all limits are independent of the values selected of the other parameters. The McStas file then needs to transform from this box parameter space to the full parameter space for every point in the optimization.

After the optimization is done in the box parameter space, the resulting optimal guide geometry description is used to run further McStas simulations to provide data for a thorough description of the guide performance.

Data visualization

The resulting data is visualized by running the generated MATLAB/iFit plotting script. This will provide figures describing performance of the guide in terms of brilliance transfer as a function of wavelength, divergence, and position. If a user specifies a source that provides absolute intensities, the guide performance will also be visualized using these units. In addition, the optimal guide geometry will be visualized.

The steps of a guide_bot run

The steps needed to run an input file and analyse the resulting data using guide_bot are fairly straight-forward:

- Create an input file with the described information
- Run the input file in MATLAB
- Send the generated folder to a supported cluster
- Run the bash script launch_all.sh
- Let the jobs complete
- Download the output folder to your own computer
- Run the analysis script to obtain the guide performance

One input file may contain only one FOM, but many input strings, making it easy to compare a selection of different geometries that are all optimized to the same FOM.

3.2.2 Examples

Here results on validation against earlier work is shown followed by two examples of guide_bot runs. The first example demonstrate the ability of guide_bot to optimize a complicated guide, while the other demonstrates how a range of optimizations can be used to evaluate the impact of the figure of merit.

Validation against earlier work

In order to validate that guide_bot works as intended, a guide optimized for an earlier publication is recreated using the software. In appendix A.4, guides consisting of a parabolic feeder that constrain the beam to a certain pinhole size followed by an elliptic guide were systematically optimized for different figure of merit. A 150 m guide is optimized for a 1×1 cm^2 sample with a $\pm 1.0°$ divergence requirement and a 3×3 cm^2 pinhole at the chopper position. The coating distribution used in the original paper was $m = 6$ in the feeder and start/end of the ellipse, with $m = 3$ in the middle part of the ellipse. However as guide_bot does not support such a distribution, it uses a $m = 6$ coating in the entire guide. This is not considered important, as the coating model used have the same reflectivity at low q regardless of the m value, and the center of the ellipse will only have low q reflections at the compared wavelength interval. A comparison between the results is displayed in figure 3.16, that shows excellent agreement between the two.

Single guide

An example of a single guide optimization is presented in order to demonstrate the ability of guide_bot to produce a highly performing guide from input with a limited information. Here the FOM was chosen to be a 1×1 cm^2 sample with a divergence requirement of $\pm 1.0°$ in the horizontal direction, and $\pm 0.75°$ in the vertical direction. The guide is optimized for brilliance transfer in the wavelength range $2 - 4$ Å. The distance between source and sample is chosen to be an ESS-relevant value of 160 m, while the distance between guide-end and sample is 40 cm. This guide uses an $m = 3$ coating everywhere simulated with the default coating model. The guide was optimized on an rectangular source, and the optimized guide was then placed on the 3 cm tall ESS Butterfly moderator where only the angle with respect to the moderator was optimized. The optimization was repeated 5 times and the one with highest FOM is presented here.

The investigated guide consists of a elliptic extraction that narrows to benefit a chopper at 7 m from the moderator with a width of 3 cm, a linear section that expands the beam before an S curved section to remove line of sight and a double ellipse with a kink in between

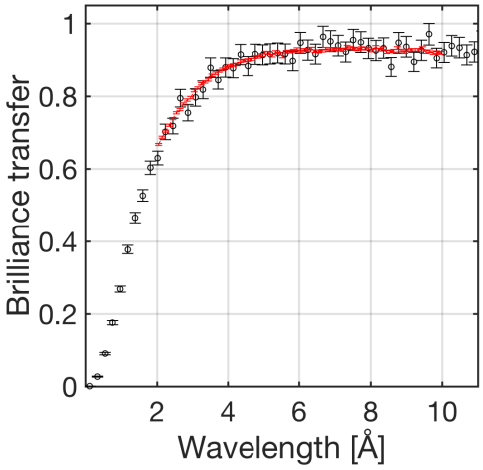

Figure 3.16: Brilliance transfer dependence on wavelength for optimized guides, the red from the original paper A.4 and black remade using guide_bot (simulated in a larger wavelength interval).

at the end. Line of sight is broken between the start of the guide and the end of the first curved module, and from the point where the curved guide changes direction of curvature and the guide end. This geometry is described with the following string:

```
E(max_smallaxis=0.1) G(start=7.0,StartWidth=0.03,length=0.1)
  S(maxStartWidth=0.06) C(los_divide=1,rots=-1) C E(minlength=20) K E
```

This is a complicated geometry, and only a few options have been used to constrain the parameter space, meaning the optimizer is given a difficult task.

The optimized guide geometry is shown in figure 3.17, and the characterization in terms of brilliance transfer is shown in figure 3.18.

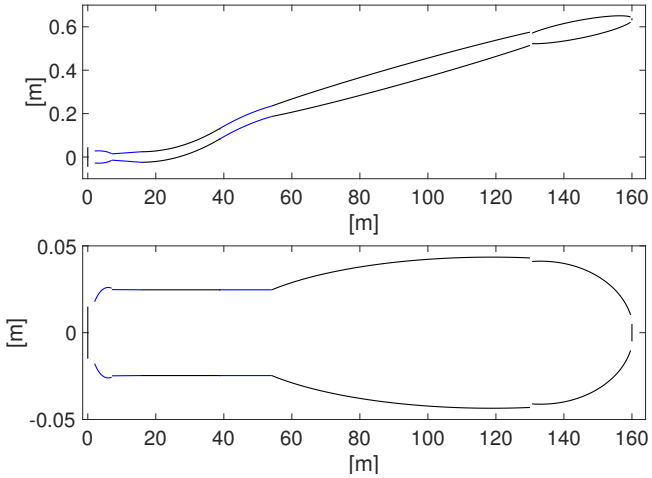

Figure 3.17: Geometry of the guide that delivered the highest brilliance transfer for the chosen FOM. Top panel is a top view, while the lower panel is from the side. The moderator is shown to the left side and the sample to the right side of the panels.

From the guide design it is intuitively clear that all parts contribute to neutron transport, making the design reasonable, but it does not resemble what would be made manually. The overall brilliance transfer is however high (about 55% at 3 Å) considering the beam requirements, small moderator height, limited coating quality, pinhole and that the guide

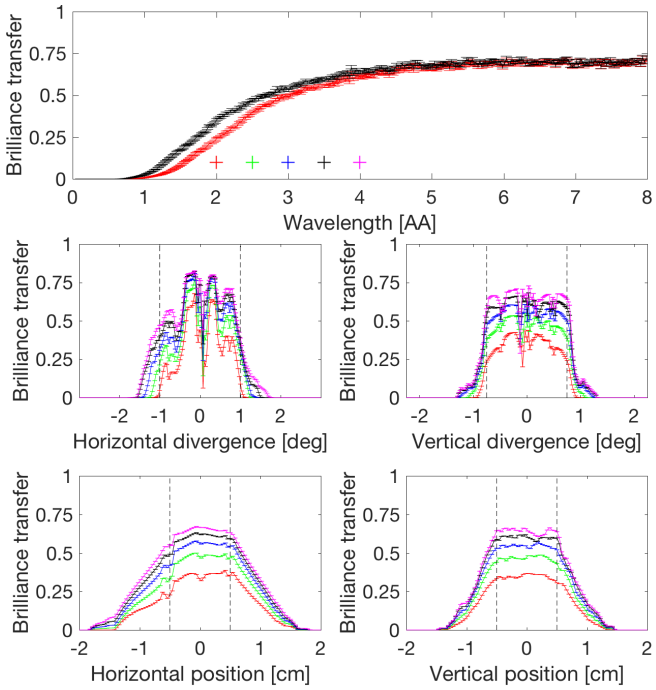

Figure 3.18: Overview of performance of the guide from Fig. 3.17 in terms of brilliance transfer on rectangular source. Top panel contains wavelength dependence, both for the requested mirror quality (black) and degraded mirror performance (red). In the remaining panels the horizontal and vertical divergence distributions as well as spatial distributions are shown for wavelength snapshots between 2 and 4 Å that corresponds to the markers in the top panel. The dashed lines show the edges of the FOM area.

breaks line of sight twice. The divergence distributions have dips and are asymmetrical, but follows the FOM very well with high brilliance transfer within, and fairly steep drops outside. The spatial distributions are more smooth, and relatively constant within the sample area.

In figure 3.19 the two-dimensional position and divergence distributions are shown, and it is again clear the optimized guide provides a beam that matches the provided FOM, but has some structure especially in the divergence space.

Acceptance diagrams are shown in figure 3.20 where the unwanted beam structure is most obvious. Two of the FOM corners are perfectly aligned with the edge of the acceptance diagrams, which is due to the dimensions of the guide-end being calculated using phase-space considerations as explained in section 3.1.2.

Figure 3.21 shows the intensity on sample relative to the total intensity leaving the guide-end, and thus provides an idea of the efficiency of the guide in terms of background generated in comparison to neutrons on sample. This particular guide has around 30% of the guide output that make it to the small sample, and in the FOM wavelength interval of 2-4 Å about 25% of the intensity from the guide hits the sample and fall within the divergence requirement.

The performance of the optimized guide on the ESS Butterfly moderator can be seen in figure 3.22. Here the beam quality is more problematic in the horizontal direction, as the structure from the more complicated source affects the result. Had the guide been optimized directly on the Butterfly moderator instead of the rectangular source, the guide geometry could have been adapted to this source. The two-dimensional position and divergence plots, and the acceptance diagrams are also created for the realistic source, but are omitted here.

With such a comprehensive description of the delivered beam for every optimized guide, the user can easily select the ones most appropriate for their instrument and continue to build on those designs.

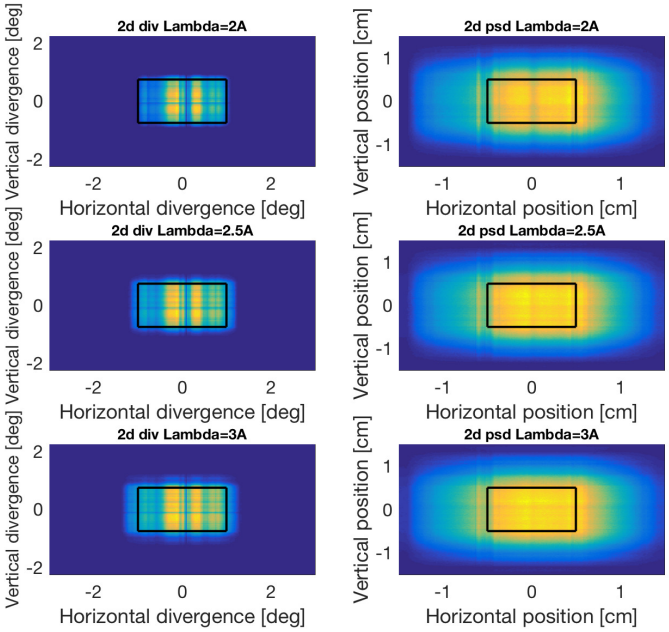

Figure 3.19: Two dimension spatial and divergence distributions for wavelength snapshots, here 2.0 Å, 2.5 Å and 3.0 Å, where the black box correspond to the FOM. Diagrams at the remaining wavelength snapshots have been omitted.

Scan of input parameters

In many situations it can be relevant to perform a scan over a range of a parameter in the FOM, as the FOM may be not be completely known in advance. Here, a guide is optimized for a horizontal divergence of $\pm 0.75°$, while the vertical divergence is scanned from $\pm 0.5°$ to $\pm 1.5°$. It is currently possible to scan sample dimensions, divergence requirements and moderator dimensions. The sample size used here is 1×1 cm^2, and the selected wavelength range is $1 - 2$ Å. This guide has 160 m between moderator and sample, and 40 cm between guide-end and sample. The McStas standard reflectivity model was used with $m = 3$ for the entire guide. The guide is optimized for a rectangular source of 10×3 cm^2, and the realistic source chosen was the 3 cm tall ESS Butterfly moderator, where only the viewing angle towards the moderator was optimized. The rectangular source size was chosen to resemble the dimensions of the cold part of the Butterfly moderator projected onto the used beam port.

The geometry is described by the following string, which correspond to a parabolic feeder that narrows the beam to 3 cm in width, an elliptic defocusing section, a curved guide and an elliptical focusing section. The gap for the chopper is forced to 10 cm length and the defocusing section is limited to a maximum of 6 cm starting width.

```
P G(start=7.0,StartWidth=0.03,length=0.1) E(maxStartWidth=0.06) C E
```

The optimization was repeated 5 times, and the best result used in order to decrease uncertainties, as it may be caught by local optima in the large parameter space. The optimized guide geometry for a vertical divergence of $\pm 1.0°$ is shown in figure 3.23.

An overview of the results is given in figure 3.24. It is expected the brilliance transfer will decrease with increasing divergence requirement as a larger phase-space volume need to be filled. It is important to notice the final intensity on sample is optimal from about 0.9° divergence requirement, but decreases at the highest divergence requirements.

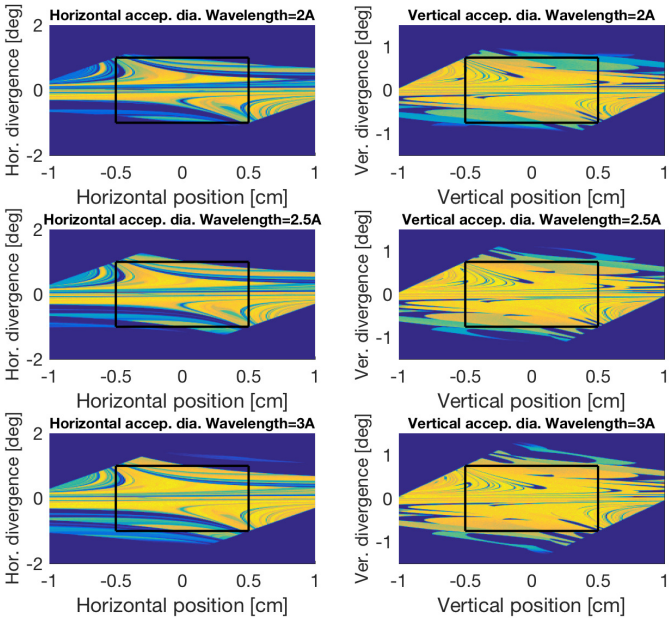

Figure 3.20: Horizontal and vertical acceptance diagrams for wavelength snapshots, here 2.0 Å, 2.5 Å and 3.0 Å, where the black box correspond to the FOM. Diagrams at the remaining wavelength snapshots have been omitted.

3.2.3 Existing use of guide_bot

Early versions of guide_bot have already been successfully used for several projects, mainly in connection with the ESS. For BIFROST A.7, HEIMDAL A.8, VESPA A.9 and ESPRESSO [71] the proposed guides were designed using guide_bot, while the MIRACLES [7] guide had brilliance transfer calculations done using guide_bot. Of these instruments, BIFROST, HEIMDAL, VESPA and MIRACLES have already been accepted for construction.

A workshop focusing on the use of guide_bot was organized by the Paul Scherrer Institute (PSI), and held in 2015. The software has been used in connection with a PSI guide upgrade project.

3.2.4 Discussion

Discussion of results

In section 3.2.2 it was shown that guide_bot could replicate a published optimization result. The similarity between the results are expected, as guide_bot merely simplifies such tasks by generating the needed code instead of it being written manually.

In the scan over vertical divergence, it was expected that the intensity on sample would increase with increasing vertical divergence requirement, but as seen in figure 3.24 this trend breaks down at the highest vertical divergence values. There are several possible explanations for this behaviour.

Since the dimensions of the guide-end are calculated from the divergence requirement, (3.1.2), the result may be suboptimal when the vertical divergence requirement is larger than what is reasonable from the small moderator.

As the FOM of the optimization is the average brilliance transfer, the entire wavelength interval is weighted equally, but the realistic source used to calculate the intensity has a different wavelength distribution. The decrease in intensity at higher divergence requirements could thus also be explained by the optimization naturally being impacted more by higher wavelengths at large divergence requirements, while the thermal ESS Butterfly spectrum have higher intensities at the lower part of the wavelength range.

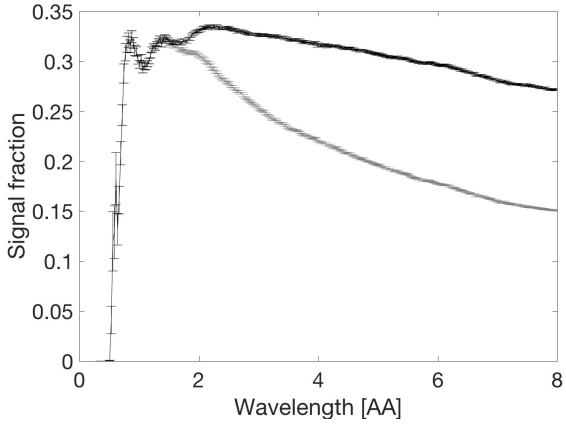

Figure 3.21: Fraction of intensity delivered by the guide on sample (black) and on sample while within the divergence limits (grey), both as a function of wavelength.

It is however also possible that the optimization is more difficult for larger divergence requirements, and that those solutions on average are further away from the true optimum. This should be investigated further.

User experience

The main goal of the program is to reduce the time spent coding between getting an idea for a guide solution and obtaining the performance of this guide optimized for a specific case. This has been achieved using code generation, meaning the user can write a relatively short and simple input file, and guide_bot will then generate the much larger amount of code needed to solve the original problem. Reproducing the examples in this paper by recreating the input files should take less than 10 minutes for a user familiar with MATLAB but not necessarily iFit or McStas.

It was considered a top priority to make guide_bot as simple to use as possible, in order to reduce the time required to learn the software, and thus allow the relevant people to design guides. Traditionally, the job of designing a guide takes months of work, and thus the amount of geometries to be investigated has been limited. Making the job faster allows for a wider range of geometries to be investigated, which will hopefully result in a better match with the instrument backend. In addition, the ease of use is extended to running on a cluster, as the optimizations are computationally heavy. The widely spread use of guide_bot on ESS projects indicates the usability of the code.

It has been a goal to keep the software modular, meaning it should have a core that is not seen by the user, and then much simpler module files that describe each type of possible guide section. The core of the program then provides the functions and routines necessary for simple module files. This has largely succeeded. However the routines for drawing the geometry of the optimized guide are part of the core instead of each module, which is a deviation from the modular philosophy. This approach makes it possible for users to contribute the majority of code for a new module, but requires the developer to add the code for plotting the geometry in the core for each addition. In similar fashion, some work may be required from the developer to include new modules in automated elimination of line of sight.

Simplicity and flexibility

The underlying software McStas was originally introduced as an alternative to writing a complete Monte Carlo ray-tracing simulation for neutron scattering from scratch, and thus provided an easier solution with less flexibility for the user. McStas still covers a great

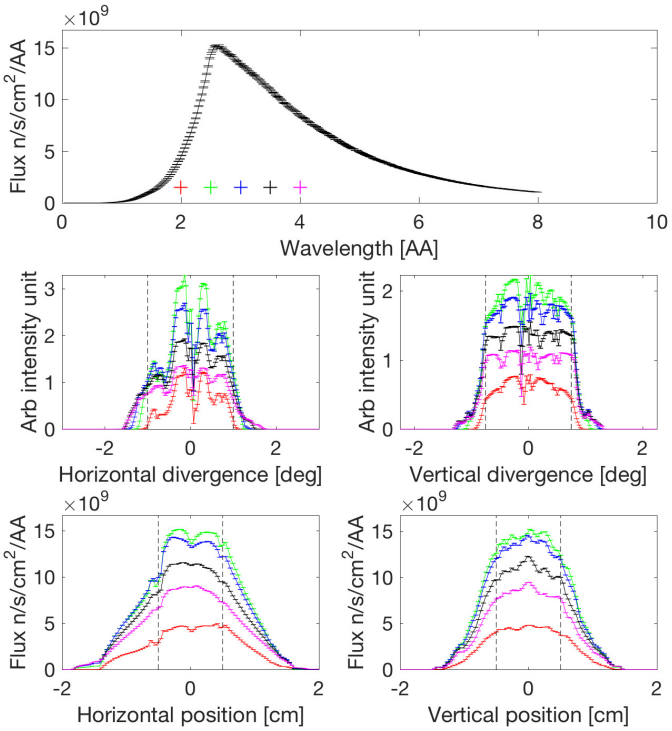

Figure 3.22: Overview of performance of the guide from Fig. 3.17, positioned on the ESS 3 cm tall Butterfly moderator. Top panel contains wavelength dependence for the requested mirror quality and markers for the wavelength snapshots used in the remaining panels. In the remaining panels the horizontal and vertical divergence distributions as well as spatial distributions are shown for wavelength snapshots that corresponds to the markers in the top panel.

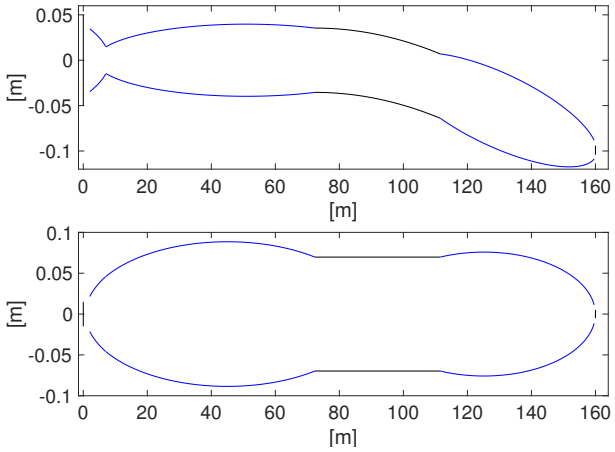

Figure 3.23: Guide geometry that delivered the highest brilliance transfer for the FOM with $\pm 1.0^\circ$ vertical divergence requirement. Top panel is a view from above, while the lower panel is from the side.

amount of possibilities, but in order to achieve the simple interface and fast performance, it has limited the infinity of options available in the C programming language.

In the same way, guide_bot simplifies the task of writing a numerical guide optimization by removing most of the flexibility that McStas and iFit provides. The simplicity of guide_bot

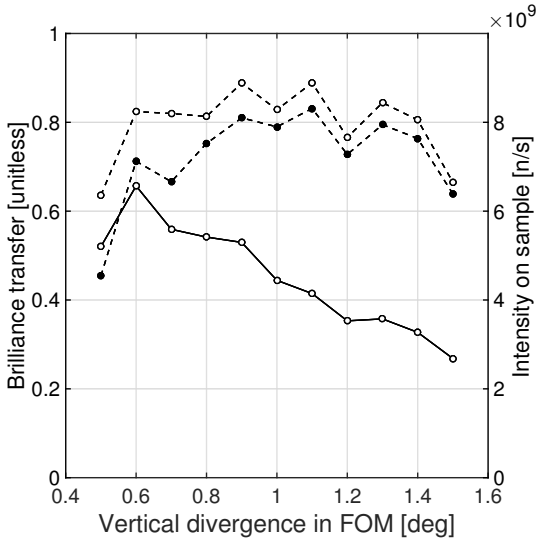

Figure 3.24: Brilliance transfer (full line, left axis) and intensity (dashed lines, right axis) for guides optimized for figure of merits with different vertical divergence requirements. The intensity results with white centers are for all neutrons that hit the sample, while the filled markers correspond to all neutrons that hit the sample and are within the divergence requirements of the appropriate FOM.

is only possible because it assumes that the user wants to optimize a guide, and that it only contains guide pieces that have been described in this context. It is thus not an attempt of replacing McStas or other tools for guide design, but to allow users whose task is within the capabilities of guide_bot to finish the task much more quickly than otherwise.

Depending on the progression of the overall instrument and facility design, the amount of a priori knowledge about the guide can vary greatly. At early stages, there will be almost no limits to the possible geometries, and in the later stages there can be a large amount of constraints to fulfil. Using guide_bot it is possible to handle these levels of a priori knowledge. This is accomplished by the options associated with each module in the input string which allow for modifying ranges for optimization or fixing certain parameters. For this reason, guide_bot can be used in most stages of the design process, but is less suitable for the final stages as it lacks the flexibility of McStas to add details.

As each task is still unique, it is important that the user can edit the McStas files generated by guide_bot to add aspects guide_bot is not able to handle. The generated McStas and iFit files are done in such a way that editing and adding to them is user friendly, and can even be a good starting point for learning to use those programs.

Outlook

As guide_bot currently only optimizes parameters describing the geometrical aspects of the guide, the next step is to include optimization of the coating distribution. Here, the resulting number of free parameters is a concern and may require the optimization to be split into several parts with some iteration between them, for example optimization of geometry and coating distribution separately. Initial work has started along this direction [75].

In addition new modules are expected to be added, for example a half ellipse module.

3.2.5 Conclusion

The program guide_bot is presented which significantly reduces the work of programming neutron guide optimizations in cases where the overall geometry can be described in the provided input scheme. This allows a comprehensive comparison between a large number of different possible guide geometries optimized for the specific instrument to be made with little effort.

Validation was performed against an earlier publication, showing that the simple guide_bot optimization yields an overall performance in agreement with the published result.

The software was demonstrated, showing that a complicated guide with a low number of constraints could be optimized to the specified figure of merit, resulting in a guide solution with high performance albeit some issues with beam quality. A scan of optimizations over the vertical divergence requirement was performed to demonstrate how such data sets can contribute to selecting the final figure of merit for an instrument.

Recently, guide_bot has been used for a wide range of tasks, successfully designing guides of several instruments accepted for construction at ESS.

3.3 ESS moderator height survey

The choice of moderator for ESS was an urgent process. Discoveries in moderator technology revealed the possibility for a large increase in brilliance for smaller moderators [5], yet limited time was available before the construction schedule would be delayed. All instrument teams were called upon to reoptimize their guide systems for a range of new moderator geometries in order to evaluate which moderator would provide the best performance for the instrument suite as a whole. Only few instrument teams were, however, able to find the time necessary for the large task, and so I was hired to use guide_bot to optimize guides for the remaining instruments. All optimizations were performed in accordance with the wishes of the instrument teams with respect to delivered beam parameters and constraints for the guides.

This section provides a summary of the work done on finding the optimal moderator height assuming use of the pancake moderator design. The complications of bi-spectral extractions are neglected, as these affect the horizontal direction. As the guide performance was calculated in terms of brilliance transfer as a function of wavelength, the resulting data set could be adapted for other spectra as a function of height. Similar work was performed on moderator widths, but these results are not presented here. The ESS management used the data generated by guide_bot as well as from participating instruments teams to choose the Butterfly moderator candidate for ESS with a height of 3 cm.

3.3.1 Moderator alternatives

Here a selection of the moderator candidates put forth by the ESS target group are briefly described in chronological order. The Butterfly moderator, which was eventually selected as the first ESS moderator, was only proposed after most of the moderator height survey was completed. The Butterfly moderator mainly affected the horizontal part which is not presented here. An illustration of the geometry of the relevant moderators are shown in figure 3.25. The spectra of the TDR and a few pancake moderators with different height are shown in figure 3.26.

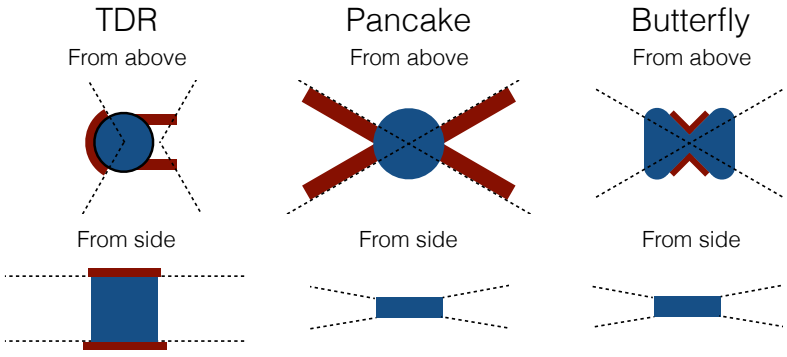

Figure 3.25: Illustration of the TDR, pancake, and butterfly ESS moderator candidates. Blue areas mark cold moderator consisting of para-hydrogen in all cases while red identifies water used as thermal moderator. The viewing angles of each moderator are depicted using dashed lines.

TDR

The baseline moderator was designed in preparation for the ESS Technical Design Report, and most early instrument proposals were optimized for this moderator system. The TDR moderator system consists of two identical moderators servicing a 60° arc in both directions with one moderator above and one below the target. The cold moderator used para-hydrogen and had a viewable surface of 12×12 cm^2, while the thermal moderator using water had the

same viable surface. The two moderators were positioned next to each other in the horizontal plane in order to facilitate bispectral extraction.

Pancake

The ESS target group found that a drastic change in moderator design philosophy could lead to a large increase in cold moderator brilliance, as described in [5]. Reducing the moderator height increased the amount of reflector material, and the used reflector material could be closer to the target. Moderators as low as 1 cm tall were found feasible. This discovery led to the design of the pancake moderator consisting of a large flat cold para-hydrogen moderator with a radius of 24 cm, and water "wings" on each side with a length of 18 cm. It was possible to allow for 120° viewing angle for these moderators, while the moderator could serve beamlines on both sides. The brilliance of the source varies significantly with moderator height as shown in figure 3.27. One of the effects responsible for the increased source brilliance is dependent on the scattering cross section for para-hydrogen decreasing sharply for very low energy neutrons. As this effect is only beneficial for the cold moderator, this source display the biggest gains for low moderator heights.

Butterfly

Further advances in moderator design led the ESS target group to the butterfly moderator design, which had an overall more complicated shape. The moderator vessels remained liquid para-hydrogen and water, but the thermal water moderator is now in the center with cold wings around. The complicated shape of the cold wings results in different perceived cold moderator widths for different beamports.

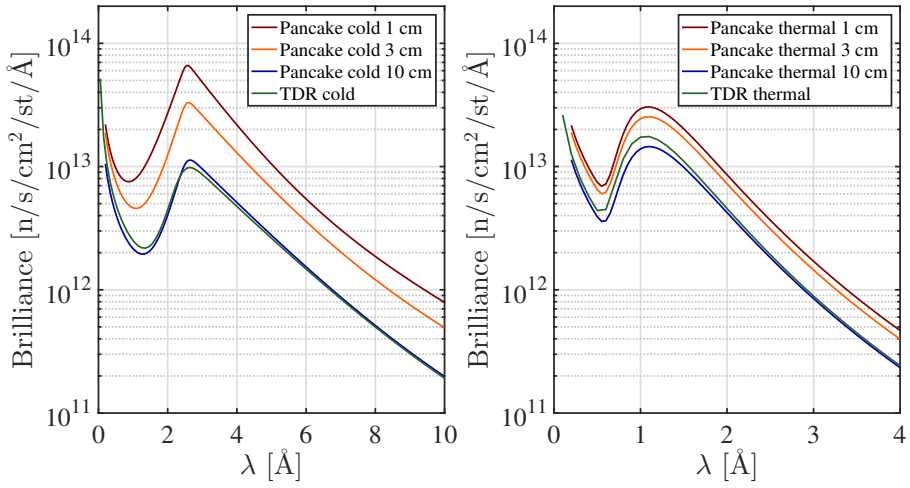

Figure 3.26: Brilliance as a function of wavelength for the TDR moderator and 3 different versions of the pancake moderator with different heights. Left shows the spectrum from the cold part of the moderator, while the right side shows the spectrum of the thermal part of the moderator.

3.3.2 Doughnut

When considering the different moderator candidates, it is also relevant to investigate if starting the guides closer to the moderator influences the result. When the guides extend closer to the moderator, the heat load increases, and technical difficulties arise from guides being very close together. Since the moderator is wider than it is tall, the benefit of having the top and bottom of the guide close to the moderator is much greater than for the sides,

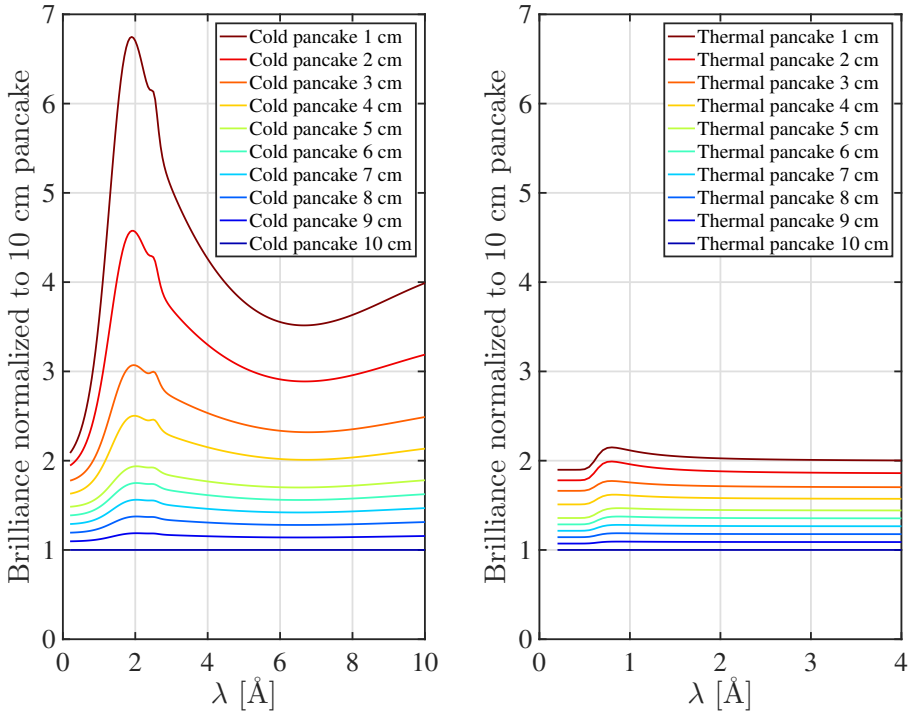

Figure 3.27: Brilliance as a function of wavelength of pancake moderators with different heights normalized to the 10 cm pancake moderator. Left side shows the spectrum from the cold part of the moderator, while the right side shows the spectrum from the thermal wing.

and it was considered to have a common top and bottom guide for all instruments nicknamed the doughnut.

The standard distance between moderator and guide at this point in the ESS project was 2 m, and starting distances as low as 1 m was investigated. Having half the distance between moderator and guide doubles the amount of phase-space received for the vertical direction according to equation (3.1.10). It is, however, not certain that guides can transport this additional phase-space volume. In order to decide if the increased risk would be worth the performance, all guide optimization made for the purpose of selecting moderators where performed for both 1 m and 2 m earliest guide starting distances. If the performance increase for guides starting closer to the moderator and optimized individually was sufficiently large, it could be considered if a common geometry could be found that would still provide performance gains worthy of the additional risk.

3.3.3 Figure of merit

In order to facilitate easy comparison between performance of many instruments on different moderators, a figure of merit is defined. The brilliance transfer, BT, is used to describe the transport from moderator to the instrument backend. The change in source brilliance is described by the source gain, SG, which is the integral over brilliance for the relevant wavelength band on a given moderator, divided by the same integral for the 10 cm tall pancake moderator. The total figure of merit is the product of these two,

$$FOM = BT \cdot SG. \tag{3.3.1}$$

When comparing a range of moderator heights, this FOM is normalized to the FOM obtained from the pancake moderator for the 10 cm height, which is considered large enough that most guides will be fully illuminated. The 10 cm tall pancake moderator has a spectrum very similar to the TDR moderator, and thus the figure of merit is a close approximation to the performance gain compared to the TDR moderator.

```
E(start=2,max_smallaxis=0.17) C(los_divide=1)
 C(rots=-1) E(max_smallaxis=0.16)
 G(start=149.95,length=0.05,StartWidth=0.026,
   EndWidth=0.026,maxStartHeight=0.055,maxEndHeight=0.055) S
```

Text block 3.1: Input string used to describe the CSPEC guide in guide_bot. Elliptical defocusing, an S curved section escaping line of sight twice followed by elliptical focusing. Close to the end a gap is introduced to facilitate the monochromating chopper, and a short straight segment ends the guide.

3.3.4 Result from CSPEC

The study for the Cold chopper Spectrometer (CSPEC) is presented here as an example of the analysis performed. The parameters describing the desired beam and constraints for the CSPEC guide are shown in table 3.3. Two wavelength ranges are given, one for which the guide system was optimized, and the one used to calculate the figure of merit for the final guide. The purpose of having both is that guides optimized for the lower end of their desired wavelength range tend to provide better results. The guide to be optimized is described by the input string shown in text block 3.1. The input string shown constrains the guide to start 2 m from the moderator. The same input string was used to optimize a guide starting 1 m from the moderator. The optimal guide for 3 cm moderator height starting 2 m from the moderator is shown in figure 3.28.

In the case of CSPEC, both the horizontal and vertical guide geometry is considered, but it is only strictly necessary to consider the vertical part, as the two are independent. In some other cases, very low requirements was set for the horizontal direction, making the brilliance transfer primarily limited by the vertical direction.

Horizontal sample size	1.9 cm
Vertical sample size	4.0 cm
Horziontal divergence	±1.00°
Vertical divergence	±1.00°
Wavelength range (optimized)	2.0 - 6.0 Å
Wavelength range (analyzed)	2.0 - 10.0 Å
Moderator to sample distance	151.4 m
Guide to sample distance	20 cm
Coating	m = 3.0

Table 3.3: Parameters used for simulation of CSPEC guides.

The results from the guide optimizations for guides starting 1 m and 2 m from the moderator are shown in figure 3.29. In both cases the figure of merit is normalized to 10 cm moderator height. The source gain increases monotonically towards lower moderator heights, but the brilliance transfer decreases monotonically. The maximum figure of merit is seen at a lower moderator height (2-3 cm) when the guide is allowed to start 1 m from the moderator, in comparison with the usual start at 2 m where the optimal height is larger (3-4 cm).

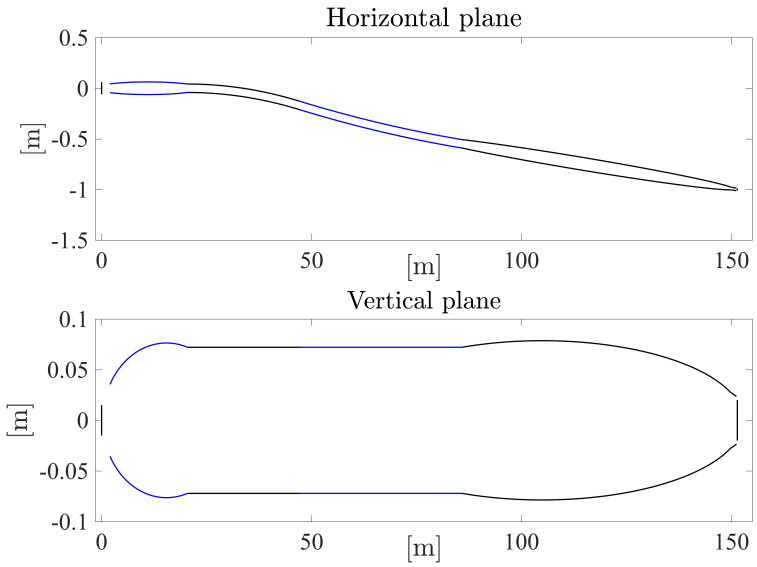

Figure 3.28: Optimized geometry of the CSPEC guide for a 3 cm high moderator with a guide start 2 m from the moderator. Showing the horizontal and vertical plane.

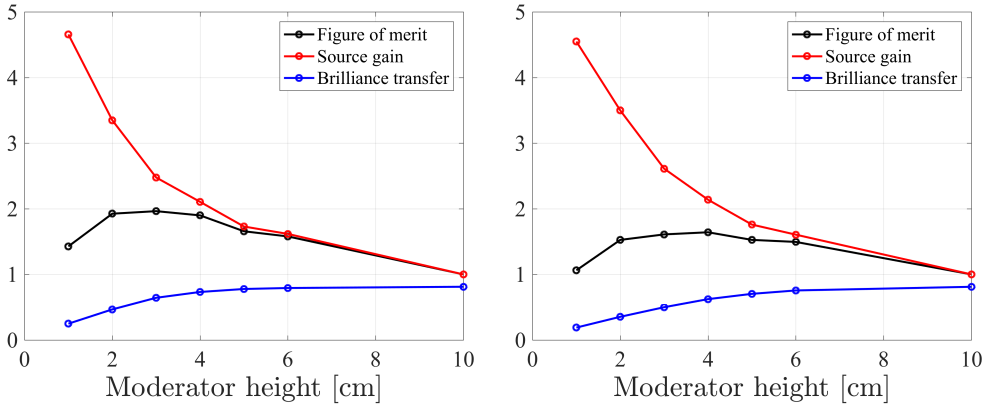

Figure 3.29: Defined figure of merit normalized to a 10 cm moderator, the source gain and the brilliance transfer. Left shows for results for guides starting 1 m from the moderator while the right shows results for guides starting 2 m from the moderator.

Instrument name	Wavelength	Sample size	Divergence
SKADI	2-10 Å	3×3 cm^2	$\pm 0.29° \times \pm 0.29°$
DREAM	0.8-4.6 Å	1×1 cm^2	$\pm 0.25° \times \pm 0.25°$
MAGIC	0.7-8 Å	1×1 cm^2	$\pm 0.3° \times \pm 0.3°$
LOKI	2-12 Å	3×3 cm^2	$\pm 0.57° \times \pm 0.57°$
NMX	1.5-3.3 Å	0.5×0.5 cm^2	$\pm 0.2° \times \pm 0.2°$
SLEIPNIR	3-19 Å	2×2 cm^2	$\pm 0.86° \times \pm 0.86°$
CAMEA	1.65-6.4 Å	1.5×1.5 cm^2	$\pm 0.75° \times \pm 1.0°$
VERITAS H	2-10 Å	1×1 cm^2	$\pm 2° \times \pm 0.75°$
Heimdal cold	4-10 Å	1×1.5 cm^2	$\pm 0.5° \times \pm 0.55°$
Heimdal thermal	0.6-2.27 Å	0.5×1.5 cm^2	$\pm 0.2435° \times \pm 1.0°$
T-REX	0.8-7.2 Å	1×3 cm^2	$\pm 1.0° \times \pm 1.0°$
ESSENSE	4-16 Å	3×3 cm^2	$\pm 0.57° \times \pm 0.57°$
CSPEC	2-10 Å	1.9×4 cm^2	$\pm 1.0° \times \pm 1.0°$
ODIN	1-7 Å	3×3 cm^2	$\pm 0.72° \times \pm 0.72°$
WANSE	2-10 Å	1.5×6 cm^2	$\pm 0.5° \times \pm 1.0°$
VOR	1-9 Å	1×1 cm^2	$\pm 0.7° \times \pm 1.05°$
FPBL (Fundamental Physics)	3-8 Å	6×6 cm^2	$\pm 0.57° \times \pm 0.57°$
MIRACLES large	2-8 Å	3×3 cm^2	$\pm 2.5° \times \pm 2.5°$
MIRACLES small	2-8 Å	1×1 cm^2	$\pm 2.5° \times \pm 2.5°$

Table 3.4: List of beam requirements for instruments investigated using guide_bot for moderator height dependence.

3.3.5 Collected results

A similar investigation was performed for all instruments in table 3.4, where constraints were discussed with the individual instruments teams. An overview of the results for guides allowed to start 1 m from the moderator can be seen in figure 3.30, while a similar overview for guides allowed to start 2 m from the moderator can be seen in figure 3.31. The benefit of starting the guide closer to the moderator is greatest at the lowest moderator heights. In the overview it can be seen that instruments with lower vertical phase-space requirements are in general the ones that prefer smaller moderators and achieve the largest figure of merit. This correlation was investigated in figure 3.32 and 3.33 for guides allowed to start 1 m and 2 m from the moderator respectively. No instruments with large vertical phase-space requirements were among the largest figure of merit gains, yet instrument with lower vertical phase-space requirements show a wide variation in maximum figure of merit gains. The possible gains are limited by both the source gain in the relevant wavelength interval, and the phase-space that can be extracted from the moderator.

All instruments have higher figure of merit at moderator heights between 3 cm and 6 cm than at the baseline 10 cm moderator height.

3.3.6 Conclusion

The guide systems for a large part of the proposed ESS instrument suite was optimized for a range of moderator heights. Guides were optimized for a starting distance of 1 m and 2 m from the moderator with the purpose of estimating the possible performance gains associated with reducing this distance. The scale of the investigation was only possible because guide_bot allowed quick guide optimizations tailored for the constraints and figure of merit of each instrument. The provided data set and other contributions was used by ESS to select a moderator height of 3 cm, and that starting guides closer than 2 m from the moderator was not worth the increased risk.

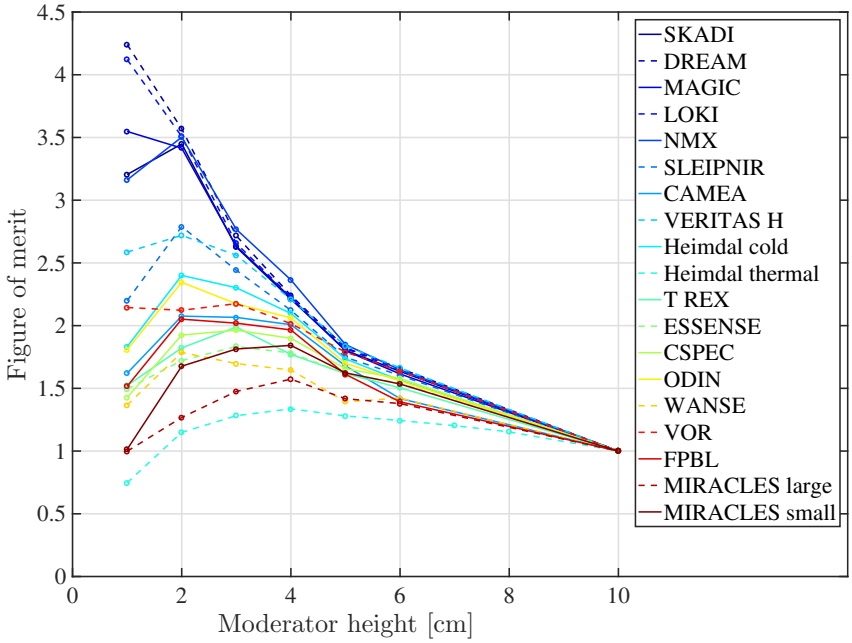

Figure 3.30: Figure of merit as a function of moderator height for guides optimized for a range of proposed and accepted ESS instruments. Here guides are allowed to start 1 m from the source.

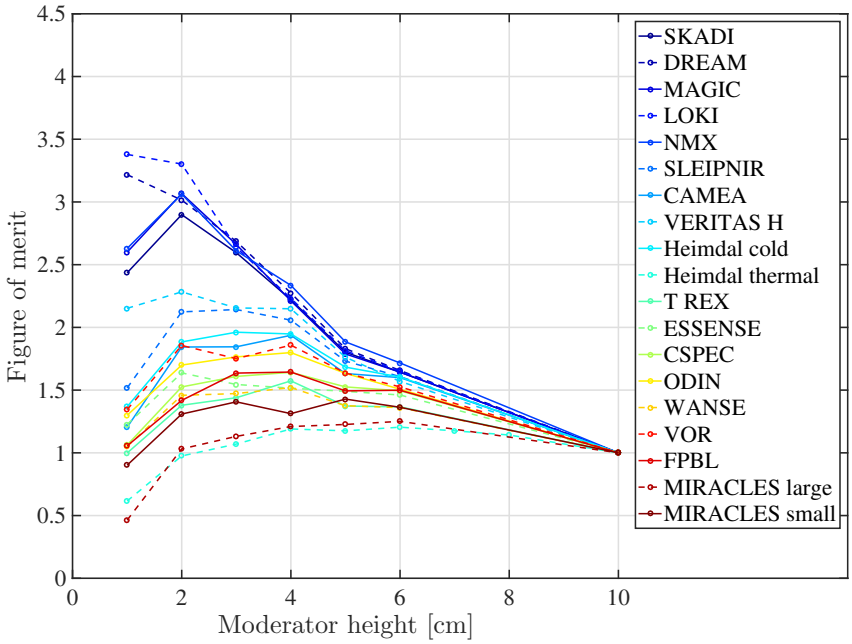

Figure 3.31: Figure of merit as a function of moderator height for guides optimized for a range of proposed and accepted ESS instruments. Here guides are allowed to start 2 m from the source.

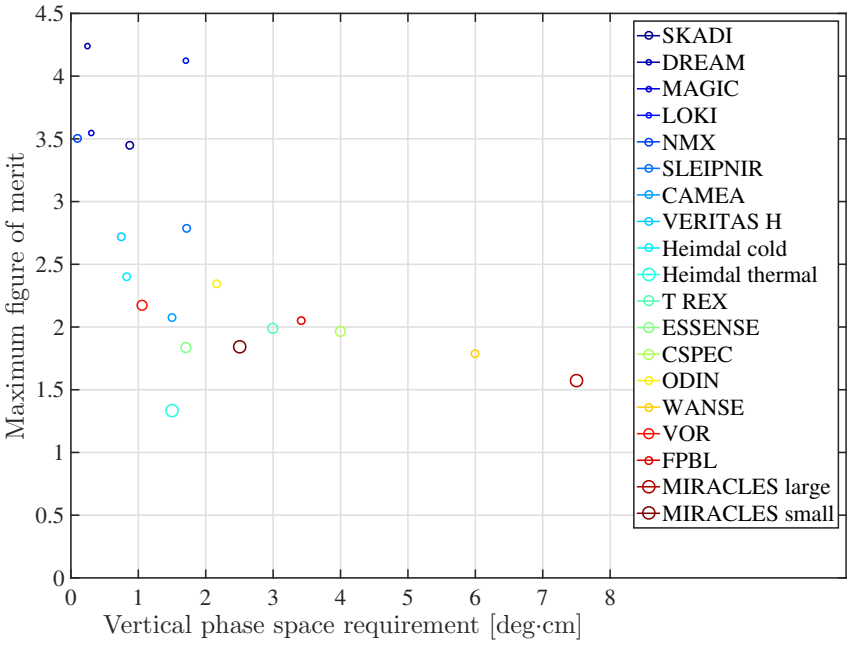

Figure 3.32: Comparison of maximum figure of merit and the vertical phase-space requirement for a range of proposed and accepted ESS instruments. The size of each circle corresponds to the moderator height that achieved the largest gain. Here for guides allowed to start 1 m from the source.

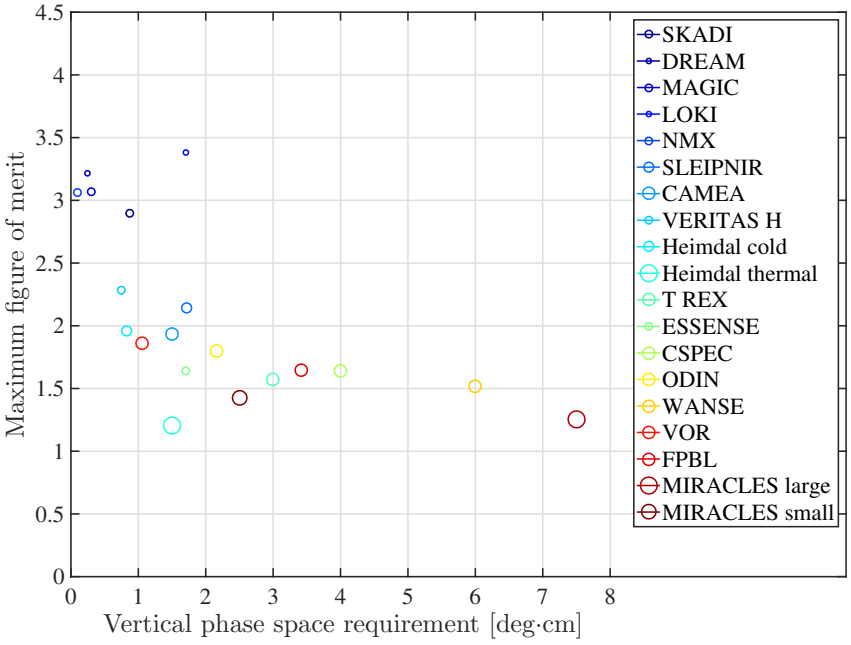

Figure 3.33: Comparison of maximum figure of merit and the vertical phase-space requirement for a range of proposed and accepted ESS instruments. The size of each circle corresponds to the moderator height that achieved the largest gain. Here for guides allowed to start 2 m from the source.

Chapter 4

McStas Union project

The Union components is a collection of McStas components that takes an alternative approach to sample simulation in McStas. In contrast to traditional sample components, the Union components are not self-contained. Instead each handles a different part of the sample simulation task and the components are then connected to accomplish the full simulation. Process components describe a scattering process such as incoherent or powder scattering. The Make_material component collects an arbitrary number of such processes and a description of absorption into a material definition. Geometry components place volumes in the McStas simulation that are assigned one of the defined material definitions. Finally a master component executes a simulation of all these volumes with multiple scattering and balancing between all processes in each material.

This approach have several inherent advantages to the traditional method. The volumes can be overlapped to create hollow and layered geometries relevant for sample environments, and the full multiple scattering between all of these is very difficult to obtain with traditional McStas samples. Since the scattering physics is separated into individual scattering processes and balancing between these is performed by the master component, writing a new process component is a much smaller task than writing a new sample component. The separation of scattering processes makes the system more flexible, it is for example easy to make mixtures of powders or twinning in crystals.

One disadvantage with the selected approach is that all simulation occurs in one master component, and it is thus difficult to follow the simulation using McStas monitors for diagnostic purposes or otherwise. To remedy this shortcoming, a suite of logging tools are available which can follow the simulation conducted by the master component.

In this chapter the Union components and the underlying algorithms are presented. The capabilities of the Union components are demonstrated by simulating the triple axis spectrometer MACS and the time of flight powder spectrometer MARI. Both simulations are compared to recent measurements, and the background present in the simulations is analyzed using the logging tools. Several sections are adapted from the paper in appendix A.3.

4.1 Component classes

The Union components are separated into different classes that each perform a different type of task, and more components of each class can be added to expand the functionality of the software. Each of the Union component classes are here described in turn. The section follows the similar section in the appendix A.3.

4.1.1 Processes

The process component defines a scattering process, and is responsible for providing a function calculating the scattering probability and a function describing a scattering event. The probability for scattering is given in terms of the inverse penetration depth as described in

section 2.1.4. The function contained in the process component for calculating scattering probability need to return μ from a given $\mathbf{k}_i$. The function describing a scattering event is more general, but needs to adhere to the common input and output of variables. Such a scattering function need to return the final wavevector and ray weight from the initial wavevector and initial weight.

Each process declares a structure that contains the user input and is passed to each function. This structure can also be used to transfer data between the two functions when necessary.

The currently available scattering processes are listed in table 4.1 together with the names of McStas components used as templates [64, 65, 76]. Not all functionality is duplicated from the originals, the incoherent process does for example not support a quasielastic energy width.

It is possible to describe a difference in orientation between different processes by giving the rotation angles in the standard McStas notation, which allows for example twinned crystals by use of two or more Single_crystal_process components.

All processes can have their statistical probability for being selected by the Monte Carlo process adjusted using suitable input. This is important when investigating weak processes that would otherwise rarely be sampled.

Name	Description	McStas component
Incoherent_process	Incoherent scattering	Incoherent
Powder_process	Bragg scattering from powder	PowderN
Single_crystal_process	Bragg scattering from single crystal	Single_crystal
Phonon_simple_process[1]	Single acustic phonon branch	Phonon_simple
AF_HB_1D_process	Antiferromagnetic 1D Heisenberg $s = 1/2$ chain	

Table 4.1: List of currently available scattering processes and the McStas components used as templates.

4.1.2 Make material

The main tasks of the Union_make_material component are to collect a number of scattering processes into a material, and provide a name that can be used to refer to this material later. The names of all scattering processes to be collected are supplied as a string in the input parameters. In addition, the inverse penetration length from absorption at the standard velocity, $v_0 = 2200$ m/s is given, $\mu_{abs\,th}$, from which the appropriate value at a given velocity, v can be found from,

$$\mu_{abs} = \mu_{abs\,th}\frac{v_0}{v}. \tag{4.1.1}$$

For a given $\mathbf{k}_i$, the inverse penetration depth for the total scattering from the material can be found,

$$\mu_s = \sum_i^N \mu_i, \tag{4.1.2}$$

where the sum is over all processes associated with the material. The total cross section is likewise, $\mu_{total} = \mu_s + \mu_{abs}$, from which the transmission probability over a path length of l can be found,

$$P_{trans} = e^{-l\mu_{total}}. \tag{4.1.3}$$

The Union_make_material component can be used to make an absorbing material without any processes.

[1] Developed by A.K. Ravn as a computing project.

4.1.3 Geometry components

Each geometry component describes a volume that is placed in the McStas simulation, and is assigned a material definition using the material name provided by the Make material component. The geometry inherits the properties of the material, including the appropriate scattering processes and absorption description. In this context the term volume refers to a geometry combined with material properties placed in simulated space.

The currently available geometry components are listed in table 4.2 and shown in figure 4.1. Adding a new geometry component takes some effort, as functions for various intersection tests with all other geometries are necessary.

Name	Description
Union_sphere	Sphere
Union_cylinder	Finite cylinder
Union_box	Box

Table 4.2: List of currently available geometry components.

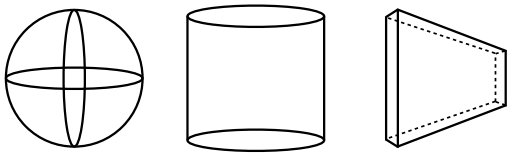

Figure 4.1: The three available geometries, (left) sphere, (middle) cylinder, (right) box. Note that the box needs to have two parallel sides with the same center.

In contrast to regular McStas components, the volumes can be defined in an arbitrary order, and are even allowed to overlap other volumes. When volumes overlap, the space that is covered more than once inherits the material definition of the volume with the highest priority, which is a unique value assigned to each volume. In this way, complicated geometries can be built from simple shapes, all with individual physical descriptions, as illustrated in figure 4.2.

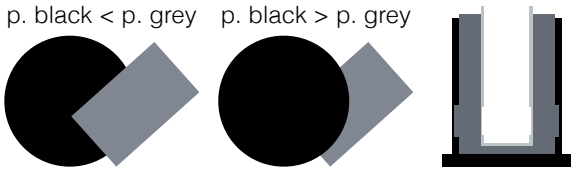

Figure 4.2: Three examples of volumes overlapping. In the left and middle, the concept is demonstrated by letting the grey and the black volume switch priority. The right panel shows how overlapping volumes of Al and vacuum can be used to build a simple cryostat, here with several layers of material, mounting plate and beam windows.

It is possible to use geometry components to define masks, as illustrated in figure 4.3. A mask is assigned to a one or more previously defined volumes, and only the parts of the masked volume covered by the mask is simulated. Volumes can have several masks, and a setting controls whether all mask volumes must cover a part of the masked volume for it to be simulated, or just any mask volume. Masks allow additional geometrical freedom, and in many cases reduce the number of volumes needed to describe a desired geometry.

A final use of the geometry components is the definition of exit volumes that allow rays to leave the Union components early if they are intersected. These can be used for example to place detectors and other components inside the overall geometry defined by the Union components.

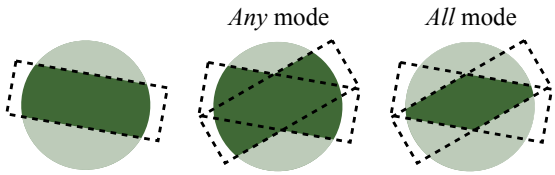

Figure 4.3: Illustration of how mask volumes can be used to chose smaller parts of a volume to be simulated, here the dashed volumes are masks, the green volume is the masked volume with the light green not simulated and the dark green simulated. Both the *any* and *all* mask modes are demonstrated.

4.1.4 Master component

The geometry components do not in themselves impact the neutron rays in the McStas simulation, instead they forward the gathered information to the Union_master component. This component contains a ray-tracing core independent from the one built into McStas, and can handle an arbitrary number of volumes with multiple scattering between them.

In order to simplify the process and geometry components, a large part of the complexity of writing a sample component was migrated to this Union_master component. Here it is shown how the scattering position and scattering process is selected.

When a ray is inside a volume, a distance to a next scattering position, l_s is selected from the appropriate distribution,

$$l_s = -\log(1-r)/\mu_{total}, \tag{4.1.4}$$

using a uniformly distributed random number between 0 and 1, r. This results in l_s being drawn from a probability distribution on the form $N\exp(-\mu_{total}l_s)$ where N is a normalization constant. If the distance l_s is smaller than the distance to the boundary of the current volume l_b, a scattering event will occur, otherwise the ray will leave the volume.

In some cases it is desired to manipulate the sampling frequency of scattering events in a certain volume, which can be done by defining a scattering probability f_s in the appropriate geometry component. This can be done by manipulating the sampling frequency and adjusting the ray weight accordingly which is common in McStas samples. The weight multiplier, π, and sampling frequency, f, must satisfy $P = \pi f$, where P is the physical probability as mentioned in 2.3.1. When the scattering process has a physical probability of P_s, the appropriate weight multiplier is,

$$P_s = f_s\pi \Rightarrow \pi = \frac{P_s}{f_s} = \frac{1-P_{trans}}{f_s} = \frac{1-e^{-\mu_{total}l_b}}{f_s}. \tag{4.1.5}$$

When a scattering event occurs, the next step is to select one of the available processes. Since absorption is excluded in this choice, the ray weight needs to be transformed accordingly. The actual probability for selecting a scattering process is $P_{scat} = \mu_s/\mu_{total}$, and the sampling frequency for selecting a scattering process is $f_s = 1$, the weight multiplier is,

$$\pi = P_{scat}/f_s = \mu_s/\mu_{total}. \tag{4.1.6}$$

Next, a Monte Carlo choice is performed to choose between the processes in the current material, each with probability $p_i = \mu_i/\mu_s$ calculated by the functions from the process components. The function describing a scattering event for the selected process is then evaluated.

As mentioned in section 2.3.1, it is possible to manipulate the sampling frequencies of the processes in a material, which is done by attributing each process a relative weight m_i, which fulfils,

$$\sum_i^N m_i = 1. \tag{4.1.7}$$

For a given $\mathbf{k}_i$, these can however not directly be used to select between the processes, as μ_i could be zero for some processes, which are then excluded from the choice. Thus, a similar parameter, t_i is defined as follows,

$$t_i = \begin{cases} m_i & \text{if } \mu_i > 0 \\ 0 & \text{otherwise} \end{cases} . \tag{4.1.8}$$

The sum over all t_i in a material is denoted T. Now a Monte Carlo choice between N possibilities with probabilities t_i/T is made, and using the final choice i, the weight is updated,

$$\pi = \frac{p_i}{f_i} = \frac{\mu_i/\mu_s}{t_i/T}, \tag{4.1.9}$$

and the function describing a scattering event for process i is evaluated.

Due to the computational requirements related to handling intersections with a large number of volumes, the Union_master component will analyse the overall system and create a simple logical network that omit most unnecessary intersection calculations. This optimization significantly improves the performance scaling, and thus large numbers of volumes can be used without excessive computational requirements. An example showing an ensemble of geometries and the resulting logical network is shown in figure 4.4, and the generation of such networks are discussed further in section 4.2.2.

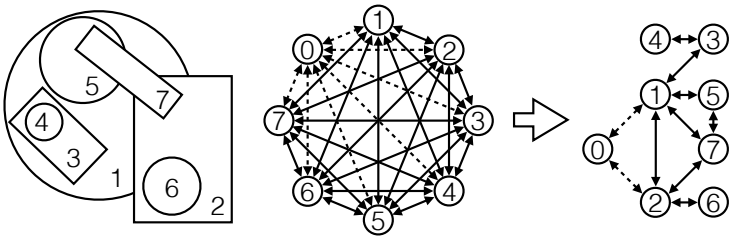

Figure 4.4: (Left) An ensemble of volumes, each named with a number that also correspond to the priority of the volume. (Middle) Worst case network where intersections with all volumes are calculated regardless of the position of the ray. Here volume 0 is the surroundings outside the ensemble. (Right) Reduced network corresponding to the depicted ensemble of volumes, here the necessary intersection calculations depend on the position of the ray.

4.1.5 Logger components

Since the Union_master component contain such a large part of the simulation, it was have chosen to add tools that are able to log what occurs in the Union_master component. Logger components save information on each scattering event and output the results as a McStas monitor. This could for example be the position of all scattering events, their scattering vector, or similar. It is possible to attach the logger component to a number of specified volumes, and even specify process names to investigate such subsets of the data. The currently available logger components are listed in table 4.3. McStas have general logger components as well [77], these do not have access to the internal information of the Union_master component, but works for all McStas components.

4.1.6 Conditional components

It can easily be investigated how certain parts of the overall geometry contribute to the total scattering, what remains is the ability to investigate what contributed to a certain part of the scattering pattern. Union conditional components can modify a logger component, so that it will only save recorded data if the final ray state adheres to some condition, for example a certain final energy range. Several conditional components can modify the same logger component, and in this case all conditions need to be fulfilled.

Name	Description
Union_logger_1D	Logs time / scattering vector
Union_logger_2DQ	Logs (q_i, q_j) for $i, j = x, y, z$
Union_logger_2D_kf	As above with final wavevector
Union_logger_2D_kf_time	As above, with time bins
Union_logger_2D_space	Logs scattering position in 2D
Union_logger_2D_space_time	As above, with time bins
Union_logger_3D_space	Logs scattering position in 3D

Table 4.3: List of currently available logger components.

There are currently two available conditional components, one that filters for time when the ray leaves the ensemble, and another that requires the ray to intersect with a virtual detector and can filter on the time of intersection.

By having loggers for position and scattering vector with conditionals filtering a certain background problem, the user can see the origin of this scattering and what succession of scattering vectors were taken. As such the combination of Union logger and Union conditional components provides powerful tools for understanding the final results.

4.2 Algorithm descriptions

The structure and logic used in the Union component is in many ways different from existing McStas components. In this section the integration with McStas is presented, as well as the propagation algorithm developed for the Union_master component, including generation of the logical networks used to reduce the computational requirements of the task. Additionally the tagging system recording ray histories is introduced.

4.2.1 McStas integration

One challenge in the structure chosen for the Union components is to forward information from one component to the next in the chain. Information is defined in the processes components, and then forwarded to the Make_material component that again forward information to geometries which in turn is collected by the Union_master. Each type of information is contained in a global list of pointers to appropriate structures. When the information is requested, for example the Make_material component looking for processes, this global list is searched by name. In this way, the Union_master component eventually receives the necessary information in the form of a list of pointers to structures describing the defined volumes. These operations can be performed in the initialize section of the components. The global lists are dynamically allocated as required, yet the information structures for each component is statically allocated in their component declare sections.

When a process component is used in an instrument file, the potentially large functions describing the scattering physics is contained in the share section of the component. Thus these functions only appear once when the c code is compiled, and only scattering functions for the used processes are compiled, in line with normal McStas philosophy. The functions describing the physics of a process is contained as function pointers in the structure describing a process. In the same manner geometry components include intersection functions in the share section, and these are contained as function pointers. This information structure makes common tasks in the Union_master component simple, as calling a physics or intersection function for a volume have the same syntax independent on the specific geometric shape or scattering type. Function pointers are used to perform logical choices in initialize where they are executed just once, instead of in the trace section where they would be evaluated millions of times.

4.2.2 Network algorithms

In the initialize section of the Union_master component the ensemble of defined volumes is analysed to reduce the number of unnecessary intersection calculations. The trivial solution to the problem is to calculate intersection times for all volumes and propagate the ray to the lowest intersection time. In the case of nested volumes, it is not necessary to calculate intersections with the volumes inside the outermost volume until the ray enters that outermost volume. When the ray is in a certain volume, n, there is a set of volumes for which an intersection calculation is necessary, here named the intersection list I_n. Likewise when a ray leaves volume with index n, it is possible to enter a certain set of other volumes, here named the destinations list D_n. As each volume have both lists, they form a logical network that describe the possible transport between the defined volumes. Here the algorithm used for generating these lists are described excluding the complexity introduced by considering mask volumes. The intersection list and destinations list are generated for a volume in an example ensemble shown in figure 4.5.

The surroundings

A volume describing the vacuum surrounding the ensemble of defined volumes is always indexed with volume number 0. In the context of list generation, this volume can be seen as covering all space. The priority of volume 0 is lower than all other volumes.

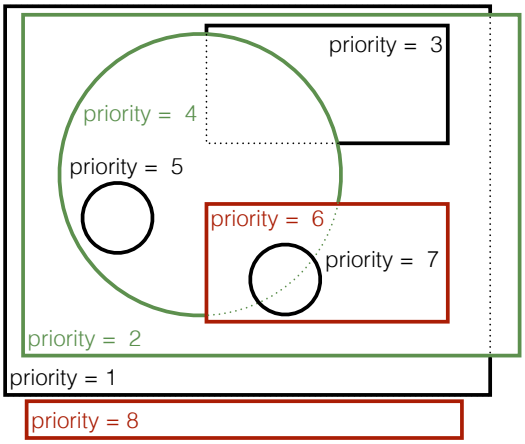

Figure 4.5: Illustration of a number of volumes, each with a denoted unique priority. The priority is here used as an identifier, so that the large circular volume with priority 4 is denoted volume 4. Dotted lines show borders of volume that are being occluded by a volume with higher priority.

Children list

If the space covered by volume i is described as a set, V_i, volume i is a child of volume n of V_i is a proper subset of V_n, $V_i \subset V_n$. This list is generated for each volume by a simple geometrical check dependent on the shapes of each volume. Every volume is a child of volume 0. The children list for volume 4 in figure 4.5 consists only of volume 5, and is here written, $C_4 = [5]$.

Parents list

A volume i is a parent to volume n if volume n appears in the children list of volume i. In figure 4.5 volume 4 has a parent list consisting of volume 0, 1 and 2, $P_4 = [0, 1, 2]$, as the surrounding vacuum covers all space.

Grandparents list

A volume i is a grandparent to volume n, if volume i appears in the parent list of volume n. Volume 4 on figure 4.5 used as an example has a grandparent list consisting of just the surrounding vacuum, $G_4 = [0]$.

Overlap list

Volume i and volume n are said to overlap if their intersection is not empty, $V_i \cap V_n \neq \emptyset$, volumes are, however, not said to overlap with themselves. The overlap list for a volume is found by checking for geometrical intersection with all other volumes. All volumes overlap the surrounding vacuum, and thus volume 0 is on all overlap lists. In figure 4.5, volume 4 overlaps all other volumes except volume 8, $O_4 = [0, 1, 2, 3, 5, 6, 7]$.

Intersection list

The intersection list for volume n is the list of volumes for which the intersection should be calculated when the ray is within volume n. The intersection list for volume n is generated as follows.

- Start with the overlap list for volume n

Starting with the overlap list of volume n is obvious, as there is no reason to calculate intersections with a volume that does not intersect volume n. For volume 4 in the example depicted on figure 4.5, a list identical to $L_4 = O_4 = [0, 1, 2, 3, 5, 6, 7]$ is made.

- Remove entries with priority less than the priority of volume n

The second step removes all volumes with a priority lower than the volume n. If a volume with lower priority intersect volume n, any intersections would be irrelevant, as the simulated material should be that of volume n regardless. In the example, the identifiers correspond to the priorities, so the remaining list is, $L_4 = [5, 6, 7]$.

- Remove entries on the remaining list that has parents on the remaining list

This third step eliminate intersections calls in cases where nested volumes occur. If a volume have a parent on the list, an intersection with that parent will always be before the volume itself. In the example, volume 7 is removed as it is a child of volume 6, $L_4 = [5, 6]$.

- The remaining list is the intersection list for volume n

Therefore the intersection list of volume 4 in figure 4.5 is $I_4 = L_4 = [5, 6]$. When the ray is in volume 4, only two volumes are relevant for intersections.

Destinations list

When a ray leaves a volume, n, by intersecting the boundary of a volume, i, it is necessary to find in what volume the ray now resides. If $n \neq i$, this is trivial, as the ray enters volume i. However, if $n = i$, it is necessary to test if the new ray position is within all other volumes, and if the ray is inside several, the next volume is the one with highest priority. To reduce this task, a destinations list is generated in the initialize section of the Union_master component that includes only the volumes the ray could enter in this situation.

- Start with the overlap list for volume n

Since the ray can not end in a volume not overlapped by volume n it is sufficient to consider only the volumes on the overlap list. For volume 4 in 4.5, a list is defined $L_4 = O_4 = [0, 1, 2, 3, 5, 6, 7]$.

- Remove volumes from intersection list n

If a volume, i is on the intersection list of n, the ray can only enter i by intersecting volume i, but the destinations list is only used when the ray intersects volume n. Hence it is not necessary to check volume i. For volume 4 in the example, volume 5 and 6 can be removed leaving, $L_4 = [0, 1, 2, 3, 7]$.

- Remove children of volumes on intersection list n

If the ray intersects volume n before any on the intersection list of volume n, the ray is outside all volumes on its intersection list, and thus also outside of any children of these volumes. In figure 4.5, volume 7 is a child of volume 6 that appear on I_4, and can thus be removed, $L_4 = [0, 1, 2, 3]$.

- Remove children of n from the remaining list

When the ray intersects volume n, it must be on the boundary of volume n, and thus can not be inside a volume that forms a proper subset of volume n. In the example on figure 4.5, this step does not remove any volumes from any destinations list. The step is only relevant when a user places a volume inside another, and assigns the inner volume with a lower priority, meaning it will not be simulated. This step is mostly a safety measure for this case.

- Remove grandparents of volume n from the remaining list

Text block 4.1: Pseudo code describing a simplified version of the multiple scattering propagation algorithm central to the Union_master component.

```
find current volume index from starting position
done = 0
while( done == 0 ) {
  calculate intersections with volumes on intersection list if not yet calculated
  find the lowest positive intersection time among these, t0
  if (A lowest intersection time is not found) {
    done = 1
  } else {
    calculate mu (inverse penetration depth) for each process in current volume
    calculate mu_sum = sum of the calculated mu values + mu_absorption*(2200/v)
    length_to_scattering = -log(1 - rand01() ) / mu_sum
    if (length_to_scattering < length_to_boundary) ) {
      select scattering process from weighted choice between mu values
      propagate ray length_to_scattering/v
      run scattering function for appropriate process -> new velocity vector
      clear table of calculated intersection times
    } else {
      propagate ray t0
      if (the next intersection is with the current volume) {
        search this volumes destinations list
        new current volume index is set
      } else {
        new current volume index corresponds to the volume that was intersected
      }
    }
  }
}
```

In order to reach a grandparent of volume n, the ray must travel through a parent of volume n, but as volume n is a proper subset of this parent, the boundary of n is contained in the parent. Thus it is unnecessary to check the grandparents on volumes still on the destinations list. In the example concerning volume 4, the surrounding vacuum denoted volume 0 can be removed, $L_4 = [1, 2, 3]$.

- Remove parents of volume n that have lower priority than other remaining parents of volume n

If there are several parents of volume n left on the list, only the one with the highest priority can be entered directly from volume n. Both volume 1 and 2 are parents to volume 4, hence the one with lowest priority is removed, $L_4 = [2, 3]$.

- The remaining list is the destinations list

The final destinations list for volume 4 in the ensemble depicted on figure 4.5 is, $D_4 = L_4 = [2, 3]$.

4.2.3 Propagation algorithm

The propagation algorithm is computationally expensive and thus heavily optimized. A simplified version is shown in text block 4.1.
A visualization of the trace algorithm in shown in figure 4.6. In the first step the ray is in the vacuum around the component, and the intersection list appropriate for this situation is used, which only contains the blue and green volumes. In step 3 the ray is propagated from the blue volume to the green, and thus uses a new intersection list. As the blue volume is not present in the new intersection list, the previously calculated intersection with it is not considered, yet as the red volume is on the intersection list, intersections with that volume is calculated. At the scattering in step 4, all previously calculated intersection times are cleared, as the ray velocity is updated. Intersections are calculated for all volumes on the

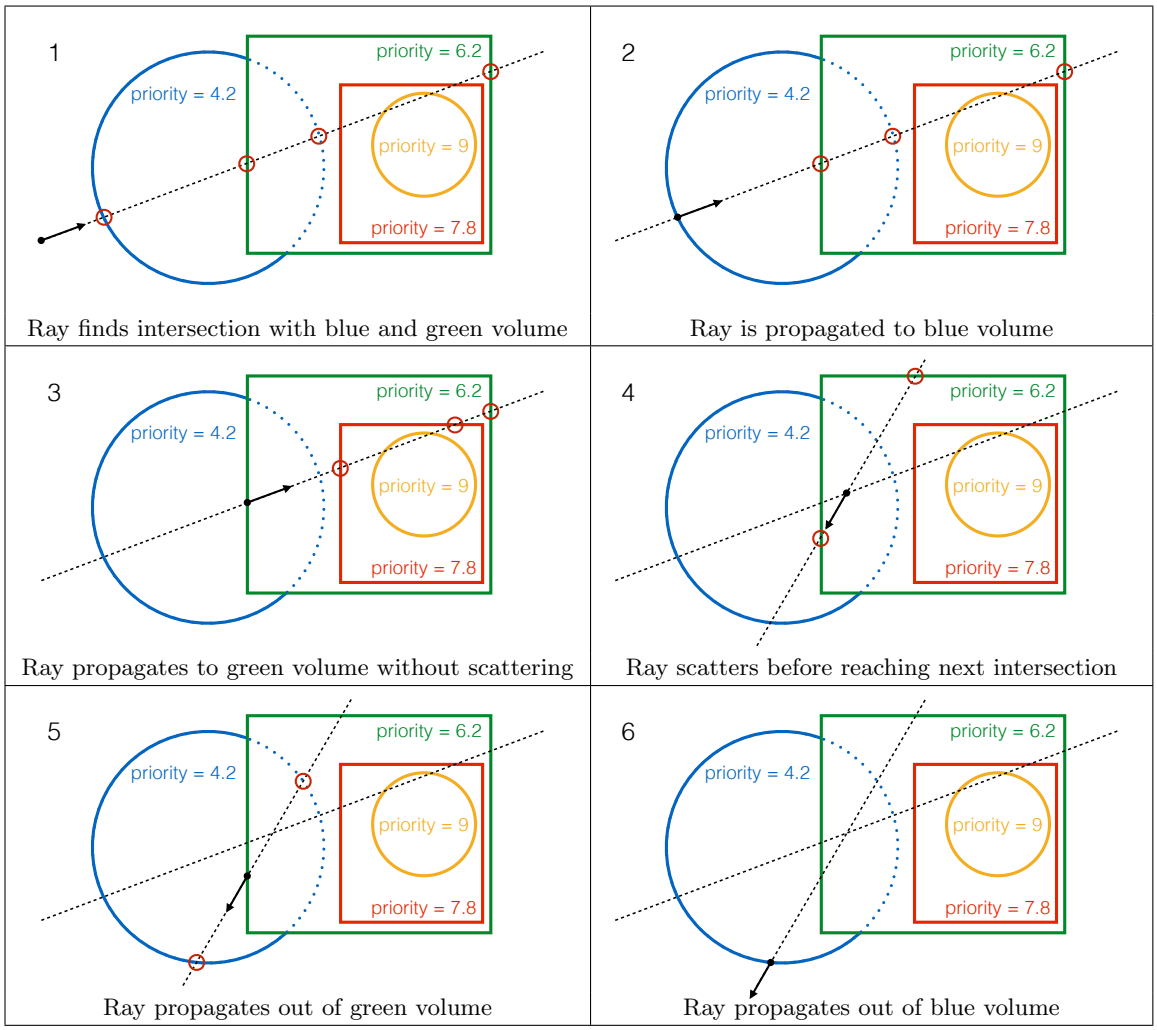

Figure 4.6: 2D visualization of the Union propagation algorithm through 4 volumes where a single scattering event occurs. The calculated intersection points are shown using red circles, and each volume have their assigned priority displayed.

intersection list of the green volume. Only after propagating out of the green volume in step 5 is the intersection time with the blue volume calculated.

In step 5 the destinations list for the green volume is searched as the ray could enter either the blue volume or the surrounding vacuum. Similarly in step 6, the destinations list for the blue volume is used, yet it is not searched as it only contains the surrounding vacuum.

Note that intersections were never calculated for the orange volume as they were not necessary in this case.

4.2.4 Search of a destinations list

The trivial way of searching a destinations list would be to check whether the position of the ray is within each of the volumes on the list, and return the volume index with the highest priority. This can, however, take some time for large destinations lists, and in the future, geometries might be added where it is more computationally expensive to check if a position is within it. For this reason, a short destinations list is created where all volumes with parents on the list is removed. The short destinations list is searched with the trivial

algorithm, yet when a ray is found to be in a volume, the children of this volume are added to the searched list. This corresponds to a tree search starting with larger volumes, and pruning branches that can not include the results, as the ray can not be in a child of a volume the ray is not within.

4.2.5 Tagging

The Union_master component records a simple history for each ray. The history consists of a series of events undertaken by a ray, which can be changing volume or a scattering event, in chronological order. All rays that propagate from volume 0 to volume 1, undergoes scattering process 2 of volume 1, then propagates back to volume 0 are considered the same history. These histories are collected and sorted after the total intensity that leaves the master component with a specific history. A sample of the top 15 histories for a simple setup is displayed in text box 4.2.

```
History file written by the McStas component Union_master
----- Description of the used volumes ---------------------------------------------------------
V0: Surrounding vacuum
V1: powder_container  Material: Al   P0: Al_incoherent P1: Al_Powder
V2: powder_inside_container  Material: Cu_powder   P0: Cu_incoherent_process P1: Cu_powder_process
----- Histories sorted after intensity --------------------------------------------------------
12221626 N I=4.188166E-06        V0
1882051  N I=1.052731E-06        V0 -> V1 -> V2 -> V1 -> V0
1517013  N I=6.213315E-07        V0 -> V1 -> V0
188661   N I=8.043799E-08        V0 -> V1 -> V2 -> P0 -> V1 -> V0
752943   N I=3.823911E-08        V0 -> V1 -> V2 -> P1 -> V1 -> V0
771437   N I=2.176363E-08        V0 -> V1 -> P1 -> V0
181532   N I=1.101451E-08        V0 -> V1 -> P1 -> V2 -> V1 -> V0
286771   N I=7.628450E-09        V0 -> V1 -> V2 -> V1 -> P1 -> V0
18736    N I=1.948079E-09        V0 -> V1 -> V2 -> P0 -> P0 -> V1 -> V0
75736    N I=1.319653E-09        V0 -> V1 -> V2 -> P1 -> P0 -> V1 -> V0
33463    N I=1.100647E-09        V0 -> V1 -> V2 -> V1 -> P1 -> V2 -> V1 -> V0
74590    N I=1.016961E-09        V0 -> V1 -> V2 -> P0 -> P1 -> V1 -> V0
301006   N I=6.623860E-10        V0 -> V1 -> V2 -> P1 -> P1 -> V1 -> V0
18169    N I=4.341707E-10        V0 -> V1 -> P1 -> V2 -> P0 -> V1 -> V0
13310    N I=4.054218E-10        V0 -> V1 -> P0 -> V0
```

Text block 4.2: Example of tagging output from the Union_master component, here for a setup consisting of an aluminium can containing a copper powder. The most common history is the ray missing the can entirely, followed by the ray passing through the entire setup. The next two histories contain a scattering event in the copper using the incoherent and powder process respectively.

The file starts with a short description of each volume including the assigned material and the scattering processes associated with that material.

The first number in a row of data is the number of rays with this history, the next is the total intensity, and then the string containing the history. VX refers to volume number X, and PX refers to process number X within the current volume. When there are volumes with different materials, PX can refer to different processes depending on which volume the ray is currently in, meaning P0 in "V0 -> V1 ->P0" and "V0 -> V2 -> P0" refers to two different processes if volume 1 and volume 2 are different materials.

In this example, $2 \cdot 10^7$ rays were simulated, but only $2.5 \cdot 10^4$ unique histories were sampled, making the data file manageable at just 2.8 MB. The size for more complicated cases can be significantly larger, and if it becomes problematic (needs to fit in memory) the number of unique histories can be limited with component input.

During the simulation the history information is recorded in a dynamically allocated tree of nodes corresponding to the volumes and processes. Each ray travels down the tree and may need to allocate new nodes if it corresponds to a unique history. When the ray leaves the Union_master component, the weight is recorded to the last node and its count is incremented. After all rays are simulated, the tree is read back and sorted before it is written to file. This system adds less than 2% of computational time.

There are many practical uses for the history information. If for example one wants to estimate the background originating from a certain part of a sample holder described by volume X, one simply adds the intensity of all histories that scattered in that volume by searching for "VX -> P". If only background at the detector is important, one can place an exit volume with number Y at the detector and add the intensities for all histories that contain the string "VX -> P" and ends in "VY". This have always been possible with McStas by tagging the neutrons manually using EXTEND, but that requires running the simulation again in order to investigate a new problem, here all histories are available after one simulation.

4.2.6 Limitations

The main limitation of the developed propagation algorithm occurs when two volumes share a surface, as the lowest intersection time is essentially determined by numerical accuracy. In such cases, the algorithm can improperly determine which volume the ray enters, and therefore the wrong intersection and destinations lists are used, leading to unphysical behaviour. When this occurs, errors are encountered and the simulations is aborted. For this reason, the current propagation algorithm do not support cases where volumes are placed so that a surface is shared, yet a movement in the order of μm is sufficient to avoid the problem.

Another issue has to do with the generation of intersection lists, which can not take so called shared children into account. One volume covered completely by another is removed, yet a volume covered completely by two volumes, but not completely by either one, is not removed. This issue does not lead to any unphysical behaviour, merely extra intersection calculations.

The algorithm does not support gravity because the underlying intersection algorithms do not. Many McStas sample components do support gravity regardless of using intersection algorithms that do not, by simply tolerating the errors introduced. The algorithm employed in the Union components is, however, sensitive to the type of error this introduces, as the ray can end outside of a volume it was meant to enter, and therefore use the wrong intersection list. For this reason, the propagation is hard coded to be linear.

A last issue has to do with the collision detection between the user defined volumes. Currently, ray-tracing methods are used to test if two cylinders intersect, which is rather slow and can fail to notice edge cases. The speed is not an issue as the code is only executed in the initialize section of the McStas file. The failure to detect a collision can, however, lead to lost rays. For this reason this ray-tracing is performed with a large number of rays on the surface of the volume.

4.3 Validation

The scattering processes included in the Union components build upon existing McStas sample components. However, the code describing Monte Carlo choices between processes, intersection algorithms, choice of scattering position and absorption have been separated from the scattering process in order to accommodate the different structure of the software. Hence, it is still prudent to validate the new software against a known reference.

The McStas instrument used for validating each process consists of a simple 1×1 mm^2 source illuminating a cylindrical sample with radius and height of 1 cm, situated 10 m from the source. A transmission detector of 1 cm height is placed 0.5 m after the sample. A cylindrical detector with a radius of 1 m and height of 10 cm measures the scattered signal. All simulations were performed using $5{\cdot}10^9$ rays. All validation is performed without gravity, as the Union components uses linear propagation regardless.

Here the processes describing incoherent scattering, powder scattering and crystal diffraction are validated. The process describing a single phonon branch is not validated here as there are significant differences in the calculation of the scattering probability. The process describing the antiferromagnetic 1D Heisenberg $s = 1/2$ chain is not validated either, as an equivalent component does not exist.

4.3.1 Incoherent scattering

Union components describing a sample with only incoherent scattering was compared to the same geometry simulated using the Incoherent McStas component. The scattering and absorption cross sections were chosen to be those of Vanadium, $\mu_{inc} = \mu_{abs\,th} = 36.73$ m^{-1}. The incoming beam was monochromatic with 10 meV energy. The transmission and scattering from the two components are compared in figure 4.7. In both cases, the results from the Union components are almost inseparable from the traditional sample component. In addition, the deviations are consistent with the Monte Carlo noise estimated by McStas.

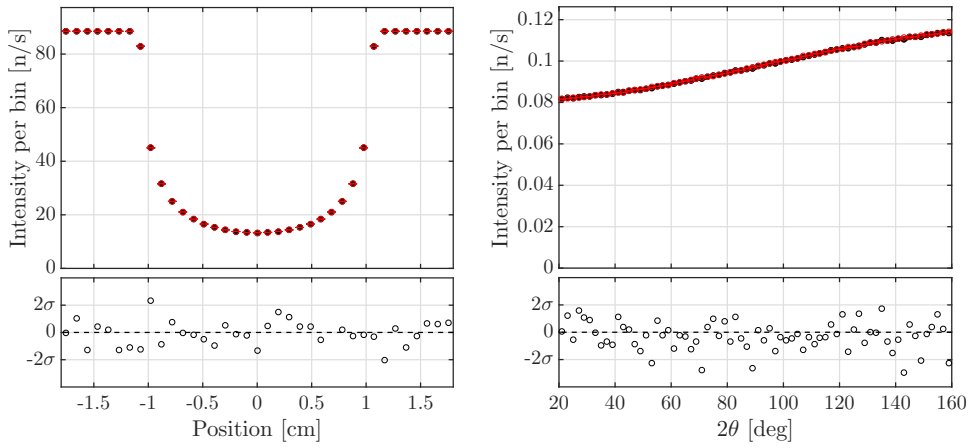

Figure 4.7: Simulation results from an incoherent scatterer with absorption simulated using Union components (black filled) and the traditional Incoherent sample component (red empty). Left side shows the described transmission detector while the right side show the scattering detector. The lower panels shows the difference between the two simulations for each point relative to the error on the difference introduced by the Monte Carlo technique.

4.3.2 Powder scattering

Here, the Union components are validated against the existing PowderN sample component. As PowderN describes both powder and incoherent scattering, the material defined using the Union components contains both processes. The powder process is based directly on the

code from the PowderN component. It is important to note that PowderN does not support multiple scattering. When using the powder process in the Union components, multiple scattering is handled by the Union_master component. To obtain a valid comparison, we add a detector that ignores multiple scattering.

This validation has been performed for many compounds. Here, the representative results for Cu and a beam with average energy of 100 meV and width 1 meV are presented. A comparison between the transmission results can be seen in figure 4.8, and in this aspect the two codes produce equivalent results. Since the PowderN component does not support

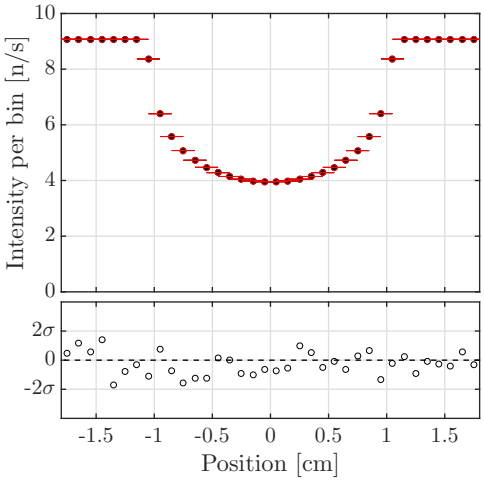

Figure 4.8: Transmission detector for Union powder sample (black filled) and traditional PowderN sample component (red empty). Lower panel shows the difference for each point relative to the error on the difference introduced by the Monte Carlo technique.

multiple scattering, a scattering detector only measuring single scattering is introduced. Results from both scattering detectors are shown in figure 4.9. In the full detector output we observe a small, but significant difference, as the multiple scattering only present in the Union version amounts to roughly 30% of the background conceived to arise from sample incoherent scattering. When only considering the single scattering events, the results from the Union components and PowderN component are in agreement. The asymmetric peak shape seen in both cases is caused by the detector height combined with the Debye-Scherrer cones.

4.3.3 Single_crystal scattering

Validation of scattering from a single crystal process is performed by comparing with the Single_crystal component which the process is based on. As the Single_crystal component simulates incoherent scattering in addition to the crystal Bragg peaks, an incoherent process is added to the Union material. Note that Single_crystal does simulate multiple scattering. Here a white beam with a homogeneous energy distribution in the interval $1 - 20$ meV illuminates a cylindrical $YBa_2Cu_3O_7$ sample oriented with the c axis along the beam direction. An isotropic mosaicity of $5' \approx 0.08°$ was used.

The transmitted beam contains both rays that never scattered, and rays that scattered an even number of times on a certain reflection. For this reason the transmission detector signal is separated into a non-scattered part and a scattered part seen in figure 4.10. Both cases show the expected agreement.

In figure 4.11 the results for a single Bragg peak is compared, showing no significant difference between the components. The asymmetric shape of the peak is due to the large sample, a large scattering cross section and the low distance to the detector. The first orders of scattering predominantly occur at the face closest to the source, while higher orders of multiple scattering are more evenly distributed over the large sample. The perceived width in scattering angle is the result of a wide distribution of spatial origins, but weighted with

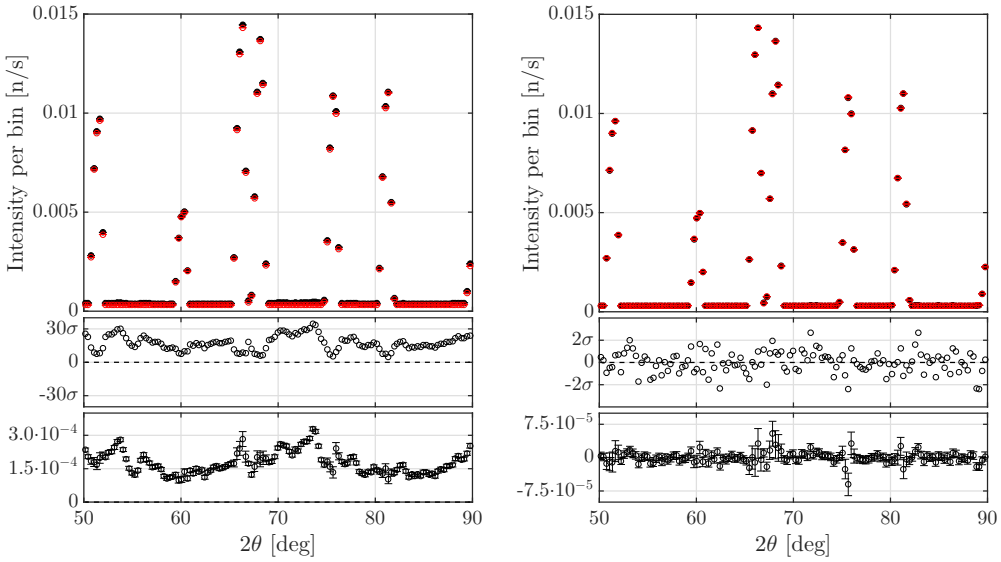

Figure 4.9: Bragg peaks simulated by Union powder sample (black filled) and PowderN (red empty). The detector results shown on the left side include all multiple scattering orders, while the right side only includes single scattering. The difference for each point relative to the error on the difference introduced by the Monte Carlo technique is shown together with the absolute difference. A positive value in the relative and absolute difference panels correspond to the Union components reporting the largest intensity.

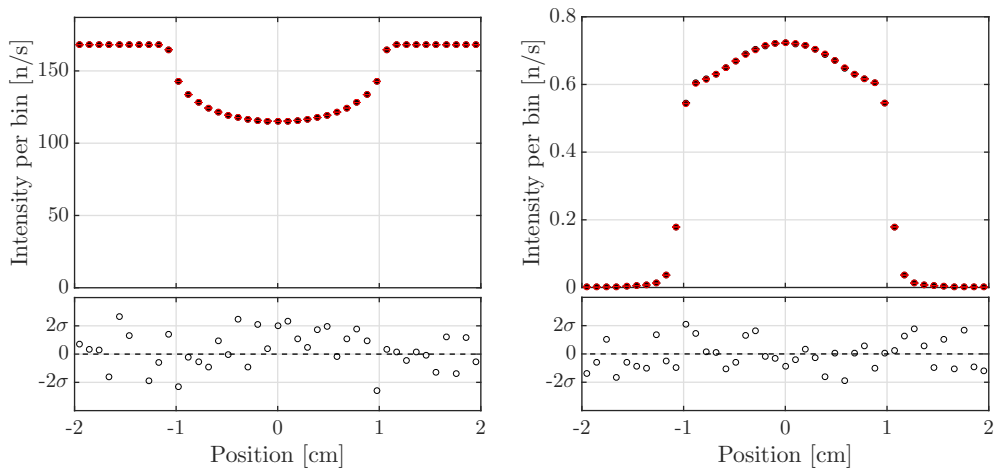

Figure 4.10: Simulated transmission results for Union components (black filled) and Single_crystal (red empty). Left side includes rays that did not scatter, while the right side display rays that did scatter. Lower panels shows the difference for each point relative to the error on the difference introduced by the Monte Carlo technique.

lower probability for higher orders of multiple scattering. The positions of the remaining Bragg peaks for the two components are identical, as shown in figure 4.12.

4.3.4 Discussion

Validation of the Union processes were done against the regular McStas components on which they were based.

The results were as expected for the Incoherent and Single crystal processes, where all deviations were consistent with the Monte Carlo noise estimated by McStas. The Powder process which was compared to the PowderN component did show some small differences

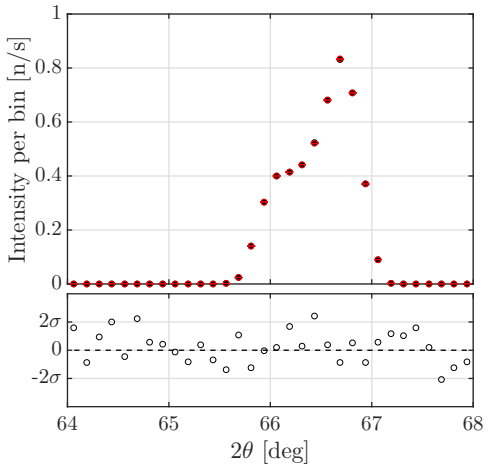

Figure 4.11: Simulated Bragg peak and incoherent background for Union components (black filled) and Single_crystal component (red empty). Lower panel shows the difference for each point relative to the error on the difference introduced by the Monte Carlo technique.

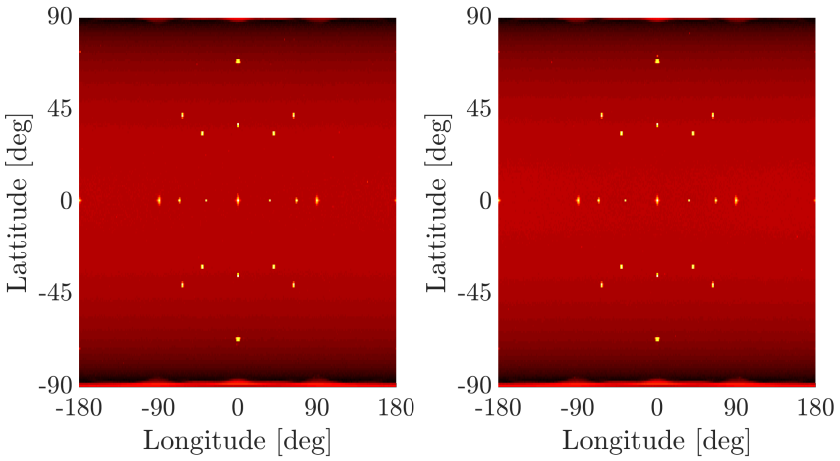

Figure 4.12: Simulation of single crystal Laue diffraction using spherical detectors covering all directions for both Union components (left) and Single_crystal (right).

that can be explained by the absence of multiple scattering in the reference component. In this case the scattering signal was validated for the first order scattering.

Further work would be required to validate the Union powder process for higher orders of scattering. This could be done either against other code that includes multiple scattering, by a detailed comparison to analytical expressions, or by experiments.

4.4 MACS

The Multi-Axis Crystal Spectrometer (MACS) at the National Institute of Standards and Technology (NIST), USA is a powerful cold triple axis spectrometer with a double focusing monochromator and 20 analyzer channels. The analysers are permanently separated by 8° and are situated in a common vessel named the "kidney" after the shape. Due to the many channels, the instrument excels at mapping out planes in reciprocal space. The instrument has, however, shown some background at low scattering vectors that was not expected by the instrument designers. For this reason, the instrument was simulated in McStas using the Union components with the hope of replicating and explaining the background issues. The McStas model is also to be used for replicating experiments when unexpected signals are measured to ascertain if they can be explained by instrument effects. Finally, the resolution functions are of interest, and beamtime has been allocated to perform a validation of the simulation with this aspect in mind.

4.4.1 Instrument overview

An overview of MACS can be seen on figure 4.13, showing the slightly unconventional setup including a translating monochromator and a center of rotation between the monochromator and sample position.

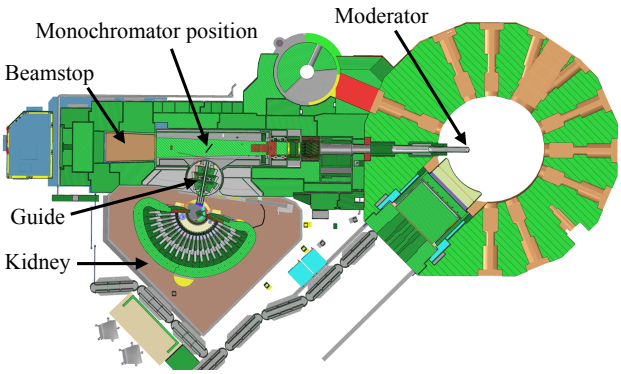

Figure 4.13: Overview of the MACS instrument from the NIST webpage [78] with additional annotations.

Source

MACS has a dedicated cold moderator [79] with a spectrum peaking at 4 meV and an elliptical shape when viewed from the MACS monochromator.

Monochromator

The monochromator consists of 21 columns of 17 2.0×2.0×0.2 cm^3 pyrolytic graphite crystals cut for the 002 reflection. The mosaicity of the crystals are 36'. Each column is mounted on a compressed aluminium support arch with a varying thickness as a function of height, resulting in adjustable vertical focusing. The columns can be rotated individually, and are kept in horizontal Rowland focusing geometry on source and sample. The monochromator is translated away from the source for decreasing energies, starting at 5.1 m for 17 meV and ending at 6.65 m for 2.4 meV. Slits are available before the monochromator to limit the illuminated area in order to control the divergence of the monochromated beam.

Guide system

No guide is used between the neutron source and monochromator, but a short guide is used between the monochromator and sample position. Due to the translation of the monochromator, the guide is rotated around a point in-between monochromator and sample. The guide has a rectangular cross section, and the angles of the vertical mirrors can be adjusted individually for each side. The exact reflectivity curve of the guide is not known, but has a m-value of 3.5.

Filters

Cooled filters are available between the source and monochromator, and between sample environment and kidney. The design include cooled beryllium, beryllium-oxide and pyrolytic graphite filters for both locations.

Sample environment

The most commonly used sample environment is a 100 mm bore cryostat and a 11.5 T cryomagnet. It was not possible to find detailed plans for either sample environment, but some information was available for the 100 mm bore cryostat. A beamstop is situated immediately outside the sample environment.

Kidney

The kidney contains 20 identical channels separated by 8°, each with a collimator entrance. An overview of the entire kidney is given in figure 4.14. A channel contains a double analyser composed of vertical focusing arrays of 9 pyrolytic graphite crystals of dimensions $2.0\times6.0\times0.2$ cm^3 as shown in figure 4.15. The used crystals have a mosaicity of 50' and the vertical focusing distance is 50 cm. The analysers are translated as a function of angle, keeping the beampath after fixed at the stationary spectroscopy detector as illustrated in figure 4.16. A diffraction detector is situated behind the first analyser, and a set of gadolinium collimator blades at a fixed position directly between the analysers are rotated according to the analyser positions. Cross talk between the channels are prevented as the kidney is constructed of boronated polyurethane with a large absorption and incoherent cross section.

4.4.2 Description of McStas simulation

The instrument responsible Jose Rodriguez made a simulation of the MACS monocrhomator [80], which was used as a starting point for the full MACS simulation. The McStas Union components were used to simulate the monochromator assembly, the sample and sample environment, and the kidney. A McStas 2.3 instrument file can have a maximum of 1000 components, and to circumvent this issue a separate instrument file is used before and after the guide. The beam after the guide is recorded in the first instrument file and loaded in the second instrument file.

Source

The elliptical shape of the source is replicated, yet the absolute source spectrum was not recreated as only a single energy was used.

Geometry

The monochromator assembly was simulated using the Union components as shown in figure 4.17. Each of the 357 monochromator crystals are individually placed with a random misalignment with a normal distribution of 0.15°. The mounting arches were simulated, albeit with constant thickness matching the total aluminium volume. The screws and shims attaching each crystal to the mounting arch were neglected due to the total component limit. The 3 hollow support columns were simulated. The horizontal and vertical focusing can be

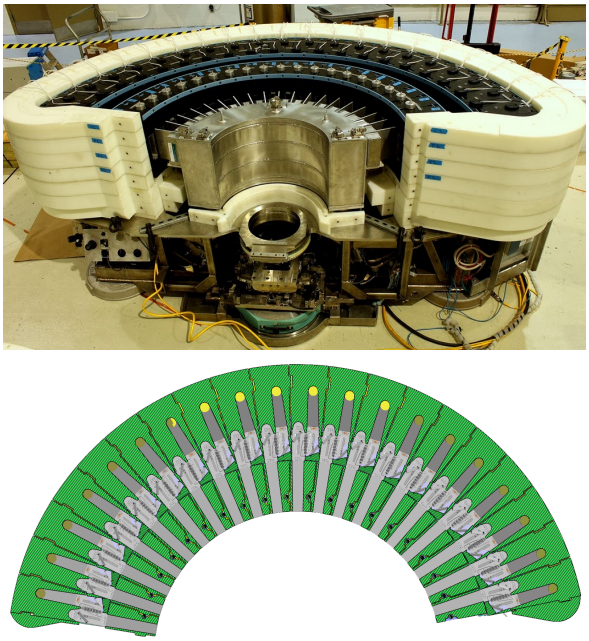

Figure 4.14: (Top) Picture of kidney assembly with filter from NIST webpage [78]. (Bottom) Cut through CAD model of the kidney showing the layout of analyzer channels.

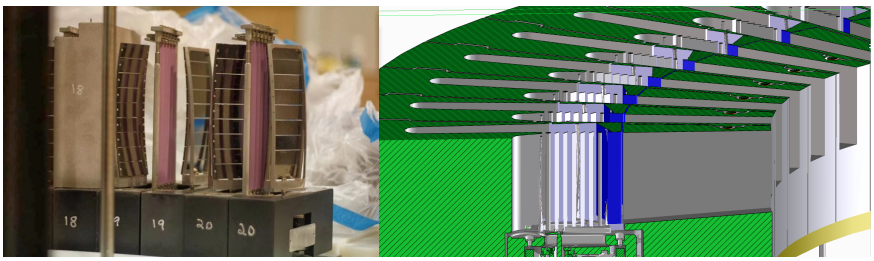

Figure 4.15: (Left) Photo of vertical focusing double analyzers from NIST webpage [78]. (Right) Cut in CAD model of kidney showing a channel for a analyzer setup, including the collimator blades, but only the frames of the crystal analyzers.

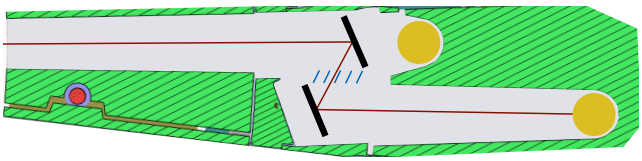

Figure 4.16: Single analyzer channel in the MACS kidney, composite image based on MACS CAD model with added analyzers (black), collimator blades (blue), detectors (yellow) and ray path (red). Both position and orientation of the analyzer depend on the selected final energy and the collimator blades are rotated to match the flight path.

disabled individually, and the slits controlling the illumination of the monochromator are included.

The guide between the monochromator and sample was simulated with adjustable angles for the two sides.

Only sparse information on the geometry of the 100 mm bore cryostat was available. The outer and inner walls were both simulated with a 2 mm thickness, and the thin heat

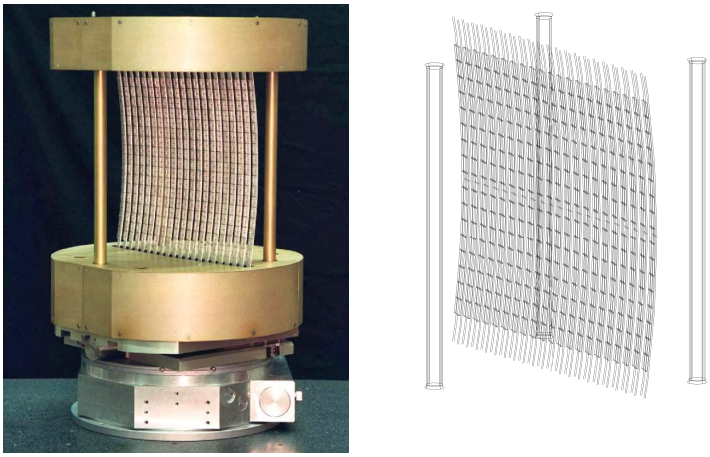

Figure 4.17: (Left) Picture of the MACS double focusing monochromator from NIST webpage [78]. (Right) McStas mcdisplay output of MACS monochromator simulated using Union components.

shield was neglected. Only the outer dimensions and the 100 mm bore cryostat are certain. Both sample and sample environment are simulated using Union components.

All 20 kidney channels are simulated simultaneously. After the sample environment, a group of filter components defining the entrance window for each channel is simulated using the Filter_gen component. Rays that do not intersect any entrance are discarded. Next a collimator with a 90' divergence limit is simulated using the Collimator_linear component.

The remaining kidney is simulated using the Union components with a separate Union_master component. The use of separate master components allows regular McStas components in between as needed here, but removes the possibility for rays returning to the sample environment from the kidney. A CAD model describing the kidney was available, and thus the channel caves could be simulated accurately as shown in figure 4.18. The vertically focusing analysers are simulated as 9 graphite single crystals each. Aluminium holders for the analyzators were not simulated. The position and angle of the analysers as a function of final energy was replicated. A set of 5 collimation blades between the analysers were simulated as thin boxes. The geometry of a single kidney channel is shown in figure 4.19.

Flat monitors with appropriate dimensions were placed in both the diffraction and spectroscopy detector positions.

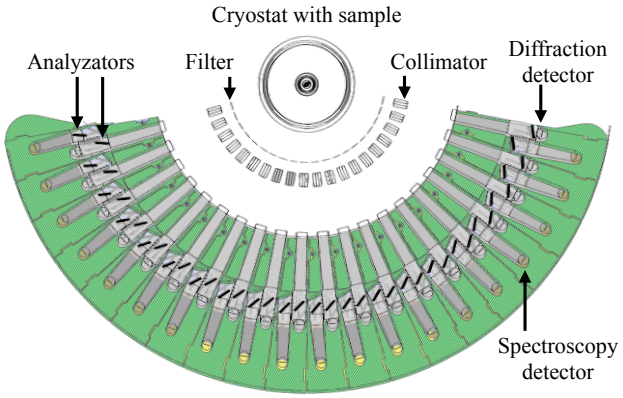

Figure 4.18: Overlay of McStas mcdisplay output and cut through CAD model of the MACS kidney. The analyzed energy for each channel is varied to show the motion of the analyzers in their caves.

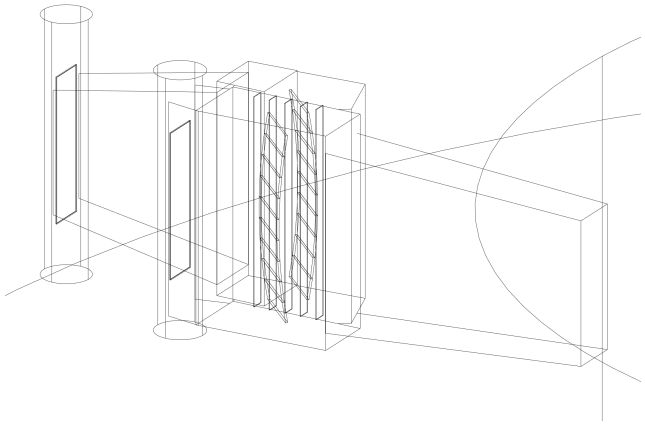

Figure 4.19: McStas mcdisplay output showing the geometry of a single kidney channel embedded in the kidney.

Materials

Here the Union material definitions are described. An overview of the inverse penetration lengths for incoherent scattering and absorption is available in table 4.4.

Both monochromator and anlyzators are made from pyrolytic graphite, but these are simulated as graphite single crystals as the Union single crystal process does not support the single crystal PG mode. The background problem encountered at low scattering vectors is not suspected to be a consequence of other Bragg peaks in the monochromator or analysers, meaning the graphite simulation should be an adequate approximation. The graphite is simulated using the appropriate standard McStas data file as a single crystal process, a incoherent process and absorption.

The aluminium is assumed to be pure, and is simulated as a perfect powder combined with an incoherent process. The standard McStas aluminium powder file is used.

The kidney is built from boronated polyurethane, for which the boron content is known. The polyurethane casting material used is, however, a commercial product where the exact formula is proprietary knowledge. Information on similar polyurethane materials was used to obtain a reasonable estimate of the incoherent and absorption cross section for the polyurethane. Due to the hydrogen and boron content, the shielding has both strong incoherent scattering and absorption.

The gadolinium coated collimator blades between the analysers are simulated as pure absorbers with very large absorption cross section.

Material	μ_{inc}	$\mu_{abs\,th}$
Aluminium	0.049 m^{-1}	1.39 m^{-1}
Boronated aluminium	0.049 m^{-1}	209 m^{-1}
Graphite	0.011 m^{-1}	0.040 m^{-1}
Boronated polyurethane	180 m^{-1}	3495 m^{-1}
Gadolinium blade	0 m^{-1}	$1.1{\cdot}10^4$ m^{-1}

Table 4.4: List of inverse penetration depth for incoherent scattering and absorption at 2200 m/s relevant for monochromator and kidney simulation.

Sample and sample holder

The McStas simulation is here used to recreate an experiment performed with a $NaCaNi_2F_7$ single crystal. A comprehensive description of the sample, its creation, and X-ray structure

measurements are available [81]. The sample has cubic symmetry with side length 10.28 Å, and the *hk* scattering plane is investigated here. The part of the sample believed to be a single crystal is still connected to a rod of polycrystalline material left over from the synthesis done in a optical floating-zone furnace. This rod was problematic during the mounting of the sample, as it was not possible to center the single crystal part while keeping the necessary orientation for the experiment. This was corrected by introducing a 8.1 mm offset of the sample environment which is rotated in its entirety. The polycrystalline rod had to be shielded due to the relatively large incoherent cross section of the material. The sample mounted on the sample holder is shown together with the simulated sample holder in figure 4.20. Figure 4.21 shows a picture of the sample holder wrapped in boronated aluminium shielding. The simulated sample and sample holder geometry relies partly on measurements and the pictures shown, and apart from the tilt in one dimension is reasonably accurate. The level of detail included on the sample holder is limited mainly be the number of geometries available due to the remaining instrument file approaching the component limit.

The form factors needed to describe the Bragg scattering is obtained using the iFit cif2hkl script on a cif file supplied by the experimental group [82]. Bragg scattering was not simulated for the polycrystalline rod, as the grain sizes are not expected to be a good approximation to a powder. The inverse penetration depth for incoherent scattering and absorption are shared among the two material descriptions and are shown in table 4.5.

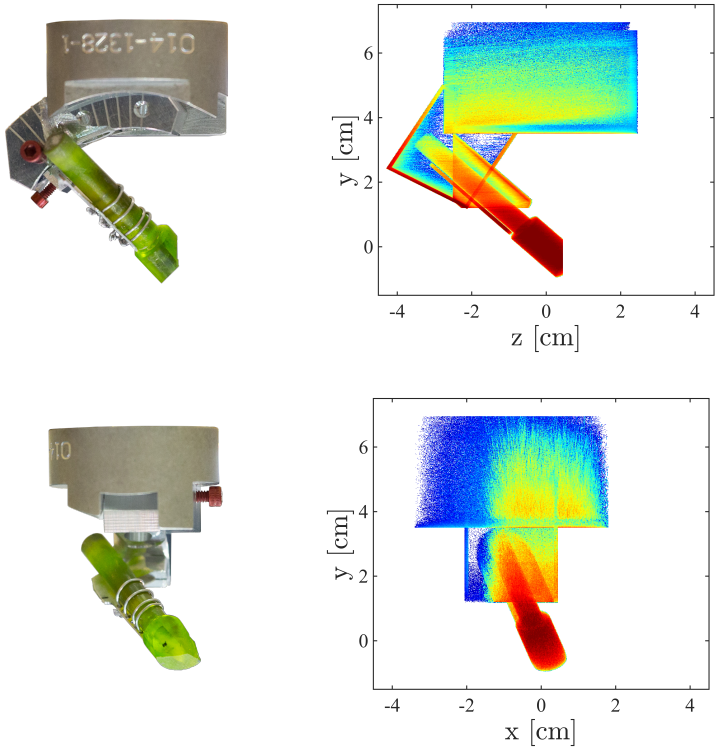

Figure 4.20: Picture of $NaCaNi_2F_7$ sample in sample-holder before shielding was added alongside the spatial scattering distribution of the simulated sample and sample holder. The simulated sample-holder includes the added shielding. The simulated spatial scattering distribution was recorded using the appropriate Union logger component and shown on a logarithmic scale over 4 orders of magnitude. The sample orientation in relation to the incoming beam correspond to an A3 angle of -90°.

Material	μ_{inc}	$\mu_{abs\,th}$
Aluminium	0.049 m^{-1}	1.39 m^{-1}
Boronated aluminium	0.049 m^{-1}	209 m^{-1}
$NaCaNi_2F_7$	8.89 m^{-1}	7.37 m^{-1}

Table 4.5: List of inverse penetration depths for incoherent scattering and absorption at 2200 m/s relevant for the sample and cryostat simulation.

Figure 4.21: $NaCaNi_2F_7$ sample in sample holder with shielding in the form of boronated aluminium. The shielding is included in the simulations shown on figure 4.20.

4.4.3 Comparison to measured data

Here the measured and simulated elastic data sets are directly compared in order to gauge the quality of the MACS instrument simulation. The elastic measurement here used as a comparison was part of a longer beamtime investigating magnetic properties of the $NaCaNi_2F_7$ sample. Preliminary results were presented [83]. This measurement is performed with a 5 meV beam using Be filters before monochromator and after the sample. The experiment was performed at a temperature of 40 K. The monochromator was not horizontally focusing, but focusing in the vertical direction was used.

MACS is often used to map planes of reciprocal space by combining a large number of A3 scans and here such a map serves as the comparison. The measured map is composed of 14 different kidney angles and 361 sample rotations over a 180° range. Only half the sample rotations are simulated, resulting in 181 sample rotations.

In order to recreate the measured data using the McStas simulation, the orientation of the crystal is necessary. This information was regretfully not recorded, and due to the cubic space group of the sample, 4 different sample rotations agree with the measured Bragg pattern. In order to determine the sample rotation retrospectively, a scan over an entire rotation was compared to the measured data. The 20 detector channels provide 20 A3 scans with different A4 values, and considering all scans, one of the 4 possible sample orientations is far more likely that the remaining. In figure 4.22 4 of the scans are shown, the first 2 of which are among the majority supporting the selected sample orientation, the third being among a few were another sample orientation would be more likely. The last shown scan includes the 400 Bragg peaks illustrating how they reduce the problem to 4 possible sample rotations due to the cubic symmetry of the sample.

The full measured data set and a simulated recreation using the conjectured sample rotation is presented in figure 4.23. The detector efficiencies for the measured data have been altered slightly using A4 plots were the detectors have significant overlap in coverage. The background measured near A4=0 is not replicated well by the simulation, as the intensity is severely underestimated. The simulation contains somewhat sharper features in the background, and in most cases there is background around these features in the measured data, with the notable exception for the area around A3=75° and A4=60° .

The data sets transformed into reciprocal space can be seen on figure 4.24. The beam at

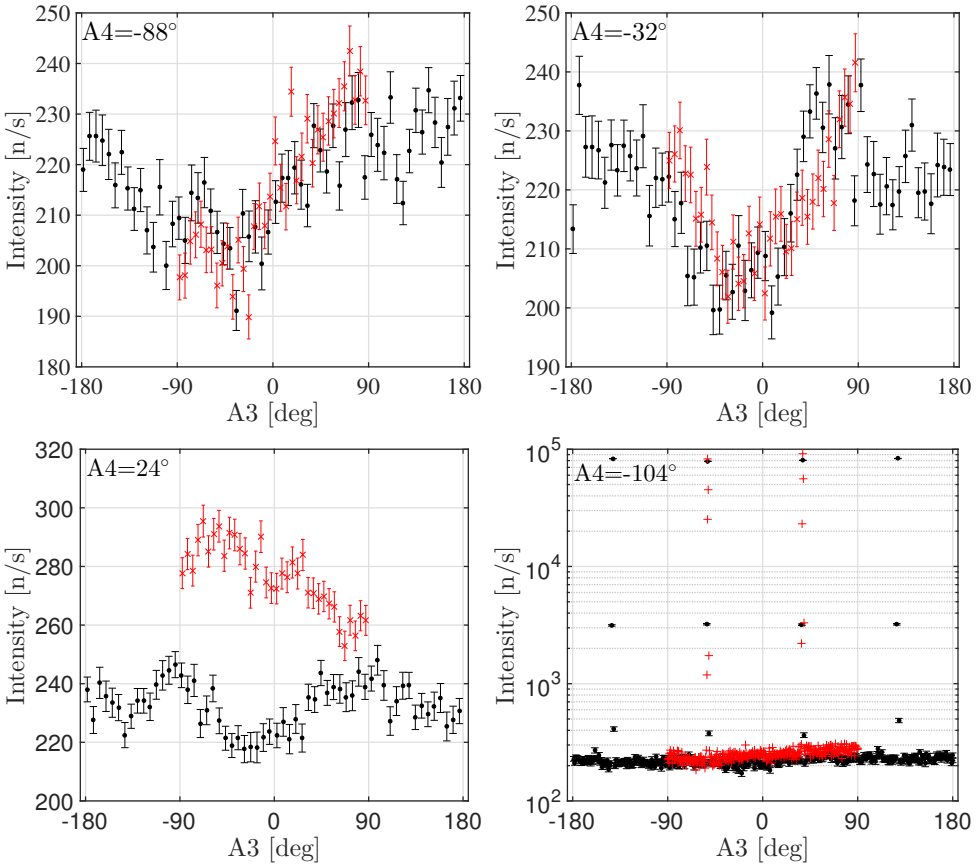

Figure 4.22: A3 scans for different detectors from one instrument configuration, red points are measured data and black simulated data. The data sets for the first 3 panels have been rebinned, and a scaling factor have been applied to all simulated data independent of A4. Due to the unknown rotation angle of the sample, the simulated data can be shifted in increments of 90°, here shown with the offset best matching the measured data when considering all 20 A3 scans.

the sample position is not symmetric when measuring the divergence as a deviation between sample position and monochromator, which would not be noticed in the real experiment as alignment would remove this offset. For the simulation a small angle was subtracted from A4 to generate the correct transformation to reciprocal space. The 220 and 400 Bragg peaks were expected, but the 200 peaks are forbidden in the space group of the sample. They are assumed to arise from multiple scattering out of the scattering plane, and are also present in the simulated data. The 3 measured Bragg peaks with lower intensity that are not at integer positions in reciprocal space were unexpected and not replicated by the simulation. Their length correspond to 131 and 111 respectively and are assumed to be from a smaller crystallite.

A close view of a number of the measured and simulated Bragg peaks are compared on figure 4.25. Here the lower number of A3 steps in the simulation is evident. The $\bar{2}20$ and $\bar{2}\bar{2}0$ peaks have similar shape and intensity. The forbidden $\bar{2}00$ and $0\bar{2}0$ peaks show large discrepancies in terms of intensity and peak width between simulation and measured data.

A integral over the h=-2 line in reciprocal space is shown in figure 4.26. Here the intensity difference between the simulated and measured $\bar{2}00$ peak is clear. The remaining simulated data does, however, agree well with measurements, including the peak width and intensity. Figure 4.27 show a comparison between the measured and simulated A4 scan for A3=79°. The scan includes the 220 peak along with the background near A4=0. The simulated contributions from the sample, inner cryostat and outer cryostat are separated

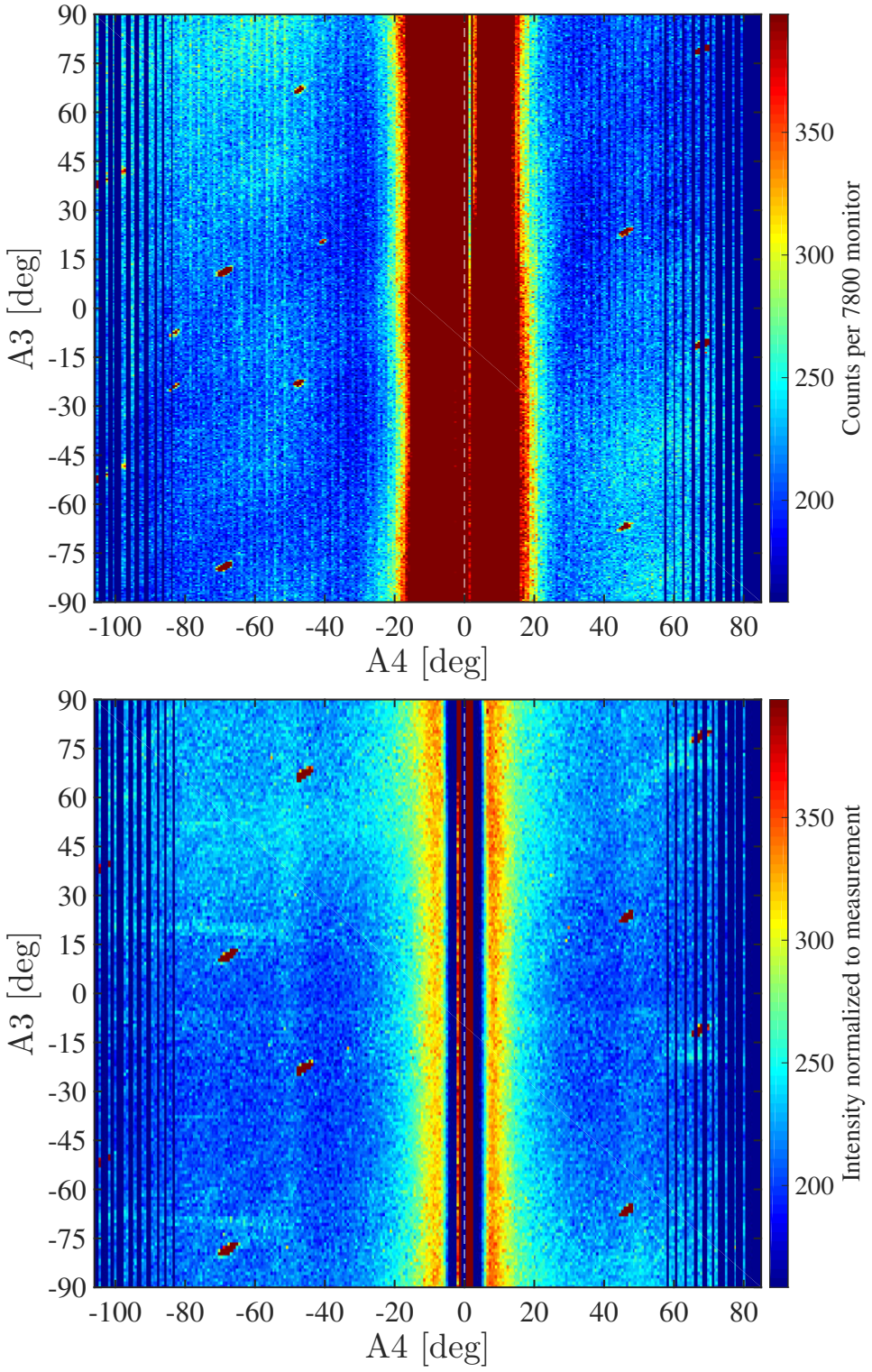

Figure 4.23: (Top) Measured elastic data set for $NaCaNi_2F_7$ with colorscale chosen to show variations in instrument background. The quick changes in intensity along A4 are due to differences in detector efficiency. (Bottom) Simulated recreation of the elastic $NaCaNi_2F_7$ data set. Intensities have been normalized to the measured data using regions without Bragg peaks.

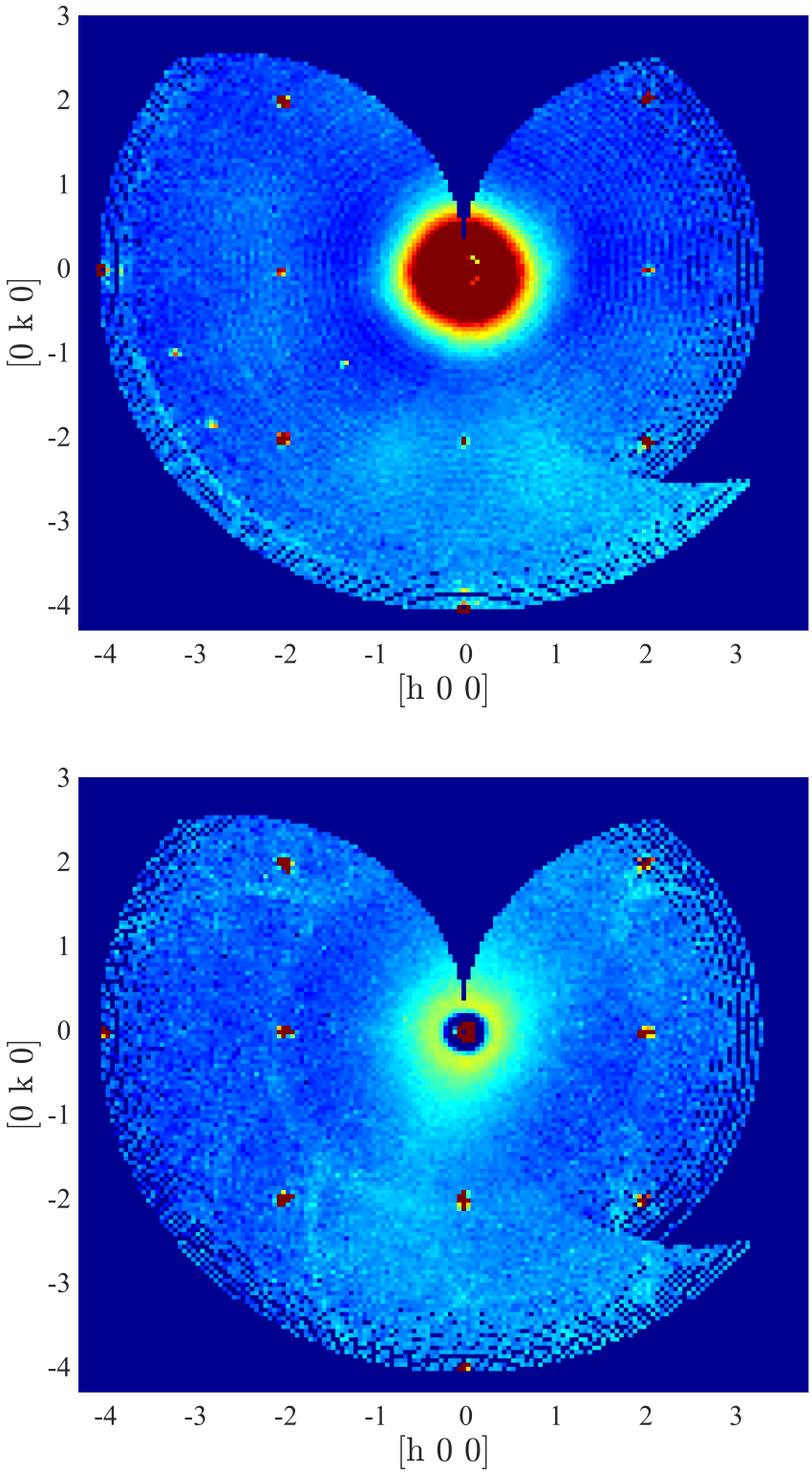

Figure 4.24: (Top) Elastic measurement of $NaCaNi_2F_7$ consisting of 14 A3 scans over 180° each with 361 sample rotations. (Bottom) Simulated recreation of the experiment, yet 181 sample rotations were used in the same interval.

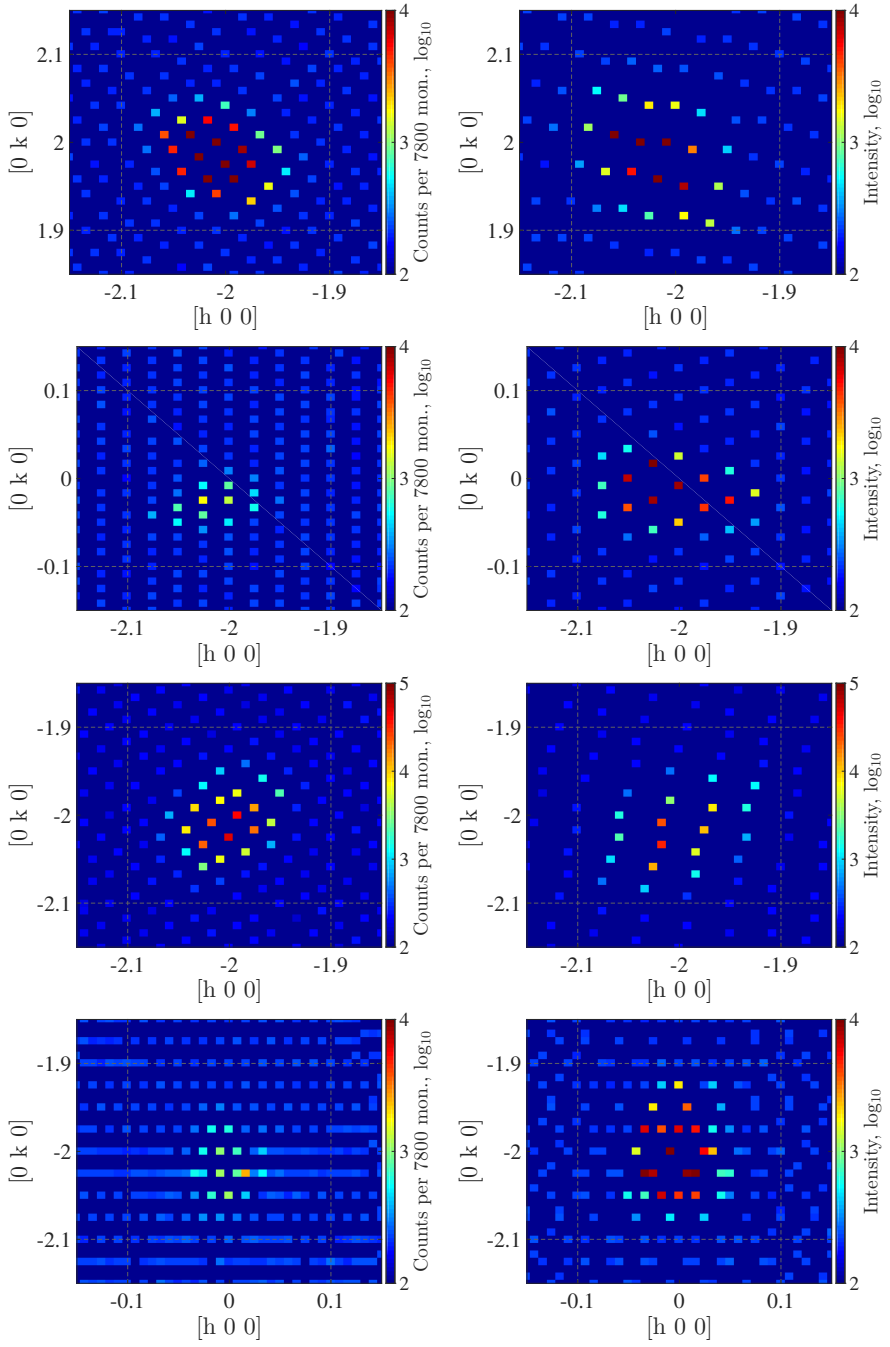

Figure 4.25: (Left column) Measured Bragg peaks binned with high resolution. (Right column) Simulated Bragg peaks binned with high resolution. Both data sets are presented on logarithmic axis, using the same intensity normalization as previously.

for the simulation. The agreement for the Bragg peak is excellent, yet the background near A4=0 is not captured well. The contributions from the cryostat do seem to match the width of the background phenomena, but is approximately a factor of 10 to weak. The increased background measured on one side of the direct beam is not captured by the simulation, and the effect is not currently understood, but could be connected to the slight asymmetry of the beam.

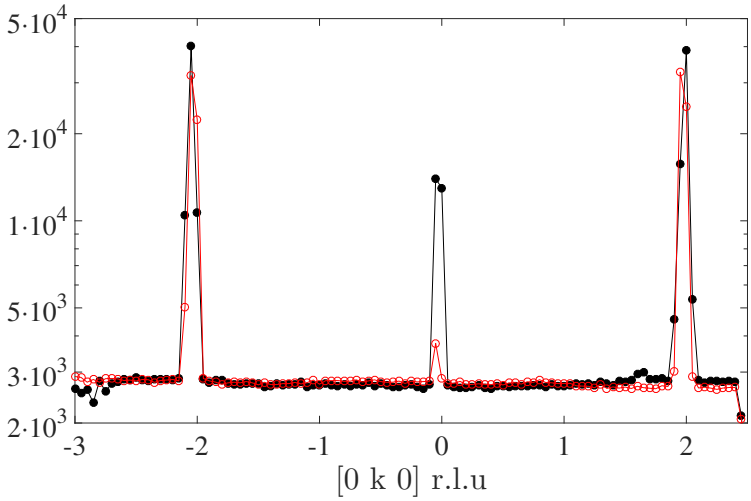

Figure 4.26: Integrated signal over h=-2±0.3 for measurement (red) and simulation (black), errorbars are neglected for clarity.

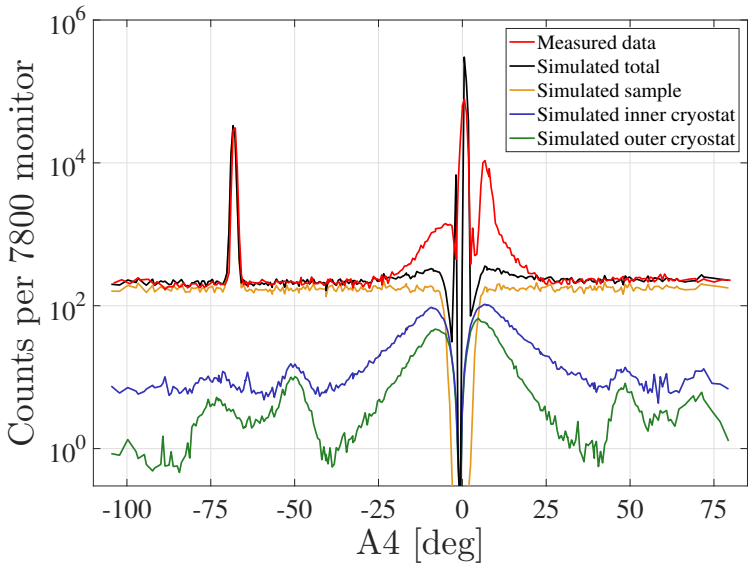

Figure 4.27: A4 scan for measured and simulated data with A3=79°, the simulated data is decomposed into the part that scattered in the sample, inner cryostat and outer cryostat. Note the sum of the three parts can be larger than the total, as some rays may scatter in more than one of these parts.

4.4.4 Analysis of simulated data

One of the main advantages of an accurate simulation is the ability to track the different contributions, understand them, and apply the knowledge to the real system. Here the Union logger and conditional components are used to analyze the data presented in 4.4.3.

In figure 4.28 the (A3,A4) plot is shown for rays that scattered in certain parts of the sample environment. From panel (a) and (b) it can be confirmed that the (200) peaks were a result of multiple scattering, as they do not appear when only single scattering events are recorded. The incoherent background from single scattering in the sample contains diagonal strips intersecting Bragg peaks with lower intensity than elsewhere. These are assumed to occur as incoherent scattering destined for these stripes would fulfil a scattering condition,

and thus have low probability for escaping the sample before being scattered again. The background pattern from the incoherent scattering originating in the polycrystalline sample part shown on panel (c) seems to be largely responsible for the recognizable features allowing the A3 angle to be found retrospectively. The effect seems to occur as the polycrystaline part of the sample is rotated in and out of the beam over the half rotation, with the shape being affected by the asymmetry of the incoming beam. Panel (d) shows scattering from the small aluminium plate used to attach the sample to the sample holder, and exposed to the direct beam. The scattering result show surprising clear peaks from the aluminium powder, which are absent when just single scattering from this part is recorded. These could be Bragg peaks from the single crystal sample that intersect the small aluminium plate, resulting in scattering at specific combinations of A3 and A4. Panels (e) and (f) show scattering from the outer and inner cryostat walls respectively, here a large background is seen at small A4 angles. Some crosses are seen for both at around A4=$\pm$70°, which are composed of a part constant in A4, and a diagonal part. These are believed to be connected with Bragg peaks from the single crystal sample out of the plane, backscattered by a powder line in the cryostat walls.

Multiple scattering in the sample

The Union logger component recording scattering vectors is used to investigate the 200 peaks further. The results are shown in figure 4.29. The logger was targeted at the sample volume and the single crystal process, and thus only records the single crystal scattering from the sample. A conditional component was used to modify the logger so that only rays that eventually reach the detector position corresponding to the $\bar{2}00$ peak are recorded. The simulation results show that the first scattering primarily occurs in $\bar{3}11$ or $\bar{3}1\bar{1}$, but some scattering from 111 and $11\bar{1}$ is observed. The second scattering event could be preceeded by an incoherent scattering event, and thus many more reflections are available, however the scattered intensity from $1\bar{1}1$ and $1\bar{1}\bar{1}$ is largest, followed by $\bar{3}\bar{1}1$ and $\bar{3}\bar{1}\bar{1}$. A scattering from $\bar{3}11$ and $1\bar{1}\bar{1}$ results in the $\bar{2}00$ investigated, and so does a scattering from $\bar{3}1\bar{1}$ and $1\bar{1}1$. This demonstrates how the Union loggers and conditional components can be used to identify the origin of multiple scattering.

Origin of background

The scattering within the sample environment is visualized on figure 4.30, where a Union logger was used to record the spatial distribution of the scattering. At the beam energy of 5 meV used here, two Bragg peaks are accessible in the aluminium, 111 with $2\theta = 119.8°$ and 200 with $2\theta = 174.6°$. The 111 reflection is clearly visible, as 3 Debye-Scherrer cones are visible from the direct beam penetrating the inner cryostat walls and the outgoing cryostat wall. The second scattering event show a lot of structure in terms of spatial distribution where the third order is more evenly distributed. The used A3 angle corresponds to a 200 peak, and the out of plane Bragg peaks are visible in the second order spatial distribution as they intersect the cryostat. The 200 peak is only visible in the third order panel, as it requires at least 2 scattering events in the sample. The 200 peak is split in the vertical direction, indicating that the Ewalds sphere could only cover the necessary reciprocal lattice vectors for the 200 reflection with a center slightly outside the scattering plane. Due to the symmetry of the crystal, an Ewalds sphere with center slightly above or below the scattering plane are possible, assuming the vertical divergence from the monochromator is sufficient, which would result in a vertically split peak.

The background at low A4 angles is investigated by recording the spatial scattering distribution for rays that end in a spectroscopy detector for a channel with A4=10°. The results are shown in figure 4.31. The first scattering shows a low intensity at the first cryostat wall encountered by the beam, probably because rays scattered here are predominately backscattered and lost. The first scattering event never occurs in the analyzer, which confirms the analyzer is not within the direct beam. The second and third order frequently occurs in the first and second analyzer respectively, which corresponds to the intended beampath. The

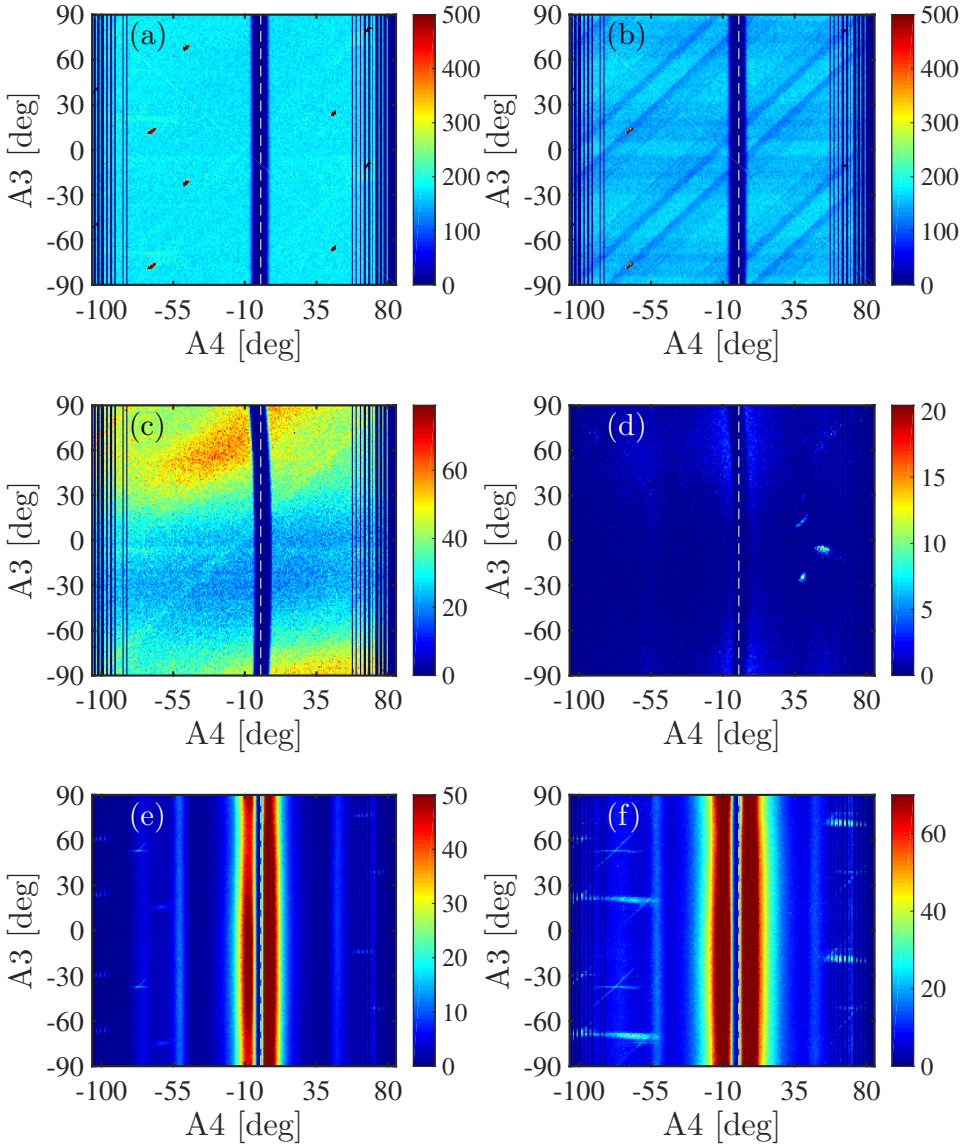

Figure 4.28: A3 A4 plots for rays that scattered in certain volumes. (a) Scattered in single crystal part of sample. (b) only single scattering in single crystal part sample. (c) polycrystaline part of sample. (d) aluminium plate holding the sample. (e) outer cryostat walls. (f) inner cryostat walls. All colorbars show intensity normalized to measured incoherent background.

scattering in the analyzers continues to higher orders due to the strong cross section provided by the Bragg peak. The origin points for higher order scattering in the cryostat align with the parts visible through the collimator. It is interesting to note that the sample is a frequent source for low scattering orders, yet the higher order scattering occurs elsewhere in the cryostat. Some low scattering intensity is recorded on the analyzers of other detector channels, one of which is exposed to the direct beam. The contributions from this scattering is minimal because the shielding between the channels have to be traversed in order to fulfil the conditional. The low angle background seem to originate from multiple scattering inside the sample environment, primarily from the cryostat walls.

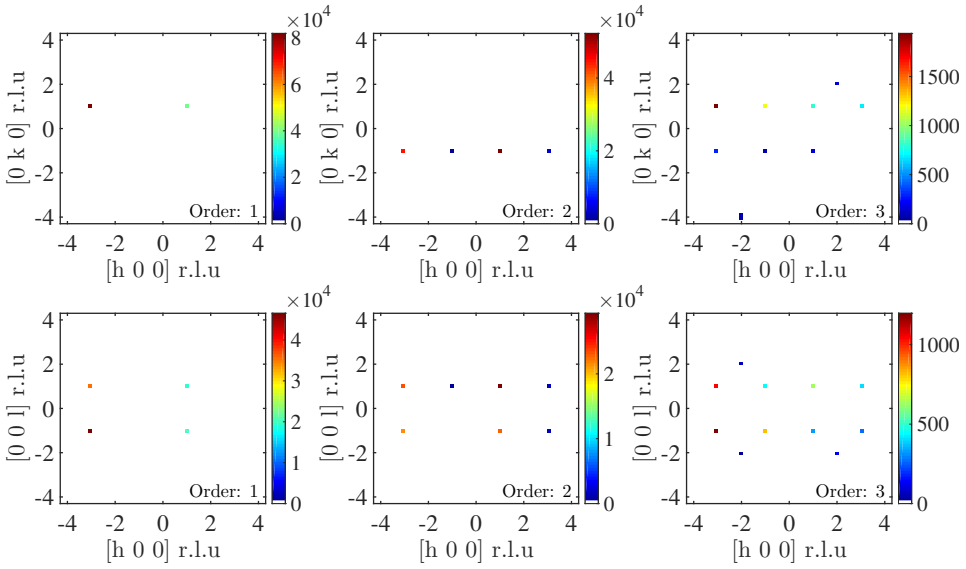

Figure 4.29: Union logger result for single crystal scattering in the sample, here shown for the hk plane integrated over all l, and the hl plane integrated over all k. A conditional component was used to modify the loggers so that only rays that contribute to the $\bar{2}00$ peak are recorded. The first 3 orders of multiple scattering are shown.

4.4.5 Discussion

The overall agreement between measured data and simulation have been noteworthy, replicating resolution functions and Bragg intensities with great accuracy. The instrument team recognized simulated spurions in the form of crosses in reciprocal space that were not visible in the measurements for this experiment, but was in other experiments and had been mistaken for sample related signal.

Two important deviations between measurement and simulation were, however, the lower background at low A4 angles and higher 200 multiple scattering peak intensity from the simulation. The simulation showed 4 different combinations of Bragg scattering resulting in the perceived 200 peak, all of which relied on out of plane reflections. Furthermore, the resulting peak was split slightly, and not completely in the plane, indicating that the center of the Ewalds sphere needed to be slightly above or below the scattering plane in order to fulfil the scattering conditions leading to the observed multiple scattering. A slight misalignment of the sample may result in only some of these multiple scattering combinations being available, and thus reducing the multiple scattering intensity for the measured data set. Simulations with misalignment could be performed to investigate the validity of this explanation.

The lower background at low A4 angles in the simulation may be connected to small angle scattering from structures in the sample environment, which was not simulated. The shape of the background is, however, replicated well by the simulation, but at an order of magnitude lower intensity. The background found in the simulation was shown to originate primarily from the sample environment.

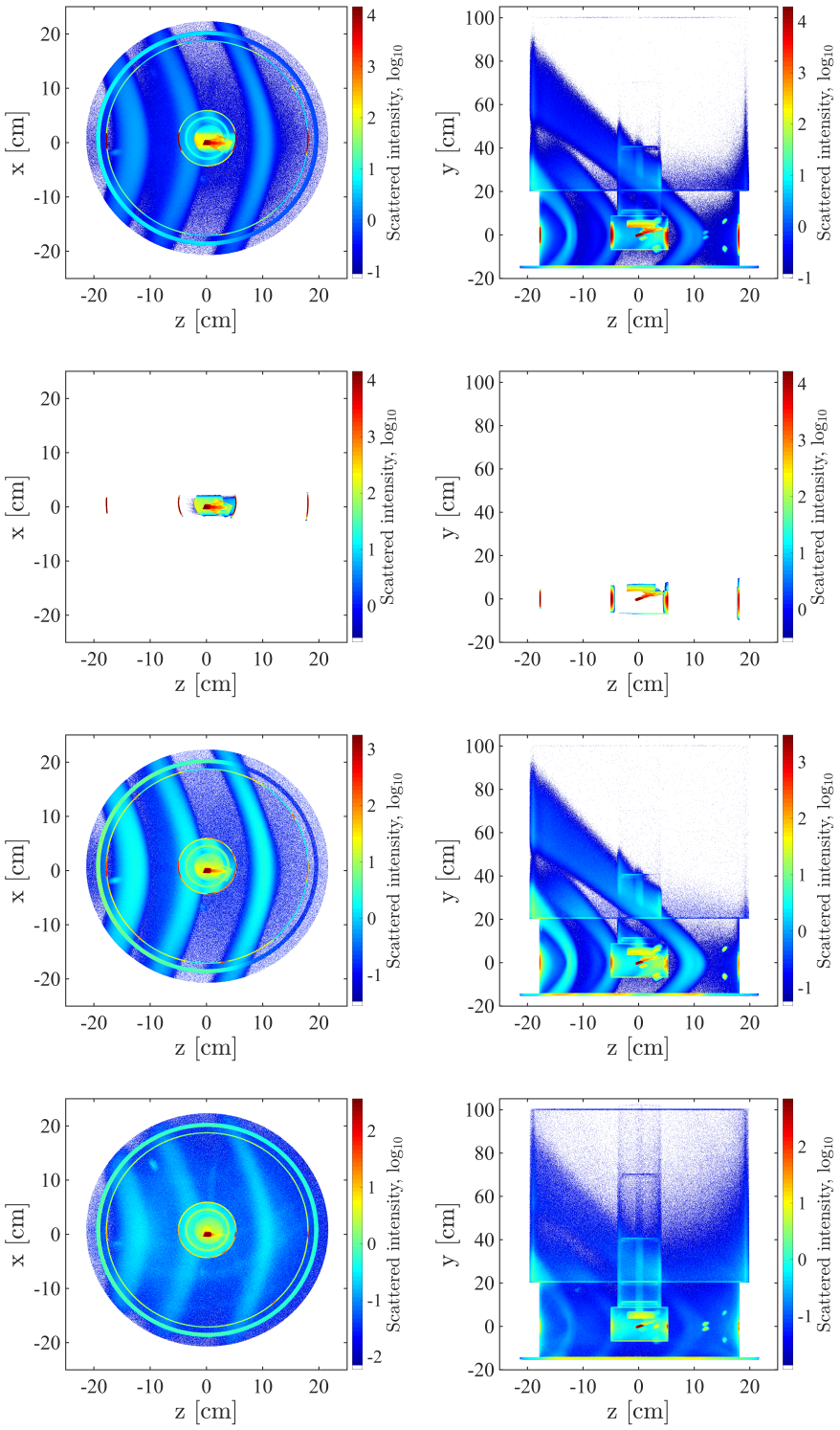

Figure 4.30: Scattering intensity for sample environment including sample, left column is from the top integrated over all heights while the right column is from the side integrated over the entire width. The first row includes all scattering, the second shows only the first scattering event, while the next two rows show the second and third scattering event respectively.

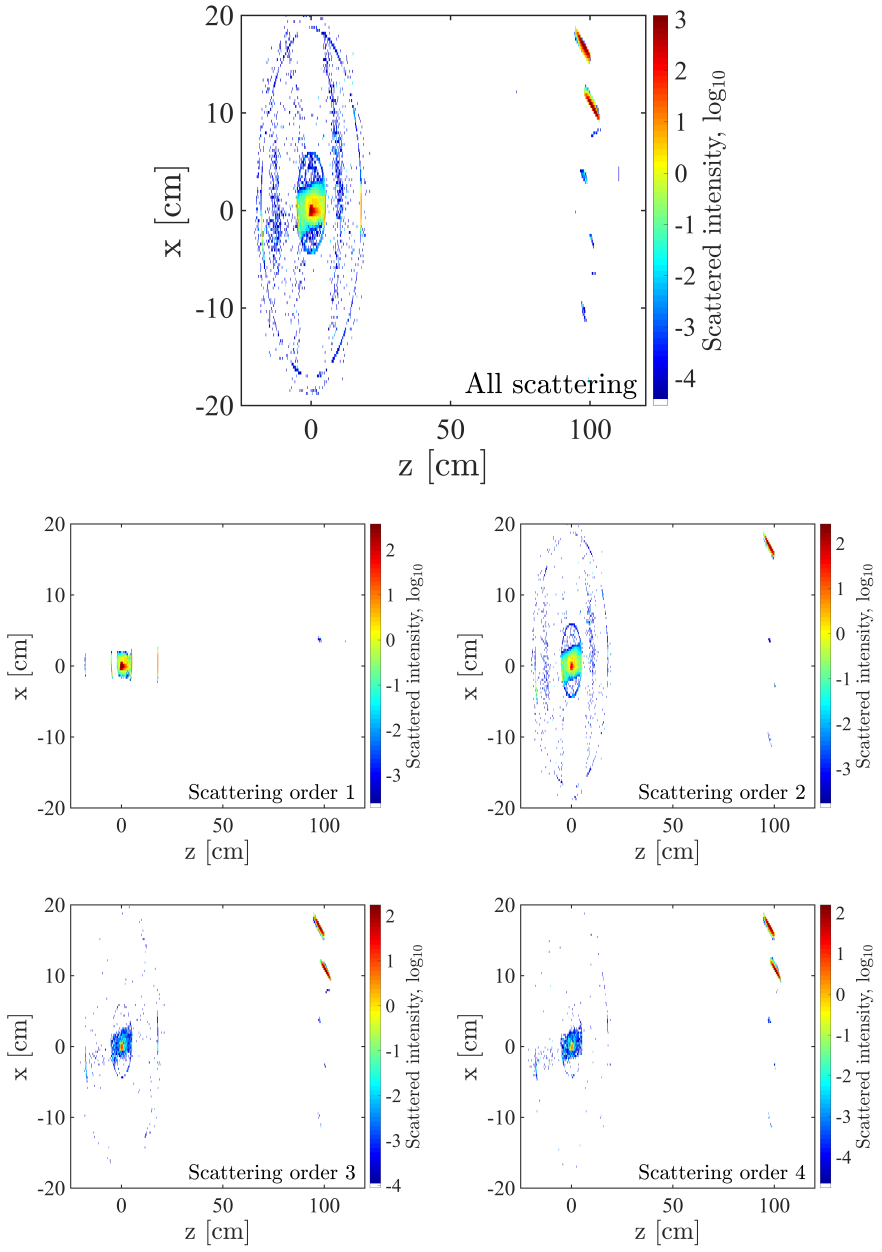

Figure 4.31: Spatial distribution of scattering for rays that end in the spectroscopy detector of a channel with A4=10°. The scattering intensity is weighted with the final weight of the ray.

4.5 MARI

In this section, the Union components are demonstrated by performing simulations of the ISIS time of flight powder spectrometer MARI [84], which is compared to an actual experiment. Furthermore, background present in the simulation is studied using the Union logger and conditional components. This section is directly based on the paper draft in appendix A.3, which was not submitted as a few slight inaccuracies in the instrument simulation were discovered shortly before submission. The discovered inaccuracies consisted of some differences in the detector geometry and some missing shielding in the sample environment. The paper is presented in its present form as there was insufficient time to obtain the accurate information on the instrument and redo the simulations before the deadline for this thesis.

4.5.1 Instrument overview

MARI uses the short pulse of the ISIS source and a single chopper to select the incoming energy as well as deduced the final neutron energy from the detection time. The trade-off between flux on sample and energy resolution can be adjusted through the rotational frequency of the chopper. The instrument is unusual as the detectors are under the sample as shown in figure 4.32.

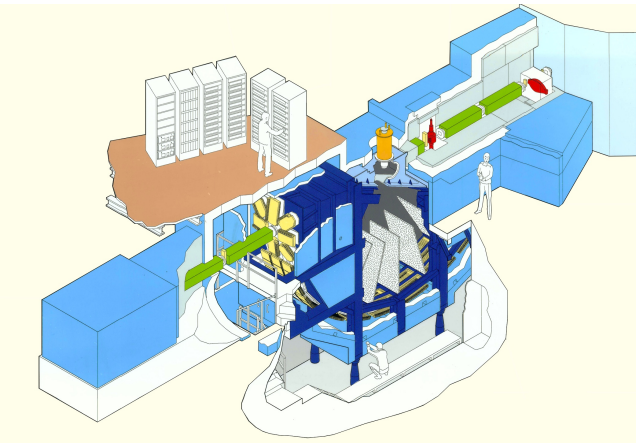

Figure 4.32: Overview of the MARI instrument from ISIS webpage [57].

4.5.2 Geometry

Here the geometry of the McStas MARI instrument model is presented.

The dedicated MARI moderator description in the ISIS source component is used with a size of 9×9 cm^2. The Fermi chopper is situated 10.05 m after the moderator and is simulated with the FermiChopper McStas component. The simulated chopper resembles the Gd chopper available at MARI. The radius is 5 cm and the 113 channels of 0.4 mm width makes up a 4.5 cm wide channel. The blades are curved with a radius of curvature of 0.8 m.

The beam defining jaws and sample position are placed 11.239 m and 11.739 m from the moderator, respectively. In all simulations for this paper, the jaws were at 4.5×4.5 cm^2.

Figure 4.33 shows an image of the simulated cryostat from the ISIS webpage [57] and the McStas Union model of the lowest parts of the cryostat.

The sample environment has an outer and inner chamber, each consisting of a cylinder on top of a sphere. The two spheres have centers 2.5 cm below the sample position and the cylinders starts at the same height. The radii and thickness of these and other geometrical details can be found in table 4.6. The outer cylinder has a window for beam entry and exit

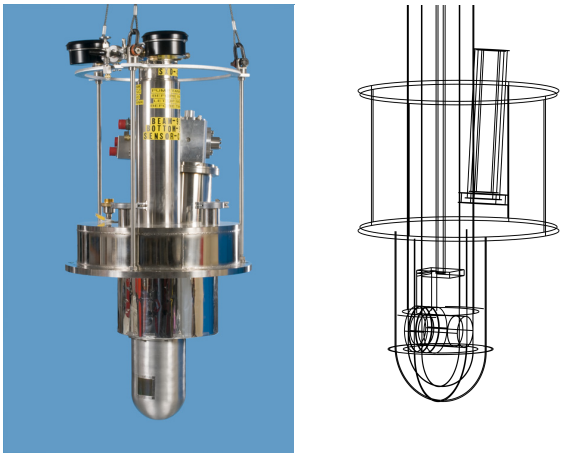

Figure 4.33: Toploading cryostat used on MARI and Union simulation of the lower part. The inner structure is visible in the Union model, showing the sample holder, sample stick and shielding blocks connecting the sample container with sample rod.

that has a width of 6 cm and a height of 5 cm. The inner cylinder is thinner at the beam height, which is ± 2.5 cm vertically from the sample position.

The lower vessel starts 13 cm above the sample position, has a height of 18.9 cm and is displaced 4.8 cm along the beam direction. The lower and upper plates are 5 mm thick. The Closed Cycle Refrigerator (CCR) starts 2.5 cm above the bottom plate of the vessel and is displaced 11.4 cm from the sample position along the beam direction. The CCR is tilted 6° from vertical towards the beam direction.

The sample container is simulated as a horizontal cylinder perpendicular to the beam direction with a length of 7.3 cm. The sample is in the circumferences of the container, and is thus hollow. The sample is 4.5 cm wide, and thus does not occupy the entire length of the container. One end of the container has a 6 cm wide collar which is connected to the sample stick with Boron-Nitride. The Boron-Nitride connecting piece is made of a cylinder with 1 cm width that connects directly to the collar and two boxes.

Description	inner radius	thickness
Outer sphere	6.90 cm	1.6 mm
Outer cylinder	6.90 cm	1.6 mm
Outer cylinder (window)	7.059 cm	0.01 mm
Inner sphere	5.00 cm	0.5 mm
Inner cylinder (beam height)	5.00 cm	0.15 mm
Inner cylinder (elsewhere)	5.00 cm	1.5 mm
Lower vessel cylinder	13.2 cm	2.5 mm
Sample can	2.09 cm	0.1 mm
Sample can collar	2.09 cm	10.1 mm
Upper CCR cylinder	2.5 cm	5 mm
Lower CCR cylinder	massive	3.4 cm
Sample stick	massive	0.7 cm

Table 4.6: Inner radius and thickness of used aluminium geometries. For massive objects, the outer radius is given as thickness.

The detectors are modelled as cylindrical monitors with a radius of 4.02 m. The high angle bank covers angles from 12° to 134° and the center detector is 30 cm wide while the side detectors are 20 cm wide and rotated plus and minus 4 degrees respectively around the beam direction. The low angle detectors covers from -12° to 12°, and there are four separate detectors rotated in 45° increments around the beam direction.

4.5.3 Materials

Here the material definitions used for the Union description of the sample environment is presented. As all materials are given a incoherent and absorption inverse penetration depth, these are collected in table 4.7.

The aluminium of which the sample environment is constructed is modelled as a powder with Bragg scattering from the standard McStas data file and an incoherent scatterer.

The Ni_3TeO_6 powder sample is modelled as Bragg scattering from a perfect powder and incoherent scattering. The Bragg scattering was described by converting a cif file obtained from the ICSD database [85, 86] into a lau file suitable for McStas using the cif2lau tool in iFit [67]. No inelastic scattering is simulated.

The vanadium calibration sample is modelled as a purely incoherent scatterer as the weak powder scattering is neglected.

The boron-nitride shielding material is modelled as an incoherent scatterer with strong absorption. The density and molar mass are used to calculate the number density, and the cross sections are taken from Ref [87]. The absorber was made using isotope pure ^{10}B for increased absorption which is taken into account.

Material	μ_{inc}	$\mu_{abs\,th}$
Aluminium	0.049 m^{-1}	1.39 m^{-1}
Ni_3TeO_6	15.1 m^{-1}	17.5 m^{-1}
Vanadium	36.7 m^{-1}	36.7 m^{-1}
Boron-nitride	80.8 m^{-1}	10100 m^{-1}

Table 4.7: List of inverse penetration depth for incoherent scattering and absorption at 2200 m/s.

4.5.4 Vanadium calibration

The calibration of the real instrument was replicated by simulating a Vanadium calibration measurement and an empty cryostat. This Vanadium calibration is simulated without the chopper and for wavelengths between 0.25 Å and 0.5 Å. The virtual detectors were calibrated to have the same systematic error as on the real instrument, by correcting with the empty cryostat simulation subtracted from the vanadium simulation.

4.5.5 Comparison with measurements

Here results from the simulated MARI instrument are compared with measurements performed on the real instrument. The empty cryostat was measured for calibration purposes, but here this measurement is the basis of the first comparison. The Gd chopper is used at 250 Hz and phased to achieve a beam energy of 34.85 meV. The real data is shown in figure 4.34, and the simulation results are shown in figure 4.35. The angular position and resolutions of the peaks match well, as do the energy shifts and energy resolution. Several peaks are split in similar fashion and their shapes generally match. The relative intensities of the peaks are, however, very different.

To investigate the angular dependence, both data sets are summed over all energy transfers, resulting in the comparison seen on figure 4.36. The simulated data have a scaling factor and a small constant background added. It is once again evident that the peak intensities does not match, but that the shape and position for the aluminium peaks does. The peaks are sharp at the positive angle side and have a tail at the low angle side which is consistent with the time tail of the used moderator.

The difference in peak intensities are expected to be caused by texture in some or all parts of the aluminium used to construct the sample environment and windows. Currently no components in McStas support simulation of textured powders, but simulations were made by increasing the scattering strength of different parts of the sample environment.

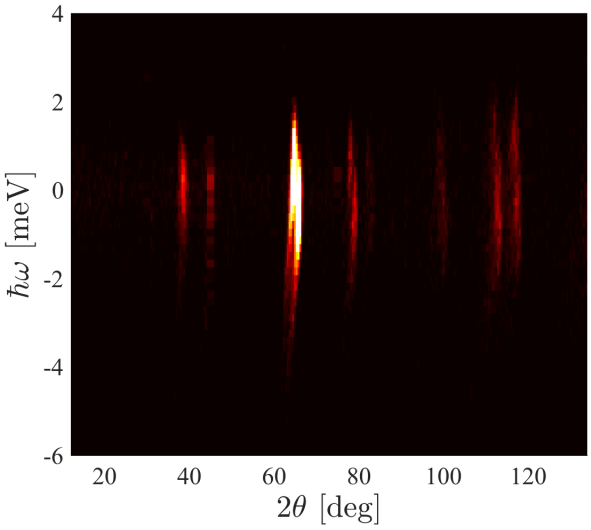

Figure 4.34: Scattering from an empty cryostat on MARI with a selected energy of 34.85 meV from the Gd chopper running at 250 Hz.

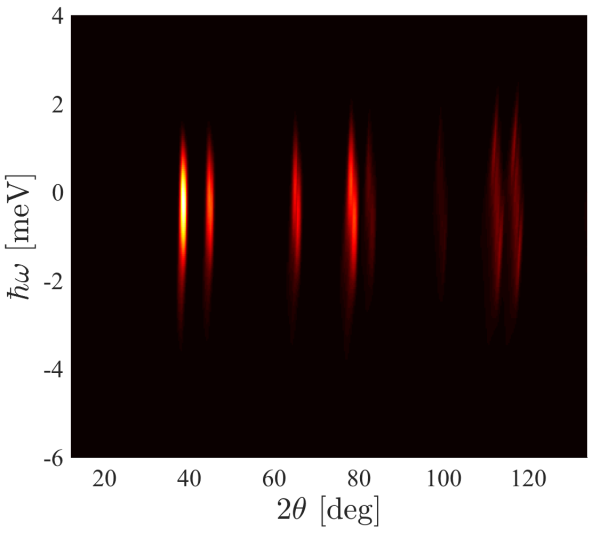

Figure 4.35: Simulation of scattering from an empty cryostat on MARI with a selected energy of 34.85 meV from the Gd chopper running at 250 Hz.

These showed that the peak separation in the data is consistent with scattering from the inner chamber walls.

The few peaks in the measurement that are one pixel wide e.g. at 109° are expected to be detector channels with slightly higher background while the small peaks at 23° and 105° may be from some other material used in a small quantity and not simulated.

The energy dependence was compared in a similar manner with a sum over all angles. The results are shown in figure 4.37, where a scaling factor was used to match the peak intensity and a small energy transfer added to facilitate easier comparison of the shape and width. The peak width is slightly wider in the simulation, but this will be influenced by the wrong Bragg peak intensities. The increased width of the simulation is most likely the result of some inaccuracy in the simulation of the chopper (where zero blade width is assumed).

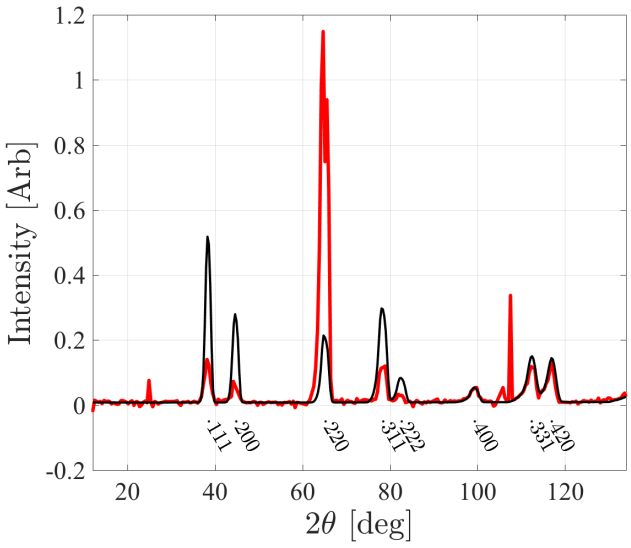

Figure 4.36: Comparison between data from an empty cryostat taken at MARI (red) and the McStas simulation using Union components (black). Here the scattering is summed over all energy transfers to view the angular dependence, which is dominated by elastic scattering and the angular resolution of the instrument. Indexing of the Al peaks is shown below the peaks.

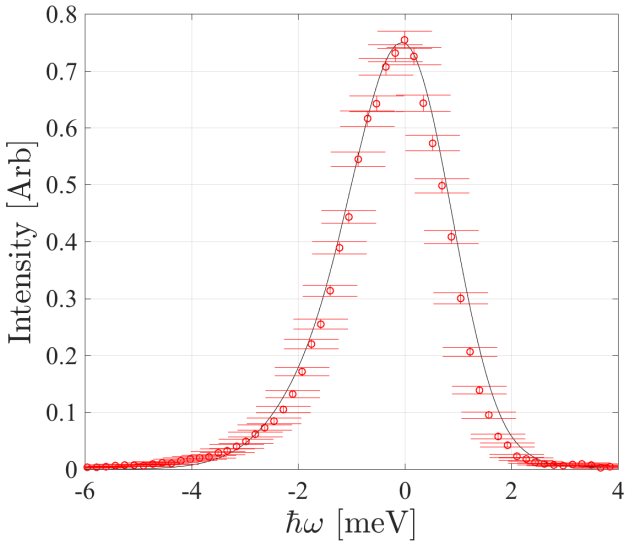

Figure 4.37: Comparison between data from empty sample environment taken at MARI (red) and the McStas simulation using Union components (black). Here the scattering is summed over all angles to view the energy dependence which is dominated by elastic scattering and the energy resolution of the instrument.

Next, the simulated MARI instrument is compared with available measurements on Ni_3TeO_6. The measurement was performed with the Gd chopper at a frequency of 250 Hz phased to provide a beam with an energy of 35.19 meV. The purpose of the experiment was to investigate the inelastic signal, the study of which will be published elsewhere [88]. Here the focus is on the elastic parts as the Union components do not include inelastic isotropic

processes yet.

The measurement were performed with a sample mass of 6.9 g placed in the circumference of the sample container with a width of 4.5 cm perpendicular to the beam and a thickness of 1.9 mm. This was replicated in the simulation.

The data sets are summed over energy to compare the angular dependence as shown in figure 4.38. A scaling factor is used to match the intensities of the two data sets and a small constant background was added to the simulation. There is a good overall agreement, but once again the differences in aluminium peak intensity are evident.

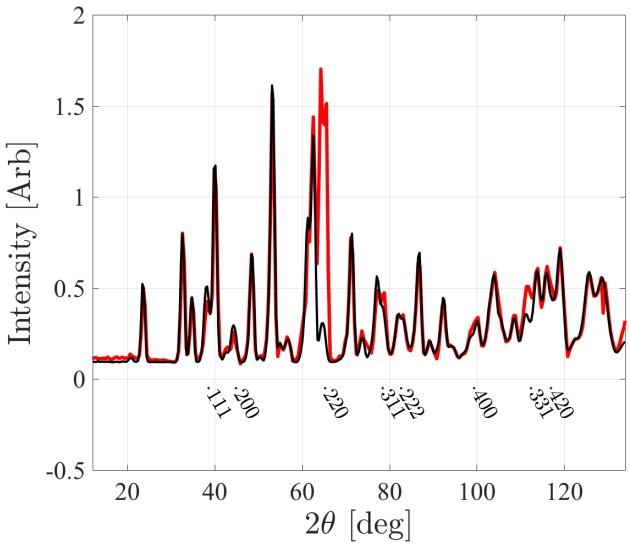

Figure 4.38: Comparison between data from Ni_3TeO_6 powder taken at MARI (red) and the McStas simulation using Union components (black). Here the scattering is summed over all energy transfers to view the angle dependence which is dominated by elastic scattering and the angular resolution of the instrument. Indexing of Al peaks are shown.

The full datasets and a comparison of the energy resolution is shown in figure 4.39, 4.40 and 4.41. The agreement is in general better than the corresponding comparison for the empty cryostat.

4.5.6 Analysis of background

With a model of the instrument available, it is interesting to map how the multiple scattering background depend on different instrument settings. On MARI, the two important choices are the incoming energy and the time resolution from the chopper. The multiple scattering is strongly dependent on the incoming energy, and it is thus selected to scan this parameter to get an overview of the multiple scattering background. A perfect source was used to simulate a very high energy resolution, so that an estimate for the multiple scattering at a broader energy resolution can be performed by integrating over the covered range. The used source component provides a constant brilliance in units $1/s/cm^2/ster./meV$.

The total single scattering and multiple scattering intensity measured by the detector is shown in figure 4.42. The measured single scattering intensity have peaks at energies where a Bragg peak enters the detector coverage at $2\theta = 134°$. The multiple scattering intensity peaks at energies corresponding to a new Bragg peak being accessible and thus a scattering angle close to 180°.

The angular dependence as a function of energy is shown in figure 4.43, where the scattering intensity is summed over all energy transfers. Here the powder scattering from aluminium dominates the plot, but as this part is not delayed significantly, this background will be located in the elastic channel. In figure 4.44, the same scan is shown, but only

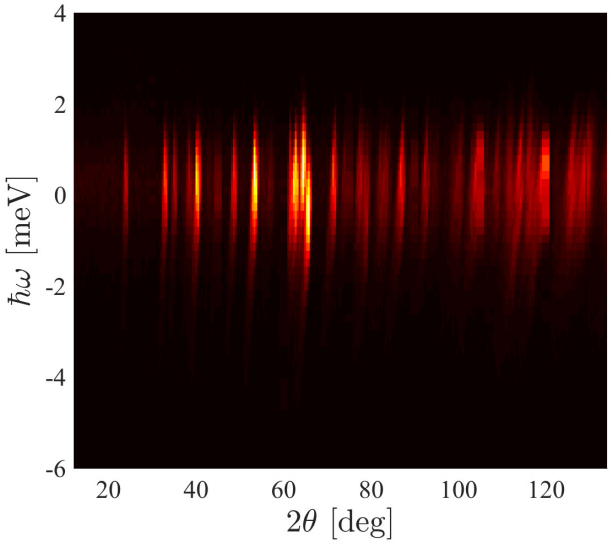

Figure 4.39: Measured scattering from cryostat and Ni_3TeO_6 sample on MARI with a selected energy of 35.19 meV from the Gd chopper running at 250 Hz.

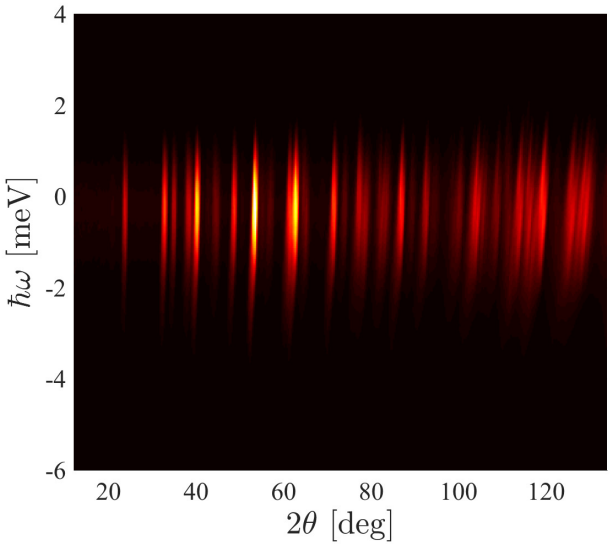

Figure 4.40: Simulated scattering from cryostat and Ni_3TeO_6 sample on MARI with a selected energy of 35.19 meV from the Gd chopper running at 250 Hz.

includes rays that underwent 2 or more scattering events. Here the structure of the multiple scattering is much more visible, and as this background can have a significant delay, it may contribute to inelastic background even though all scattering was elastic.

As expected the background from multiple scattering is completely absent at energies where there are no Bragg scattering in aluminium i.e. below 3.7 meV. Conversely, the background is almost uniform at large incoming energies as there is a great number of different Bragg peaks that can be accessed, and thus a large number of different combinations seem to diminish the structure. In the region of 5 meV to 50 meV, however, the relatively low number of accessible Bragg peaks makes the structure more pronounced. In addition, it seems that the largest background occurs at energies where a Bragg peak corresponds

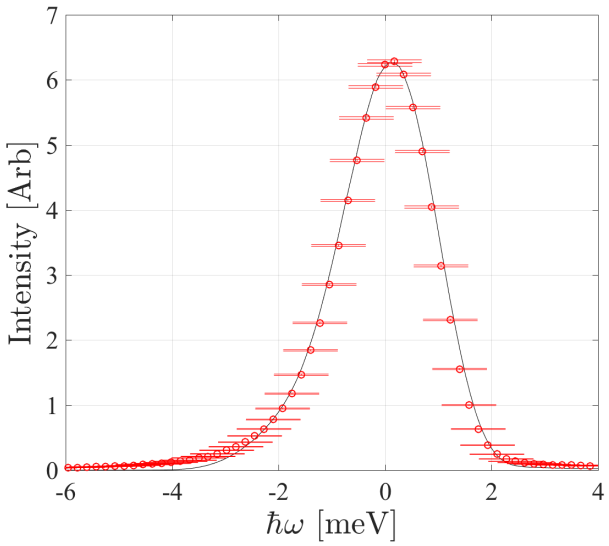

Figure 4.41: Comparison between data taken at MARI (red) and the McStas simulation using Union components (black), here the scattering is summed over all angles to view the energy dependence which is dominated by elastic scattering and the energy resolution of the instrument.

to a scattering angle of 180°.In addition to the low energies (<4 meV) and high energies (>50 meV), a few energies are comparatively free from background and can be recommended for measurements, 9 meV, 13 meV, 23 meV, 35 meV, and around 40 meV.

Union logger components are used to record the scattering positions in the sample environment at the same energy as the simulation, 35 meV. The results are shown in figure 4.45 and 4.46. These contain a surprising amount of complexity, as the illumination of the sample environment originates from the many layers of material in the beam. First order scattering appears only in the directly illuminated parts, the two windows, sample container and the edge of the absorbing connecting piece. The second order scattering is highly structured as a consequence of the sharp Bragg peaks from the parts illuminated by the beam. Here the shadow from the absorber is visible as an asymmetry between the two sides when seen from above. In contrast the third order is more evenly distributed over the entire sample environment.

Next the multiple scattering present in the MARI simulation of the empty sample environment is investigated by plotting the detector signal on a logarithmic scale as seen on figure 4.47. Here many multiple scattering features are visible, and it is clear how they have a potential for being mistaken as an inelastic signal. The measured data on the empty cryostat hardly contained any counts outside the elastic line, and thus a comparison to the measured data is not feasible. This could be explained either by the measurement being too short or because additional shielding not simulated were installed. The latter was confirmed by the instrument scientist, yet simulations were performed without the shielding, and now serves to show the multiple scattering that would occur without such shielding.

In order to investigate the multiple scattering signal further, a simulation of the empty sample environment was performed with an artificial source with perfect time structure and energy resolution of 0.01 meV. This serves to remove the smearing from energy resolution and inherent time structure of the moderator, making the perceived energy transfer a clear measure of added distance to the neutron flight path. The resulting detector output is shown in figure 4.48. Here, the multiple scattering features are clear and an analysis of this output is simpler as the peaks can be easily distinguished.

In order to understand these features one can filter the McStas monitors used to only view events that had certain number of scattering events, were scattered in certain volumes,

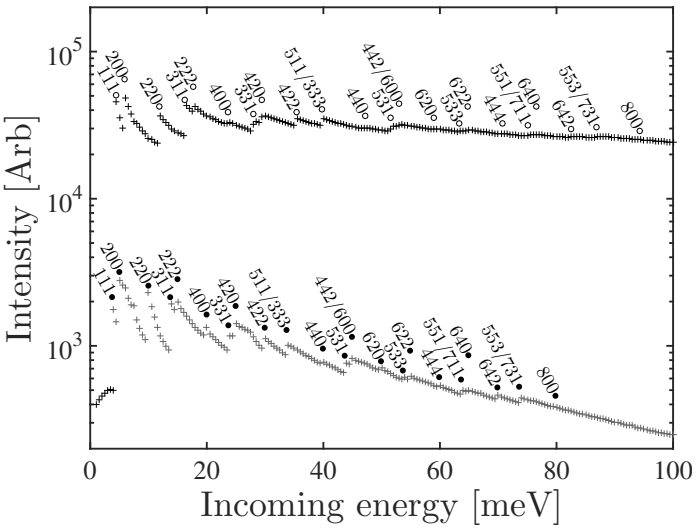

Figure 4.42: Total measured single scattering intensity (black) and multiple scattering intensity (grey) as a function of incoming energy. Errorbars not shown as they were negligible. Simulated with a unrealistically narrow energy band of 0.01 meV on the MARI instrument model. The Miller indices for aluminium Bragg peaks at $2\theta = 180^\circ$ is shown with filled circles and $2\theta = 134^\circ$ is shown with empty circles.

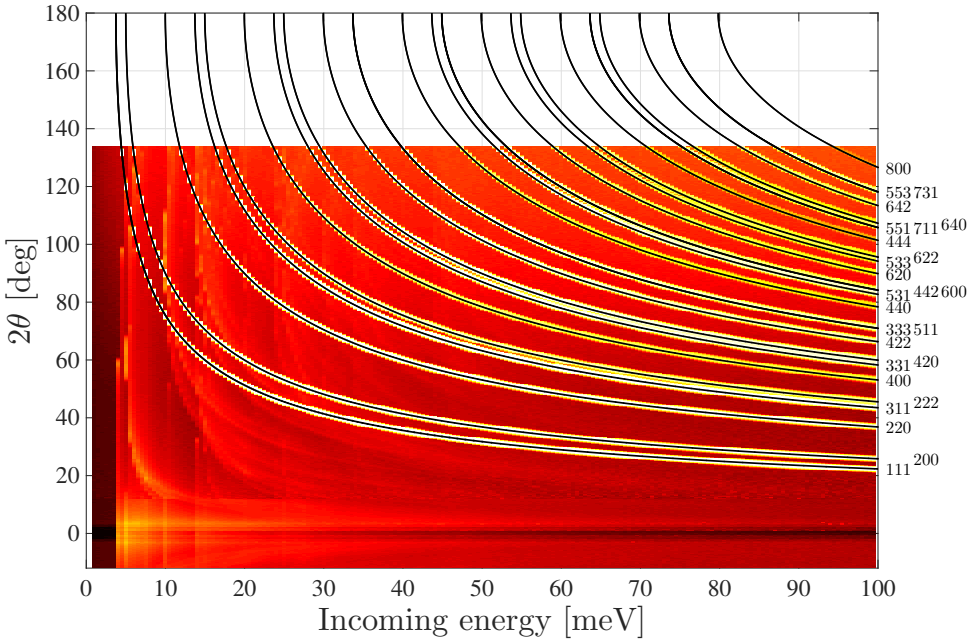

Figure 4.43: Detector output as a function of detected scattering angle over a range of incoming energies. Simulated with a narrow energy band of 0.01 meV on the MARI instrument model. The overlay shows expected Bragg scattering from aluminium with the corresponding Miller indices.

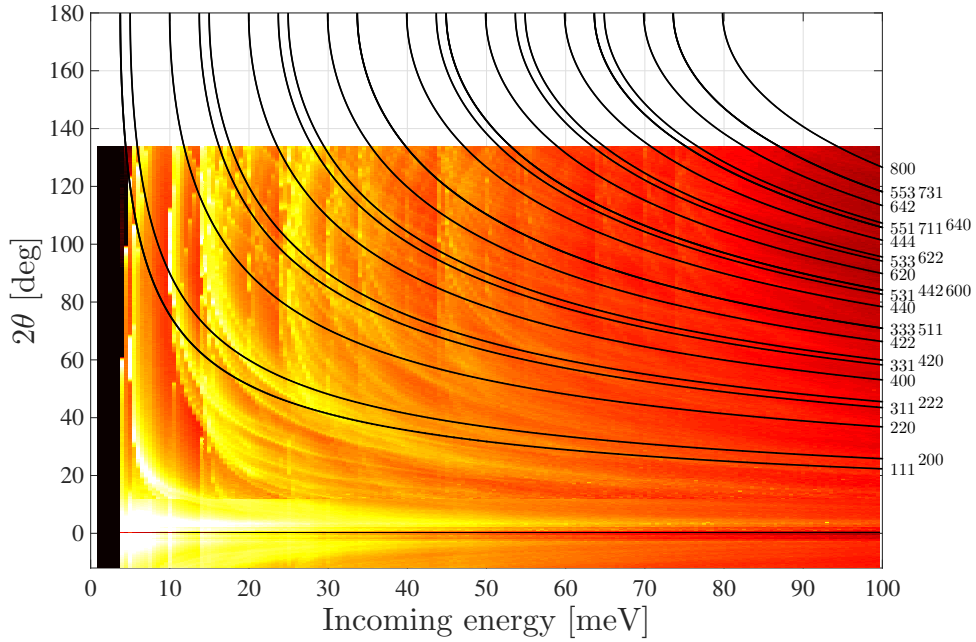

Figure 4.44: Detector output as a function of detected scattering angle over a range of incoming energies. Simulated with a narrow energy band of 0.01 meV on the MARI instrument model. Here only rays that scattered more than once are recorded. The overlay shows expected Bragg scattering from aluminium with the corresponding Miller indices.

or took part in some specified process. Figure 4.49 shows the part of the detector output that had a scattering in the CCR. All contributions from the CCR appear well outside the elastic line as rays need to add a significant path length to reach the CCR before ending at the detectors.

The capabilities of the conditional components are demonstrated by investigating the origin of two marked peaks in figure 4.48. Each peak is assigned a series of Union logger components and a conditional component that ensure the loggers only record events that are within the boundaries marked A and B respectively on figure 4.48. The spatial origins for peak A is shown in figure 4.50, showing that the first scattering occurs in the Al window and sample container, while the second occurs at the lower vessel. The distribution of scattering among the powder lines in aluminium are displayed in table 4.8. The reference column shows the probability distribution among the Bragg peaks for all scattering, not just the part that satisfy the conditional. For this conditional, the first order scattering has a higher probability for low angles of scattering, while the second order is primarily from the 311 reflection.

The spatial origins for peak B is shown in figure 4.51. The first scattering primarily occurs after the beam has travelled halfway through the cryostat, and on panel (e) it is even visible that half of the sample container has a lower probability to contribute to peak B, as the rays need to travel through the Boron-Nitride sample holder. The second scattering most frequently occur at the top plate of the simulated vessel, with some on the CCR itself. The distribution of scattering among the aluminium powder lines can be seen in table 4.9. The first scattering is often the 311 reflection that yields the necessary scattering angle to hit the top of the sample environment. In order to contribute to the investigated peak, the ray must end on the detector below the sample environment, and thus must backscatter. More than 80% of the second order events used the 511 or 333 reflection that share a scattering angle of 158°. The third order scattering has a distribution closer to the reference, but still with a higher probability for back scattering.

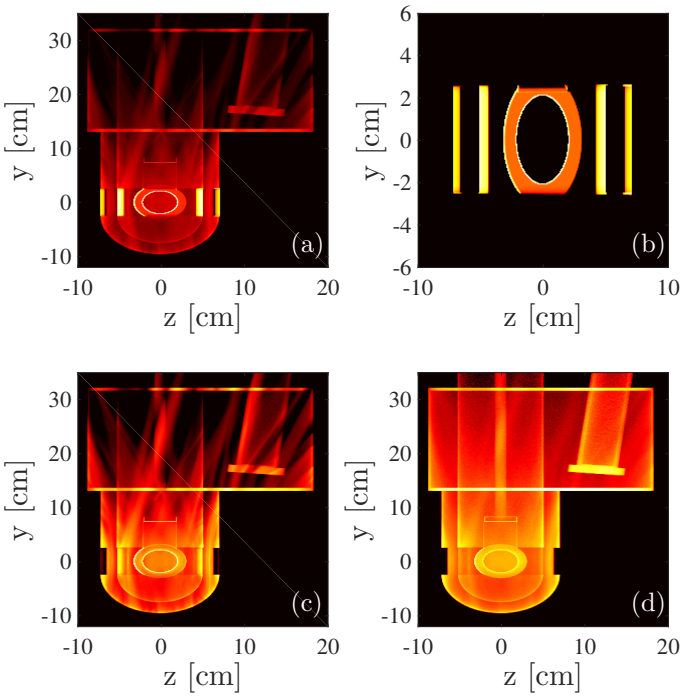

Figure 4.45: Scattering positions within the sample environment seen from the side. The colorscale is logarithmic and measures the amount of scattered intensity within a certain region of space. Here separated into all orders in panel (a), while 1st order is shown in (b), 2nd order in (c) and 3rd order in (d). Note that panel (b) is zoomed onto the sample and sample environment windows, because this is the only directly illuminated area. The colour scales are individual for each panel.

Miller indices	2θ	1st order	2nd order	3rd order	Reference
111	38.2°	29.7%	1.2%	16.4%	14.2%
200	44.4°	10.4%	0.7%	12.0%	9.2%
220	64.5°	6.5%	0.8%	9.2%	11.1%
311	77.5°	17.6%	72.2%	17.3%	19.0%
222	81.7°	3.4%	4.0%	6.0%	5.1%
400	98.1°	1.8%	0.6%	3.1%	3.3%
331	111°	6.9%	4.0%	10.0%	10.1%
420	115°	6.8%	11.6%	10.6%	9.8%
422	135°	9.0%	2.9%	7.5%	9.0%
511/333	158°	8.0%	1.9%	8.0%	9.1%

Table 4.8: Table over distribution of scattering per powder line for conditional A. The reference column is the probability for all scattering without any conditional.

4.5.7 Discussion

The comparison between the simulated and measured MARI experiment did show that many aspects were replicated well by the simulation, but still had a shortcoming in the description of the empty sample environment. As mentioned, it is believed the primary reason for this discrepancy is due to texture in the aluminium introduced in production. This explanation alone is however not sufficient to explain the discrepancy, as this should not change the ratio between the intensities of the 200 and 400 peaks, yet these are different in measurement and simulation. The most probable explanations would be an error in the simulation code or an unknown difference between the simulated and real scattering system.

Since the used experiment was not performed with the intention of being replicated

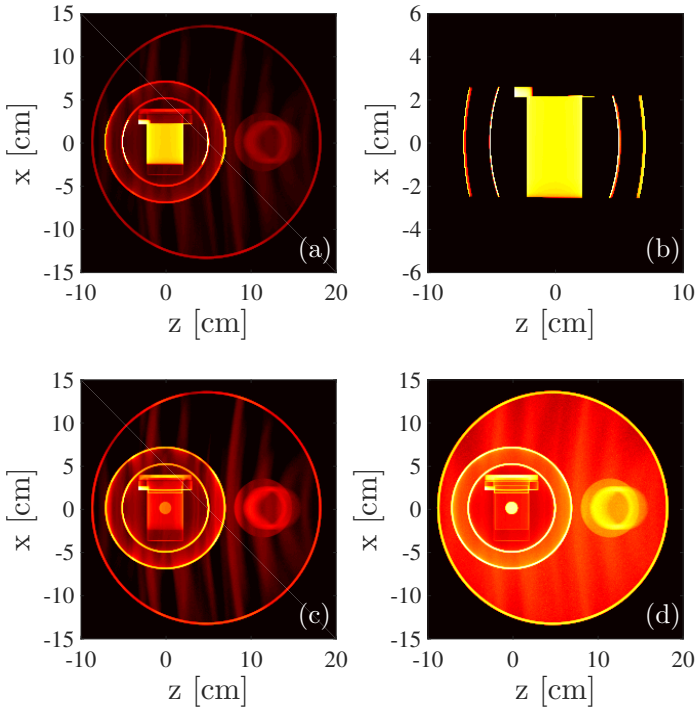

Figure 4.46: Scattering positions within the sample environment seen from the top. The colorscale is logarithmic and measures the amount of scattered intensity within a certain region of space. Here separated into all orders in panel (a), while 1st order is shown in (b), 2nd order in (c) and 3rd order in (d). Note that panel (b) is zoomed onto the sample and sample environment windows, because this is the only directly illuminated area. The colour scales are individual for each panel.

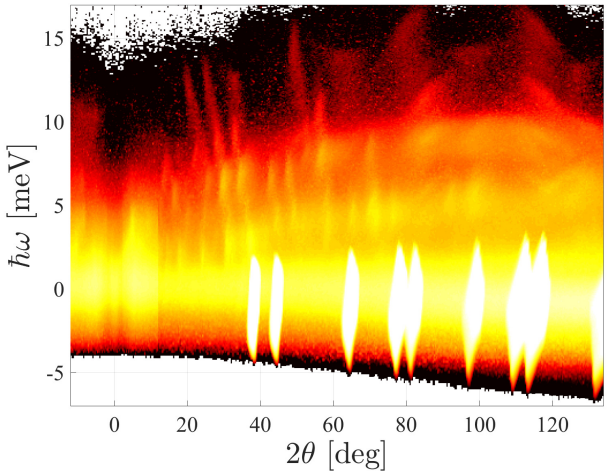

Figure 4.47: Output from simulation of an empty cryostat on the MARI instrument on a logarithmic scale from 2 to 7 orders of magnitude below the aluminium Bragg peaks.

by simulation, some details were not measured and are impossible to reconstruct to full accuracy.

A dedicated experiment on MARI or on another beamline would be needed to perform a detailed experimental validation of the Union components, and such endeavours are always

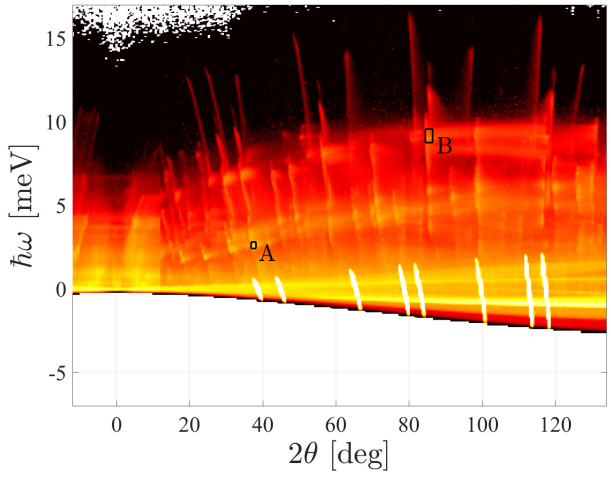

Figure 4.48: Output from simulation of an empty cryostat on a logarithmic scale from 2 to 7 orders of magnitude below the aluminium Bragg peaks. Here a source without time distribution and a narrow energy interval is used to show the multiple scattering features in more detail. The peaks marked A and B are investigated further in figure 4.50 and 4.51, respectively.

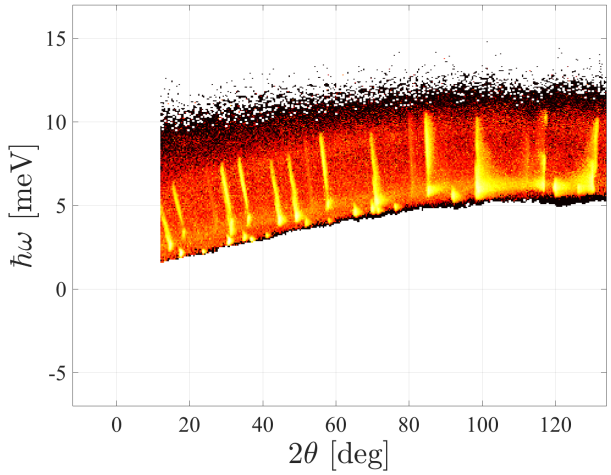

Figure 4.49: Output from simulation of an empty cryostat on a logarithmic scale, here filtered to only show events that scattered in the CCR. Only the center high angle detector bank which covers 12° to 134° is used.

a prudent exercise for the McStas package overall[69].

The analysis of the multiple scattering background from the MARI cryostat served as a demonstration of both the new possibilities brought to McStas by the Union components and the relevance of the problem they solve. It is now possible to easily model complex sample environments which yield the full multiple scattering signal and can be analyzed in great detail.

The background analysis done does not correspond to the real instrument due to some shielding not being simulated, and thus serves to show what this shielding can prevent. Future simulations will include the additional shielding, and a rerun of the scans over the incoming energy shown in figure 4.44 can become a useful tool for selecting the best pos-

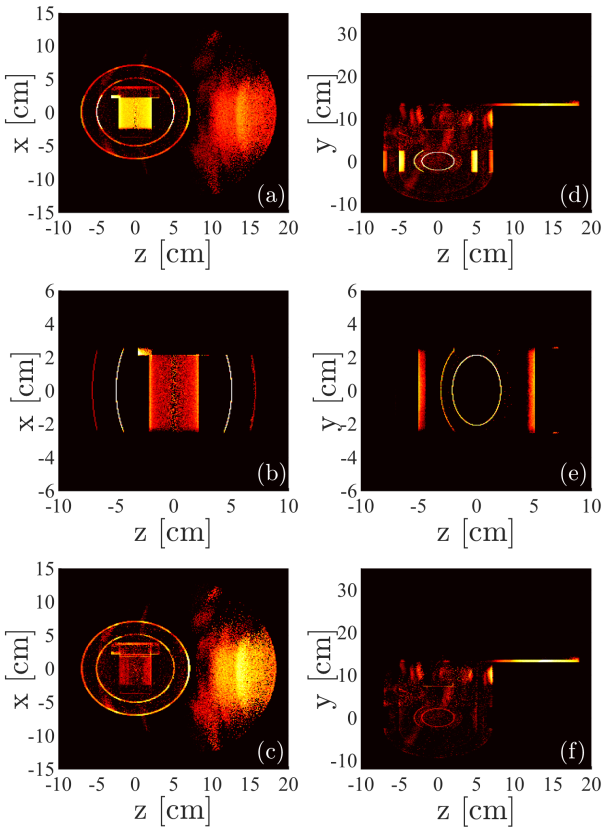

Figure 4.50: Scattering positions within the sample environment for rays that satisfy conditional A shown in figure 4.48. Panel (a) through (c) are from a top view, (a) being all scattering, (b) only first order scattering (zoomed) and (c) second order scattering. Likewise panel (d) through (f) are from the side, and (d) is all orders of scattering, (e) only first order (zoomed), and (f) only second order.

sible energy. Furthermore, the full data set for each energy will be available, allowing the researchers to view the expected multiple scattering and make sure it is not located in the $(\hbar\omega, 2\theta)$ regions that are most important for their experiment.

The investigations of the two peaks in figure 4.48 showed their origins to be related to the vessel above the sample, not usually suspected of being a major background source. The instrument responsible have commented that shielding not simulated should prevent scattering from the upper vessel, which also explains why these multiple scattering peaks were absent in the measured data.

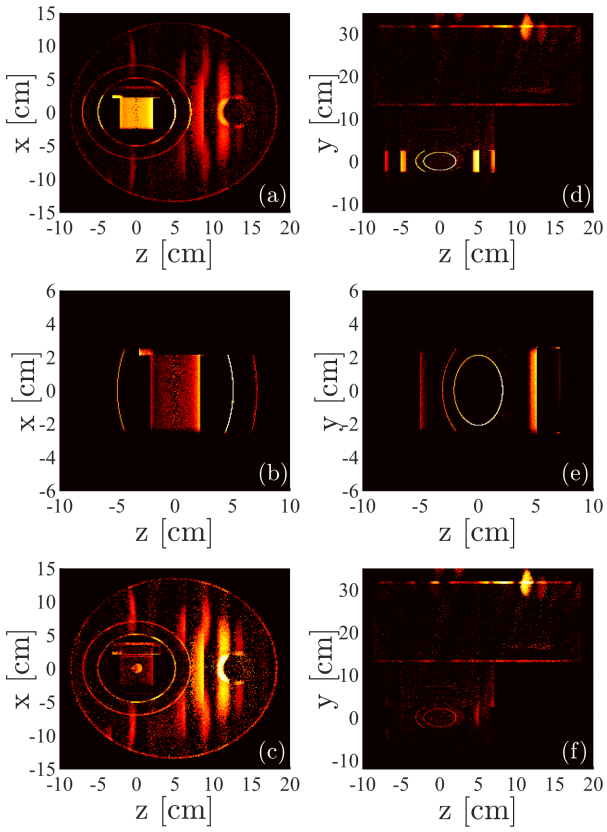

Figure 4.51: Scattering positions within sample environment for rays that satisfy conditional B shown in figure 4.48. Panel (a) through (c) are from a top view, (a) being all scattering, (b) only first order scattering and (c) second order scattering. Likewise panel (d) through (f) are from the side, and (d) is all orders of scattering, (e) only first order, and (f) only second order.

Miller indices	2θ	1st order	2nd order	3rd order	Reference
111	38.2°	5.0%	4.3%	14.2%	14.2%
200	44.4°	3.3%	2.4%	6.9%	9.2%
220	64.5°	4.9%	2.1%	6.9%	11.1%
311	77.5°	62.6%	3.2%	14.8%	19.0%
222	81.7°	9.7%	0.9%	4.1%	5.1%
400	98.1°	4.2%	0.5%	2.4%	3.3%
331	111°	3.1%	1.4%	8.1%	10.1%
420	115°	2.7%	1.5%	8.4%	9.8%
422	135°	2.2%	1.4%	9.1%	9.0%
511/333	158°	2.4%	82.3%	25.1%	9.1%

Table 4.9: Table over distribution of scattering per powder line for conditional B. The reference column is the probability for all scattering without any conditional.

4.6 Discussion on Union components

In this section the Union components are discussed in the light of the performed simulations of the MACS and MARI instruments and subsequent comparison to measurements.

4.6.1 Added capabilities from the Union components

The recreations of experiments performed on MACS and MARI serves to demonstrate the capabilities available in McStas through the Union components. A new level of detail in simulation of thermal background can be attained. The most obvious improvements arises from the complex geometry that can be described with relative ease, but it is also important to consider the benefits of being able to add an arbitrary number of processes to the same geometry. Doing so without the Union components required additional logic to switch between several sample components in the same position, and each ray would thus only be allowed to do multiple scattering in the selected sample component. With the framework developed for the Union components, scenarios such as twinned crystals or elastic-inelastic multiple scattering can easily be simulated, but have not yet been performed. The separation of scattering physics into processes also simplifies the addition of new physics to the project, as a developer can focus on a specific type of scattering instead of having to balance several existing types. There are, however, also disadvantages in splitting up the code, as some tasks may be easier to do by expanding existing code. The many shorter pieces of code describing scattering physics is, however, much easier to understand than the traditional large sample components that also mix geometry calculations and Monte Carlo sampling manipulation into the code. It remains to be seen if McStas contributors will select to work with entire sample components or will work in the Union framework.

With the increased capabilities available through the Union components, the amount of information relevant for simulating an experiment have increased dramatically. Something as simple as sample holders have rarely been simulated because the tools were not available, and thus it is not considered relevant to accurately preserve the information. The advent of inexpensive 3D scanners may help to rectify this somewhat, as the sample holder can be scanned for with an accuracy better than 0.5 mm, greatly exceeding the accuracy achieved in this thesis. Handheld scanners can also be used to scan instrument geometry, such as a goniometer or other open form of sample environment. Software could be made to decompose the scanned geometry into the shapes supported by the Union components with some resolution requirements. The user would just need to assign material definitions to each geometry.

The Union loggers and conditionals are powerful tools as demonstrated with the background analysis of MACS and MARI. McStas already had logger components for regular use [77], but they do not have access to other than the global variables, and no alternative to the conditionals exist. The Union loggers can be attached to certain geometries and processes, and many useful limits can be used. As seen the scattering in a system can be displayed spatially, in reciprocal space and as a function of scattering order. The conditional components adds an additional level of convenience, as the user can investigate what part of the scattering system contribute to certain recorded features.

4.6.2 User experience

The user experience is an important aspect of any piece of software, as a user will always balance the effort required to use the software with the benefits of doing so. The data input method developed for the Union components follows the McStas conventions to a large extent, but have some significant differences as a consequence of the different structure. Several possible input schemes were presented to current McStas users, and their critique was used to streamline the user experience. The most important difference is the need to link components together, which did exist previously in McStas, but only for single components. In the Union components an arbitrary number of processes need to be linked together to create a material. This is accomplished by entering the component names of the processes

into the input of the Make_material component using a comma separated string. Setting up the geometry is considered easier than usual, as the number of available parameters is low and each geometrical shape has an independent component. This provides the necessary context to the user, greatly increasing the readability of the code. Furthermore, an effort was made to display comprehensive error messages in all cases where it can be determined that the user made a mistake. These error messages include a probable reason for the failure, and when possible a list of allowed options as alternatives to the problematic input. This could for example be a misspelled process name entered into the Make_material component, where both the wrong process name is displayed along with a list of defined processes. Some issues with usability remain, but these are mostly relegated to advanced use of the software including several Union_master components and masks. Changes in the input system are expected as feedback from users is imminent after the recent public release of the software in McStas 2.4 [16].

4.6.3 Performance

One of the main benefits of using McStas for instrument simulations is the performance of the software. Simulations are to be feasible on a laptop, and jeopardizing this notion is not an option. The time spent in the trace section when executing the MARI instrument model with $1 \cdot 10^6$ rays and without chopper is less than 6 seconds on the authors laptop. A simulation with the chopper is faster as only a small fraction of the simulated rays reach the sample environment. The MARI model consists of 27 volumes, and the execution time is within the order of magnitude expected for a McStas instrument. The MACS monochromator model composed of 426 volumes can simulate the standard $1 \cdot 10^6$ rays in less than 20 seconds. This time is despite having open slits and only simulating a narrow energy band around the selected energy, resulting in the largest amount of scattering events possible. The MACS backend with 694 volumes simulates the $1 \cdot 10^6$ rays in just 11 seconds, there is, however, a large number of rays lost in the collimation between sample environment and kidney, as only 157 rays are detected in the spectroscopy detectors. Obtaining a total of $1 \cdot 10^4$ rays in the spectroscopy channels of the MACS backend model thus takes 12 minutes. It is evident that the performance scaling with the number of volumes is sufficiently good to make it relevant to study complex geometries on a laptop.

The Union components does, however, add a large amount of possible paths through the scattering system, which in turn requires a larger number of simulated rays to sample all possibilities. Furthermore, since multiple scattering is one of the main benefits, the use of focusing which forces scattering into certain solid angles (usually onto a detector) will significantly change the results. For these reasons, the computational requirements for using the Union components are in practice larger than for typical McStas simulations, but still within reason.

4.6.4 New McStas use cases

The introduction of the Union components opens new potential use cases for McStas, the most obvious of which is design of sample environments. The level of fidelity achievable should be sufficient to model for example the influence of different beam window designs or how parts not directly in the beampath affect the background. Furthermore designers of sample environments have the entire library of McStas instruments available to test their designs on different instruments.

Instrument designers can also start using McStas for basic shielding calculations to for example eliminate cross talk between detector channels. It has even been suggested to simulate a crude environment of the instrument including air scattering and the immediate surroundings. It is, however, to be stressed that only thermal neutrons are modelled, and thus does not allow estimation of dose levels from fast neutron, gamma radiation or similar.

4.6.5 Outlook

Including a broader library of inelastic processes is the highest priority, as these are necessary to perform virtual experiments on spectrometers. This could include existing McStas sample components that are converted to process components or entirely new code. The any-shape geometry option available in other McStas components should be included as a geometry component in the Union components.

Future expansions could include surface effects such as refraction and reflectivity, which would allow some optics to be incorporated into sample environment models. Simulation of bispectral extraction can be complicated due to the difficulty in predicting the order of scattering, and thus often includes some logic written by the user. The possibility of simulating optics with the Union components would make simulation of bispectral extraction much simpler.

Finally the validation effort should be continued as beamtime for dedicated validation experiments has been offered both on the MACS and MARI instrument.

4.7 Conclusion on Union components

With the release of the Union components, the capabilities of McStas have increased significantly due to the addition of multiple scattering in complex geometries. This has been achieved while decreasing the work required to add new scattering physics to the package, as geometry and scattering is separated in the Union components. Scattering physics is further divided into processes of which an arbitrary number can be used in the same geometry with automatic balancing between these. This allows investigation of multiple scattering in twinned crystals and other complicated systems. An emphasis on user experience have made the software accessible, and code optimization using logical networks have kept the computational requirement low. The Union components were demonstrated by recreating data from recent experiments on the triple axis spectrometer MACS and time of flight powder spectrometer MARI. Both simulated recreations showed overall agreement with the measurements albeit with some deviations. The background on the instruments were analysed using the included tools, demonstrating the ability to determine the origin of scattering signals and background.

Bibliography

[1] G. J. Russell, Proceedings of ICANS-XI, Tsukuba 1990 (1991) 291–299.

[2] S. Peggs, ESS Technical Design Report, 2013. URL: http://eval.esss.lu.se/cgi-bin/public/DocDB/ShowDocument?docid=274.

[3] L. S. Waters, G. W. McKinney, J. W. Durkee, M. L. Fensin, J. S. Hendricks, M. R. James, R. C. Johns, D. B. Pelowitz, Hadronic Shower Simulation Workshop 896 (2007) 81–90.

[4] S. Agostinelli, J. Allison, K. Amako, J. Apostolakis, H. Araujo, P. Arce, M. Asai, D. Axen, S. Banerjee, G. Barrand, F. Behner, L. Bellagamba, J. Boudreau, L. Broglia, A. Brunengo, H. Burkhardt, S. Chauvie, J. Chuma, R. Chytracek, G. Cooperman, G. Cosmo, P. Degtyarenko, A. Dell'Acqua, G. Depaola, D. Dietrich, R. Enami, A. Feliciello, C. Ferguson, H. Fesefeldt, G. Folger, F. Foppiano, A. Forti, S. Garelli, S. Giani, R. Giannitrapani, D. Gibin, J. Gomez Cadenas, I. Gonzalez, G. Gracia Abril, G. Greeniaus, W. Greiner, V. Grichine, A. Grossheim, S. Guatelli, P. Gumplinger, R. Hamatsu, K. Hashimoto, H. Hasui, A. Heikkinen, A. Howard, V. Ivanchenko, A. Johnson, F. Jones, J. Kallenbach, N. Kanaya, M. Kawabata, Y. Kawabata, M. Kawaguti, S. Kelner, P. Kent, A. Kimura, T. Kodama, R. Kokoulin, M. Kossov, H. Kurashige, E. Lamanna, T. Lampen, V. Lara, V. Lefebure, F. Lei, M. Liendl, W. Lockman, F. Longo, S. Magni, M. Maire, E. Medernach, K. Minamimoto, P. Mora de Freitas, Y. Morita, K. Murakami, M. Nagamatu, R. Nartallo, P. Nieminen, T. Nishimura, K. Ohtsubo, M. Okamura, S. O'Neale, Y. Oohata, K. Paech, J. Perl, A. Pfeiffer, M. Pia, F. Ranjard, A. Rybin, S. Sadilov, E. di Salvo, G. Santin, T. Sasaki, N. Savvas, Y. Sawada, S. Scherer, S. Sei, V. Sirotenko, D. Smith, N. Starkov, H. Stoecker, J. Sulkimo, M. Takahata, S. Tanaka, E. Tcherniaev, E. Safai Tehrani, M. Tropeano, P. Truscott, H. Uno, L. Urban, P. Urban, M. Verderi, A. Walkden, W. Wander, H. Weber, J. Wellisch, T. Wenaus, D. Williams, D. Wright, T. Yamada, H. Yoshida, D. Zschiesche, Nuclear Instruments and Methods in Physics Research A 506 (2003) 250–303. doi:10.1016/S0168-9002(03)01368-8.

[5] K. Batkov, A. Takibayev, L. Zanini, F. Mezei, Nuclear Instruments and Methods in Physics Research, Section A: Accelerators, Spectrometers, Detectors and Associated Equipment 729 (2013) 500–505. URL: http://dx.doi.org/10.1016/j.nima.2013.07.031. doi:10.1016/j.nima.2013.07.031.

[6] T. Kittelmann, I. Stefanescu, K. Kanaki, M. Boin, R. Hall-Wilton, K. Zeitelhack, Journal of Physics: Conference Series 513 (2014) 022017. doi:10.1088/1742-6596/513/2/022017.

[7] N. Tsapatsaris, P. K. Willendrup, R. E. Lechner, H. N. Bordallo, EPJ Web of Conferences 83 (2015) 03015. URL: http://www.epj-conferences.org/10.1051/epjconf/20158303015. doi:10.1051/epjconf/20158303015.

[8] A. Fedrigo, D. Colognesi, M. Bertelsen, M. Hartl, K. Lefmann, P. P. Deen, M. Strobl, F. Grazzi, M. Zoppi, Review of Scientific Instruments 87 (2016) 065101. URL: http://dx.doi.org/10.1063/1.4952430. doi:10.1063/1.4952430.

[9] P. Freeman, J. Birk, M. Markó, M. Bertelsen, J. Larsen, N. Christensen, K. Lefmann, J. Jacobsen, C. Niedermayer, F. Juranyi, H. Ronnow, EPJ Web of Conferences 83 (2015) 03005. URL: http://www.epj-conferences.org/10.1051/epjconf/20158303005. doi:10.1051/epjconf/20158303005.

[10] S. L. Holm, K. Lefmann, P. F. Henry, M. Bertelsen, J. Schefer, M. Christensen, Nuclear Instruments and Methods in Physics Research, Section A: Accelerators, Spectrometers, Detectors and Associated Equipment 828 (2016) 229–241. URL: http://dx.doi.org/10.1016/j.nima.2016.05.046. doi:10.1016/j.nima.2016.05.046.

[11] J. Fenske, M. Rouijaa, J. Šaroun, R. Kampmann, P. Staron, G. Nowak, J. Pilch, P. Beran, P. Šittner, P. Strunz, H.-G. Brokmeier, V. Ryukhtin, L. Kadeávek, M. Strobl, M. Müller, P. Lukáš, A. Schreyer, Journal of Physics: Conference Series 746 (2016) 012009. doi:10.1088/1742-6596/746/1/012009.

[12] W. Schweika, N. Violini, K. Lieutenant, C. Zendler, D. Nekrassov, A. Houben, P. Jacobs, P. F. Henry, Journal of Physics: Conference Series 747 (2016) 012013. doi:10.1088/1742-6596/746/1/012013.

[13] M. Boehm, P. Steffens, J. Kulda, M. Klicpera, S. Roux, P. Courtois, P. Svoboda, J. Saroun, V. Sechovsky, Neutron News 26 (2015) 18–21. doi:10.1080/10448632.2015.1057050.

[14] P. Fouquet, G. Ehlers, B. Farago, C. Pappas, F. Mezei, Journal of Neutron Research 15 (2007) 39–47. doi:10.1080/10238160601048791.

[15] R. I. Bewley, J. W. Taylor, S. M. Bennington, Nuclear Inst. and Methods in Physics Research, A 637 (2011) 128–134. URL: http://dx.doi.org/10.1016/j.nima.2011.01.173. doi:10.1016/j.nima.2011.01.173.

[16] McStas webpage, 2017. URL: www.mcstas.org.

[17] K. Lefmann, K. Nielsen, Neutron News 10 (1999) 20–23. URL: http://dx.doi.org/10.1080/10448639908233684. doi:10.1080/10448639908233684.

[18] P. K. Willendrup, E. Farhi, K. Lefmann, Physica B: Condensed Matter 350 (2004) 735–737. doi:10.1016/j.physb.2004.03.193.

[19] P. K. Willendrup, E. B. Knudsen, E. Klinkby, T. Nielsen, E. Farhi, U. Filges, K. Lefmann, Journal of Physics: Conference Series 528 (2014) 12035. URL: http://stacks.iop.org/1742-6596/528/i=1/a=012035?key=crossref.7e8a18cec79f974db19c2eee9bb52ada. doi:10.1088/1742-6596/528/1/012035.

[20] P. Willendrup, E. Farhi, E. B. Knudsen, U. Filges, K. Lefmann, Journal of Neutron Research 17 (2014) 35–43. URL: http://dx.doi.org/10.3233/JNR-130004. doi:10.3233/JNR-130004.

[21] J. Šaroun, J. Kulda, Physica B: Condensed Matter 234-236 (1997) 1102–1104. doi:10.1016/S0921-4526(97)00037-9.

[22] J. Šaroun, J. Kulda, Neutron ray-tracing simulations and data analysis with RESTRAX, 2004. doi:10.1117/12.560925.

[23] D. Wechsler, G. Zsigmond, F. Streffer, J. A. Stride, F. Mezei, Physica B: Condensed Matter 276-278 (2000) 71–72. doi:10.1016/S0921-4526(99)01332-0.

[24] G. Zsigmond, K. Lieutenant, F. Mezei, Neutron News 13 (2002) 11–14. URL: http://www.tandfonline.com/doi/abs/10.1080/10448630208218488. doi:10.1080/10448630208218488.

[25] C. Zendler, K. Lieutenant, D. Nekrassov, M. Fromme, Journal of Physics: Conference Series 528 (2014) 12036. URL: http://stacks.iop.org/1742-6596/528/i=1/a=012036. doi:10.3233/JNR-130005.

[26] H. Schober, E. Farhi, F. Mezei, P. Allenspach, K. Andersen, P. M. Bentley, P. Christiansen, B. Cubitt, R. K. Heenan, J. Kulda, P. Langan, K. Lefmann, K. Lieutenant, M. Monkenbusch, P. Willendrup, J. Saroun, P. Tindemans, G. Zsigmond, Nuclear Instruments and Methods in Physics Research, Section A: Accelerators, Spectrometers, Detectors and Associated Equipment 589 (2008) 34–46. doi:10.1016/j.nima.2008.01.102.

[27] J. Šaroun, J. Kulda, Physica B: Condensed Matter 385-386 (2006) 1250–1252. doi:10.1016/j.physb.2006.06.022.

[28] J. Stahn, T. Panzner, U. Filges, C. Marcelot, P. Böni, Nuclear Instruments and Methods in Physics Research, Section A: Accelerators, Spectrometers, Detectors and Associated Equipment 634 (2011) 12–16. doi:10.1016/j.nima.2010.06.221.

[29] C. Zendler, K. Lieutenant, D. Nekrassov, L. D. Cussen, M. Strobl, Nuclear Instruments and Methods in Physics Research, Section A: Accelerators, Spectrometers, Detectors and Associated Equipment 704 (2013) 68–75. URL: http://dx.doi.org/10.1016/j.nima.2012.11.180. doi:10.1016/j.nima.2012.11.180.

[30] A. C. Komarek, P. Böni, M. Braden, Nuclear Instruments and Methods in Physics Research, Section A: Accelerators, Spectrometers, Detectors and Associated Equipment 647 (2011) 63–72. doi:10.1016/j.nima.2011.04.022.

[31] K. Lefmann, K. H. Klenø, J. O. Birk, B. R. Hansen, S. L. Holm, E. Knudsen, K. Lieutenant, L. von Moos, M. Sales, P. K. Willendrup, K. H. Andersen, Review of Scientific Instruments 84 (2013) 055106. doi:10.1063/1.4803167.

[32] N. Stüßer, M. Bartkowiak, T. Hofmann, Nuclear Instruments and Methods in Physics Research, Section A: Accelerators, Spectrometers, Detectors and Associated Equipment 748 (2014) 39–45. URL: http://dx.doi.org/10.1016/j.nima.2014.02.028. doi:10.1016/j.nima.2014.02.028.

[33] P. M. Bentley, S. J. Kennedy, K. H. Andersen, D. M. Rodríguez, D. F. R. Mildner, Nuclear Instruments and Methods in Physics Research, Section A: Accelerators, Spectrometers, Detectors and Associated Equipment 693 (2012) 268–275. doi:10.1016/j.nima.2012.07.002.

[34] C. Zendler, D. Nekrassov, K. Lieutenant, Nuclear Instruments and Methods in Physics Research, Section A: Accelerators, Spectrometers, Detectors and Associated Equipment 746 (2014) 39–46. URL: http://dx.doi.org/10.1016/j.nima.2014.01.044. doi:10.1016/j.nima.2014.01.044.

[35] L. D. Cussen, D. Nekrassov, C. Zendler, K. Lieutenant, Nuclear Instruments and Methods in Physics Research, Section A: Accelerators, Spectrometers, Detectors and Associated Equipment 705 (2013) 121–131. URL: http://dx.doi.org/10.1016/j.nima.2012.11.183. doi:10.1016/j.nima.2012.11.183.

[36] M. Bertelsen, H. Jacobsen, U. Bengaard Hansen, H. Hoffmann Carlsen, K. Lefmann, Nuclear Instruments and Methods in Physics Research, Section A: Accelerators, Spectrometers, Detectors and Associated Equipment 729 (2013) 387–398. URL: http://dx.doi.org/10.1016/j.nima.2013.07.062. doi:10.1016/j.nima.2013.07.062.

[37] M. Bertelsen, K. Lefmann, Nuclear Instruments and Methods in Physics Research, Section A: Accelerators, Spectrometers, Detectors and Associated Equipment 830 (2016) 313–324. URL: http://dx.doi.org/10.1016/j.nima.2016.06.003. doi:10.1016/j.nima.2016.06.003.

[38] U. B. Hansen, M. Bertelsen, J. Stahn, K. Lefmann, Nuclear Instruments and Methods in Physics Research Section A: Accelerators, Spectrometers, Detectors and Associated Equipment 852 (2017) 46–56. URL: http://linkinghub.elsevier.com/retrieve/pii/S016890021730181X. doi:10.1016/j.nima.2017.01.075.

[39] S. Holm, N. Rasmussen, L. Høpfner, M. Bertelsen, J. Voigt, K. Andersen, K. Lefmann, Nuclear Instruments and Methods in Physics Research, Section A: Accelerators, Spectrometers, Detectors and Associated Equipment 782 (2015) 1–8. doi:10.1016/j.nima.2015.01.045.

[40] K. H. Klenø, K. Lieutenant, K. H. Andersen, K. Lefmann, Nuclear Instruments and Methods in Physics Research, Section A: Accelerators, Spectrometers, Detectors and Associated Equipment 696 (2012) 75–84. URL: http://dx.doi.org/10.1016/j.nima.2012.08.027. doi:10.1016/j.nima.2012.08.027.

[41] N. Stüßer, T. Hofmann, Nuclear Instruments and Methods in Physics Research, Section A: Accelerators, Spectrometers, Detectors and Associated Equipment 727 (2013) 84–89. URL: http://dx.doi.org/10.1016/j.nima.2013.06.026. doi:10.1016/j.nima.2013.06.026.

[42] S. Mühlbauer, P. G. Niklowitz, M. Stadlbauer, R. Georgii, P. Link, J. Stahn, P. Böni, Nuclear Instruments and Methods in Physics Research, Section A: Accelerators, Spectrometers, Detectors and Associated Equipment 586 (2008) 77–80. doi:10.1016/j.nima.2007.11.047.

[43] H. Jacobsen, K. Lieutenant, C. Zendler, K. Lefmann, Nuclear Instruments and Methods in Physics Research, Section A: Accelerators, Spectrometers, Detectors and Associated Equipment 717 (2013) 69–76. URL: http://dx.doi.org/10.1016/j.nima.2013.03.048. doi:10.1016/j.nima.2013.03.048.

[44] A. Houben, W. Schweika, T. Brückel, R. Dronskowski, Nuclear Instruments and Methods in Physics Research, Section A: Accelerators, Spectrometers, Detectors and Associated Equipment 680 (2012) 124–133. doi:10.1016/j.nima.2012.03.015.

[45] J. Copley, P. Verkerk, A. van Well, H. Fredrikze, Computer Physics Communications 40 (1986) 337–357. doi:10.1016/0010-4655(86)90118-9.

[46] P. Seeger, Physica B: Condensed Matter 283 (2000) 433–435. URL: http://linkinghub.elsevier.com/retrieve/pii/S0921452600003823. doi:10.1016/S0921-4526(00)00382-3.

[47] P. Seeger, L. Daemen, T. Thelliez, R. Hjelm, Neutron News 13 (2002) 20–23. doi:10.1080/10448630208218490.

[48] P. A. Seeger, Nuclear Instruments and Methods in Physics Research Section A: Accelerators, Spectrometers, Detectors and Associated Equipment 510 (2003) 290–299. doi:10.1016/S0168-9002(03)01814-X.

[49] P. A. Seeger, L. L. Daemen, Proc. SPIE 5536, Advances in Computational Methods for X-ray and Neutron Optics 5536 (2004) 109–123. doi:10.1117/12.559817.

[50] J. Y. Y. Lin, H. L. Smith, G. E. Granroth, D. L. Abernathy, M. D. Lumsden, B. Winn, A. A. Aczel, M. Aivazis, B. Fultz, Nuclear Instruments and Methods in Physics Research, Section A: Accelerators, Spectrometers, Detectors and Associated Equipment 810 (2016) 86–99. URL: http://dx.doi.org/10.1016/j.nima.2015.11.118. doi:10.1016/j.nima.2015.11.118.

[51] K. Lefmann, Neutron scattering: Theory, Instrumentation, and Simulation, course notes, Univ. Cph., 2017. URL: http://vnt.nmi3.org/wiki.

[52] G. Squires, Introduction to the Theory of Thermal Neutron Scattering, Cambridge University Press, 1972.

[53] H. Börner, J. Brown, C. J. Carlile, R. Cubitt, R. Currat, A. J. Dianoux, B. Farago, A. W. Hewat, J. Kulda, E. Lelièvre-Berna, G. J. McIntyre, S. A. Mason, R. P. May, A. Oed, J. R. Stewart, F. Tasset, J. Tribolet, I. Anderson, D. Dubbers, R. S. Eccelston, M. Johnson, C. C. Wilson, G. Lander, H. Rauch, R. B. Von Dreele, W. Waschkowski, Neutron Data Booklet, second ed., Institut Laue-Langevin, 2003.

[54] J. Stahn, Slides from talk named: "A neutron polariser based on magnetically remanent Fe/Si supermirrors" given at ILL, Grenoble, Jan 18th., 2006.

[55] ILL webpage, 2017. URL: `https://www.ill.eu`.

[56] Y. G. Dragunov, I. Tretiyakov, A. Lopatkin, N. Romanova, I. Lukasevich, V. Ananyev, A. V. Vinogradov, A. Dolgikh, L. Yedunov, Y. Pepelyshev, A. Rogov, E. Shabalin, A. Zaikin, I. Golovnin, Atomic Energy 113 (2012) 29–34.

[57] ISIS webpage, 2017. URL: `http://isis.stfc.ac.uk`.

[58] JPARC webpage, 2017. URL: `https://j-parc.jp/index-e.html`.

[59] SNS webpage, 2017. URL: `https://neutrons.ornl.gov`.

[60] PSI webpage, 2017. URL: `https://www.psi.ch`.

[61] ESS Webpage, 2017. URL: `https://europeanspallationsource.se`.

[62] E. Klinkby, B. Lauritzen, E. Nonbøl, P. Kjær Willendrup, U. Filges, M. Wohlmuther, F. X. Gallmeier, Nuclear Instruments and Methods in Physics Research, Section A: Accelerators, Spectrometers, Detectors and Associated Equipment 700 (2013) 106–110. URL: `http://dx.doi.org/10.1016/j.nima.2012.10.052`. doi:`10.1016/j.nima.2012.10.052`.

[63] T. Kittelmann, E. Klinkby, E. B. Knudsen, P. Willendrup, X. X. Cai, K. Kanaki, Computer Physics Communications 218 (2017) 17–42. URL: `http://dx.doi.org/10.1016/j.cpc.2017.04.012`. doi:`10.1016/j.cpc.2017.04.012`.

[64] A. Ravn, K. Lefmann, Unpublished (2017).

[65] P. Willendrup, E. Farhi, E. Knudsen, U. Filges, K. Lefmann, Component Manual for the Neutron Ray-Tracing Package McStas, version 2.3, Technical Report, Technical University of Denmark, 2016.

[66] E. Farhi, C. Monzat, R. Arnerin, T. V. Vuure, C. Castán-guerrero, C. Hennane, Journal of Neutron Research 17 (2014) 63–74. doi:`10.3233/JNR-130007`.

[67] E. Farhi, Y. Debab, P. Willendrup, Journal of Neutron Research 17 (2014) 5–18. doi:`10.3233/JNR-130001`.

[68] K. Lefmann, P. Willendrup, L. Udby, B. Lebech, K. Mortensen, J. Birk, K. H. Klenø, E. Kndusen, P. Christiansen, J. Šaroun, J. Kulda, U. Filges, M. Konnecke, P. Tregenna-Piggott, J. Peters, K. Lieutenant, G. Zsigmond, P. Bentley, E. Farhi, Journal of Neutron Research 16 (2008) 97–111. doi:`10.1080/10238160902819684`.

[69] L. Udby, P. K. Willendrup, E. Knudsen, C. Niedermayer, U. Filges, N. B. Christensen, E. Farhi, B. O. Wells, K. Lefmann, Nuclear Instruments and Methods in Physics Research Section A: Accelerators, Spectrometers, Detectors and Associated Equipment 634 (2011) 138–143. doi:`10.1016/j.nima.2010.06.235`.

[70] E. Farhi, V. Hugouvieux, M. R. Johnson, W. Kob, Journal of Computational Physics 228 (2009) 5251–5261. URL: `http://dx.doi.org/10.1016/j.jcp.2009.04.006`. doi:`10.1016/j.jcp.2009.04.006`.

[71] M. Guthrie, M. Baldini, C. Bull, P. Henry, S. Klotz, J. Loveday, P. Noguera, J. Luis Martínez Peña, J. Pedro de Vicente, ESS Instrument Construction Proposal (2015). doi:105281/zenodo.154478.

[72] J. Copley, Journal of neutron research 1 (1993) 21–36. URL: http://iospress.metapress.com/index/6565XG7534404605.pdf.

[73] K. Klenø, Exploration of the challenges of neutron optics and instrumentation at long pulsed spallation sources, Ph.D. thesis, University of Copenhagen, Niels Bohr Institute, 2013.

[74] SLURM webpage, 2017. URL: https://slurm.schedmd.com.

[75] M. Andreas Olsen, Optimizing neutron guide performance and price using guide_bot and CoatingWriter (Bachelor thesis Univ. Cph.), 2016.

[76] P. Willendrup, U. Filges, L. Keller, E. Farhi, K. Lefmann, Physica B: Condensed Matter 385-386 (2006) 1032–1034. doi:10.1016/j.physb.2006.05.329.

[77] E. Bergbäck Knudsen, E. Bryndt Klinkby, P. Kjær Willendrup, Nuclear Instruments and Methods in Physics Research, Section A: Accelerators, Spectrometers, Detectors and Associated Equipment 738 (2014) 20–24. doi:10.1016/j.nima.2013.11.071.

[78] NIST webpage, 2017. URL: https://www.ncnr.nist.gov/.

[79] MACS cold source, 2017. URL: https://www.ncnr.nist.gov/expansion/coldsource.html.

[80] J. Rodriguez, D. Adler, P. Brand, C. Broholm, J. Cook, C. Brocker, R. Hammond, Z. Huang, P. Hundertmark, J. Lynn, N. Maliszewskyj, J. Moyer, J. Orndorff, D. Pierce, T. Pike, G. Scharfstein, S. Smee, R. Vilaseca, Measurement Science and Technology 19 (2008) 034023. doi:10.1088/0957-0233/19/3/034023.

[81] J. Krizan, R. Cava, Physical Review B - Condensed Matter and Materials Physics 92 (2015) 014406. doi:10.1103/PhysRevB.92.014406.

[82] Personal communication with Allen Scheie and Kemp Plumb, 2016.

[83] K. Plumb, A. Scheie, J. Krizan, J. Rodriguez-Rivera, Y. Qiu, R. Cava, C. Broholm, Talk titled: "Magnetic excitations from a pyrochlore Heisenberg antiferromagnet", 2017. URL: http://meetings.aps.org/Meeting/MAR17/Session/E48.1.

[84] M. Arai, Advances in Colloid and Interface Science 71-72 (1997) 209–232. doi:10.1016/S0001-8686(97)90018-X.

[85] G. Bergerhoff, I. D. Brown, Acta Crystallographica Section A Foundations of Crystallography 37 (1981) C342–C342. doi:10.1107/S0108767381089411.

[86] ICSD database, 2017. URL: https://icsd.fiz-karlsruhe.de.

[87] NIST cross section database, 2017. URL: https://www.ncnr.nist.gov/resources/n-lengths/.

[88] A. Ravn, K. Røhl, M. Retuerto, T. Guidi, J. Taylor, A. Piovani, H. Leeberg, J. Birk, K. Lefmann, (In preperation) (2017).

UNIVERSITY OF COPENHAGEN
FACULTY OF SCIENCE

Appendix

Software for simulation and design of neutron scattering instrumentation

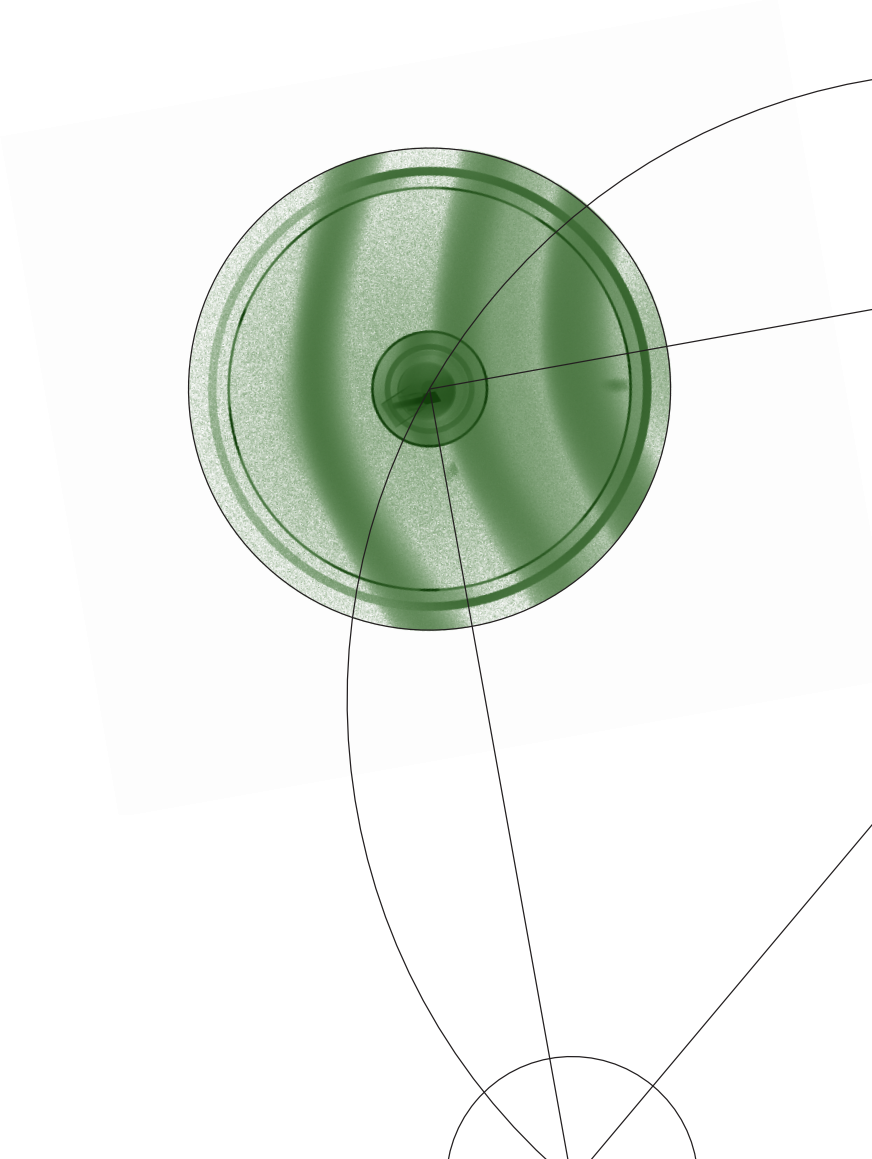

PhD Thesis

Mads Bertelsen
Nano-Science Center
Niels Bohr Institute
University of Copenhagen

A.1: **Constraining neutron guide optimizations with phase-space considerations** M. Bertelsen, K. Lefmann. Nuclear Instruments and Methods in Physics Research Section A: Accelerators, Spectrometers, Detectors and Associated Equipment, Vol. 830, (2016), DOI: 10.1016/j.nima.2016.06.003

A.2: **The automatic neutron guide optimizer guide_bot** (accepted) M. Bertelsen. Nuclear Instruments and Methods in Physics Research Section A: Accelerators, Spectrometers, Detectors and Associated Equipment, (2017), DOI: 10.1016/j.nima.2017.06.012

A.3: **Expanding the McStas sample simulation logic with McStas Union components** (in preparation), M. Bertelsen, K. Lefmann. Review of Scientific Instruments.

A.4: **Exploring performance of neutron guide systems using pinhole beam extraction** M. Bertelsen, H. Jacobsen, U.B. Hansen, H.H. Carlsen, K. Lefmann. Nuclear Instruments and Methods in Physics Research Section A: Accelerators, Spectrometers, Detectors and Associated Equipment, Vol. 729, (2013) DOI: 10.1016/j.nima.2013.07.062

A.5: **Neutron guide-split: A high performance guide bundle concept for elliptical guides** S. L. Holm, N. Rasmussen, L. Høpfner, M. Bertelsen, J. Voigt, K. H. Andersen, K. Lefmann. Nuclear Instruments and Methods in Physics Research Section A: Accelerators, Spectrometers, Detectors and Associated Equipment, Vol. 782, (2015), DOI: 10.1016/j.nima.2015.01.045

A.6: **Simulation of waviness in neutron guides** U.B. Hansen, M. Bertelsen, E.B. Knudsen, K. Lefmann. Journal of Neutron Research, Vol. 18, (2016) DOI: 10.3233/JNR-150023

A.7: **CAMEA ESS - The Continuous Angle Multi-Energy Analysis Indirect Geometry Spectrometer for the European Spallation Source** P. G. Freeman, J. O. Birk, M. Mark, M. Bertelsen, J. Larsen, N. B. Christensen, K. Lefmann, J. Jacobsen, Ch. Niedermayer, F. Juranyi, H. M. Ronnow. European Physical Journal Web of Conferences, Vol. 83, (2015), DOI: 10.1051/epjconf/20158303005

A.8: **HEIMDAL: A thermal neutron powder diffractometer with high and flexible resolution combined with SANS and neutron imaging - Designed for materials science studies at the European Spallation Source** S.L. Holm, K. Lefmann, P.F. Henry, M. Bertelsen, J Schefer, M. Christensen. Nuclear Instruments and Methods in Physics Research Section A: Accelerators, Spectrometers, Detectors and Associated Equipment, Vol. 828, (2016), DOI: 10.1016/j.nima.2016.05.046

A.9: **VESPA: The vibrational spectrometer for the European Spallation Source** A. Fedrigo, D. Colognesi, M. Bertelsen, M. Hartl, K. Lefmann, P. Deen, M. Strobl, F. Grazzi, M. Zoppi. Review of Scientific Instruments, Vol. 87(6), (2016), DOI: 10.1063/1.4952430

A.10: **Neutron guide shielding for the bifrost spectrometer at ESS** K. Mantulnikovs, M. Bertelsen, C.P. Cooper-Jensen, K. Lefmann and E.B. Klinkby. Journal of Physics: Conference Series, Vol. 746, (2016), DOI: 10.1088/1742-6596/746/1/012027

A.11: **An optional focusing SELENE extension to conventional neutron guides: A case study for the ESS instrument BIFROST** U. B. Hansen, M. Bertelsen, J. Stahn, K. Lefmann. Nuclear Instruments and Methods in Physics Research Section A: Accelerators, Spectrometers, Detectors and Associated Equipment, Vol. 852, (2017), DOI: 10.1016/j.nima.2017.01.075

A.12: **On the nature of magnetic stripes in cuprate superconductors** (submitted), H. Jacobsen, S.L. Holm, M.-E. Lăcătuşu, M. Bertelsen, M. Boehm, R. Toft-Petersen, J.-C. Grivel, S. B. Emery, L. Udby, B.O. Wells, K. Lefmann. Physical Review Letters, (2017)

A.13: **Field-induced inter-planar correlations in the high-temperature superconductor La1.88Sr0.12CuO4** A. T. Roemer, P. Jensen, H. Jacobsen, L. Udby, B. M. Andersen, M. Bertelsen, S. L. Holm, N. B. Christensen, R. Toft-Petersen, M. Skoulatos, M. Laver, A. Schneidewind, P. Link, M. Oda, M. Ido, N. Momono, K. Lefmann. Phys. Rev. B 91, (2015)

Appendix A

Publications

A.1 Constraining neutron guide optimizations with phase-space considerations

This paper is based on calculations and in part simulations included in my master thesis titled "Optimizing neutron guides using the minimalist principle and guide_bot", yet was improved in many ways. The focusing factor was introduced, allowing for continuous tuning of the expected focusing capabilities of the optimized guide. Scans of optimizations were redone, and the study of signal fraction was added. The paper was published in Nuclear Instruments and Methods in Physics Research, Section A.

Abstract

We introduce a method named the Minimalist Principle that serves to reduce the parameter space for neutron guide optimization when the required beam divergence is limited. The reduced parameter space will restrict the optimization to guides with a minimal neutron intake that are still theoretically able to deliver the maximal possible performance. The geometrical constraints are derived using phase-space propagation from moderator to guide and from guide to sample, while assuming the optimized guides will achieve perfect transport of the limited neutron intake.

Guide systems optimized using these constraints are shown to provide performance close to guides optimized without any constraints, however the divergence received at the sample is limited to the desired interval, even when the neutron transport is not limited by the supermirrors used in the guide.

As the constraints strongly limit the parameter space for the optimizer, two control parameters are introduced that can be used to adjust the selected subspace, effectively balancing between maximizing neutron transport and avoiding background from unnecessary neutrons. One parameter is needed to describe the expected focusing abilities of the guide to be optimized, going from perfectly focusing to no correlation between position and velocity. The second parameter controls neutron intake into the guide, so that one can select exactly how aggressively the background should be limited.

We show examples of guides optimized using these constraints which demonstrates the higher signal to noise than conventional optimizations. Furthermore the parameter controlling neutron intake is explored which show that the simulated optimal neutron intake is close to the analytically predicted, when assuming that the guide is dominated by multiple scattering events.

My contribution

Performed the entire study and wrote the manuscript with supervision from Kim Lefmann.

Nuclear Instruments and Methods in Physics Research A 830 (2016) 313–324

Contents lists available at ScienceDirect

Nuclear Instruments and Methods in Physics Research A

journal homepage: www.elsevier.com/locate/nima

Constraining neutron guide optimizations with phase-space considerations

Mads Bertelsen *, Kim Lefmann

Nanoscience Center and eScience Center, Niels Bohr Institute, University of Copenhagen, Universitetsparken 5, 2100 Copenhagen, Denmark

ARTICLE INFO

Article history:
Received 23 February 2016
Received in revised form
18 May 2016
Accepted 1 June 2016
Available online 2 June 2016

Keywords:
Neutron guide
Neutron optics
Phase-space
Neutron instrumentation
McStas
IFit

ABSTRACT

We introduce a method named the Minimalist Principle that serves to reduce the parameter space for neutron guide optimization when the required beam divergence is limited. The reduced parameter space will restrict the optimization to guides with a minimal neutron intake that are still theoretically able to deliver the maximal possible performance. The geometrical constraints are derived using phase-space propagation from moderator to guide and from guide to sample, while assuming that the optimized guides will achieve perfect transport of the limited neutron intake.

Guide systems optimized using these constraints are shown to provide performance close to guides optimized without any constraints, however the divergence received at the sample is limited to the desired interval, even when the neutron transport is not limited by the supermirrors used in the guide.

As the constraints strongly limit the parameter space for the optimizer, two control parameters are introduced that can be used to adjust the selected subspace, effectively balancing between maximizing neutron transport and avoiding background from unnecessary neutrons. One parameter is needed to describe the expected focusing abilities of the guide to be optimized, going from perfectly focusing to no correlation between position and velocity. The second parameter controls neutron intake into the guide, so that one can select exactly how aggressively the background should be limited.

We show examples of guides optimized using these constraints which demonstrates the higher signal to noise than conventional optimizations. Furthermore the parameter controlling neutron intake is explored which shows that the simulated optimal neutron intake is close to the analytically predicted, when assuming that the guide is dominated by multiple scattering events.

1. Introduction

The European Spallation Source [1] will be the first neutron source to utilize a long pulse design [2], and as the time structure favours long time of flight instruments [3,4], it has spawned a renewed interest in neutron guide design [5–9]. Recent findings suggesting novel moderator geometries with limited height [10] have yet again posed new challenges in guide design. Monte Carlo ray tracing techniques have been used for decades, starting with NISP [11] and later McStas [12–15], Vitess [16,17] and ResTrax [18], but it is only in recent years that the use of numerical optimizers [19,20] has become a standard tool of the trade. The optimizer will control parameters in the guide model, and run the underlying ray tracer for each step in order to maximize a particular figure of merit (FOM), often taken to be flux on sample within a wavelength interval.

This optimization technique caused guides to reach new performance levels, and it became relevant to compare the quality of the beam with the theoretical maximum, which can be described using Liouville's theorem [21]. The so-called brilliance transfer [22] is bounded between zero and unity, and expresses the ratio of phase-space density at the moderator and sample for a given closed phase-space volume. The requirement of a closed phase-space volume meant the FOM was changed to the neutron intensity within a fixed sample area, divergence interval, and wavelength interval.

Unfortunately, guides designed using numerical optimizers in this way are only guaranteed to provide a high neutron brilliance, not a low background. A neutron source generates a large number of high energy particles that can only be suppressed by large quantities of shielding, but the typical unrestrained solution from the optimizer would have an abnormally large guide entrance near the moderator, which allows also a large amount of these particles to enter the guide system. In addition, the improved transport efficiency of these guides allows for a high number of thermal

* Corresponding author.
E-mail address: mads.bertelsen@gmail.com (M. Bertelsen).

http://dx.doi.org/10.1016/j.nima.2016.06.003
0168-9002/

neutrons transported that does not contribute to the FOM, and thus becomes a secondary source of background close to the neutron instrument. In addition it was observed that running the same optimization several times would give rise to very different guide geometries with strikingly similar performance, making it prudent to optimize the same guide geometry several times in order to get a solution with reasonable background characteristics.

The long term solution to these problems is obviously to include detailed background simulations in the Monte Carlo ray tracing simulation of each guide [23,24] in the optimization procedure, but as this requires unrealistic amounts of computing power and considerable amounts of specialized code for every guide geometry, a simpler solution is highly relevant.

We here propose a principle where analytical calculations on the propagation of phase-space volumes using acceptance diagrams [25] are used to constrain the optimizer to guides with a reasonable balance between neutron intake and the ability to reach a brilliance transfer of unity. This is done by considering propagation from the moderator to the guide, and from the guide to the sample. Inside the guide, it is assumed the optimizer will find a solution that transports the entire neutron intake to the end of the guide. The balance between background reduction and performance can be tuned using two control parameters with intuitive meanings, instead of manually scanning e.g. the entrance dimensions of the guide. We show that this method will effectively reduce the parameter space of the optimizer to guides with minimal background, still potentially able to reach a brilliance transfer of unity. Hence we call the method the "Minimalist Principle" (MP).

This describes the ideas necessary for understanding the MP before deriving it, and then show examples on guides optimized under varying circumstances to highlight the benefits of this alternative method for guide optimization.

2. Reasoning behind the Minimalist Principle

It follows from Liouville's theorem that the phase-space density at the sample cannot exceed that of the phase-space density near the moderator. If one requires a neutron beam described by a closed phase-space volume, it follows that there is a maximum possible neutron flux in this phase-space volume. This limit is the foundation of the MP, as there is a point where additional neutron intake cannot possibly contribute to the brilliance transfer.

When optimizing a guide system with the FOM chosen as the number of neutrons in such a phase-space volume, there is a corresponding maximum FOM. It is of interest to find a guide which delivers a FOM close to this maximum, but it is also important to limit the potential background from the neutron source. The background can be split into high energy particles that should be absorbed by shielding, and unwanted cold and thermal neutrons are to be reflected by the neutron mirrors. The high energy background is not taken into account in this paper, but is expected to be handled by choosing a guide geometry that allows sufficient shielding between moderator and sample.

In the MP, geometrical constraints on the guide geometry are designed to minimize the background from unnecessary cold and thermal neutrons. This is done by only transporting the neutrons necessary to fully illuminate the FOM phase-space volume. In order to calculate which neutrons are necessary, the phase-space volume corresponding to the FOM is propagated from the sample back to the end of the guide by acceptance diagrams. This yields the phase-space volume the guide should be able to deliver, and as this volume has a certain spatial width, the dimensions of the end of the guide can be determined, which is the first important constraint.

As it is theoretically possible for a guide to transport a phase-space volume without increasing its size or decreasing its phase-space density, the size of the phase-space volume that enters the guide should be at least equal to the size of the phase-space volume that the guide must deliver. If the size of the incoming phase-space volume is smaller than needed, it is not possible to reach the maximum FOM. By providing the guide with a phase-space volume of the same size as the one it has to deliver, the optimal brilliance transfer should be achievable. Increasing the incoming phase-space volume at this point would only increase the background if a perfect brilliance transfer is already achieved. As the incoming phase-space volume size depends on the size of the guide entrance, the distance to the source and the source dimensions, this requirement results in a constraint on these parameters.

A guide that only delivers the exact phase-space volume needed to evenly illuminate the sample is considered truly focusing. Such guides exist, for example the Selene guide system as described in [26]. A truly focusing guide will work through single reflections per guide element, because multiple reflections will destroy the necessary perfect correlations in phase-space.

Most guide designs rely on multiple reflections. Even a perfect elliptical guide will have large amounts of the intensity from this process for anything but point sources [8]. An ideal multiple reflecting guide is assumed to have a divergence distribution that is independent of position, or at least a weaker correlation than that of a truly focusing guide. Without the focusing ability, the delivered phase-space needs to be larger than for a focusing guide in order to cover the FOM. The exact size of this larger phase-space volume is again derived using acceptance diagrams.

Guides designed using the MP constraints have a more direct control over the outgoing divergence, which will be limited to the divergence limits of the FOM in the case of a perfect guide. In practice there will be unwanted neutrons at higher divergences than requested on some parts of the sample, but very limited in comparison to a guide optimized without any constraints. In addition, the amount of neutrons entering the guide is as low as possible, under the condition that the guide is still theoretically able to achieve the maximum possible FOM. This causes lower neutron losses along the guide than traditional geometries, yielding a guide which is highly efficient in terms of neutrons delivered in relation to background generated from absorbing these neutrons either in the guide or near the sample. It will also reduce radiation damage on the supermirrors and necessary shielding along the guide.

3. Derivation of the Minimalist Principle

In this section appropriate terminology and notation is introduced, followed by a derivation of the MP using acceptance diagrams.

3.1. Phase-space terminology

A phase-space is a space spanned by canonical variable pairs, here position and velocity are used [27]. The z direction is selected to be along the beam direction, and the 5 dimensional phase-space consists of $(x, y, \eta_x, \eta_y, \lambda)$ where the wavelength is often ignored as it does not change inside a neutron guide system. For a comprehensive description see [28]. When assuming rectangular cross sections of the guides, the x and y components are independent and the phase-space is split into two subspaces, (x, η_x) and (y, η_y). A closed set in a space is referred to as a phase-space volume. The size of a phase-space volume is defined to be the volume of this

closed set in the phase-space. The phase-space density of phase-space volume is the amount of neutrons per second with trajectories within the volume divided with the size of the phase-space volume. The size of a phase-space volume α is here denoted $V(\alpha)$ and the density is denoted $\rho(\alpha)$.

The phase-space volume that enters the guide is called α and the phase-space volume leaving the guide is called β. The FOM phase-space volume at the sample is called Ω, and is assumed to be a rectangle in space with a position independent symmetric divergence requirement. The brilliance transfer can be written as $\rho(\Omega)/\rho(\Omega_M)$ with Ω_M being the FOM phase-space volume, but translated to the moderator surface.

With this terminology Liouville's theorem [21] states the size of a phase-space volume is constant. With the chosen notation, Liouville's theorem for a guide without gaps can be written as

$$V(\alpha) = V(\beta) \tag{1}$$

$$\rho(\alpha) \geq \rho(\beta). \tag{2}$$

3.2. Notation

The MP considers the beam propagation before and after the guide, and thus assumes a generic guide setup as seen in Fig. 1, where the shape and the length of the guide are arbitrary, but the dimensions at both ends are known. For now it is assumed the guide is closed meaning without gaps, but the appropriate corrections are described later in the section. All parts of the source, guide and sample are assumed rectangular, meaning that horizontal and vertical components of the neutron trajectory can be calculated independently. All calculations are done for a single direction, but are valid for both if gravity is neglected.

The width of the moderator in the relevant direction is denoted M, and the distance between the moderator and guide is denoted L_M. The width of the start and end of the guide is denoted W and U. The distance between the end of the guide and the sample is L_S, and is often small. The width of the sample is denoted S and together with the divergence requirement, ϕ, describes the FOM. It is assumed the guide is placed with the center of the guide entrance aligned with the center of the moderator, and the center of the end of the guide is aligned with the center of the sample.

3.3. Beam propagation without guide

A neutron beam with a given width and divergence distribution will propagate under simple rules from classical mechanics. The divergent beam can be easily visualized by acceptance diagrams [25], as shown for the x direction in Fig. 2. The wavelength range is ignored as it does not influence the trajectories when gravity is neglected. Under these conditions the ideal spatial and divergence distributions are top hat functions. When the beam propagates, the diagram shears as shown. When propagating a neutron a distance L, the divergence η_x is unchanged while the transverse distance travelled can be calculated from

$$\Delta x = L\tan(\eta_x). \tag{3}$$

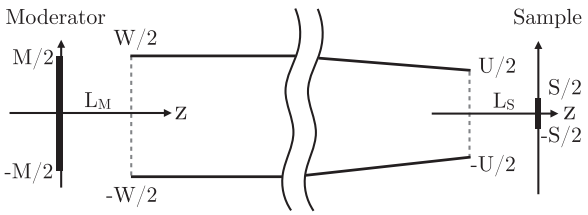

Fig. 1. A sketch of the generic guide system investigated when using the MP, and the variables used to describe it.

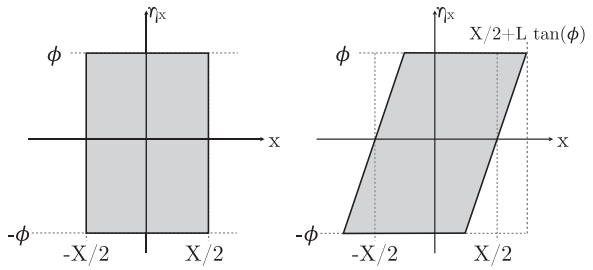

Fig. 2. Acceptance diagrams showing propagation without guide. The left side shows a beam at $z = z_0$ with width X and a uniform divergence distribution between $-\phi$ and ϕ . The phase-space at $z = z_0 + L$ is shown on the right side, where the propagation of the beam has caused a shearing of the phase-space volume, which can be calculated from Eq. (3).

Thus a beam where the highest divergence is ϕ and the lowest is $-\phi$ will be $2L\tan(\phi)$ wider when propagated a distance L, as shown in Fig. 2.

3.4. Propagation between sample and guide

When considering propagation from the end of the guide to the sample with the objective to reach a brilliance transfer of unity, the entire FOM must be covered, and since the neutrons at the extremes of the divergence interval are translated by Eq. (3), the guide should be $2\Delta x$ wider than the sample:

$$U = S + 2L_s\tan(\phi). \tag{4}$$

Any neutrons outside the FOM phase-space volume are considered background, so it is important to find the smallest possible phase-space volume that will still cover the FOM. Here a phase-space volume with the dimension U and entire divergence range $[-\phi; \phi]$ is denoted β_M and is propagated from the end of the guide to the sample, which can be seen in Fig. 3. When using a rectangular phase-space volume at the end of the guide, it is clear that the FOM is covered, but that some of the propagated phase-space is outside the FOM area. By propagating the FOM volume back to the end of the guide, the smallest possible phase-space volume is found, here denoted β_F.

The volumes β_M and β_F correspond to two extremes in terms of focusing ability. The β_F volume corresponds to perfectly focusing, as the entire phase-space volume exactly covers the FOM volume when propagated to the sample. The β_M volume corresponds to the case of a guide relying on multiple reflections, as the correlations between position and divergence are smeared out. In order to generalize this we introduce the focusing parameter, Y, that describes a linear transition from the focusing case to the multiple reflecting case, so that the size of the needed phase-space volume at the end of the guide can be written as

$$V(\beta_F) = 2S\phi \tag{5}$$

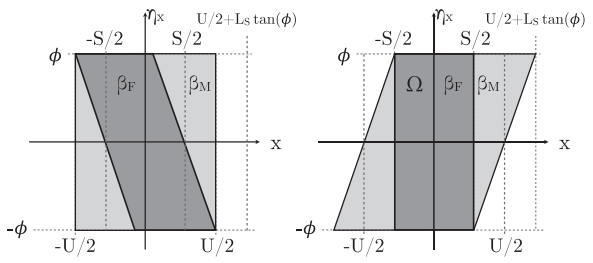

Fig. 3. Acceptance diagram for a guide of width U illuminating a sample of width of S from a distance of L_S. The left part is at the end of the guide, while the right side is at the sample position. The light grey area is the phase-space volume designated β_M while the dark grey is the phase-space volume designated β_F, and the latter corresponds perfectly to the FOM phase-space volume at the sample position, Ω.

$$V(\beta_M) = 2U\phi = 2(S + 2L_S\tan(\phi))\phi \quad (6)$$

$$V(\beta) = 2(S + 2YL_S\tan(\phi))\phi. \quad (7)$$

Thus $Y=0$ corresponds to perfectly focusing, while $Y=1$ corresponds to a guide completely dominated by multiple reflections. The appropriate value of Y will depend on the geometry of the entire moderator, guide, sample system including the selected FOM, and is not known. It is intended that a reasonable value of Y should be found from experience with similar cases. The highest possible value of $Y=1$ will still be an aggressive reduction of unwanted neutrons.

3.5. Supplying the needed phase-space volume size

As the phase-space volume size $V(\beta)$ is known at the end of the guide, it is of interest to determine the minimal phase-space size needed at the start of the guide $V(\alpha)$ in order to illuminate the FOM phase-space volume.

From Liouville's theorem it is known that phase-space density cannot be increased, and thus the best case is no reduction in phase-space density under transport. If one assumes a perfect guide, it should only be necessary to supply a phase-space volume with a size identical to the needed phase-space volume:

$$V(\alpha) = V(\beta) \quad (8)$$

$$\rho(\alpha) = \rho(\beta) \quad (9)$$

This is a very ambitious requirement, and will only result in guides with a high brilliance transfer if a suitable geometry is within the specified parameter space, and the mirror quality is sufficient. One can relax the requirement by introducing an illumination factor k, so that

$$V(\alpha) = kV(\beta). \quad (10)$$

Here a guide optimized using the constraint with $k < 1$ should not be able to reach a brilliance transfer of unity, unless the focusing parameter Y has been set too high for the selected guide geometry. Setting $k=1$ corresponds to the case discussed so far. Using $k > 1$, will introduce additional background but may also increase the FOM.

We have experienced that adjusting the parameter k for a range of guide optimizations is superior to adjusting the guide opening manually, as one is always aware of the balance between FOM and background when using k-adjustments.

3.6. Propagating from moderator to guide

In order to calculate the size of the phase-space volume received by the guide, the known phase-space volume at the moderator is propagated to the start of the guide. It is assumed that the moderator emits neutrons in every direction with equal probability, and thus the phase-space volume emitted is not closed in the divergence direction. There is thus effectively no top or bottom in the acceptance diagram. For the small divergence values needed here, we assume that the sides are straight lines. The acceptance diagram is propagated forward a distance of L_M. From Fig. 2, the slope can be calculated as

$$a = \frac{\Delta\eta_x}{\Delta x} = \frac{\phi}{L_M\tan(\phi)} \approx \frac{1}{L_M}, \quad (11)$$

with divergence measured in radians. The size of the phase-space volume α which enters the guide is calculated using the appropriate acceptance diagram in Fig. 4. The area of the parallelogram is

$$V(\alpha) = aMW = MW/L_M. \quad (12)$$

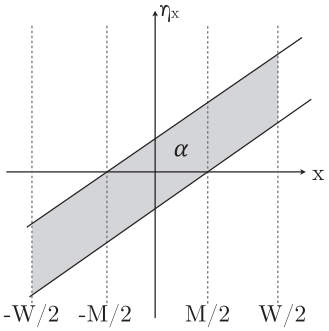

Fig. 4. Acceptance diagram for a distance L_M after a moderator of width M. A guide with width W starts here, and the phase-space volume which enters the guide is denoted α.

3.7. Applying the Minimalist Principle

The preceding calculations are sufficient to use the MP, as one uses the derived equations as constraints in the parameter space describing the guide geometry. Assuming that a truly focusing guide can use the entire incoming phase-space volume size, a combination of Eqs. (7), (10) and (12) gives

$$V(\alpha) = kV(\beta_F) \Rightarrow WM/L_M = 2kS\phi. \quad (13)$$

In addition Eq. (4) should also be used to ensure not to waste phase-space volume size by illuminating an area larger than the sample:

$$U = S + 2L_S\tan(\phi). \quad (14)$$

By applying both equations (for both x and y directions) the number of free parameters to be optimized is reduced by 4, which can in many cases be essential. In addition only the guides which can potentially reach the best possible FOM without over-illuminating the guide entrance are investigated. The 4 free parameters are effectively replaced by 4 tunable parameters that should not be selected by the optimizer, an illumination factor for each direction, and a focusing factor for each direction.

3.8. Gaps in the guide

If the guide is not closed, but contains gaps for choppers or similar, it is not a reasonable assumption that phase-space volume is conserved along the guide. It can be handled by applying the MP on the closed guide on each side of the gap, starting from the sample. The guide piece between the sample and the gap will have a constraint to determine the end of the guide, but will not have any constraints for selecting the size of the guide opening after the gap, which can be chosen by the optimizer. This guide piece will need a phase-space volume of a certain size which can be calculated from Eq. (7). The guide piece between the moderator and gap will consider the guide opening after the gap as the sample, and from the dimensions chosen, a divergence requirement can be calculated from the necessary phase-space volume size, and the MP can thus be applied to the first guide piece. There is, however, the issue of selecting a reasonable value of the focusing parameter Y, in this work $Y=1$ (non-focusing) has been used for gaps.

3.9. Kink in the guide

A surprisingly efficient way of escaping line of sight is to simply have a kink in the guide instead of a long bending section. Here a kink is defined as a gap between two guides, where the second guide has a new direction. After using the MP on the guide after

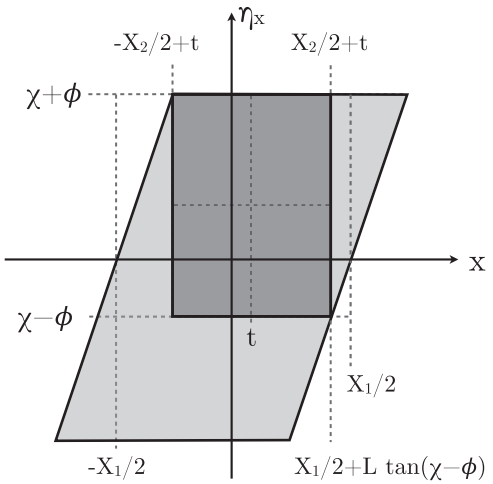

Fig. 5. The acceptance diagram after a kink with length L and angular change χ. The guide before the kink ends with dimension X_1 just large enough to evenly illuminate a guide with width X_2 and divergence requirement ϕ angled χ relative to the first guide. The light grey box is the output of the first guide, while the dark grey box is the needed phase-space volume for the second.

the kink, the needed divergence can be calculated from its phase-space volume size requirement and start width. It is then of interest to calculate the width and needed divergence from the first guide so that this requirement is met. This is achieved by the appropriate phase-space diagram in Fig. 5, where a guide with divergence requirement ϕ is kinked an angle of χ. The guide before the kink has the width X_1, while the width of the guide after the kink is denoted X_2. The second guide is translated a distance t in order to minimize the needed phase-space volume from the first guide. The derivation is done only for the case of multiple scattering guides, meaning a focusing parameter of $Y=1$, and is a generalization of the case discussed in Section 3.4.

The beam needed at the guide after the kink will have an increased width when propagated back to the guide before the kink of $2L\tan(\phi)$ from Eq. (3), and thus $X_1 = X_2 + 2L\tan(\phi)$. The necessary translation is found from Fig. 5, as it must satisfy,

$$t + X_2/2 = X_1/2 + L\tan(\chi-\phi) \Rightarrow t = L\tan(\phi) + L\tan(\chi-\phi) \approx L\chi. \quad (15)$$

The needed phase-space volume size for the guide before the kink is $2X_1(\phi+\chi)$. In this derivation it is implicitly assumed that the second guide will need a symmetric phase-space volume, as the area directly under the dark grey box in Fig. 5 would also be received by the second guide, but is assumed to be absorbed due to the high divergence relative to the second guide. This can however give some asymmetry at higher wavelengths in kinked guides.

4. The Minimalist Principle in practice

We now present examples of guides optimized with the MP, both to show how they differ from guides optimized without these constraints and to explore the parameters used to adjust the optimization within the MP.

4.1. Effect of the Minimalist Principle

In order to demonstrate the MP, a guide is optimized with and without the constraint in Eq. (10). This will show how the amount of unnecessary neutrons is limited, as there will not be a limit on neutron intake in the reference case. In order to illustrate how the illumination factor affects the results, the optimization using the MP is done with both $k=1$ and $k=1.25$.

The guide geometry to be optimized consists of a focusing piece (a "feeder" [29,30]) before a gap at 5.9 m followed by an elliptic section, a curved guide, and an elliptic section. The gap length is 20 cm, and the following elliptic guide section has a starting width of 3 cm. The guide stops 50 cm before the sample, and is not allowed to start closer than 2 m from the moderator. The guides are curved so that line of sight through the guide is eliminated 5 m before the end. The remaining geometrical parameters are controlled by the optimizer. The FOM is a 1.5×1.5 cm^2 area with a divergence requirement of 0.75° horizontally and 1.0° vertically. The wavelength range 1.5–4 Å. The moderator is a 12×12 cm^2 square, and the sample is situated 150 m from the moderator. The supermirror coating of the guide is $m=3$ everywhere with $q_c=0.0217$ Å^{-1} [31, Chapter 3.2-9], being the critical scattering vector for the Ni vacuum interface. The guide is assumed multiple reflecting, and uses $Y=1$ when the MP is applied. These requirements are similar to a large amount of guides optimized for ESS instruments using the TDR [1] moderator description. The optimizations were done using McStas [12–15] and iFit [19], the resulting guide geometries are shown in Fig. 6.

The brilliance transfer as a function of wavelength for the optimized guides is shown in Fig. 7. The brilliance transfer for the guides optimized with the MP normalized to the guide optimized without is seen in Fig. 8. Here the amount of useful neutrons the three guides deliver to the sample is compared, as only neutrons which are within the spatial and divergence requirement are considered.

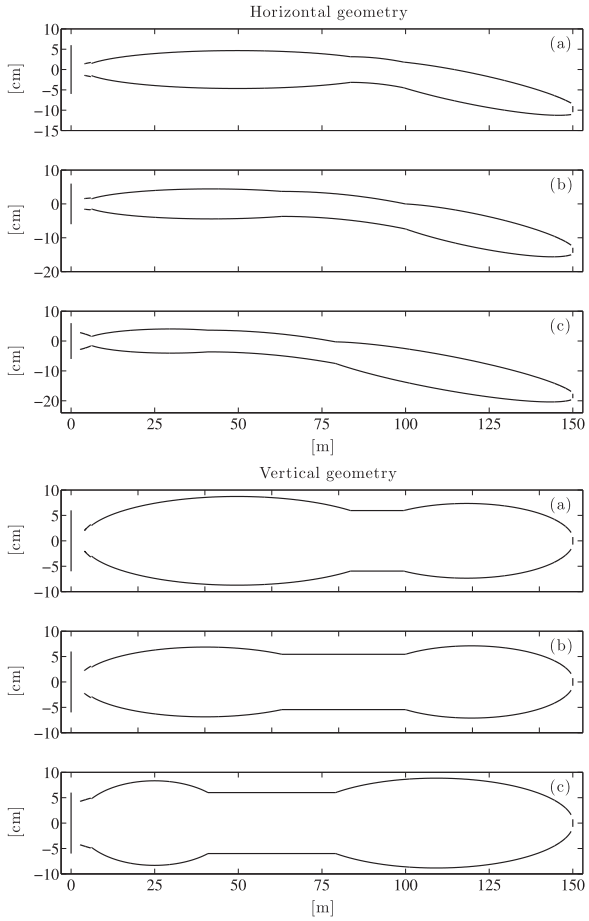

Fig. 6. Geometry of the three guides to be compared: (a) is with the MP and $k=1$ where (b) is with $k=1.25$ and (c) is without the MP.

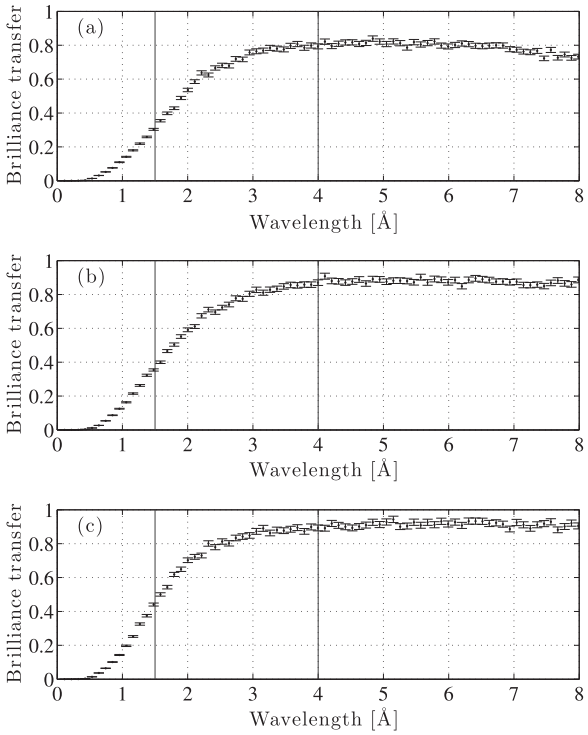

Fig. 7. Brilliance transfer as a function of wavelength for the three guides optimized under different conditions. Graph (a) is with the MP and $k=1$ where (b) is with $k=1.25$ and (c) is without the MP. All guides were optimized for the wavelength band 1.5–4 Å.

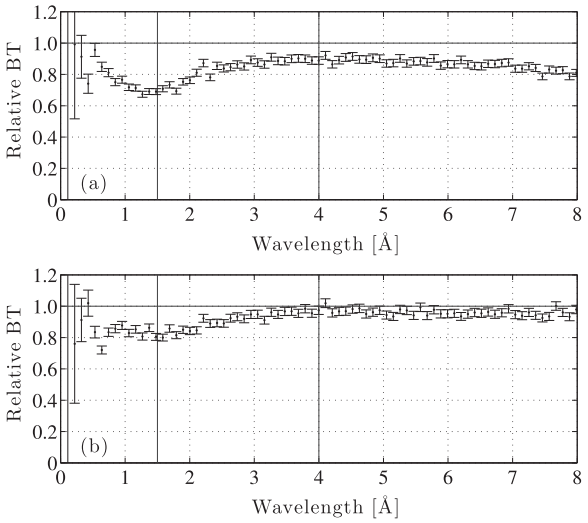

Fig. 8. Brilliance transfer as a function of wavelength for the two guides optimized with the MP normalized to the brilliance transfer of the guide optimized without. Graph (a) is for $k=1$ while (b) was optimized using $k=1.25$.

It is clear that the guide optimized without the MP has the highest brilliance transfer at all wavelengths, but the difference down to the guide with $k=1.25$ is quite small. The guide with $k=1$ has an integrated brilliance transfer of 80% of the guide optimized without the MP. The small decrease in brilliance transfer at larger wavelengths for the guide with $k=1$ is caused by gravity and not punished by the optimizer as the FOM wavelength range is 1.5–4 Å.

Fig. 9 shows the horizontal acceptance diagrams used to compare the guides performance in terms of homogeneity of divergence and spatial distributions. As the acceptance diagram shows a larger phase-space volume than the FOM, they also show neutrons transported that did not enter the FOM. The guide optimized without the MP has the most homogeneous phase-space volume inside the FOM box, as the guides designed with the MP have some structure in the form of thin lines with lower brilliance transfer. However, for many applications these small features are of little importance as they are much smaller than the instrument resolution.

The guides optimized with the MP have far fewer neutrons transported outside the FOM box. At low wavelengths where the transported divergence is limited by the coating of the supermirrors, the solutions are very similar. At higher wavelengths, the guide optimized without the MP starts to expand the divergence distribution beyond what was requested, while the guide optimized with $k=1$ does not have any additional phase-space volume size to allow for that, and thus has a divergence which matches the requested even at larger wavelengths. The guide optimized with $k=1.25$ does go to higher divergence than requested, but still reaches a limit where the divergence is not increased further (not shown).

Note that the corners of the FOM box are just covered by the transported phase-space volume because Eq. (4) was used, even when optimizing without the MP.

The behaviour shown in the acceptance diagrams signifies that the guides designed with the MP would have an advantage in terms of signal to noise. This is explored as a function of wavelength in Fig. 10 where the neutrons within the FOM volume is counted as signal, and noise is counted as all other neutrons in a 10×10 cm^2 area centred at the sample position. This area corresponds to typical sample environment sizes where slits are commonly used to reduce the background from the unnecessary neutrons, and here we explore how much this task can be reduced by using the MP. As with the acceptance diagrams we see similar performance in the low wavelength region where the performance is limited by the supermirrors, but at higher wavelengths the unwanted high divergence neutrons in the reference case results in a large advantage for the guides optimized with the MP. When comparing the two guides optimized with the MP, we see the highest signal to noise for the guide optimized with $k=1$ as expected from the derivation, but the guide with $k=1.25$ is close. This indicates that illumination factors slightly above 1 are very interesting, as the performance is improved with only a small loss in signal to noise.

4.2. The effect of the illumination factor

We now investigate how guides optimized by using the MP perform as a function of the illumination factor, k. Four different guide geometries are optimized using the MP for a range of k values. The FOM is a 2×2 cm^2 area with a divergence requirement of 0.75° for both directions and a wavelength range of 1–4 Å. The source is 12×12 cm^2, and the sample is located 160 m from it. A coating of $m=3.5$ was used in the entire guide.

- Elliptic guide.
- Parabolic defocusing to curved guide followed by parabolic focusing.
- Parabolic feeder ending at 6.5 m from the source connected to a 1 m straight 3 cm wide guide followed by an elliptic guide.
- Guide composed of three sections with flat mirrors.

Fig. 11 shows the resulting brilliance transfer for these guides optimized over a range of illumination factor values with the focusing factor $Y=0$, meaning the guides are assumed truly focusing. Examples of the optimized geometries are shown in Fig. 12. It is expected that the brilliance transfer should asymptotically reach a saturation value at high illumination factors where

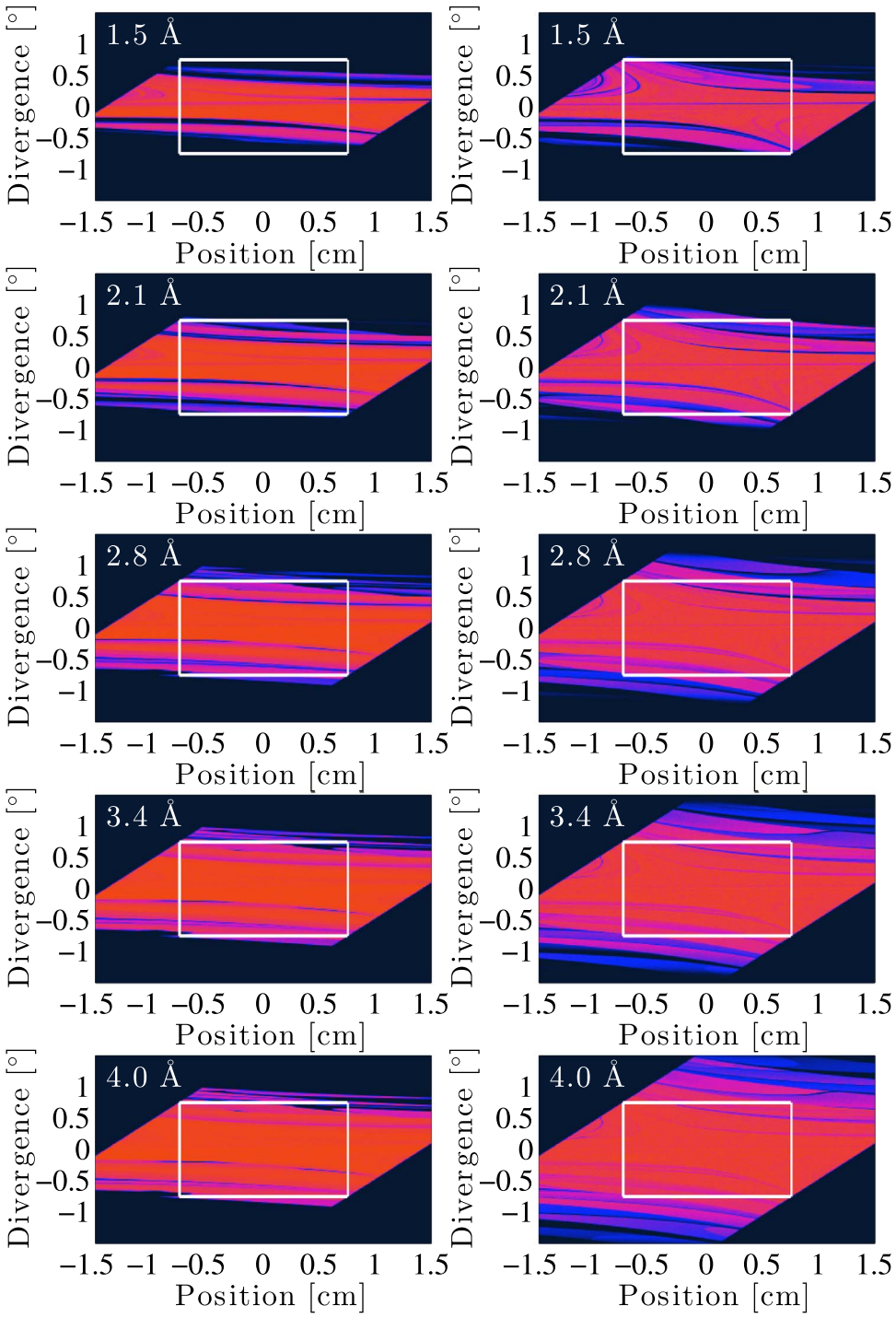

Fig. 9. Horizontal acceptance diagrams for the sample position for two different guides shown for five different wavelengths (rows). The left column is for a guide optimized with the MP and $k=1$, while the column to the right is for a guide optimized without any restrictions on the incoming phase-space volume.

additional incoming neutrons simply does not add to the brilliance transfer.

In Fig. 13 a similar scan has been made, but with a focusing factor of $Y=1$, assuming that the guides are not able to focus on the sample. The optimal geometries are similar to the results for the truly focusing case shown in Fig. 12, but their entrances have a slightly larger solid angle as seen from the moderator. In this case the brilliance transfer of all guides levels off at higher illumination factors as they approach a saturation brilliance transfer. The tapered guide clearly reaches a limit earlier than the remaining guides in this comparison. At low illumination factors, the elliptic guides perform better than expected, as the brilliance transfer exceeds the minimalist factor, which means it must have some focusing ability. The important prediction of the MP is that the start of the flat part of the brilliance transfer curve should be at or close to $k=1$, after which there should be diminishing returns of accepting more neutrons into the guide. For the tested guides this seems to happen somewhere in the range $k = [1: 1.25]$, which is close to the prediction.

The brilliance transfer saturates well below the actual performance limit of unity from Liouville's theorem. This can be explained by the high requirements for the guide compared to the

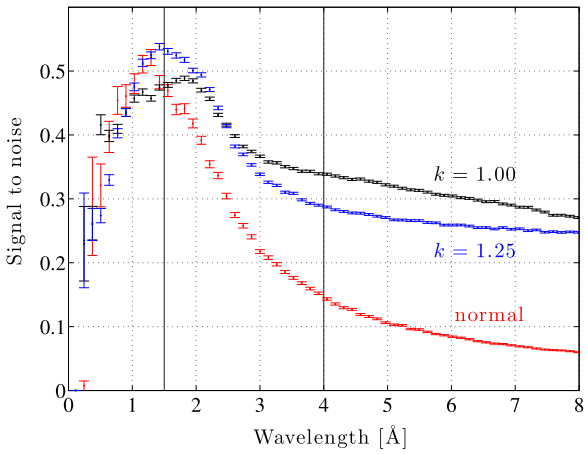

Fig. 10. Signal to noise for a guide designed without the use of the MP compared to two guides designed using the MP, but with illumination factors of $k=1$ and $k=1.25$ respectively.

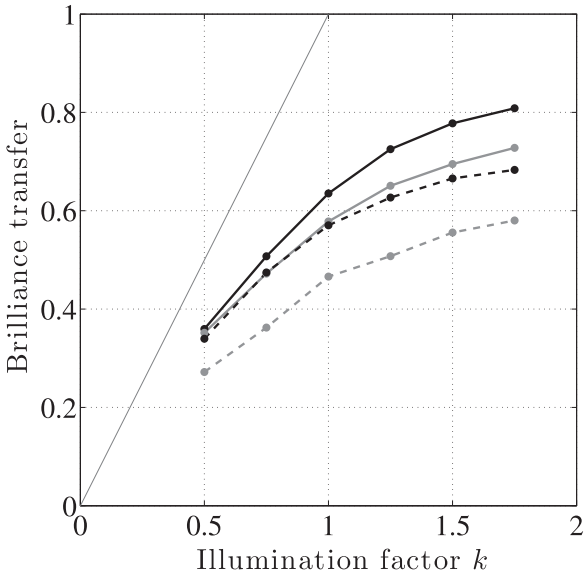

Fig. 11. Scans of the illumination factor k for four different guide geometries which are all assumed truly focusing, $Y=0$. From highest performance to lowest there is the elliptic guide (black), the curved with parabolic focusing (grey), the elliptic guide with feeder (black dashed) and the straight tapered (grey dashed). All brilliance transfers are for the entire wavelength range of 1–4 Å. Examples of the geometry of each guide are displayed in Fig. 12.

used mirror quality. A brilliance transfer above 80% (70% without line of sight through guide) is, however, a respectable performance in this case, and is achieved with an overillumination of 25% this corresponds to 1. $25^2 \approx 1.56$ times more neutrons than with $k=1$, a factor of k for each direction.

As the brilliance transfer values in both Figs. 11 and 13 are averages over the wavelength band, they do hide some complexity. Over the wavelength range the brilliance transfer of the guides changes from being limited by the supermirror quality to being limited by neutron intake, and both contribute to the values shown in the figures. We have, however, selected not to show brilliance transfer for smaller wavelength ranges as they are similar to the averaged case.

4.3. Analysing guide data using the Minimalist Principle

Here we investigate the relation between the phase-space intake recommended by the MP, and those selected by an optimizer

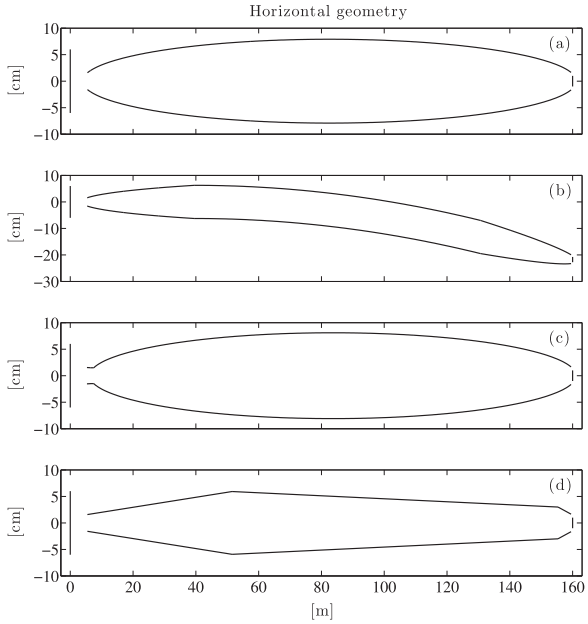

Fig. 12. Examples of the geometry of the four investigated guides with the focusing parameter $Y=0$ and all with illumination factor $k=1$. The elliptic guide (a), the curved with parabolic focusing (b), the elliptic guide with feeder (c) and the straight tapered (d).

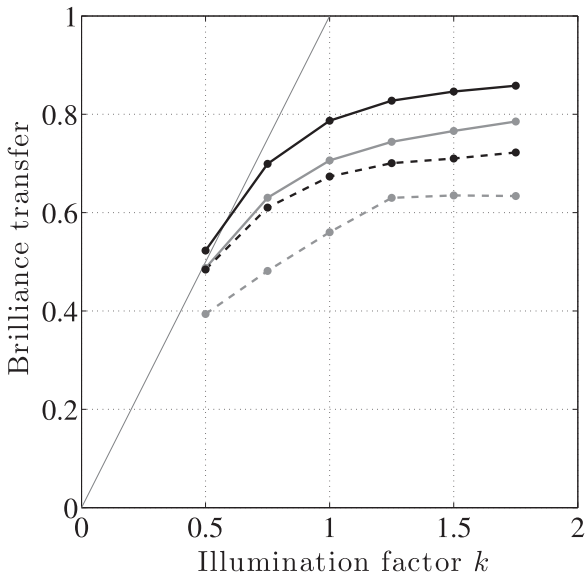

Fig. 13. Scans of the illumination factor k for four different guide geometries which are all assumed multiple scattering, $Y=1$. From highest performance to lowest there is the elliptic guide (black), the curved with parabolic focusing (grey), the elliptic guide with feeder (black dashed) and the straight tapered (grey dashed). All brilliance transfers are for the entire wavelength range of 1–4 Å. The geometries are similar to the truly focusing case shown in Fig. 12. Here we see the brilliance transfer reaching a plateau just above $k=1$.

without the derived constraints. Data from a previous publication [29] is analysed, as it contains a large amount of guides optimized for different FOM's without use of the MP. The optimized guides all have a pinhole at 6.0 m from the moderator, and an elliptic guide to transport from pinhole to sample. The performance increase gained by inserting a parabolic feeder before this pinhole was investigated. The phase-space volume size received by each guide will be compared to the phase-space volume size recommended by the MP under different assumptions.

Even though there is a small gap between the pinhole and the start of the elliptical guide, this is not taken into account when

applying the MP because the relation between pinhole size and opening of the elliptic guide behind can be chosen by the optimizer such that no neutrons are lost.

With this assumption, the MP will recommend the required phase-space at the start of the guide to be equal to the phase-space volume size required at the end of the guide. This phase-space volume size is calculated using Eq. (7). Here we investigate the data for the extreme cases of no focusing, $Y=1$, and perfect focusing $Y=0$.

Since the minimalist concept was not used to optimize the guides in Ref. [29], the phase-space volume size which enters the guide is not in general equal to the minimalist requirements. In the following the size of the received phase-space volume is calculated using Eq. (12).

For guides optimized without using the minimalist concept, a unitless scalar, P, is defined, that describes the ratio between the phase-space volume size received by the guide and the size recommended by the MP with $k=1$. It is clear that the value of P will depend upon the focusing parameter, Y, the FOM and the geometry of the guide and moderator.

Since the guides investigated in Ref. [29] are identical in the horizontal and vertical directions, the phase-space volume sizes for one of these are calculated and squared in order to get the full phase-space volume size. The value is calculated using Eqs. (12) and (7):

$$P = \frac{\text{recieved PS size}}{\text{needed PS size}} = \left(\frac{WM}{2\phi L_M (S + 2YL_S \tan(\phi))} \right)^2. \quad (16)$$

The value of P will be compared to the brilliance transfer obtained for each individual guide, here denoted B. When calculating the brilliance transfer, the FOM phase-space volume is used, here with a sample area of 1×1 cm^2, a wavelength interval of 2–10 Å and the specified divergence requirement.

If the assumptions are fulfilled for guides optimized using the MP, the relation $P \geq B$ should be true, as any non-ideal guide would lose some phase-space density under reflections. Since $B \leq 1$, it is expected the data will be close to but below $B=P$ for $P \leq 1$, and $B=1$ for $P > 1$. This prediction is referred to as the theory line. When the assumptions used are not fulfilled, it is possible for data points to lie above the $B=P$ line, for example by using a focusing factor larger than appropriate. The value of B will however never exceed the Liouville limit ($B=1$).

For guides optimized without the MP, the situation is not as clear because they can have a guide end which is narrower than the minimalist constraint, and thus gain some efficiency at the cost of inhomogeneous sample illumination. Because of this, guides with $Y > 0$ can have $B > P$ when $P < 1$, even when delivering a rectangular shaped phase-space volume at the end of the guide, but the divergence distribution will be dependent on position. When assuming a guide is truly focusing ($Y=0$), the minimalist limit reduces to the Liouville limit, and thus every data point must be below or at the theory line, regardless of using the MP or not.

In Fig. 14, the brilliance transfer is plotted against the ratio of received to needed phase-space size, P when using $Y=0$ in Eq. (16). Here two groups of guides separated in P are clearly visible, and correspond to guides with and without feeder. The guides without feeder are much closer to fulfilling the assumptions, as they are closer to the theory line. It is clear that an assumption of a perfectly focusing guide is better for a single ellipse than a feeder followed by an ellipse, but it is still surprising that most feeder guides received phase-space volume sizes more than a factor of hundred over the theoretically needed. It can be argued that a higher coating m-value would cause the guides without feeder to approach the theory line, but it is hardly relevant as expensive $m=6$ coatings are used.

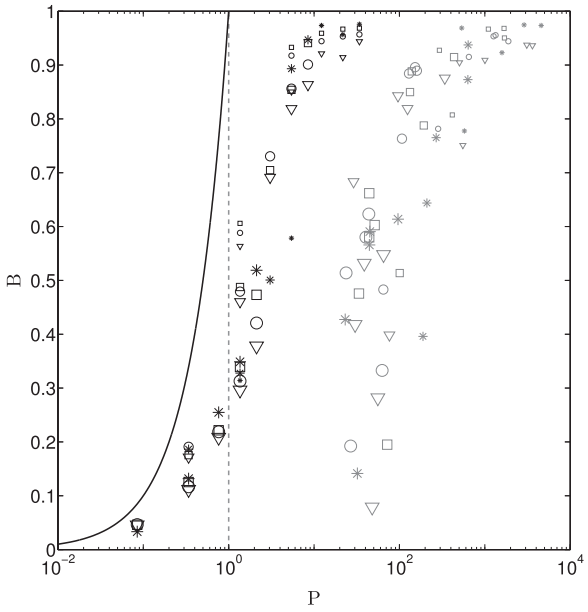

Fig. 14. Comparison of optimized brilliance transfer obtained, B, and ratio P between incoming and required phase-space volume size, for the guides [29]. Here the guides are assumed truly focusing and the entire incoming phase-space size volume is expected to be useful. The solid black line is the maximal performance achievable according to the MP under the stated assumptions. The marker symbols are explained in Table 1.

Table 1
The markers used in Figs. 14 and 15 to indicate which guide from [29] each point corresponds to. Each marker appears 5 times, reflecting 5 pinhole settings.

Property	Marker description			
Guide	Black No feeder		Grey Feeder	
Divergence	±0.5° Small	±1.0° Medium	±2.0° Large	
Length	24 m Star	75 m Square	150 m Circle	300 m Triangle

In Fig. 15 a similar plot is made, but using $Y=1$ in Eq. (16), corresponding to guides without any focusing ability, which thus need a larger phase-space volume, decreasing the value of P for each guide. Under these assumptions P will also depend on the distance between the end of the guide and the sample L_S, which is 50 cm in all cases shown here. It is worth noting that the difference between the needed phase-space volume in the focusing and multiple reflecting case is proportional to this distance.

The guides without feeder have brilliance transfer which surpass the theory for lower values of P, either because of focusing or higher efficiency from inhomogeneous illumination of the sample.

The brilliance transfer for the guides without feeder saturates close to $P=1$. This is the most important prediction of the theory. Had a guide of this geometry been designed to be at $P=1$, it would be able to achieve a brilliance transfer of approximately 95%, where solutions with $P=10$ are only a few percent better. To obtain these last few percent in brilliance transfer one would have to accept a 10 times increase in neutrons that enters the guide, and thus almost 90% of these would have to be absorbed along the guide or in slits near the instrument which will only contribute to unwanted background.

The guides that use a feeder are not close to the theory line. This implies that they are not particularly efficient in terms of the amount of neutrons accepted by the guide to reach a certain brilliance transfer. If the optimizer system is not punished for the

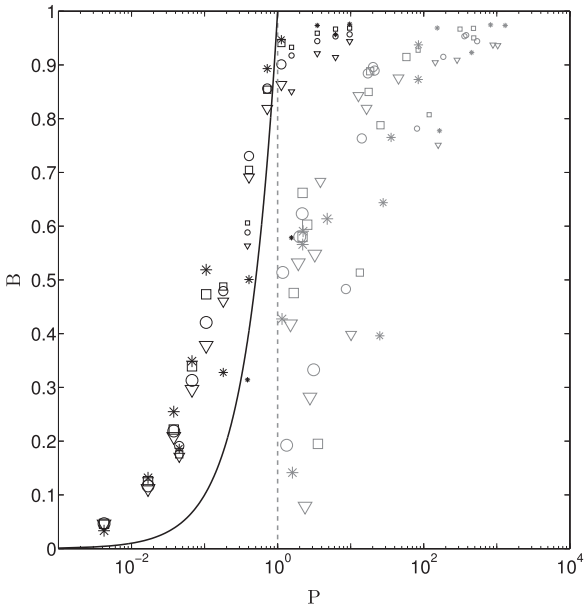

Fig. 15. Comparison of optimized brilliance transfer obtained, B, and ratio P between incoming and required phase-space volume size, for the guides in [29]. Here the guide is assumed multiple reflecting and the entire incoming phase-space size volume is expected to be useful. The solid black line is the maximal performance achievable according to the MP under the stated assumptions. The marker symbols are explained in Table 1.

over intake, it is clear that very large intake values can be obtained. If the minimalist concept was used to optimize such a guide, the constraints would force the guide to be more conservative with the phase-space intake, and most likely find solutions closer to the theory line, but probably with lower brilliance transfer.

5. Discussion

Using the MP changes the way a guide is designed. There are several new choices to be made and consequences which should be understood. This section will discuss the problems it solves as well as the problems it generates.

5.1. Performance

Guides optimized without the MP have every geometrical parameter available to the optimizer. Thus the minimalist optimization will happen in a subspace of the parameter space and should therefore not be able to surpass this method in terms of brilliance transfer on sample. The success of the MP depends on its ability to select a parameter space which ensures minimal background while still allowing for performance close to the global optimum.

From the comparison between a guide optimized with the MP and without, we clearly see the expected increase of signal to noise, mostly for higher wavelengths as the guides can transfer neutrons with divergence beyond the requested. This excess divergence is however avoided when using the MP. The increase in signal to noise from the MP thus starts at the wavelength where the typical reflections for reaching a divergence higher than FOM are within the critical scattering vector of the supermirrors, making the relevance of the MP highly dependent on the FOM, mirror choice and wavelength band.

From the acceptance diagrams we see the behaviour close to the theoretical prediction for $Y=1$, meaning the guides are not focusing. The loss in performance when using the most aggressive background suppression, $k=1$ was only 20% when averaging over the relevant wavelength band, and with the slight increase to $k=1.25$, we see a performance loss of less than 10%.

The scan of the illumination factor k showed the expected results when using $Y=1$, as a plateau occurred where additional incoming neutrons did not add significantly to the brilliance transfer. Furthermore, the point at which this happens was close to the theoretically predicted from the MP. The scan with $Y=0$ did not correspond well with the theory, which can be explained either by the used guides not being focusing, or a failure of the theory to accurately describe the data in this limit.

The MP was used to view data from a previous publication [29] in a different way, and showed that the addition of a parabolic focusing element before the pulse-shaping chopper does increase brilliance transfer, it is also very inefficient in terms of the ratio between neutrons entering the guide, and hitting the sample. The guides without a focusing element were much closer to the theory, but again only when they were considered multiple scattering ($Y=1$), and in this case the MP accurately predicted the optimal neutron intake. The brilliance transfer as a function of intake was surprisingly sharp, as just a small decrease from the optimal value would lower performance drastically, while a small increase would have little effect.

5.2. Advantages and disadvantages

The MP as presented here is per construction used to find the limit where only an ideal guide would be able to deliver the perfect result, here being a brilliance transfer of unity. It is the task of the optimizer to find such a solution, and it may not even be in the given parameter space.

Since the brilliance transfer is limited to be less than unity, it is very clear from the optimization results that the guide is close to the optimal. In the case where the brilliance transfer is not satisfactory, it is possible to increase the size of the incoming phase-space volume with the illumination factor, k. The FOM increases when the guide is supplied a larger phase-space volume ($k > 1$), this may be necessary. If the FOM does not increase, the limitation could be insufficient coating quality. This makes it imperative to calculate the brilliance transfer and not just the intensity on sample, as the brilliance transfer indirectly shows the losses in the guide, when $k=1$.

Working in units of the illumination factor will make it easy to balance between efficient low background guide (k close to unity) and overillumination of the guide entrance which give higher performance and background (larger k). Without this information, the optimizer will search among guides with vastly different efficiencies, or a needlessly restricted parameter space.

Using the MP will stop the optimizer searching among guides which do not receive sufficient phase-space ($k < 1$) to obtain the maximal FOM. Experience with very small moderators does, however, show that $k < 1$ can be beneficial, as $k=1$ can lead to unreasonably large guide entrances that results in high angles of incidence, meaning the goal of a brilliance transfer at unity is unrealistic in any case.

Selecting a reasonable value for the focusing parameter Y before an optimization is necessary, as letting this parameter be determined by the optimizer will almost certainly result in the uncorrelated value $Y=1$, because this will allow both higher signal and background, where the FOM only considers the signal. When using a FOM that punishes background intensity, it may be reasonable to let the focusing parameter be a free parameter. A classical straight guide with parallel mirrors will not focus in any way, and thus needs $Y=1$, where the Selene type guide system [26] is truly focusing and can still perform perfectly with $Y=0$. In

addition this consideration should include the size of the moderator, which e.g. in the case of a single ellipse will determine the correlation between position and divergence necessary for fully exploiting the focusing abilities.

In addition there are real-world problems to consider when recommending building a guide on the limit of what is possible in terms of efficiency. Misalignment of guide segments in a guide designed without the MP is not problematic with today's precision [22]. When designing a guide with the MP and a minimalist factor of $k=1$, the guide will not be overilluminated, and thus any amount of phase-space lost will decrease performance. Because of this it is advised to check guides designed using k close to 1 for sensitivity to alignment, which may be improved by increasing the value of k.

In any case the simple equations derived for the MP will help understanding the consequences of pre-selected parameters. For example how the distance between the sample and guide will affect the signal to noise ratio for a multiple reflecting guide. Reducing this distance improves the efficiency of such guides, especially for small samples, as it lowers the required phase-space volume size. This fact may be missed in usual optimizations.

5.3. Outlook

The Minimalist Principle could be expanded to either take coating values of the guide into account, or to calculate the necessary coating values within the guide. Here the most important part would be the first and last reflections. At the moderator a limited coating m value effectively reduces the ingoing phase-space volume by limiting the maximum possible divergence, this could be added to the model by adjusting the acceptance diagram in Fig. 4. Alternatively one could calculate the appropriate coating for the start of the guide from these figures, but this would change the coating for each optimization step, which would need a cost function in the figure of merit. In a similar way one can calculate the appropriate coating for the last part of the guide by propagating the FOM phase-space volume back from the sample into the guide and find the angle of incidence for the last reflections.

It would be interesting to calculate the necessary shielding for guides designed with and without the MP, as the reduced amount of background along the guide should lower this requirement. The cost of shielding is roughly equivalent to that of the guide, so savings here can be quite significant.

As it is time consuming to do a full guide optimization, and adding the MP constraints to the optimization can be difficult, a program called guide_bot is under development which will write the McStas and iFit codes necessary for running such optimizations. Here it will be possible to create optimizations with or without the MP, minimizing the effort needed to evaluate if the MP is of benefit in a specific case.

6. Conclusion

Basic constraints on the geometrical parameters describing a neutron guide to be optimized were derived under the assumption of a FOM at the sample position which has limits in both position and divergence. These constraints ensure that only a minimal amount of neutrons are allowed to enter the guide while still allowing for a performance close to the theoretical limit. It was shown to be practically applicable in realistic examples using Monte Carlo ray-tracing simulation, where it was demonstrated that the resulting guides clearly limit excessive divergence, even at higher wavelengths, while suffering very little performance loss.

Acknowledgement

We thank Phil Bentley, Ken H. Andersen, Leo Cussen, Pascale P. Deen, Werner Schweika, Peter K. Willendrup, Jochen Stahn, Sonja L. Holm and Kaspar H. Klenø for engaging in discussion on the paper's subject. We thank the ESS DMSC for providing computing power. We would like to thank the Danish Agency for Research and Innovation for their support through the contribution to the ESS update phase. This work is supported by the Univ. Copenhagen 2016 project under “CONeXT”.

References

[1] S. Peggs, ESS Technical Design Report ⟨http://eval.esss.lu.se/cgi-bin/public/DocDB/ShowDocument?docid=274⟩, 2013.
[2] F. Mezei, Physica B: Condens. Matter 234–236 (1997) 1227–1232, http://dx.doi.org/10.1016/S0921-4526(97)00271-8 (URL ⟨⟩).
[3] H. Schober, E. Farhi, F. Mezei, P. Allenspach, K. Andersen, P.M. Bentley, P. Christiansen, B. Cubitt, R.K. Heenan, J. Kulda, P. Langan, K. Lefmann, K. Lieutenant, M. Monkenbusch, P. Willendrup, J. Saroun, P. Tindemans, G. Zsigmond, Nucl. Instrum. Methods Phys. Res. Sect. A: Accel. Spectrom. Detect. Assoc. Equip. 589 (2008) 34–46, http://dx.doi.org/10.1016/j.nima.2008.01.102.
[4] K. Lefmann, K.H. Klenø, J.O. Birk, B.R. Hansen, S.L. Holm, E. Knudsen, K. Lieutenant, L. Von Moos, M. Sales, P.K. Willendrup, K.H. Andersen, Rev. Sci. Instrum. (2013), http://dx.doi.org/10.1063/1.4803167.
[5] K.H. Klenø, K. Lieutenant, K.H. Andersen, K. Lefmann, Nucl. Instrum. Methods Phys. Res. Sect. A: Accel. Spectrom. Detect. Assoc. Equip. 696 (2012) 75–84, http://dx.doi.org/10.1016/j.nima.2012.08.027.
[6] A. Houben, W. Schweika, T. Brückel, R. Dronskowski, Nucl. Instrum. Methods Phys. Res. Sect. A: Accel. Spectrom. Detect. Assoc. Equip. 680 (2012) 124–133, http://dx.doi.org/10.1016/j.nima.2012.03.015.
[7] P.M. Bentley, S.J. Kennedy, K.H. Andersen, D.M. Rodríguez, D.F.R. Mildner, Nucl. Instrum. Methods Phys. Res. Sect. A: Accel. Spectrom. Detect. Assoc. Equip. 693 (2012) 268–275, http://dx.doi.org/10.1016/j.nima.2012.07.002 ().
[8] L.D. Cussen, D. Nekrassov, C. Zendler, K. Lieutenant, Nucl. Instrum. Methods Phys. Res. Sect. A: Accel. Spectrom. Detect. Assoc. Equip. 705 (2013) 21–131, http://dx.doi.org/10.1016/j.nima.2012.11.183.
[9] N. Stüßer, M. Bartkowiak, T. Hofmann, Nucl. Instrum. Methods Phys. Res. Sect. A: Accel. Spectrom. Detect. Assoc. Equip. 748 (2014) 39–45, http://dx.doi.org/10.1016/j.nima.2014.02.028.
[10] K. Batkov, A. Takibayev, L. Zanini, F. Mezei, Nucl. Instrum. Methods Phys. Res. Sect. A: Accel. Spectrom. Detect. Assoc. Equip. 729 (2013) 500–505, http://dx.doi.org/10.1016/j.nima.2013.07.031.
[11] P. Seeger, Physica B: Condens. Matter 283 (2000) 433–435, http://dx.doi.org/10.1016/S0921-4526(00)00382-3 (URL ⟨⟩).
[12] McStas Webpage ⟨www.mcstas.org⟩.
[13] K. Lefmann, K. Nielsen, Neutron News 10 (1999) 20–23, http://dx.doi.org/10.1080/10448639908233684.
[14] P. Willendrup, E. Farhi, K. Lefmann, Physica B: Condens. Matter 350 (2004) 735–737, http://dx.doi.org/10.1016/j.physb.2004.03.193.
[15] P. Willendrup, E. Farhi, E. Knudsen, U. Filges, K. Lefmann, J. Neutron Res. 17 (2014) 35–43, http://dx.doi.org/10.3233/JNR-130004.
[16] D. Wechsler, G. Zsigmond, F. Streffer, J.A. Stride, F. Mezei, Physica B: Condens. Matter 276-278 (2000) 71–72, http://dx.doi.org/10.1016/S0921-4526(99)01332-0.
[17] G. Zsigmond, K. Lieutenant, F. Mezei, Neutron News 13 (2002) 11–14, http://dx.doi.org/10.1080/10448630208218488 (URL ⟨⟩).
[18] J. Šaroun, J. Kulda, Physica B: Condens. Matter 234-236 (1997) 1102–1104, http://dx.doi.org/10.1016/S0921-4526(97)00037-9.
[19] E. Farhi, Y. Debab, P. Willendrup, J. Neutron Res. 17 (2014) 5–18, http://dx.doi.org/10.3233/JNR-130001.
[20] K. Lieutenant, C. Zendler, S. Manoshin, M. Fromme, A. Houben, D. Nekrassov, J. Phys.: Conf. Ser. 528 (2014) 12036. http://dx.doi.org/10.3233/JNR-130005.
[21] L. Landau, E. Lifshitz, Course of Theoretical Physics. Volume 5: Statistical Physics, 3rd ed., Pergamon, The Boulevard, Langford Lane, Kidlington, Oxford OX5 1GB 30, UK; Corporate Drive, Suite 400, Burlington, MA 01803, USA, 1951, ISBN: 978-0-7506-3372-7.
[22] K. Klenø, Exploration of the challenges of neutron optics and instrumentation at long pulsed spallation sources (Ph.D. Thesis), University of Copenhagen, Niels Bohr Institute, 2013.
[23] L.S. Waters, G.W. McKinney, J.W. Durkee, M.L. Fensin, J.S. Hendricks, M.R. James, R.C. Johns, D.B. Pelowitz, Hadronic Shower Simulation Workshop vol. 896, 2007, pp. 81–90.
[24] E. Klinkby, B. Lauritzen, E. Nonbøl, P. Kjær Willendrup, U. Filges, M. Wohlmuther, F.X. Gallmeier, Nucl. Instrum. Methods Phys. Res. Sect. A: Accel. Spectrom. Detect. Assoc. Equip. 700 (2013) 106–110, http://dx.doi.org/10.1016/j.nima.2012.10.052.
[25] J. Copley, J. Neutron Res. 1 (1993) 21–36 (URL: ⟨⟩).
[26] J. Stahn, T. Panzner, U. Filges, C. Marcelot, P. Böni, Nucl. Instrum. Methods Phys.

Res. Sect. A: Accel. Spectrom. Detect. Assoc. Equip. 634 (2011) 12–16, http://dx.doi.org/10.1016/j.nima.2010.06.221.
[27] F. Reif, Fundamentals of Statistical and Thermal Physics, Waveland Press, Inc., 4180 IL Route 83, Suite 101, Long Grove, IL 60047-9580, USA, 1965.
[28] F. János, Physica B 386 (2006) 1253–1255, http://dx.doi.org/10.1016/j.physb.2006.06.023.
[29] M. Bertelsen, H. Jacobsen, U. Bengaard Hansen, H. Hoffmann Carlsen, K. Lefmann, Nucl. Instrum. Methods Phys. Res. Sect. A: Accel. Spectrom. Detect. Assoc. Equip. 729 (2013) 387–398, http://dx.doi.org/10.1016/j.nima.2013.07.062.
[30] H. Jacobsen, K. Lieutenant, C. Zendler, K. Lefmann, Nucl. Instrum. Methods Phys. Res. Sect. A: Accel. Spectrom. Detect. Assoc. Equip. 717 (2013) 69–76, http://dx.doi.org/10.1016/j.nima.2013.03.048.
[31] H. Börner, J. Brown, C.J. Carlile, R. Cubitt, R. Currat, A.J. Dianoux, B. Farago, A.W. Hewat, J. Kulda, E. Lelièvre-Berna, G.J. McIntyre, S.A. Mason, R.P. May, A. Oed, J. R. Stewart, F. Tasset, J. Tribolet, I. Anderson, D. Dubbers, R.S. Eccelston, M. Johnson, C.C. Wilson, G. Lander, H. Rauch, R.B. Von Dreele, W. Waschkowski, Neutron Data Booklet, 2nd ed., Institut Laue-Langevin, Old City Publishing, 628 North Second Street, Philadelphia, PA 19123, USA, 2003.

A.2 The automatic neutron guide optimizer guide bot

This paper was accepted for publication in Nuclear Instruments and Methods A. The paper is based partly on content from my master thesis titled "Optimizing neutron guides using the minimalist principle and guide_bot". The software package guide_bot was further developed significantly after the submission of the master thesis adding such features as additional sources, support for newer McStas releases, support for other clusters and additional optimization options. In the paper, only the simulation validating guide_bot against earlier publications were from the master thesis, the remaining simulations were performed after the submission of the master thesis.

Abstract

The guide optimization software guide bot is introduced, the main purpose of which is to reduce the time spent programming when performing numerical optimization of neutron guides. A limited amount of information on the overall guide geometry and a figure of merit describing the desired beam is used to generate the code necessary to solve the problem. A generated McStas instrument file performs the Monte Carlo ray-tracing, which is controlled by iFit optimization scripts. The resulting optimal guide is thoroughly characterized, both in terms of brilliance transfer from an idealized source and on a more realistic source such as the ESS Butterfly moderator. Basic MATLAB knowledge is required from the user, but no experience with McStas or iFit is necessary. This paper briefly describes how guide bot is used and some important aspects of the code. A short validation against earlier work is performed which shows the expected agreement. In addition a scan over the vertical divergence requirement, where individual guide optimizations are performed for each corresponding figure of merit, provides valuable data on the consequences of this parameter. The guide bot software package is best suited for the start of an instrument design project as it excels at comparing a large amount of different guide alternatives for a specific set of instrument requirements, but is still applicable in later stages as constraints can be used to optimize more specific guides.

My contribution

The content of the publication were all performed by myself as I am the sole author.

The automatic neutron guide optimizer guide_bot

Mads Bertelsen[a,*]

[a]Nanoscience Center and eScience Center, Niels Bohr Institute, University of Copenhagen, Universitetsparken 5, 2100 Copenhagen, Denmark

Abstract

The guide optimization software guide_bot is introduced, the main purpose of which is to reduce the time spent programming when performing numerical optimization of neutron guides. A limited amount of information on the overall guide geometry and a figure of merit describing the desired beam is used to generate the code necessary to solve the problem. A generated McStas instrument file performs the Monte Carlo ray-tracing, which is controlled by iFit optimization scripts. The resulting optimal guide is thoroughly characterized, both in terms of brilliance transfer from an idealized source and on a more realistic source such as the ESS Butterfly moderator. Basic MATLAB knowledge is required from the user, but no experience with McStas or iFit is necessary. This paper briefly describes how guide_bot is used and some important aspects of the code. A short validation against earlier work is performed which shows the expected agreement. In addition a scan over the vertical divergence requirement, where individual guide optimizations are performed for each corresponding figure of merit, provides valuable data on the consequences of this parameter. The guide_bot software package is best suited for the start of an instrument design project as it excels at comparing a large amount of different guide alternatives for a specific set of instrument requirements, but is still applicable in later stages as constraints can be used to optimize more specific guides.

Keywords: Neutron guide, Neutron optics, Software, Neutron instrumentation, McStas, iFit

1. Introduction

Neutron guides are part of almost every neutron scattering experiment as they transport the neutrons from the source to the instrument. Their design have been unchanged for many years, but due to recent advancements the geometrical part of their design has been revisited [1–8]. Using advanced ballistic shapes instead of simple parallel mirrors, the performance and possibilities have increased dramatically. Each guide is tailored to each instrument and considerable resources are devoted to both design and construction.

The neutron guide allows instruments to be situated further from the source, which is beneficial as more instruments can use a single source, it allows time of flight instruments on pulsed sources to reach the length required for their desired resolution and the instruments escape the high radiation environment near the neutron source. Transporting the neutron beam some distance reduces the background, but it is also important to design the guide in a way that allows for shielding between the moderator and the experiment. This is known as "breaking line of sight". This will suppress all background that is not able to be reflected by neutron supermirrors, such as fast neutrons, and is an important feature of most modern guides. Neutrons that are reflected by the supermirrors, but appear outside the desired beam description are described as thermal background and should be limited. This type of background can be completely avoided using the Selene concept [7, 8] where two 1-sided elliptic mirrors are used to image the source to the sample, but this concept has limitations on the divergence that can be delivered. The thermal background can also be controlled using the Minimalist Principle [9] which describes analytical constraints that will limit the neutron intensity entering the guide to a minimum with only a small loss in usable intensity.

Today a large amount of guide design is being performed in relation to the European Spallation Source (ESS) [10]. The neutron guide design work is predominantly performed using Monte Carlo ray-tracing simulations [11–20], and often numerical optimizers [21, 22]. These packages enable the user to build a guide system section by section, and have relatively limited computational requirements. Numerical optimization is thus feasible on a single computer in the order of hours. Such an optimization will maximize a scalar value called the figure of merit (FOM), most commonly the intensity within a certain sample area, divergence range and wavelength range.

The current challenge in guide design has become to select the best possible guide among the vast number of possibilities. This includes investigating how much the background and cost can be limited before the performance of the instrument is jeopardized. Even though the number of possibilities is great, often only a few solutions are conjectured, optimized and then compared, hardly exploring the full solution space.

Here the program guide_bot is presented which automates the geometrical part of guide optimization and simplifies this task so that no prior experience with the underlying ray-tracing software is necessary. The numerical simulations are done using generated McStas [11–15] and iFit [22] files, while plotting is done within MATLAB. The input method is flexible enough to cover most relevant guide types and allows the entire range

*Corresponding author
Email address: mads.bertelsen@gmail.com (Mads Bertelsen)

from optimization of all geometrical parameters to a fixed geometry. It is possible to investigate different methods of breaking line of sight as well as adjust the point at which the line of sight is measured. The background from thermal neutrons that does not contribute to the FOM can be minimized by enabling simultaneous use of the Minimalist Principle [9]. Examples are shown that demonstrate the optimized guides provide an overall high performance within the given FOM. Several guides have been designed using guide_bot [23–26].

The aim is to enable a guide designer to investigate orders of magnitude more geometries in a similar time, leading to more informed decisions when selecting the final geometry for the guide of a neutron instrument under construction or upgrade.

2. guide_bot

The main task of guide_bot is to quickly optimize the geometrical part of neutron guide design for a specified overall geometry. This is accomplished by having the program read a simple input file describing the problem and generate the code needed to complete that task; which will in turn solve the original problem when the generated code is compiled and executed. guide_bot itself runs in MATLAB, but the generated code is in multiple programming languages linked together by scripts that are easily executed. The required ray-tracing simulation is performed using the generated McStas instrument file that describe the desired guide system. Generated iFit scripts control both the guide optimization and visualization of results.

MATLAB was selected because it has the necessary plotting functionality, and is widely used in the community. The add-on iFit [22] enable control of McStas through MATLAB, and has comprehensive optimization libraries. The clusters available at the ESS Data Management and Software Centre and Paul Scherrer Institute Scientific Computing group both use the queue management system SLURM [27] which is supported by guide_bot.

The following sections will describe the important parts of the code and the use of guide_bot.

2.1. guide_bot input file

The input file is a short MATLAB script the contents of which the user will edit to correspond to the desired guide geometry and optimization. The mandatory input consists of describing a FOM, which here refers to a closed phase-space volume, meaning a fixed area, divergence range and wavelength range. The average brilliance transfer [9] is calculated by normalizing the intensity in one phase-space volume with the intensity in the same phase-space volume placed at the source.

The total length between source and sample is fixed as is the distance between guide-end and sample. The distance between source and guide start is optimized, however the user must define the interval of allowed starting distances.

A homogeneous rectangular source is always used for calculation of brilliance transfer, and the dimensions of this source are given as input. In addition, a more realistic source is chosen which is used for calculation of the absolute intensities. In most cases the optimization is performed on the rectangular source. However the optimization can be performed on the ESS TDR and Butterfly sources[11, 28] including optimizing the angle at which the guide views the moderator. Optionally, the optimization can be performed on the rectangular source, and the optimized guide is then placed on the realistic source where only this angle is optimized.

Module	Explanation	McStas component
S	Straight guide	guide_gravity
E	Elliptic guide	Elliptic_guide_gravity
P	Parabolic guide	Elliptic_guide_gravity
G	Gap	Arm
K	Kink	Arm
C	Curved guide	Bender
Slit	Slit	Slit
Selene	Selene guide	Elliptic_guide_gravity / Arm / Slit

Table 1: The available modules of which an input string describing a guide can be assembled.

The guide geometry is described using a character string, which corresponds to a linear succession of guide elements. The following input string will generate an optimization of a guide consisting of a straight section using flat mirrors, a curved guide section and finally an elliptic guide section.

```
S C E
```

A single part of such an input string (separated by spaces) is referred to as a module, and the currently available modules in guide_bot are listed in table 1.

In the example, no details other than selecting the sequence of guide elements are given. Hence, the resulting guide optimization will have all possible geometrical parameters for the 3 modules as free parameters in the numerical optimization. This may not be appropriate for a particular application, as certain constraints could be needed. These are incorporated for each module by adding options. In the following input string, such options are used to constrain the optimization, both by adjusting the optimization limits and by locking certain parameters.

```
S(maxStartHeight=0.1)
 C(maxlength=20,start=6.5,StartWidth=0.03) E
```

This input string adds a height limit to the start of the first straight section of 10 cm and locks the starting position of the curved section to 6.5 m from the source. Furthermore, the width of the curved guide at its starting position is locked to 3 cm, while its length is limited to a maximum of 20 m. The full list of available options is described in the manual distributed with the software [11].

If an input string contains a curved section or a kink, both commonly used to break line of sight through a guide, guide_bot will assume breaking line of sight is the intention and dynamically select a curvature or angle deviation just sufficient to break line of sight between the start and end of the full guide. The guide curvature or angle deviation will thus depend on, for example, the guide width and where in the guide the curved sec-

tion is placed. It is possible to adjust this behaviour by selecting, e.g., a smaller section of the guide line of sight should be broken over or to break line of sight multiple times in different sections. This system can be disabled by selecting suitable options. Further details are described in Appendix A.

2.2. McStas instrument file

The McStas instrument file contains the necessary input parameters in the basis appropriate for the numerical optimizer, and the code for transforming these parameters to the type needed for the individual McStas components. The instrument file also contains a piece of ray-tracing code that will control how line of sight is broken for this particular user input.

Each of the modules used in the geometry input string will typically correspond to a single instance of a McStas component in the instrument file, and the components used for each module are listed in table 1.

Most of the written McStas instrument file is intended to be human readable, especially the trace section containing the McStas components. The initialize section containing the transformation of the parameter space and the added ray-tracer is, however, not meant to be changed by the user.

2.3. Butterfly source

The current ESS baseline moderator, nicknamed the butterfly, have been included in the McStas package from version 2.3, and is depicted in figure 1. The thermal water moderator is located between two para-H_2 moderator wings. Each beamline is aimed at a spot between the thermal moderator and the cold moderator wing closest to corresponding beamport. Hence it is important to select an appropriate viewing angle so that the optical axis of the guide views the correct moderator, which can be optimized by guide_bot.

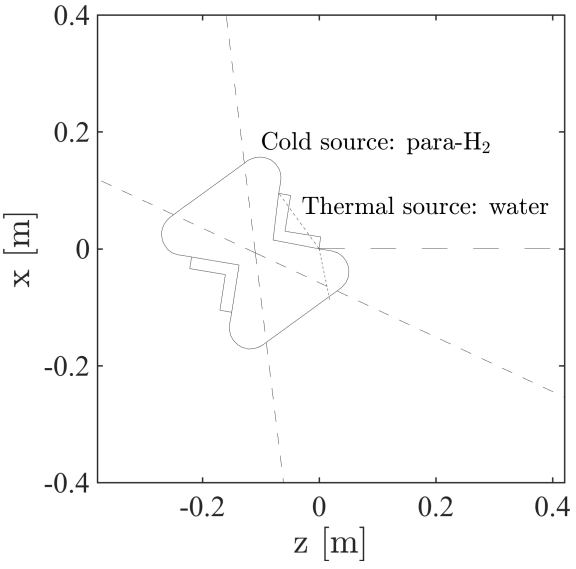

Figure 1: McStas mcdisplay output for butterfly moderator component, here oriented for the North sector beamline 5.

Constant	Description	Value
R_0	Low angle reflectivity	0.99
q_c	Critical scattering vector	0.0217 Å^{-1}
W	Width of cut-off	0.003 Å^{-1}
α	Reflectivity slope	6.07 Å

Table 2: Standard constants used for the reflectivity model (1), where the critical scattering vector q_c is from [29].

2.4. Reflectivity curves

The supermirror reflectivity $R(q)$ is a unit-less quantity that describes the probability for a neutron to be reflected by a supermirror as a function of the scattering vector q perpendicular to the supermirror. Supermirrors are characterised by their effective critical edge mq_c, which is given as a multiple of the critical scattering vector from the Nickel-Vacuum interface, q_c. The constant m is named the m-value.

Since the neutron ray-tracing is performed by McStas, the reflectivity models available in guide_bot are those implemented in most McStas components. There are two models available, a fully adjustable first order model, and a second order model with only the m-value as a free parameter.

The standard McStas reflectivity model described by equation (1) is used as default, and the resulting reflectivity curves are shown in figure 2 with the default constants in table 2. The reflectivity below q_c is described with the R_0 parameter, while the slope of the reflectivity curve between q_c and mq_c is denoted α. The finite width of the critical edge at $q = mq_c$ is denoted W. The user can adjust these constants if needed to obtain a description closer to the currently available mirror quality.

$$R(q) = \begin{cases} R_0 & \text{if } q < q_c \\ R_0(1 - \tanh((q - mq_c)/W))(1 - \alpha(q - q_c))/2 & \text{otherwise} \end{cases} \quad (1)$$

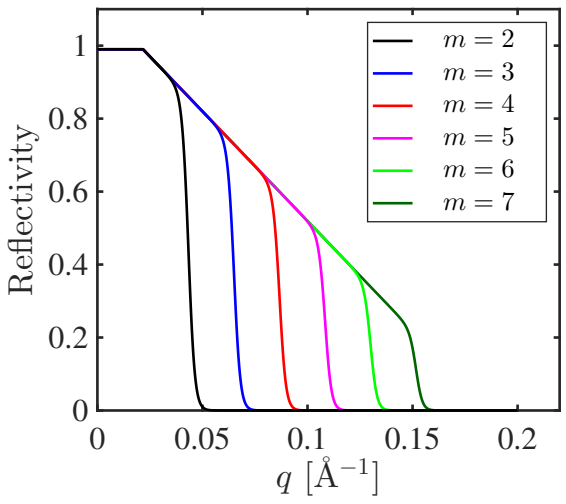

Figure 2: Reflectivity curves for a range of m-values using the standard McStas reflectivity model with the default reflectivity constants in guide_bot.

Alternatively the user can select a second order model that fits measured reflectivity data [30]. In this model the m-value is given, and the remaining constants are calculated based on this choice, resulting in the reflectivity curves shown in figure 3.

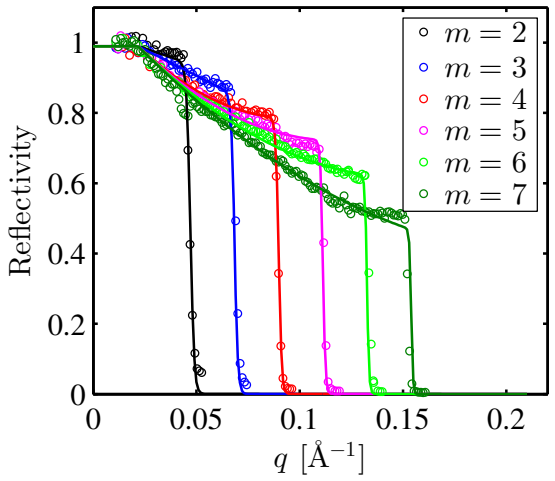

Figure 3: Reflectivity data and model available in most McStas components, figure from [30].

In order to show the robustness of optimized guides, the performance is evaluated both with the selected mirror quality and an artificially degraded description, where the m-value is reduced by 20%, and the reflectivity slope is increased by 40%. When using the second order reflectivity model there is however no parameter describing the slope, so only the m-value is reduced and in most cases this actually decreases the reflectivity slope which should be kept in mind.

2.5. iFit optimization

The iFit files control the generated McStas files by setting up a numerical optimization using the appropriate parameter space and a particle swarm optimization algorithm. All variables to be optimized are specified with their constant limits, meaning that the limits do not depend on values of other parameters. A parameter space is used where all variables can be varied in their entire range independently. This is here referred to as a "box parameter space". It will be discussed in Appendix B how guide_bot constructs such a space.

After the optimization is done in the box parameter space, the resulting optimal guide geometry description is used to run further McStas simulations to provide data for a thorough description of the guide performance.

2.6. Data visualization

The resulting data is visualized by running the generated MATLAB/iFit plotting script. This will provide figures describing performance of the guide in terms of brilliance transfer as a function of wavelength, divergence, and position. If a user specifies a source that provides absolute intensities, the guide performance will also be visualized using these units. In addition, the optimal guide geometry will be visualized.

3. Examples

Here results on validation against earlier work is shown followed by two examples of guide_bot runs. The first example demonstrate the ability of guide_bot to optimize a complicated guide, while the other demonstrates how a range of optimizations can be used to evaluate the impact of the figure of merit.

3.1. Validation against earlier work

In order to validate that guide_bot works as intended, a guide optimized for an earlier publication is recreated using the software. In Ref [31], guides consisting of a parabolic feeder that constrain the beam to a certain pinhole size followed by an elliptic guide were systematically optimized for different figure of merit. A 150 m guide is optimized for a 1×1 cm^2 sample with a $\pm 1.0^\circ$ divergence requirement and a 3×3 cm^2 pinhole at the chopper position. The coating distribution used in the original paper was $m = 6$ in the feeder and start/end of the ellipse, with $m = 3$ in the middle part of the ellipse. However as guide_bot does not support such a distribution, it uses a $m = 6$ coating in the entire guide. This is not considered important, as the coating model used have the same reflectivity at low q regardless of the m value, and the center of the ellipse will only have low q reflections at the compared wavelength interval. A comparison between the results is displayed in figure 4, that shows excellent agreement between the two.

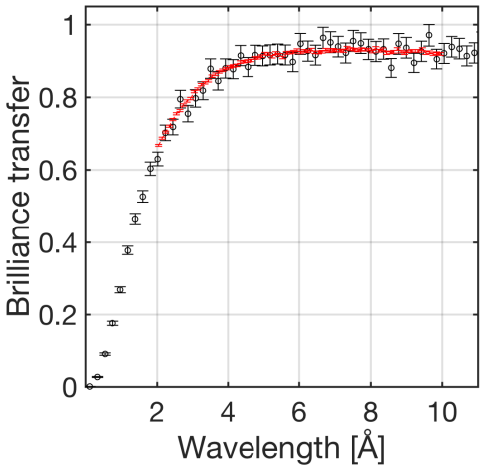

Figure 4: Brilliance transfer dependence on wavelength for optimized guides, the red from the original paper [31] and black remade using guide_bot (simulated in a larger wavelength interval).

3.2. Single guide

An example of a single guide optimization is presented in order to demonstrate the ability of guide_bot to produce a highly performing guide from input with a limited information. Here the FOM was chosen to be a 1×1 cm^2 sample with a divergence requirement of $\pm 1.0^\circ$ in the horizontal direction, and $\pm 0.75^\circ$ in the vertical direction. The guide is optimized for brilliance transfer in the wavelength range 2 – 4 Å. The distance between

source and sample is chosen to be an ESS-relevant value of 160 m, while the distance between guide-end and sample is 40 cm. This guide uses an $m = 3$ coating everywhere simulated with the default coating model. The guide was optimized on an rectangular source, and the optimized guide was then placed on the 3 cm tall ESS Butterfly moderator where only the angle with respect to the moderator was optimized. The optimization was repeated 5 times and the one with highest FOM is presented here.

The investigated guide consists of a elliptic extraction that narrows to benefit a chopper at 7 m from the moderator with a width of 3 cm, a linear section that expands the beam before an S curved section to remove line of sight and a double ellipse with a kink in between at the end. Line of sight is broken between the start of the guide and the end of the first curved module, and from the point where the curved guide changes direction of curvature and the guide end. This geometry is described with the following string:

```
E(max_smallaxis=0.1)
 G(start=7.0,StartWidth=0.03,length=0.1)
 S(maxStartWidth=0.06) C(los_divide=1,rots=-1) C
 E(minlength=20) K E
```

This is a complicated geometry, and only a few options have been used to constrain the parameter space, meaning the optimizer is given a difficult task.

The optimized guide geometry is shown in figure 5, and the characterization in terms of brilliance transfer is shown in figure 6.

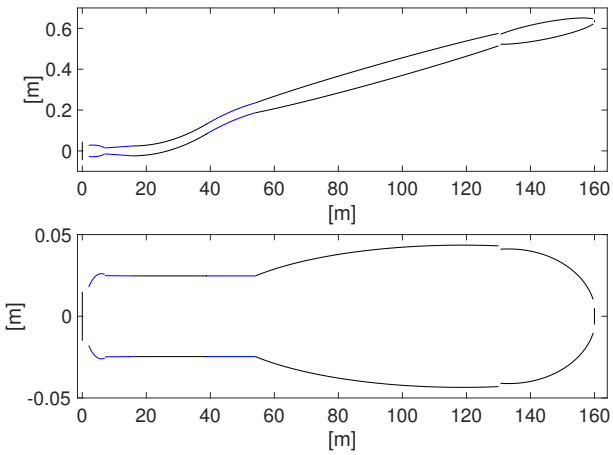

Figure 5: Geometry of the guide that delivered the highest brilliance transfer for the chosen FOM. Top panel is a top view, while the lower panel is from the side. The moderator is shown to the left side and the sample to the right side of the panels.

From the guide design it is intuitively clear that all parts contribute to neutron transport, making the design reasonable, but it does not resemble what would be made manually. The overall brilliance transfer is however high (about 55% at 3 Å) considering the beam requirements, limited coating quality, pinhole and that the guide breaks line of sight twice. The divergence distributions have dips and are asymmetrical, but follows the FOM

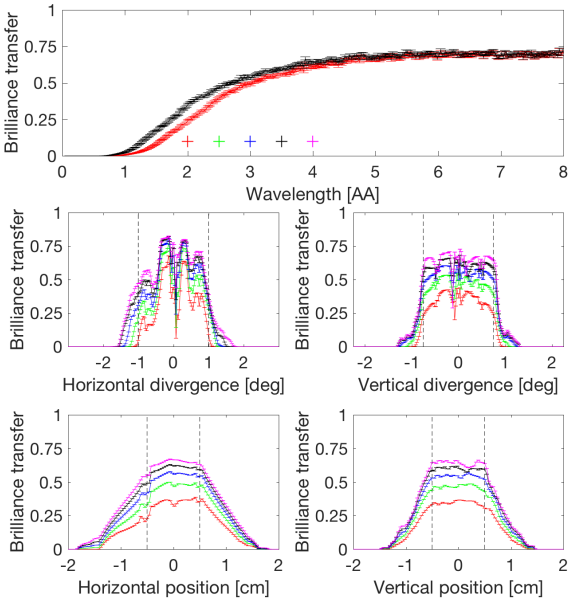

Figure 6: Overview of performance of the guide from Fig. 5 in terms of brilliance transfer on rectangular source. Top panel contains wavelength dependence, both for the requested mirror quality (black) and degraded mirror performance (red). In the remaining panels the horizontal and vertical divergence distributions as well as spatial distributions are shown for wavelength snapshots between 2 and 4 Å that corresponds to the markers in the top panel. The dashed lines show the edges of the FOM area.

very well with high brilliance transfer within, and fairly steep drops outside. The spatial distributions are more smooth, and relatively constant within the sample area.

In figure 7 the two-dimensional position and divergence distributions are shown, and it is again clear the optimized guide provides a beam that matches the provided FOM, but has some structure especially in the divergence space.

Acceptance diagrams are shown in figure 8 where the unwanted beam structure is most obvious. Two of the FOM corners are perfectly aligned with the edge of the acceptance diagrams, which is due to the dimensions of the guide-end being calculated using phase-space considerations as explained in Appendix C.

Figure 9 shows the intensity on sample relative to the total intensity leaving the guide-end, and thus provides an idea of the efficiency of the guide in terms of background generated in comparison to neutrons on sample. This particular guide has around 30% of the guide output that make it to the small sample, and in the FOM wavelength interval of 2-4 Å about 25% of the intensity from the guide hits the sample and fall within the divergence requirement.

The performance of the optimized guide on the ESS Butterfly moderator can be seen in figure 10. Here the beam quality is more problematic in the horizontal direction, as the structure from the more complicated source affects the result. Had the guide been optimized directly on the Butterfly moderator instead of the rectangular source, the guide geometry could have been adapted to this source. The two-dimensional position and

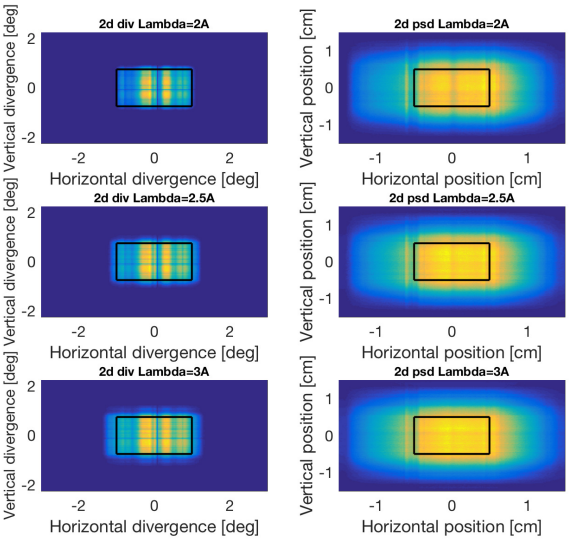

Figure 7: Two dimension spatial and divergence distributions for wavelength snapshots, here 2.0 Å, 2.5 Å and 3.0 Å, where the black box correspond to the FOM. Diagrams at the remaining wavelength snapshots have been omitted.

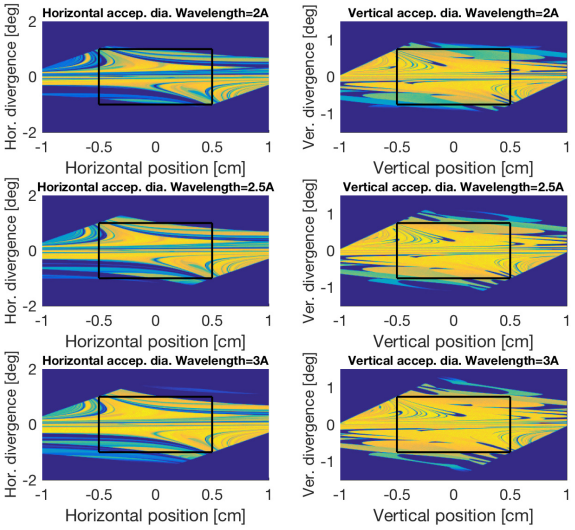

Figure 8: Horizontal and vertical acceptance diagrams for wavelength snapshots, here 2.0 Å, 2.5 Å and 3.0 Å, where the black box correspond to the FOM. Diagrams at the remaining wavelength snapshots have been omitted.

divergence plots, and the acceptance diagrams are also created for the realistic source, but are omitted here.

With such a comprehensive description of the delivered beam for every optimized guide, the user can easily select the ones most appropriate for their instrument and continue to build on those designs.

3.3. Scan of input parameters

In many situations it can be relevant to perform a scan over a range of a parameter in the FOM, as the FOM may be not be completely known in advance. Here, a guide is optimized for a horizontal divergence of ±0.75°, while the vertical divergence is scanned from ±0.5° to ±1.5°. It is currently possible to scan sample dimensions, divergence requirements and moderator dimensions. The sample size used here is 1×1 cm^2, and the selected wavelength range is 1 – 2 Å. This guide has 160 m between moderator and sample, and 40 cm between guide-end and sample. The McStas standard reflectivity model was used with $m = 3$ for the entire guide. The guide is optimized for a rectangular source of 10×3 cm^2, and the realistic source chosen was the 3 cm tall ESS Butterfly moderator, where only the viewing angle towards the moderator was optimized. The rectangular source size was chosen to resemble the dimensions of the cold part of the Butterfly moderator projected onto the used beam port.

The geometry is described by the following string, which correspond to a parabolic feeder that narrows the beam to 3 cm in width, an elliptic defocusing section, a curved guide and an elliptical focusing section. The gap for the chopper is forced to 10 cm length and the defocusing section is limited to a maximum of 6 cm starting width.

```
P G(start=7.0,StartWidth=0.03,length=0.1)
E(maxStartWidth=0.06) C E
```

The optimization was repeated 5 times, and the best result used in order to decrease uncertainties, as it may be caught by local optima in the large parameter space. The optimized guide geometry for a vertical divergence of ±1.0° is shown in figure 11.

An overview of the results is given in figure 12. It is expected the brilliance transfer will decrease with increasing divergence requirement as a larger phase-space volume need to be filled. It is important to notice the final intensity on sample is optimal from about 0.9° divergence requirement, but decreases at the highest divergence requirements.

4. Discussion

4.1. Discussion of results

In section 3.1 it was shown that guide_bot could replicate a published optimization result. The similarity between the results are expected, as guide_bot merely simplifies such tasks by generating the needed code instead of it being written manually.

In the scan over vertical divergence, it was expected that the intensity on sample would increase with increasing vertical divergence requirement, but as seen in figure 12 this trend breaks down at the highest vertical divergence values. There are several possible explanations for this behaviour.

Since the dimensions of the guide-end are calculated from the divergence requirement, Appendix C, the result may be suboptimal when the vertical divergence requirement is larger than what is reasonable from the small moderator.

As the FOM of the optimization is the average brilliance transfer, the entire wavelength interval is weighted equally, but the realistic source used to calculate the intensity has a different

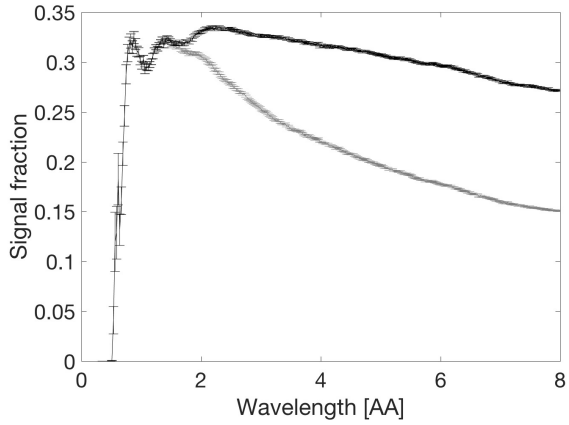

Figure 9: Fraction of intensity delivered by the guide on sample (black) and on sample while within the divergence limits (grey), both as a function of wavelength.

wavelength distribution. The decrease in intensity at higher divergence requirements could thus also be explained by the optimization naturally being impacted more by higher wavelengths at large divergence requirements, while the thermal ESS Butterfly spectrum have higher intensities at the lower part of the wavelength range.

It is however also possible that the optimization is more difficult for larger divergence requirements, and that those solutions on average are further away from the true optimum. It should be investigated further.

4.2. User experience

4.2.1. Automate everything

The main goal of the program is to reduce the time spent coding between getting an idea for a guide solution and obtaining the performance of this guide optimized for a specific case. This has been achieved using code generation, meaning the user can write a relatively short and simple input file, and guide_bot will then generate the much larger amount of code needed to solve the original problem. Reproducing the examples in this paper by recreating the input files should take less than 10 minutes for a user familiar with MATLAB but not necessarily iFit or McStas.

4.2.2. Usability

It was considered a top priority to make guide_bot as simple to use as possible, in order to reduce the time required to learn the software, and thus allow the relevant people to design guides. Traditionally, the job of designing a guide takes months of work, and thus the amount of geometries to be investigated has been limited. Making the job faster allows for a wider range of geometries to be investigated, which will hopefully result in a better match with the instrument backend. In addition, the ease of use is extended to running on a cluster, as the optimizations are computationally heavy. The widely spread use of guide_bot on ESS projects indicates the usability of the code.

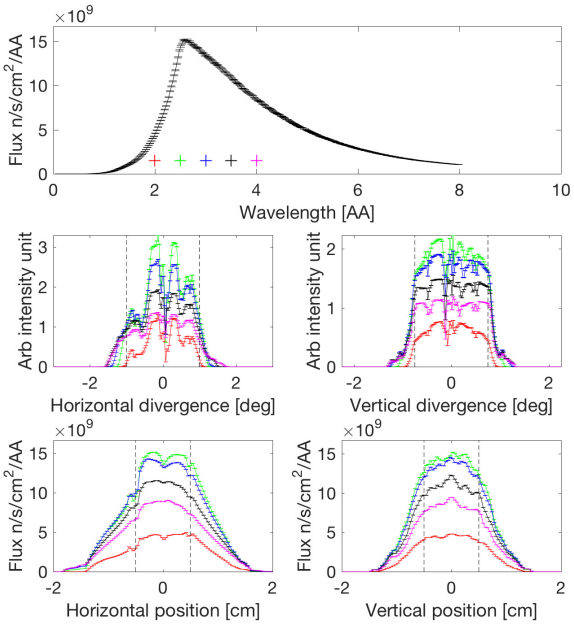

Figure 10: Overview of performance of the guide from Fig. 5, positioned on the ESS 3 cm tall Butterfly moderator. Top panel contains wavelength dependence for the requested mirror quality and markers for the wavelength snapshots used in the remaining panels. In the remaining panels the horizontal and vertical divergence distributions as well as spatial distributions are shown for wavelength snapshots that corresponds to the markers in the top panel.

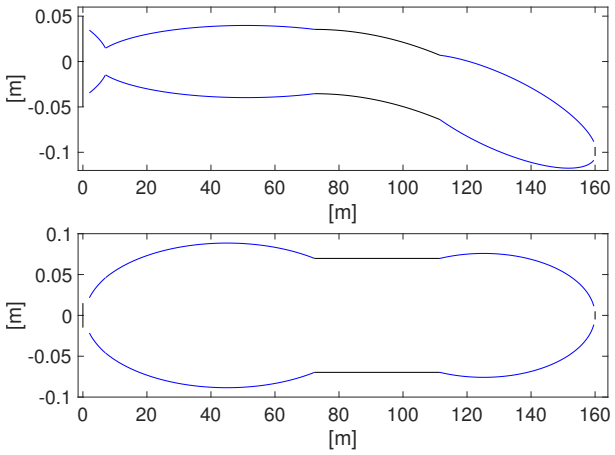

Figure 11: Guide geometry that delivered the highest brilliance transfer for the FOM with ±1.0° vertical divergence requirement. Top panel is a view from above, while the lower panel is from the side.

4.2.3. Modularity

It has been a goal to keep the software modular, meaning it should have a core that is not seen by the user, and then much simpler module files that describe each type of possible guide section. The core of the program then provides the functions and routines necessary for simple module files. This has largely succeeded. However the routines for drawing the geometry of the optimized guide are part of the core instead of each module, which is a deviation from the modular philosophy. This approach makes it possible for users to contribute the majority

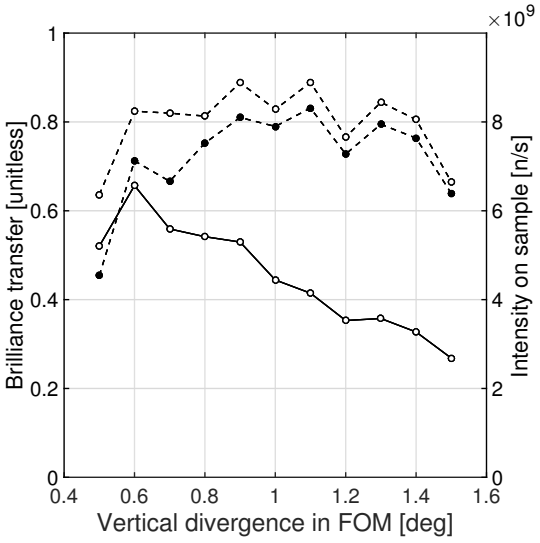

Figure 12: Brilliance transfer (full line, left axis) and intensity (dashed lines, right axis) for guides optimized for figure of merits with different vertical divergence requirements. The intensity results with white centers are for all neutrons that hit the sample, while the filled markers correspond to all neutrons that hit the sample and are within the divergence requirements of the appropriate FOM.

of code for a new module, but requires the developer to add the code for plotting the geometry in the core for each addition. In similar fashion, some work may be required from the developer to include new modules in automated elimination of line of sight.

4.3. Simplicity and flexibility

4.3.1. Balance between simplicity and flexibility

The underlying software McStas was originally introduced as an alternative to writing a complete Monte Carlo ray-tracing simulation for neutron scattering from scratch, and thus provided an easier solution with less flexibility for the user. McStas still covers a great amount of possibilities, but in order to achieve the simple interface and fast performance, it has limited the infinity of options available in the C programming language.

In the same way, guide_bot simplifies the task of writing a numerical guide optimization by removing most of the flexibility that McStas and iFit provides. The simplicity of guide_bot is only possible because it assumes that the user wants to optimize a guide, and that it only contains guide pieces that have been described in this context. It is thus not an attempt of replacing McStas or other tools for guide design, but to allow users whose task is within the capabilities of guide_bot to finish the task much more quickly than otherwise.

4.3.2. Handle all levels of a priori knowledge

Depending on the progression of the overall instrument and facility design, the amount of a priori knowledge about the guide can vary greatly. At early stages, there will be almost no limits to the possible geometries, and in the later stages there can be a large amount of constraints to fulfil. Using guide_bot it is possible to handle these levels of a priori knowledge. This is accomplished by the options associated with each module in the input string which allow for modifying ranges for optimization or fixing certain parameters. For this reason, guide_bot can be used in most stages of the design process, but is less suitable for the final stages as it lacks the flexibility of McStas to add details.

4.3.3. User interaction with generated code

As each task is still unique, it is important that the user can edit the McStas files generated by guide_bot to add aspects guide_bot is not able to handle. The generated McStas and iFit files are done in such a way that editing and adding to them is user friendly, and can even be a good starting point for learning to use those programs.

4.4. Outlook

As guide_bot currently only optimizes parameters describing the geometrical aspects of the guide, the next step is to include optimization of the coating distribution. Here, the resulting number of free parameters is a concern and may require the optimization to be split into several parts with some iteration between them, for example optimization of geometry and coating distribution separately. Initial work has started along this direction [32].

In addition new modules are expected to be added, for example a half ellipse module.

5. Conclusion

The program guide_bot is presented which significantly reduces the work of programming neutron guide optimizations in cases where the overall geometry can be described in the provided input scheme. This allows a comprehensive comparison between a large number of different possible guide geometries optimized for the specific instrument to be made with little effort.

Validation was performed against an earlier publication, showing the simple guide_bot optimization yielding an overall performance in agreement with the published result.

The software was demonstrated, showing that a complicated guide with a low number of constraints could be optimized to the specified figure of merit, resulting in a guide solution with high performance albeit some issues with beam quality. A scan of optimizations over the vertical divergence requirement was performed to demonstrate how such data sets can contribute to selecting the final figure of merit for an instrument.

Recently, guide_bot has been used for a wide range of tasks, successfully designing guides of several instruments accepted for construction at ESS.

Acknowledgement

I thank Ken Andersen, Phillip Bentley, Jonas Okkels Birk, Kaspar H. Klenø and Peter K. Willendrup for fruitful discussion on the article subject. I thank my supervisor Kim Lefmann for advice and comments to the manuscript. I further thank

Niko Tsapatsaris, Jonas Okkels Birk, Martin Olsen, Manuel Morgano, Emmanouela Rantsiou, Leland Harriger and Kaspar H. Klenø for beta testing the software and reporting bugs. I thank ESS DMSC and PSI for providing computational resources. This work was supported by the ESS and by the ESS Design Update Program through the Danish Agency for Science and Innovation.

Appendix A. Dynamic line of sight elimination

When optimizing a guide that eliminates line of sight, many geometrical parameters influence whether line of sight can be drawn or not. A short algorithm written to the McStas initialize file is used to check if the guide blocks line of sight by checking all relevant sight lines. Instead of providing the curvature as a free parameter in the optimization, the McStas file will find the smallest curvature that will eliminate line of sight. This is achieved by starting with a nearly straight guide and increasing the curvature until line of sight is blocked. By default line of sight is broken between the start of the guide at the moderator and exit at the sample, but line of sight can be broken between two points specified in the options for the relevant modules. In addition, line of sight can be broken several times, as long as the sections do not overlap. Multiple curved sections can even work together in breaking line of sight, in that case the ratio between their curvatures is optimized as a free parameter. The importance of this is that all guides compared by the optimizer will have similar background characteristics, which is chosen by the user, instead of a large variation in background suppression.

Appendix B. Optimizing in a hyper-box parameter space

A numerical optimization takes place in a parameter space, and it is an important choice which parameter space is used. As the optimizer will take a range for each parameter to be optimized, and these are considered independent, it is necessary that every possible value in these ranges corresponds to a valid guide geometry, regardless of all other selected values. This is no problem for the width and height of all guides, but for example the horizontal(vertical) small axis of an elliptic guide can be problematic, as it cannot be lower than both the start and end width(height). In the same way the lengths of the modules have an overall constraint of keeping a total guide length fixed.

The parameter space including all geometrical variables to be entered into the McStas components is referred to as the full parameter space, here with N dimensions. A number of constraints, k, is taken into account. These originate from the basic guide problem, but can also be given by the user through options in the input string. A space with dimensionality $N - k$ is created where all points adhere to these constraints, and this is called the reduced parameter space. In this reduced parameter space, the limits on each parameter may depend on the value selected by another, which as discussed is not allowed. The solution used in guide_bot is to transform this reduced parameter space to a box parameter space of the same dimensionality where all limits are independent of the values selected of the other parameters. The McStas file then needs to transform from this box parameter space to the full parameter space for every point in the optimization.

The length of each module is the most important problem of this type, as there are many constraints to consider. The distance between source and sample is known, but there is a range of allowed distances between source and guide. Using the options, it is possible to set a fixed length of a module, or modify the range of allowed lengths. Likewise, the distance between the source and the starting position of a module can be fixed or have its range modified. The reduced parameter space is built so that the absolute length of one module is given, and the remaining are given as a fraction that describes how much of the available length they should occupy, in addition to their minimum length. Generated code in the McStas initialize section transform these fractions to absolute lengths, which corresponds to the transformation from the reduced box parameter space to the full parameter space.

Appendix C. Minimalist algorithms

The Minimalist principle [9] is supported in guide_bot. This requires a calculation of the necessary phase-space starting at the sample and ending at the source. This will effectively add constraints limiting the intake of phase-space to the necessary volume. The kink module uses the phase-space propagation considerations from [9] to calculate the translation and size increase for a certain kink angle and length. In addition, the dimensions at the end of the guide, W, are calculated using equation (C.1),

$$W = S + 2L \tan \phi \tag{C.1}$$

where S is the sample size, L is the distance between the guide end and sample and ϕ the divergence in the appropriate plane. The use of the Minimalist Principle to calculate the necessary phase-space intake of the guide and the calculations for the dimensions at the end of the guide can be enabled separately. For the examples shown in this paper, the restriction on phase-space intake was disabled.

References

[1] L. D. Cussen, D. Nekrassov, C. Zendler, K. Lieutenant, Nuclear Instruments and Methods in Physics Research, Section A: Accelerators, Spectrometers, Detectors and Associated Equipment 705 (2013) 121–131. URL: http://dx.doi.org/10.1016/j.nima.2012.11.183. doi:10.1016/j.nima.2012.11.183.

[2] P. M. Bentley, S. J. Kennedy, K. H. Andersen, D. M. Rodríguez, D. F. R. Mildner, Nuclear Instruments and Methods in Physics Research, Section A: Accelerators, Spectrometers, Detectors and Associated Equipment 693 (2012) 268–275. doi:10.1016/j.nima.2012.07.002.

[3] K. H. Klenø, K. Lieutenant, K. H. Andersen, K. Lefmann, Nuclear Instruments and Methods in Physics Research, Section A: Accelerators, Spectrometers, Detectors and Associated Equipment 696 (2012) 75–84. URL: http://dx.doi.org/10.1016/j.nima.2012.08.027. doi:10.1016/j.nima.2012.08.027.

[4] A. Houben, W. Schweika, T. Brückel, R. Dronskowski, Nuclear Instruments and Methods in Physics Research, Section A: Accelerators, Spectrometers, Detectors and Associated Equipment 680 (2012) 124–133. doi:10.1016/j.nima.2012.03.015.

[5] N. Stüßer, M. Bartkowiak, T. Hofmann, Nuclear Instruments and Methods in Physics Research, Section A: Accelerators, Spectrometers, Detectors and Associated Equipment 748 (2014) 39–45. URL: http://dx.doi.org/10.1016/j.nima.2014.02.028. doi:10.1016/j.nima.2014.02.028.

[6] H. Schober, E. Farhi, F. Mezei, P. Allenspach, K. Andersen, P. M. Bentley, P. Christiansen, B. Cubitt, R. K. Heenan, J. Kulda, P. Langan, K. Lefmann, K. Lieutenant, M. Monkenbusch, P. Willendrup, J. Saroun, P. Tindemans, G. Zsigmond, Nuclear Instruments and Methods in Physics Research, Section A: Accelerators, Spectrometers, Detectors and Associated Equipment 589 (2008) 34–46. doi:10.1016/j.nima.2008.01.102.

[7] J. Stahn, T. Panzner, U. Filges, C. Marcelot, P. Böni, Nuclear Instruments and Methods in Physics Research, Section A: Accelerators, Spectrometers, Detectors and Associated Equipment 634 (2011) 12–16. doi:10.1016/j.nima.2010.06.221.

[8] U. B. Hansen, M. Bertelsen, J. Stahn, K. Lefmann, Nuclear Instruments and Methods in Physics Research Section A: Accelerators, Spectrometers, Detectors and Associated Equipment (2017). URL: http://linkinghub.elsevier.com/retrieve/pii/S016890021730181X. doi:10.1016/j.nima.2017.01.075.

[9] M. Bertelsen, K. Lefmann, Nuclear Instruments and Methods in Physics Research, Section A: Accelerators, Spectrometers, Detectors and Associated Equipment 830 (2016) 313–324. URL: http://dx.doi.org/10.1016/j.nima.2016.06.003. doi:10.1016/j.nima.2016.06.003.

[10] ESS Webpage, 2017. URL: https://europeanspallationsource.se.

[11] McStas webpage, 2017. URL: www.mcstas.org.

[12] K. Lefmann, K. Nielsen, Neutron News 10 (1999) 20–23. URL: http://dx.doi.org/10.1080/10448639908233684. doi:10.1080/10448639908233684.

[13] P. Willendrup, E. Farhi, K. Lefmann, Physica B: Condensed Matter 350 (2004) 735–737. doi:10.1016/j.physb.2004.03.193.

[14] P. K. Willendrup, E. B. Knudsen, E. Klinkby, T. Nielsen, E. Farhi, U. Filges, K. Lefmann, Journal of Physics: Conference Series 528 (2014) 12035. doi:10.1088/1742-6596/528/1/012035.

[15] P. Willendrup, E. Farhi, E. B. Knudsen, U. Filges, K. Lefmann, Journal of Neutron Research 17 (2014) 35–43. URL: http://dx.doi.org/10.3233/JNR-130004. doi:10.3233/JNR-130004.

[16] D. Wechsler, G. Zsigmond, F. Streffer, J. A. Stride, F. Mezei, Physica B: Condensed Matter 276-278 (2000) 71–72. doi:10.1016/S0921-4526(99)01332-0.

[17] G. Zsigmond, K. Lieutenant, F. Mezei, Neutron News 13 (2002) 11–14. URL: http://www.tandfonline.com/doi/abs/10.1080/10448630208218488. doi:10.1080/10448630208218488.

[18] J. Šaroun, J. Kulda, Physica B: Condensed Matter 234-236 (1997) 1102–1104. doi:10.1016/S0921-4526(97)00037-9.

[19] P. Seeger, Physica B: Condensed Matter 283 (2000) 433–435. URL: http://linkinghub.elsevier.com/retrieve/pii/S0921452600003823. doi:10.1016/S0921-4526(00)00382-3.

[20] P. M. Bentley, K. H. Andersen, Nuclear Instruments and Methods in Physics Research, Section A: Accelerators, Spectrometers, Detectors and Associated Equipment 602 (2009) 564–573. doi:10.1016/j.nima.2009.01.013.

[21] C. Zendler, K. Lieutenant, D. Nekrassov, M. Fromme, Journal of Physics: Conference Series 528 (2014) 12036. URL: http://stacks.iop.org/1742-6596/528/i=1/a=012036. doi:10.3233/JNR-130005.

[22] E. Farhi, Y. Debab, P. Willendrup, Journal of Neutron Research 17 (2014) 5–18. doi:10.3233/JNR-130001.

[23] P. Freeman, J. Birk, M. Markó, M. Bertelsen, J. Larsen, N. Christensen, K. Lefmann, J. Jacobsen, C. Niedermayer, F. Juranyi, H. Ronnow, EPJ Web of Conferences 83 (2015) 03005. URL: http://www.epj-conferences.org/10.1051/epjconf/20158303005. doi:10.1051/epjconf/20158303005.

[24] S. L. Holm, K. Lefmann, P. F. Henry, M. Bertelsen, J. Schefer, M. Christensen, Nuclear Instruments and Methods in Physics Research, Section A: Accelerators, Spectrometers, Detectors and Associated Equipment 828 (2016) 229–241. URL: http://dx.doi.org/10.1016/j.nima.2016.05.046. doi:10.1016/j.nima.2016.05.046.

[25] A. Fedrigo, D. Colognesi, M. Bertelsen, M. Hartl, K. Lefmann, P. P. Deen, M. Strobl, F. Grazzi, M. Zoppi, Review of Scientific Instruments 87 (2016) 065101. URL: http://dx.doi.org/10.1063/1.4952430. doi:10.1063/1.4952430.

[26] M. Guthrie, M. Baldini, C. Bull, P. Henry, S. Klotz, J. Loveday, P. Noguera, J. Luis Martínez Peña, J. Pedro de Vicente, ESS Instrument Construction Proposal (2015). doi:105281/zenodo.154478.

[27] SLURM webpage, 2017. URL: https://slurm.schedmd.com.

[28] S. Peggs, ESS Technical Design Report, 2013.

[29] H. Börner, J. Brown, C. J. Carlile, R. Cubitt, R. Currat, A. J. Dianoux, B. Farago, A. W. Hewat, J. Kulda, E. Lelièvre-Berna, G. J. McIntyre, S. A. Mason, R. P. May, A. Oed, J. R. Stewart, F. Tasset, J. Tribolet, I. Anderson, D. Dubbers, R. S. Eccelston, M. Johnson, C. C. Wilson, G. Lander, H. Rauch, R. B. Von Dreele, W. Waschkowski, Neutron Data Booklet, second ed., Institut Laue-Langevin, 2003.

[30] H. Jacobsen, K. Lieutenant, C. Zendler, K. Lefmann, Nuclear Instruments and Methods in Physics Research, Section A: Accelerators, Spectrometers, Detectors and Associated Equipment 717 (2013) 69–76. URL: http://dx.doi.org/10.1016/j.nima.2013.03.048. doi:10.1016/j.nima.2013.03.048.

[31] M. Bertelsen, H. Jacobsen, U. Bengaard Hansen, H. Hoffmann Carlsen, K. Lefmann, Nuclear Instruments and Methods in Physics Research, Section A: Accelerators, Spectrometers, Detectors and Associated Equipment 729 (2013) 387–398. URL: http://dx.doi.org/10.1016/j.nima.2013.07.062. doi:10.1016/j.nima.2013.07.062.

[32] M. Andreas Olsen, Optimizing neutron guide performance and price using guide_bot and CoatingWriter (Bachelor thesis), 2016.

A.3 Expanding the McStas sample simulation logic with McStas Union components

This is a draft of a paper intended for Review of Scientific Instruments which introduces the McStas Union components and compares simulations of the MARI powder spectrometer with measured data. The publication of the paper was halted as a small inaccuracy in the placement of the side detectors in the MARI simulation could affect the comparison between measurement and simulation. Furthermore it was found that additional shielding was installed in the sample environment which was not included in the simulation. Simulations with the additional shielding may be compared to the existing simulations without in order to quantify the effectiveness of the installed shielding and demonstrate this new use case of the McStas simulation package.

Abstract

We introduce the Union components that initiate a new level of detail in sample simulation in the leading neutron scattering simulation package McStas. These components allow the construction of complex geometries composed of volumes with independent physical properties and native multiple scattering between them. The Union components separate the task of a regular McStas sample component into several component instances. Process components describe scattering processes such as incoherent scattering, powder scattering, single crystal diffraction etc., but has no geometrical representation. Creating such a process component is thus simpler than creating a full sample component. The make_material component is used to collect an arbitrary number of processes and an absorption cross section to form a material definition. The material definitions are assigned to geometry components that describe the geometry of the system using simple shapes such as spheres, cylinders and boxes. As these geometries are allowed to overlap, complex geometries can be assembled from a number of these geometry components. The Union master component contains an independent ray tracing core that will simulate the entire system. A suite of logging tools are included in the Union components, these tools can investigate how the simulation progressed and will explain the origin of features observed in the simulation output e.g. background events. We have validated this new method against traditional McStas components. We demonstrate the new possibilities by comparing a virtual experiment on the ISIS powder spectrometer MARI with existing data. The virtual experiment matches almost every aspect of the real data, with the notable exception of the Bragg peak intensities from the empty sample environment which is expected to be caused by aluminium texture not included in the model. The incoming energy is mapped up to 100 meV, showcasing the strong dependence on energy of the multiple scattering and providing guidance in selecting energies with minimal background. We furthermore study the MARI model using the introduced logging tools and explain the origin of two background features originating from parts of the sample environment not illuminated by the direct beam.

My contribution

Wrote the manuscript and performed all simulations under the supervision of Kim Lefmann.

Expanding the McStas sample simulation logic with McStas Union components

Mads Bertelsen,[1, a)] Tatiana Guidi,[2] and Kim Lefmann[1]
[1)] *Nano-Science Center, Niels Bohr Institute, University of Copenhagen, Universitetsparken 5, 2100 Copenhagen Ø, Denmark*
[2)] *ISIS facility, Rutherford Appleton Laboratory, Chilton, Didcot, OX11 0QX Oxfordshire, UK*

(Dated: June 19, 2017)

We introduce the Union components that initiate a new level of detail in sample simulation in the leading neutron scattering simulation package McStas. These components allow the construction of complex geometries composed of volumes with independent physical properties and multiple scattering between them. The Union components separate the task of a regular McStas sample component into several component instances. *Process* components describe scattering processes such as incoherent scattering, powder scattering, single crystal diffraction etc., but has no geometrical representation. Creating such a process component is thus simpler than creating a full sample component. The *make_material* component is used to collect an arbitrary number of processes and an absorption cross section to form a material definition. The material definitions are assigned to *geometry components* that describe the geometry of the system using simple shapes such as spheres, cylinders and boxes. As these geometries are allowed to overlap, complex geometries can be assembled from a number of these geometry components. The *Union master component* contains an independent ray tracing core that will simulate the entire system. A suite of logging tools are included in the Union components, these tools can investigate how the simulation progressed and will explain the origin of features observed in the simulation output e.g. background events. We have validated this new method against traditional McStas components. We demonstrate the new possibilities by comparing simulations of the the ISIS powder spectrometer MARI with existing data. The simulations match almost every aspect of the real data, with the notable exception of the Bragg peak intensities from the empty sample environment which is expected to be caused by aluminium texture not included in the model. The incoming energy is mapped up to 100 meV, showcasing the strong dependence on energy of the multiple scattering and providing guidance in selecting energies with minimal background. We furthermore study the MARI model using the introduced logging tools and explain the origin of two background features originating from parts of the sample environment not illuminated by the direct beam.

I. INTRODUCTION

The field of neutron scattering instrumentation design have in recent years relied heavily on Monte Carlo ray-tracing packages for simulation of expected performance, both in terms of intensity and resolution. Such simulations can include effects nearly impossible to describe analytically, such as non-Gaussian resolutions, secondary extinction and multiple scattering within the sample. They do, however, have a tendency to focus on the intended beampath through the instrument as it includes the important signal, but not all of the background that frequently originates from unintended beampaths e.g. related to multiple scattering in sample environment.

The most common neutron ray-tracing packages McStas[1–5], RESTRAX/SIMRES[6,7] and VITESS[8–10] were created to simulate a linear succession of modular components separated in space. This approach has obvious advantages for software performance, and it also simplifies user contributions of components, as each component can assume that the ray starts outside its volume and that no other component occupy the same region of space. While this solution has carried neutron ray-tracing simulation far, there are some inherent limitations that we here wish to address and remedy.

In McStas the linear succession of components dictates a certain order of components which the ray interacts with in turn, unless additional logic is added by the user. Each component include multiple scattering internally, but it makes multiple scattering between components a difficult task. Some components allow a so called concentric geometry, where an outer layer of material surrounds some components, and can thus scatter both when the ray enters, and when it leaves, but not in an arbitrary order.

As the components are not allowed to overlap, it is not possible to build a general geometry from smaller building blocks, but rather required that the entire geometry is described in a single component. This has the effect of complicating (especially sample) components as each can take a number of shapes. Likewise, sample components are further complicated by having to simulate all desired types of scattering in a single piece of code. This has made it unnecessarily difficult to write advanced sample components, as the developer has to balance a number of different types of scattering rather than just focusing

[a)] mads.bertelsen@gmail.com

on adding the single scattering type that was missing in the package.

Neutron scattering simulation tools with larger emphasis on multiple scattering does exist, the earliest of which named MSCAT[11] was published in 1986. The ray-tracing package NISP[12–15] does not assume a linear succession of components and allow overlapping of geometries, but is not updated for modern operating systems. In a recent publication, the MCViNE package[16] demonstrated multiple scattering between different components and a tree like structure for scattering logic, which does solve the mentioned issues, but usage of the package is not widespread.

In this paper, we introduce advanced multiple scattering to the most widely used neutron ray-tracing package McStas in the form of the Union project that completely rethinking how the component structure is used. The McStas Union project is a collection of McStas components that separate geometry from the scattering process while allowing geometries to overlap. A ray-tracing core independent from the McStas core is used to simulate multiple scattering between all these geometries until the ray leaves, which effectively circumvents the assumption of a linear succession of components, while maitaining the possibility of a performance-enhancing linear flow in the remainder of the simulation. The separation of scattering and geometry is meant to simplify the task of adding new physics or geometry to the project. The scattering is further divided into individual scattering processes, and writing such a process is kept as easy as possible, only requiring a description of the neutron scattering cross section as a function of wavevector and a description of a single scattering event.

The output from simulations with intricate geometry, many different materials, and unlimited multiple scattering has the potential to become very complicated. It is possible to filter the simulation output to rays that interacted with certain marked geometries or processes, but this may not be sufficient to understand the interplay between different parts. For this reason, a suite of Union components capable of monitoring the ray-tracing simulation are provided. These can for example show the spatial distribution of scattering or the distribution of momentum transfer. In addition, one can select parts of the simulation output and thoroughly investigate the many different ray paths that contributed to that specific part of the output.

The combination of multiple scattering and the ability to create complicated geometrical assemblies is highly relevant for the core McStas task of instrument design, as it will give a more accurate description of unexpected background that may be critical for instrument performance. These new possibilities also make it attractive to design sample environments directly in McStas as the geometrical tools necessary are now available along with a large library of instruments to test the sample environment. Finally, the Union components will increase the accuracy of virtual experiments, bringing McStas closer to being used directly as part of data reduction or analysis[17].

In this paper the Union components are introduced and validated against existing McStas sample components. A simulation including vanadium normalization is performed on the ISIS powder spectrometer MARI and favourably compared to experimental data. The multiple scattering background present in the MARI instrument model is analyzed using the tools provided by the Union components.

II. UNION COMPONENTS IN INSTRUMENT FILE

A schematic view of a McStas instrument file is shown in figure 1 where the linear succession of components can be seen. The only possible change from the specified order would be if a component is skipped because the ray did not intersect with a certain part of the instrument, unless the user manually programs such additional logic. The McStas package includes the GROUP keyword that can set components in parallel, but the ray can thus only interact with a single component in the group. The approach used by the Union project is seen in figure 2, where ray-tracing for the defined Union components occurs in a single master component. The master component circumvents the McStas ray-tracing core in order to achieve multiple scattering between a number of components. A number of McStas Union components can be used together with regular McStas components as part of the linear succession of components, for example by simulating sample environment plus sample within an existing instrument.

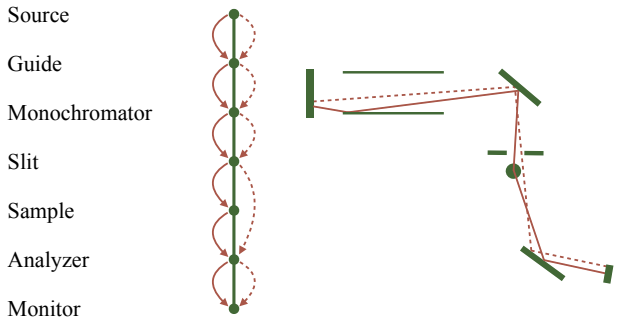

Figure 1. (Left) A sketch demonstrating the linear succession of components in a McStas instrument file and how two different rays pass through the instrument. (Right) A sketch of the two rays in the simulated instrument.

III. UNION COMPONENTS

In this section, each type of Union component is described in turn. The main reason for splitting the code

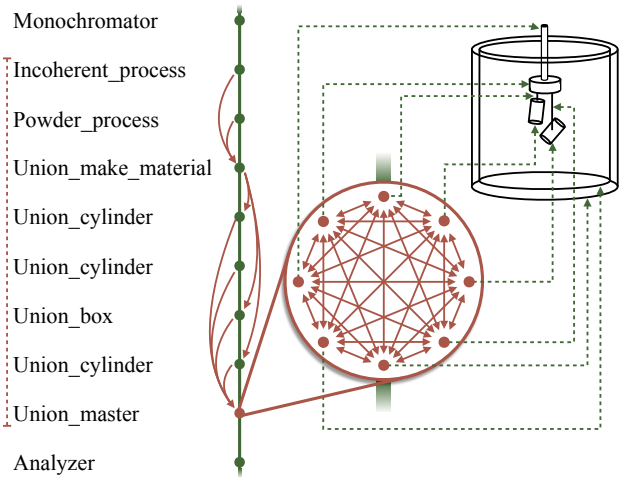

Figure 2. Sketch of an instrument file including Union components that forward information to a single master component wherein a separate ray-tracing core simulates the defined system.

over multiple collaborating components is to facilitate scalable, clear input of parameters. This approach is a major difference between the Union McStas components and previous components in terms of practical usage.

The component types are used in a specific order, as one first defines a number of physical processes using process components, then collects these into a material, and finally one places volumes with individual material descriptions in the simulation by using geometry components.

A. Scattering process components

A scattering process component has no physical shape and only needs to describe the probability for scattering and what happens in a scattering event, each of which is described by a separate function. The inverse penetration depth, μ, is used to describe the scattering probability, and is defined as,

$$\mu(\vec{k}_i) = n\sigma(\vec{k}_i) = \frac{N\sigma(\vec{k}_i)}{V}. \quad (1)$$

Where some number of scatterers (or possibly unit cells), N is observed in some volume V. The specific cross section σ may in general depend on the initial wavevector $\vec{k}_i$. A process component contains a function that returns the inverse penetration depth μ .

The second function included in a process component describes a scattering event by updating the initial wavevector to the final wavevector. This scattering funciton have access to the weight multiplier of the ray, π, which can be updated when manipulating the MC sampling frequency f of an event, as they must satisfy $p = \pi f$, where p is the physical probability[18,20].

It is possible to transfer variables between the two functions, and to store permanent information that can be used in subsequent function calls.

The currently available scattering processes are listed in table I together with the names of McStas components used as templates[18–20]. Not all functionality is duplicated from the originals, the incoherent process does for example not support a quasielastic energy width. Currently, all processes are elastic, inelastic processes are however supported by the Union infrastructure and will be added at later stages of development and through user contributions.

It is possible to describe a difference in orientation between different processes by giving the rotation angles in the standard McStas notation, which allows for example twinned crystals by use of two or more Single_crystal_process components.

When a process is very weak, it will not be sampled frequently by the Monte Carlo process unless its sampling probability is manipulated. This can be done for all processes and is explained in section III D.

Name	McStas component
Incoherent_process	Incoherent
Powder_process	PowderN
Single_crystal_process	Single_crystal

Table I. List of currently available scattering processes and the McStas components they used as template.

B. Union_make_material component

The main tasks of the Union_make_material component are to collect a number of scattering processes into a material, and provide a name that can be used to refer to this material later. The names of all scattering processes to be collected are supplied as a string in the input parameters. In addition, the inverse penetration length from absorption at the standard velocity, $v_0 = 2200$ m/s is given, $\mu_{abs\,th}$, from which the appropriate value at a given velocity, v can be found from,

$$\mu_{abs} = \mu_{abs\,th}\frac{v_0}{v}. \quad (2)$$

For a given $\vec{k}_i$, the inverse penetration depth for the total scattering from the material can be found,

$$\mu_s = \sum_i^N \mu_i, \quad (3)$$

where the sum is over all processes associated with the material. The total cross section is likewise, $\mu_{total} = \mu_s + \mu_{abs}$, from which the transmission probability over a path length of l can be found,

$$P_{trans} = e^{-l\mu_{total}}. \quad (4)$$

C. Geometry components

Each geometry component describes a volume that is placed in the McStas simulation, and is assigned a material definition using the material name provided by the Make material component. The geometry inherits the properties of the material, including the appropriate scattering processes and absorption description. In this context a volume is refers to a geometry combined with material properties placed in simulated space.

The currently available geometry components are listed in table II and shown in figure 3. Adding a new geometry component takes some effort, as functions for various intersection tests with all other geometries are necessary.

Name	Description
Union_sphere	Sphere
Union_cylinder	Finite cylinder
Union_box	Box

Table II. List of currently available geometry components.

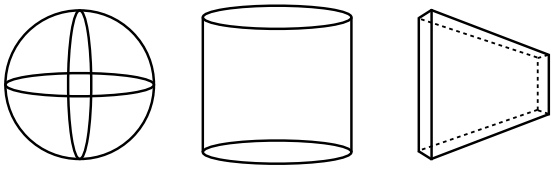

Figure 3. The three available geometries, (left) sphere, (middle) cylinder, (right) box. Note that the box needs to have two parallel sides with the same center.

In contrast to regular McStas components, the volumes can be defined in an arbitrary order, and are even allowed to overlap other volumes. When volumes overlap, the space that is covered more than once inherits the material definition of the volume with the highest priority, which is a unique value assigned to each volume. In this way, complicated geometries can be built from simple shapes, all with individual physical descriptions, as illustrated in figure 4.

D. Union_master component

The geometry components do not in themselves impact the neutron rays in the McStas simulation, instead they forward the gathered information to the Union_master component. This component contains a ray-tracing core independent from the one running other McStas components, and can handle an arbitrary number of volumes with multiple scattering between them. All propagation within the Union_master component is linear as gravity is neglected.

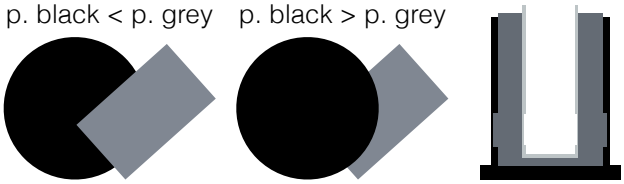

Figure 4. Three examples of volumes overlapping. In the left and middle, the concept is demonstrated by letting the grey and the black volume switch priority. The right panel shows how overlapping volumes of Al and vacuum can be used to build a simple cryostat, here with several layers of material, mounting plate and beam windows.

In order to simplify the process and geometry components, a large part of the complexity of writing a sample component was migrated to this Union_master component. Here we show how the scattering position and scattering process is selected.

When a ray is inside a volume, a distance to a next scattering position, l_s is selected from the appropriate distribution,

$$l_s = -\log(1-r)/\mu_{total}, \tag{5}$$

using a uniformly distributed random number between 0 and 1, r. This results in l_s being drawn from a probability distribution on the form $N\exp(-\mu_{total}l_s)$ where N is a normalization constant. If the distance l_s is smaller than the distance to the boundary of the volume l_b, a scattering event will occur, otherwise the ray will leave the volume.

In some cases it is desired to manipulate the sampling frequency of scattering events in a certain volume, which can be done by defining a scattering probability f_s in the appropriate geometry component. This can be done by manipulating the sampling frequency and adjusting the ray weight accordingly which is common in McStas samples. When the scattering process has a physical probability of p_s, the appropriate weight multiplier is,

$$p_s = f_s\pi \Rightarrow \pi = \frac{p_s}{f_s} = \frac{1-P_{trans}}{f_s} = \frac{1-e^{-\mu_{total}l_b}}{f_s}. \tag{6}$$

When a scattering event occurs, the next step is to select one of the available processes. Since we exclude absorption in this choice, the ray weight needs to be transformed accordingly. The actual probability for selecting a scattering process is $P_{scat} = \mu_s/\mu_{total}$, and as we define the sampling frequency for selecting a scattering process to $f_s = 1$, the weight multiplier is,

$$\pi = P_{scat}/f_s = \mu_s/\mu_{total}. \tag{7}$$

Next, a Monte Carlo choice is performed to choose between the processes in the current material, each with probability $p_i = \mu_i/\mu_s$ calculated by the functions from the process components. The function describing a scattering event for the selected process is then evaluated.

As mentioned in section III A, it is possible to manipulate the sampling frequencies of the processes in a material, which is done by attributing each process a relative weight m_i, which fulfils,

$$\sum_i^N m_i = 1. \tag{8}$$

For a given $\vec{k}_i$, these can however not directly be used to select between the processes, as μ_i could be zero for some processes, which are then excluded from the choice. Thus, a similar parameter, t_i is defined as follows,

$$t_i = \begin{cases} 0 & \text{if } \mu_i = 0 \\ m_i & \text{otherwise} \end{cases}. \tag{9}$$

The sum over all t_i in a material is denoted T. Now a Monte Carlo choice between N possibilities with probabilities t_i/T is made, and using the final choice i, the weight is updated,

$$\pi = \frac{p_i}{f_i} = \frac{\mu_i/\mu_s}{t_i/T}, \tag{10}$$

and the function describing a scattering event for process i is evaluated.

Due to the computational requirements related to handling intersections with a large number of volumes, the Union_master component will analyse the overall system and create a simple logical network that omit most unnecessary intersection calculations. This optimization significantly improves the performance scaling, and thus large numbers of volumes can be used without excessive computational requirements. An example showing an ensemble of geometries and the resulting logical network is shown in figure 5.

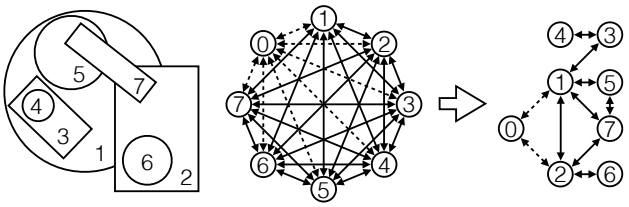

Figure 5. (Left) An ensemble of volumes, each named with a number that also correspond to the priority of the volume. (Middle) Worst case network where intersections with all volumes are calculated regardless of the position of the ray. Here volume 0 is the surroundings outside the ensemble. (Right) Reduced network corresponding to the depicted ensemble of volumes, here the necessary intersection calculations depend on the position of the ray.

E. Union logger components

Since the Union_master component contain such a large and important part of the full McStas simulation, we have chosen to add tools that are able to log what occurs in the Union_master component. Logger components saves information on each scattering event and output the results as a McStas monitor. This could for example be the position of all scattering events, their scattering vector, or similar. It is possible to attach the logger component to a number of specified volumes, and even specify process names to investigate such subsets of the data. The currently available logger components are listed in table III.

Name	Description
Union_logger_1D	Logs time / scattering vector
Union_logger_2DQ	Logs (q_i, q_j) for i,j = x,y,z
Union_logger_2D_kf	As above with final wavevector
Union_logger_2D_kf_time	As above, with time bins
Union_logger_2D_space	Logs scattering position in 2D
Union_logger_2D_space_time	As above, with time bins
Union_logger_3D_space	Logs scattering position in 3D

Table III. List of currently available logger components.

F. Union conditional components

It can easily be investigated how certain parts of the overall geometry contribute to the total scattering, what remains is the ability to investigate what contributed to a certain part of the scattering pattern. Union conditional components can modify a logger component, so that it will only save recorded data if the final ray state adhere to some condition, for example a certain final energy range. Several conditional components can modify the same logger component, and in this case all conditions need to be fulfilled.

There are currently two available conditional components, one that filters for time when the ray leaves the ensemble, and another that requires the ray to intersect with a virtual detector and can filter on the time of intersection.

By having loggers for position and scattering vector with conditionals filtering a certain background problem, the user can inspect the origin of this scattering and what succession of scattering vectors were taken. As such the combination of Union logger and Union conditional components provides powerful tools for understanding the final results.

IV. VALIDATION

The scattering processes included in the Union components build upon existing McStas sample components. However, the code describing Monte Carlo choices between processes, intersection algorithms, choice of scattering position and absorption have been separated from

the scattering process in order to accommodate the different structure of the software. Hence it is still prudent to validate the new software against known references.

The McStas instrument used for validating each process consists of a simple 1×1 mm^2 source illuminating a massive cylindrical sample with radius and height of 1 cm, situated 10 m from the source. A transmission detector of 1 cm height is placed 0.5 m after the sample. A cylindrical detector with a radius of 1 m and height of 10 cm measures the scattered signal. All validation is performed without gravity, as the Union components does not support parabolic propagation. All simulations were performed with $5 \cdot 10^9$ rays

A. Incoherent scattering

Union components describing a sample with only incoherent scattering was compared to the same geometry simulated using the Incoherent McStas component. The scattering and absorption cross sections were chosen to be those of Vanadium, $\mu_{inc} = \mu_{abs\,th} = 36.73$ m^{-1}. The incoming beam was monochromatic with 10 meV energy. A comparison between the transmission from the two components are shown in figure 6, while the scattered intensity is compared in figure 7. The incoherently scattered intensity varies slightly with scattering angle due to self-absorption in the sample. The absorption is most prominent for forward scattering. For both the transmission and scattering cases, the results from the Union components are almost inseparable from the traditional sample component. In addition, the deviations are consistent with the Monte Carlo noise estimated by McStas.

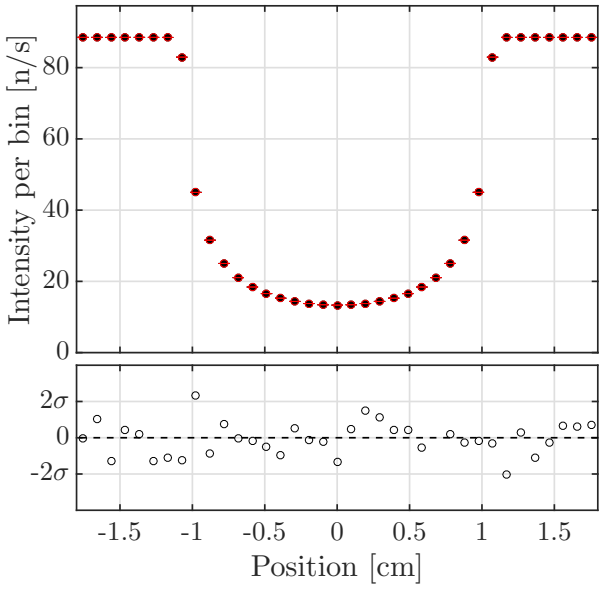

Figure 6. Comparison of transmission through an incoherent scatterer with absorption simulated using Union components (black filled) and the McStas library Incoherent sample component (red empty). The lower panel shows the difference between the two simulations for each point relative to the error on the difference introduced by the Monte Carlo technique.

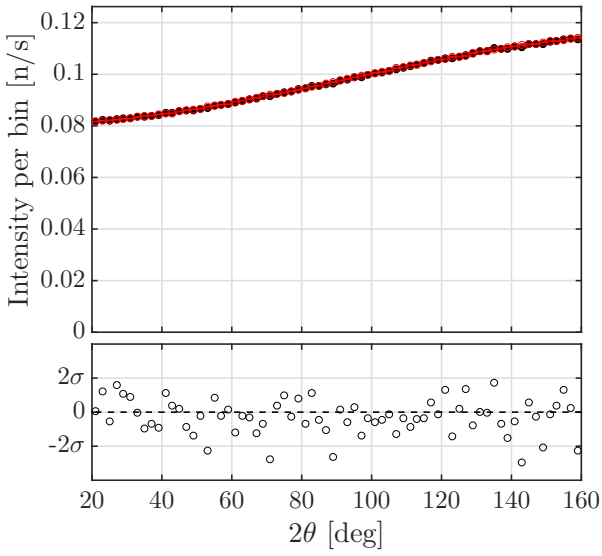

Figure 7. Comparison of scattering from incoherent scatterer with absorption simulated using Union components (black filled) and the McStas library Incoherent sample component (red empty) as a function of scattering angle 2θ. The lower panel shows the difference between the two simulations for each point relative to the error on the difference introduced by the Monte Carlo technique.

B. Powder scattering

Here, the Union components are validated against the existing PowderN sample component. As PowderN describes both powder diffraction and elastic incoherent scattering, the material defined using the Union components contains both processes. The powder diffraction process is based directly on the code from the PowderN component. It is important to note that PowderN does not support multiple scattering. When using the powder process in the Union components, multiple scattering is handled by the Union_master component. To obtain a valid comparison, we add a detector that ignores multiple scattering.

This validation has been performed for many compounds. Here, the representative results for Cu and a 100±0.5 meV beam are presented. A comparison between the transmission results can be seen in appendix figure 27, and in this aspect the two codes produce equivalent results.

Parts of the scattered intensity is shown in appendix figure 28. Here we observe a small, but significant difference, as the multiple scattering only present in the Union version amounts to roughly 30% of the background con-

ceived to arise from sample incoherent scattering. When only considering the single scattering events, as seen in figure 8, the different versions agree as expected. The asymmetric peak shape seen at low scattering angles is caused by the detector height combined with the Debye-Scherrer cones.

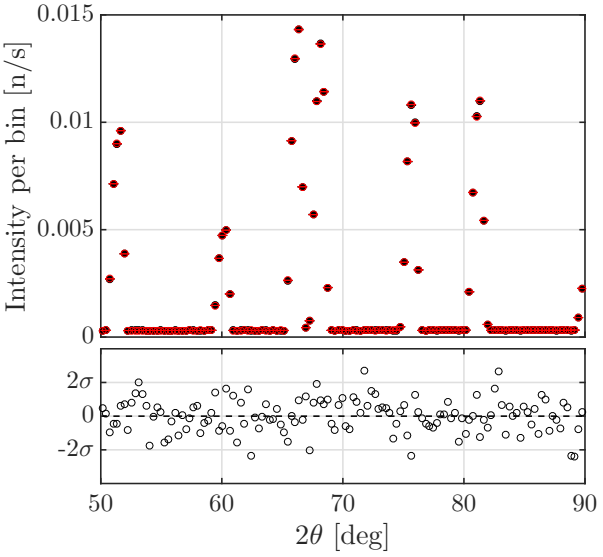

Figure 8. Bragg peaks simulated by Union powder sample (black filled) and McStas library component PowderN (red empty), here only single scattering events are recorded. Lower panel shows the difference for each point relative to the error on the difference introduced by the Monte Carlo technique.

C. Single crystal diffraction

Validation of scattering from a single crystal process is performed by comparing with the Single_crystal component which the process is based on. As the Single_crystal component simulates incoherent scattering in addition to the crystal Bragg peaks, an incoherent process is added to the Union material. Note that Single_crystal does simulate multiple scattering. Here a white beam with a homogeneous energy distribution in the interval $1-20$ meV illuminates a cylindrical $YBa_2Cu_3O_7$ sample oriented with the c axis along the beam direction. An isotropic mosaicity of 5 arcmin was used.

The transmitted beam contains both rays that never scattered, and rays that scattered an even number of times on a certain reflection. For this reason the transmission detector signal is separated into a non-scattered part seen in appendix figure 29 and a scattered part seen in figure 9. Both cases show the expected agreement.

In figure 10 the results for a single Bragg peak is compared, showing no significant difference between the components. The skewed shape of the $\bar{1}02$ Bragg peak shown is due to the large size of the sample which causes the

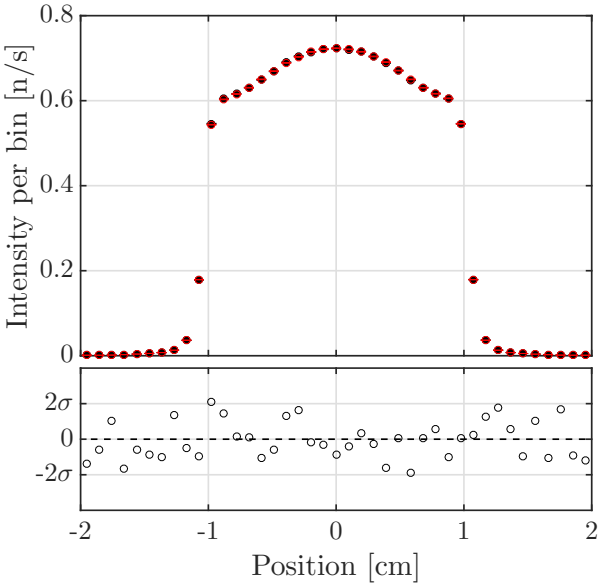

Figure 9. Simulated transmission for rays that did scatter, results for Union components (black filled) and the McStas library component Single_crystal (red empty). Lower panel shows the difference for each point relative to the error on the difference introduced by the Monte Carlo technique.

majority of scattering to originate from the side cloest to the source. Since the distance to the detector is small, the skewed distribution of origins is measured as a distribution in angle. The positions of the remaining Bragg peaks for the two components are identical, as shown in the Laue diffraction pattern in appendix figure 30.

V. SIMULATING THE MARI SPECTROMETER

Here the Union components are demonstrated by performing simulations of the ISIS time of flight powder spectrometer MARI[21] which is compared to an actual experiment. Furthermore, we study the background present in the simulations using the Union logger and conditional components.

A. MARI geometry

Here the geometry of the McStas MARI instrument model is presented.

The dedicated MARI moderator description in the ISIS source component is used with a size of 9×9 cm^2. The Fermi chopper is situated 10.05 m after the moderator and is simulated with the FermiChopper McStas component. The simulated chopper resembles the Gd chopper available at MARI. The radius is 5 cm and the 113 channels of 0.4 mm width makes up a 4.5 cm wide channel. The blades are curved with a radius of curvature of 0.8 m.

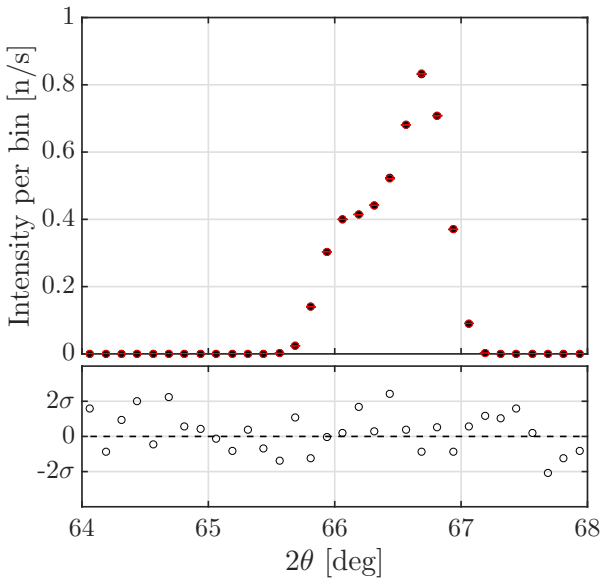

Figure 10. Simulated Bragg peak and incoherent background for Union components (black filled) and the McStas library component Single_crystal (red empty). Lower panel shows the difference for each point relative to the error on the difference introduced by the Monte Carlo technique.

The beam defining jaws and sample position are placed 11.239 m and 11.739 m from the moderator, respectively. In all simulations for this paper, the jaws were at 4.5×4.5 cm^2.

Figure 11 shows an image of the simulated cryostat from the ISIS webpage[22] and the McStas Union model of the lowest parts of the cryostat.

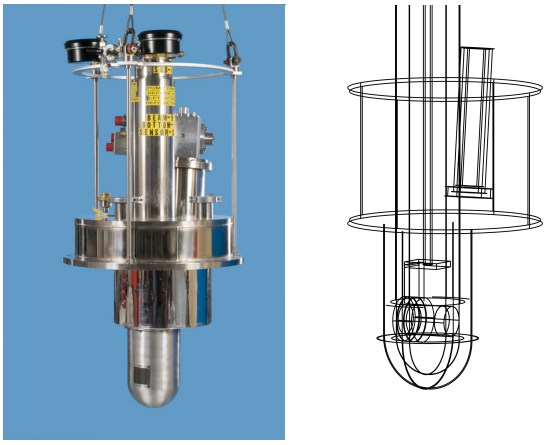

Figure 11. Toploading cryostat used on MARI and Union simulation of the lower part. The inner structure is visible in the Union model, showing the sample holder, sample stick and shielding blocks connecting the sample container with sample rod.

The sample environment has an outer and inner chamber, each consisting of a cylinder on top of a sphere. The two spheres have centers 2.5 cm below the sample position and the cylinders starts at the same height. The radii and thickness of these and other geometrical details can be found in table IV. The outer cylinder has a window for beam entry and exit that has a width of 6 cm and a height of 5 cm. The inner cylinder is thinner at the beam height, which is ± 2.5 cm vertically from the sample position.

The lower vessel starts 13 cm above the sample position, has a height of 18.9 cm and is displaced 4.8 cm along the beam direction. The lower and upper plates are 5 mm thick. The Closed Cycle Refrigerator (CCR) starts 2.5 cm above the bottom plate of the vessel and is displaced 11.4 cm from the sample position along the beam direction. The CCR is tilted 6° from vertical towards the beam direction.

The sample container is simulated as a horizontal cylinder perpendicular to the beam direction with a length of 7.3 cm. The sample is in the circumferences of the container, and is thus hollow. The sample is 4.5 cm wide, and thus does not occupy the entire length of the container. One end of the container has a 6 cm wide collar which is connected to the sample stick with Boron-Nitride. The Boron-Nitride connecting piece is made of a cylinder with 1 cm width that connects directly to the collar and two boxes.

Description	inner radius	thickness
Outer sphere	6.90 cm	1.6 mm
Outer cylinder	6.90 cm	1.6 mm
Outer cylinder (window)	7.059 cm	0.01 mm
Inner sphere	5.00 cm	0.5 mm
Inner cylinder (beam height)	5.00 cm	0.15 mm
Inner cylinder (elsewhere)	5.00 cm	1.5 mm
Lower vessel cylinder	13.2 cm	2.5 mm
Sample can	2.09 cm	0.1 mm
Sample can collar	2.09 cm	10.1 mm
Upper CCR cylinder	2.5 cm	5 mm
Lower CCR cylinder	massive	3.4 cm
Sample stick	massive	0.7 cm

Table IV. Inner radius and thickness of used aluminium geometries. For massive objects, the outer radius is given as thickness.

The detectors are modelled as cylindrical monitors with a radius of 4.02 m. The high angle bank covers angles from 12° to 134° and the center detector is 30 cm wide while the side detectors are 20 cm wide and rotated plus and minus 4 degrees respectively around the beam direction. The low angle detectors covers from -12° to 12°, and there are four separate detectors rotated in 45° increments around the beam direction.

B. MARI materials

Here the material definitions used for the Union description of the sample environment is presented. As all materials are given a incoherent and absorption inverse penetration depth, these are collected in table V.

The aluminium of which the sample environment is constructed is modelled as a powder with Bragg scattering from the standard McStas data file and an incoherent scatterer.

The Ni_3TeO_6 powder sample is modelled as Bragg scattering from a perfect powder and incoherent scattering. The Bragg scattering was described by converting a cif file obtained from the ICSD database[23,24] into a lau file suitable for McStas using the cif2lau tool in iFit[25]. No inelastic scattering is simulated.

The vanadium calibration sample is modelled as a purely incoherent scatterer as the weak powder scattering is neglected.

The boron-nitride shielding material is modelled as an incoherent scatterer with strong absorption. The density and molar mass are used to calculate the number density, and the cross sections are taken from Ref 26. The absorber was made using isotope pure ^{10}B for increased absorption which is taken into account.

Material	μ_{inc}	$\mu_{abs\,th}$
Aluminium	0.049 m^{-1}	1.39 m^{-1}
Ni_3TeO_6	15.1 m^{-1}	17.5 m^{-1}
Vanadium	36.7 m^{-1}	36.7 m^{-1}
Boron-nitride	80.8 m^{-1}	10100 m^{-1}

Table V. List of inverse penetration depth for incoherent scattering and absorption at 2200 m/s.

C. MARI Vanadium calibration

The calibration of the real instrument was replicated by simulating a Vanadium calibration measurement and an empty cryostat. This Vanadium calibration is simulated without the chopper and for wavelengths between 0.25 Å and 0.5 Å. The virtual detectors were calibrated to have the same systematic error as on the real instrument, by correcting with the empty cryostat simulation subtracted from the vanadium simulation.

D. MARI comparison with measurements

Here we compare results from the simulated MARI instrument with measurements performed on the real instrument. The empty cryostat was measured for calibration purposes, but here this measurement is the basis of our first comparison. The Gd chopper is used at 250 Hz and phased to achieve a beam energy of 34.85 meV. The real data is shown in figure 12, and the simulation results are shown in figure 13. The angular position and resolutions of the peaks match well as do the energy shifts and energy resolution. Several peaks are split in similar fashion and their shapes generally match. The relative intensities of the peaks are, however, very different.

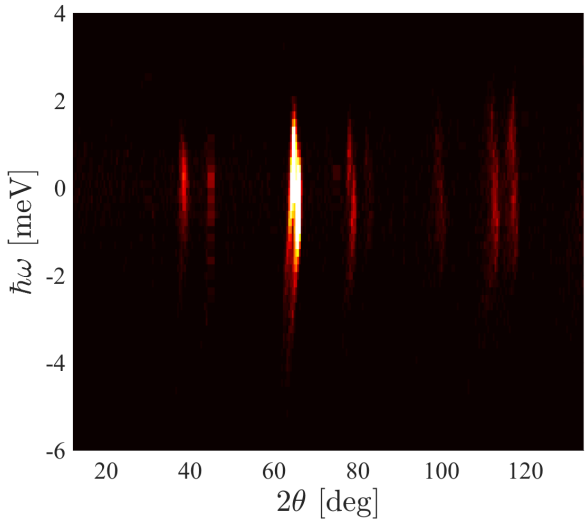

Figure 12. Scattering from an empty cryostat on MARI with a selected energy of 34.85 meV from the Gd chopper running at 250 Hz.

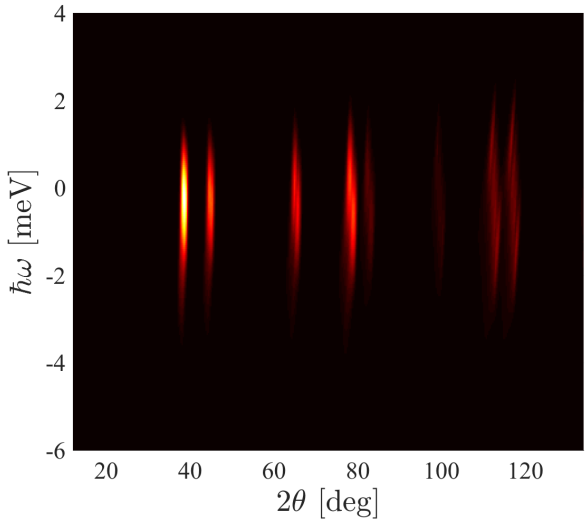

Figure 13. Simulation of scattering from an empty cryostat on MARI with a selected energy of 34.85 meV from the Gd chopper running at 250 Hz.

To investigate the angular dependence, both data sets are summed over all energy transfers, resulting in the

comparison seen in figure 14. The simulated data have a scaling factor and a small constant background added. It is once again evident that the peak intensities does not match, but that the shape and position for the aluminium peaks do. The peaks are sharp at the positive angle side and have a tail at the low angle side which is consistent with the time tail of the used moderator.

The difference in peak intensities are expected to be caused by texture in some or all parts of the aluminium used to construct the sample environment and windows. Currently no components in McStas support simulation of textured powders, but simulations were made by increasing the scattering strength of different parts of the sample environment. These showed that the peak separation in the data is consistent with scattering from the inner chamber walls.

The few peaks in the measurement that are one pixel wide e.g. at 109° are expected to be detector channels with slightly higher background while the small peaks at 23° and 105° may be from some other material used in a small quantity and not simulated.

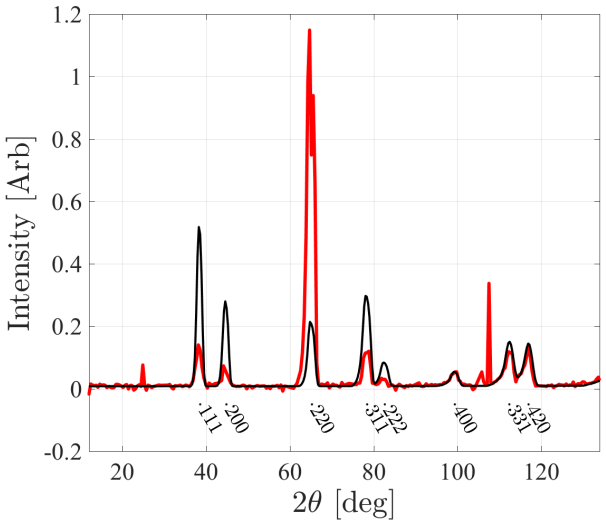

Figure 14. Comparison between data from an empty cryostat taken at MARI (red) and the McStas simulation using Union components (black). Here the scattering is summed over all energy transfers to view the angular dependence, which is dominated by elastic scattering and the angular resolution of the instrument. Indexing of the Al peaks is shown below the peaks.

The energy dependence was compared in a similar manner with a sum over all angles. The results are shown in figure 15, where a scaling factor was used to match the peak intensity and a small energy transfer added to facilitate easier comparison of the shape and width. The peak width is slightly wider in the simulation, but this will be influenced by the wrong Bragg peak intensities. The increased width of the simulation is most likely the result of some inaccuracy in the simulation of the chopper (where zero blade width is assumed).

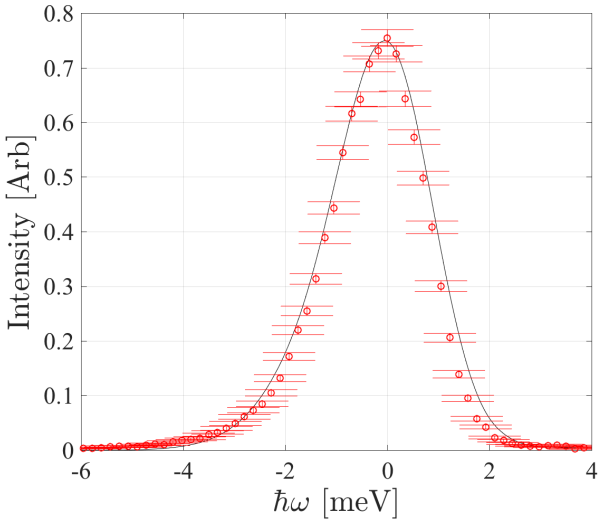

Figure 15. Comparison between data from empty sample environment taken at MARI (red) and the McStas simulation using Union components (black). Here the scattering is summed over all angles to view the energy dependence which is dominated by elastic scattering and the energy resolution of the instrument.

Next, the simulated MARI instrument is compared with available measurements on Ni_3TeO_6. The measurement was performed with the Gd chopper at a frequency of 250 Hz phased to provide a beam with an energy of 35.19 meV. The purpose of the experiment was to investigate the inelastic signal, the study of which will be published elsewhere[27]. Here the focus is on the elastic parts as the Union components do not include inelastic processes yet.

The measurement were performed with a sample mass of 6.9 g placed in the circumference of the sample container with a width of 4.5 cm perpendicular to the beam and a thickness of 1.9 mm. This was replicated in the simulation.

The data sets are summed over energy to compare the angular dependence as shown in figure 16. A scaling factor is used to match the intensities of the two data sets and a small constant background was added to the simulation. There is a good overall agreement, but once again the differences in aluminium peak intensity are evident.

The full datasets and a comparison of the energy resolution is shown in appendix figure 31, 32 and 33. The agreement is in general better than the corresponding comparison for the empty cryostat, figure 12, 13 and 15.

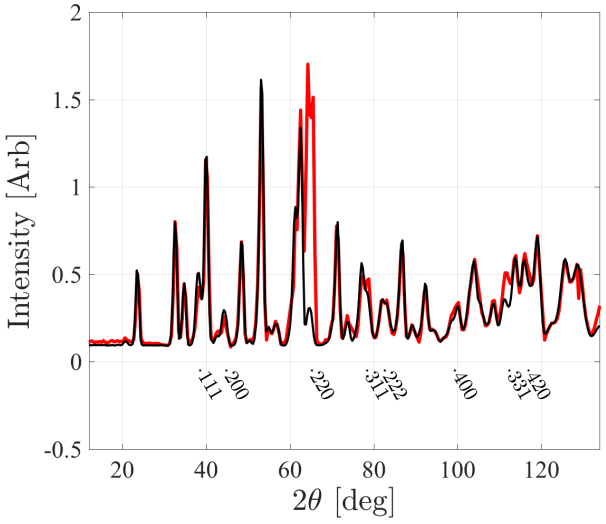

Figure 16. Comparison between data from Ni_3TeO_6 powder taken at MARI (red) and the McStas simulation using Union components (black). Here the scattering is summed over all energy transfers to view the angle dependence which is dominated by elastic scattering and the angular resolution of the instrument. Indexing of Al peaks are shown.

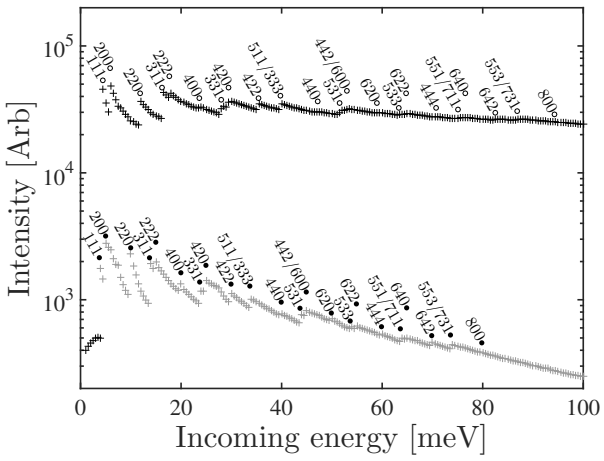

Figure 17. Total measured single scattering intensity (black) and multiple scattering intensity (grey) as a function of incoming energy. Errorbars not shown as they were negligible. Simulated with a unrealistically narrow energy band of 0.01 meV on the MARI instrument model. The Miller indices for aluminium Bragg peaks at $2\theta = 180°$ is shown with filled circles and $2\theta = 134°$ is shown with empty circles.

E. Analysis of background

With a model of the instrument available, it is interesting to map how the multiple scattering background depend on different instrument settings. On MARI, the two important choices are the incoming energy and the time resolution from the chopper. The multiple scattering is strongly dependent on the incoming energy, and it is thus selected to scan this parameter to get an overview of the multiple scattering background. A perfect source was used to simulate a very high energy resolution, so that an estimate for the multiple scattering at a broader energy resolution can be performed by integrating over the covered range. The used source component provides a constant brilliance in units $1/s/cm^2/ster./meV$.

The total single scattering and multiple scattering intensity measured by the detector is shown in figure 17. The measured single scattering intensity have peaks at energies where a Bragg peak enters the detector coverage at $2\theta = 134°$. The multiple scattering intensity peaks at energies corresponding to a new Bragg peak being accessible and thus a scattering angle close to 180°.

The angular dependence as a function of energy is shown in figure 18, where the scattering intensity is summed over all energy transfers. Here the powder scattering from aluminium dominates the plot, but as this part is not delayed significantly, this background will be located in the elastic channel. In figure 19, the same scan is shown, but only includes rays that underwent 2 or more scattering events. Here the structure of the multiple scattering is much more visible, and as this background can have a significant delay, it may contribute to inelastic background even though all scattering was elastic.

As expected the background from multiple scattering is completely absent at energies where there are no Bragg scattering in aluminium i.e. below 3.7 meV. Conversely, the background is almost uniform at large incoming energies as there is a great number of different Bragg peaks that can be accessed, and thus a large number of different combinations seem to diminish the structure. In the region of 5 meV to 50 meV, however, the relatively low number of accessible Bragg peaks makes the structure more pronounced. In addition, it seems that the largest background occurs at energies where a Bragg peak corresponds to a scattering angle of 180°.In addition to the low energies (<4 meV) and high energies (>50 meV), a few energies are comparatively free from background and can be recommended for measurements, 9 meV, 13 meV, 23 meV, 35 meV, and around 40 meV.

Union logger components are used to record the scattering positions in the sample environment at the same energy as the simulation, 35 meV. The results are shown in figure 20 and 21. These contain a surprising amount of complexity, as the illumination of the sample environment originates from the many layers of material in the beam. First order scattering appears only in the directly illuminated parts, the two windows, sample container and the edge of the absorbing connecting piece. The second order scattering is highly structured as a consequence of the sharp Bragg peaks from the parts illuminated by the beam. Here the shadow from the absorber is visible as an asymmetry between the two sides when seen from above. In contrast the third order is more evenly

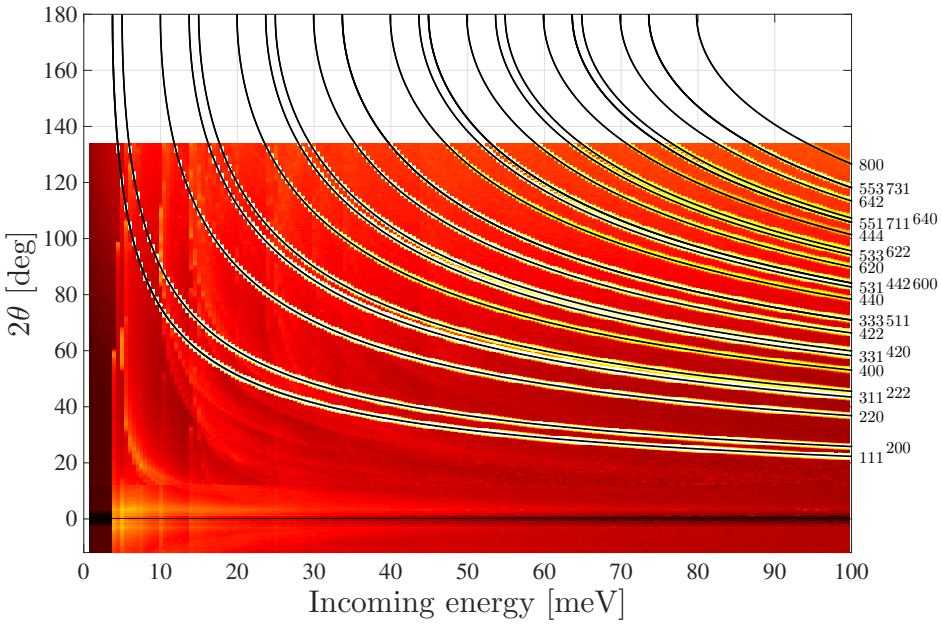

Figure 18. Detector output as a function of detected scattering angle over a range of incoming energies. Simulated with a narrow energy band of 0.01 meV on the MARI instrument model. The overlay shows expected Bragg scattering from aluminium with the corresponding Miller indices.

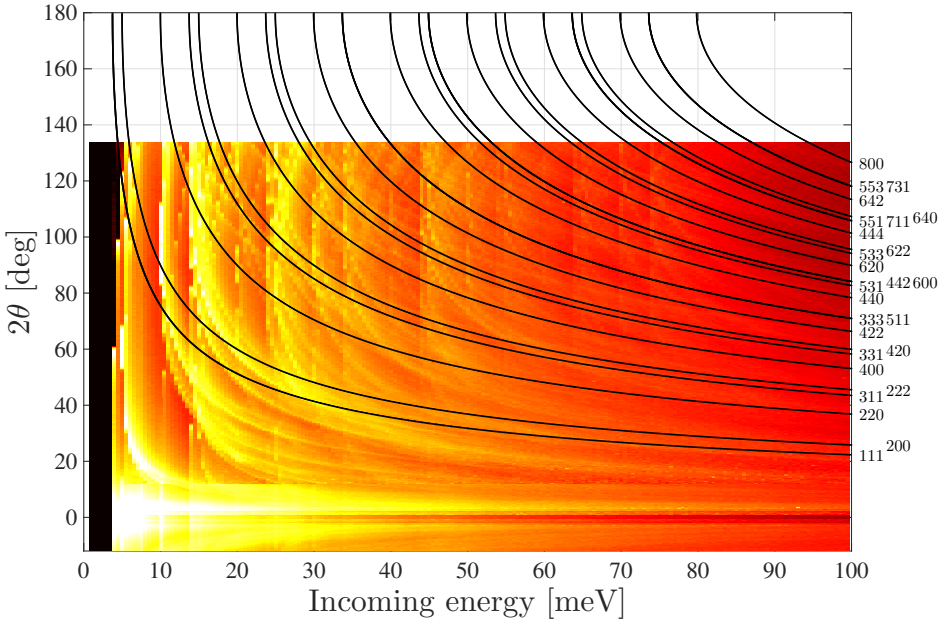

Figure 19. Detector output as a function of detected scattering angle over a range of incoming energies. Simulated with a narrow energy band of 0.01 meV on the MARI instrument model. Here only rays that scattered more than once are recorded. The overlay shows expected Bragg scattering from aluminium with the corresponding Miller indices.

distributed over the entire sample environment.

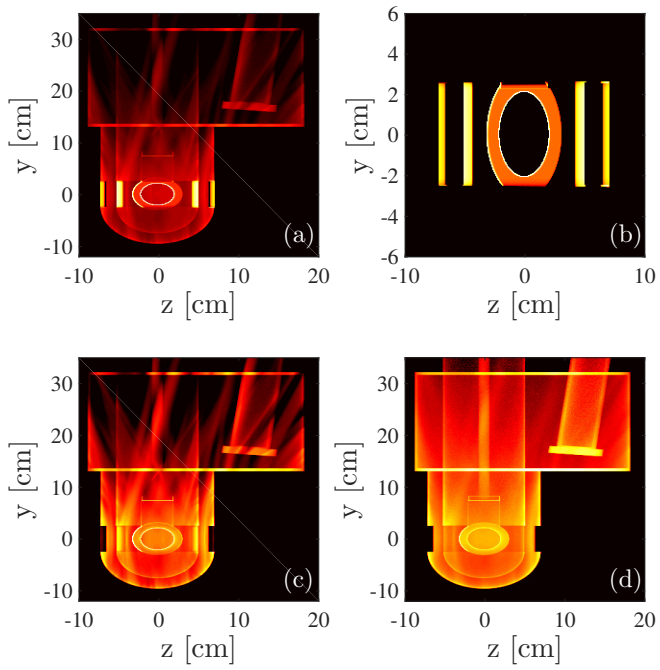

Figure 20. Scattering positions within the sample environment seen from the side. The colorscale is logarithmic and measures the amount of scattered intensity within a certain region of space. Here separated into all orders in panel (a), while 1st order is shown in (b), 2nd order in (c) and 3rd order in (d). Note that panel (b) is zoomed onto the sample and sample environment windows, because this is the only directly illuminated area. The colour scales are individual for each panel.

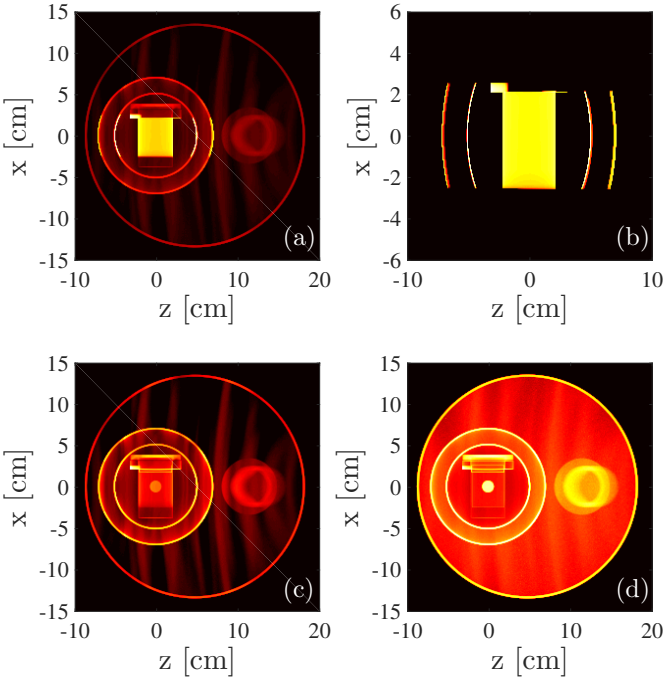

Figure 21. Scattering positions within the sample environment seen from the top. The colorscale is logarithmic and measures the amount of scattered intensity within a certain region of space. Here separated into all orders in panel (a), while 1st order is shown in (b), 2nd order in (c) and 3rd order in (d). Note that panel (b) is zoomed onto the sample and sample environment windows, because this is the only directly illuminated area. The colour scales are individual for each panel.

Next the multiple scattering present in the MARI simulation of the empty sample environment is investigated by plotting the detector signal on a logarithmic scale as seen on figure 22. Here many multiple scattering features are visible, and it is clear how they have a potential for being mistaken as an inelastic signal. The measured data on the empty cryostat hardly contained any counts outside the elastic line, and thus a comparison to the measured data is not feasible. This could be explained either by the measurement being too short or because additional shielding not simulated were installed. The latter was confirmed by the instrument scientist, yet simulations were performed without the shielding, and now serves to show the multiple scattering that would occur without such shielding.

In order to investigate the multiple scattering signal further, a simulation of the empty sample environment was performed with an artificial source with perfect time structure and energy resolution of 0.01 meV. This serves to remove the smearing from energy resolution and inherent time structure of the moderator, making the perceived energy transfer a clear measure of added distance to the neutron flight path. The resulting detector output

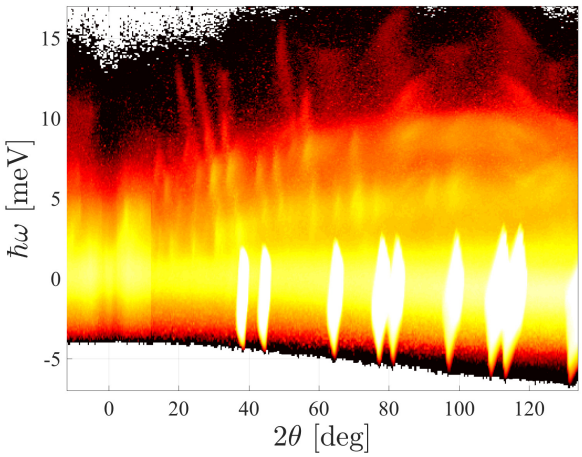

Figure 22. Output from simulation of an empty cryostat on the MARI instrument on a logarithmic scale from 2 to 7 orders below the aluminium Bragg peaks.

is shown in figure 23. Here, the multiple scattering fea-

tures are clear and an analysis of this output is simpler as the peaks can be easily distinguished.

In order to understand these features one can filter the McStas monitors used to only view events that had certain number of scattering events, were scattered in certain volumes, or took part in some specified process. On figure 24 we show the part of the detector output that had a scattering in the CCR. All contributions from the CCR appear well outside the elastic line as rays need to add a significant path length to reach the CCR before ending at the detectors.

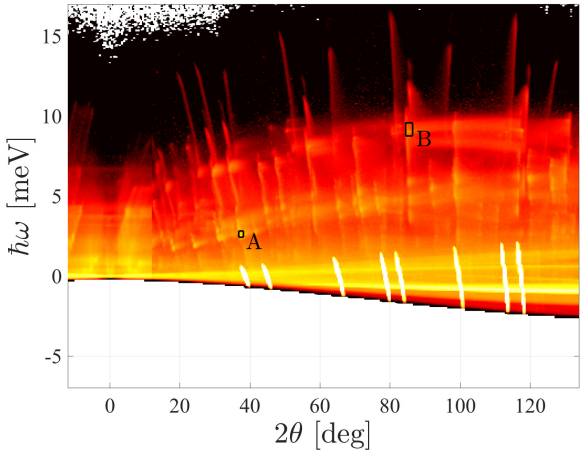

Figure 23. Output from simulation of an empty cryostat on a logarithmic scale from 2 to 7 orders below the aluminium Bragg peaks. Here a source without time distribution and a narrow energy interval is used to show the multiple scattering features in more detail. The peaks marked A and B are investigated further in figure 25 and 26, respectively.

The capabilities of the conditional components are demonstrated by investigating the origin of two marked peaks in figure 23. Each peak is assigned a series of Union logger components and a conditional component that ensure the loggers only record events that are within the boundaries marked A and B respectively on figure 23. The spatial origins for peak A is shown in figure 25, showing that the first scattering occurs in the Al window and sample container, while the second occurs at the lower vessel. The distribution of scattering among the powder lines in aluminium are displayed in table VI. The reference column shows the probability distribution among the Bragg peaks for all scattering, not just the part that satisfy the conditional. For this conditional, the first order scattering has a higher probability for low angles of scattering, while the second order is primarily from the 311 reflection.

The spatial origins for peak B is shown in figure 26. The first scattering primarily occurs after the beam has travelled halfway through the cryostat, and on panel (e) it is even visible that half of the sample container has a lower probability to contribute to peak B, as the rays

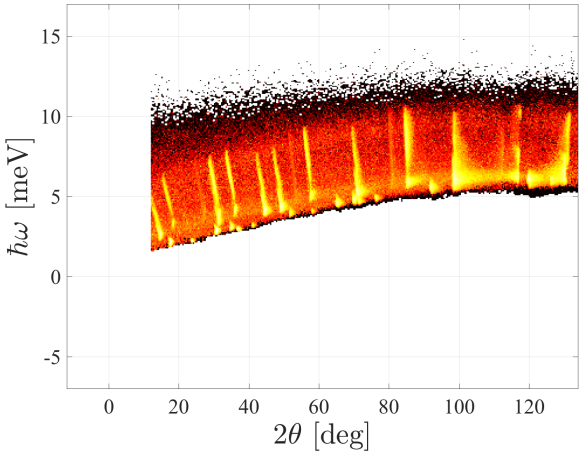

Figure 24. Output from simulation of an empty cryostat on a logarithmic scale, here filtered to only show events that scattered in the CCR. Only the center high angle detector bank which covers 12° to 134° is used.

Miller indices	2θ	1st order	2nd order	3rd order	Reference
111	38.2°	29.7%	1.2%	16.4%	14.2%
200	44.4°	10.4%	0.7%	12.0%	9.2%
220	64.5°	6.5%	0.8%	9.2%	11.1%
311	77.5°	17.6%	72.2%	17.3%	19.0%
222	81.7°	3.4%	4.0%	6.0%	5.1%
400	98.1°	1.8%	0.6%	3.1%	3.3%
331	111°	6.9%	4.0%	10.0%	10.1%
420	115°	6.8%	11.6%	10.6%	9.8%
422	135°	9.0%	2.9%	7.5%	9.0%
511/333	158°	8.0%	1.9%	8.0%	9.1%

Table VI. Table over distribution of scattering per powder line for conditional A. The reference column is the probability for all scattering without any conditional.

need to travel through the Boron-Nitride sample holder. The second scattering most frequently occur at the top plate of the simulated vessel, with some on the CCR itself. The distribution of scattering among the aluminium powder lines can be seen in table VII. The first scattering is often the 311 reflection that yields the necessary scattering angle to hit the top of the sample environment. In order to contribute to the investigated peak, the ray must end on the detector below the sample environment, and thus must backscatter. More than 80% of the second order events used the 511 or 333 reflection that share a scattering angle of 158°. The third order scattering has a distribution closer to the reference, but still with a higher probability for back scattering.

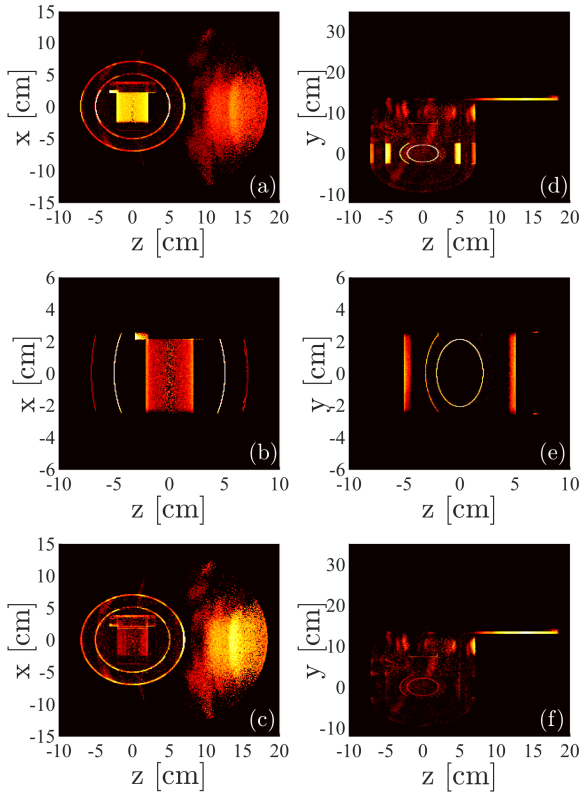

Figure 25. Scattering positions within the sample environment for rays that satisfy conditional A shown in figure 23. Panel (a) through (c) are from a top view, (a) being all scattering, (b) only first order scattering (zoomed) and (c) second order scattering. Likewise panel (d) through (f) are from the side, and (d) is all orders of scattering, (e) only first order (zoomed), and (f) only second order.

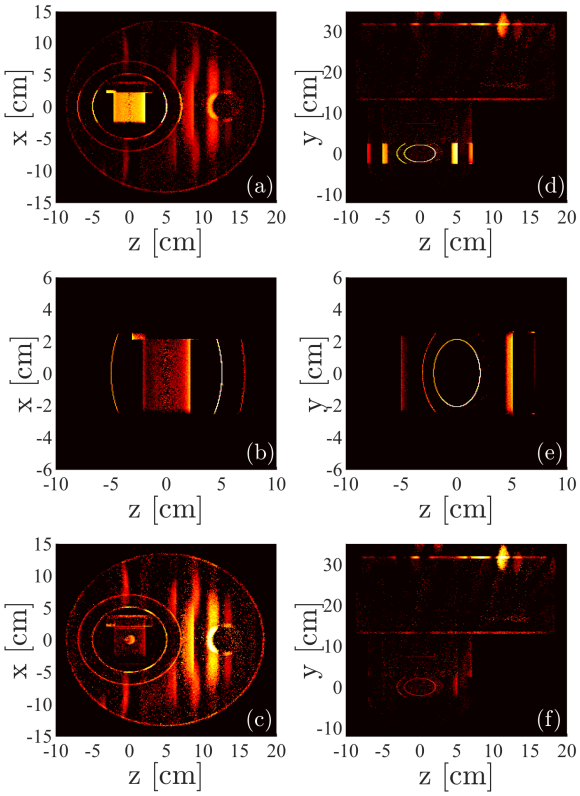

Figure 26. Scattering positions within sample environment for rays that satisfy conditional B shown in figure 23. Panel (a) through (c) are from a top view, (a) being all scattering, (b) only first order scattering and (c) second order scattering. Likewise panel (d) through (f) are from the side, and (d) is all orders of scattering, (e) only first order, and (f) only second order.

Miller indices	2θ	1st order	2nd order	3rd order	Reference
111	38.2°	5.0%	4.3%	14.2%	14.2%
200	44.4°	3.3%	2.4%	6.9%	9.2%
220	64.5°	4.9%	2.1%	6.9%	11.1%
311	77.5°	62.6%	3.2%	14.8%	19.0%
222	81.7°	9.7%	0.9%	4.1%	5.1%
400	98.1°	4.2%	0.5%	2.4%	3.3%
331	111°	3.1%	1.4%	8.1%	10.1%
420	115°	2.7%	1.5%	8.4%	9.8%
422	135°	2.2%	1.4%	9.1%	9.0%
511/333	158°	2.4%	82.3%	25.1%	9.1%

Table VII. Table over distribution of scattering per powder line for conditional B. The reference column is the probability for all scattering without any conditional.

VI. DISCUSSION

A. Validation against existing McStas components

Validation of the Union processes were done against the regular McStas components of which they were based.

The results were as expected for the Incoherent and Single crystal processes, where all deviations were consistent with the Monte Carlo noise estimated by McStas. The Powder process which was compared to the PowderN component did show some small differences that can be explained by the absence of multiple scattering in the reference component. In this case the scattering signal was validated for the first order scattering.

Further work would be required to validate the Union powder process for higher orders of scattering. This could be done either against other code that includes multiple scattering, by a detailed comparison to analytical expres-

sions, or by an experiment.

B. Simulation compared to MARI measurement

The comparison between the simulated and measured MARI experiment did show that many aspects were replicated well by the simulation, but still had a shortcoming in the description of the empty sample environment. As mentioned, we believe the primary reason for this discrepancy is due to texture in the aluminium introduced in production. This explanation alone is however not sufficient to explain the discrepancy, as this should not change the ratio between the intensities of the 200 and 400 peaks, yet these are different in measurement and simulation. The most probable explanations would be an error in the simulation code or an unknown difference between the simulated and real scattering system.

Since the used experiment was not performed with the intention of being replicated by simulation, some details were not measured and are impossible to reconstruct to full accuracy.

A dedicated experiment on MARI or on another beamline would be needed to perform a detailed experimental validation of the Union components, and such endeavours are always a prudent exercise for the McStas package overall[28].

C. Demonstration of Union components

The analysis of the multiple scattering background from the MARI cryostat served as a demonstration of both the new possibilities brought to McStas by the Union components and the relevance of the problem they solve. It is now possible to easily model complex sample environments which yield the full multiple scattering signal and can be analyzed in great detail.

The background analysis done does not correspond to the real instrument due to some shielding not being simulated, and thus serves to show what this shielding can prevent. Future simulations will include the additional shielding, and a rerun of the scans over the incoming energy shown in figure 19 can become a useful tool for selecting the best possible energy. Furthermore, the full data set for each energy will be available, allowing the researchers to view the expected multiple scattering and make sure it is not located in the $(\hbar\omega, 2\theta)$ regions that are most important for their experiment.

The investigations of the two peaks in figure 23 showed their origins to be related to the vessel above the sample, not usually suspected of being a major background source. Shielding may, however, already have been in place at MARI to avoid this background.

These new capabilities allow McStas to become part of the design of sample environments as they can be modelled to a reasonable precision and can be tested on the comprehensive library of McStas instruments.

The accuracy that can be achieved in virtual experiments is significantly increased by the multiple scattering in complex geometries, but also the possibility for multiple scattering between an arbitrary number of processes. This serves to enhance all use cases for virtual experiments including experiment planing, evaluating proposals, and even as a means of data reduction[17].

D. Collaboration on scattering processes

It has been a high priority to lower the barrier of entry for contributing new physics to the Union components. This was achieved by moving the geometry and many technical Monte Carlo sampling tasks away from the process components. It is the hope of the authors that this will allow a broader part of the neutron scattering community to contribute scattering processes relevant for their work into the pool of McStas functionality.

E. Performance of Union components

One of the main benefits of using McStas for instrument simulations is the performance of the software. Simulations are to be feasible on a laptop, and jeopardizing this notion is not an option. The MARI model runs the standard $1 \cdot 10^6$ rays in 6 seconds on the authors laptop[29], which is within the order of magnitude expected for simple McStas instruments. Simulations have been performed with more that 600 volumes, and these are still manageable on a laptop, as great care have been placed on scalability with increasing number of volumes.

The Union components does, however, add a large amount of possible paths through the scattering system, which in turn requires a larger number of simulated rays to sample all possibilities. Furthermore, since multiple scattering is one of the main benefits, the use of focusing which forces scattering in certain solid angles (usually onto a detector) will significantly change the results. For these reasons, the computational requirements for using the Union components are in practice larger than for typical McStas simulations, but still within reasonable computational requirements.

F. Outlook

The most important task yet to be done in the Union project is a full validation of the multiple scattering model in a dedicated validation experiment. This will require a detailed description of the sample environment to be available and an accurate model of the instrument. It is, however, important in order to build trust in the accuracy of the software.

The process library is to be expanded with with inelastic processes, greatly improving the possible virtual experiments.

In terms of new features there are ideas for an expansion including surface effects as this will expand the use cases for the software to include super mirrors for optics (both inside sample environment, but also for extraction systems) and samples for reflectometry. In addition, the material refractive index could be included.

The performance of the code is expected to improve with further revisions as debugging tools can be removed.

VII. CONCLUSION

The McStas Union components were introduced and the differences from previous McStas implementations highlighted, primarily the full multiple scattering among a large number of volumes, the balancing between an arbitrary number of scattering processes in a material, and the easier addition of new scattering processes.

Validation of the incoherent, powder and single_crystal scattering processes were performed, showing high agreement with a few discrepancies that will be investigated further.

Simulations of the ISIS powder time of flight spectrometer MARI were performed and compared to measurements showing agreement in all aspects, but the peak intensities of aluminium in the empty cryostat. This is probably partly explained by the texture introduced in production of the sample environment, but may also be due to inaccuracies in the simulated system.

Furthermore the multiple scattering background from the used cryostat were investigated showing a surprisingly rich structure. A scan of the incoming energies revealed a strong dependence on this parameter and small energy intervals of comparatively low background were identified. The Union logger and conditional components were further used to analyse two multiple scattering peaks and it was identified that the vessel above the sample container contributed to both.

ACKNOWLEDGEMENTS

We thank Henrik Jacobsen, Jonas O. Birk, Peter K. Willendrup and Erik B. Knudsen for discussions on the topic of this paper. We thank Jonathan Taylor for detailed information about MARI and the procedures commonly used for calibration and data analysis. We thank Maria Retuerto and Christopher Rhl Andersen for their work on preparing the sample. We thank the ESS DMSC for providing computing power, and the Danish Agency for Research and Innovation for their support through the contribution to the ESS update phase.

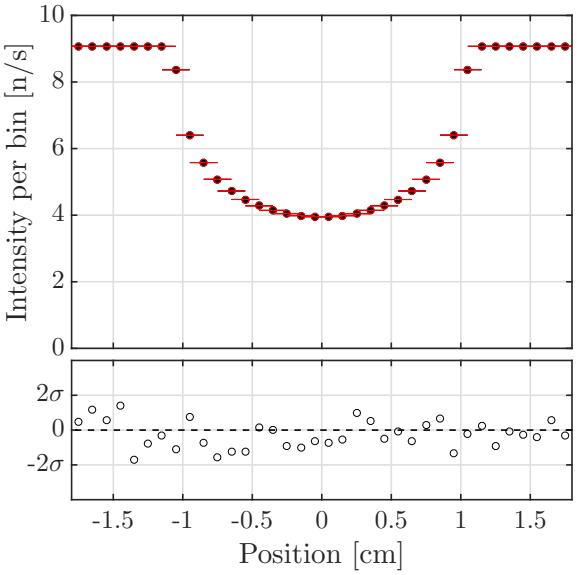

Figure 27. Transmission detector for Union powder sample (black filled) and traditional PowderN sample component (red empty). Lower panel shows the difference for each point relative to the error on the difference introduced by the Monte Carlo technique.

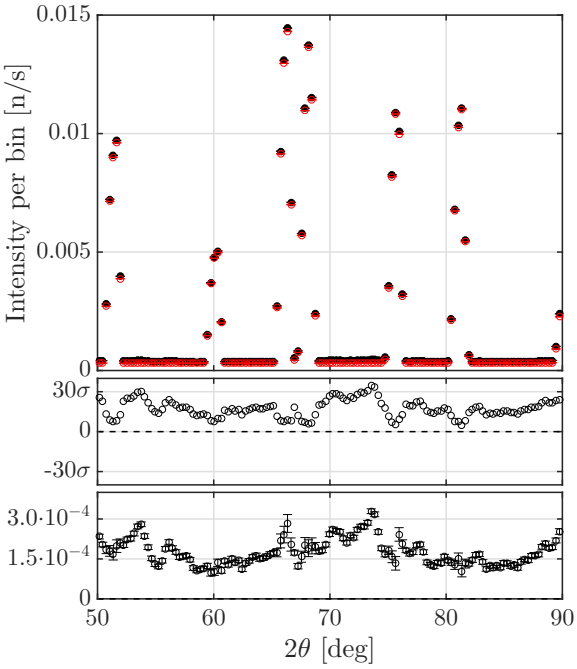

Figure 28. Bragg peaks simulated by Union powder sample (black filled) and PowderN (red empty). Middle panel shows the difference for each point relative to the error on the difference introduced by the Monte Carlo technique. The bottom panel shows the absolute difference, with a positive value being higher intensity for the Union powder sample.

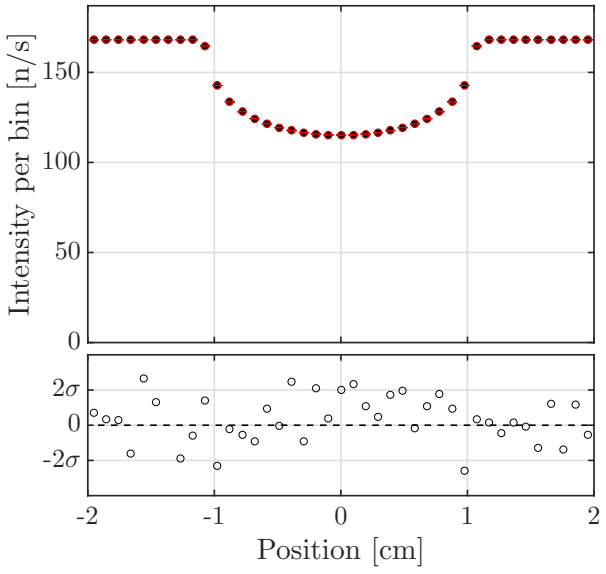

Figure 29. Simulated transmission for rays that did not scatter, results for Union components (black filled) and Single_crystal (red empty). Lower panel shows the difference for each point relative to the error on the difference introduced by the Monte Carlo technique.

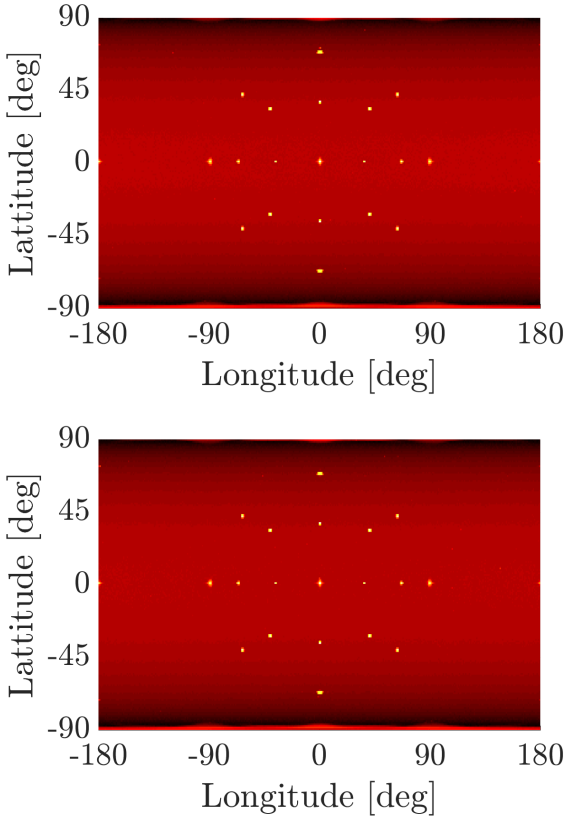

Figure 30. Simulation of single crystal diffraction using spherical detectors covering all directions for both Union components (top) and Single_crystal (bottom).

Appendix A: Additional figures

Appendix B: Additional features

Explanation of further features that may be important for certain users, but did not fit into the narrative of the manuscript.

1. Masks

It is possible to place Mask volumes in the simulation that does not have a specified material, but instead masks a number of other volumes. A masked volume is only simulated in the regions covered by both the original volume and the mask. This can for example be used to create thin windows in limited parts of a sample environment.

In addition several mask volumes can mask a single volume, and depending on user input they all need to cover the same region for that region to be simulated, or just one mask and the original volume need to cover a region.

2. Exit geometry

It is possible to mark a volume as an Exit volume by giving the material definition "Exit". When a ray intersects such an exit volume, the ray leaves the current Union_master component. This is useful for example when placing a detector inside a sample environment or similar.

3. Activation counter

Under normal circumstances, each geometry component will only be used by the next Union_master component. Thus several sets of volumes each with their own master can be used to simulate several independent areas with multiple scattering. This could for example be a separate monochromator assembly and sample environment. It is however possible to adjust a quantity named the activation counter for a volume to alter this behaviour, as the activation counter selects how many of the next master components a geometry component participates in. In the example with the monochromator and sample environment, one could have an activation_counter of 2 for volumes describing a filter between them, and these would be simulated in both assemblies.

This feature along with exit volumes provides a powerful tool for including regular McStas components inside

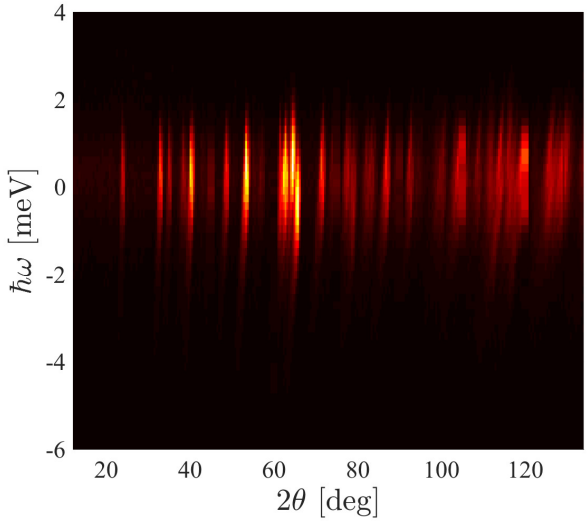

Figure 31. Measured scattering from cryostat and Ni_3TeO_6 sample on MARI with a selected energy of 35.19 meV from the Gd chopper running at 250 Hz.

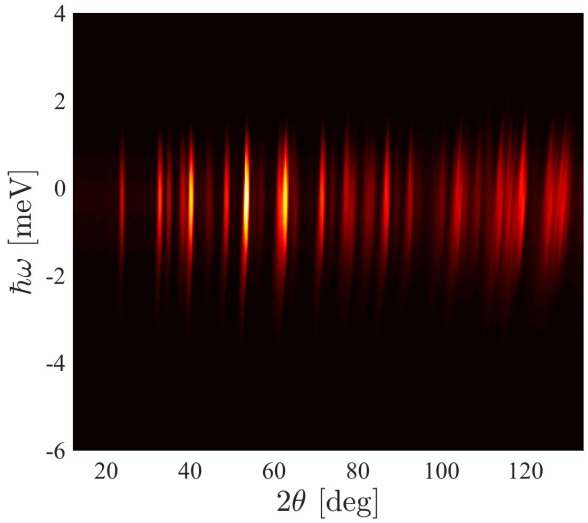

Figure 32. Simulated scattering from cryostat and Ni_3TeO_6 sample on MARI with a selected energy of 35.19 meV from the Gd chopper running at 250 Hz.

a large ensemble of Union components. A large number of volumes with activation counter set to 2 could be used with an exit volume that has activation counter 1 and is placed around a regular component. The next Union_master component will thus simulate the ensemble as normal, until the exit volume may be reached, where the ray is handled by the regular McStas component. After the ray leaves the regular McStas component, it is sent to the next Union_master that can continue the simulation within the same ensemble of volumes, but without the exit volume. The issue with this approach is that the regular McStas component will effectively become invisible for the rays after their first interaction, but this is appropriate in many cases, for example monitors or a resolution sample.

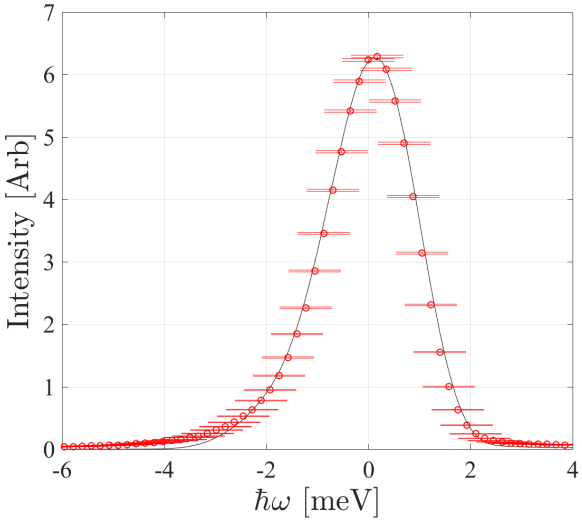

Figure 33. Comparison between data from Ni_3TeO_6 powder taken at MARI (red) and the McStas simulation using Union components (black). Here the scattering is summed over all angles to view the energy dependence which is dominated by elastic scattering and the energy resolution of the instrument.

4. Tagging

The Union_master component records a simple history for each ray. The history consists of a series of events undertaken by a ray, which can be changing volume or a scattering event, in chronological order. All rays that propagate from volume 0 to volume 1, undergoes scattering process 2 of volume 1, then propagates back to volume 0 are considered the same history. These histories are collected and sorted after the total intensity that leaves the master component with a specific history. A sample of the top 15 histories for a simple setup is displayed in text box 1.

The file starts with a short description of each volume including the assigned material and the scattering processes associated with that material.

The first number in a row of data is the number of rays with this history, the next is the total intensity, and then the string containing the history. VX refers to volume number X, and PX refers to process number X within the current volume. When there are volumes with different materials, PX can refer to different processes depending on which volume the ray is currently in, meaning P0 in

```
History file written by the McStas component Union_master
----- Description of the used volumes -----------------------------------------------------------
V0: Surrounding vacuum
V1: powder_container  Material: Al   P0: Al_incoherent P1: Al_Powder
V2: powder_inside_container  Material: Cu_powder   P0: Cu_incoherent_process P1: Cu_powder_process
----- Histories sorted after intensity ----------------------------------------------------------
12221626 N I=4.188166E-06        V0
1882051  N I=1.052731E-06        V0 -> V1 -> V2 -> V1 -> V0
1517013  N I=6.213315E-07        V0 -> V1 -> V0
188661   N I=8.043799E-08        V0 -> V1 -> V2 -> P0 -> V1 -> V0
752943   N I=3.823911E-08        V0 -> V1 -> V2 -> P1 -> V1 -> V0
771437   N I=2.176363E-08        V0 -> V1 -> P1 -> V0
181532   N I=1.101451E-08        V0 -> V1 -> P1 -> V2 -> V1 -> V0
286771   N I=7.628450E-09        V0 -> V1 -> V2 -> V1 -> P1 -> V0
18736    N I=1.948079E-09        V0 -> V1 -> V2 -> P0 -> P0 -> V1 -> V0
75736    N I=1.319653E-09        V0 -> V1 -> V2 -> P1 -> P0 -> V1 -> V0
33463    N I=1.100647E-09        V0 -> V1 -> V2 -> V1 -> P1 -> V2 -> V1 -> V0
74590    N I=1.016961E-09        V0 -> V1 -> V2 -> P0 -> P1 -> V1 -> V0
301006   N I=6.623860E-10        V0 -> V1 -> V2 -> P1 -> P1 -> V1 -> V0
18169    N I=4.341707E-10        V0 -> V1 -> P1 -> V2 -> P0 -> V1 -> V0
13310    N I=4.054218E-10        V0 -> V1 -> P0 -> V0
```

Text box 1. Example of tagging output from the Union_master component, here for a setup consisting of an aluminium can containing a copper powder. The most common history is the ray missing the can entirely, followed by the ray passing through the entire setup. The next two histories contain a scattering in the copper using the incoherent and powder process respectively.

"V0 -> V1 ->P0" and "V0 -> V2 -> P0" refers to two different processes if volume 1 and volume 2 are different materials.

In this example, $2 \cdot 10^7$ rays were simulated, but only $2.5 \cdot 10^4$ unique histories were sampled, making the data file manageable at just 2.8 MB. The size for more complicated cases can be significantly larger, and if it becomes problematic (needs to fit in memory) the number of unique histories can be limited with component input.

There are many practical uses for the history information. If for example one wants to estimate the background originating from a certain part of a sample holder described by volume X, one simply adds the intensity of all histories that scattered in that volume by searching for "VX -> P". If only background at the detector is important, one can place an exit volume with number Y at the detector and add the intensities for all histories that contain the string "VX -> P" and ends in "VY". This have always been possible with McStas by tagging the neutrons manually using EXTEND, but that requires running the simulation again in order to investigate a new problem, here all histories are available after one simulation.

REFERENCES

[1] "McStas webpage," (2017), www.mcstas.org.

[2] K. Lefmann and K. Nielsen, "McStas, a general software package for neutron ray-tracing simulations," Neutron News, **10**, 20–23 (1999), ISSN 1044-8632.

[3] P. Willendrup, E. Farhi, and K. Lefmann, "McStas 1.7 - A new version of the flexible Monte Carlo neutron scattering package," Physica B: Condensed Matter, **350**, 735–737 (2004), ISSN 09214526.

[4] P. K. Willendrup, E. B. Knudsen, E. Klinkby, T. Nielsen, E. Farhi, U. Filges, and K. Lefmann, "New developments in the McStas neutron instrument simulation package," Journal of Physics: Conference Series, **528**, 012035 (2014), ISSN 1742-6588.

[5] P. Willendrup, E. Farhi, E. B. Knudsen, U. Filges, and K. Lefmann, "McStas: Past, present and future," Journal of Neutron Research, **17**, 35–43 (2014).

[6] J. Šaroun and J. Kulda, "RESTRAX a program for TAS resolution calculation and scan profile simulation," Physica B: Condensed Matter, **234-236**, 1102–1104 (1997), ISSN 09214526.

[7] J. Saroun and J. Kulda, "Neutron ray-tracing simulations and data analysis with RESTRAX," (2004).

[8] D. Wechsler, G. Zsigmond, F. Streffer, J. A. Stride, and F. Mezei, "Monte-Carlo simulations for instrumentation at pulsed and continuous sources," Physica B: Condensed Matter, **276-278**, 71–72 (2000), ISSN 09214526.

[9] G. Zsigmond, K. Lieutenant, and F. Mezei, "Monte Carlo simulations of neutron scattering instruments by VITESS: Virtual instrumentation tool for ESS," Neutron News, **13**, 11–14 (2002), ISSN 1044-8632.

[10] C. Zendler, K. Lieutenant, D. Nekrassov, and M. Fromme, "VITESS 3 - Virtual instrumentation tool for the European Spallation Source," Journal of Physics: Conference Series, **528**, 12036 (2014), ISSN 14772655.

[11] J. Copley, P. Verkerk, A. van Well, and H. Fredrikze, "Improved Monte Carlo calculation of multiple scattering effects in thermal neutron scattering experiments," Computer Physics Communications, **40** (1986), ISSN 00104655, doi:10.1016/0010-4655(86)90118-9.

[12] P. Seeger, "Neutron instrument simulations in the next millennium," Physica B: Condensed Matter, **283**, 433–435 (2000), ISSN 09214526.

[13] P. Seeger, L. Daemen, T. Thelliez, and R. Hjelm, "NISP : The neutron instrument simulation package at Los Alamos National Laboratory Scientific Reviews NISP : The Neutron Instrument Simulation Package at Los Alamos," Neutron News, **13**, 20–23 (2002).

[14] P. A. Seeger, "Scattering and multiple scattering in NISP," Nuclear Instruments and Methods in Physics Research Section A: Accelerators, Spectrometers, Detectors and Associated Equipment, **510**, 290–299 (2003).

[15] P. A. Seeger and L. L. Daemen, "The neutron instrument simulation package, NISP," Proc. SPIE 5536, Advances in Compu-

tational Methods for X-ray and Neutron Optics, **5536**, 109–123 (2004), ISSN 0277786X.

[16] J. Y. Y. Lin, H. L. Smith, G. E. Granroth, D. L. Abernathy, M. D. Lumsden, B. Winn, A. A. Aczel, M. Aivazis, and B. Fultz, "MCViNE - An object oriented Monte Carlo neutron ray tracing simulation package," Nuclear Instruments and Methods in Physics Research, Section A: Accelerators, Spectrometers, Detectors and Associated Equipment, **810**, 86–99 (2016), ISSN 01689002, arXiv:arXiv:1504.02776v1.

[17] K. Lefmann, P. Willendrup, L. Udby, B. Lebech, K. Mortensen, J. Birk, K. Klenø, E. Kndusen, P. Christiansen, J. Saroun, J. Kulda, U. Filges, M. Konnecke, P. Tregenna-Piggott, J. Peters, K. Lieutenant, G. Zsigmond, P. Bentley, and E. Farhi, "Virtual experiments : the ultimate aim of neutron ray-tracing simulations," Journal of Neutron Research, **16**, 97–111 (2008).

[18] A. Ravn, P. K. Willendrup, K. Nielsen, B. H. Larsen, A. B. Abrahamsen, L. Arleth, H. Ronnow, and K. Lefmann, "On Monte Carlo ray-tracing simulation of neutron scattering samples," Unpublished (2011).

[19] P. Willendrup, U. Filges, L. Keller, E. Farhi, and K. Lefmann, "Validation of a realistic powder sample using data from DMC at PSI," Physica B: Condensed Matter, **385-386**, 1032–1034 (2006), ISSN 09214526.

[20] P. Willendrup, E. Farhi, E. Knudsen, U. Filges, and K. Lefmann, "Component Manual for the Neutron Ray-Tracing Package McStas, version 2.3," Tech. Rep. (Technical University of Denmark, 2016).

[21] M. Arai, "Dynamic structure factor of non-crystalline and crystalline systems as revealed by MARI, a neutron chopper instrument," Advances in Colloid and Interface Science, **71-72**, 209–232 (1997), ISSN 00018686.

[22] "ISIS webpage," (2017), http://isis.stfc.ac.uk.

[23] G. Bergerhoff and I. D. Brown, "Inorganic Crystal Structure Database," Acta Crystallographica Section A Foundations of Crystallography, **37**, C342–C342 (1981), ISSN 0108-7673.

[24] "ICSD database," (2017), https://icsd.fiz-karlsruhe.de.

[25] E. Farhi, Y. Debab, and P. Willendrup, "IFit: A new data analysis framework. Applications for data reduction and optimization of neutron scattering instrument simulations with McStas," Journal of Neutron Research, **17**, 5–18 (2014), ISSN 14772655.

[26] "NIST cross section database," (2017), https://www.ncnr.nist.gov/resources/n-lengths/.

[27] Ravn, A.K., K. Røhl, T. Guidi, and K. Lefmann, "Paper on Ni3TeO6 results," (2017).

[28] L. Udby, P. K. Willendrup, E. Knudsen, C. Niedermayer, U. Filges, N. B. Christensen, E. Farhi, B. O. Wells, and K. Lefmann, "Nuclear Instruments and Methods in Physics Research A Analysing neutron scattering data using McStas virtual experiments," Nuclear Instruments and Methods in Physics Research Section A: Accelerators, Spectrometers, Detectors and Associated Equipment, **634**, 138–143 (2011).

[29] These simulations are performed without chopper so that all rays reach the sample environment.

A.4 Exploring performance of neutron guide systems using pinhole beam extraction

This paper was included in my master thesis titled "Optimizing neutron guides using the minimalist principle and guide_bot", and is thus not to be included in the assessment of this thesis, it is however included for completeness. The paper was published in Nuclear Instruments and Methods in Physics Research, Section A.

Abstract

We perform an optimization of pinhole neutron guide systems under systematically varying conditions. It is investigated how neutron guide systems consisting of a parabolic feeder inside the biological shielding followed by a pinhole and an elliptical guide perform with different pinhole sizes and divergence requirements. We have clarified in which situations such a guide system is a viable choice and when the parabolic feeder is necessary in terms of neutron transport. The advantage of this design is the reduction of background from fast thermal neutrons compared to a system without a pinhole, hence the smallest possible pinhole is of interest. It is found that instruments with divergence requirements of $\pm 1.0^\circ$ will have excellent neutron transport with a 3×3 cm^2 pinhole, while lower divergence requirements of $\pm 0.5^\circ$ can do with a smaller pinhole of 2×2 cm^2. The feeder effectively reduces the necessary pinhole size, and is especially beneficial for short instruments. In addition to these qualities, a feeder will often smoothen the divergence profile, mostly for longer instruments.

My contribution

The goal was to study a certain guide geometry in connection to the guide task force at ESS. Kim Lefmann took the task upon his group, and the task was shared among H. Jacobsen, U. B. Hansen and myself who took decisions on how to approach the simulation task supervised by K. Lefmann. H. Carlsen wrote the Elliptical_guide_gravity component that I validated. I wrote the McStas instrument file which was the core of the simulation, and participated in discussions on analysing the results. I wrote the entire manuscript.

Nuclear Instruments and Methods in Physics Research A 729 (2013) 387–398

Contents lists available at ScienceDirect

Nuclear Instruments and Methods in Physics Research A

journal homepage: www.elsevier.com/locate/nima

Exploring performance of neutron guide systems using pinhole beam extraction

Mads Bertelsen [a,b,*], Henrik Jacobsen [a,b], Ursula Bengaard Hansen [a,b], Henrik Hoffmann Carlsen [a], Kim Lefmann [a,b]

[a] Nanoscience Center and eScience Center, Niels Bohr Institute, University of Copenhagen, Denmark
[b] ESS Design Update Program, Denmark

ARTICLE INFO

Article history:
Received 30 January 2013
Received in revised form
16 July 2013
Accepted 20 July 2013
Available online 26 July 2013

Keywords:
Neutron optics
Ballistic neutron guides
Elliptical guides
ESS
McStas
IFit

ABSTRACT

We perform an optimization of pinhole neutron guide systems under systematically varying conditions. It is investigated how neutron guide systems consisting of a parabolic feeder inside the biological shielding followed by a pinhole and an elliptical guide perform with different pinhole sizes and divergence requirements. We have clarified in which situations such a guide system is a viable choice and when the parabolic feeder is necessary in terms of neutron transport. The advantage of this design is the reduction of background from fast thermal neutrons compared to a system without a pinhole, hence the smallest possible pinhole is of interest. It is found that instruments with divergence requirements of $\pm 1.0^\circ$ will have excellent neutron transport with a $3\times 3\,\mathrm{cm}^2$ pinhole, while lower divergence requirements of $\pm 0.5^\circ$ can do with a smaller pinhole of $2\times 2\,\mathrm{cm}^2$. The feeder effectively reduces the necessary pinhole size, and is especially beneficial for short instruments. In addition to these qualities, a feeder will often smoothen the divergence profile, mostly for longer instruments.

1. Introduction

In the design of instrumentation for a pulsed neutron source, the background flash from the pulse is a major concern. The main constituents are gamma radiation and fast neutrons, which both require large quantities of shielding to be suppressed. These background contributors can however propagate freely within the guide itself. Hence, a guide system consisting of a highly transporting single long ellipse [1,2] may lead to intolerably large background levels [3].

It is possible to increase the amount of shielding between moderator and sample by using a guide system that narrows down to a small pinhole at some point as suggested in Ref. [4]. Such a pinhole could also be beneficial for a pulse shaping chopper, which is positioned as close to the moderator as the primary shielding will allow. In order to achieve the smallest possible pinhole while still maintaining a high transport efficiency, a system with a narrowing "feeder" could be needed in order to lead the neutron trajectories through the pinhole, effectively by increasing the divergence of the beam. Such narrowing guide systems have been investigated in the form of double trumpets with flat sides for example in Ref. [5].

In this paper the effect of a pinhole and a parabolic feeder is investigated with computer simulations. An elliptical guide is used to transport the high-divergence neutrons from the pinhole to the sample. This system is then optimized for a large range of pinhole sizes, guide lengths, and divergence requirements.

2. Description and simulation of the guide system

The instrument parameters are chosen to resemble a typical instrument foreseen for the European Spallation Source (ESS) [6,7]. This implies that no optical element can start closer than 2 m from the moderator and that the first chopper can be located at 6 m. The square pinhole is placed at 5.9 m, and different sizes are investigated with side lengths varying from 1 cm to 5 cm in 1 cm increments. In addition, the divergence requirement is varied independently between $\pm 0.5^\circ$, $\pm 1.0^\circ$ and $\pm 2.0^\circ$. This is done for different instrument lengths, which are denoted by the distance between chopper and sample, here chosen to be 24 m, 75 m, 150 m and 300 m. In order to highlight the effect of the feeder, each instrument is optimized also without the parabolic feeder; in total 120 guide systems. To enable the large amount of simulations, all guides are modelled without choppers, which are assumed not to affect the relative performance of the guides.

* Corresponding author at: Nanoscience Center and eScience Center, Niels Bohr Institute, University of Copenhagen, Denmark. Tel.: +45 31691008.
E-mail addresses: mads.bertelsen@gmail.com, zxj803@alumni.ku.dk (M. Bertelsen).

0168-9002/$ - see front matter © 2013 Elsevier B.V. All rights reserved.
http://dx.doi.org/10.1016/j.nima.2013.07.062

The intensity on the sample is given in terms of the brilliance transfer which means that the density in five-dimensional phase space (position, divergence, wavelength) is normalized to the phase space density at the moderator. The limit on the spatial dimensions is the sample size while the limit in divergence is the divergence requirement of the instrument. The limits for the wavelength are simply the wavelength band used. The brilliance transfer can be shown as a function of one or more of these dimensions by summing over the remaining dimensions. This value has an intrinsic upper limit of 100%, which is the maximal theoretical transport efficiency allowed by Liouville's theorem [8]. The performance should, however, also be compared to a less restricted guide system, and thus a single elliptical guide starting at 2 m was simulated as a reference.

3. Instrument details

A sketch of the simulated system can be seen in Fig. 1 for one specific instrument length. The moderator is a simple 12×12 cm^2 square moderator with uniform divergence and wavelength distribution. The wavelength band used is 2–10 Å, and all wavelengths are weighted equally in the optimizations. The sample is a 1×1 cm^2 square and the figure of merit is neutron intensity on sample within the given maximum divergence. Even though neutron transport is not perfectly symmetric due to gravity, it was chosen to keep the guide system square by locking the horizontal and vertical free geometrical parameters together. This effectively halves the amount of free parameters and thus greatly reduces the computation time for the optimizations.

The parabolic feeder starts 2 m from the moderator, and the width at this point is a free parameter. The feeder ends at 5.9 m just before the pinhole, and the position of the focus point close to the pinhole is a free parameter. The elliptical guide starts 20 cm after the pinhole, and ends 50 cm before the sample to allow for sample environment, slits, and monitor. The focal points and small axis of the elliptical guide are free parameters. In total, there are five free parameters with the feeder and three free parameters without.

The simulated supermirrors have a critical scattering vector of reflection of $Q_c = mQ_{Ni}$, where m is a number in the range 1–7 and $Q_{Ni} = 0.0217$ Å^{-1} is the critical scattering angle of nickel. The feeder uses $m=6$ supermirrors, while the elliptical guide uses $m=6$ for the first and last 10% of the length, and $m=3$ in the remaining part. The high m values were chosen so that the guide system was not limited by too poor coating. It has been shown that the m values needed in an elliptical guide can be minimized dramatically from this value without losing much performance [9], and it is expected to be possible with this design as well. In the used model, the slope of the reflectivity does not depend on the m value. Both feeder and guide are simulated without waviness in the supermirrors.

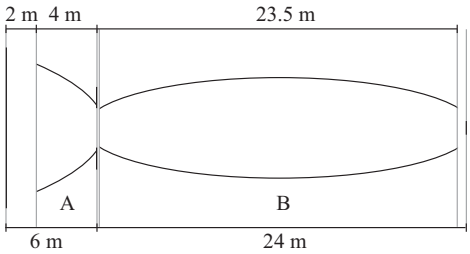

Fig. 1. A sketch of the guide system consisting of the parabolic feeder (A) and an elliptical guide (B) separated by a pinhole situated at the end of the feeder. There is 20 cm separation between the feeder and guide. This specific sketch is the optimized geometry for a 24 m instrument with 3×3 cm^2 pinhole and $\pm 1.0^\circ$ divergence requirement.

4. Computing

The simulations were done in the Monte Carlo ray-tracing simulation package McStas 1.12c [10–12]. The feeder and elliptical guide were both simulated by a new component distributed with McStas 2.0 [13], *Guide_elliptical*, which uses the Newton–Raphson method [14] to iteratively find intersections between the perfect elliptical guide and neutron rays affected by gravity. For this reason there are no guide segments in neither the feeder nor elliptical guide in the simulated guide system. This component uses approximately the computation time of 10 small guide segments made with the *Guide_gravity* component, but to make a sufficiently smooth guide, in excess of 100 segments are needed. Thus the performance of the overall simulation was greatly improved making the large number of optimizations possible. The optimizations and data plotting were performed using iFit [15] for MATLAB. The computations were carried out on the 500 core cluster of the ESS Data Management and Software Center [16].

5. Simulation data

We here show the main results of the simulation work. In every case, only the performance of the optimized guides are considered. In general the simulated neutron intensity is displayed in terms of the brilliance transfer, which has been computed as the intensity at the sample position (within decided wavelength, area, and divergence limits) divided by the similar intensity at the moderator.

5.1. Wavelength dependence of brilliance transfer

In Fig. 2 the brilliance transfer as a function of wavelength is displayed for a single configuration, 24 m with a 1×1 cm^2 pinhole and optimized for a divergence requirement of $\pm 0.5^\circ$. The solid black curve which is without a feeder has an almost constant brilliance transfer of around 30%, which is quite low for this divergence requirement. The dashed red curve is with a feeder which has a much higher brilliance transfer for the entire wavelength range. The brilliance transfer for the guide with feeder is more wavelength dependent, going from a brilliance transfer of

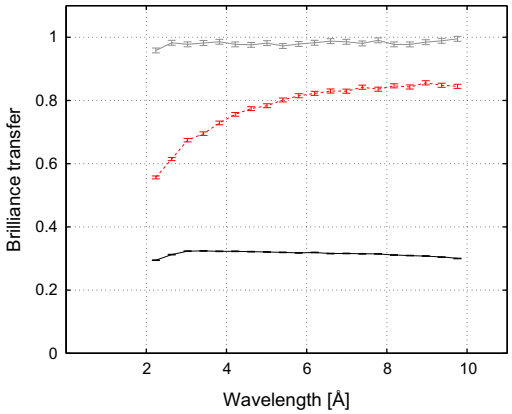

Fig. 2. Brilliance transfer as a function of wavelength for a 24 m instrument with 1×1 cm^2 pinhole and optimized for a $\pm 0.5^\circ$ divergence requirement. The dashed red curve is with the feeder while the solid black is without, and the solid gray curve is the reference elliptical guide without the space restriction. (For interpretation of the references to color in this figure caption, the reader is referred to the web version of this article.)

52% at 2 Å to 85% at 10 Å. The reference guide shown as a solid gray curve has almost perfect brilliance transfer, which is possible without the restriction of having a narrowing pinhole.

The same information as in Fig. 2 is shown for all simulated configurations in Figs. 3–6 for instrument lengths 24 m, 75 m, 150 m and 300 m respectively. The dependence on pinhole size and divergence is explicitly shown in each figure. Results for the 24 m instrument are shown in Fig. 3, where each row represents one divergence requirement and each column is one pinhole size. The bottom row corresponds to a divergence requirement of $\pm 0.5^\circ$, for which the brilliance transfer exceeds 89% over the full 2–10 Å wavelength range with a pinhole of 2×2 cm^2 and a feeder, while a 3×3 cm^2 pinhole is needed to obtain a similar performance without a feeder. A less extreme difference is seen at $\pm 1.0^\circ$ divergence, but the feeder still represents a large improvement for pinhole sizes of 3×3 cm^2 or less. It is noted that the feeder is better suited for longer wavelengths, as it adds almost nothing to

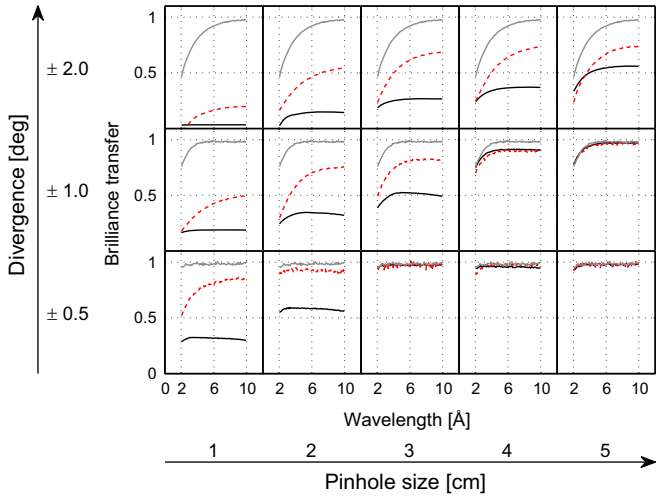

Fig. 3. Brilliance transfer for a 24 m instrument as a function of wavelength. The dashed red curve is with the feeder while the solid black is without, and the solid gray curve is the reference elliptical guide. The individual plots each resemble that of Fig. 2 but for a range of pinhole sizes (displaced horizontally) and divergence requirements (displaced vertically).

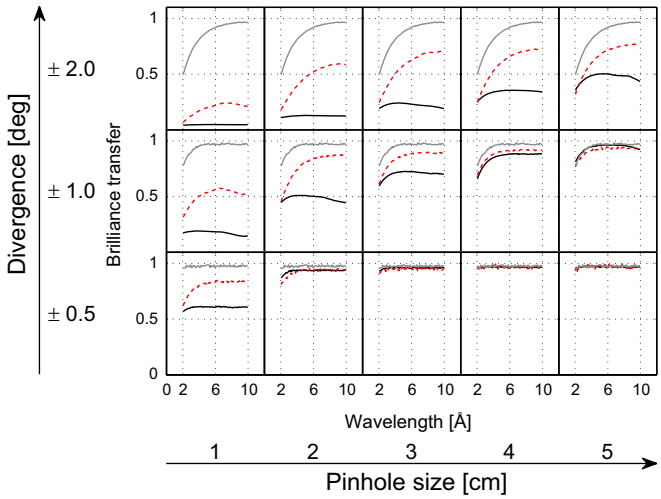

Fig. 4. Brilliance transfer for a 75 m instrument as a function of wavelength. The dashed red curve is with the feeder while the solid black is without, and the solid gray curve is the reference elliptical guide. The individual plots each resemble that of Fig. 2 but for a range of pinhole sizes, divergence requirements and instrument length.

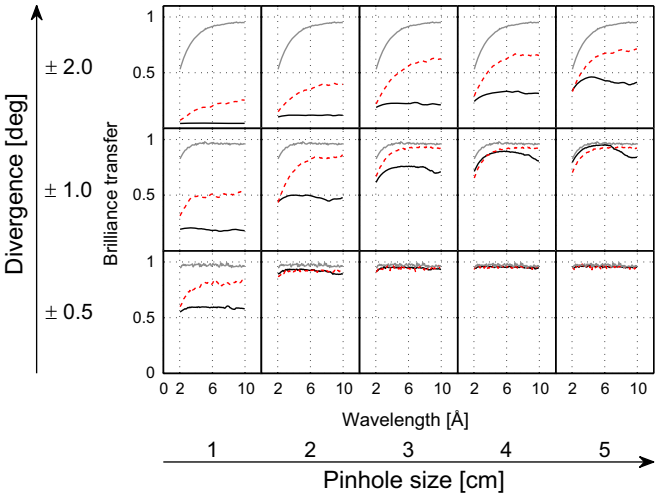

Fig. 5. Brilliance transfer for a 150 m instrument as a function of wavelength. The dashed red curve is with the feeder while the solid black is without, and the solid gray curve is the reference elliptical guide. The individual plots each resemble that of Fig. 2 but for a range of pinhole sizes, divergence requirements and instrument length.

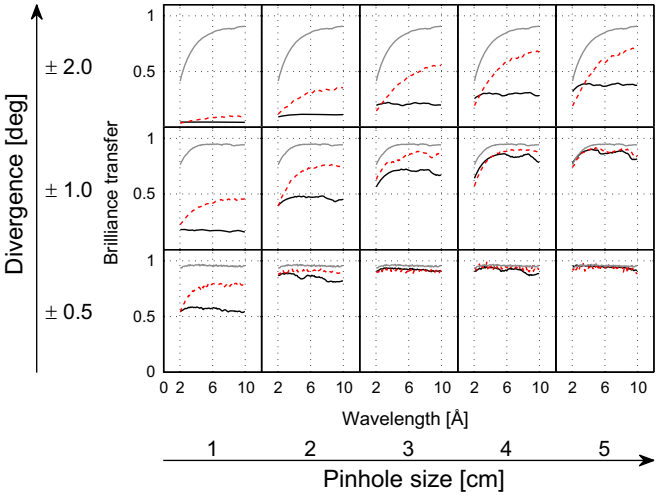

Fig. 6. Brilliance transfer for a 300 m instrument as a function of wavelength. The dashed red curve is with the feeder while the solid black is without, and the solid gray curve is the reference elliptical guide. The individual plots each resemble that of Fig. 2 but for a range of pinhole sizes, divergence requirements and instrument length.

the transmission of the 2 Å neutrons when the divergence is $\pm 1.0^\circ$ or more.

In the case of the 75 m instrument, Fig. 4, it is remarkable that for the low divergence ($\pm 0.5^\circ$), most of the simulated guides yield almost perfect brilliance transfer. The only exception is at 1×1 cm^2 pinhole, where the feeder is a considerable improvement, but still does not reach the reference performance. There is naturally $\pm 0.6^\circ$ divergence at 5.9 m from the 12×12 cm^2 moderator, which is the reason a perfect brilliance transfer is possible without the feeder. The 1×1 cm^2 pinhole does however not perform as well, simply because of the increase in phase-space volume requirement caused by the distance between the guide end and sample. At higher divergences the necessary pinhole size is larger, 3×3 cm^2 would be acceptable for the $\pm 1.0^\circ$ case. The feeder is always an improvement at the extreme $\pm 2.0^\circ$ divergence, but the guide system never quite does a convincing job when compared with the reference guide. In some cases the guide system has a brilliance transfer which decreases towards high wavelength. This effect is caused by gravitation, as test simulations

without gravity yielded monotonically increasing brilliance transfers as a function of wavelength.

For the 150 m instrument, Fig. 5 results are in general similar to the 75 m system. All guide systems have good brilliance transfers (above 90%) for divergence below $\pm 0.5^\circ$ and a pinhole size of 2×2 cm^2 or more, and thus the feeder is unnecessary here. At a divergence requirement of $\pm 1.0^\circ$ the feeder does remarkably well at low pinhole sizes, increasing the performance almost to the reference level at 3×3 cm^2 pinhole. At $\pm 2.0^\circ$, the feeder is an improvement, but seems limited to around 71% of the reference guide performance, even at the maximum pinhole size of 5×5 cm^2.

The 300 m guide system as shown in Fig. 6 performs quite similar to the 150 m system, however the maximal brilliance transfers achieved is a few percent lower because of the increased number of reflections. It should however be noted that a 300 m guide can perform quite close to the theoretically possible value of unity, at least for divergencies up to $\pm 1.0^\circ$.

5.2. Divergence dependence of brilliance transfer

For the same guides as were optimized and presented in Section 5.1, we here show the obtained brilliance transfer as a function of vertical divergence. The data are averaged over wavelength, position and horizontal divergence within the decided limits. The divergence distributions are always shown over the entire $\pm 2.0^\circ$ vertical divergence range, but the brilliance transfer is only summed over the divergence requirement in the horizontal divergence. The horizontal divergence plots are quite similar to the vertical, but are symmetrical as gravity does not affect them directly. Here, they add no new information, and we omit them.

In Fig. 7 the brilliance transfer as a function of vertical divergence is shown for a 24 m instrument with 1×1 cm^2 pinhole and optimized for a $\pm 0.5^\circ$ divergence requirement. The data is averaged over the entire wavelength interval, 2–10 Å. The divergence distribution for the guide without feeder (solid black curve) is quite problematic as the big dip around 0° divergence will make the resolution function more complicated. The instrument with feeder described by the dashed red curve does much better as the shape is much more smooth. The reference elliptical guide also has a simple shape with a very even distribution. The reference guide provides a high brilliance transfer even at divergencies outside the $\pm 0.5^\circ$ interval for which it was optimized, this is not a problem since neutrons with too high divergence can be removed by (distance) collimation.

Figs. 8–11 contain information similar to Fig. 7 but for all the simulated configurations as in the previous section.

In Fig. 8, the brilliance transfer dependence on vertical divergence for the 24 m instrument is shown. Notice how the solid black curve representing a guide without the feeder has quite uneven divergence distributions for small pinholes, mostly in the form of a low intensity region near zero divergence. In most cases, a feeder rectifies this, even while improving the overall transmission. In some cases ($\pm 1.0^\circ$, 2×2 cm^2 pinhole and $\pm 0.5^\circ$, 4×4 cm^2 pinhole), the feeder adds some structure to the divergence distribution in the form of small amplitude oscillations. These are unwanted, but are not punished directly in the optimization. A careful re-optimization of one particular guide system has for all cases tested been able to remove these features without compromising the overall transmission, since there are in general multiple different solutions with similar figures of merit. Due to

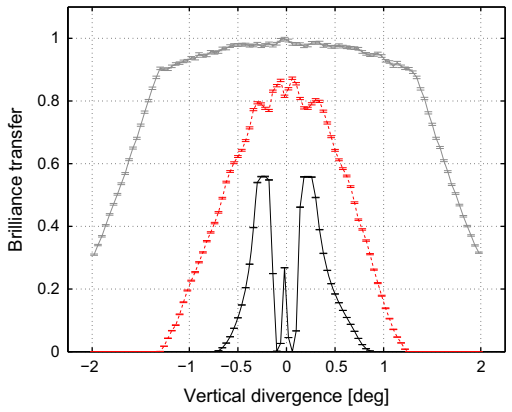

Fig. 7. Brilliance transfer as a function of vertical divergence for a 24 m instrument with 1×1 cm^2 pinhole and optimized for a $\pm 0.5^\circ$ divergence requirement. The dashed red curve is with the feeder while the solid black is without, and the solid gray curve is the reference elliptical guide. (For interpretation of the references to color in this figure caption, the reader is referred to the web version of this article.)

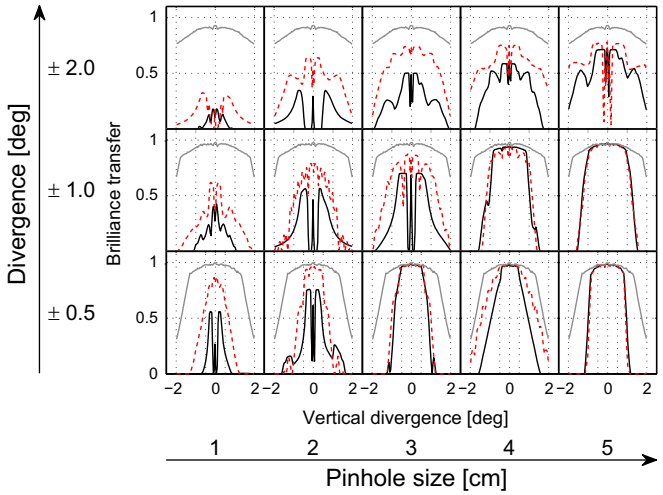

Fig. 8. Brilliance transfer for a 24 m instrument as a function of vertical divergence. The dashed red curve is with the feeder while the solid black is without, and the solid gray curve is the reference elliptical guide. The individual plots each resemble that of Fig. 7 but for a range of pinhole sizes and divergence requirements.

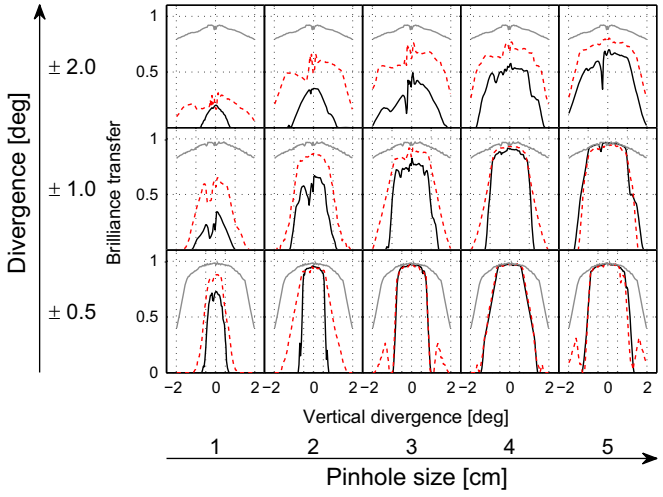

Fig. 9. Brilliance transfer for a 75 m instrument as a function of vertical divergence. The dashed red curve is with the feeder while the solid black is without, and the solid gray curve is the reference elliptical guide. The individual plots each resemble that of Fig. 7 but for a range of pinhole sizes, divergence requirements and instrument length.

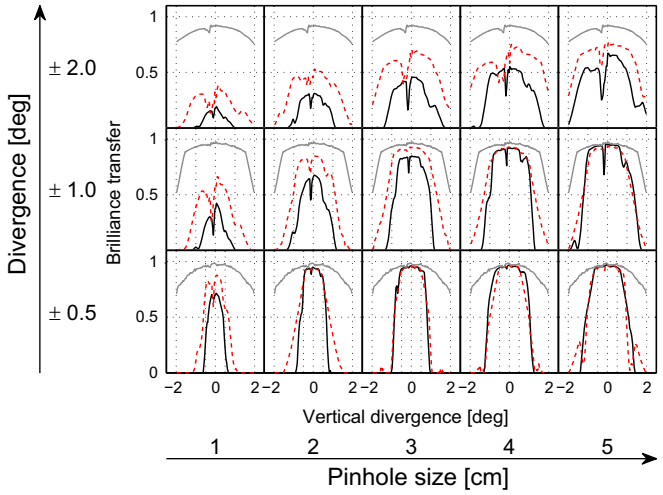

Fig. 10. Brilliance transfer for a 150 m instrument as a function of vertical divergence. The dashed red curve is with the feeder while the solid black is without, and the solid gray curve is the reference elliptical guide. The individual plots each resemble that of Fig. 7 but for a range of pinhole sizes, divergence requirements and instrument length.

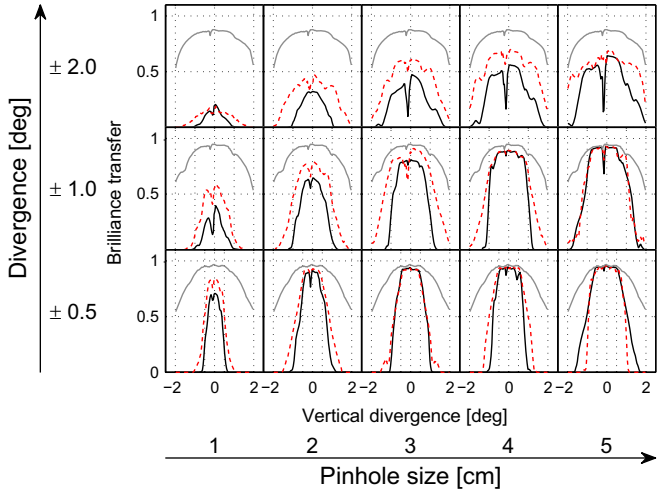

Fig. 11. Brilliance transfer for a 300 m instrument as a function of vertical divergence. The dashed red curve is with the feeder while the solid black is without, and the solid gray curve is the reference elliptical guide. The individual plots each resemble that of Fig. 7 but for a range of pinhole sizes, divergence requirements and instrument length.

the sheer amount of work, we did, however, not reoptimize all affected simulations for smooth divergence distributions.

In Figs. 9 and 10 the vertical divergence is shown for the 75 m and 150 m instruments, respectively. Here, the effect of gravity is more visible because of the longer flight path. In some cases, mostly with $\pm 2.0^\circ$, the divergence distribution is more skewed when the feeder is used. This happens because the feeder transport more high wavelength neutrons, which are in turn affected more by gravity. For the divergencies $\pm 1.0^\circ$ and lower, the divergence profiles seem quite smooth, with the exception of some $1 \times 1\ \mathrm{cm}^2$ pinhole results. In some cases the feeder does yield some unwanted wings in the profile, but this only happens in cases where the pinhole is larger than necessary.

The vertical divergence distribution for the 300 m instrument is shown in Fig. 11 and is similar to the distributions for 75 m and 150 m, but a little more smeared out. With the feeder most of these distributions would provide smooth resolution functions, as the feeder seems to fill out the dip commonly seen close to zero divergence.

5.3. Moving the slit closer to the moderator

For the purpose of increasing the effective divergence leaving the pinhole, one could consider moving the pinhole closer to the moderator. We here show a few set-ups that exemplify how and when this scheme has a possibility of producing useful results. We choose to place the pinhole at 3.44 m in order to increase the effective divergence to $1.0^\circ \times 1.0^\circ$ at the pinhole position. Two 150 m guides without feeder were optimized, one with $\pm 1.0^\circ$ divergence requirement and $2 \times 2\ \mathrm{cm}^2$ pinhole and the other with $\pm 2.0^\circ$ divergence requirement and $3 \times 3\ \mathrm{cm}^2$ pinhole. The brilliance transfer as a function of wavelength can be seen in Fig. 12. For the guide with $\pm 1.0^\circ$ divergence requirement and $2 \times 2\ \mathrm{cm}^2$ pinhole, moving the slit closer to the moderator reduced the brilliance transfer significantly. For the guide with $\pm 2.0^\circ$ divergence requirement and $3 \times 3\ \mathrm{cm}^2$ pinhole the brilliance transfer did increase, but only marginally.

5.4. Moving both slit and guide closer to the moderator

For completeness we also investigate how the two guides perform when both the slit and guide start are moved closer to the moderator. The slit is located 3.44 m from the moderator with the guide starting 20 cm after. As shown in Fig. 13 this improves performance over the similar system starting further from the moderator which is not surprising. The improvements are comparable to going one step up in slit size in Fig. 5.

In Table 1 the width of the guide at 6.1 m from the moderator is shown. This position is chosen because it is the ideal placement for a pulse shaping chopper under the restrictions imposed on ESS instruments. The chopper will perform better for a narrow guide. For the situations with a large distance between slit and guide start, the width at 6.1 m is more than twice that of the situations with 20 cm between slit and guide. If a feeder is not used and a narrow guide at the first chopper position is required, it seems that starting the guide early is better than just placing the slit early as both the brilliance transfer is higher and the guide at the chopper point is narrower. If the divergence requirement is low, it would also be acceptable to simply start the guide narrow at 6.1 m.

5.5. Specific information on selected guides

In this section detailed results from a few guides are shown in order to check for potential problems which cannot be spotted in the more general data. Spatial and divergence distributions are shown in one dimension with wavelength snapshots, meaning that only neutrons in a very narrow wavelength band were simulated, here 2.0 Å, 3.0 Å, 4.5 Å and 8.0 Å all with a width of 0.01 Å. In the plots the wavelength bands are shown in blue, purple, orange and green which in black/white corresponds to a lighter tone of gray for higher wavelengths. In this way chromatic effects are easily visualized. The spatial and divergence distributions are also shown as brilliance transfer in two-dimensional plots averaged over the entire wavelength band to check the homogeneity. Acceptance diagrams showing the brilliance transfer vs. position and divergence for the same orientation show the phase space for horizontal and vertical directions which can have problematic correlations. Every two-dimensional plot has a white square which shows the limits for which the instrument was optimized. In the two-dimensional brilliance plots we integrate the brilliance transfer over the three dimensions of the figure of merit box which is not shown. Notice that the two-dimensional plots have individual color scales and thus only the structure is visible, absolute comparisons should be done between one-dimensional plots. The chosen configurations are

- 24 m, $\pm 0.5^\circ$, $2 \times 2\ \mathrm{cm}^2$ pinhole without feeder,
- 24 m, $\pm 0.5^\circ$, $2 \times 2\ \mathrm{cm}^2$ pinhole with feeder,

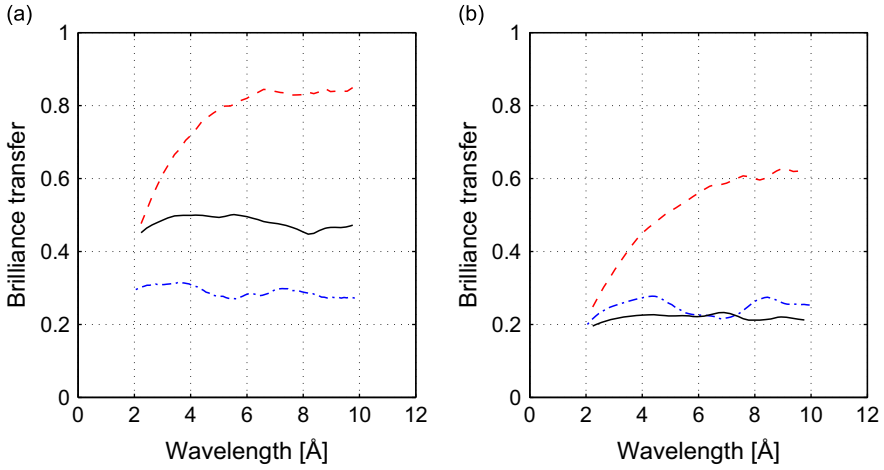

Fig. 12. Brilliance transfer as a function of wavelength for two different 150 m guides. Subplot (a) is for a divergence requirement of $\pm 1.0^\circ$ and 2×2 cm^2 pinhole while (b) is for $\pm 2.0^\circ$ and 3×3 cm^2 pinhole. The red dashed line is with the slit at 5.9 m and with feeder where the black line is without the feeder. The blue dash/dotted line is with the slit at 3.44 m and the guide starting at 6.1 m. (For interpretation of the references to color in this figure caption, the reader is referred to the web version of this article.)

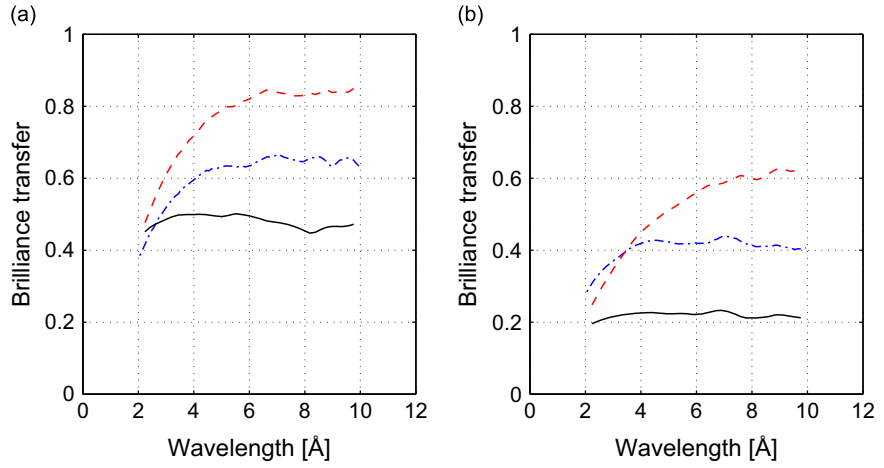

Fig. 13. Brilliance transfer as a function of wavelength for two different 150 m guides. Subplot (a) is for a divergence requirement of $\pm 1.0^\circ$ and 2×2 cm^2 pinhole while (b) is for $\pm 2.0^\circ$ and 3×3 cm^2 pinhole. The red dashed line is with the slit at 5.9 m and with feeder where the black line is without the feeder. The blue dash/dotted line is with the slit at 3.44 m and the guide starting at 3.64 m. (For interpretation of the references to color in this figure caption, the reader is referred to the web version of this article.)

Table 1
Width of two optimized guides at the first chopper position when using different slit and guide start positions. The guide described with (a) has a divergence requirement of $\pm 1.0^\circ$ and a 2×2 cm^2 pinhole while (b) is for $\pm 2.0^\circ$ and 3×3 cm^2. Both guides are 150 m long.

Guide	Slit position (m)	Guide start (m)	Width at 6.1 m (cm)
(a)	5.9	6.1	2.3
	3.44	6.1	5.8
	3.44	3.64	2.5
(b)	5.9	6.1	3.4
	3.44	6.1	9.3
	3.44	3.64	3.8

- 150 m, $\pm 0.5^\circ$, 2×2 cm^2 pinhole without feeder,
- 150 m, $\pm 1.0^\circ$, 3×3 cm^2 pinhole with feeder,
- 150 m, $\pm 2.0^\circ$, 3×3 cm^2 pinhole with feeder.

Results for these five guides are presented in Figs. 14–28. Each guide is described with three figures showing divergence, position and acceptance diagrams which show the correlations between the position and divergence. The difference between the two 24 m instruments is the addition of a feeder, but notice that the elliptical guide between the pinhole and sample does not have the same parameters because each was optimized individually.

In Figs. 14–16 the results for the 24 m instrument without feeder is shown. The spatial and divergence distributions are achromatic with the exception of a wing seen in the vertical divergence plot and a slight shift in the vertical position. The two-dimensional plots show quite some unwanted structure, only the spatial distribution seems acceptable. These problems would result in an unnecessarily complicated resolution function.

Figs. 17–19 show the solution when a feeder is added. Again there are some small wings in the divergence profile in Fig. 17 which are wavelength dependent. The acceptance diagrams in Fig. 19 show much less structure, meaning that the sample is illuminated homogeneously in phase space, at least inside the figure of merit box.

The remaining guides are 150 m with the optimal combination of pinhole and divergence requirement, as judged from the overview plot in Fig. 5. Here the guide for the lowest divergence, $\pm 0.5^\circ$, does not need a feeder, but the guides for higher divergence requirements do. The low divergence results are shown in Figs. 20–22, which look nearly optimal in every way except the vertical divergence distribution which does have some small

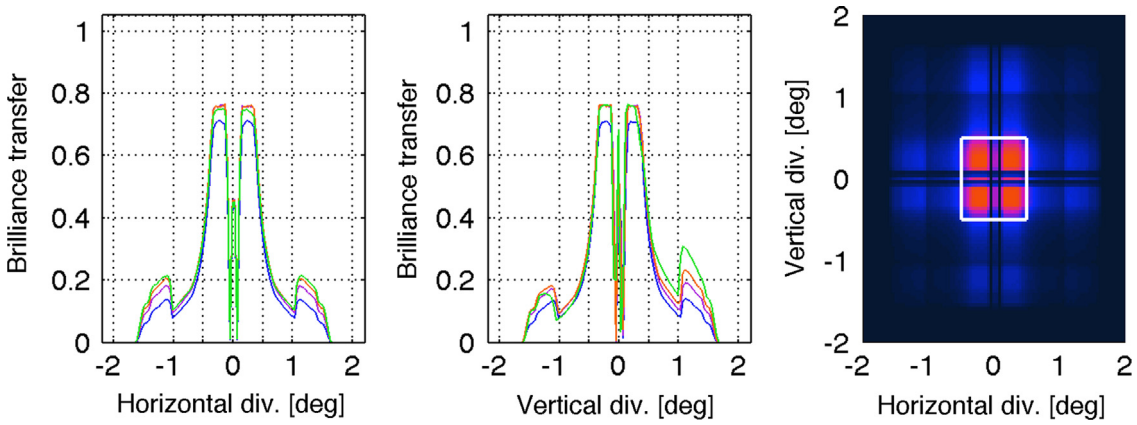

Fig. 14. Data on the divergence for a 24 m guide without feeder optimized for $\pm 0.5^\circ$ divergence requirement with 2×2 cm^2 pinhole.

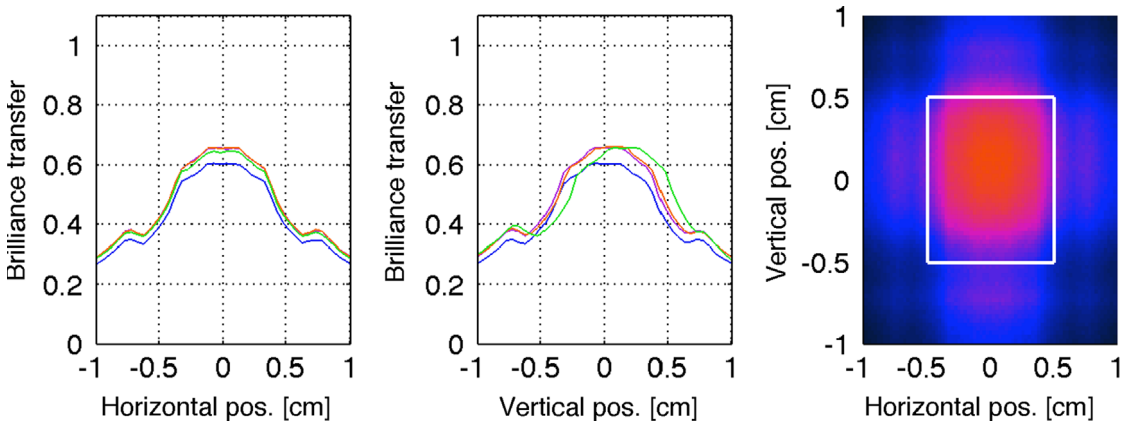

Fig. 15. Data on the spatial distribution for a 24 m guide without feeder optimized for $\pm 0.5^\circ$ divergence requirement with 2×2 cm^2 pinhole.

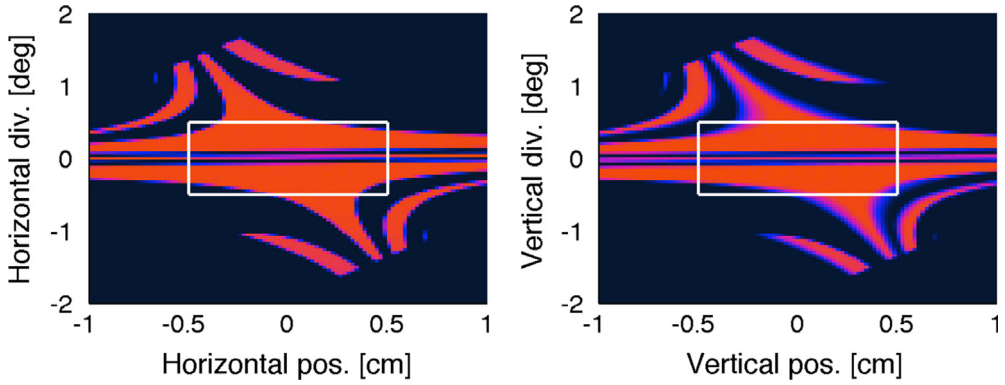

Fig. 16. Acceptance diagrams for a 24 m guide without feeder optimized for $\pm 0.5^\circ$ divergence requirement with 2×2 cm^2 pinhole.

wavelength dependent dips caused by gravity, most are however outside the $\pm 0.5^\circ$ interval which the guide is optimized for.

For the 150 m $\pm 1.0^\circ$ case, Figs. 23–25, the situation is similar for the two-dimensional plots, but there are some chromatic effects in the divergence distribution, where not only the transmission is wavelength dependent, but also the shape. At low wavelength (the blue/dark curve) the distribution looks Gaussian, but at the highest wavelength (green) the distribution is almost flat across $\pm 1.0^\circ$. This may complicate the part of the data analysis related to the momentum transfer, $\vec{q}$, when this guide is used e.g. for a chopper spectrometer. There are no significant problems to be spotted in any of the other plots.

The results for the highest divergence, $\pm 2.0^\circ$, Figs. 26–28 do however have significant issues on nearly every plot. The vertical divergence distribution has the most noticeable problem as a strongly wavelength dependent dip near -0.5° is quite problematic. The two-dimensional plots have a lot of structures in general, only the spatial distribution seems acceptable. Notice that the figure of merit box on the acceptance diagram has some corners where no neutrons are detected – this means that there are no neutrons with very high upward divergence at the bottom of the sample and vice versa.

6. Discussion

In general, the addition of a feeder should never decrease the overall performance as it expands the parameter space for the

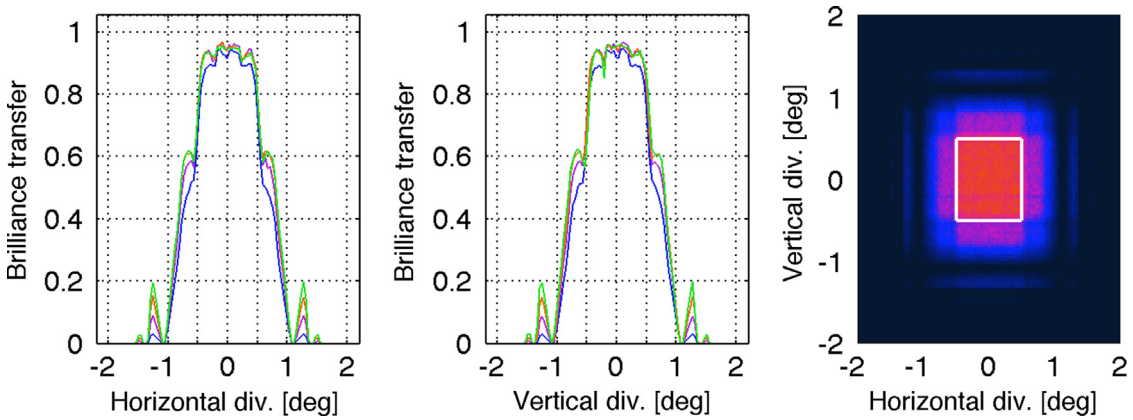

Fig. 17. Data on the divergence for a 24 m guide with feeder optimized for $\pm 0.5^{\circ}$ divergence requirement with 2×2 cm^2 pinhole.

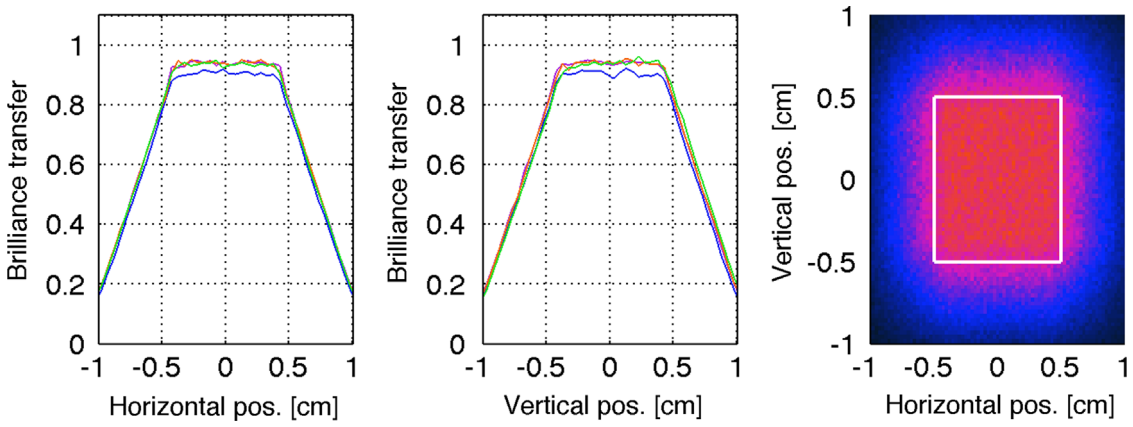

Fig. 18. Data on the spatial distribution for a 24 m guide with feeder optimized for $\pm 0.5^{\circ}$ divergence requirement with 2×2 cm^2 pinhole.

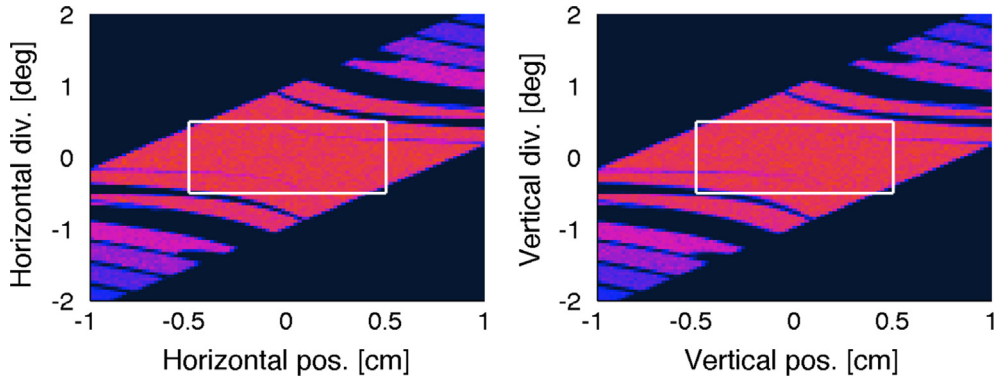

Fig. 19. Acceptance diagrams for a 24 m guide with feeder optimized for $\pm 0.5^{\circ}$ divergence requirement with 2×2 cm^2 pinhole.

optimization, still including the optimum from the instrument without a feeder. For reasons of maintenance and background from unwanted cold/thermal neutrons, the addition of a feeder should, however, correspond to a significant improvement in order to be recommended. The feeder systems are not expected to surpass the traditional elliptical guide starting at 2 m in the simulated performance as the latter does not have the restriction of a small pinhole. However, in many cases the brilliance transfer nearly equals that of the reference single ellipse guide, which is a most satisfying result.

In order to obtain a near-perfect brilliance transfer, it is a requirement that enough neutrons enter the guide, but that does not guarantee a perfect result which is evident in the results from the guides simulated with a feeder. The feeder will allow the optimizer to select a width of the feeder which will deliver the required phase-space volume. As the sample is 1×1 cm^2, the phase-space volume required at the sample position is this area multiplied by the divergence requirement. There is however a distance of 50 cm between the end of the guide and the sample, which will for non-focusing guides increase the required phase-space volume. An effective required beamsize can be calculated by $d + 2l\phi$, where d is the sample size, l is the distance between guide end and sample, and ϕ is the divergence requirement (in radians). Thus the effective beamsize needed is 1.8 cm for the $\pm 0.5^{\circ}$ requirement, 2.7 cm for the $\pm 1.0^{\circ}$ requirement and 4.5 cm for the $\pm 2.0^{\circ}$ instrument (given the needed divergence is supplied).

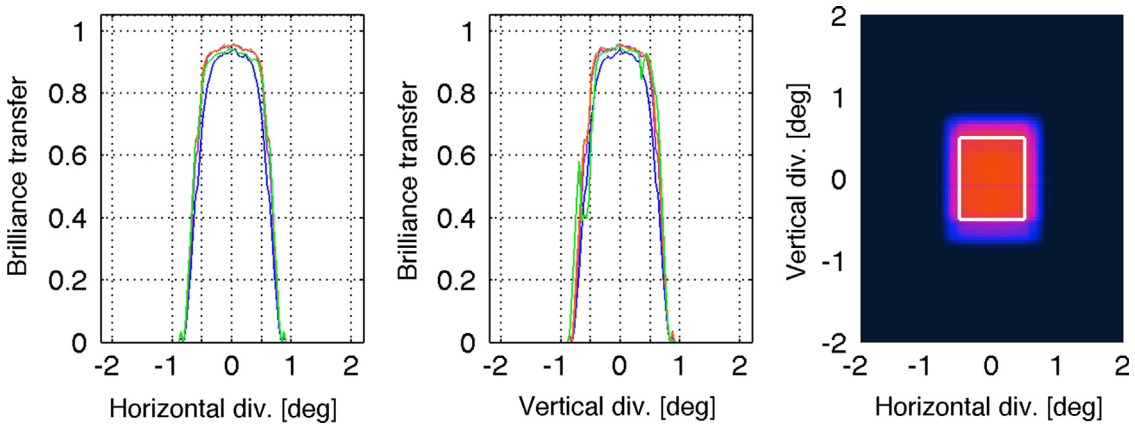

Fig. 20. Data on the divergence for a 150 m guide without feeder optimized for $\pm 0.5^{\circ}$ divergence requirement with 2×2 cm^2 pinhole.

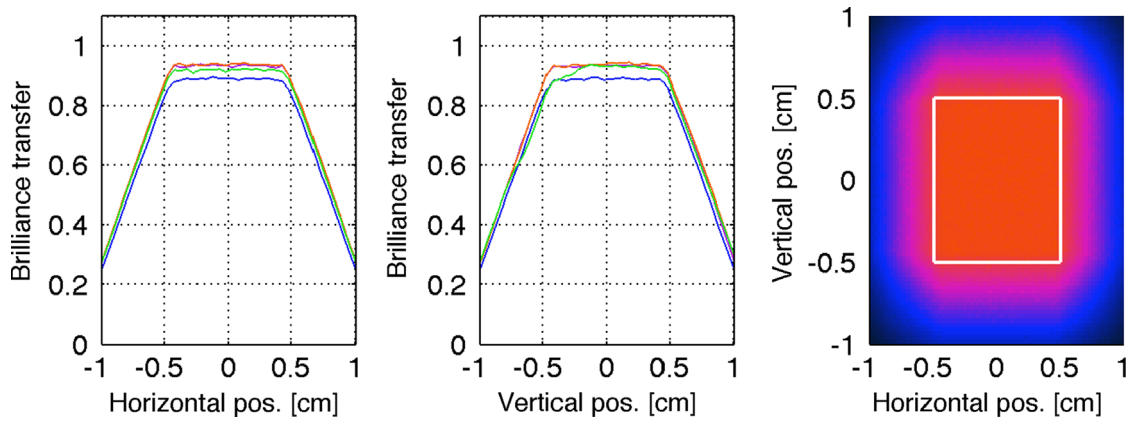

Fig. 21. Data on the spatial distribution for a 150 m guide without feeder optimized for $\pm 0.5^{\circ}$ divergence requirement with 2×2 cm^2 pinhole.

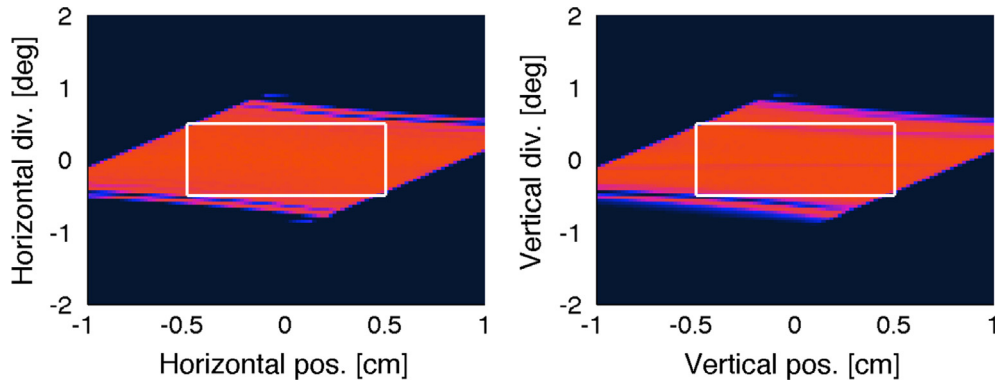

Fig. 22. Acceptance diagrams for a 150 m guide with feeder optimized for $\pm 0.5^{\circ}$ divergence requirement with 2×2 cm^2 pinhole.

This explains why the smallest pinhole of 1×1 cm^2 was never able to reach perfect brilliance transfer at the lowest divergence requirement, even though the needed divergence was present.

Our results show that in most cases it is possible to select a reasonable pinhole size for a given combination of instrument length and divergence requirement. For the case of low divergence, $\pm 0.5^{\circ}$, a pinhole of 2×2 cm^2 is sufficient, and the 24 m instrument will need a feeder, where the 75 m, 150 m and 300 m instruments will not. The 24 m instrument could select a pinhole of 3×3 cm^2 instead of the feeder to obtain a comparable performance. When the divergence requirement is $\pm 1.0^{\circ}$, the required pinhole size increases. For the 24 m instrument, a 4×4 cm^2 pinhole without a feeder will yield around 95% of the reference performance, while a 3×3 cm^2 pinhole with feeder will only provide 80%. From the gathered data it is not possible to determine which of these options will provide the best signal-to-background ratio. The 3×3 cm^2 pinhole with feeder will bring the longer instruments to around 90% of reference performance.

For the highest divergence, $\pm 2.0^{\circ}$, it is hard to select the pinhole size perfectly as the performance never becomes comparable to the traditional elliptical guide. It is obvious that a feeder is necessary in every case. For all instrument lengths a pinhole of 3×3 cm^2 seems optimal as further increases in size does not increase performance significantly. This kind of solution will only yield 50–65% of the performance offered by a traditional elliptical guide. One could search for other guide systems which include a pinhole and better performance in these circumstances as Liouville's theorem allows room for improvement.

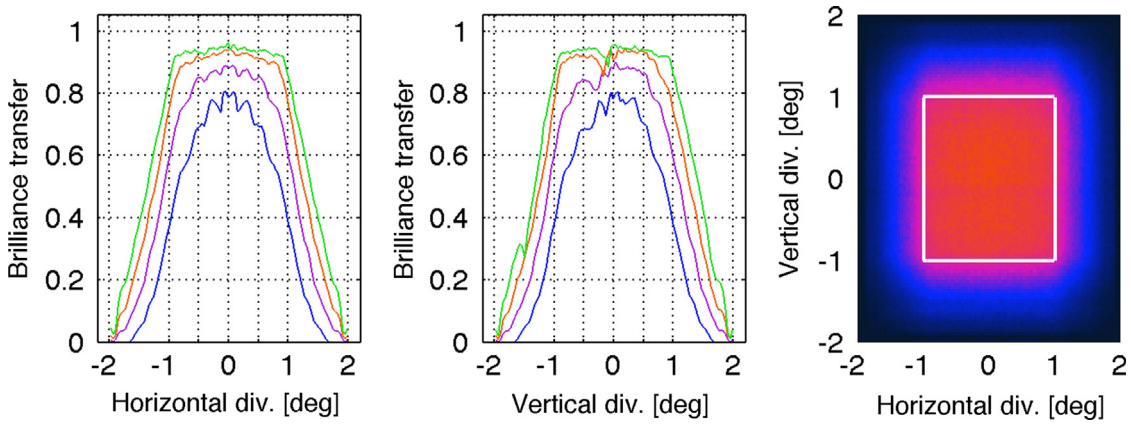

Fig. 23. Data on the divergence for a 150 m guide with feeder optimized for $\pm 1.0^{\circ}$ divergence requirement with 3×3 cm^2 pinhole. (For interpretation of the references to color in this figure caption, the reader is referred to the web version of this article.)

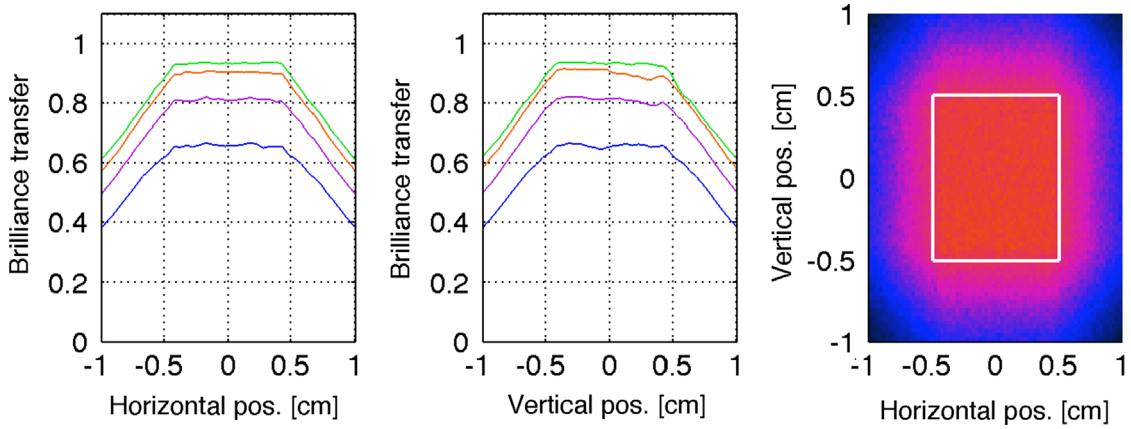

Fig. 24. Data on the spatial distribution for a 150 m guide with feeder optimized for $\pm 1.0^{\circ}$ divergence requirement with 3×3 cm^2 pinhole. (For interpretation of the references to color in this figure caption, the reader is referred to the web version of this article.)

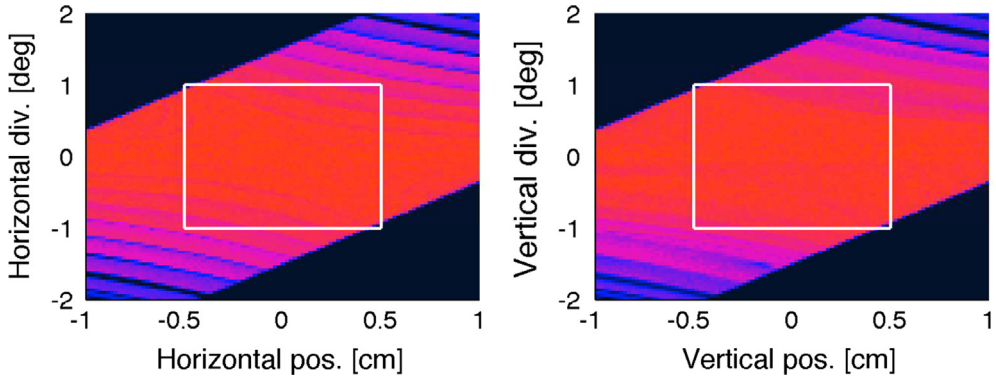

Fig. 25. Acceptance diagrams for a 150 m guide with feeder optimized for $\pm 1.0^{\circ}$ divergence requirement with 3×3 cm^2 pinhole.

The guides investigated are not focusing as the elliptic shape might suggest, as the outgoing beam is divergent [20]. It can be seen from the acceptance diagrams in Figs. 16, 19, 22, 25, and 28 that moving the sample closer to the guide would be beneficial. With a truly focusing guide, there would be an optimal position at the sample position. It is however not possible to increase the brilliance transfer beyond 1, which means that substituting the end of a guide which has the brilliance transfer close to 1 with a focusing device will not have a significant effect.

Problems with irregular divergence distributions occur for many of the simulated guides in this study. It is most common for guides with the smallest pinhole, 1×1 cm^2, or the highest possible divergence requirement, $\pm 2.0^{\circ}$. The short instrument (24 m) was most problematic in this regard. There are however many smooth divergence distributions both with and without feeder. The examples show that these can be smooth even for individual wavelengths and not just when averaged over the entire wavelength band. The work done by Cussen et al. [20] suggests that smooth divergence distributions from elliptical guides are unlikely. In this work, we have optimized additional parameters, including the position of the focal points, and have found that smooth divergence and large brilliance transfers are simultaneously possible. The guides investigated in Ref. [20] were, however, much closer to the moderator, 20 cm as opposed to 6.1 m

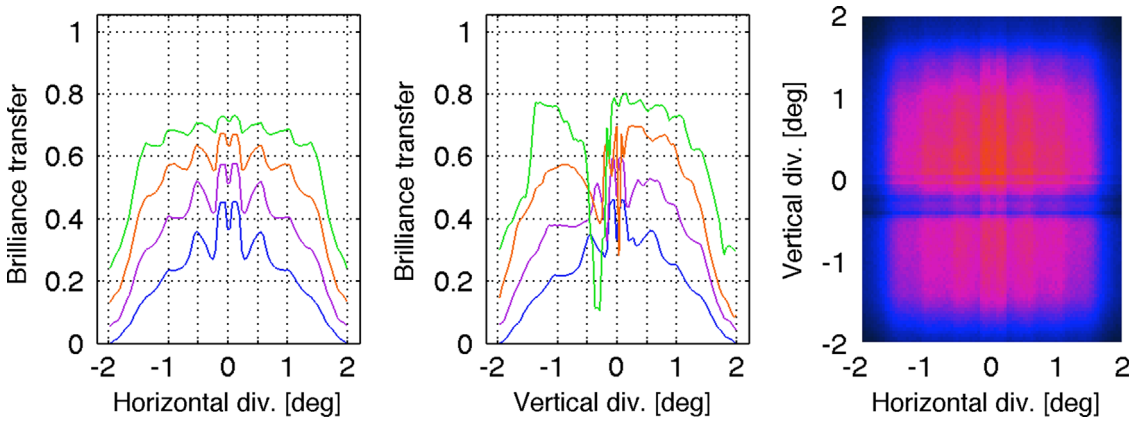

Fig. 26. Data on the divergence for a 150 m guide with feeder optimized for $\pm 2.0^{\circ}$ divergence requirement with 3×3 cm^2 pinhole.

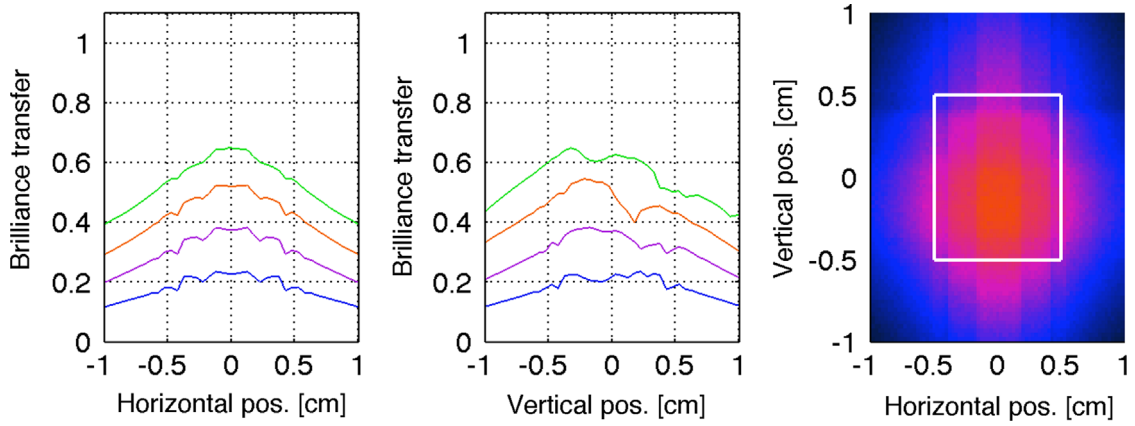

Fig. 27. Data on the spatial distribution for a 150 m guide with feeder optimized for $\pm 2.0^{\circ}$ divergence requirement with 3×3 cm^2 pinhole.

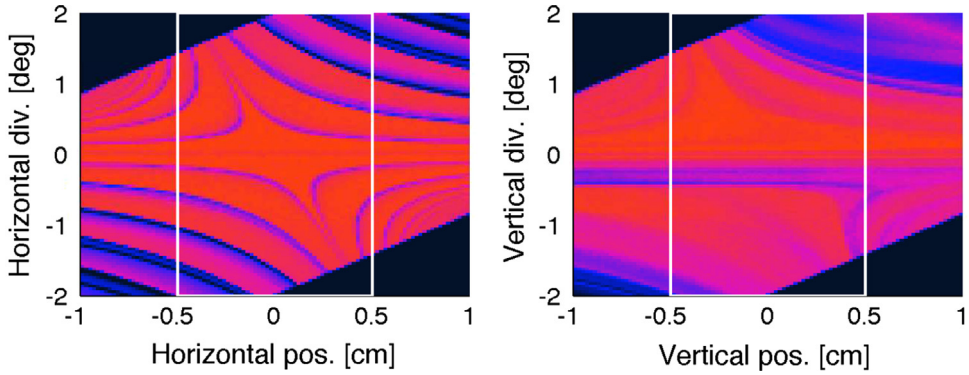

Fig. 28. Acceptance diagrams for a 150 m guide with feeder optimized for $\pm 2.0^{\circ}$ divergence requirement with 3×3 cm^2 pinhole.

in this work, which may affect the divergence distribution. Further research is needed in order to determine how to ensure smooth and simple divergence distributions from realistic elliptical guides.

When performing the optimizations on rather similar guide systems, it became evident that in general many different solutions can be found which will provide similar figures of merit. This reflects itself in the topological differences of the divergence plots, where the found solutions may vary significantly, even while only changing the pinhole size by one step. Although confusing at first sight, this is encouraging, as it allows one to add further requirements on the figure of merit in order to select between these many solutions. For example estimated cost [17], background [18] or even requirements on the smoothness of the curves could be included, presumably without lowering the brilliance transfer significantly.

One remaining problem with the discussed guide systems is that they do not block line of sight between sample and moderator. There are several recent ideas which could rectify this problem. The approach of a beamstop in the center of the elliptical guide [3] seems suited for this geometry, as the view to the moderator is by the pinhole. It is also possible to bend the elliptical guide vertically to take advantage of gravitation, but the effect of this is wavelength dependent and only works for guides exceeding ~150 m in length [2]. Another option is to use a double ellipse after the pinhole [4] which effectively adds a second pinhole. It would also be possible to introduce an angle between the ellipses sufficient for

escaping line of sight [19], but as the symmetry is broken the optimal ellipses are not necessarily the same, either by coating or geometry. We have work in progress concerning how such systems should be optimized [21]. Further work is needed in order to determine how these solutions would work in combination with the feeder geometry and how they would affect the fast-neutron background.

7. Conclusion

We have successfully shown that guide systems with a small pinhole at the position of the pulse shaping chopper are a viable solution in terms of cold neutron transport. By making the pinhole a part of the primary shielding, the background from fast neutrons can presumably be reduced significantly. It was found that for a low divergence requirement, $\pm 0.5^\circ$, a pinhole of 2×2 cm^2 will be sufficient for the four instrument lengths, 24 m, 75 m, 150 m and 300 m where only 24 m would benefit significantly from a feeder. For the higher divergencies, a 3×3 cm^2 pinhole with a feeder seems optimal for every guide length. At $\pm 1.0^\circ$ divergence requirement the performance is around 90% of the reference guide, except for the 24 m instrument, which is at 80%. The 24 m instrument could alternatively use a larger pinhole, 4×4 cm^2, but without the feeder for better performance with higher background. For $\pm 2.0^\circ$ divergence requirement this configuration yields 50–65% of the brilliance transfer from a traditional elliptical guide. These systems are thus best suited for instruments with divergence requirements up to $\pm 1.0^\circ$.

Acknowledgments

We thank Phil Bentley, Ken H. Andersen, Leo Cussen, Pascale Deen, Werner Schweika, Klaus Lieutenant and Kaspar H. Klenø for engaging in discussion on the article subject and commenting on results. We thank Peter K. Willendrup and Emmanuel Farhi for technical help with software and the ESS DMSC for providing computing power. We would like to thank the Danish Agency for Research and Innovation for their support through the contribution to the ESS update phase.

References

[1] C. Schanzer, P. Boni, U. Filges, T. Hils, Nuclear Instruments and Methods in Physics Research Section A 529 (2004) 63.
[2] K.H. Klenø, K. Lefmann, Journal of Physical Society of Japan 80 (2011) SB004.
[3] U. Filges, Unpublished, 2012.
[4] A. Houben, W. Schweika, T. Brückel, R. Dronskowski, Nuclear Instruments and Methods in Physics Research Section A 680 (2012) 124.
[5] R.E. Lechner, Advanced neutron sources, in: D.K. Hyer (Ed.), Proceedings of ICANS-X, Institute of Physics, Bristol, 1989, pp. 843–848.
[6] ⟨http://europeanspallationsource.se/⟩.
[7] H. Schober, et al., Nuclear Instruments and Methods in Physics Research Section A 589 (2008) 34.
[8] L.D. Landau, E.M. Lifshitz, 3rd ed.,Statistical Physics, vol. 1, Elsevier, 1951.
[9] K.H. Klenø, Ph.D. Thesis, University of Copenhagen, July 2013.
[10] ⟨www.mcstas.org⟩.
[11] K. Lefmann, K. Nielsen, Neutron News 10/3 (1999) 20.
[12] P.K. Willendrup, E. Farhi, K. Lefmann, Physica B 350 (2004) E735.
[13] P.K. Willendrup, et al., Journal of Neutron Research, http://dx.doi.org/10.3233/JNR-130004 (preprint).
[14] K.F. Riley, M.P. Hobson, S.J. Bence, Mathematical Methods for Physics and Engineering, 3rd ed., Cambridge, 2007, p. 990.
[15] E. Farhi, Y. Debab, P. Willendrup, Journal of Neutron Research 17 (2012).
[16] ⟨http://www.ess-dmsc.eu⟩.
[17] K.H. Klenø, Simulating Neutron Guide for the European Spallation Source, M.Sc. Thesis, University of Copenhagen, 2008.
[18] E. Klinkby, et al., Nuclear Instruments and Methods in Physics Research Section A 700 (2013) 106–110, http://dx.doi.org/10.1016/j.nima.2012.10.052.
[19] S.L. Holm, N. Rasmussen, L. Høpfner, J. Voigt, K.H. Andersen, K. Lefmann, Journal of Applied Crystallography, submitted for publication.
[20] L.D. Cussen, et al., Nuclear Instruments and Methods in Physics Research Section A (2012), http://dx.doi.org/10.1016/j.nima.2012.11.183.
[21] M. Bertelsen, K. Lefmann, Journal of Applied Crystallography in preparation.

A.5 Neutron guide-split: A high performance guide bundle concept for elliptical guides

This paper provides an alternative method of sharing the phase-space extracted from a source among several instruments, as guides are normally split spatially, but here the large divergence of an elliptical guide is shared. The idea was simulated by modifying guide_bot generated instrument files to adhere to the additional constraints presented by having multiple guides after a single large elliptic guide. The paper was published in Nuclear Instruments and Methods in Physics Research, Section A.

Abstract

We present a new guide-split concept for transporting cold and thermal neutrons to multiple instruments from a single beam port at a neutron facility without compromising the useful neutron brilliance notably for any of the instruments. Elliptical guides are capable of transporting an almost completely filled phase space within a large divergence ($\pm 2^\circ$ for cold neutrons). It is therefore possible to place several secondary guides side by side pointing in slightly different directions using the end of a primary guide as a virtual source. The instruments placed at the secondary guides hence exploit different parts of the phase space transported by the primary guide. In addition, the resulting kink between the primary and secondary guide eliminates line of sight. Using ray-tracing simulations of three different set-ups (with two, four, and eight secondary guides) we show that it is possible to illuminate at least eight sample positions from one beam port with a brilliance transfer above 90% on each sample on a 150 m long instrument. This has been done for a phase space volume comprised of an area of 1×1 cm^2 and a maximum divergence of $\pm 0.5^\circ$ within a wavelength band of 4.25-5.75 Å. We show, by a full virtual experiment, an example of applying the guide-split concept to an instrument proposed for the European Spallation Source, namely a magnetism diffractometer.

My contribution

Performed all optimizations presented in the paper and commented on the manuscript.

Nuclear Instruments and Methods in Physics Research A 782 (2015) 1–8

Contents lists available at ScienceDirect

Nuclear Instruments and Methods in Physics Research A

journal homepage: www.elsevier.com/locate/nima

Neutron guide-split: A high performance guide bundle concept for elliptical guides

Sonja L. Holm [a,b,*], Nina Rasmussen [a,b], Louise Høpfner [a,b], Mads Bertelsen [a,b,d], Jörg Voigt [c], Ken H. Andersen [d], Kim Lefmann [a,b]

[a] Nano-Science Center, Niels Bohr Institute, University of Copenhagen, Universitetsparken 5, 2100 Copenhagen Ø, Denmark
[b] ESS Design Update Program, Denmark
[c] Jülich Centre for Neutron Science JCNS, 52425 Jülich, Germany
[d] European Spallation Source ESS AB, 22100 Lund, Sweden

ARTICLE INFO

Article history:
Received 11 July 2014
Received in revised form
3 January 2015
Accepted 9 January 2015
Available online 17 January 2015

Keywords:
McStas
Monte Carlo
Ray tracing
Neutron guide
ESS

ABSTRACT

We present a new guide-split concept for transporting cold and thermal neutrons to multiple instruments from a single beam port at a neutron facility without compromising the useful neutron brilliance notably for any of the instruments.

Elliptical guides are capable of transporting an almost completely filled phase space within a large divergence ($\pm 2^\circ$ for cold neutrons). It is therefore possible to place several secondary guides side by side pointing in slightly different directions using the end of a primary guide as a virtual source. The instruments placed at the secondary guides hence exploit different parts of the phase space transported by the primary guide. In addition, the resulting kink between the primary and secondary guide eliminates line of sight.

Using ray-tracing simulations of three different set-ups (with two, four, and eight secondary guides) we show that it is possible to illuminate at least eight sample positions from one beam port with a brilliance transfer above 90% on each sample on a 150 m long instrument. This has been done for a phase space volume comprised of an area of $1 \times 1\ \mathrm{cm}^2$ and a maximum divergence of $\pm 0.5^\circ$ within a wavelength band of 4.25–5.75 Å. We show, by a full virtual experiment, an example of applying the guide-split concept to an instrument proposed for the European Spallation Source, namely a magnetism diffractometer.

1. Introduction

With the construction of the European Spallation Source (ESS) [1], the field of neutron scattering is on the verge of entering a new era. ESS will be the world's first high-power long-pulse spallation source and hence offers a large number of new scientific possibilities. For any neutron source there is an upper limit to the number of instruments due to the geometry of the moderator, reflector, and beam extraction system. However, it is possible to increase the instrument capacity by use of the guide systems, e.g. by the design described in this paper.

The design of neutron guides has gone through many transformations since the first straight, constant-cross-section guides in the sixties [2,3]. The realization that a removal of the sample from line-of-sight to the source leads to a significant reduction of the background noise from fast neutrons and gamma radiation, gave rise to a curved version of the constant-cross-section guide which is still the standard guide design at many neutron facilities. With the addition of the super-mirror coating in the seventies [4,5], another vital step in the improvement of neutron guides was taken, increasing dramatically the reflection angle and thus the divergence and intensity transported by the guide. In recent years ballistic guides with straight tapering [6,7], parabolic tapering [8,9] and full elliptical [8–11] geometries have been investigated and implemented with the aim of reducing transport losses and improving divergence profiles in guide systems.

The concept of placing several instruments on the same beam port using straight or curved guides is well known. These guide bundles are found at most facilities e.g. at ILL [12] and enable a sharing of the neutron flux amongst the instruments placed on a single beam port. The primary guide is wider than needed for a single instrument, and the splitting of the guide is essentially performed by dividing the guide with an additional mirror. In effect, this performs a spatial separation of the phase space transported by the primary guide into the secondary guides.

The guide-split concept presented here facilitates a similar increase in the instrument capacity of a neutron source by

* Corresponding author.

http://dx.doi.org/10.1016/j.nima.2015.01.045
0168-9002/

allowing several instruments to use the same beam port. Our idea is to implement a primary elliptical guide that feeds a number of secondary guides. These secondary guides are rotated around an axis at the end of the primary guide using this as a new virtual source. In effect, at this virtual source, the phase space is divided between the secondary guides by separating in divergence space.

While the classical guide bundle concept couples well into constant-cross-section secondary guides, the guide-split concept presented here couples well into elliptical secondary guides. Due to the superior performance of elliptical guides over long distances, one can expect that the neutron transport of the double-elliptical guide-split system has very small losses.

In this paper, we show that the guide-split concept has indeed very good transport properties for cold neutrons. In addition, examples of ESS instruments that could be placed on a guide-split system are presented, along with a simple virtual experiment for the magnetism diffractometer suggested in the Technical Design Report (TDR) for ESS [13].

2. The guide-split concept

Elliptical guides are capable of transporting an almost completely filled phase space within a large divergence ($\eta = \pm 2^\circ$), for cold neutrons [9]. The end of a primary elliptical guide can therefore be used as a virtual source. Consequently, it is possible to place several secondary guides side by side oriented along slightly different directions, and hence exploit different divergence parts of the transported phase space. An illustration of this guide arrangement is shown in Fig. 1.

The guide-split can be realized in numerous variations with many different shapes of the primary and secondary guides in different ballistic combinations, e.g. elliptic, parabolic, or linearly tapering. However, only the double ellipse case is investigated here, as this is the natural choice because of the limited size of the virtual source.

2.1. The guide-split set-up

Three guide-split set-ups where the guide junction supports two, four, or eight secondary guides have been investigated, each with a total length (distance from moderator to sample) of 150 m. A horizontal cut of the guide junctions is illustrated in Fig. 1. In this study, we have chosen to let the distance from the moderator to the splitting point be around 100 m. Other guide length ratios are also feasible (e.g. 50 m or 75 m from the moderator to the splitting point of a 150 m guide).

The guide parameters of the set-up are restricted by the requirement that the secondary guides cannot overlap. An illustration used in the geometrical considerations of a two-split set-up is shown in Fig. 2. Ignoring the substrate thickness, we use $d \geq 0$, for the two- and four-split set-up and $d \geq w$ for the eight-split option.

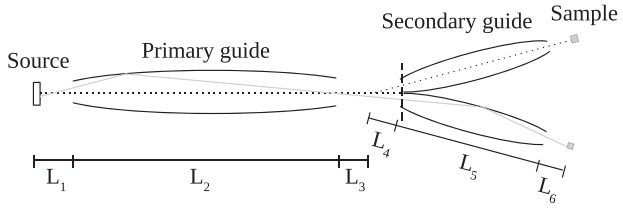

Fig. 1. Layout of the guide-split set-up with two secondary elliptical guides. The dotted line represents the primary axis through one instrument, the gray line is an example of a neutron path through the guide system, and the dashed line marks the entrance of the secondary guides. A zoom of the junction area is shown in Fig. 3. Each of the sibling instruments on the secondary guides retain a high brilliance transfer (~ 90%). L_i represents the naming of various distances, discussed in the text.

The rotation angles are small (0.4°) in all three test cases but sufficient to break line-of sight once through the guide system. Due to the symmetric nature of the set-up, only selected simulated data are presented: the guide rotated to the left in the two-split version, the lower left corner of the four-split, and the middle and lower left guide in the eight-split set-up as highlighted in Fig. 3. Gravity will affect the neutron flight paths in long guides. However, due to multiple reflections in the elliptical guides, the resulting effect of gravity is very minor. All simulations presented here do take gravity into account.

No guide is simulated in the middle of the eight-split variation, due to line-of-sight considerations. It is likely, however, that a secondary parabolic-curved-parabolic guide geometry, to avoid line-of-sight, will perform adequately at this position.

3. Ray-tracing simulations

The numerical optimizations were performed using the ray-tracing package McStas [14,15] and executed on the computer cluster of the ESS Data Management and Software Center [16].

Brilliance transfer, used in our figure of merit for the optimization, is defined as the transmission of a closed four-dimensional phase space volume (2D position, 2D divergence) through a guide system to the sample within a certain wavelength band [17]. We have chosen to optimize for a maximum divergence of $\pm 0.5^\circ$; a wavelength band from 4.25 Å to 5.75 Å; and a sample size of 1×1 cm^2. These parameters match the requirements of the magnetism diffractometer described in the ESS TDR [13].

The elliptical guide component used in the simulation has a perfect elliptical shape in the x- and y-directions and a rectangular cross-section [18]. For simplicity the m-value is set to be a high

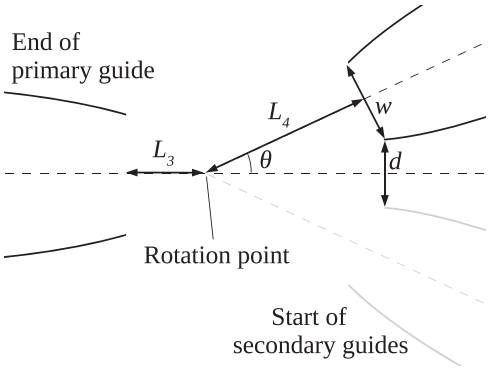

Fig. 2. Top view of the guide junction. θ is the rotation angle of the secondary guide, L_3 is the length from the end of the first guide to the rotation point, L_4 is the length from the rotation point to the secondary guide entrance, w is the width of the secondary guide entrance, and d is the distance between the outermost secondary guides.

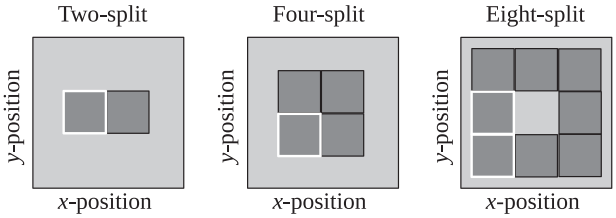

Fig. 3. Sketch of the cross-sections of the secondary guide junction for the two-, four- and eight-split variations of the set-up. The position of this vertical cut is marked with a dashed line in Fig. 1. The guide positions marked with white outlines are simulated and the corresponding results presented in this paper. The two positions in the eight split option are referred to as the side and the corner positions.

Table 1
The parameters used for the three different set-ups. The parameters marked with an asterisks have not been optimized. See Figs. 1 and 2 for a graphical explanation of the lengths.

Layout option	Two-split	Four-split	Eight-split
Parameters of the primary guide			
L_1, distance from moderator to guide entrance (m)	3.17	3.18	3.11
L_2, length of the primary guide (m)	91.83	91.81	91.89
L_3, distance from exit to rotation point (m)	0.58	0.26	0.21
Distance from focal point to guide entrance (hori) (m)	5.42	4.88	3.44
Distance from focal point to guide entrance (verti) (m)	15.0	4.02	6.66
Distance guide exit to focal point (hori) (m)	1.92	1.43	3.40
Distance guide exit to focal point (verti) (m)	21.3	1.56	4.06
Small axis, half width (hori) (cm)	10.2	12.3	9.8
Small axis, half width (verti) (cm)	8.66	13.0	9.05
Parameters of the secondary guide			
θ, angular rotation of secondary guides (deg)	0.4	0.4	0.4
L_4, distance from rotation point to entrance (m)	*3	*3	*5
L_5, length of the secondary guide (m)	50.42	50.74	48.8
L_6, distance from guide exit to sample (m)	*1	*1	*1
Distance from focal point to guide entrance (hori) (m)	1.70	2.18	2.25
Distance from focal point to guide entrance (verti) (m)	31.2	1.49	2.11
Distance guide exit to focal point (hori) (m)	1.00	1.34	1.62
Distance guide exit to focal point (verti) (m)	1.23	1.72	1.72
Small axis, half width (hori) (cm)	5.04	4.43	3.98
Small axis, half width (verti) (cm)	5.67	3.91	3.86

value of $m=4$ (reflectivity 79% at $q=mQ_c$, as described in [17]) for all guides. When making a specific design of an instrument, however, the coating should be cost-optimized. In the simulations we have used the ESS 12×12 cm^2 cold moderator description from 2012, as defined in McStas 2.0 [19].

The preliminary optimization of the guide systems was performed by scanning the parameters one at a time. During these optimizations the parameter space (lengths, focal points, angles) was found to have large regions with brilliance transfers above 90%.

In the final optimization of the three set-ups the program guide_bot [20] and the package iFit [21] were used. Many solutions with high brilliance transfers were found with this method and the final solution was manually selected such that a smooth divergence distribution at the sample position was obtained. The final parameters of the guides are listed in Table 1.

The two eight-split options will obviously share the same primary guide and hence we choose only to make one optimization for the two positions. The corner option was optimized and the side option was simulated with the same parameters but with another kink rotation.

4. Results of the guide-split simulations

The main result in this study is how the brilliance transfer depends on the wavelength for the three optimized guide systems. Our data are shown in Fig. 4. The guide-split concept shows excellent performance for cold neutrons ($\lambda>3$ Å). The brilliance transfers obtained (for the chosen phase space of 1×1 cm^2, $\pm0.5^\circ$, and $\lambda=4.25$–5.75 Å) in the optimizations are 95% for the two-split, 94% for the four-split, and 93%, 91% for the two eight-split options, respectively. For thermal neutrons ($\lambda=1.5$ Å) the brilliance transfer is still acceptable: 82% for the two-split, 71% for the four-split, and 71%, 59% for the two eight-split options.

It is desirable to have a homogeneously filled four-dimensional phase space at the sample position within the wavelength band

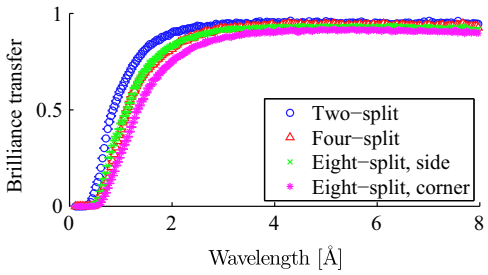

Fig. 4. The brilliance transfer at the sample position for the two-, four-, and eight-split options as a function of wavelength.

used. The brilliance transfer as a function of each of the four parameters is displayed in Fig. 5 for three wavelength snap shots (1.5 Å, 3 Å, and 4.5 Å). In the optimizations we have obtained a flat divergence and position distribution in the desired ranges ($\pm$ 0.5° and $\pm$0.5 cm) in all four test cases for the cold wavelength band ($\lambda\geq3$ Å), while a shorter wavelength of 1.5 Å gives few non-ideal features in both position and divergence profiles.

A simulation with $m=1$ was made to see the impact of the coating value for the guides. We found only a few percentage difference to the $m=4$ results within the cold wavelength band. The lower wavelengths however are not transported well for the low m coating.

We have investigated the performance of the three guide-split set-ups with regard to sample illumination, divergence distribution, and their correlations (acceptance diagrams). The results are shown in Fig. 6 for neutrons within the wavelength interval for which the set-ups have been optimized (4.25–5.75 Å). It is observed that for all three guide set-ups, the neutron phase space is very uniformly filled.

In Fig. 7 the phase spaces, perpendicular to the axis of the primary guide, at the entrance of the secondary guides, are displayed. The guide openings of the secondary guides, that were used to produce the results in Figs. 5 and 6, are indicated with black lines on the position axes. On the divergence axes the black lines show the zero divergence in the secondary guides and on sample positions. Note that the vertical acceptance diagram for the two split is atypical because the entrance height of the secondary guide was not limited, and is here over twice as large as the others.

5. Performance of guide split systems

As seen from the data in Figs. 4–6, the guide-split idea is certainly useful for the case of two- and four-split elliptical guides. This is judged on the basis of the brilliance transfer values over a large wavelength range. In addition, for the chosen sample size of 1×1 cm^2, the illumination is very smooth both in divergence and position. The same is true for the eight-split option, although the brilliance transfer is slightly smaller, in particular towards the shorter wavelengths.

A slightly larger brilliance transfer of the two-split variation is observed (see Fig. 4). This is to be expected, since in the two-split set-up, the secondary guides are more favorably placed in the vertical divergence space. It can be argued that the four-split – or even eight-split – options are the better choices due to the increased amount of instruments and utilized neutrons. Neither of the variations provides as high a brilliance transfer as a single elliptical guide, although the transmission in excess of 90% for $\lambda\geq3$ Å must be seen as a most satisfactory result. In addition, all variations provide a strong total utilization of the generated neutrons, when the increase in instrument number is considered.

The guide-split concept also works for straight and curved constant-cross-section secondary guides, although with slightly lower brilliance transfers of $\sim$80%, with losses mostly at the highest divergence values (data not shown). In contrast, the

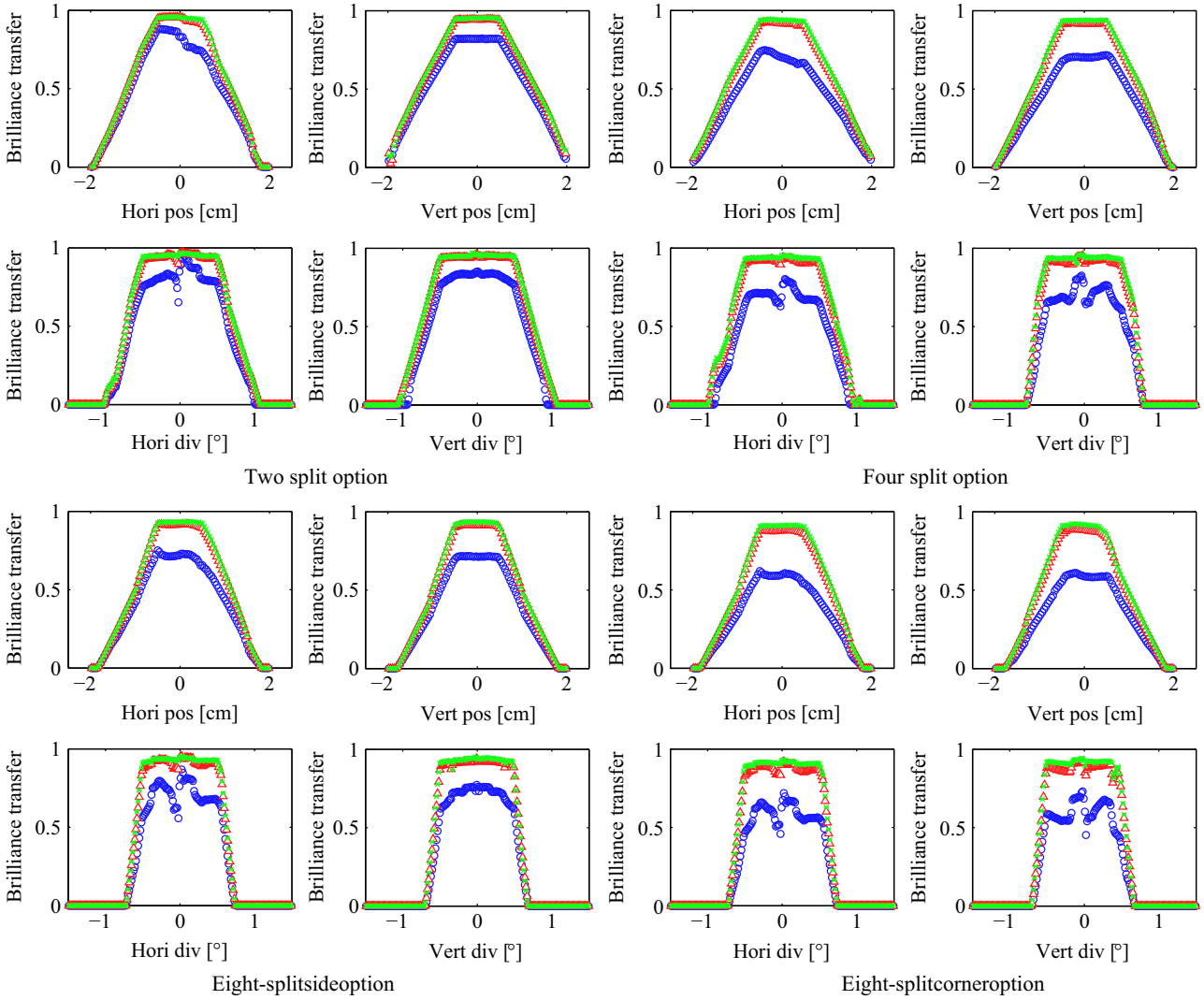

Fig. 5. Brilliance transfer at the sample position as a function of horizontal and vertical positions and divergences. The dimensions of the phase space have summed from -0.5° to 0.5° or from -0.5 cm to 0.5 cm for neutrons within three narrow wavelength bands at 1.5 Å (blue circles), 3 Å (red triangles), and 4.5 Å (green x's). (For interpretation of the references to color in this figure caption, the reader is referred to the web version of this article.)

elliptical secondary guides have no problem in transporting $\pm 0.5^\circ$ divergence, and can even accommodate higher divergences, also for the present optimization. It is uncertain how well the guide-split set-up will work when optimized for higher divergences but it is likely to be successful for cold neutrons ($\lambda \geq 3$ Å). The limiting factor is the maximal divergence from the primary guide where the phase space is filled (divergence up to $\pm 2^\circ$) [9].

Another advantage of the guide-split system is that the guide-split concept has the possibility to be combined with the guide-feeder concept for beam extraction in elliptical guides [18]. Here, another virtual source is present close to the surface of the biological shielding, 6 m from the moderator surface.

6. Wavelength bands, choppers, and resolution

In the present plans for the ESS, guide bundles are not foreseen. Part of the reason is the need to select pulse lengths and wavelength bands using choppers placed close to the source.

The restriction of the wavelength band can be partly lifted when implementing the guide-split at the long instruments for ESS, as one can allow a general, broader primary wavelength band up to the guide split position. The width of the primary band amounts to $\Delta\lambda_p = T/(\alpha L_{sc})$, where L_{sc} is the distance between the source and the secondary band chopper and α is defined as $\alpha = m_n/h = 253$ μs/m/Å. The width of this wavelength band at ESS is 2.77 Å if the guide split position is at $L_{sc} = 100$ m, or 5.54 Å for $L_{sc} = 50$ m. This primary wavelength band is selected by common bandwidth choppers placed in the first part of the guide; the more narrow secondary bands of width $\Delta\lambda = T/(\alpha L) = 1.88$ Å (for $L = 150$ m) are chosen individually within the primary band by choppers placed in the secondary guides, allowing some independence in choice of wavelengths for the sibling instruments. A time-of-flight diagram of the full arrangement is shown in Fig. 8.

The most important limiting factor for placing an instrument on a guide-split system is the instrument resolution. Many long-pulse instrument designs require a pulse-shaping chopper (or set of choppers) early in the guide system to define the time (and hence wavelength) resolution of the primary beam [22]. If several instruments would need to agree on a common pulse shaping opening time, this would compromise the instrument flexibility. Hence, for these types of instruments the guide-split system may not be the better choice. However, some instrument classes exist, which either work without pulse shaping, or where pulse shaping can be moved to after the guide-split position. We will discuss these instrument types below.

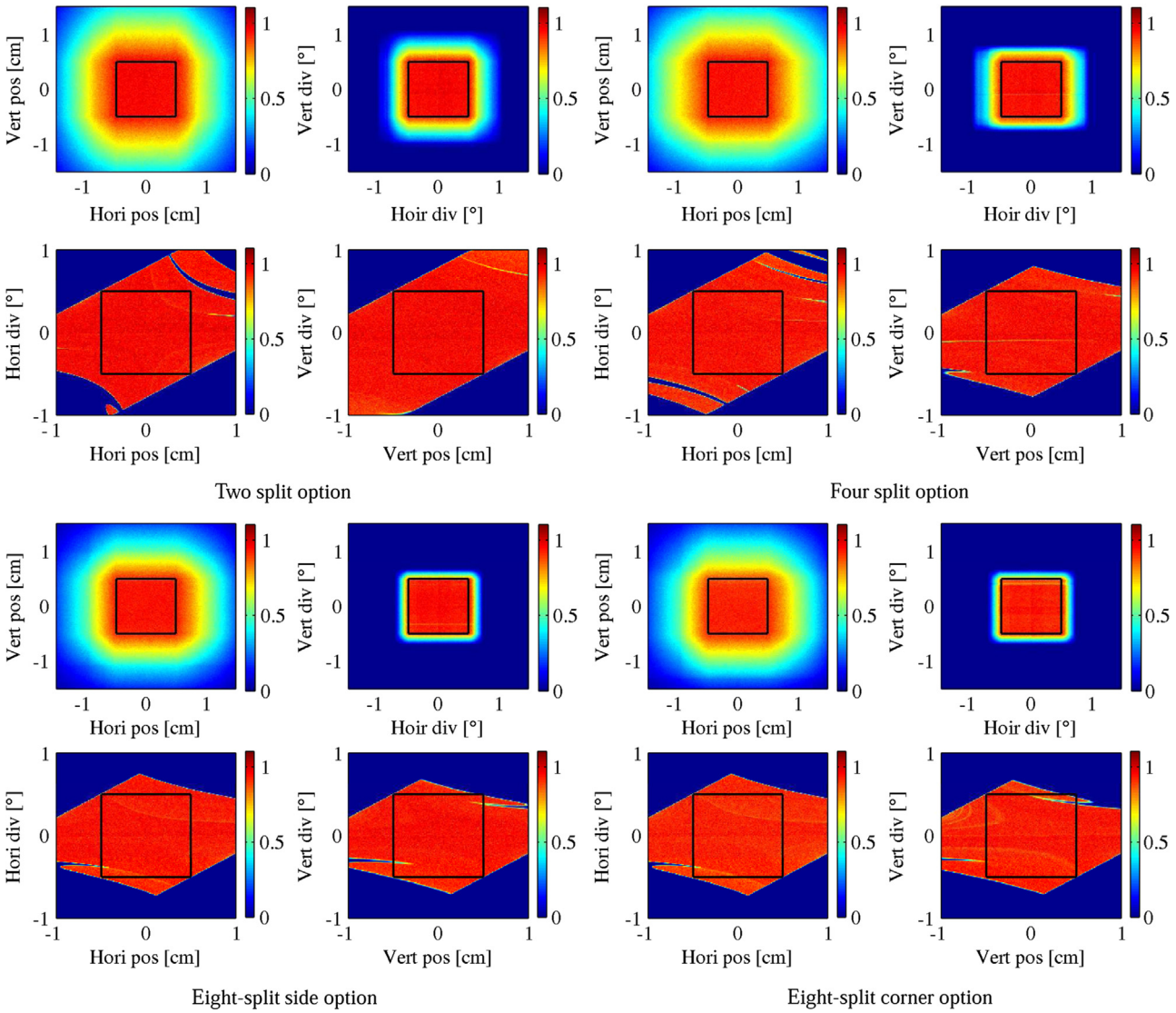

Fig. 6. Brilliance transfer obtained from the position, divergence, and acceptance monitors at the sample position for the four different secondary guides considered. The black squares indicate the edges of the phase space volume used in the optimizations. The data has been summed up inside the chosen phase space volume in the dimensions not shown in the 2D plots (1×1 cm^2, $\pm 0.5^\circ$, and 4.25–5.75 Å). The color scales represent the brilliance transfer values. Some of the pixels have an apparent brilliance transfer above unity due to statistical fluctuations in the simulations. (For interpretation of the references to color in this figure caption, the reader is referred to the web version of this article.)

7. Applications of guide-split at ESS

For all the long instruments (>75 m) chosen for the instrument suite at ESS it would be worth the effort to explore the possibility of building a guide system that can be turned into a guide-split system at a later point. In this way it will be possible to build additional instruments at a reduced cost since most of the guide and shielding is already in place.

The examples below describe four types of long cold-neutron instruments for ESS described in the TDR [13], using a wavelength band of around 3–6 Å. One of these, a magnetism diffractometer, has been simulated in detail.

7.1. Monochromator instruments

One instrument with a monochromator has been suggested for ESS: a monochromatic powder diffractometer [13]. This instrument utilizes the high time-integrated flux of the ESS source and therefore needs no pulse shaping chopper, while second and third order neutrons are still discriminated by time-of-flight. In addition the guide-split concept opens up the possibility of having a "farm" of several similar monochromator instruments e.g. triple-axis-spectrometers [23].

The usefulness of the split guide for these instruments depends only on the brilliance transfer, which is excellent (see Fig. 4), and on the transported divergence, which might be a limiting factor in the vertical direction if a focusing monochromator is foreseen. The vertical dimension of a two-split guide system is free to be optimized independently of the horizontal guide shape, whence a large vertical divergence would be possible [9].

7.2. Cold crystal-analyzer spectrometer

A 165 m long inverse geometry instrument with a triple-axis-like backend and small sample size (CAMEA) has been suggested for ESS [13,24,25]. Detailed simulations are presented in Ref. [26,27]. In general, this instrument type is well matched to the wavelength and divergence ranges, and to the limited beam spot size that the guide-split system will provide. In addition, this instrument can accept limited or no pulse shaping.

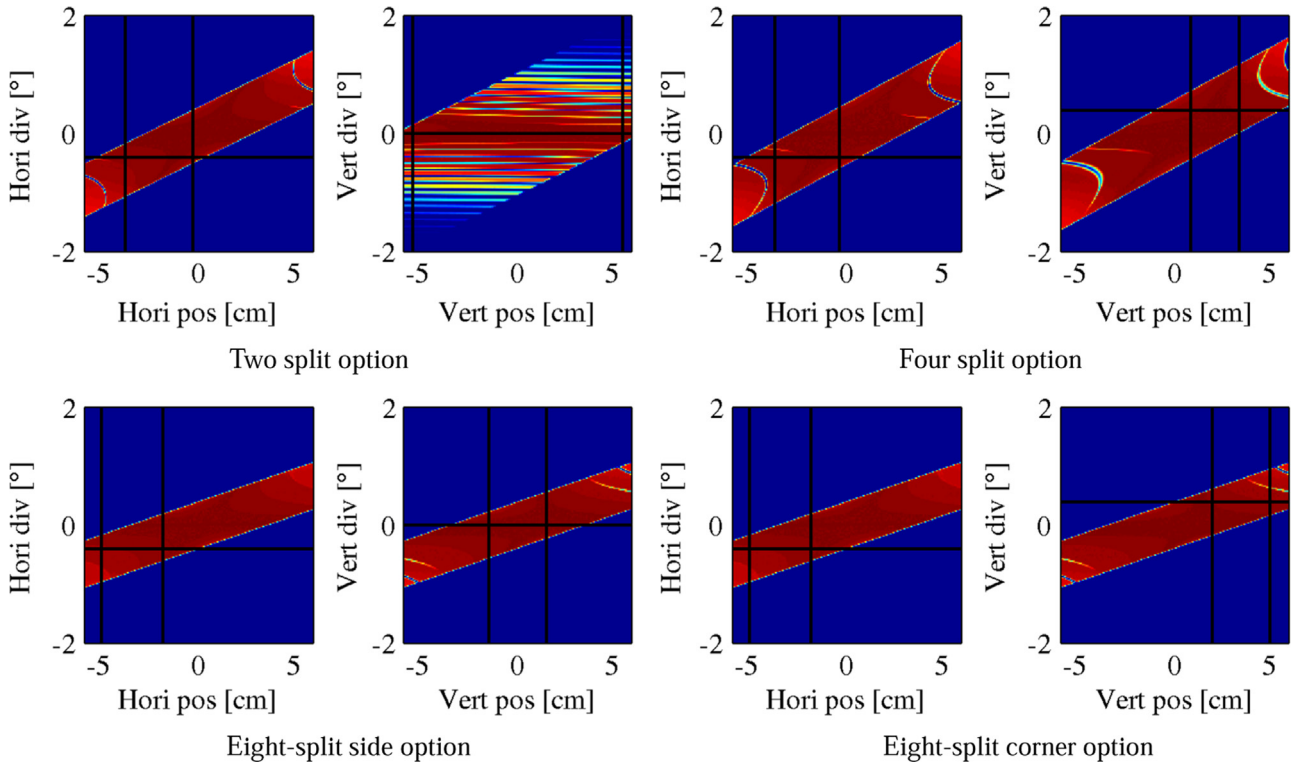

Fig. 7. The acceptance diagrams of the beam profile just at the entrance of the secondary guides for the wavelength band between 4.25 Å and 5.75 Å. The vertical lines mark the spatial opening of the secondary guides and the horizontal lines indicate where the new zero point for the divergence is.

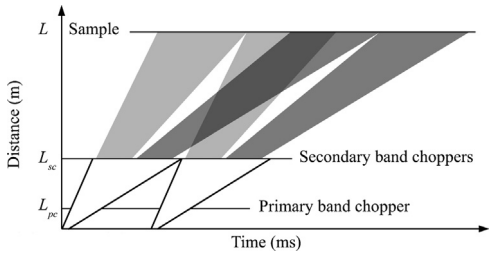

Fig. 8. A time-of-flight diagram showing how two sibling instruments can have a flexible selection of their wavelength bands despite a shared primary pulse shaping chopper. The light gray band shows a short wavelength choice and the dark gray band is a long wavelength choice. For clarity we use $L_{sc}/L = 1/3$ instead of the value 2/3 as used in the simulations.

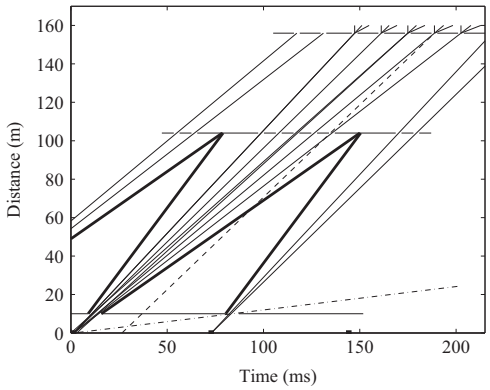

Fig. 9. Time-distance diagram for a 165 m long cold neutron chopper spectrometer. We show a wavelength band of 3.0–5.7 Å, narrowing down to 3.55–5.3 Å after the guide split, with 5 monochromatic pulses in this range. Parts of the preceding and following source pulses are shown. The dashed line represents a theoretical path a neutron would need to take to perform "cross-talk" between different chopper channels. The dashed-dotted line with a much smaller slope than the main neutron paths shows a possible frame overlap.

7.3. Cold chopper spectrometer

Another instrument that could be accommodated by the guide-split set-up would be the Cold Chopper Spectrometer [13]. Due to the long source pulse at ESS, chopper spectrometers will use the repetition-rate multiplication (RRM) method, where a pair of fast, counter-rotating choppers at the end of the second guide produces several monochromatic pulses on the sample for each source pulse [28].

When used in a guide-split set-up, the pulse shaping chopper can be positioned just after the guide split, in order to decouple the instrument resolution from the other instruments on the same guide system. A time-distance-diagram for such an instrument is displayed in Fig. 9. As illustrated by the dashed line the neutrons that may provide "cross-talk" between the designated time-distance channels of the utilized scheme cannot originate from the main source pulse. This is due to the fact that the pulse-shaping chopper is situated far from the moderator. The two chopper pairs therefore select the wavelength of the incoming neutrons uniquely, from the given moderator pulse within the band limited by the band width selection.

This instrument is quite similar to one of the cold chopper spectrometers proposed for ESS [29], and also rather similar to a simpler suggestions for a long-pulsed chopper spectrometers, simulated earlier [30]. Since a chopper spectrometer would typically accept a large vertical divergence and a medium (or large) horizontal divergence, a two-split guide would be preferred as discussed in Section 7.1.

7.4. Single crystal magnetism diffractometer

This section presents a study of a simple magnetism diffractometer for ESS. The instrument design is inspired by the Single-Crystal magnetism diffractometer described in the TDR [13]. The

instrument specifications match that of the WISH instrument at ISIS in high flux mode [31]. For simplicity we only present simulated results using a powder sample.

The detector is cylindrical with a height of 1 m and a radius of 2.2 m. There are 855 pixels covering 2π giving a horizontal pixel size of 16 mm (vertical pixel size is 10 cm). The instrument length is $L=156$ m.

The maximum width of the wavelength band of the instrument when using every source pulse is given by $\Delta\lambda = T/(\alpha L) = 1.88$ Å, where $T=71.4$ ms is the time between pulses. To avoid frame overlap, a slightly smaller wavelength band is used in practice ($\Delta\lambda = 1.80$ Å). In order to cover a larger q-range with the instrument the wavelength band can be shifted by phasing the band choppers.

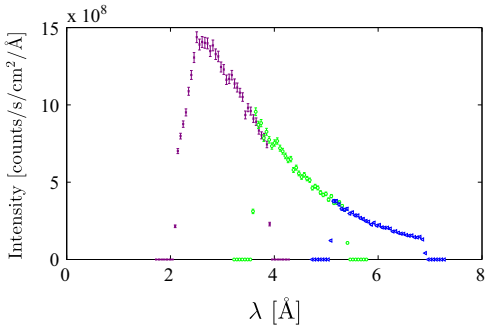

Fig. 10. Simulated wavelength spectrum at the 1×1 cm^2 sample position for the magnetism diffractometer, running with three different wavelength bands (2.1–3.9 Å, 3.6–5.4 Å, and 5.1–6.9 Å) selected by the band choppers.

With three wavelength intervals one can cover from 2.1 to 6.9 Å, which corresponds to a q-range from 0.91 to 5.98 Å^{-1} (when using scattering angles, 2θ, between 30° and 180°). In Fig. 10 the simulated flux on the sample is shown for three different wavelength bands.

In the simulations the instrument is placed on the 4-split guide system giving a divergence at the sample position of $\pm0.5°$. We consider only the high flux mode where no pulse shaping is used ($\tau=2.86$ ms). The wavelength resolution of the instrument is then $\delta\lambda/\lambda = \tau/(\alpha L\lambda) = 1.6\%$ for $\lambda=4.5$ Å. This resolution would be insufficient for most powder experiments but adequate for many single crystal magnetism experiments.

To simulate a full experiment, we use a standard NaCaAlF powder sample with realistic scattering power, and including incoherent scattering, [32] in a cylindrical container with a 10 mm height and a 10 mm diameter. The detector output is shown in Fig. 11 as a $(2\theta,t)$ diagram (raw data output), a $(2\theta,q)$ diagram (data ready to be refined), and the same data collapsed along 2θ onto q. A discussion on how to analyze 2D time-of-flight powder data can be found in Ref. [33]. In the one-dimensional data the peak shapes have the expected width of 0.06 Å^{-1} at $q=3$ Å^{-1} and are seen to have a slight asymmetry at high q, which originates from the pulse shape. The neutron detector count rate is 5×10^6 neutrons per second for the full spectrum on the detector, allowing collection of data with reasonable statistics (4×10^5 counts) from just a single source pulse.

7.5. Other options

Like the guide bundle, the guide-split set-up facilitates an increased number of instruments at a neutron source. This could

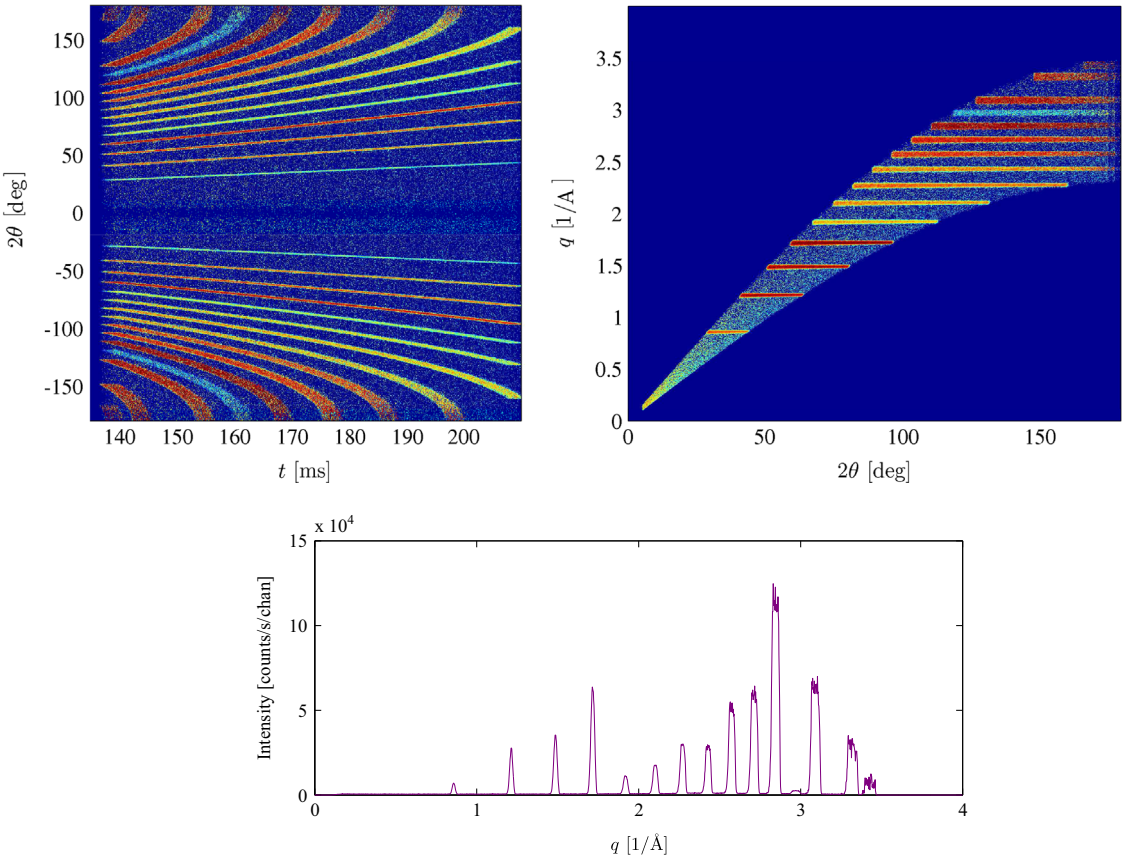

Fig. 11. Data from a simulation run on the magnetism diffractometer using the wavelength band 3.2–5.0 Å on a NaCaAlF sample (10 mm high cylinder with a 10 mm diameter). The color scale on the two color plots are logarithmic to enhance details. Top left: raw simulated data $(2\theta,t)$. Top right: transformed data $(2\theta,q)$ which is a more useful representation for refinement. Bottom: one-dimensional data obtained by projecting the top right data onto the q-axis, resembling the usual presentation of powder diffraction data. (For interpretation of the references to color in this figure caption, the reader is referred to the web version of this article.)

be used to build beam-lines that would otherwise not be built at a dedicated beam port, for example,

- Laue stations for crystal alignment.
- In-house test beam-lines for optics and other beam components.
- Dedicated student beam lines for educational purposes.

The guide-split set-up could also be used for bispectral instruments (working wavelength range 1.5–3.5 Å), including the accepted Macromolecular Diffractometer (NMX) and the Bispectral Powder Diffractometer [13] as it was recently shown that bispectral extraction feeds well into elliptical guides [34,17]. Thermal neutrons (wavelengths below 1.5 Å) do not seem to be well transported by the split guides that we have investigated. However, the current version of the guide-split was not optimized for this wavelength range, so future developments may improve this performance.

8. Conclusions

We have shown by simulations that it is feasible to split neutron guides by using a virtual source from a primary elliptical guide, in particular for cold neutrons with a divergence up to $\pm 0.5^\circ$ (1° FWHM) at the sample position. The elliptical set-up variations were found to have a brilliance transfer above 90% for the two-split, four-split and eight-split systems. The divergence distribution of these variations at the sample position is uniform for cold neutrons. We have demonstrated the use of this guide system by full simulations of a magnetism diffractometer for ESS. The guide for this instrument has an excellent performance.

The guide-split set-up offers the possibility of an increased amount of instruments, each out of line-of-sight, at the cost of a slightly reduced intensity at the sample position of each instrument. The lower intensity does not originate from lower brilliance transfer, but from a (possibly) reduced maximum divergence. Further studies are needed to quantify this divergence limitation.

The guide-split concept enables several instruments to share the same beam port. For sibling time-of-flight instruments the users would have to stay within the same primary wavelength band determined by pulse shaping choppers placed in the shared guide when operating the instrument. However, these constraints are tolerable and will not overshadow the advantage of the increase of the total number of instruments. Furthermore, the cost of the individual instruments will be reduced due to the fact that the primary guide and shielding are shared between instruments.

Acknowledgments

This work was supported by the Danish Ministry of Science and Innovation through the Danish in-kind program for the ESS design-update.

References

[1] ESS Web Page, ⟨http://ess-scandinavia.eu⟩, 2014.
[2] J. Christ, T. Springer, Nukleonik 4 (1962) 23.
[3] H. Maier-Leibnitz, T. Springer, Journal of Nuclear Energy 17 (1963) 217.
[4] F. Mezei, et al., Communications on Physics 1 (1976) 81.
[5] F. Mezei, P. Dagleish, Communications on Physics 2 (1977) 41.
[6] F. Mezei, et al., Journal of Neutron Research 6 (1997) 3.
[7] H. Abele, et al., Nuclear Instruments and Methods in Physics Research Section A 562 (2006) 407.
[8] C. Schanzer, et al., Nuclear Instruments and Methods in Physics Research Section A 529 (2004) 63.
[9] K.H. Klenø, et al., Nuclear Instruments and Methods in Physics Research Section A 696 (2012) 75. http://dx.doi.org/10.1016/j.nima.2012.08.027, URL: ⟨http://linkinghub.elsevier.com/retrieve/pii/S0168900212008959⟩.
[10] P. Böni, Nuclear Instruments and Methods in Physics Research Section A 586 (1) (2008) 1. http://dx.doi.org/10.1016/j.nima.2007.11.059, URL: ⟨http://linkinghub.elsevier.com/retrieve/pii/S0168900207023790⟩.
[11] D. Rodriguez, S. Kennedy, P. Bentley, Journal of Applied Crystallography 44 (2011) 727.
[12] P.M. Bentley, et al., Journal of Applied Crystallography 44 (2011) 483.
[13] ESS Technical Design Report, Technical Design Report for the European Spallation Source, URL: ⟨http://eval.esss.lu.se/cgi-bin/public/DocDB/ShowDocument?docid=274⟩, April 2013.
[14] K. Lefmann, K. Nielsen, Neutron News 10 (3) (1999) 20. http://dx.doi.org/10.1080/10448639908233684, URL: ⟨http://www.tandfonline.com/doi/abs/10.1080/10448639908233684⟩.
[15] P. Willendrup, et al., Physica B: Condensed Matter 350 (2004) 735.
[16] DMSC Web Page, ⟨http://www.ess-dmsc.eu⟩, 2014.
[17] H. Jacobsen, K. Lieutenant, C. Zendler, K. Lefmann, Nuclear Instruments and Methods in Physics Research Section A 717 (2013) 69.
[18] M. Bertelsen, et al., Nuclear Instruments and Methods in Physics Research Section A 729 (2013) 387.
[19] P. Willendrup, et al., Journal of Neutron Research 17 (2014) 35.
[20] M. Bertelsen, et al. (2015), in preparation.
[21] E. Farhi, et al., Journal of Neutron Research 17 (2013) 5.
[22] H. Schober, et al., Nuclear Instruments and Methods in Physics Research Section A 589 (2008) 34.
[23] A. Hiess, Personal Communication, 2014.
[24] H. Rønnow, et al., ESS Instrument Construction Proposal, Camea, URL: ⟨http://infoscience.epfl.ch/record/190509/files/MASTERInstrument_Construction_Proposalfinal.pdf⟩, March 2014.
[25] P. Freeman, J.O. Birk, M. Marko, M. Bertelsen, J. Larsen, N.B. Christensen, K. Lefmann, J. Jacobsen, Ch. Nidermayer, F. Juranyi, H.M. Rønnow, EPJ Web of Conferences 83 (2015) 03005.
[26] J.O. Birk, Camea, Ph.D. thesis, University of Copenhagen, Niels Bohr Institute, 2014.
[27] J.O. Birk, M. Marko, P.G. Freeman, J. Jacobsen, R.L. Hansen, N.B. Christensen, Ch. Niedermayer, M. Månsson, H.M. Rønnow, K. Lefmann, Review of Scientific Instruments 85 (2014) 113908.
[28] F. Mezei, M. Russina, in: Proceedings of the SPIE, vol. 4785, 2002, p. 24.
[29] J. Voigt, et al., Nuclear Instruments and Methods in Physics Research Section A 741 (2014) 26. http://dx.doi.org/10.1016/j.nima.2013.12.036.
[30] K. Lefmann, H. Schober, F. Mezei, Measurement Science and Technology 19 (2008) 034025.
[31] L.C. Chapon, P. Manuel, P.G. Radaelli, C. Benson, L. Perrott, S. Ansell, N. J. Rhodes, D. Raspino, D. Duxbury, E. Spill, J. Norris, Neutron News 22 (2) (2011) 22. http://dx.doi.org/10.1080/10448632.2011.569650, URL: ⟨http://www.tandfonline.com/doi/abs/10.1080/10448632.2011.569650⟩.
[32] P. Willendrup, et al., Physica B: Condensed Matter 385–386 (2006) 1032.
[33] A. Houben, et al., Nuclear Instruments and Methods in Physics Research Section A 680 (2012) 124.
[34] C. Zendler, K. Lieutenant, D. Nekrassov, L. Cussen, M. Strobl, Nuclear Instruments and Methods in Physics Research Section A 704 (2013) 68.

A.6 Simulation of waviness in neutron guides

This paper was partly a response to unphysical behaviour discovered in the McStas package when angles of incidence became similar than the simulated waviness of supermirrors. In these cases negative outgoing angles could be selected when a small random angle was added to the incidence angle, and rays were thus escaping the guide. This only occurs in rare cases, as the beam divergence is usually much larger than the waviness. A more thorough theoretical investigation identified the issue, and the findings are reported in this paper as well as results from guide simulations using an improved waviness model. The paper was published in the journal of Neutron Research.

Abstract

As the trend of neutron guide designs points towards longer and more complex guides, imperfections such as waviness becomes increasingly important. Simulations of guide waviness has so far been limited by a lack of reasonable waviness models. We here present a stochastic description of waviness and its implementation in the McStas simulation package. The effect of this new implementation is compared to the guide simulations without waviness and the simple, yet unphysical, waviness model implemented in McStas 1.12c and 2.0.

My contribution

Implemented the waviness theory into the McStas guide component used for the study and commented on the manuscript.

Journal of Neutron Research 18 (2015) 45–59
DOI 10.3233/JNR-150023
IOS Press

Simulation of waviness in neutron guides

Ursula Bengaard Hansen [a,*], Mads Bertelsen [a], Erik Bergbäck Knudsen [b] and Kim Lefmann [a]

[a] *Niels Bohr Institute, University of Copenhagen, Universitetsparken 5, Denmark*
[b] *Department of Physics, Technical University of Denmark, Lyngby, Denmark*

Abstract. As the trend of neutron guide designs points towards longer and more complex guides, imperfections such as waviness becomes increasingly important. Simulations of guide waviness has so far been limited by a lack of reasonable waviness models. We here present a stochastic description of waviness and its implementation in the McStas simulation package. The effect of this new implementation is compared to the guide simulations without waviness and the simple, yet unphysical, waviness model implemented in McStas 1.12c and 2.0.

Keywords: Waviness, neutron guides, super mirror, Monte Carlo simulations

1. Introduction

Neutron reflecting guides are most valuable to neutron scattering science, since they transport the neutrons from the source (moderator) surroundings to a low-background region, often 20 to 100 meters away. For time-of-flight neutron instruments, also the sheer instrument length is of value, since it gives an important contribution to improving the instrument resolution.

It is common experience that the transport efficiency of neutron guides degrades with their length. This can partially be explained by multiple reflections, causing unavoidable losses even when using mirrors with almost-perfect reflectivity. However, recent designs of elliptic, parabolic, and other types of ballistic guides [2,3,8,17,19] have been able to reduce the number of reflections dramatically. Much simulation work has been performed along these routes, and also the first physical realisations of elliptical guides have proven of great benefit [5,10].

Other causes of loss in neutron guide transport are imperfections of the guides, like misalignment or waviness. The effect of misalignment has to some extent been understood for straight guides [1], and back-of-the-envelope calculations show that present-day values of waviness are unproblematic for straight guides. However, concerns have been raised about the severity of imperfect guide conditions for complex guide shapes like the parabolic or elliptic ones. The actual relevance of this is emphasised, as these ballistic guide types are foreseen to be used for a significant part of the instruments at the European Spallation Source (ESS), with guide lengths up to 165 m [14,20].

Simulation of guide waviness has until now been hampered by the lack of a trustworthy description of waviness from individual mirrors, and simple attempts have been found to give physically invalid results [13] as we will discuss in the following. We here suggest an approximate model for waviness and present the implementation within the McStas package [16,21]. We will present and discuss the relevant effects of waviness: reflection angle, illumination corrections, mirror shading, and multiple reflections. Finally, we show the effect of waviness in a few realistic guide systems. Our aim with this work is to provide an effective description of the reflectivity as a function of waviness.

*Corresponding author. E-mail: uhansen@nbi.ku.dk.

1.1. Description of reflectivity and waviness

In most neutron ray-tracing packages, the specular reflectivity of neutron guides is modelled by a piecewise linear function [9,16] that depends only on the length of the neutron scattering vector, q:

$$R(q) = \begin{cases} R_0 & (q \leqslant Q_c), \\ R_0[1 - \alpha(q - Q_c)] & (Q_c < q \leqslant mQ_c), \end{cases} \tag{1}$$

where the critical scattering vector for natural abundance Ni is $Q_{c,Ni} = 0.0217$ Å^{-1}. Expressions with quadratic terms in q have also been used with only minor changes in performance [11,12].

For a perfect surface, the low-q reflectivity is unity, $R_0 = 1$. However, roughness on length scales smaller than the neutron coherence length will reduce the reflectivity from this value, typical values lie in the range $R_0 = 0.990$–0.995.

What we here understand as waviness is a local deviation of the surface normal of the neutron guide, on the sub-mm to cm range, larger than the neutron coherence length. At this length scale, one can assume that the neutron reflects from a single point at the surface. Typical mean waviness values (FWHM) are of the order 10^{-4} to 10^{-5} radians [18].

In our description of waviness, we assume that the whole guide substrate and coating have the same angular deviation as the guide surface. Hence, the reflectivity function, $R(q)$, depends only on the scattering vector q and is unaffected by waviness. Instead, waviness affects the angle between the neutron and the guide surface at the reflection point. Thereby it also changes the value of q and the direction of the neutron after reflection – with direct consequences for the transport properties of the guide. We assume that all rays are reflected at the surface of the guide piece, effectively this means that we assume that each layer of the supermirror has the same profile as the surface.

2. An algorithm for waviness simulations

As we are only interested in an average description of waviness, we require that the guide waviness can be described stochastically. In other words, we do not need to create and store a complete description of the guide surface height on sub-mm scaled grid. In addition, we require the algorithm to be scale invariant, i.e. it does not depend upon the length scale of the waviness, only on the root-mean-square waviness value, w.

When discussing the waviness problem we will solely focus on the longitudinal waviness, i.e. the waviness from rotation around on the axis transverse to the neutron beam path. The transverse waviness will not affect the illumination but only contribute through a very small alteration of the beam direction, which we will ignore in this analysis.

As an introduction, we describe the presently used, but physically wrong algorithm, that nevertheless fulfils these requirements. We investigate by analytics and simple ray-tracing what causes the algorithm to fail, and use this as a starting point to suggest a series of improvements in order to reach an algorithm that is in correspondence with the ray-tracing results.

2.1. The Gaussian waviness model

A somewhat inaccurate stochastic algorithm for the simulation of waviness was implemented in McStas 1.12c in the component *Guide_wavy* [9]. The main steps are:

1. Calculate the intersection point between the neutron and the average guide surface.
2. Calculate the angle of incidence θ_i with the average guide surface using the guide normal vector $\mathbf{n}$ and the direction of the incoming neutron wave vector $\mathbf{k}_i$.

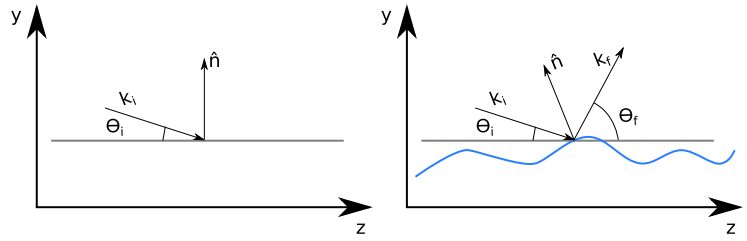

(a) Step 1-2. (b) Step 3-4.

Fig. 1. Schematic drawings of the waviness algorithm implemented in *Guide_wavy*. $\mathbf{k}_\mathrm{i}$ and θ_i ($\mathbf{k}_\mathrm{f}$ and θ_f) denote the initial (final) wave vector and angle respectively. First the intersection point and the angle of incidence is found (left). Then the guide normal vector $\hat{n}$ is randomly modified and the exit angle θ_f and the final wave vector is calculated. The nominal neutron direction is along z. The drawing is stretched along y for clarity.

3. Rotate $\mathbf{n}$ by a random angle, sampled from a Gaussian distribution of width w to reach the local surface normal $\mathbf{n}$.
4. Calculate the exit angle, θ_f, and the final neutron wave vector, $\mathbf{k}_\mathrm{f}$, by requiring specular (and elastic) reflectivity of the modified surface, see Fig. 1.
5. Calculate $\mathbf{q} = \mathbf{k}_\mathrm{i} - \mathbf{k}_\mathrm{f}$ and $R(q)$ and use this to modify the beam intensity.

However plausible, this algorithm yields unphysical results. The problem lies in step 3. The probability for the neutron ray to intersect the guide surface is implicitly assumed not to depend upon the local guide normal vector (from now on denoted the local waviness value). This leads to highly unphysical situations. For example, the neutron may reflect from a surface which is locally parallel to $\mathbf{k}_\mathrm{i}$. In addition it will be possible for low θ_i values to generate negative values of θ_f.

2.2. *Analysis of the beam illumination of a wavy surface*

In order to arrive at a waviness algorithm based on a stochastic theorem, we start by accounting for the beam illumination. The total illumination of a neutron ray of nominal incidence angle θ_i on a guide piece of length L is

$$\tilde{f} = \frac{L\sin(\theta_\mathrm{i})}{L} \approx \theta_\mathrm{i} \tag{2}$$

as we everywhere work in the small-angle approximation. We now imagine that the relative height of the guide surface can be written as $h(z)$, where we use periodic boundary conditions, $h(0) = h(L)$. We use the McStas convention where $\hat{\mathbf{z}}$ is along the main neutron flightpath. The local inclination is then given as $\theta_w = \frac{\mathrm{d}h(z)}{\mathrm{d}z} = h'(z)$. The local illumination of this piece of guide of length $\mathrm{d}z$ can in the small angle approximation be written as

$$\mathrm{d}f = \mathrm{d}z(\theta_\mathrm{i} + \theta_w). \tag{3}$$

The probability $\mathrm{d}P$ for a general neutron ray to reflect from this particular piece of guide is its fraction of the total illumination

$$\mathrm{d}P = \frac{\mathrm{d}f}{f} = \frac{1 + h'(z)/\theta_\mathrm{i}}{L}\,\mathrm{d}z. \tag{4}$$

The integral of (4) over the full length of the guide piece, L, gives

$$\int_0^L \mathrm{d}P(z) = \int_0^L \frac{1 + h'(z)/\theta_\mathrm{i}}{L}\,\mathrm{d}z = 1 \tag{5}$$

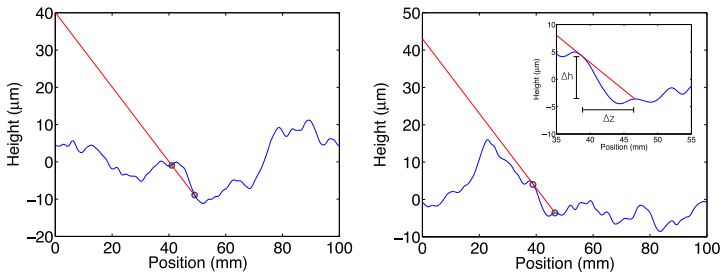

Fig. 2. Illustration of the problem with negative illumination and shading in waviness simulation for a surface with $w = 1$ mrad and $L = 100$ mm. We show two random, but static waviness profiles, $h(z)$ (blue), with the same low incoming neutron angle, $\theta_i = w$ (red). Left panel shows an illegal situation where the beam at $z = 41$ mm intersects the surface 'from below'. Right panel illustrates shading effects; the whole surface range $z = 38.6$ to 46.6 mm is out of reach for a neutron ray of the shown value of θ_i.

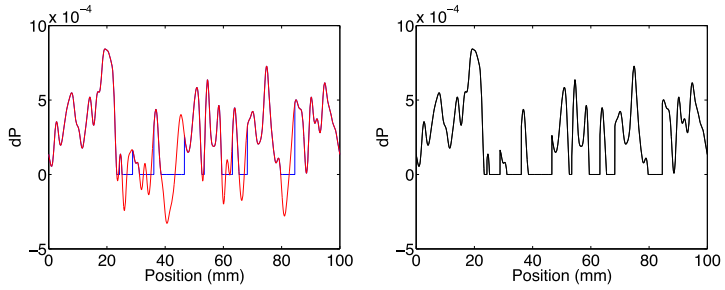

Fig. 3. Illustration of the influence of waviness shading on the beam illumination for a surface with $w = 1$ mrad and $L = 100$ mm. Left panel shows the 'bare' illumination probability (4) (red) and the shading corrections to this equation (blue) for the same surface as in Fig. 2 (right). Right panel shows the modified dP value (black).

as the integral over $h'(z)$ vanishes due to the periodic boundary conditions of $h(z)$. In addition, we note that our model is scale invariant, as it depends only on the values of $h'(z)$, whose magnitude is determined by the waviness w, and not on the guide piece length, L.

A necessary requirement for describing a correct waviness reflectivity algorithm is to be able to sample the local inclination according to the probability distribution (4). However, for small values of θ_i, (4) can give the unphysical value $dP < 0$. This implies that the local inclination angle of the guide surface is higher than the incoming angle. Thus, this part of the surface cannot be reached, as illustrated in Fig. 2. In fact, this implies that also other parts of the guide surface are out of reach, or "shaded". Also for the shaded part of the guide surface, the physical reflection probability must be zero, $dP = 0$. The figure also shows that the condition for the end of the shaded region is $\theta_i + \Delta h/\Delta z = 0$, corresponding to

$$\int_a^b \frac{1 + h'(z)/\theta_i}{L} \, dz = 0, \tag{6}$$

where a and b are the beginning and end of the shaded region, respectively. Hence, by replacing dP by zero in the shaded region, (5) is still fulfilled, which was also verified numerically. This replacement of dP is shown in Fig. 3 for the particular guide profile example shown in the right part of Fig. 2. Here, the shaded region is between $z = 38.6$ and 46.6 mm is assigned the corrected value $dP = 0$.

We choose, without loss of generality, to shift the endpoints of the periodic static surface so that the function $h(z)$ does not cause shading at the upper end of the interval.

2.3. A static model for random wavy surfaces

In order to simulate the effects of shading in wavy surfaces, we must be able to generate these surfaces. Waviness is a random phenomenon arising when manufacturing the neutron guide surfaces. It therefore makes sense to model waviness as a stochastic process (see for instance [7]) along the length of the guide surface.

Our starting assumption is that the height variations of the imperfect surface may be written as a sum of independent stochastic processes $h_n(z)$ with amplitudes a_n and random phases Φ_n:

$$h(z) = \sum_{n=1}^{n_{\max}} h_n(z) = \sum_{n=1}^{n_{\max}} a_n \sin\left(2\pi \frac{n}{L} z + \Phi_n\right) \tag{7}$$

which means that waviness may be expressed as:

$$h'(z) = \sum_{n=1}^{n_{\max}} 2\pi \frac{n}{L} a_n \cos\left(2\pi \frac{n}{L} z + \Phi_n\right). \tag{8}$$

This definition may obviously be interpreted as a Fourier series of the surface profile. Denoting the distribution of the phases by f_Φ the expectation, E, of the part processes is:

$$m_{h'_n}(z) = \mathrm{E}\big(h'_n(z)\big) = \int 2\pi \frac{n}{L} a_n \cos\left(2\pi \frac{n}{L} z + \phi\right) f_\Phi(\phi)\, \mathrm{d}\phi. \tag{9}$$

If we now assume the random phases to be uniformly distributed, the expectation of the sum process $m_h(z) = 0$. Similarly, the autocovariance function of the sum process (8) is:

$$\gamma(s,t) = \sum_{n=1}^{n_{\max}} \mathrm{E}\big(h'_n(s)\big)\mathrm{E}\big(h'_n(t)\big) - m_{h'_n}(s) m_{h'_n}(t), \tag{10}$$

where each of the elements in the sum is

$$\gamma_n(s,t) = \int_0^{2\pi} 2\pi \frac{n}{L} a_n \cos\left(2\pi \frac{n}{L} s + \phi\right) 2\pi \frac{n}{L} a_n \cos\left(2\pi \frac{n}{L} t + \phi\right) \frac{1}{2\pi}\, \mathrm{d}\phi \tag{11}$$

$$= 2\pi \frac{n^2}{L^2} a_n^2 \int_0^{2\pi} \frac{1}{2}\left(\cos\left(2\pi \frac{n}{L}(s+t) + 2\phi\right) + \cos\left(2\pi \frac{n}{L}(s-t)\right)\right) \mathrm{d}\phi \tag{12}$$

$$= 2\pi^2 \frac{n^2}{L^2} a_n^2 \cos\left(2\pi \frac{n}{L}(s-t)\right). \tag{13}$$

Thus,

$$\gamma(s,t) = \frac{2\pi^2}{L^2} \sum_{n=1}^{n_{\max}} n^2 a_n^2 \cos\left(2\pi \frac{n}{L}(s-t)\right) = \gamma(\tau); \quad \tau = s - t \tag{14}$$

which also proves that the sum process is stationary as the autocovariance function only depends on the distance between two samples, not on the absolute location along z. The stationarity property also proves our earlier statement that we may choose to shift the generated surface $h(z)$ so we avoid shading in the beginning of the considered interval.

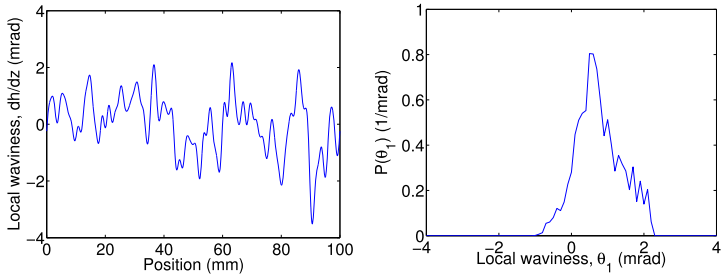

Fig. 4. Results from waviness shading simulation for one surface with $w = \theta_i = 1$ mrad. Left panel shows the waviness profile, $h'(z)$, along the surface. Right panel shows a weighted histogram of the local waviness value at the point of intersection with the neutron beam.

Waviness, w, is generally specified as a standard deviation of the angle variations along the length of a guide. In terms of the defined stochastic process, this is simply $w^2 = \gamma(0)$. What remains is to define the amplitudes (or Fourier coefficients) of the part processes. The spectral properties hereof must depend on the actual neutron guide manufacturing procedure. For simplicity, here we choose

$$a_n \propto \frac{\exp(-n/n_0)}{n} \tag{15}$$

which indicates a fairly uniform weighting of low frequency components while suppressing high frequency variations, which are generally not significant for the purpose of describing waviness. To simulate a guide, we generate a realisation of Eq. (8) with amplitude coefficients given by (15) normalised to the desired waviness using (14). It is worth to notice that this model is scale invariant and only depends on w, hence all profile simulations have been scaled to reasonable length scales [4]. The surface profiles in Fig. 2 and in the remainder of this report are generated in this way, using $n_0 = 10$ and $n_{\max} = 25$. At these values the results converged. A fully stochastic description of waviness should also allow for random fluctuations in the amplitude coefficients, but as we will show in the following, the proposed model, while simple, works quite well and is a significant improvement to the schemes that have been used so far.

2.4. Simulation of shading effects in the static, random model

We have performed simulations of waviness shading on a series of surfaces. For each surface, we have calculated $\mathrm{d}P(z)$ and used weighted histograms to calculate the probability function $P(\theta_w)$, describing the frequency each surface orientation is getting hit by the neutron ray. Figure 4 shows the result from one such simulation with a low incidence angle, $\theta_i = w$. The peaks in $P(\theta_w)$ corresponds to the positions where the local waviness profile is peaking. As expected from the illumination analysis, $P(\theta_w)$ vanishes below the value $\theta_w = -\theta_i$.

However, Fig. 4 shows only a single surface. For a stochastic model, all surface patterns should be represented. We simulate this by generating the average of $P(\theta_w)$ over a large number of static surfaces. Such an average is seen in Fig. 5(b). We immediately notice that the distribution vanishes at $\theta_w = -\theta_i$ as it should, and that it otherwise seems like a skewed Gaussian with a centre slightly larger than zero.

A simple test expression to model the simulated distribution of θ_w is found by multiplying a normal distribution of $\theta_w(z)$ with the illumination probability (4):

$$f(\theta_w) \propto \mathrm{d}P(\theta_w) g(\theta_w, w) \propto \frac{1 + h'(z)/\theta_i}{L} \exp\bigl(-\theta_w^2/\bigl(2w^2\bigr)\bigr). \tag{16}$$

In Fig. 5, we have overlaid a scaled version of the function (16) to the simulated data, and the agreement is found to be surprisingly good. For small incidence angles, $\theta_i/w = 0.5$, there are small deviations at low values of θ_w, where

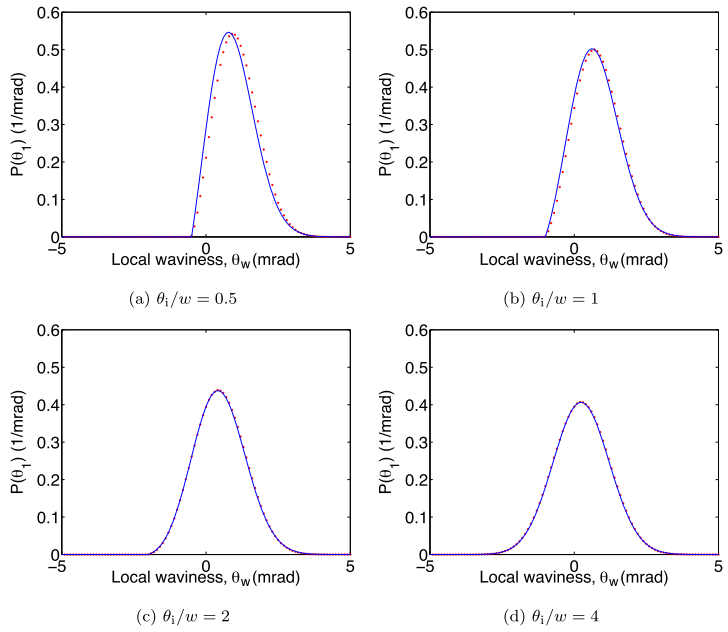

(a) $\theta_i/w = 0.5$ (b) $\theta_i/w = 1$

(c) $\theta_i/w = 2$ (d) $\theta_i/w = 4$

Fig. 5. Distribution of local waviness values. Dots show results from $5 \cdot 10^4$ waviness shading simulations for surfaces generated with $w = 1$ mrad and $\theta_i/w = 0.5$, 1, 2 and 4. The solid line are scaled versions of Eq. (16).

the simulated waviness is lower than the model, which in effect shifts the simulated waviness slightly to the right. This is an effect of the shading, which preferably appear at low θ_w values reducing the reflectivity. Figure 5 also shows similar comparisons for higher values of the beam incidence angle. For $\theta_i/w = 2$ or higher, the right-shift has almost vanished. This validates the picture of shading as the cause of the right-shift. We have not found a (simple) functional form of $f(\theta_w)$ that matches the simulated distribution better than Eq. (16).

2.5. *Correction for multiple reflections*

Unfortunately, knowledge about the distribution of the waviness angle θ_w is insufficient to constitute a complete waviness algorithm. In addition, we must account for the neutron rays that are reflected multiple times. The necessity for this originates from a simple consideration: Imagine a beam of nominal incident angle θ_i being reflected at the local waviness angle θ_w. Then, the local angle of incidence is $\theta = \theta_i + \theta_w$, leading to an outgoing angle of

$$\theta_f = \theta_i + 2\theta_w \tag{17}$$

(see Fig. 1). For negative values of θ_w this may result in negative values of θ_f, meaning that the neutron ray continues down towards the mirror. With the exception of reflections at the very end of the mirror, there will be (at least) one other reflection before the neutron ray has left the mirror.

To quantify the effect of this, we have employed a simple ray-tracing method when simulating the wavy surfaces. We chose the initial intersection point in accordance with the illumination and shading discussed above and construct the angle of the outgoing neutron ray according to (17). We then follow the outgoing ray over an extended surface that spans over a length of $2L$. We check across the surface height curve if the ray collides with the surface again. If there is such a multiple collision, another outgoing angle is calculated according to (17), and the ray-tracing continues. Two examples of these simulations are given in Fig. 6.

We have performed a series of simulations with varying incident angles, θ_i, with $N = 10^4$ simulations per angle, to obtain the fraction of multiply reflected rays. The results are shown in Fig. 7. We observe that the degree of

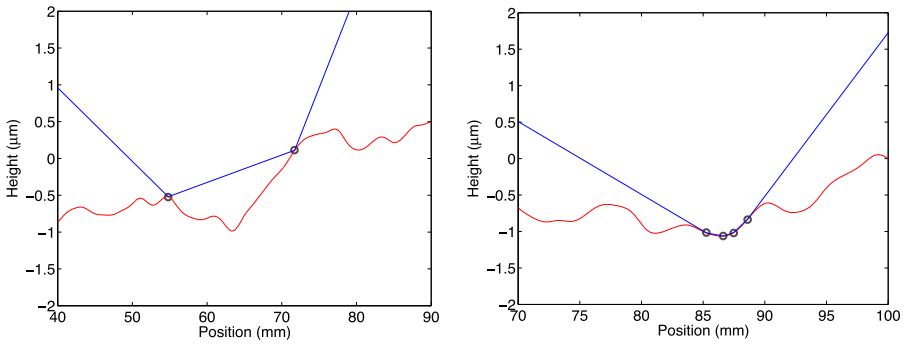

Fig. 6. Two examples of multiple reflections simulated with $\theta_w/w = 1$ mrad and a repetition period $L = 100$ mm. Left panel shows a typical double reflection. Right panel illustrates the rare occasion of many close multiple reflections.

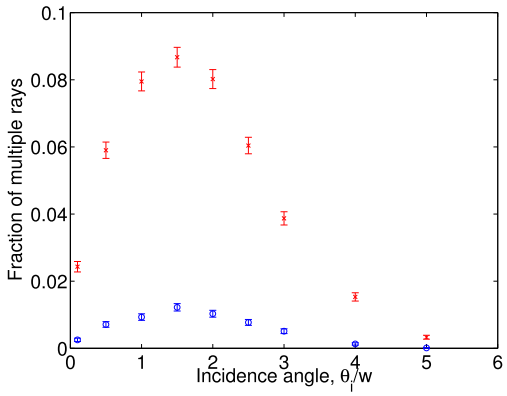

Fig. 7. Simulated fraction of multiple reflections as a function of incident angle, θ_i. Red crosses represents all multiple events, while blue circles are events with three or more reflections.

multiple reflection is highest, just below 10%, for $\theta_w/w \approx 1.5$, to decay to zero for $\theta_w/w = 0$, and for angles higher than $\theta_w/w \approx 5$. This is in agreement with expectations, since rays with very low angles will reflect only from the tops of the height curve, $h(z)$, on the side with $\theta_w > 0$ due to shading, while high incident angles will reflect with high outgoing angles without chance for having a second reflection, $\theta_i > 2|\theta_w|$, leaving Eq. (17) always positive. Figure 7 also shows that the ratio of rays with more than two reflections in general behaves as the ratio of all multiple reflections. The maximum is of the order 1%, occurring also around $\theta_w/w \approx 1.5$.

Our most important result, however, is the distribution of final reflections angles, $P(\theta_f)$. A naive prediction of the shape of this simulation would come from taking only the illumination argument into account, ignoring shading and multiple scattering. Here we combine (16) and (17) to reach

$$f(\theta_f) \propto \exp\bigl(-(\theta_f - \theta_i)^2/(8w^2)\bigr)\left(1 + \frac{(\theta_f - \theta_i)}{2\theta_i}\right). \tag{18}$$

Figure 8(b) shows the simulated distribution overlaid with Eq. (18). We observe that the simulations show a vanishing probability for a reflection at $\theta_f = 0$, as one must require, while the naive prediction (18) has a finite probability at negative θ_f values, as it does not include multiple reflections.

The full analytical description of the illumination, shading, and multiples into one equation is a complex task that we have no intention of performing. However, we have performed a minimal change of (18) to make it vanish

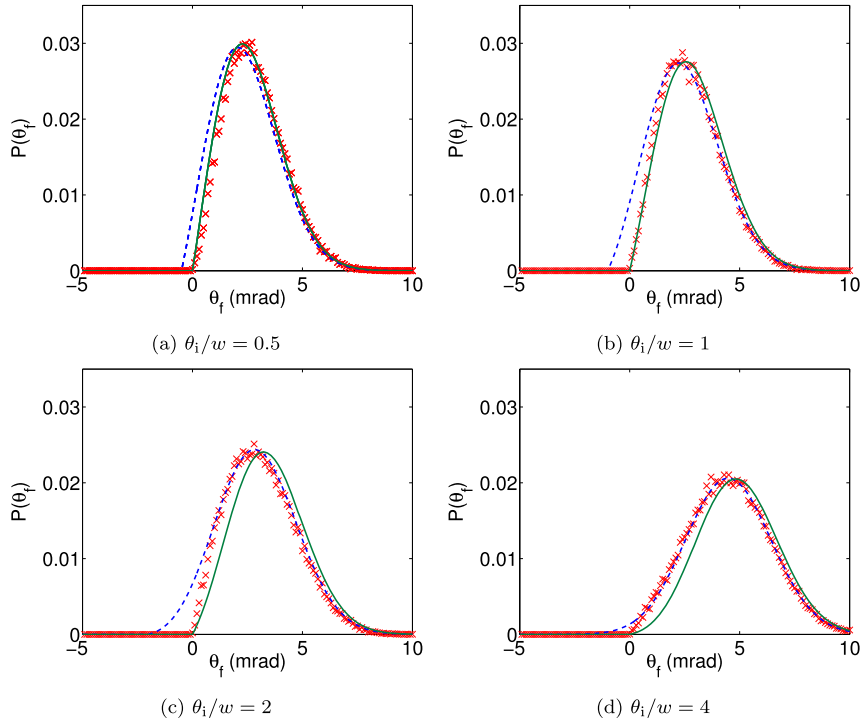

(a) $\theta_i/w = 0.5$ (b) $\theta_i/w = 1$

(c) $\theta_i/w = 2$ (d) $\theta_i/w = 4$

Fig. 8. Distribution of outgoing angles of neutron rays, θ_f, reflected from a wavy surface with $w = 1$ mrad, $\theta_i/w = 0.5$, 1, 2 and 4. Red crosses represents results from simulations with $N = 5 \cdot 10^4$ rays, the blue dashed line is the prediction (18) taking only the illumination into account, while the green line is our conjecture, (19).

at $\theta_f = 0$:

$$f(\theta_f) \propto \exp\left(-(\theta_f - \theta_i)^2/(8w^2)\right)\left(\frac{\theta_f}{2\theta_i}\right). \tag{19}$$

Figure 8 show that this equation in fact describes the simulated distribution of the outgoing angle θ_f quite well for $\theta_i/w = 1$. Hence, we use (19) as a first order conjecture for the true outcome of the reflection from wavy surfaces.

We have as well performed simulations of other values of θ_i/w: 0.5, 2, and 4. All these results are shown along with the predictions (18) and (19) in Fig. 8. We see that for the high angles of incidence, θ_i, the naive prediction (18) in general works better than the conjecture (19).

3. A new approximate algorithm for waviness simulation

Our objective is now to find a functional form that can effectively describe $P(\theta_f)$ as a function of θ_i and w. From our simulations we see that $P(\theta_f)$ approaches zero for $\theta_f \to 0$. For small θ_i it increases linearly with θ_f to a maximum slightly above θ_i and then decreases in a Gaussian manner. In the other end of the spectrum, when θ_i is large, $P(\theta_f)$ can be described by a Gaussian with a width w centred at θ_i. Both observations are in accordance with the simple considerations discussed earlier. We have made no attempt to understand the details the shape of $P(\theta_f)$ in the intermediate region.

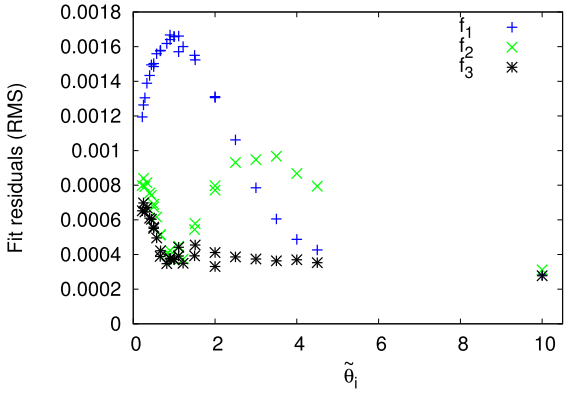

Fig. 9. The root mean square of the fits to f_1 (blue +), f_2 (green ×) and f_3 (black ∗) as a function of incoming angle $\tilde{\theta}_\mathrm{i}$.

As a starting point we have modified the expression (18) in order to reproduce the observed behaviour. We have produced three alternatives:

$$f_1(\tilde{\theta}_\mathrm{f}) = \alpha_1 \exp\bigl(-(\tilde{\theta}_\mathrm{f} - \kappa_1\tilde{\theta}_\mathrm{i})^2/8\bigr)\left(1 + \frac{(\tilde{\theta}_\mathrm{f} - \tilde{\theta}_\mathrm{i})}{2\tilde{\theta}_\mathrm{i}}\right), \tag{20}$$

$$f_2(\tilde{\theta}_\mathrm{f}) = \alpha_2 \exp\bigl(-(\tilde{\theta}_\mathrm{f} - \kappa_2\tilde{\theta}_\mathrm{i})^2/8\bigr)\left(\frac{\tilde{\theta}_\mathrm{f}}{2\tilde{\theta}_\mathrm{i}}\right), \tag{21}$$

$$f_3(\tilde{\theta}_\mathrm{f}) = \alpha_3 \exp\bigl(-(\tilde{\theta}_\mathrm{f} - \kappa_3\tilde{\theta}_\mathrm{i})^2/8\bigr)\tanh(\beta_3\tilde{\theta}_\mathrm{f}/\tilde{\theta}_\mathrm{i}), \tag{22}$$

where $\tilde{\theta}_\mathrm{i}$ and $\tilde{\theta}_\mathrm{f}$ are the dimensionless variables $\tilde{\theta}_\mathrm{i} = \theta_\mathrm{i}/w$ and $\tilde{\theta}_\mathrm{f} = \theta_\mathrm{f}/w$ respectively.

A series of simulations with $\tilde{\theta}_\mathrm{i}$ going from 0.22 to 10 was made and each simulation was fitted to the expressions (20), (21) and (22). In all cases the $\alpha_{1,2,3}$, $\beta_{1,2,3}$ and $\kappa_{1,2,3}$ are fitting parameters that are free to vary. Figure 9 shows the root mean square of the residuals for each fit. It is clear that the expression f_3 has the best performance over the whole range. This can also be seen in the individual simulations, in Fig. 10 examples where $\tilde{\theta}_\mathrm{i} = 0.22$, 1, 2.5 and 4.5 are shown. We therefore choose $f_3(\tilde{\theta}_\mathrm{f})$ as our model for describing $P(\theta_\mathrm{f})$ when simulating waviness.

The value of the fitting parameters α_3, β_3 and κ_3 varies with $\tilde{\theta}_\mathrm{i}$. In order to make an algorithm that provides $P(\tilde{\theta}_\mathrm{f})$ for any given $\tilde{\theta}_\mathrm{i}$, the $\tilde{\theta}_\mathrm{i}$ dependence of the parameters α_3, β_3 and κ_3 was each fitted to an effective model that could approximate the numerical results. This turned out to be:

$$\begin{aligned}
\alpha_3(\tilde{\theta}_\mathrm{i}) &= \begin{cases} a_1 & \text{for } \tilde{\theta}_\mathrm{i} < 0.78, \\ a_2\tilde{\theta}_\mathrm{i}^{-a_3} + a_4 & \text{otherwise}, \end{cases} \\
\beta_3(\tilde{\theta}_\mathrm{i}) &= \begin{cases} b_1\tilde{\theta}_\mathrm{i}^{b_2} + b_3 & \text{for } \tilde{\theta}_\mathrm{i} < 1.38, \\ b_4\tilde{\theta}_\mathrm{i}^{b_5} + b_6 & \text{for } 1.38 < \tilde{\theta}_\mathrm{i} < 4.5, \\ b_7 & \text{otherwise}, \end{cases} \\
\kappa_3(\tilde{\theta}_\mathrm{i}) &= k_1\tilde{\theta}_\mathrm{i}^{k_2} + 1.
\end{aligned} \tag{23}$$

The results for each expression in (23) can be seen in Fig. 11 and the corresponding parameters in Table 1.

The validity of this model is tested by its strength to predict the simulations made in Section 2.5. In Fig. 12 the new model is compared to that of McStas 1.12c for $\tilde{\theta}_\mathrm{i} = 0.22$, 1, 2.5 and 4.5. The results from the new model over

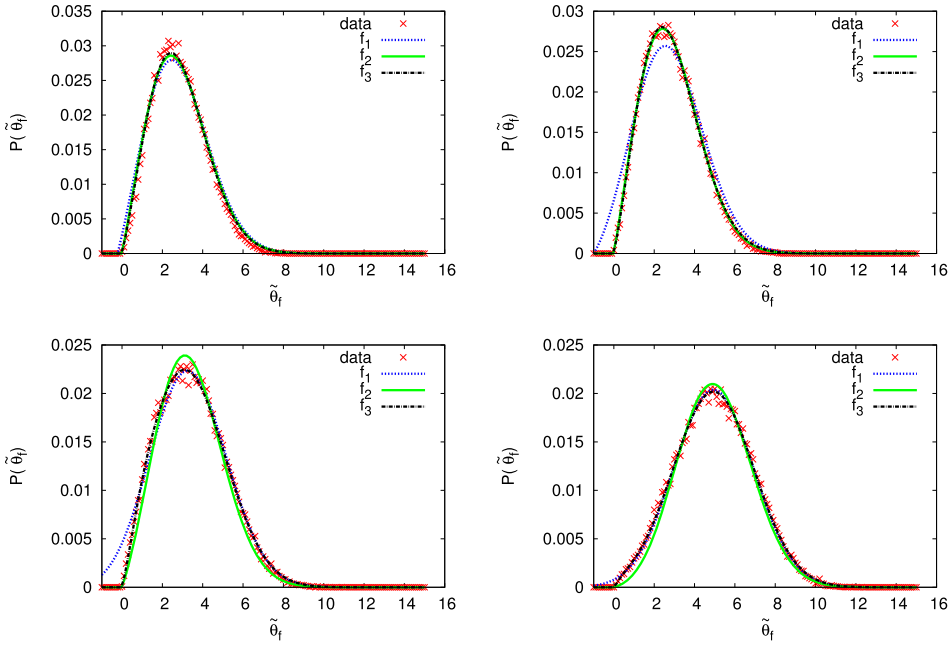

Fig. 10. Simulated data for $\tilde{\theta_i} = 0.22$, 1, 2.5 and 4.5 with $N = 5 \cdot 10^4$ rays along with fits to f_1 (blue dashed line), f_2 (green solid line) and f_3 (black dot dashed line).

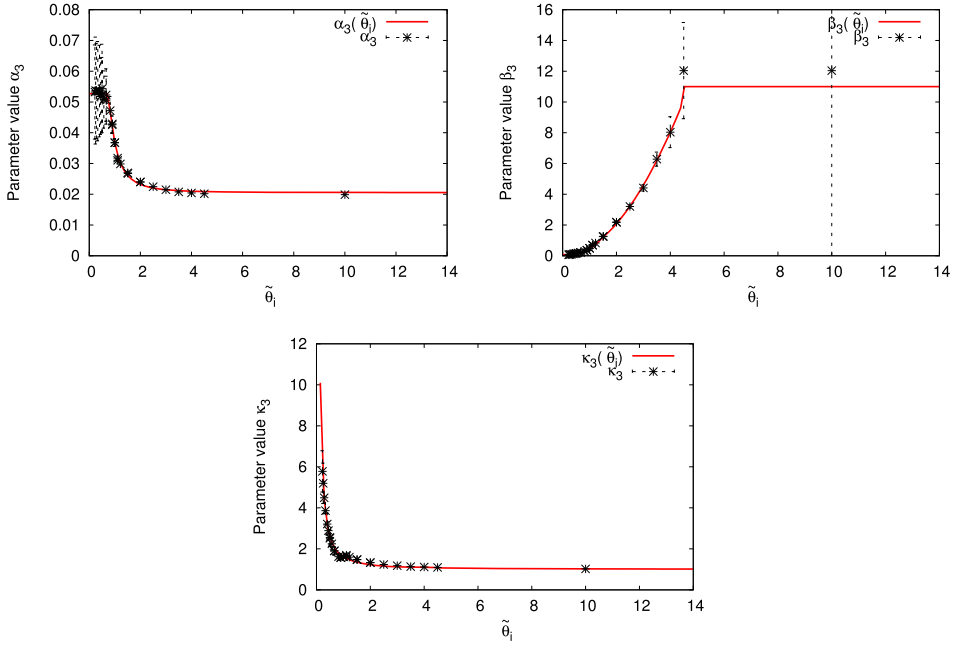

Fig. 11. The parameters α_3, β_3, and κ_3 of expression (22) as a function of $\tilde{\theta_i}$ (black $*$) where the error bars denotes the uncertainty on the parameter in the fits to (22) along with the power law fits to (23) (red line).

Table 1
The parameters of the new waviness model used in Eqs (22) and (23)

$\alpha_3(\tilde{\theta}_i)$	a_1	a_2	a_3	a_4			
	0.0527	0.0162	2.6	0.0205			
$\beta_3(\tilde{\theta}_i)$	b_1	b_2	b_3	b_4	b_5	b_6	b_7
	0.395	2.5	0.076	0.541	1.9	0.007	11
$\kappa_3(\tilde{\theta}_i)$	k_1	k_2					
	0.61	1.39					

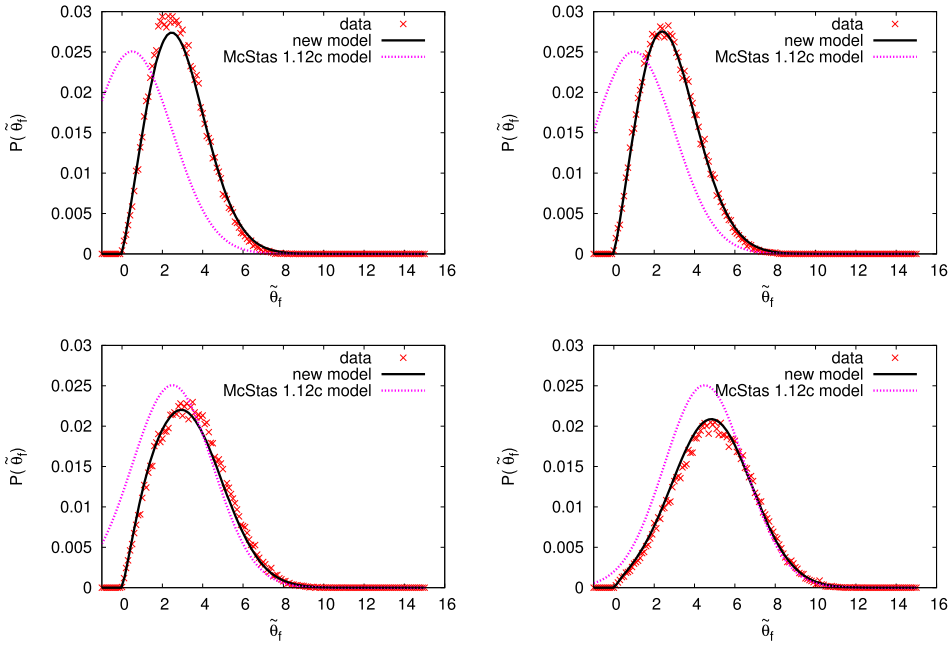

Fig. 12. Simulated data for $\tilde{\theta}_i = 0.22$, 1, 2.5 and 4.5 with $N = 5 \cdot 10^4$ rays along with the model of McStas 1.12c (magenta dashed line) and the prediction by the new algorithm (black line).

the whole range are sufficiently close to the simple ray tracing simulations that we do not need to refine the model further.

It should be noted that in the McStas 1.12c model, described in Section 2.1, the parameter w was taken to be the width of the distribution of final angles. In the new model w is the average inclination (rms) of the surface, which gives a width of $2w$. We have corrected for this in our comparison in Fig. 12.

4. Implementation of waviness in McStas

The algorithm describing $P(\tilde{\theta}_f)$ from Eq. (22) along with a *hit and miss* [6] sampling routine, were implemented in a straight guide in McStas. First the outcome of a single reflection from a wavy surface for an extremely narrow and well collimated beam was compared to the simulations made in Section 2.5. Figure 13 shows examples for $\tilde{\theta}_i = 1$ and $\tilde{\theta}_i = 10$. The implementation of waviness in McStas clearly reproduces the simulations from Section 2.5.

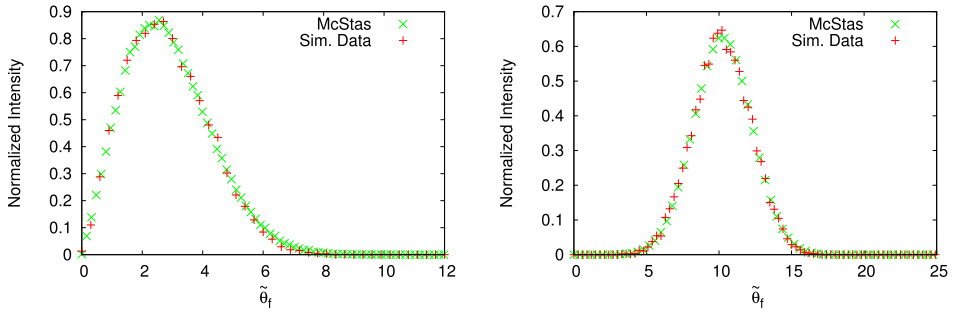

Fig. 13. Simulated data with $N = 5 \cdot 10^4$ rays (red) and normalised neutron counts from McStas (red) made with $N = 10^6$ rays for $\tilde{\theta}_i = 1$ (left) and $\tilde{\theta}_i = 10$ (right).

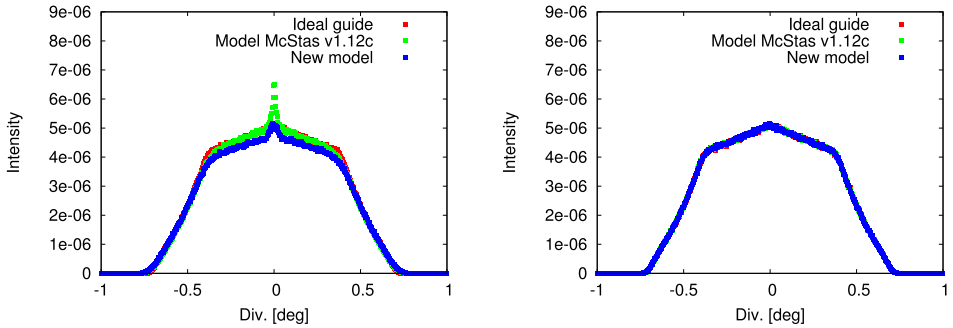

Fig. 14. Intensity as a function of divergence after an ideal guide without waviness (red), with the McStas 1.12c waviness description (green) and with the new waviness description (blue) for $w = 10^{-4}$ (left) and $w = 10^{-6}$ rad (right). The simulations were made with 10^7 neutron rays each.

4.1. Example guide simulations

At last, we show simulations of a 150 m long straight guide with a cross section of $0.05 \times 0.05\ \mathrm{m}^2$ starting 4 m from a $0.1 \times 0.1\ \mathrm{m}^2$ moderator using only 4 Å neutrons. The guide has a coating described by (1) with $m = 2$, $Q_c = 0.0217$, $R_0 = 0.99$, $W = 0.003$ and $\alpha = 2.0$. Simulations were done without waviness, with the McStas 1.12c waviness description (see Section 2.1) and with the new description developed in Section 3, respectively.

When simulating long neutron guides, there is a significant difference between the new and the McStas 1.12c waviness descriptions for large waviness values, $w = 10^{-4}$ rad, as shown in Fig. 14. In the old version we see a large unphysical peak around 0° divergence which would lead to a brilliance transfer (defined as neutron flux within a small $2D$ divergence interval and wavelength interval) larger than unity. This, in turn is a violation the Liouville theorem [15]. The reason for this is the oversampling of low values of θ_f caused by a mistake in the algorithm.

The main consequence of waviness is in the case of the new description reduced intensity as expected, but no violation of the Liouville theorem. The difference between the two descriptions diminishes for smaller values of w, an example with a very low waviness $w = 10^{-6}$ rad is also shown in Fig. 14.

5. Summary

We have performed analytical and simple ray-tracing analysis of the waviness problem relevant for simulations of neutron supermirror reflectivity. The simulations provided a distribution of outgoing angles for a given incoming

angle and waviness. It was found that the shape of the distribution evolved as a function of incoming angle.

For each incident angle the distribution was fitted to a expressions whose parameters was taken to be dependent on the incoming angle. This dependence was fitted as well, which resulted in an effective description of the simulated probability distribution of outgoing angles as a function of the incoming angles and waviness.

A routine sampling of the outgoing angle for a given incoming angle and waviness was implemented in a straight-guide component in McStas. There is good accordance between the McStas simulations of a single reflection on a wavy surface of a narrow beam and the ray-tracing simulations described in this work.

The unphysical behaviour of the McStas 1.12c waviness model for large waviness values is no longer present in the new model. Instead, the main consequence of waviness is a reduced intensity as expected from simple physical arguments.

Acknowledgements

This project has been funded by the University of Copenhagen 2016 program through the project CoNeXT. CoNeXT is a University of Copenhagen interfaculty collaborative project, which is fertilising the ground and harvesting the full potential of the new neutron and X-ray research infrastructures close to Copenhagen University. We also thank the Danish Agency for Research and Innovation for their support through the contribution to the ESS design update phase.

References

[1] P.M. Allenspach, P. Böni and K. Lefmann, Loss mechanisms in supermirror neutron guides, *Proc. SPIE* **4509** (2001), 157–165.
[2] M. Bertelsen, H. Jacobsen, U.B. Hansen, H.H. Carlsen and K. Lefmann, Exploring performance of neutron guide systems using pinhole beam extraction, *Nuclear Instruments and Methods in Physics Research Section A: Accelerators, Spectrometers, Detectors and Associated Equipment* **729** (2013), 387–398.
[3] P. Böni, New concepts for neutron instrumentation, *Nuclear Instruments and Methods in Physics Research Section A: Accelerators, Spectrometers, Detectors and Associated Equipment* **586**(1) (2008), 1–8.
[4] P. Böni, D. Clemens, H. Grimmer and H. Van Swygenhoven, Morphology of glass surfaces: influence on the performance of supermirrors, in: *Proceedings of ICANS-XIII*, 1995, pp. 279–287.
[5] L.C. Chapon, P. Manuel, P.G. Radaelli, C. Benson, L. Perrott, S. Ansell, N.J. Rhodes, D. Raspino, D. Duxbury, E. Spill and J. Norris, Wish: The new powder and single crystal magnetic diffractometer on the second target station, *Neutron News* **22**(2) (2011), 22–25.
[6] G. Cowan, *Statistical Data Analysis*, Clarendon Press/Oxford University Press, Oxford/New York, 1998.
[7] D.R. Cox and H.D. Miller, *The Theory of Stochastic Processes*, Chapman & Hall, 1965.
[8] L.D. Cussen, D. Nekrassov, C. Zendler and K. Lieutenant, Multiple reflections in elliptic neutron guide tubes, *Nuclear Instruments and Methods in Physics Research Section A: Accelerators, Spectrometers, Detectors and Associated Equipment* **705** (2013), 121–131.
[9] E. Farhi, P. Willendrup, E. Knudsen and K. Lefmann, User and programmers guide to the neutron ray-tracing package McStas, version 1.12, 2011.
[10] R.M. Ibberson, Design and performance of the new supermirror guide on HRPD at ISIS, *Nuclear Instruments and Methods in Physics Research Section A: Accelerators, Spectrometers, Detectors and Associated Equipment* **600**(1) (2009), 47–49.
[11] H. Jacobsen, K. Lieutenant, C. Zendler and K. Lefmann, Bi-spectral extraction through elliptic neutron guides, *Nuclear Instruments and Methods in Physics Research Section A: Accelerators, Spectrometers, Detectors and Associated Equipment* **717** (2013), 69–76.
[12] H. Jacobsen, K. Lieutenant, C. Zendler and K. Lefmann, Corrigendum to "Bi-spectral extraction through elliptic neutron guides" [Nucl. Instr. and Meth. A 717 (2013) 69–76], *Nuclear Instruments and Methods in Physics Research Section A: Accelerators, Spectrometers, Detectors and Associated Equipment* **743** (2014), 160.
[13] K.H. Klenø, Exploration of the challenges of neutron optics and instrumentation at long pulsed spallation sources, PhD thesis, University of Copenhagen, 2013.
[14] K.H. Klenø, K. Lieutenant, K.H. Andersen and K. Lefmann, Systematic performance study of common neutron guide geometries, *Nuclear Instruments and Methods in Physics Research Section A: Accelerators, Spectrometers, Detectors and Associated Equipment* **696** (2012), 75–84.
[15] L.D. Landau, L.P. Pitaevskii and E.M. Lifshitz, *Statistical Physics*, Butterworth-Heinemann, Oxford, 1980.
[16] K. Lefmann and K. Nielsen, McStas, a general software package for neutron ray-tracing simulations, *Neutron News* **10**(3) (1999), 20–23.
[17] S. Mühlbauer, M. Stadlbauer, P. Böni, C. Schanzer, J. Stahn and U. Filges, Performance of an elliptically tapered neutron guide, *Physica B: Condensed Matter* **385–386** (2006), 1247–1249.

[18] C. Schanzer, Waviness of neutron guides/mirror optics, Personal communication, SwissNeutronics.
[19] C. Schanzer, P. Böni, U. Filges and T. Hils, Advanced geometries for ballistic neutron guides, *Nuclear Instruments and Methods in Physics Research Section A: Accelerators, Spectrometers, Detectors and Associated Equipment* **529**(1–3) (2004), 63–68.
[20] The European Spallation Source, *ESS Technical Design Report*, 2013.
[21] P. Willendrup, E. Farhi, E. Knudsen, U. Filges and K. Lefmann, Mcstas: Past, present and future, *Journal of Neutron Research* **17**(1) (2014), 35–43.

A.7 CAMEA ESS - The continuous angle multi-energy analysis indirect geometry spectrometer for the European Spallation Source

Publication of the CAMEA instrument design proposed and accepted for construction at the ESS. The instrument uses time of flight to measure the initial neutron energy and an array of crystal analysers to select final energies. The analysers are placed such that a range of scattering angles are covered, and several layers of analysers cover a number of investigated final energies. The name of the instrument was later changed to BIFROST. The paper was published in EPJ Web of Conferences.

Abstract

The CAMEA ESS neutron spectrometer is designed to achieve a high detection efficiency in the horizontal scattering plane, and to maximize the use of the long pulse European Spallation Source. It is an indirect geometry time-of-flight spectrometer that uses crystal analysers to determine the final energy of neutrons scattered from the sample. Unlike other indirect geometry spectrometers CAMEA will use ten concentric arcs of analysers to analyse scattered neutrons at ten different final energies, which can be increased to 30 final energies by use of prismatic analysis. In this report we will outline the CAMEA instrument concept, the large performance gain, and the potential scientific advancements that can be made with this instrument.

My contribution

Participated in design meetings for the instrument and designed the guide through many iterations with the remaining instrument team. Final tweaks to the guide design shown in the publications were made by Jonas O. Birk using the guide_bot software package developed by me. Commented on the manuscript.

EPJ Web of Conferences **83**, 03005 (2015)
DOI: 10.1051/epjconf/20158303005

CAMEA ESS – The continuous angle multi-energy analysis indirect geometry spectrometer for the European Spallation Source

P.G. Freeman[1,a], J.O. Birk[2], M. Markó[3], M. Bertelsen[2], J. Larsen[4], N.B. Christensen[4], K. Lefmann[2], J. Jacobsen[2], Ch. Niedermayer[3], F. Juranyi[3] and H.M. Ronnow[1,b]

[1] Laboratory for Quantum Magnetism, ICMP, École Polytechnique Fédérale de Lausanne (EPFL), 1015 Lausanne, Switzerland
[2] Niels Bohr Institute, University of Copenhagen, Universitetsparken 5, 2100 Copenhagen, Denmark
[3] Laboratory of Neutron Scattering, Paul Scherrer Institute, 5232 VilligenPSI, Switzerland
[4] Department of Physics, Technical University of Denmark, Kongens Lyngby 2800, Denmark

Abstract. The CAMEA ESS neutron spectrometer is designed to achieve a high detection efficiency in the horizontal scattering plane, and to maximize the use of the long pulse European Spallation Source. It is an indirect geometry time-of-flight spectrometer that uses crystal analysers to determine the final energy of neutrons scattered from the sample. Unlike other indirect geometry spectrometers CAMEA will use ten concentric arcs of analysers to analyse scattered neutrons at ten different final energies, which can be increased to 30 final energies by use of prismatic analysis. In this report we will outline the CAMEA instrument concept, the large performance gain, and the potential scientific advancements that can be made with this instrument.

1. Introduction

For measuring excitations such as phonons and magnons in materials there are two dominant types of inelastic neutron spectrometers presently in use, i) direct geometry time-of-flight (ToF) spectrometers and ii) triple-axis spectrometers (TAS). Direct ToF instruments compensate a low incident neutron flux from using monochromatic pulses, by detecting the scattered neutrons of all energies over a large solid angle in position sensitive detectors. In contrast TAS focus a continuous high flux monochromatic beam of neutrons on a sample but have a low detection coverage of counting neutrons at one final neutron energy at one position, or tens of angles in the case of multiplexed TAS [1–3].

The European Spallatioon Source (ESS) will be a 5 MW long pulse spallation neutron source, and will have the world's highest peak brightness for cold neutrons [4]. The time averaged cold neutron flux of the ESS will also be greater than that of world leading continuous sources such as the Insitut Laue-Langevin high flux reactor. The instrument design phase for the ESS is an ideal opportunity to consider new possibilities for instrument concepts.

Researchers of magnetism are the largest user community of single crystal spectrometers. This community often use applied magnetic fields to tune the magnetic properties of materials across phase transitions in to new phases of matter, where inelastic neutron scattering uniquely determines the nature of the magnetic phase. Cryomagnets used in these experiments however restrict the access for neutrons. For example, currently the highest vertical field cryomagnetic for neutron spectroscopy is the 16 T "Fat Sam" produced by Bruker, for the Spallation Neutron Source (SNS) as a collaborative project between the Swiss Neutron Scattering Society (SGN/SSDN) and the Oak Ridge National Laboratory [5]. This magnet has a vertical opening angle of $\pm 4^\circ$. When used on the direct geometry ToF Cold Chopper Neutron Spectrometer (CNCS) at SNS, 75% of CNCS's detectors out of the horizontal plane are blocked, reducing the instruments efficiency. TAS spectrometers operate in the horizontal plane and are therefore less restricted by the neutron access of split-pair cryomagnets. A similar situation holds for using anvil cells for extreme pressure to tune magnetic properties of materials [6]. TAS spectrometers are the instrument of choice for these types of experiments, however a TAS would not take advantage of the pulsed nature of the ESS. This provides an initial motivation to examine optimizing a spallation source instrument that maximizes the neutron count rate within the horizontal plane.

2. Concept

We directed our attention to indirect geometry ToF spectrometry where the final energy of the neutron is determined by a crystal analyser. Present indirect spectrometers analyse neutrons scattered from a sample at one final fixed energy, from knowing the final energy and the time-of-flight the scattering process is determined. Present indirect ToF spectrometers are inefficient as the scattered neutron energy is only analysed once, any neutron that does not have the correct final energy only increases the background signal. We note that the indirect spectrometers such as PRISMA (ISIS) [8] and CQS (Los Alamos) [9] did work with variable final neutron

[a] e-mail: paul.freeman@epfl.ch
[b] e-mail: henrik.ronnow@epfl.ch

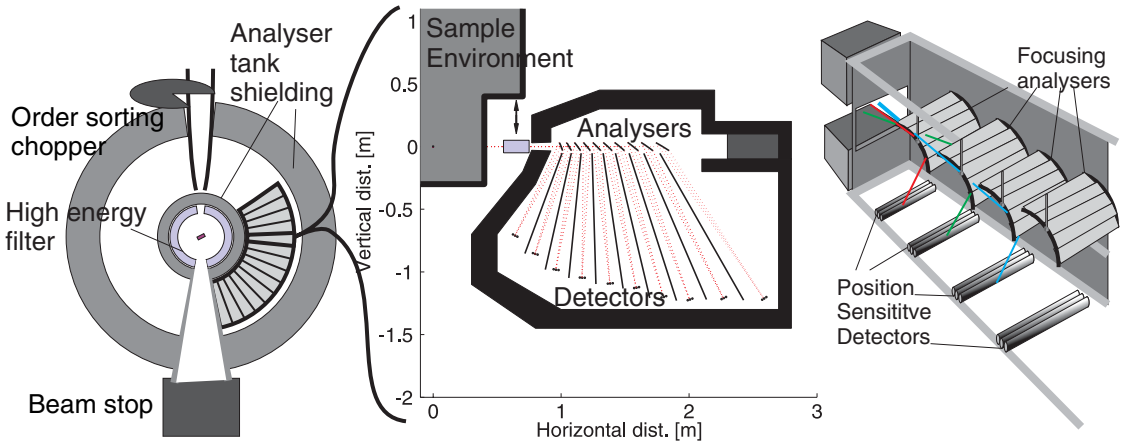

Figure 1. Left: a simplified overview of the CAMEA spectrometer from the end of the neutron guide, not to scale. The sample is surrounded on one side by the analyser-detector chamber that covers a large angle within the horizontal plane. Centre: a cross section to scale of one 9° multi-analyser-detector module is shown on the right. There is large 90 cm diameter space for sample environment, and a removable cooled Be high energy filter placed in front of the entry to the secondary spectrometer. We show how 10 analysers sat behind each other working at different final neutron energies can geometrically be spaced with neutron shielding between the analyser to detector channels. After the last analyser the neutrons are directed into a get lost tube into a beamstop. Right: a simplified three-dimensional sketch of the analyser and detector setup in a module of the secondary spectrometer for the first four of ten analysers, omitting all flight-path definition elements for the purpose of clarity.

energies, but only analysed a scattered neutron's energy a single time. The majority of spallation source indirect ToF spectrometers are ultra high resolution backscattering spectrometers, or vibrational spectrometers that measure phonon density of states. Neither of these two instrument classes are ideally suited for mapping phonon or magnon dispersion curves in single crystals, however the back scattering spectrometer Osiris at the ISIS facility is successfully used to study magnetic excitations in single crystals [7].

The essential evolution in neutron instrumentation of CAMEA is the secondary spectrometer:

1) Vertically scattering analysers that allows for increased coverage of in plane scattering.
2) Multiple concentric arcs of analysers sat behind each other to perform multiple final energy analysis.
3) Use of Position Sensitive Detectors (PSDs) for quasi-continuous angular coverage.
4) Prismatic analysis from a distance collimated analyser allowing multi-energy analysis from a single analyser.
5) An order sorting chopper that enables use of first and second order reflections off the analysers.

Neutrons have large penetration depths, for analyser crystals of pyrolytic graphite (PG) of 1 mm thickness mounted on 1 mm Si wafers, the transmission rate we have experimentally determined as $> 98\%$. Typically 2 mm PG analyser crystals are used, but reducing to 1 mm halves the cost, increases transmission, for only a small cost in reflectivity. We propose an instrument with 10 concentric arcs of analysers that direct analysed neutrons vertically into detectors, if a neutron scattered from the sample is not at the energy of the first analyser the neutron is transmitted to be analysed by up to nine further analysers working at different final energies. Scattering vertically has been shown not to reduce energy resolution when studying samples of small vertical height (<1 cm) [3]. The increased efficiency of this Multi-Energy Analysis for 10 energies gives a gain factor > 9.1, considering transmission rates. In Fig. 1a we sketch an overview of the secondary spectrometer, and in Fig. 1b we outline how ten analysers placed behind each other can be positioned.

Continuous Angular coverage is obtained by using PSDs that are arranged tangentially, as shown in the right panel of Fig. 1. The position along the PSD that the neutron is detected determines the angle at which the neutron was scattered from the sample, and knowing the sample orientation the wavevector of the scattered neutrons is determined. To map out excitations in $(h,\ k,\ \omega)$ of a single crystal a sample rotation scan is performed, in the same way as a scan of a reciprocal plane is produced on a multiplexed spectrometer such as MACS or Flatcone [2,3]. In Fig. 2 we show how the magnetic dispersion from a one dimensional spin system can be measured without the need for a sample rotation scan. For Continuous Angular coverage we need to resolve the issue of dead angles between segment wedges of the secondary spectrometer. Continuous Angular coverage can be achieved in two ways, 1) re-position the secondary spectrometer so that the dead angles and active angles swap positions, 2) in a sample rotation scan we can use the detected neutrons observed by different analysers to create a continuous map of the excitations measured with different final neutron energies.

3. Design

The specifics of the secondary spectrometer of CAMEA-ESS are shown in Fig. 1a Each segment of the secondary spectrometer consists of fifteen wedges of 9° width covering a horizontal scattering angle of 3–135°. Each wedge consists of 10 PG analysers sat behind each other, with each analyser working at a different final neutron

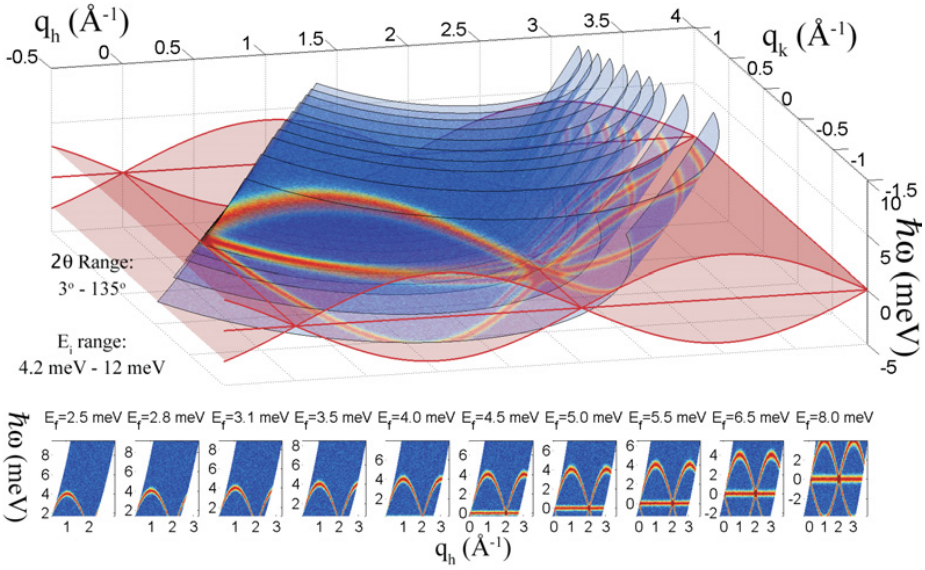

Figure 2. A diagram to represent the measuring capabilities of CAMEA measuring the magnon spin excitation spectrum of a one dimensional spin system, in a single point scan. The main figure shows the surfaces in reciprocal space mapped by CAMEA, and the red surface represents the magnon dispersion. Below the main figure shows the projected excitation spectrums measured by the ten different analysers of CAMEA. No spinon continuum excitation is included, and dead angles between the analyser sections have been omitted (equivalent to measuring two points, the second being where the dead angles and active analyser angles of the secondary spectrometer swap position).

energy, and three linear PSDs for each analyser. In this way we have ten concentric arcs of analysers working at ten final neutron energies.

Analysers will be constructed of PG crystals mounted on Si wafers, five or more blades will be used in a vertical focusing Rowland geometry covering $\sim \pm 1.4^\circ$ vertically, to focus the analysed neutrons into three PSD tubes arranged to be parallel to the analysers. An analyser wedge of 9° width will consist of 6° active analyser, and 3° of dead angle for support structures, etc.. As the energy resolution of the secondary spectrometer is limited by distance collimation, the three PSD tubes are at a different scattering angle from a single analyser arc, so each PSD detects a different final neutron energy. This prismatic analysis allows for 30 final energies to be examined by CAMEA at a higher energy resolution [10].

For the primary spectrometer, CAMEA will be placed on cold neutron moderator. The neutron guide was optimised by simulations using the McStas package and the optimizer package GuideBot [11, 12]. A wide range of guide shapes were examined, and the best guide shape identified [13]. From the neutron moderator there is a guide feeder to a virtual source at 6.5 m [14], where a pulse shaping chopper is placed at the closest possible distance to the moderator. To be able to use the full length of the 2.86 ms neutron pulse of the 14 Hz ESS, filling the counting window, a pulse shaping chopper at 6.3 m gives a natural length of 165 m [15]. The neutron guide is then two ellipses separated by a small angular kink in the guide to remove line-of-sight from the neutron source. Elliptical guides reduce neutron losses by reducing the number of reflections required along the guide's length, and the pinch point between the ellipses provide background reduction. A bandwidth chopper will be placed in the kink section of the guide, and the instrument requires three frame overlap choppers, that can be positioned in the first ellipse.

A prototype of the secondary spectrometer of CAMEA has been built, and tested on the MARS spectrometer at the SINQ neutron source, Paul Scherrer Institut, Switzerland. The results of this testing validates the CAMEA design and will be reported in detail elsewhere [18]. In addition to this, analytical calculations of CAMEA have been performed [19].

For any spectrometer background reduction is critical, and requires a clear strategy to achieve. A set of beam definition jaws at the end of the guide section will define the beam divergence that reaches the sample position, as has been implemented on WISH at the ISIS facility [20]. The divergence jaws are followed by diaphragm to define the beam size at the sample position. Any neutrons that pass straight through the sample will be directed along a get lost tube to the beam stop. The secondary spectrometer will either be in an Ar atmosphere or under vacuum to remove background from air scattering of neutrons. Line-of-sight between the PSDs and the sample position will be shielded by neutron absorbing materials. Radial collimation between the sample and analysers, and cross talk collimation inside the secondary spectrometer are foreseen. A removable Be-filter can be placed in the scattered neutron beam to remove high energy neutrons, although this restricts CAMEA to working with the first seven analysers. The effectiveness of our background reduction strategy has been confirmed in our prototype testing of CAMEA, where a the background count rate is 5×10^{-5} times that from the incoherent scattering from a vanadium sample.

The energy range can be expanded to measure excitations of thermal energies on CAMEA using the

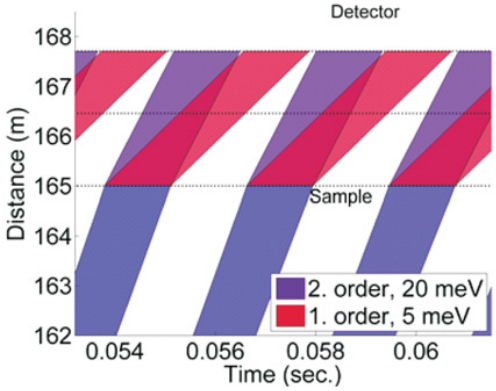

Figure 3. Time-of-flight diagram of the order sorting chopper and the 7th PG(002) $E_f = 5$ meV analyser. At 162 m the chopper divides the pulse into ~ 26 pulses per source pulse, at 3 m from the detector the neutrons hit the sample and scatters. The time distance diagram clearly shows how the neutrons that scatter of the analyser at 166.5 m by the first and second order reflections are detected over unique time windows at the detector. The time gaps between the signals at the detector are necessary due to a small time broadening of the signals that is mainly due to the choppers open and closing time.

order sorting chopper. If thermal neutrons are scattered off the sample, the scattered neutrons can be analysed by the PG(002) or PG(004) analyser reflections with $E_f(PG(004) = 4 \times E_f(PG(002))$, and we cannot directly differentiate between them. In Fig. 3 we show a time-distance plot for the order sorting chopper. The order sorting chopper for CAMEA consists of two counter rotating disc choppers that run at 180 Hz with two symmetric openings, effectively 360 Hz a non-integer multiple of the the source's repetition rate. The time distance plot of Fig. 3 for the $E_f(PG(002)) = 5$ meV shows that neutrons that arrive at the detector at a given time are uniquely determined from the PG(002) or PG(004) analyser reflection. Using the order sorting chopper CAMEA has analysers working from $E_f = 2.5$ meV to 32 meV. The order sorting chopper however reduces the incident neutron intensity by 59% when placed 3 m from the sample position. The greater the distance for the order sorting chopper to the sample position, the greater the reduction in incident neutrons, 3 m represents a safe distance from stray fields from future >20 T cryomagnet possibilities.

4. Performance

In table one we outline specifications of the CAMEA spectrometer. Ten analysers represents a compromise on coverage, the cost increase of the analyser for increasing sample to analyser distance, and the reduced performance due to transmission losses. The CAMEA analyser resolution is limited by distance collimation, not mosaic quality, so 60′ mosaic PG crystals can be used to improve count rates without reducing the energy resolution. When the primary and secondary resolutions are matched, CAMEA will achieve a higher energy resolution than than triple-axis spectrometers, whose energy resolution is limited by mosaic quality.

If the full ESS pulse width is used the primary spectrometer energy resolution is 4%, with 1.8×10^{10} neutrons $s^{-1}\,cm^{-2}$ for a 1.7 Å bandwidth centred at 3 Å [13]. We consider the simulated performance of ThALES the upgraded IN14 at the ILL, which to the best of our knowledge will be the highest flux cold TAS in the world with a monochromatic flux maximum of 3.5×10^8 [16], a factor of 50 lower than the maximum polychromatic flux of CAMEA. The energy resolution of the primary spectrometer of CAMEA can be improved to 0.8% to match the secondary spectrometer, with the primary resolution being directly proportional to the pulse width from the pulse shaping chopper. For example the flux for 2% total energy resolution on CAMEA is 0.9×10^{10}. Due to the high flux of CAMEA special care must be taken with regards to activation. A simple mechanical interlock device has been designed for removing active samples from the instrument to an active sample store on the instrument zone, removing the need to directly handle samples [21]. Indirect handling of active samples can be avoided by use of a robotic arm for sample removal. Design of instrument components and sample environment also requires attention to the choice of materials placed in the neutron beam.

Within $\pm 1.4^\circ$ vertical range of CAMEA, and taking into account transmission rates, we estimate the solid angle gain of CAMEA over Flatcone to be 36 [3], or 23 over MACS at NIST [2]. Comparing CAMEA's flux gain for 2% energy resolution, and the increased solid angle coverage gives a gain factor of ~ 900 compared to ThALES using Flatcone, provided all detected signal is of use in both cases. With this gain factor CAMEA will enable inelastic neutron scattering on samples of **1 mm^3** and smaller as a routine measurement. Neutron simulations were also used to compare CAMEA to a 150 m long cold direct ToF spectrometer that uses Repetition Rate Multiplication, with a large vertical coverage of $\pm 30^\circ$, at the ESS. These simulations indicated within the horizontal plane CAMEA has a 22 times higher count rate than the direct ToF [17]. If we consider the total counts of the direct ToF ESS spectrometer including a large vertical angular coverage, CAMEA has a slightly higher count rate.

Polarized inelastic neutron scattering will be available for CAMEA from the beginning. The incident neutron beam will be polarized by a polarizing supermirror S-bender, inserted near the end of the guide by a guide changer, a setup successfully used on instruments such as FLEXX [22]. Polarization analysis of the scattered beam will be performed by a wide angle polarized supermirror analyser replacing the Be filter, which is equivalent to the setup used on the D7 instrument [23]. We chose a polarized supermirror analyser over a wide angle He-3 polarization cell, to enable the use of cryomagnets which produce stray fields, and to keep a large sample environment space available with the polarized option.

5. Scientific demand for extreme conditions

The CAMEA geometry is especially suitable for inelastic neutron scattering in applied magnetic fields, and under

Table 1. Specifications for the CAMEA instrument at the ESS.

Primary Spectrometer	
Moderator	Cold
Wavelength Range (Energy Range)	1 Å to 8 Å (81.8 meV to 1.3 meV)
Bandwidth	1.7 Å
Neutron Guide	165 m – Parabolic feeder to double elliptical guide
Line-of-Sight Removal	Kink between elliptical guide sections
Number of Choppers	7, operating from 840 rpm to 12600 rpm
Beam Divergence	2.0° vertical, 1.5° horizontal
Divergence Control	5 divergence jaws intergrated into the end of the guide
Incoming Energy Resolution	Adjustable from 0.1% to 3% at 5 meV
Polarizer	Removeable polarizing supermirror s-bender
Sample	
Maximum Flux on Sample Position	1.8×10^{10} n/s/cm^2/1.7 Å
Wavector Range at Elastic Position	PG(002) reflections: 0.058 Å^{-1} to 3.6 Å^{-1}
(Including PG(004) reflections)	PG(004) reflections: 0.12 Å^{-1} to 7.26 Å^{-1}
Background Count Rate	$< 5\times10^{-5}$ comparted to the elastic signal of vanadium (result obtained from prototype testing)
Beam Size at Sample position	1.5 cm × 1.5 cm
Beam Size Resolution Optimization	0.1 cm × 0.1 cm–1.0 cm × 1.0 cm
Sample Environment Space	90 cm diameter with possible side access
Secondary Spectrometer	
Collimation	Radial collimation after Sample
	Cross-talk collimation in secondary spectrometer
Filter	Removable cooled Be-filter before analyzers
Analyser crystals	2 m^2 cooled Pyrolytic Graphite (PG)
	60″ mosaic using (002) and (004) reflections
Detectors	2.5 m^2 position sensitive ^{3}He at 7 bar
Number of Analyzer Arcs	10
Number of Analyzer-Detector Segments	15 (9.0° per segment, 6.0° active)
Sample to Analyzer Distances	1.00 m to 1.79 m
Analyzer to detector Distances	0.8 m to 1.45 m
Horizontal Angular Coverage	3° to 135°
Horizontal Angular Resolution	0.79° to 0.46°
Vertical Angular Coverage	± 1.4°
Final Neutron Energy PG(002)	2.5, 2.8, 3.1, 3.5, 4.0, 4.5, 5.0, 5.5, 6.5, 8.0 meV
Final Neutron Energy Range PG(002) and PG(004)	2.5 meV to 32 meV
Secondary Energy Resolution	0.77% to 1.3%
Polycrystal Elastic Wavevector Resolution	1.1% for E_f = 5.0 meV
Time Resolution	20 μs
Neutron Polarization	Polarizing supermirrors

Table 2. Demand for several European based cold TAS and indirect geometry spectrometers that measure magnetic excitations in single crystals, and the demand for extreme environments conditions on these instruments. The overload of an instrument is defined as the number of days applied for experiments divided by the total number of days available to perform experiments.

Instrument (Instute/Neutron Source)	Overload	Magnetic fields (% of proposals)	Pressure (%)	$\leq$ 1, K (%)	Polarized neutrons (%)
RITA-II, TASP (PSI)	2.5	34	4	19	N/a
PANDA (FRM-II)	2.7	30	5	20	N/a
IN14 (ILL)	2.5	30–40	< 5	60	20–25
IN12 (JCNS@ILL)	2.6	24	0	28	10
Osiris (ISIS)	2	40	0	40	Planned
FLEX (HZB)	1.5	56	0	20	Commissioning

extreme pressure. In table two we outline the results of a survey into the use of extreme environments on cold inelastic neutron spectrometers in Europe. Typically there are overload factors of 2.5 for these instruments, with $\sim$ 33% requesting the use of a cryomagnet. The lack of demand for use of high pressure for neutron spectroscopy is likely due to the highly restrictive sample volume of pressures cells, and the present need for large single crystals for inelastic studies. In September 2012 attendees of an ESS Science Symposium on Strongly Correlated Electron Systems were asked to name three instruments you would like to have at the ESS, and a spectrometer for extreme conditions was one of the three instruments [24]. There is a significant scientific demand for spectroscopy under extreme conditions in Europe, which the ESS can accommodate through CAMEA.

6. Scientific capabilities of CAMEA

The massive gain factor of CAMEA ESS has the potential to enable scientific discoveries in several fields of research, a few of which are discussed below.

The present user community for using extreme environments in inelastic neutron scattering is based in the magnetic scattering community, which includes magnetic materials, strongly correlated electron systems, superconductors, quantum magnets, etc. CAMEA offers this community high counting rates to study weak excitations to a level of accuracy that present instrumentation cannot reach, bridging the gap between the accuracy theoretical calculations can reach and present inelastic neutron scattering. Alternatively rapid mapping of excitations will be enabled for parametric studies of dynamics across critical transitions, providing a unique tool to study wavevector and energy evolution across transitions. The large gain factor of the instrument and the low background count rate will unlock the ability to study magnet materials under extreme pressure.

At present the sample size required for inelastic neutron scattering is prohibitive, limiting the technique to crystals grown by techniques such as floating zone mirror light furnaces. The ability to study samples of less than 1 mm^3 opens up the possibility for sample growth for neutron scattering in both material discovery and soft matter. For example it will be possible to study materials grown by high-pressure synthesis (which is how the highest Tc iron-based superconductors were first crystalized) and hydrothermal synthesis (which is how the best known realization of a kagome quantum magnet is synthesized) CAMEA will enable neutron scattering to be be part of the iterative process to discover new materials classes. This will lead to input from inelastic neutron scattering immediately after materials are discovered, or directly lead to discovery of materials. At present a large amount of experimental and theoretical work is wasted due to incorrect assumptions made about the spin and lattice interactions in materials, inelastic neutron scattering unambiguously resolves these issues.

CAMEA has the potential to open up the application of neutron spectroscopy in new fields of reasearch including biophysical studies of collective dynamics in membranes. In membranes collective dynamics are believed to drive transport of molecules, pore opening, membrane fusions and protein-protein interactions [29], which can be determined by inelastic neutron scattering. At present studies of collective dynamics in membranes by neutrons is restricted to model systems which can be prepared in large multi-layer stackes, the small sample capability of CAMEA will enable studies of the actual membranes of interest.

There exist a great hitherto unaccommodated interest to study lattice dynamics in simple materials under extreme pressure, and for geo- and planetary science related studies such as hydrogen diffusion in materials of the Earths upper mantle. CAMEA is ideally suited for both of these purposes. Despite the fact that water is vital for life on Earth we have little knowledge on the extent of the water cycle in the Earths mantle. Estimates on the water in the mantle wildly vary from ten percent to two and a half times the water on the Earths surface [25]. The uptake of water into the material of the Earths mantle greatly influences the properties of the materials, which has consequences for flow of material and sound velocities in the mantle, studying these materials has the potential to provide great insight into plate-tectonics and seismic activity [25,26]. To study the effects of hydrogen on the different phases of the material of the Earth's mantle requires performing neutron scattering at pressure up to 30 GPa for temperatures of the order of 2000 K. The experimental conditions imply a pressure cell with a sample volume $< 5\,mm^3$ [27], and an instrument resolution of a cold TAS is required, well within CAMEA's capability [28].

Table 3. Desirable sample environments for CAMEA, within predicted technical developments.

Sample Environment	Performance
Low Temperatue	Dilution to <100 mK
Magnetic fields	Vertical >20 T
Pressure	30 GPa with 5 mm^3 sample, T = 3–2000 K 10 GPa with 50 mm^3 sample, T = 0.1–1800 K
Magnetic Field and Pressure	>10 T with upto 10 GPa T = 0.1–350 K

In table 3 we outline some of the desirable sample environment for CAMEA to perform these experiments.

For time dependent studies the time resolution of CAMEA is only from the secondary spectrometer, and of the order of 20 μs. An analyser arc of CAMEA measures one excitation energy for a time of the order of the 2.86 ms source pulse width with 20 μs resolution, that is the time dependence of excitations at ten different energies are simultaneously measured. This capability of CAMEA opens up experimental possibilities in inelastic neutron scattering for example in soft matter stimulated out of equilibrium by pump-probe techniques, or studying excitations in pulsed high magnetic fields beyond 30 T.

7. Conclusion

CAMEA provides an evolution in cold neutron indirect spectroscopy by performing analysis of the energy of the scattered neutrons at 10 final energies, that can be increased to 30 energies by prismatic analysis. This instrument has been designed through simulations, with validation of the simulations of the secondary spectrometer achieved by prototype testing on the MARS spectrometer at the SINQ neutron source of the Paul Scherrer Insitut. Compared to present cold multiplexed TAS CAMEA has three orders of magnitude gain. At the ESS the in plane count rate of CAMEA is over an order of magnitude higher than cold direct geometry ToF spectrometers, and is equivalent to the total count rate of a cold direct ToF spectrometer. CAMEA therefore enables inelastic neutron scattering on samples of less than 1 mm^3 as a routine measurement, enabling experiments in fields of research such material discovery , soft matter, and extreme pressure studies in magnetism, and geoscience. Finally

we note that the secondary spectrometer of CAMEA can be implemented as a multiplexing option for a TAS instrument, that could perform within a factor of 100 of CAMEA at the ESS. A CAMEA TAS is being built for the the RITA-II spectrometer at SINQ neutron source, P.S.I., Switzerland.

The work presented here is part of the European Spallation Source Design Update Programs of Switzerland and Denmark.

References

[1] M. Jimnez-Ruiz, and A. Hiess, Physica B: Condensed Matter, **385-386**, 1086–1088 (2006); K. Lefmann, D. McMorrow, H. M. Rønnow, K. Nielsen, K. Clausen, B. Lake, and G. Aeppli, Physica B: Condensed Matter, **283**, 343–354 (2000); C.R.H. Bahl, K. Lefmann, A.B. Abrahamsen, H.M. Rønnow, F. Saxild, T.B.S. Jensen, L. Udby, N.H. Andersen, N.B. Christensen, H.S. Jakobsen, T. Larsen, P.S. Häfliger, S. Streule, Ch. Niedermayer, Nucl. Instr. Meth. A, **246**, 452-462 (2006); K. Lefmanna, Ch. Niedermayer, A.B. Abrahamsen, C. R. H. Bahla, N. B. Christensena, H.S. Jacobsen, T.L. Larsen, P. Häfliger, U. Filges, and H.M. Rønnow, Physica B: Condensed Matter, **385-386**, 1083-1085 (2006). K. Lefmann, U. Filges, F. Treue, J. Kirkensgaard, B. Plesner, K. Hansen, and K. Klenø, Nucl. Instr. Meth. A, **634**, S1–S6, (2011)

[2] J. A. Rodriguez, D. M. Adler, P. C. Brand, C. Broholm, J. C. Cook, C. Brocker, R. Hammond, Z. Huang, P. Hundertmark, J. W. Lynn, N. C. Maliszewskyj, J. Moyer, J. Orndorff, D. Pierce, T. D. Pike, G. Scharfstein, S. A. Smee and R. Vilaseca, Meas. Sci. Technol. **19**, 034023 (2008)

[3] M. Kempa, B. Janousova, J. Saroun, P. Flores, M. Boehm, F. Demmel, and J. Kulda, Physica B: Condensed Matter, Proceedings of the Eighth International Conference on Neutron Scattering, **385-386(0)**, 1080–1082 (2006)

[4] S. Peggs, R. Kreier, C. Carlile, R. Miyamoto, A. Paahlsson, M. Trojer, and J. G. Weisend II, ESS Technical Design Report. Tech. rep. ESS. (2013)

[5] P. Allenspach, M. Zolliker, and U. Filges, Swiss Neutron News **36**, 14 (2009)

[6] S. Klotz, J. M. Besson, G. Hamel, R. J. Nelmes, J. S. Loveday, W. G. Marshall and R. M. Wilson, Appl. Phys. Lett. **66**, 1735 (1995)

[7] M. T. F. Telling and K. H. Andersen, Phys. Chem. Chem. Phys. **7**, 1255 (2004); R. Coldea, D. A. Tennant, E. M. Wheeler, E. Wawrzynska, D. Prabhakaran, M. T. F. Telling, K. Habicht, P. Smedibidl, and K. Kiefer, Science **327**, 177 (2010)

[8] U. Steigenberger, M. Hagen, R. Caciuffo, C. Petrillo, F. Cilloco and F. Sachetti F Nucl. Instrum. Methods B **53** 87 (1991); M.J. Bull, M.J. Harris, U. Steigenberger, M. Hagen, C. Petrillo, and F. Sacchetti, Physica B **234-236**, 1061 (1997)

[9] R. A. Robinson, R. Pynn and J. Eckert, Nuclear Instruments and Methods in Physics Research A **241**, 312 (1985)

[10] J. O. Birk, *et. al.*, article in preparation

[11] K. Lefmann and K. Nielsen, Neutron News **10**, 20, (1999); P. Willendrup, E. Farhi and K. Lefmann, Physica B **350**, 735 (2004)

[12] M. Bertelsen, GuideBot software, University of Copenhagen, 2014

[13] J. O. Birk and M. Bertelsen, CAMEA Guide Report, `http://infoscience.epfl.ch/record/190503?ln=en`

[14] M. Bertelsen, H. Jacobsen, U.B. Hansen, H.H. Carlsen, and K. Lefmann, Nucl. Instr. Meth. A **729**, 387-398 (2013)

[15] K. Lefmann, K. H. Klenø, J. O. Birk, B. R. Hansen, S. L. Holm, E. Knudsen, K. Lieutenant, L. von Moos, M. Sales, P. K. Willendrup, and K. H. Andersen, Rev. Sci. Instrum. **84**, 055106 (2013)

[16] M. Boehm, A. Hiess, J. Kulda, S. Roux and J. Saroun, Meas. Sci. Technol. **19**, 034024 (2008); M. Boehm (Insitut Laue-Langevin) personal communication

[17] J. O. Birk, CAMEA: Comparison to the Colder Chopper Spectrometer, `https://infoscience.epfl.ch/record/190496?ln=en`

[18] M. Marton article in preparation; M. Marton, Building and Testing a Prototype for CAMEA, `http://infoscience.epfl.ch/record/197952?ln=en`

[19] M. Marton, Analytical Calculations for CAMEA, `https://infoscience.epfl.ch/record/190497?ln=en`

[20] L. C. Chapon, P. Manuel, P.G. Radaelli, C. Benson, L. Perrott, S. Ansell, N.J. Rhodes, D. Raspino, D. Duxbury, E. Spill, J. Norris, Neutron News **22:2**, 22 (2011)

[21] J. O. Birk, CAMEA: Technical Solutions, `http://infoscience.epfl.ch/record/190506?ln=en`

[22] M. Skoulatos, and K. Habicht, Nucl. Instrum. Methods B **647**, 100 (2011)

[23] J. R. Stewart, P. P. Deen, K. H. Andersen, H. Schober, J.-F. Barthélémy, J. M. Hillier, A. P. Murani, T. Hayes and B. Lindenau, J. Appl. Cryst. **42**, 69-84 (2009)

[24] A. Boothroyd, T. Perring, S. Hayden, D. McMorrow, P. Deen, A. Hiess, Report on the ESS Symposium on Spin Dynamics (Abingdon, 2012)

[25] M. Hirschmann and D. Kohlstedt, Physics Today **65 (3)**, 40 (2012)

[26] D. G. Pearson, F. E. Brenker, F. Nestola, J. McNeill, L. Nasdala, M. T. Hutchison, S. Matveev, K. Mather, G. Silversmit, S. Schmitz, B. Vekemans, and L. Vincze, Nature **507**, 221 (2014)

[27] S. Klotz (University Pierre and Marie Curie) personal communication

[28] L. E. Bove, S. , Phys. Rev. Lett. **111**, 185901 (2013)

[29] Neutron Applications, Neutron Scatterng Applications and Techniques, V. García Sakai, C. Alba-Simionesco, S.-H. Chen. (Springer Science and Business Media, 2012) M.C. Rheinstädter, Chapter 10 Lipid Membrane Dynamics, Dynamics of Soft Matter

A.8 HEIMDAL: A thermal neutron powder diffractometer with high and flexible resolution combined with SANS and neutron imaging - Designed for materials science studies at the European Spallation Source

Presentation of the HEIMDAL instrument accepted for construction at the ESS. The instrument combines thermal neutron powder scattering, cold SANS and imaging for simultaneous measurements over a wide range of length scales. The instrument require a challenging thermal guide and a separate cold guide that provide two beams on the same sample with a 3.5° angular separation. The paper was published in Nuclear Instruments and Methods in Physics Research, Section A.

Abstract

HEIMDAL will be a multi length scale neutron scattering instrument for the study of structures covering almost nine orders of magnitude from 0.01 nm to 50 mm. The instrument is accepted for construction at the European Spallation Source (ESS) and features a variable resolution thermal neutron powder diffractometer (TNPD), combined with small angle neutron scattering (SANS) and neutron imaging (NI). The instrument uses a novel combination of a cold and a thermal guide to fulfill the diverse requirements for diffraction and SANS. With an instrument length of 170 m, HEIMDAL will take advantage of the high neutron flux of the long pulse at ESS, whilst maintaining a high q-resolution due to the long flight path. The q-range coverage is up to 20 Å 1 allowing low-resolution PDF analysis. With the addition of SANS, HEIMDAL will be able to cover a uniquely broad length scale within a single instrumental setup. HEIMDAL will be able to accommodate modern materials research in a broad variety of fields, and the task of the instrument will be to study advanced functional materials in action, as in situ and in operandi at multiple length scales (0.01-100 nm) quasi simultaneously. The instrument combines state-of-the-art neutron scattering techniques (TNPD, SANS, and NI) with the goal of studying real materials, in real time, under real conditions. This article describes the instrument design ideas, calculations and results of simulations and virtual experiments.

My contribution

Designed the thermal guide through many iterations with the remaining instrument team. Ran the full instrument simulations combining the guide and backend. Commented on the manuscript.

Nuclear Instruments and Methods in Physics Research A 828 (2016) 229–241

Contents lists available at ScienceDirect

Nuclear Instruments and Methods in Physics Research A

journal homepage: www.elsevier.com/locate/nima

HEIMDAL: A thermal neutron powder diffractometer with high and flexible resolution combined with SANS and neutron imaging – Designed for materials science studies at the European Spallation Source

Sonja L. Holm [a,*], Kim Lefmann [a], Paul F. Henry [b], Mads Bertelsen [a,b], Jürg Schefer [c], Mogens Christensen [d]

[a] Nano-Science Center, Niels Bohr Institute, University of Copenhagen, Universitetsparken 5, 2100 Copenhagen Ø, Denmark
[b] European Spallation Source ERIC, 22100 Lund, Sweden
[c] Laboratory for Neutron Scattering and Imaging, Paul Scherrer Institute, 5232 Villigen, Switzerland
[d] Department of Chemistry & Interdisciplinary Nanoscience Center (iNANO), Langelandsgade 140, 8000 Aarhus C, Denmark

ARTICLE INFO

Article history:
Received 12 February 2016
Received in revised form
10 May 2016
Accepted 10 May 2016
Available online 13 May 2016

Keywords:
ESS
Neutron instrumentation
McStas
Powder diffraction
SANS
Imaging
Materials science
In situ

ABSTRACT

HEIMDAL will be a multi length scale neutron scattering instrument for the study of structures covering almost nine orders of magnitude from 0.01 nm to 50 mm. The instrument is accepted for construction at the European Spallation Source (ESS) and features a variable resolution thermal neutron powder diffractometer (TNPD), combined with small angle neutron scattering (SANS) and neutron imaging (NI). The instrument uses a novel combination of a cold and a thermal guide to fulfill the diverse requirements for diffraction and SANS. With an instrument length of 170 m, HEIMDAL will take advantage of the high neutron flux of the long pulse at ESS, whilst maintaining a high q-resolution due to the long flight path. The q-range coverage is up to 20 $Å^{-1}$ allowing low-resolution PDF analysis. With the addition of SANS, HEIMDAL will be able to cover a uniquely broad length scale within a single instrumental set-up. HEIMDAL will be able to accommodate modern materials research in a broad variety of fields, and the task of the instrument will be to study advanced functional materials in action, as *in situ* and *in operandi* at multiple length scales (0.01–100 nm) quasi simultaneously. The instrument combines state-of-the-art neutron scattering techniques (TNPD, SANS, and NI) with the goal of studying real materials, in real time, under real conditions. This article describes the instrument design ideas, calculations and results of simulations and virtual experiments.

1. Introduction

Advances in materials science come through an in-depth understanding of the relationships between structure and properties. Profound insights into these relationships are a common goal across condensed matter science, from high precision crystallography to fast kinetics studies, and are a prerequisite for the rational design of new and improved materials. Traditionally, materials have been studied at equilibrium, far from operating conditions, but growing efforts seeks to investigate materials under more realistic conditions and on multiple length scales, a trend pioneered by developments at synchrotron sources [1–4].

The intention with HEIMDAL is to build a neutron instrument able to access a wide length scale provided by the combination of thermal neutron powder diffraction (TNPD), small angle neutron scattering (SANS), and neutron imaging (NI). Multiple length scales are crucial to expand the understanding of advanced functional materials under external stimuli such as gas flow, pressure, or temperature, which can be difficult to recreate exactly in subsequent experiments. A classic example is heterogeneous catalysis, which depends on the atomic structure of catalytic nanocrystallites in a microporous matrix. All length scales are relevant for the efficiency of the catalytic process; therefore, in-depth knowledge into the structure and functionality requires multiple length scale coverage with sufficiently good time resolution. In these types of systems HEIMDAL will be a game-changer in neutron scattering, because it will provide new capabilities for investigating multiple dimensions at fast time scales. Topics of particular interest are materials containing light elements, related to energy, composites, matrix embedded systems, phase transition and nucleation, and magnetic materials.

* Corresponding author.

http://dx.doi.org/10.1016/j.nima.2016.05.046
0168-9002/

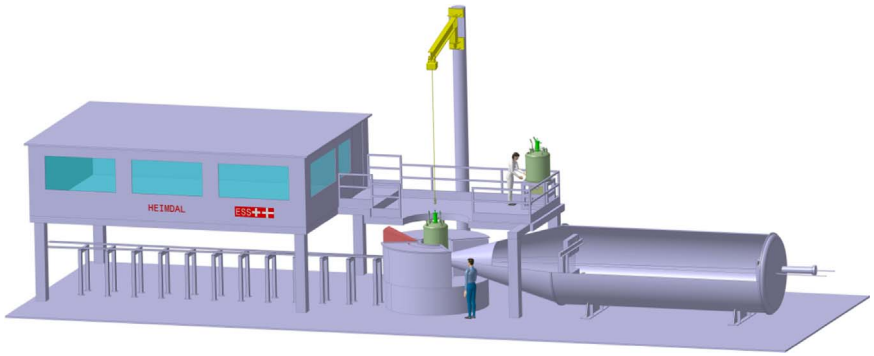

Fig. 1. Illustration of the HEIMDAL experimental station. Drawn in collaboration with Peter Keller, Laboratory for Scientific Developments and Novel Materials, Paul Scherrer Institut, Switzerland.

Neutrons are an ideal probe for *in situ* and *in operandi* studies inside bulky sample environments. However, only few neutron instruments existing today are capable of covering multiple length scale in real time as the experimental techniques of TNPD, SANS, and NI have highly different requirements to the incoming neutron beam. Therefore, all existing instruments covering broad length scales are focused towards either SANS or TNPD (*e.g.*, NOVA, i-Materia at J-Parc [5,6] or NIMROD at ISIS [7]). The HEIMDAL design uses an entirely novel concept, where two independent guides view the cold and thermal moderators independently. The two beams are extracted from the same beam port, and can be individually optimized without compromising the capability of either technique. This unique combination of three different neutron scattering techniques in a single setup will enable HEIMDAL to cover the atomic regime (0.01–5 nm) with TNPD, the nanometer regime (2–100 nm) with SANS, and structural features in direct space from 0.05 to 50 mm with NI. The total length scale coverage thus spans nine orders of magnitude, with minor gaps in the μm range.

The name HEIMDAL originates from the Norse Mythology. In Asgard, the home of the gods, HEIMDAL is the guardian of the rainbow bridge Bifrost that spans the worlds of gods and men. He has the most keen senses among gods, a vision so powerful that he can see and hear the grass grow in real time [8].

In the following sections we shall go though the design considerations, calculations, and simulations done in order to propose this instrument for construction at the ESS, starting with the instrument concept. After that we present the unique guide system and the chopper set-up of the instrument, before going into details with first the powder diffractometer, then the SANS set-up, and finally the imaging insert. Finally full virtual experiments, performed using the Monte Carlo ray tracing software McStas [9,10], will be presented for the TNPD and SANS set-up along with a discussion of the software needs associated with the data analysis.

2. The instrument concept

The powder diffraction part of the instrument is by far the most demanding due to the high resolution requirements. Therefore, the instrument design is based around an optimized, high performance thermal powder diffractometer, modified in order to also accommodate SANS and NI around a single sample position.

The source at ESS will run with a pulse period of $T=71$ ms and a pulse length $\tau = 2.86$ ms. The benefits and challenges of such a time structure are described in [11–13], and the long pulse at ESS is, at first glance, not ideal when building high resolution powder diffraction instruments; As such an instrument requires a combination of good resolution ($\sigma d/d \approx 0.1\%$), wide reciprocal space coverage, and access to as high a q as possible (at least 15 Å^{-1}). However, a long pulse source combined with a pulse shaping (PS) chopper close to the source and a long flight path between the moderator and the sample provides a tailored, well-defined pulse with high time-resolution (and thereby a good q-resolution) for the instrument. The q_{max} of the instrument is determined by the moderator configuration and the efficiency of the beam transport system. The design results in a relatively narrow wavelength band ($\Delta\lambda = 1.74$ Å) that can be matched to the q-range of interest with regard to the sample.

The major advantage of the long-pulse spallation source/PS chopper combination is that the pulse length can be matched to the requirements of the material. Therefore, the instrument configuration can be changed from high-resolution (short pulse with lower intensity) to high count-rate (long pulse with lower resolution) simply through chopper rephasing, adding a degree of operational flexibility not possible using current generation time-of-flight diffractometers.

A significant benefit of the HEIMDAL design is that a simple analytical two dimensional peak profile function can describe the raw data, due to the relatively simple chopper system and the cylindrical detector geometry. The wide detector angular coverage (10–170°), coupled with the instrument wavelength band (see next section) allows a q-range of 0.73–19.87 Å^{-1} to be covered, ideal for most aspects of chemical crystallography while also suitable for some low resolution pair distribution function (PDF) analysis. Additional backscattering detectors (highlighted in red in Fig. 1) are placed above and below the incoming guide to provide improved counting statistics for data collected at high q, critical to high-resolution chemical crystallography and PDF.

For SANS, a separate guide delivers cold neutrons to the sample position, where the angle between the incoming thermal and cold beams is 3.5°. This ensures that the direct beam from the thermal guide will not contaminate the SANS signal on the detector, while retaining sufficient space upstream of the sample for incident beam tailoring using apertures and minimizing the curvature of the cold guide. The main SANS detector (1×1 m^2) is situated 10 m from the sample position, giving a q_{min} limit of 8.6×10^{-4} Å^{-1} using 11 Å wavelength neutrons and a 15 mm radius beamstop 0.2 m from the detector. Additional detector panels are placed in the vacuum tank 4 m from the sample position to cover the q-range between that accessible by the main SANS detector and the wide angle diffraction detectors.

A model drawing of the experimental area of HEIMDAL is presented in Fig. 1.

2.1. Instrument length and wavelength band

To obtain high resolution TNPD at a long pulsed source, it is necessary to build a very long instrument or make drastic modifications to the pulse shape after the source. We have chosen to

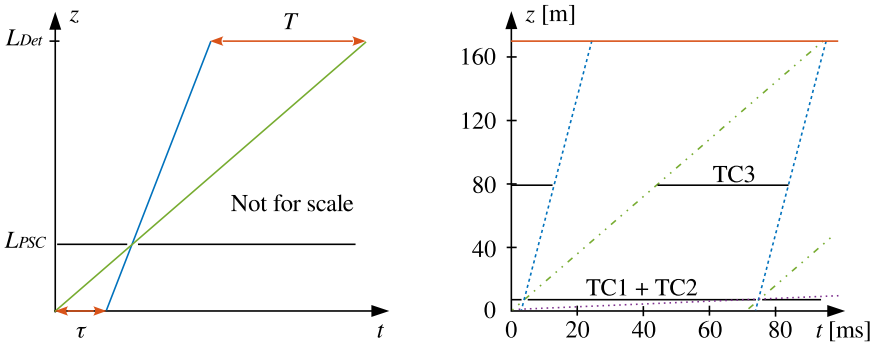

Fig. 2. Time-of-flight diagrams where the neutron position (z) along the neutron guide is plotted as a function of flight time (t). Left: A ToF diagram displaying the triangles used in the calculations of the natural instrument length. Right: A 168.8 m long diffraction instrument with a PS chopper at 6.5 m and a mean wavelength of $\lambda = 1.5$Å. There are two pulses present in the diagram. The two black horizontal lines mark the time where the choppers (TC1, TC2, TC3) are closed and the red line at 168.8 m mark the detector position. The path of the shortest wavelength let through the chopper system is marked with the blue dashed lines and the long wave length limit is marked with the green dash-dotted lines. The pink dotted line corresponds to 45 Å neutrons escaping through the first part of the chopper system. (For interpretation of the references to color in this figure legend, the reader is referred to the web version of this article.)

combine the two approaches as it keeps the design for TNPD simple.

Many overall parameters for the entire ESS instrument suite have already been decided, *e.g.* the pulse period and length [13,14] from these parameters we can calculate many of the instrument parameters for the TNPD.

The PS chopper, cutting the long pulse from the moderator short, has to be placed as close to the source as possible in order to obtain the largest possible bandwidth. The closest position for the PS chopper is $L_{chop} = 6.5$ m away from the moderator due to the biological shielding around the target station (the monolith). From this restriction we can calculate the natural instrument length, where the time window is completely filled without causing frame overlap. Hence the wavelength frame multiplication [16,17] (which shortens the instrument dramatically) and other elaborate chopper systems were not included in the design. We use the neutron time-of-flight (ToF) equation $t = \alpha\lambda L$, where $\alpha = h/m_n = 0.2528\frac{\text{ms}}{\text{Å m}}$. The opening time of the PS chopper is assumed to be close to zero and using the principle of similar triangles shown in Fig. 2 we obtain $L_{chop}/\tau = (L_{det} - L_{chop})/T$ and the instrument length can be calculated to be

$$L_{det} = \left(\frac{T}{\tau} + 1\right)L_{chop} \tag{1}$$

giving a full instrument length of $L_{det} = 168.8$ m.

The width of the wavelength band can be calculated using $\Delta\lambda = T/(\alpha L) = 1.74$ Å, where $L = L_{det} - L_{chop}$. For the thermal part of the instrument $\lambda = 1.5$ Å is used as the mean wavelength so the wavelength band coincides with the peak brightness of the thermal moderator. This gives a thermal wavelength band of 0.63–2.37 Å. The cold wavelength band has the same width (1.74 Å), but it can be tuned using the cold chopper system. The wavelength operation range for the SANS will be between 4 Å and 11 Å.

In order to obtain the 3.5° separation of the two guides at the sample position it is necessary to bend the guides apart (in particular the cold-neutron guide) and subsequently back together (see Fig. 3). This can be realized without benders as the instrument is long. See Section 4.2 for a more detailed description of the cold guide.

3. TNPD design

Users will have the possibility to run the TNPD part of the instrument in different resolution settings. A trade-off between high resolution and high flux will have to be considered for every

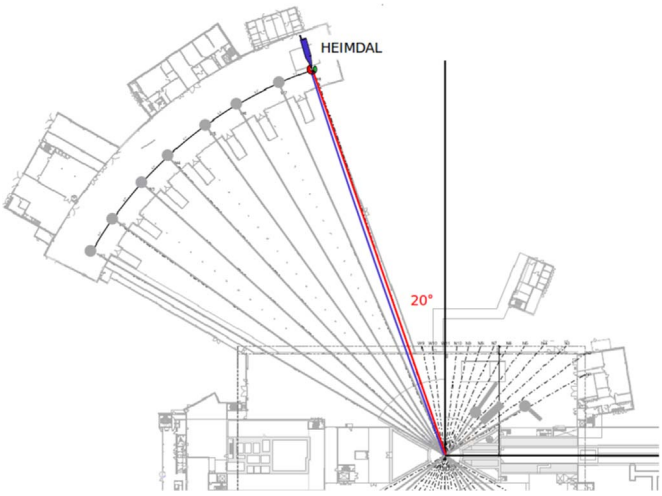

Fig. 3. Illustration of the guide system drawn on top of the ESS building layout (top view). The cold (blue line) and thermal (red line) guides start at the same beamport coming out from the source bend away from each other and come together again at the sample separated by an angle of 3.5°. From [15]. (For interpretation of the references to color in this figure legend, the reader is referred to the web version of this article.)

experiment. In this section we describe the considerations and calculations done in order to obtain the optimal instrument resolution and flux conditions.

3.1. TNPD instrument resolution calculations

The overall limiting factor of the instrumental resolution is the detector. The pixel size together with the distance between the sample and the detector determine its effective contribution to the resolution. The size of the sample will lead to an additional smearing of the signal on the detector. The other contributions to the total resolution function (*i.e.* time uncertainty and beam divergence on sample) can be adjusted to get the desired instrument resolution at the cost of neutron flux.

We shall now calculate the overall instrument resolution function ($\Delta d/d$) using error propagation of Bragg's law, resolution matching of the contributing terms, and the choice of the detector design. It is important to distinguish between the differential δ, the standard deviation, σ, and the FWHM when calculating the full resolution function of the instrument. In order to perform statistical calculations on solid ground all further calculations are performed using the standard deviation (σ).

A transformation of Bragg's law using the ToF equation ($t = \alpha\lambda L$)

gives $t = 2\alpha L d \sin\theta$. The contributions to the d-spacing resolution is derived by error propagation. The error in flight path $(\sigma L/L)^2 \sim 10^{-9}$ is negligible at this long instrument. Both the incoming divergence on the sample and the sample size together with the detector geometry contribute independently to the uncertainty in the in-plane scattering angle (σ_θ). The angular contribution is split into two terms while the time uncertainty (from pulse width) gives a third term to the resulting uncertainty in lattice spacing [18]:

$$\left(\frac{\sigma_d}{d}\right)^2 = \left(\frac{\frac{1}{2}\sigma_{2\theta_i}}{\tan\theta}\right)^2 + \left(\frac{\frac{1}{2}\sigma_{2\theta_f}}{\tan\theta}\right)^2 + \left(\frac{\sigma_t}{t}\right)^2. \tag{2}$$

The subscripts i and f denote the incoming and outgoing sides with respect to the sample respectively.

The time uncertainty (σ_t) can be controlled with PS chopper close to the source and the incoming divergence ($\sigma_{2\theta_i}$) can be modified with collimation. Therefore the limiting factor of the total resolution (2) stems from the uncertainty of scattered beam direction ($\sigma_{2\theta_f}$) which depends on the size of the sample, s, and the size of the detector pixels in the horizontal direction, p, together with the sample to detector distance, r. In order to calculate $\sigma_{2\theta_i}$ for this set-up, we first consider the geometry for distance collimation between sample and detector as shown in Fig. 4 and reach

$$\eta^{max}_{min} = \operatorname{atan}\left(\frac{s \pm p}{2r}\right) \approx \frac{|s \pm p|}{2r}. \tag{3}$$

The contribution from the out of plane scattering is ignored as it is a second order effect, except close to backscattering. More on this can be found in Section 3.5.

The beam intensity hitting the sample as a function of divergence has a trapezoid shape, with full intensity when $\eta \in [-\eta_{min}; \eta_{min}]$ and no intensity when $\eta < -\eta_{max}$ or $\eta > \eta_{max}$ as shown in Fig. 4. The variance of this distribution can be calculated [18]:

$$\sigma^2_{2\theta_f} = \frac{\eta^2_{\max}}{6} + \frac{\eta^2_{\min}}{6} = \frac{1}{12}\frac{s^2 + p^2}{r^2}. \tag{4}$$

The pixel size is chosen from a projection of present-day detector technology to have 3 mm width, and the sample width is set to the match pixel size, giving $p = s = 3$ mm. The radius of the simple cylindrical detector is chosen to be $r = 1.5$ m to limit the overall detector cost. Since the two first terms of the resolution Eq. (2) depends on the scattering angle ($1/tan(\theta)$), we cannot obtain resolution matching for all values of θ. The choice have been made to fulfill the resolution matching condition at $2\theta = 90°$. The instrument resolution is in this case $(\sigma_d/d)^2 = 5.00\cdot10^{-7}$ corresponding to a (σ_d/d) of 0.07%. The optimal horizontal divergence of the incoming beam for the high resolution case is $\sigma_{2\theta_f} = 0.047°$ which corresponds to a FWHM of 0.11°.

The full opening time of the resolution chopper can also be calculated when the resolution matching condition is upheld for the uncertainty of the flight time so that $1/3(\sigma_d/d)^2 = (\sigma t/t)^2$ (from (2)), where t is the flight time of the mean wavelength ($\lambda_{mean} = 1.5$ Å) from the PS chopper at $L_{chopper} = 6.5$ m to the detector. Using the ToF equation the flight time is $t_{chop2det} = 61.53$ ms and hence the width of the opening time has to be $\sigma_t = 25.1$ μs. The transmission function of a disc chopper with an opening that matches the guide cross section has a triangular shape with full intensity at $t = 0$ and no intensity when $t < -t_{\max}$ or $t > t_{\max}$. The variance of this function can be calculated to $\sigma_t^2 = \frac{1}{6}t^2_{\max}$ [18]. The full opening time of the PS chopper is therefore $\Delta t = 2t_{\max} = 123.1$ μs.

3.2. Instrument resolution settings – guide and chopper system requirements

We foresee the normal operation of the instrument to be in one of three different modes; "high resolution", "high flux", and "medium mode". The high resolution mode is intended for crystallographic studies related to accurate structure determination, nuclear densities, and atomic displacement factors. In order to measure with a short data acquisition time the TNPD can be run in high flux mode where the instrument resolution is relaxed. The high flux mode is intended for time resolved measurements of fast kinetics and low resolution PDF, where peak resolution is less significant for the interpretation of the data. The medium setting of the instrument is for *insitu* studies in materials science, chemistry and physics. The medium and high flux modes utilizes best the length of the long pulse at ESS.

The instrument resolution tuning can be done by changing the speed and hence the opening time of the PS chopper, by allowing a larger incoming divergence on the sample, and by changing the size of the sample. For this to be possible, the guide and chopper system has to fulfill several conditions.

The PS chopper is a pair of counter rotation disc choppers placed 6.5 m from the source. In order to produce the short pulse length, for the high resolution mode, the opening in the choppers has to be small (we choose $b = 38$ mm) and the width of the guide has to match this opening. A height of 60 mm have been chosen for the guide at this point.

To sample a constant wavelength range the choppers must spin at a multiple of the source frequency (14 Hz). We can find a set of suitable parameters for the choppers using $b = \nu\cdot 2\pi r\cdot\Delta t$; the full radii of the choppers be $R = 0.38$ m and the beam center position $r = 0.35$ m from the center of the disc. When running at $\nu = 140$ Hz (10 times the source frequency) the full opening time of the choppers is $\Delta t = 123$ μs which matches the required opening time for the natural high resolution setting. The medium and high flux opening times can be obtained spinning the choppers at two and one times the source frequency, respectively.

In order to maximize the count rate in the high flux mode, the guide has to be able to transport neutrons with a divergence up the limits of high flux mode $\sigma_{2\theta} = 0.47°$. The divergence can be reduced, for the medium and high resolution modes, using the resolution jaw concept (slits in the guide) like the one implemented at the cold-neutron powder diffraction instrument Wish at ISIS [19].

As described in the previous section the natural high resolution calculations are based on the choice of the smallest sample size

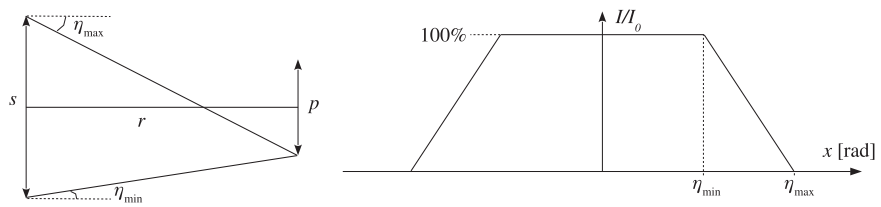

Fig. 4. Left: A sketch showing the relevant angles, η, arising from the sample width, s, the pixel size, p and the detector radius, r. Right: Intensity as a function of divergence. An expression for η_{min} and η_{max} are given in (3).

Table 1
Key numbers for the three modes of the TNPD. Δt is the full opening time of the PS choppers and $\sigma_{2\theta}$ is the standard deviation of the incoming divergence on the sample. The sample is a cylinder with a diameter, d, and the hight, h. The results of the virtual experiment described below gives these relative uncertainties, $\frac{\sigma_d}{d}$, for the 90° detector bank and the backscattering bank at 170° for $\lambda = 1.5$Å, as well as the flux on the sample position.

Instrument mode	Δt [μs]	$\sigma_{2\theta}$ [°]	$d \times h$ [mm^2]	$\frac{\sigma_d}{d}$ at 90° [%]	$\frac{\sigma_d}{d}$ at 170° [%]	Flux [n/s/cm^2]
High resolution	123	0.047	3×10	0.091	0.044	$7.1 \cdot 10^6$
Medium mode	617	0.235	5×20	0.36	0.14	$5.1 \cdot 10^8$
High flux	1234	0.470	5×20	0.66	0.24	$1.4 \cdot 10^9$

and the matching pixel size. For the medium and high flux mode the calculated sample sizes for which resolution matching is obtained are very large ($s_{medium} = 21$ mm and $s_{flux} = 42$ mm) where the pixel size remain constant. We have therefore decided not to fulfill resolution matching for the sample size but limit the size to the realistic value of 5×20 mm^2 for the examples calculated here.

Table 1 shows a summary of the key numbers for the three operation modes of the TNPD. The opening time of the PS choppers and the incoming divergence on the sample have been calculated so that they contribute equally to the resolution in the high flux and the medium mode. The relative uncertainties for the two cases for a scattering angle of $2\theta = 90°$, where the resolution matching is fulfilled in the high resolution mode, and for a scattering angle of $2\theta = 170°$ (near backscattering) where the highest resolution is obtained are the result of the virtual experiment described below. The flux numbers at the sample position are also obtained using McStas simulations.

3.3. Thermal guide optimization

The optimization for the HEIMDAL guide has been done with the Matlab-McStas based software package Guide_Bot [20,21]. The moderator at ESS was updated to the "butterfly" configuration in April 2015. As the butterfly moderator component for McStas is still under development, our optimization was done using the flux curve from the Technical design report for ESS 2013 [14]. However we have changed the dimensions of the moderators to the new size of the bottom thermal moderator described in the new ESS Butterfly Moderator Configuration Baseline [22]. We presume that HEIMDAL will be placed in Experimental Hall 3 at the northernmost position [15] (see Fig. 3), thus the bottom thermal moderator will have an effective width of =126 mm and height of =60 mm. The change to the butterfly moderator geometry will also require a shift of the starting points of the two guides, as the thermal and cold source have switched places. Preliminary studies indicate that this can be rather straightforwardly incorporated into the current guide design by mirroring the entire instrument.

The guide will start 2 m from the moderator as radiation damage gets too severe closer to the moderator. The distance from the guide end to the sample is $d = 1.6$ m in order to be able to shield off the unwanted neutrons before the backscattering detector. Other solutions to minimize the background are not yet investigated.

At the PS chopper position, 6.5 m from the moderator, a 0.1 m gap is made in the guide to give room for the choppers. The divergence criteria for the optimization is calculated using (Eqs. (3) and 4) to get $\eta_{min} = |s - \sqrt{12r^2\sigma_{2\theta}^2 - s^2}|/(2d) = 0.7196°$, where $d = 1.6$ m is the distance from the guide end to the sample, $s = 5$ mm is the width of the sample and $\sigma_{2\theta} = 0.47°$ is the optimal angular uncertainty for the high flux mode. This gives a guide width of 45.19 mm at the end of the guide.

A high priority area in phase space (horizontal divergence of $\pm 0.5°$, vertical divergence of $\pm 0.081°$ ($=\sqrt{3}\sigma_{2\theta}$ high resolution), height of 10 mm and width of 3 mm) has been set to have the same weight in the optimization as the remainder of the full phase space volume in order to ensure a high performance for the high resolution setting.

For simplicity, the super mirrors used for the thermal guide have a m-value of 5 everywhere. In a later cost/performance optimization we expect this number to be heavily reduced in the majority of the mirrors without significant loss of useful neutrons. The dimensions of the height and width of the guide have been limited to be less than 0.1×0.1 m^2 before the PS chopper, inside the monolith, and 0.2×0.2 m^2 after the chopper. In the optimization we have chosen to reduce the background at the sample position by requiring that the guide is bend out of line-of-sight. Other options could also be implemented to eliminate the background coursed by fast neutrons and gamma radiation emitted from the source, like a prompt pulse chopper (T_{zero} chopper).

A summary of all the fixed parameters for the guide optimization is listed in Table 2, and the resulting geometry of the optimized thermal guide can be seen in Fig. 5. The performance of this guide as a function of wavelength is shown in Fig. 6 for the three instrument resolution modes as well as the divergence and spatial distributions for a range of wavelength snapshots. For the high resolution setting of the instrument the horizontal

Table 2
Summary of fixed parameters used in the Guide_bot optimization for the thermal guide.

Moderator to sample	167.3 m
Moderator to guide start	2 m
Guide end to sample	1.6 m
Space for resolution chopper centered at 6.5 m from moderator	0.1 m
Moderator height	60 mm
Moderator width	126 mm
Guide height at chopper position	60 mm
Guide width at chopper position	38 mm
Sample height	20 mm
Sample width	5 mm
Horizontal divergence on sample (η_{min})	0.7196°
Vertical divergence on sample (η_{min})	1.0°
Out of line-of-sight	–
m-value for the guide	5
Wavelength band	0.63–2.37 Å
Upper limit for the guide height before chopper (inside bunker)	0.1 m
Upper limit for the guide width before chopper	0.1 m
Upper limit for the guide height after chopper (outside bunker)	0.2 m
Upper limit for the guide width after chopper	0.2 m
High priority area sample height	10 mm
High priority area sample width	3 mm
High priority area horizontal divergence on sample	0.081°
High priority area vertical divergence on sample	0.5°

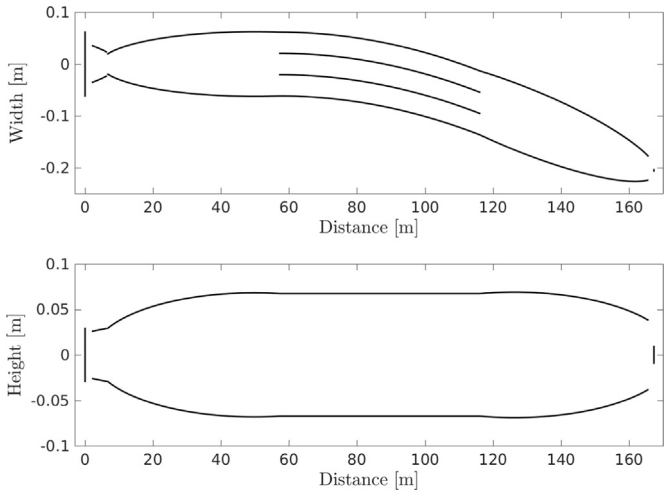

Fig. 5. Geometry of the thermal guide. The top view shows a feeder followed by an elliptic defocusing system, a curved guide to escape line of sight and then a elliptic section that will refocus the beam. The bottom panel shows the side view where the beam height is first expanded elliptically, followed by a constant section, and then an elliptical compression section.

divergence and position have a flat top and are symmetrical, which is necessary in order to get symmetrically shaped peaks on the detector. For the two other modes the neutron intensity is prioritized at the expense of the shape of the distributions. The limits of $\pm 1^\circ$ for the vertical divergence is larger than what the guide can transport. This is due to small hight of the moderator (6 cm) and the narrow opening at the chopper position. The resulting brilliance transfer is therefore not close to one as the required phase space is not filled.

The resulting flux numbers on the sample position for the three modes of operation are listed in Table 1 as well as the relative uncertainty at two scattering angles (90° and 170°) for $\lambda = 1.5$ Å. The simulation result of $\delta d/d = 0.09\%$ is a little larger than the calculated $\delta d/d = 0.07\%$ which is coursed by the shape of the distribution of the divergence of the incoming beam, square and trapezoid respectively.

A pair of counter rotating disc choppers have a transmission that is highest in the center of the beam and falls of linearly towards the edges in the horizontal direction. This effect was not taken into account in the guide optimization. It would be interesting to study how this can be exploited to make a more efficient guide for the full set-up. Furthermore, a study of the positions for the resolution jaws should be done to minimize the background from the unwanted neutrons while maintaining the collimation properties.

3.4. Chopper system

In order to deliver the desired pulse to the sample position a minimum of three sets of choppers are necessary: a pair of PS choppers as described earlier, a pulse selection chopper, and a wavelength definition chopper.

The main purpose of TC2 at 7 m is to suppress all the unwanted extra pulses created by TC1. TC2 will have the same dimensions as TC1, but rotating at a much lower speed as it will follow the source frequency of 14 Hz. The two choppers will produce blurry edges in the wavelength distribution, these can be removed by a wavelength definition chopper (TC3). TC3 is placed at the narrow part of the guide system around 79 m from the moderator.

Frame overlap will occur for neutrons with wavelengths around 45 Å. However, the flux from the thermal source at this wavelength will be extremely low and there is therefore no need to suppress these very slow neutrons. This behavior of long wavelength neutrons are shown in the time distance diagram in Fig. 2.

3.5. Diffraction detectors

Neutron detection is currently a very fast progressing field and it is not certain what will be the best detector for HEIMDAL at the time of its construction, so for these calculations a simple cylinder powder diffraction detector detector with a pixel width of $p=3$ mm and a radius of $r=1.5$ m has been chosen.

The detector will cover one side of the sample with scattering angles from 10 to 170° and have a height of 1 m giving a coverage of $\pm 18^\circ$ out of the horizontal plane. The pixel size will be 3×10 mm^2 in order to match the sample size and the resolution criteria. In order to have better statistics for the high q-values a set of backscattering detectors are placed above and below the guide. The dedicated backscattering detectors are shown in Fig. 7.

The initial detector coverage will be one side fully covered (~ 4 m^2) plus the backscattering detector (0.5 m^2) and from 170° to 150° on the right hand side adding another 0.5 m^2. The limited vertical coverage allows for a highly vertical divergent beam that increases the flux at the sample position. This high vertical divergence is acceptable as it only gives small losses in the horizontal resolution, because the part of the Debye-Scherrer cones intersecting the detector are almost vertical (except close to backscattering where a different detector is used). A schematic drawing of the TNPD detector set-up is shown in Fig. 7.

4. SANS design

The requirements from the diffraction part of the instrument determines the instrument length from moderator to sample to 168 m. This is unusually long for SANS, and makes this part of the instrument quite different from dedicated SANS machines.

4.1. Wavelength band, resolution, and collimation

The SANS resolution can in principle be calculated from equation (2), used for the diffraction resolution. However, it is not generally useful in this context, since $\delta q/q$ ($=\delta d/d$) diverges at the scattering angle goes to zero. Instead, we observe that the relative wavelength uncertainty for SANS at present instruments rather relaxed; up to $\delta\lambda/\lambda \approx 10\%$ and that the collimation contribution to the resolution can always be sufficiently limited.

For our long guide, we need no pulse shaping chopper, since the full pulse length gives a $\delta\lambda/\lambda = 1.5\%$ for $\lambda = 4.5$Å (and 0.6% at 11 Å), which will give us an instrument with a much better resolution than present day instruments, in particular at high q-values.

To collimate the beam, a standard pinhole system for SANS is foreseen. One pinhole to be positioned 10 m before the sample, identical to the sample to detector distance. Another pinhole is placed as close to the sample as allowed by the sample environment, which is about 0.5 m. Pinholes in between these two main pinholes will be inserted to reduce stray-neutron background. A possible beam-defining pinhole very close to the sample, *e.g.* 0.1 m, would have to be shared between the SANS and TNPD beams, the centers of which are at that distance only 6 mm apart. This will for most experiments not be a viable solution.

4.2. Cold guide and chopper system

The SANS and TNPD parts of the instrument use completely

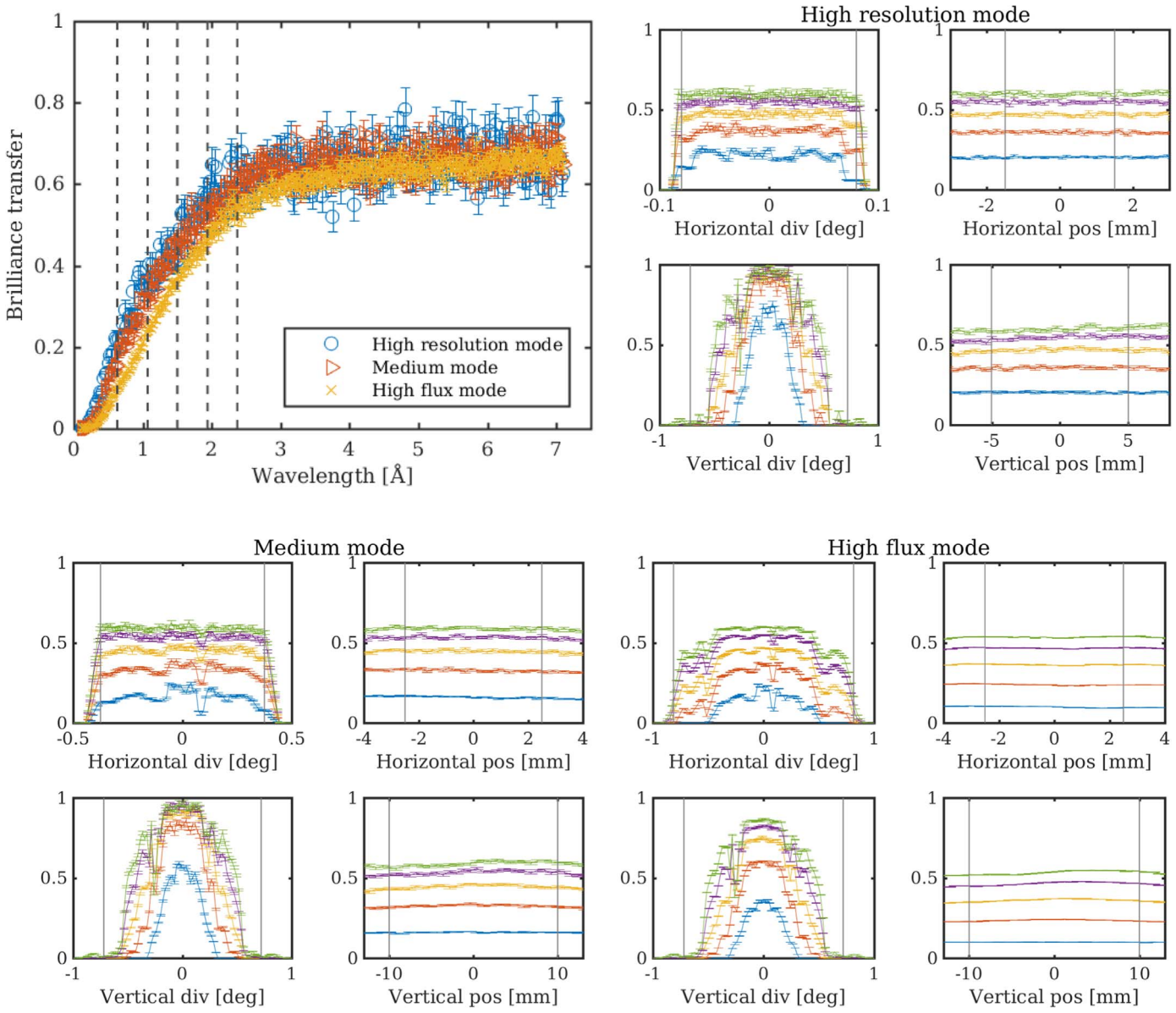

Fig. 6. The brilliance transfer as a function of wavelength for the three modes of operation is shown in the top left figure. The three other panels show the divergence and spatial distributions in terms of brilliance transfer for the five wavelength snapshots indicated with dashed lines in the top left figure. The solid gray vertical lines indicate the limits for the brilliance transfer phase space volumes used for each wavelength snapshot. The blue lines correspond to 0.63 Å, the read 1.07 Å, the yellow 1.5 Å, the purple 1.94 Å and the green 2.37 Å. (For interpretation of the references to color in this figure legend, the reader is referred to the web version of this article.)

different chopper settings and beam divergence criteria. It is therefore not possible to lead the two beams through the same guide without large sacrifices in neutron flux. However, the new pancake moderator design with a cold and a thermal target placed above and below the tungsten target respectively facilitate the extraction of two different guides from one port. This allows utilizing the optimized upper cold moderator for the SANS setup and the optimized lower thermal moderator for the thermal beam [22].

The designed SANS guide has $m=2$, dimensions of $w \times h = 20 \times 20\ \mathrm{mm}^2$ and a curvature radius of $R=1.2$ km, which is necessary to bring the beam back on the sample with an angle of 3.5° to the thermal guide. In our simulations we record the neutron intensity within the divergence range of ±0.2° in both vertical and horizontal direction, matching the divergence of SANS in low-resolution mode. We assume perfect low-angle reflectivity, as an upper limit for the guide performance, since we have no information on the quality of the actual guide. This method should, however, be taken with a certain amount of care, due to the many reflections (the average number of reflections is 61) present in the guide system. The analytical cut-off wavelength of such a guide is given by [27] $\lambda_c = 4\pi\sqrt{2w/R}/(mQ_{\mathrm{Ni}})$, giving the value $\lambda_c = 1.18$ Å for our guide parameters.

However, due to the very long curved section (almost 150 m), the usual approximation to a curved guide with a series of straight sections is problematic. The repeated encounter of reflections that are slightly away from the ideal circular arc will result in a severe loss of neutron flux, as illustrated by the simulated transmission of 4 Å neutrons, Fig. 8. We see that to obtain a brilliance transfer above 80%, we would need to operate with guide sections shorter than 100 mm, which is obviously not a practical solution. Instead, the guide will either have to be continuously curved or consist of linear pieces separated by solid-state benders. That choice will depend upon detailed budgeting that is only made in a later phase of the project.

In the remainder of this article, we adopt a continuously curved

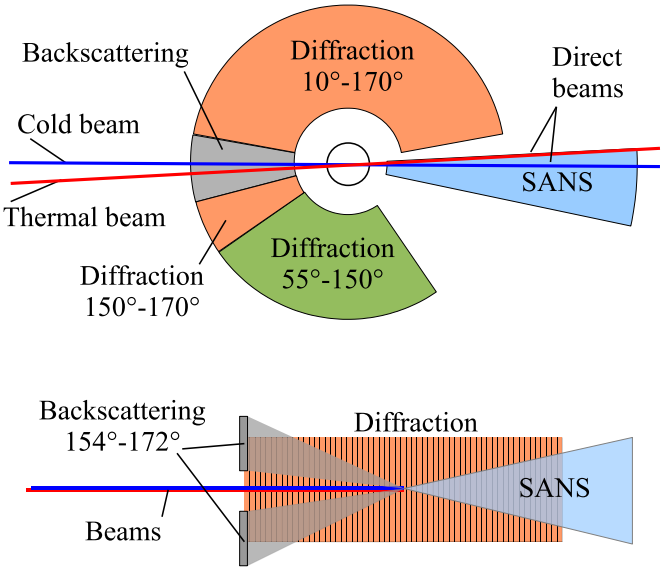

Fig. 7. Diffraction detector setup view from above (top), and from the side (bottom). The primary diffraction banks are shown in orange and the back scattering detectors placed above and below the incoming beams are drawn in gray. The green diffraction bank indicates area for future upgrade. The nose of the SANS detector is shown in blue. (For interpretation of the references to color in this figure legend, the reader is referred to the web version of this article.)

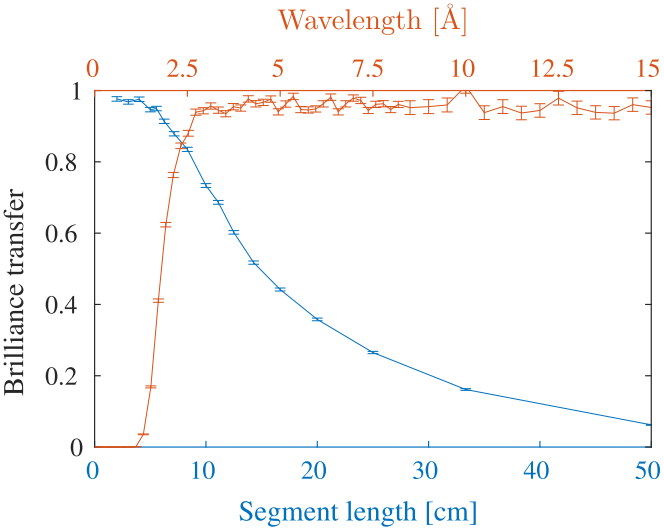

Fig. 8. Brilliance transfer through the curved SANS guide as a function of guide segment length (blue) and wavelength (red). When obtaining the wavelength dependence of the brilliance transfer of the guide the segment length was fixed to 4 cm and for the segment length dependence the wavelength was fixed to. (For interpretation of the references to color in this figure legend, the reader is referred to the web version of this article.)

SANS guide. The wavelength dependence of the brilliance transfer of the final guide is seen in Fig. 8. We see that the transfer is above 90% for wavelengths down to 2.5 Å, which is very reasonable for a guide with such a long curved section. It is likely that the coating profile of the guide can be further optimized, *e.g.* that the coating values can be decreased along the inner walls.

In the SANS guide, three slow disc choppers are needed: two wavelength band definition choppers (CC1 and CC3), and a frame overlap chopper (CC2); each with a radius of R=0.35 m and spinning at the source frequency of 14 Hz. CC1 must be placed rather close to the moderator, to limit the amount of frame overlap to be removed later. We choose to place it 14 m from the

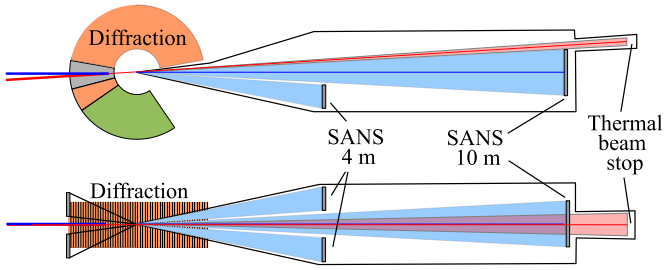

Fig. 9. SANS detector setup view from above (top), and from the side (bottom). The thermal beam passes by the SANS detectors which can also be seen in Fig. 15.

moderator. The chopper will allow the full 2.86 ms pulse to reach the sample for the chosen wavelength band of $\Delta\lambda$ = 1.7Å. CC3 is placed halfway between the moderator and the sample and will serve to define more sharply the selected wavelength band. Frame overlap is found when slow neutrons from one pulse match the burst time of CC1 meant for neutrons from the next pulse. To remove these, a frame-overlap chopper (CC2) is placed 18 m from the source.

4.3. SANS detectors and reciprocal space coverage

To collect small-angle scattering data, HEIMDAL uses dedicated small-angle scattering detectors placed in two positions: 1) A flat 1×1 m^2 panel detector placed 10 m from the sample with a pixel size of 4×4 mm^2. 2) Three flat panel side detectors (1×0.5 m^2) placed 4 m from the sample, displaced away from the central beam. The geometry of the set-up as seen in Fig. 9. The possible fourth panel is missing, allowing to install a “get lost” beam tube geometry for the thermal beam, which passes through the SANS tank. The flat panel detectors are likely to be based on state-of-the-art ^{10}B technology at the time of the detector purchase. Another option is ^{3}He, which, however, has the limitation of a slower count rate.

It should be noted that it might be required to develop a SANS detector design much like LOKI, the SANS instrument proposed for ESS [23].

The diffraction detectors are used to extend the angular range of the small angle scattering data, allowing a very broad q-range to be covered in a single setting, despite the limited wavelength

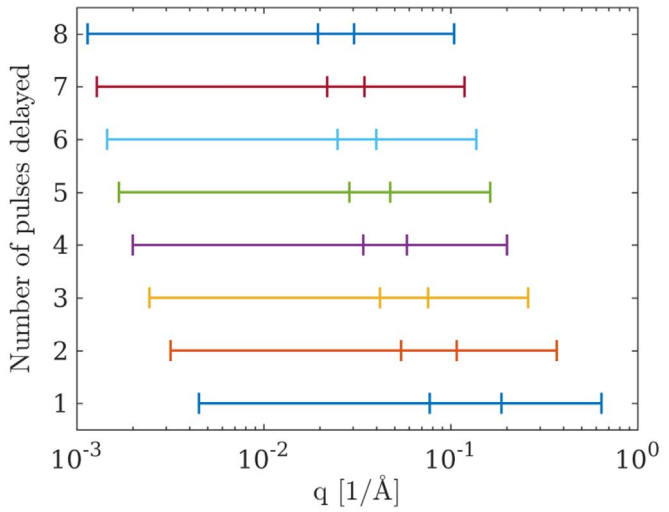

Fig. 10. The q-coverage of the two SANS detectors for different wavelength intervals selected by suppression of one thermal pulse. When delaying the cold pulse by one thermal frame, the wavelength band is from 2.37 Å to 3.94 Å corresponding to the q-range displayed at 1. By an eight frame delay the band is from 14.56 Å to 15.52 Å. The ToF diagram of a two frame delay is displayed in Fig. 11.

band. Taking the beam stop into account, the resulting coverage is from q_{min}(11 Å, SANS)=9·10^{-4}Å^{-1} to q_{max}(4 Å, NPD)=3.1Å^{-1}. Using only a single pulse in the wavelength range 9.1–10.8 Å gives full coverage in the region $9 \cdot 10^{-4}$–1.4 Å^{-1}.

The q-ranges accessible when using the narrow cold wavelength bands accessible for one suppressed thermal pulse is shown in Fig. 10. When delaying the cold pulse by one thermal frame, the wavelength band is from 2.37 Å to 3.94 Å and by an eight frame delay the band is from 14.56 Å to 15.52 Å on the center detector 10 m from the sample. A single narrow wavelength band pressed in between two thermal pulses, is sufficient for collection of SANS data for most systems. If necessary a wider wavelength band is possible through additional pulse suppression, as discussed later.

5. Neutron imaging option

The imaging option is operated as an add-on unit, which can be activated on demand, but not operated in sequence with the 14 Hz ESS pulse frequency. The imaging camera will be placed within the sample chamber normally kept under vacuum. For the operation of the SANS mode, the camera has to be moved completely out of the beam area. This can be solved by approaching a parking position, which is beyond the beam, but still within the vacuum chamber.

In the operating position, the NI camera should be placed as close as possible to the sample to avoid loss of resolution. The design will allow both neutron beams (thermal and cold) to be used for imaging, even with the 3.5° offset of the two beams. Possible detectors are the Timepix/Medipix detector or a small imaging detector using a CCD camera viewing a scintillation plate over an optical mirror [24]. The Timepix/Medipix detector has two main advantages: 1) it allows time resolved Bragg edge imaging and 2) it can be placed much closer to sample, due to the absence of spacious mirror setups, which allows higher resolution. The intended resolution is ~50 μm for samples up to 50 × 50 mm^2. The Bragg-edge imaging will inherently have a good wavelength resolution, $\Delta\lambda/\lambda$ = 1.5%, at 4.5 Å due to the length of the instrument.

By removing the front aperture of the cold guide, a single pinhole camera can be made with a L/D = 350 using a 20 mm aperture. A horizontal and vertical divergence of HFWHM = VFWHM = 0.5° gives an illuminated area with radius of approximately 60 mm. The beam divergence can be reduced by placing an aperture closer to the sample.

6. Instrument operation and data

In the operation of the instrument, neutrons can arrive to the sample from only one beam at a time, in order to correctly convert the time-of-flight to wavelength. In other words, each time window on the detector will be dedicated to either small angle scattering or powder diffraction. To ensure this, the frame-overlap choppers will suppress pulses in either of the powder and small angle scattering beams. For this reason, the choppers need to run slower, at integer fractions of the source frequency. The selection of the pulses determines the operation mode of the instrument, as illustrated with three of many different scenarios in Fig. 11.

In either operational mode, all data will be collected in event mode, where the arrival time of each single neutron is recorded along with the position on the detector. The neutron information will be coupled with metadata from the experiment like which pulse was selected, the sample temperature, pressure, gas flow *etc*.

Below, we will discuss typical data from the SANS and powder diffraction modes separately.

6.1. Diffraction detector

The diffraction detectors can be divided into two set of detectors: the cylindrical detectors surrounding the sample and the flat backscattering detectors, behind the samples. Due to the sample size optimization there are different requirements to pixel size for the different detector sets.

The cylindrical detector covers a range from 10° to 170°, the detector has a height of 1.0 m and is around 4 m in circumference, when placed 1.5 m from the sample. The pixel size will be 3 × 10 mm^2 to match the sample size. This gives approximately 130.000 pixels. A McStas simulation of HEIMDAL, showing typical instantaneous (monochromatic) diffraction data from the cylinder detector is shown in Fig. 12.

HEIMDAL is in addition equipped with dedicated backscattering detectors to improve resolution and q-coverage. The dedicated backscattering detectors placed above and below the incident beam will have a pixel resolution of 3 × 3 mm^2 to account for the circular projection of the Debye-Scherrer cone. The backscattering data will provide high resolution data and improve statistics for the high-q data.

6.2. Data analysis

For a perfect homogenous powder the full data set will be integrated along the Debye-Scherrer cone to produce a 1D pattern per time slot. The collected powder patterns are stacked to produce a 2D pattern with 2θ as function of wavelength or time-of-

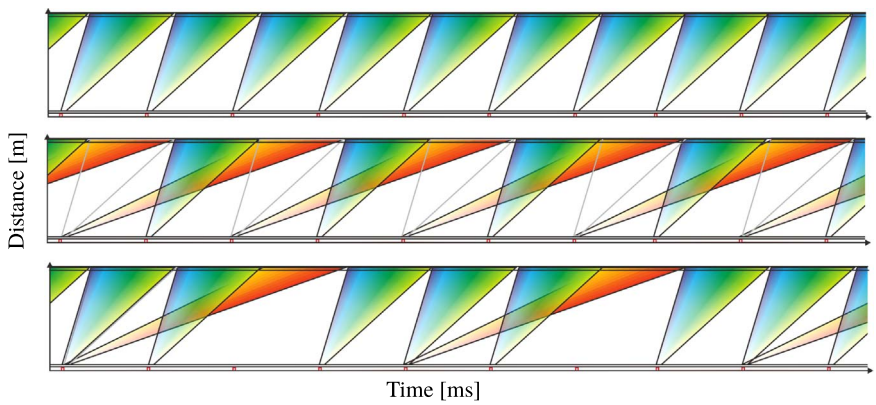

Fig. 11. ToF diagrams for three different operation modes of the two HEIMDAL beams: (top) pure powder diffraction; (middle) alternating powder diffraction and SANS; (bottom) three of four pulses are used for powder diffraction, the fourth for SANS.

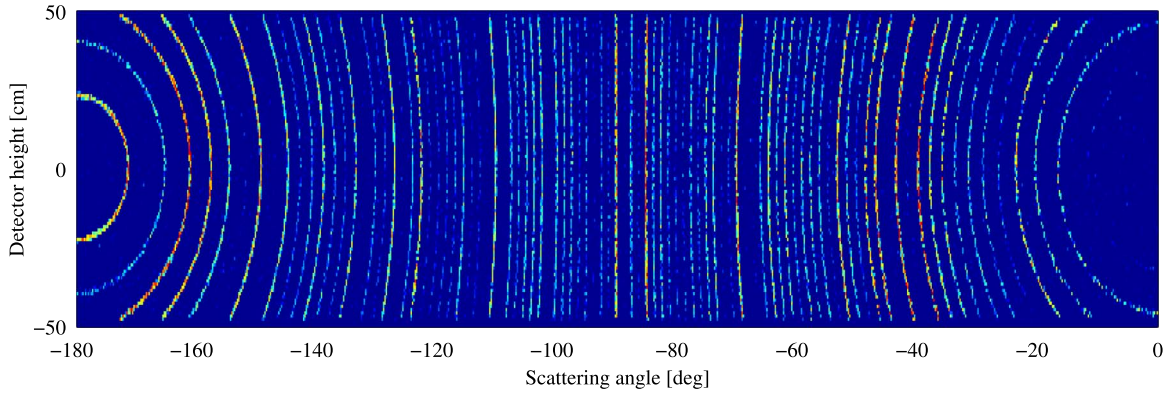

Fig. 12. Simulated data on the cylinder detector of a snapshot in time, corresponding to $\lambda = 1.5$Å . The data is a ray-tracing simulation of TPD run in high resolution mode with a 3×10 mm^2 cylindrical sample of $Na_2Al_{12}Ca_3F_{14}$.

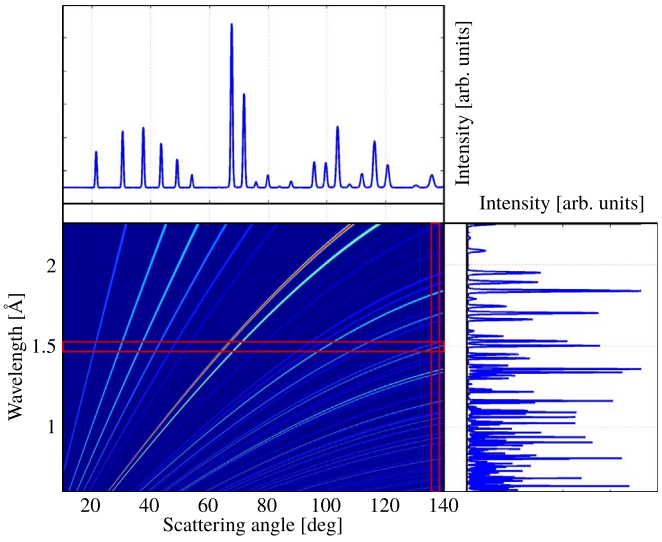

Fig. 13. Simulation of powder diffraction data of LaB_6, the 2D pattern shows 2θ at various wavelengths. The integrated area shown in red corresponds to conventional data measured at constant wavelength or constant angle, typical for instrument at reactor and spallation sources, respectively. The figure above corresponds to constant wavelength, while the figure to the right is the time-of-flight data in the backscattering detector at constant angle. (For interpretation of the references to color in this figure legend, the reader is referred to the web version of this article.)

flight. A simulation of such data is shown in Fig. 13, where we for convenience have used only the cylinder detector.

The cuts in the 2D map represent 1D data conventionally produced at a monochromatic instrument with a fixed wavelength (top) and a backscattering bank for a time-of-flight instrument (right). For HEIMDAL, we propose a different data reduction strategy, where the data is fitted in 2D. The reason for this is that merging all data into 1-dimensional diffraction patterns significantly reduces the information, because the data to be merged have very different resolution.

In 2D data analysis, the data is best viewed when plotted for the scattering angle, 2θ, and the scattering vector, q. The resulting simulated 2D powder diffraction patterns are shown in Fig. 14 for the three instrument settings as well as the 1D q dependence obtained by a summation along 2θ from 10° to 180°.

6.3. Total scattering

Combing the cylindrical and backscattering detectors will provide sufficient q-range coverage to allow collection of total scattering data to be used for Pair Distribution Function (PDF) analysis or Debye Function fitting. For the PDF analysis broad q-coverage is important and the proposed $q_{max} = 20$ Å^{-1} is lower than what is normally used for total scattering using neutron diffraction. The proposed q-range should, however, be well suited to investigate *e.g.* liquids and nanomaterials. The peak resolution in reciprocal space is less important for total scattering data compared to high counting statistics and q-coverage and therefore it should be possible to do PDF analysis based on the summed 2D diffraction data to gain counting statistics.

6.4. SANS detector

The central SANS detector is foreseen to have a size of 1×1 m^2 with a pixel resolution of 4×4 mm^2. The detector configuration is shown in Fig. 15 (left), the gap at the right hand side is needed to allow the thermal beam to pass through the SANS tank. Fig. 15 (right) shows the detector coverage possible using the four SANS detectors and the diffraction detectors, overlayed with instantaneous (monochromatic) SANS data. One challenge in the SANS data analysis will be the scaling between the SANS detectors and the diffraction detectors to give the huge single shot maximal reciprocal space coverage.

In general the event data collected on the SANS detector must be azimuthally integrated and converted into scattering vector (q). For aligned nanostructures it may be advantageous to perform semi-azimuthal integrations. The data treatment and analysis should be very similar to the procedures used for instruments at other facilities such as D33 at ILL [25] and 2D SANS at ISIS [26].

6.5. Sample geometry and sample environment

Conventionally, different sample geometries are used for NPD and SANS. Typical for NPD is a cylindrical geometry giving uniform scattering in all directions, while SANS uses thin flat sample geometry to have an even attenuation across the entire surface of the sample. In our simulations, we are optimizing for a cylindrical sample with dimensions of 5 mm diameter and 20 mm of height. When working with non-hydrogenous samples in SANS it is not necessary to work with thin samples and the variation in thickness across a cylindrical sample can relatively easy be corrected for, specially when using an almost monochromatic beam as is the case for the narrow bandwidth of HEIMDAL. Flat samples as traditionally used by SANS are naturally also usable, but the detector coverage (diffraction detectors) is likely limited to 45° or less due to angular variation in attenuation. Flat samples would not be good for the 90° detector banks. However we foresee that the data reduction software should be capable of dealing with different sample geometries and attenuation corrections from sample environment and sample.

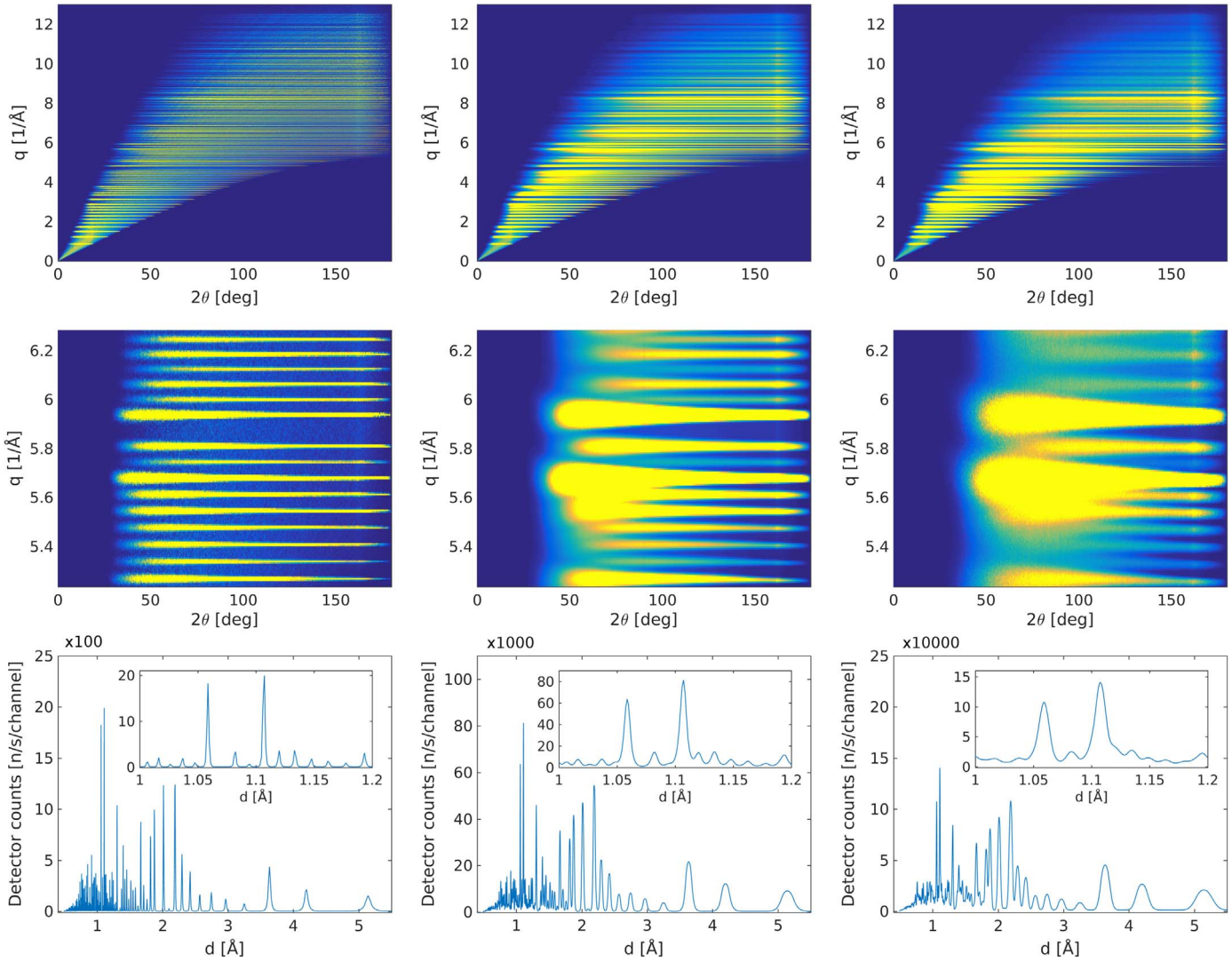

Fig. 14. Virtual data from the HEIMDAL TNPD simulation in the three operation modes with a cylindrical $Na_2Al_{12}Ca_3F_{14}$ sample. The simulated detector is run in event mode and neutrons are assigned a q-value calculated from the pixel position on the detector and the time delay from the chopper to the detector. The shape of the Debye-Scherrer cones are taken into account. The three plot on the left are data from the high resolution mode, the center plots are from the medium mode, and on the right are the high flux mode data. The 2D maps at the top are the full data sets and the center plots are a smaller sample of the data. The bottom plots show the data summed from 10° to 180° and converted from q-value to d-spacing. The insert show the same data as displayed in the center panels. The somewhat stronger scattering intensity at 17° and 163° this happens just where the size of the Debye-Scherrer cone matches the detector hight.

The volume between the sample and the detector, from 0.5 m to 1.5 m radius, will be filled with Ar to avoid scattering from moisture and nitrogen in the air. In the standard configuration a radial collimator: 600 mm high and 300 mm wide, with a blade separation of 1° will be installed 0.5 m from the sample. The radial collimator can be automatically shifted in and out of diffracted beam. This possibility gives an option for easily changing to another collimation system to fit the sample size and the sample environment. Ideally, it should be possible to build the collimators into the sample environment and make it easily interchangeable. The immediate volume around the sample and sample environment will be evacuated. A vanadium window will seal between the pre-vacuum around the sample and the Ar in the vacuum diffraction detector tank.

A key element for the success of HEIMDAL will be access to specialized sample environment allowing manipulation of the sample in order to perform *in situ* and *in operandi* measurements. Therefore HEIMDAL must be built to accommodate a flexible sample environment. The geometry of the detectors should be particularly suited as they allow top and 35° side access, while the detector opening is 18° above and below the scattering plane. The side access gives optical access to the sample and facilitate neutron diffraction experiments combined with UV–vis, IR, or Raman scattering. The geometry makes HEIMDAL ideal for accepting sample environment where access to the scattering plane is limited like high field magnets and pressure cells. The target with regards to conventional sample environment is covering the temperature range from 10 mK to 2000 K and having vertical magnetic fields up to 15 T, while pressures cells should allow studying samples under 25 GPa. An automatic sample change should allow experiments being performed in the range 2–400 K allowing a high through-put of experiments and potentially allow mail-in service.

In addition to these standard sample environments, it is expected that users will bring in their own equipment for specialized *in situ* or *in operandi* studies. Here chemical reaction cells for *in situ* studies of crystal growth in various media and pressures are foreseen. The instrument should be equipped with a gas rig for purging different inert and reactive gasses over the sample along with gas analysis techniques such as mass spectrometry and gas

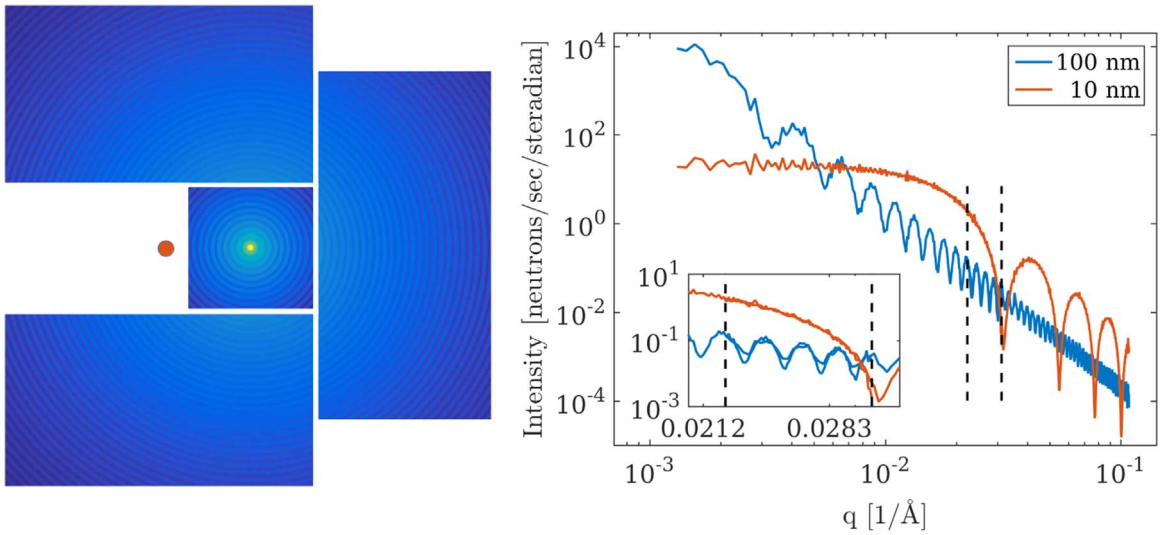

Fig. 15. Left: The SANS detector coverage in perspective, the quadratic back most detector is 1×1 m^2 and placed 10 m from the sample position, while the rectangular shaped detectors are 1×0.5 m^2 and placed 4 m from the sample. They therefore appear larger in the figure. The red dot indicates the position of the direct thermal beam. The data displayed is a snap shot taken at $\lambda = 10$Å from a simulation using a sample of nanoparicles with sizes of 100 nm. Right: A radial integration of the simulated data of two particle sizes, 10 nm and 100 nm, at a snap shot with a wavelength of $\lambda = 10$Å. The black dashed lines show where the center detector stops and the outer detector begins. The overlap region displayed in the insert occurs as the distance to the corner of the center detector is further away than the closes point of the side detector. (For interpretation of the references to color in this figure legend, the reader is referred to the web version of this article.)

chromatography. Thermogravimetry (TG) and differential calorimetric scanning DSC can also be combined with neutron scattering. Battery charge and discharge cell for following intercalation and deintercalation of Li-ion batteries, electric fields for studying the cycling piezo electric materials, catalytic reactors to follow catalyst materials *in operandi* and many more that will be built and designed by the user in collaboration with the instrument team to accommodate a specific science case, where the virtues of HEIMDAL will allow completely new science.

Space will be allocated close to the instrument to set up the sample environment for the following experiment, including control through the instrument software. Special care has to be taken for controlling and monitor the sample environment, both, on-line and off-line. It is important that the software control allows parallel operations of different sample environment: The running experiment and the standby experiment. The pretested sample environment should be easily transferable to the beam position. This minimizes the down time between experiments. It is envisaged that the complete sample environment can be tested off-line including all cables connections. As the previous beamtime ends the entire sample environment can be pulled out of the instrument and the next sample environment can be inserted with a minimum of setup time. In this fashion, it is also envisioned, that long term experiments could be inserted at HEIMDAL multiple times (days, weeks, months after the beginning of the chemical reaction) without removing the sample from the sample environment.

7. Conclusion

HEIMDAL is a novel instrument concept combining thermal powder neutron diffraction (TPND) with small neutron angle scattering (SANS) and neutron imaging (NI). The highly different conditions needed for TPND and SANS is overcome by using two guides, where the guide for TPND is looking at the thermal moderator and uses a pulse shaping chopper to shorten the pulse in order to produce sharp pulses as needed for diffraction. Flexible collimation will be implemented as movable jaws inside the last part of the guide. The SANS will be fed from a cold guide looking onto the cold moderator. The cold guide is curved and at the sample position the two guides are intersecting with an angle of 3.5°. The cold guide will be equipped with double pinhole collimation to create a highly parallel beam for the SANS setup. NI is an add-on feature that will enable users to inspect samples during experiments using the Bragg-edge imaging technique. The simultaneous capabilities of TPND and SANS will allow for completely new science as it will cover multiple length scales and allow studying dynamical processes of real materials in real time, under real conditions.

Acknowledgments

The authors like to thank Ken Andersen and Werner Schweika for fruitful discussions during the development of the instrument concept. The project was supported by the Danish contribution to the ESS Design Update Phase under the Danish Agency for Science and Innovation, and the Danish National Research Foundation (Center for Materials Crystallography, DNRF93). Work in Switzerland for the ESS is funded by the Swiss State Secretariat for Education, Research and Innovation SERI.

References

[1] A.M. Beale, et al., J. Am. Chem. Soc. 128 (2006) 12386–12387.
[2] David S. Wragg, et al., Angew. Chem. Int. Ed. 51 (2012) 7956–7959.
[3] I. Halasz, et al., Nat. Protoc. 8 (2013) 1718–1729.
[4] K.W. Chapman, et al., J. Appl. Crystallogr. 48 (2015) 1619–1626.
[5] T. Ishigaki, et al., Nucl. Instrum. Methods Phys. Res. A 600 (2009) 189–191.
[6] T. Hattori, et al., J. Phys. : Conf. Ser. 215 (2010) 012024.
[7] D.T. Bowron, et al., Rev. Sci. Instrum. 81 (2010) 033905.
[8] ⟨https://en.wikipedia.org/wiki/HEIMDALIr⟩, 2015.
[9] K. Lefmann, K. Nielsen, Neutron News 10 (3) (1999) 20–23.
[10] P.K. Willendrup, E. Farhi, K. Lefmann, Physica B 350 (2004) e735.
[11] F. Mezei, J. Neutron Res. 6 (1–3) (1997) 3–32.
[12] H. Schober, et al., Nucl. Instrum. Methods Phys. Res. Sect. A 589 (1) (2008) 34–46.
[13] K. Lefmann, et al., Rev. Sci. Instrum. 84 (2013) 055106.
[14] S. Peggs et al., ESS Technical Design Report, ISBN 978-91-980173-2-8, Lund, 2013.
[15] Private Communication with Ken Andersen, ESS, October 2015.
[16] F. Mezei, et al., Proc. SPIE 4785 (2002) 24–33.

[17] K. Lieutenant, et al., J. Neutron Res. 14 (2006) 177–191.
[18] S.L. Holm, M.Sc. thesis, Niels Bohr Institute, University of Copenhagen, 2013, ⟨http://xns.nbi.ku.dk/student_theses⟩.
[19] L.C. Chapon, et al., Neutron News 22 (2011) 22–25.
[20] M. Bertelsen, M.Sc. thesis, Niels Bohr Institute, University of Copenhagen, 2014, ⟨http://xns.nbi.ku.dk/student_theses⟩.
[21] E. Farhi, et al., J. Neutron Res. 17 (2013) 5–18.
[22] Internal Report: New ESS Moderator Baseline by Ken Andersen, 2015.
[23] A. Jackson et al., LoKI – A Broad Band High Flux SANS Instrument for the ESS, subm. Proc ICANS XXI, 2015.
[24] ⟨https://en.wikipedia.org/wiki/Medipix⟩, 2016.
[25] C.D. Dewhurst, Meas. Sci. Technol. 19 (2008) 034007-1–034007-8.
[26] R.K. Heenan et al., Proc. ICANS-XVII, 2006, pp. 780–785.
[27] D.F.R. Mildner, Nucl. Instrum. Methods 200 (1982) 167.

A.9 VESPA: The vibrational spectrometer for the European Spallation Source

Presentation of the VESPA instrument accepted for construction at ESS. The spectrometer measures initial energy using time of flight, and filters final energies using crystal analyzers. The analyzers and their detectors are in a so-called time focusing geometry, reducing the error in the time measurement. The science case of the instrument requires high energies, and it was chosen to have direct line of sight through the guide. The paper was published in Review of Scientific Instruments.

Abstract

VESPA, *Vibrational Excitation Spectrometer with Pyrolytic-graphite Analysers*, aims to probe molecular excitations via inelastic neutron scattering. It is a thermal high resolution inverted geometry time-of-flight instrument designed to maximise the use of the long pulse of the European Spallation Source. The wavelength frame multiplication technique was applied to provide simultaneously a broad dynamic range (about 0-500 meV) while a system of optical blind choppers allows to trade flux for energy resolution. Thanks to its high flux, VESPA will allow the investigation of dynamical and in situ experiments in physical chemistry. Here we describe the design parameters and the corresponding McStas simulations.

My contribution

Designed the guide system for the instrument under constraints discussed with the remaining instrument team. Provided figures on guide geometry used in the final manuscript. Commented on the final version of the manuscript.

REVIEW OF SCIENTIFIC INSTRUMENTS **87**, 065101 (2016)

VESPA: The vibrational spectrometer for the European Spallation Source

Anna Fedrigo,[1,2,3,a)] Daniele Colognesi,[2] Mads Bertelsen,[1,3] Monika Hartl,[3] Kim Lefmann,[1] Pascale P. Deen,[3] Markus Strobl,[1,3] Francesco Grazzi,[2] and Marco Zoppi[2]
[1]*Niels Bohr Institute, University of Copenhagen, 2100 Copenhagen Ø, Denmark*
[2]*Istituto dei Sistemi Complessi, Consiglio Nazionale delle Ricerche, 50019 Sesto Fiorentino, Italy*
[3]*European Spallation Source ESS AB, SE-221 00 Lund, Sweden*

(Received 11 February 2016; accepted 9 May 2016; published online 2 June 2016)

VESPA, *Vibrational Excitation Spectrometer with Pyrolytic-graphite Analysers*, aims to probe molecular excitations via inelastic neutron scattering. It is a thermal high resolution inverted geometry time-of-flight instrument designed to maximise the use of the long pulse of the European Spallation Source. The wavelength frame multiplication technique was applied to provide simultaneously a broad dynamic range (about 0-500 meV) while a system of optical blind choppers allows to trade flux for energy resolution. Thanks to its high flux, VESPA will allow the investigation of dynamical and *in situ* experiments in physical chemistry. Here we describe the design parameters and the corresponding McStas simulations. *Published by AIP Publishing.* [http://dx.doi.org/10.1063/1.4952430]

I. INTRODUCTION

VESPA—*Vibrational Excitation Spectrometer with Pyrolytic-graphite Analysers*—is a concept for a thermal neutron vibrational spectrometer at the European Spallation Source (ESS) in Sweden.[1] It is a high-resolution, high-intensity, broadband inverse geometry neutron spectrometer that will be focused on neutron vibrational spectroscopy (NVS) fully utilizing the new and upcoming high-power spallation source ESS. While a thermal instrument may seem an illogical choice to build at a neutron facility optimised for cold neutrons, the ESS brilliance into the thermal range will be sufficient to cover, achieving both high intensity and high resolution, the so-called "vibrational fingerprint region" (i.e., 60-220 meV ≈ 500-1800 cm^{-1}), a region most important to identify functional chemical groups.[2] Moreover, the instrument aims at *in situ* measurements, especially in the field of catalysis, materials for renewable energies, and also for applied scientific and industrial research.

In state-of-the-art research, it is quite common to combine *in situ* spectroscopy with other techniques to observe processes in realistic situations and sometimes with very complex samples. VESPA will be able to offer equivalent *in situ* spectroscopy techniques using neutrons thereby providing all the advantages of neutrons for vibrational spectroscopy when quantitative results are needed and/or optically dense materials are investigated. The flux available at VESPA using the time structure of ESS makes much anticipated time-resolved studies feasible, and kinetic phenomena at medium time scales will become observable. Catalytic reactions and thermal decomposition of hydrogen storage materials are only two of the scientifically very interesting examples for these types of experiments.[3]

NVS provides information on chemical bonding, intramolecular and intermolecular interactions, and general vibrational dynamics of atoms in molecules. This will address common research topics such as the aforementioned hydrogen storage and catalysis but also hydrogen bonding in drugs and pharmaceuticals, surface chemistry, thermoelectric and photovoltaic effects in materials and energy storage to name a few.[4] Due to the high neutron flux at modern spallation sources, it is possible to probe elements other than hydrogen.[5] For example, geologically important gases such as CO_2 and their interaction with minerals under normal and high pressure can be measured. This currently creates a high scientific impact as the carbon sequestration is one of the mechanisms playing an important role in geochemistry with respect to global warming.

NVS is the analogue of combined infrared (IR) and Raman spectroscopy with the source of radiation being neutrons instead of photons. Optical spectroscopy is used extensively in educational settings, in research, or industrial laboratories. Raman and IR spectroscopy have become essential tools not only in chemistry but also in medical applications, forensics, environmental compliance, and quality control to cite but a few common uses. The applications in the investigation of solids and liquids, soft matter, complex fluids, and biomaterials are well-known.[6] While the standard resolving power of commercially available Raman instruments used in almost every chemistry laboratory around the world (of the order of 0.2-0.5 meV or 0.1 meV for high resolution instruments)[7] is still better than the energy resolution of the best performing NVS instruments currently operating (rated around 0.3-6 meV at 15 and 250 meV, respectively),[8] it is not better by a large margin.

In comparison to optical vibrational spectroscopy, NVS offers features that not only balance but often outperform the corresponding ones of optical spectroscopy.[7] The advantage of using neutrons over photons lies mainly in the high sensitivity of neutrons to hydrogen, hydrogen being the nucleus with the largest cross section for neutrons. The lack of excitation rules for neutron scattering, in comparison to the restrictive excitation rules in optical spectroscopy, enables the observation of modes only weakly active in optical spectros-

a)E-mail: anna.fedrigo@nbi.ku.dk

copy. This is a huge advantage not only over light but also X-rays, especially in surface science and catalysis. It becomes easy, for example, to observe small amounts of hydrogen-containing molecules on solid surfaces even containing high-Z metals. Optical radiation and X-rays are strongly adsorbed by samples leading to unwanted photochemical effects and possibly redox processes in the sample, which does not happen when using neutrons.

The neutron nucleus interaction is well described within nuclear reaction theory.[9] As a result, it is possible to quantitatively determine the modes, position, and intensity of excitations probed by neutrons. This is a much more difficult endeavour for the photon-electron interaction. As such, there is a well understood interpretation of neutron spectra using theoretical calculations and makes it possible to use NVS as a tool for benchmarking density functional theory (DFT) methods and atomic potentials. NVS has no selection rules since neutron cross sections do not suffer the well-known restrictions,[10] which sometimes hinder the observation of critical modes in high symmetry molecules when using optical spectroscopy. The NVS signal strength depends on cross section and amplitude of motion. As such, bending modes in the fingerprint region are often more easily observed than with optical methods. Neutrons carry momentum and produce a spectrum averaged over the entire Brillouin zone, a distinct and unique advantage in the determination of the phonon density of states of a sample and the corresponding thermodynamic properties. The low momentum transfer in optical spectroscopy limits these probes to the gamma point in the first Brillouin zone ($q = 0$). Last but not least, neutrons have high penetrating power, which allows the use of bulky, dense sample environment. Optical spectroscopies require complex sample holders with optical access to the sample. This is an advantage that should not be underestimated since a lot of *in situ* experimental setups in areas such as catalysis, photochemistry, and energy storage are quite elaborate and optical windows are not always possible.

The ESS source and the instrument characteristics of VESPA will provide high-intensity flux in the fingerprint region of spectroscopy. VESPA will offer an unparalleled, constant relative energy resolution as low as $\Delta E/E_0 = 0.5\%$ over most of its energy transfer range; a comparison with the current best performing NVS instrument is reported later in Figure 7. Thanks to its flux and such excellent energy resolution, VESPA will allow the detection of smaller and smaller amounts of samples, a crucial feature to compete with optical spectroscopies and to measure novel, cutting edge materials often only available in very small quantities. The flexible chopper configuration of VESPA in conjunction with the long pulse structure of the ESS source will enable the user to trade resolution for count rate. While this feature is common on direct inelastic neutron spectrometers, VESPA is the first proposed instrument that will bring it to NVS. In addition, the instrument will be provided with features that proved very useful at world leading instruments such as VISION. These features include diffraction banks, an automatic sample changer, a customised sample environment for high pressure or *in situ* electrochemistry. In particular, VESPA will allow the use of anvil cells to achieve high pressures in the GPa range, a research area that is currently being explored with NVS at VISION (SNS). The diffraction banks will allow phase identification as well as basic pair-distribution function (PDF) analysis for non-crystalline samples. These combined features are generally sought after by many researchers in this field.

With the MAX IV synchrotron coming online next year and the close proximity between ESS and MAX IV, using X-ray absorption fine structure XAFS in connection with NVS as a complimentary technique will be a great asset to surface science research areas such as catalysis. The benefits will only increase with the possibility of a high-throughput at the XAFS BALDER[11] and VESPA beamlines.

II. INSTRUMENT OVERVIEW

VESPA is an inverted geometry time-of-flight (ToF) spectrometer, which is the most effective solution for a spectroscopy instrument on a spallation source when a wide range of energy-transfer coverage is required,[12] such as for neutron vibrational spectroscopy.

The mode of operation of the instrument is pictured in Figure 1. With each proton pulse hitting the ESS tungsten target, spallation neutrons are produced and thermalized by the H_2O moderator. Each of the neutrons from the pulses originating at the moderator M travels down the beamline at a speed determined by its energy and hits the sample S with varying energy E_0, depending on time. The scattered energy E_1 of the neutrons recorded is fixed and defined by the Bragg angle $2\theta_A$ of the crystal analyser A and filtered through a beryllium bandpass filter before hitting the detector D. By measuring the total flight time t of the neutrons at the detector, their incident energies E_0 can be determined. The

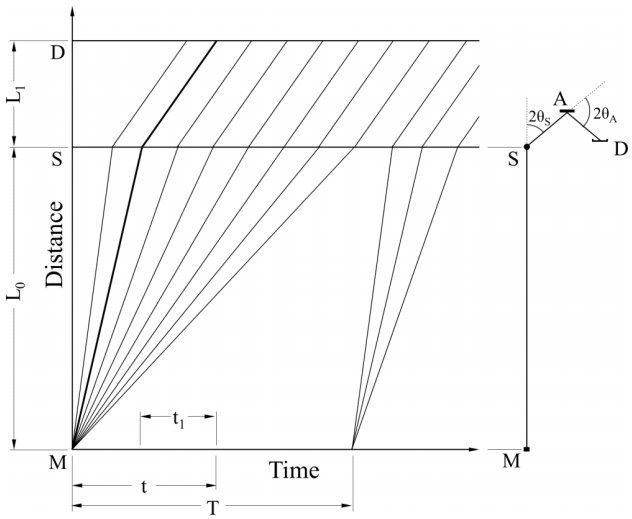

FIG. 1. Time-distance diagram of an inverted geometry neutron spectrometer. L_0 represents the primary path from the moderator M to the sample S; L_1 is the secondary path, the distance from S to the analyser A to the detector D. By measuring the total flight time t (where $t = t_0 + t_1$), it is possible to calculate the incident energy E_0. T is the period of the source while t_0 and t_1 are the primary and secondary flight time, respectively.

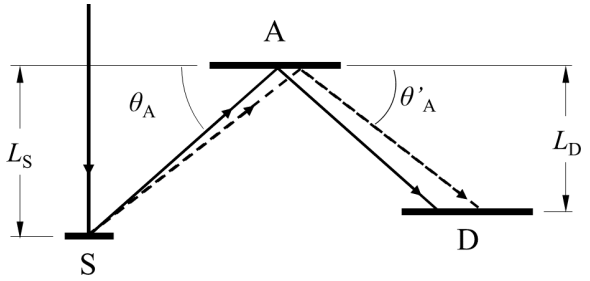

FIG. 2. Schematic of the time focussing principle. From the sample S, two scattered neutrons are taken into account and their flightpath is shown by the solid and dashed lines (of which the dashed path is clearly longer). From Bragg's law, and considering that $\theta_A > \theta'_A$, the wavelength of the neutron scattered at θ'_A must be shorter than the one scattered at θ_A. Therefore its energy and hence its velocity are greater, compensating for a longer path length.

energy transfer E from the neutron to the sample via inelastic scattering can then be calculated ($E = E_0 - E_1$).

The same conceptual design is used for the spectrometers TOSCA[13] at ISIS and VISION[8] at SNS and permits on these machines the measurement of an extensive energy transfer range up to ≈500 meV with energy resolution $\Delta E/E_0$ ranging between 1% and 2%. Thanks to the high flux provided by the ESS spallation source, VESPA aims to outperform the current vibrational spectrometers both in term of brightness and resolution in the fingerprint region.

The secondary spectrometer of VESPA hosts the sample, analyser, and detector planes in a parallel configuration, as pictured in Figure 2. This configuration allows for the exploitation of the time focussing principle,[14,9] which is also a feature of TOSCA and of most crystal analyser instruments.

The secondary path L_1 from the sample to the detector is given by

$$L_1 = \frac{(L_S + L_D)}{\sin\theta_A}, \tag{1}$$

where L_S and L_D are the vertical distances sample to analyser and analyser to detector respectively, and θ_A is analyser angle. The de Broglie wavelength of the scattered neutron can be written as

$$\lambda_1 = \frac{2\pi\hbar}{m_n v_1} = \left(\frac{2\pi\hbar}{m_n}\right)\left(\frac{t_1}{L_1}\right), \tag{2}$$

where λ_1 and v_1 are, respectively, the wavelength and velocity of the neutrons selected by the crystal analyser, $\hbar$ the reduced Planck constant, and m_n the mass of the neutron. By substituting Eqs. (1) and (2) into Bragg's law ($n\lambda = 2d \sin\theta$), we obtain

$$\left(\frac{2\pi\hbar}{m_n}\right)\left(\frac{t_1}{L_1}\right) = 2d_{PG}\frac{L_S + L_D}{L_1}, \tag{3}$$

where in our case, d_{PG} is the interplanar spacing of the analyser (Pyrolytic Graphite). Therefore t_1 is constant and independent of the energy of the scattered neutron. This is important because it reduces the relative time uncertainty in case of high energy transfers, thereby improving the energy resolution.

With respect to VISION and TOSCA, the novelty in the design of VESPA concerns mainly the primary spectrometer, which is designed to take advantage of the long pulse structure of the ESS beam by:

- Use of the wavelength frame multiplication WFM technique;
- Use of a pulse-shaping double chopper system PSC;
- Use of elliptical guides to transport neutrons;
- Increase of solid-angle coverage of the analyser-detector system (secondary spectrometer) with the possibility of an additional set of analyser-detector banks.

Compared to the other instruments at the ESS, VESPA belongs to the medium-length category. The instrument length has been optimised to provide a broad spectral range (E_0 = 3-503 meV) while maintaining the desired energy resolution ($\Delta E/E_0 \approx$ 0.5%-1.3%). The moderator-to-sample distance is 59 m with a sample-to-detector distance of ca. 1 m. A general overview of the instrument is presented in Figure 3.

The secondary spectrometer consists of four different annular sets of analysers-filter-detector banks, each set placed symmetrically with respect to the sample, two in backward (130° and 150° scattering angle $2\theta_S$) and two in forward scattering ($2\theta_S$ = 30° and 50°) geometry. Due to the double detector bank set on VESPA, a broader solid angle can be covered compared to TOSCA and VISION. In addition, it will be possible to increase the count rate of the secondary spectrometer even more by adding, downstream of the 30° and 150°scattering angle arms, a second crystal analyser bank in transmission, as proposed on the CAMEA/BIFROST instrument.[15] This additional bank will not work in time focussing.

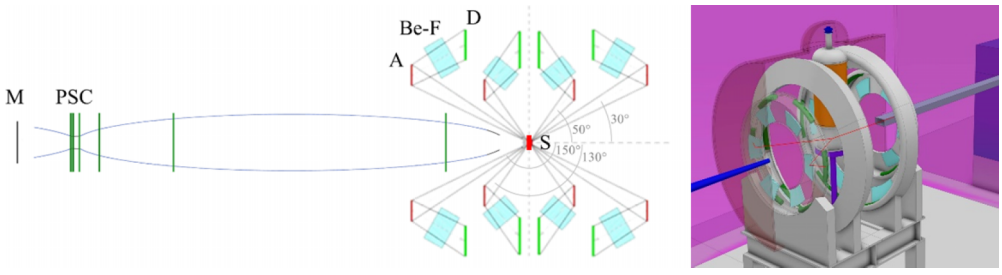

FIG. 3. (Left) Simplified overview of VESPA (not to scale). Neutrons are transported from the moderator M to the samples S through an elliptic guide. The secondary spectrometer consists of four sets of analyser-filter-detector banks radially placed around the sample. Choppers are marked by dark green. (Right) 3D representation of the secondary spectrometer; for simplicity, only two of the four banks are illustrated.

Most design features meant to improve the instrument performance are based on the specific neutron optics and chopper system to be utilized at the ESS. These are dealt with in more detail Secs. III–IV. Below we report corresponding instrumental details and Monte Carlo simulations using the ray-tracing package McStas.[16–18]

III. MODERATOR AND NEUTRON GUIDE SYSTEM

Beam extraction from the ESS thermal moderator has been optimised to maximise the neutron flux in the fingerprint region. McStas simulations of the beamline were performed using the ESS 3 cm-high thermal "pancake" moderator.[19]

The extraction and efficient long-distance transport of the neutron beam is possible, thanks to the elliptical neutron guides.[20,21] The guide-system starts at 2 m from the moderator with the extraction guide (or "feeder")[22] that focuses the primary beam to a 3×6 cm^2 window at 6.8 m, i.e., an intermediate position between the optically blind WFM pulse shaping choppers. Doing so, the accuracy of the pulse-shaping choppers (PSCs) is improved.[23] The extraction guide ends at 6.45 m from the moderator, just before the 1.1 m long straight section where the PSCs are positioned. From here, a long elliptical guide transfers the neutron flux to the position of the sample, 59 m away from the moderator. The guide system was developed making use of a combination of analytical calculations,[24] McStas simulations (version 2.1) and the McStas optimisation software guide_bot.[25] The neutron transport was optimised for full weight in the wavelength range from 0.6 to 1.0 Å and with a linear decrease to zero at 4.7 Å. The resulting geometry is shown in Figure 4. Elliptical guides significantly improve the beam transport, and the direct line of sight to the moderator preserves the thermal flux. All guides are assumed to have an $m = 4$ surface coating. An additional improvement on the neutron transport can be achieved by choosing greater m values, in the very beginning and end of the ellipse, where the neutrons have a higher average reflection angle.[21]

IV. CHOPPER SYSTEM

The *wavelength frame multiplication* (WFM) technique[23,26,27] was proposed to produce a broad wavelength spectrum for different instruments installed on long pulse target stations. The same concept is applied in the case of VESPA to extend the energy-transfer range within the pulse repetition time of ESS. By splitting the pulse in 3 sub-frames, we achieve, in addition to a broader wavelength spectrum, a shortening of the natural instrument length[28,29] and a consequent reduction of neutron transport issues for high energy neutrons. Combining WFM with pulse-shaping double choppers in optically blind mode[30,23] enables us to define a constant resolution over the whole energy range and allows pushing the energy resolution down to $\Delta E/E_0 \approx 0.5\%$.

The versatility of VESPA in trading flux for resolution is due to this chopper system, which consists of three types of choppers arranged as following:

- Optically blind WFM pulse-shaping choppers (PSCs) placed as close to the moderator as possible;
- A bandwidth chopper (BWC) located after the PSCs;

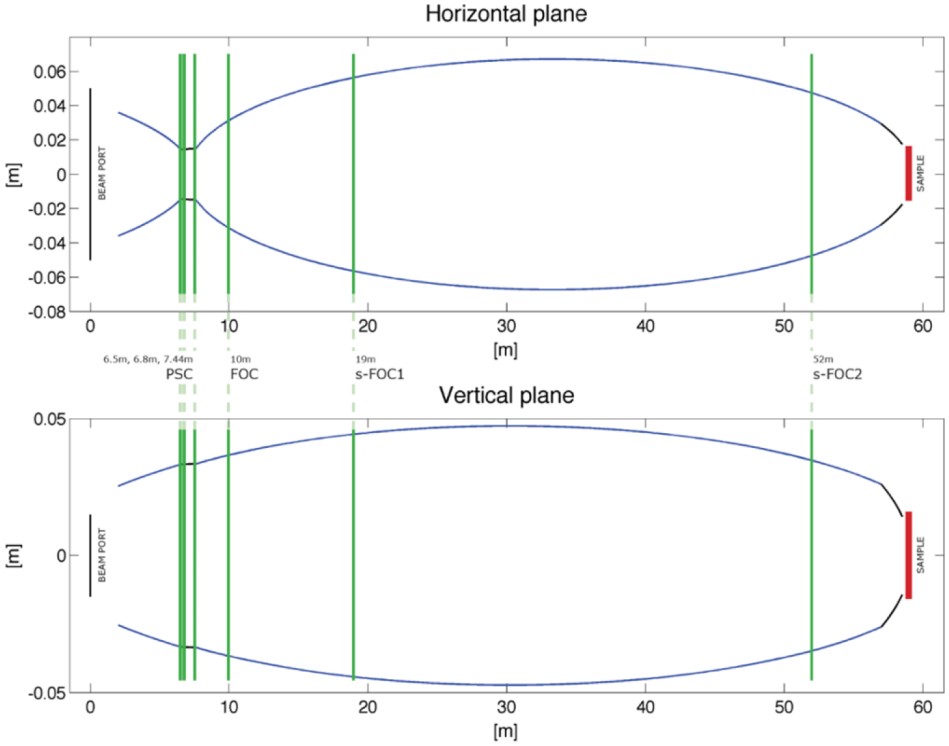

FIG. 4. Sketch of the guide system (to scale) seen from above (horizontal plane) and from a lateral view (vertical plane). Straight neutron guides (in black), used at the PSC position and in the last focussing section onto the sample, are not part of the overall ellipse. The choppers are shown by green vertical lines.

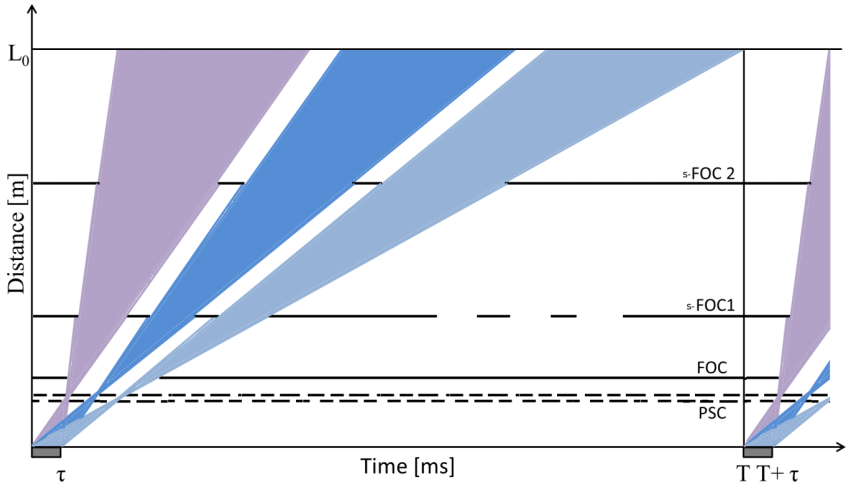

FIG. 5. Space-time diagram showing the three sub-frames and the chopper positions and the neutron time-distribution at sample position (to scale). L_0 is 59 m, T and τ are 71.43 and 2.86 ms, respectively.

- 2 sub-frame overlap choppers (s-FOC1 and s-FOC2) situated after the WBC to keep the sub-frames well separated in time.

A schematic view of the chopper positions in the time-of-flight (ToF) diagram is pictured in Figure 5.

The PSC system makes use of an optical blind chopper pair that provides neutrons with constant ToF resolution: $\delta t(\lambda)/t_0(\lambda)$ = constant, where $\delta t(\lambda)$ is the wavelength dependent opening time of the window and $t_0(\lambda)$ the corresponding wavelength dependent time of flight from the pulse shaping chopper to the sample. The midpoint between the choppers to the sample position defines the ToF starting point,[30] which, however, differs from frame to frame.[23] The distance z_0 between the optical blind pulse shaping choppers defines the constant ToF resolution of the system.

The instrument is provided with three PSC choppers at 6.5, 6.8, and 7.44 m from the moderator, allowing three different resolution settings. Only two choppers at a time will be used, the third will be left in an open position. This way it will be possible to vary the instrument resolution between three settings: low ($\Delta E/E_0 \approx 1.3\%$), medium ($\Delta E/E_0 \approx 0.9\%$), and high resolution ($\Delta E/E_0 \approx 0.5\%$). The values for the different configurations are reported in Table I.

In addition to the WFM pulse-shaping choppers (PSCs), a wavelength band chopper—or bandwidth chopper—(WBC) and two sub-frame overlap choppers (s-FOCs) are needed to keep the three bands well separated in time over the length of the flightpath. All choppers are made of counter-rotating double discs of 70 cm of diameter, with 3 windows each (except for the bandwidth chopper WBC that has only 1 window) and running at a multiple of the source frequency. Counter rotating double disc choppers provide double opening and closing speed compared to single disc choppers, minimizing the opening and closing time of the beam windows, thus giving an improved trapezoidal transmission profile. This is particularly important for high resolutions and in general if the running frequency is limited and the guide cross sections are relatively large as it is the case for WBC, s-FOC1, and s-FOC2 that are located in the wide parts of the elliptic neutron guides. All specifications of the choppers are listed in Table II.

TABLE I. Parameters for low, mid, and high resolution configuration of VESPA. WFM-PSC1 and WFM-PSC2 indicate the position of the chopper in use, their distance is z_0, while L_{ToF} represents the flight path from the mid-point between the pulse shaping choppers to the sample.

	Low-Res ($\Delta E/E_0 = 1.3\%$)	Mid-Res ($\Delta E/E_0 = 0.9\%$)	High-Res ($\Delta E/E_0 = 0.5\%$)
WFM-PSC1 (m)	6.50	6.80	6.50
WFM-PSC2 (m)	7.44	7.44	6.80
z_0 (m)	0.94	0.64	0.30
L_{ToF} (m)	52.03	51.88	52.35

The primary spectrometer was simulated using McStas, and results at the sample position are shown below for the three resolution configurations. The targeted nominal operation power of ESS for which the brightness is calculated is 5 MW. The parameters for the choppers used are the ones listed in Tables I and II. In Figure 6 (left), we report the simulated flux distribution at the sample position as a function of time. The three sub-frames appear well separated in time, allowing to unequivocally determine the neutron energy from ToF, and avoiding at the same time the interference with the prompt pulse of the moderator, which interests the first 6 ms (including the "tail") of the 71.429 ms source cycle. In Figure 6 (right), we show the same data as a function of the neutron wavelength.

The wavelength intervals are well superimposed at their edges so that the total available spectral range is fully covered with only minor dips in intensity where consecutive frames overlap. As expected from the intrinsic features of the ESS source, the intensity distribution of the flux decreases above 50 meV but still remains optimal up to $E_0 \approx 150$ meV (Figure 7). This is a direct consequence of the ESS design (over-moderated source) and the transport of neutrons over such distance. In the same graph, the corresponding McStas simulations for VISION are reported for comparison and they suggest that due to the effect of the

TABLE II. VESPA chopper scheme and specifications. The chopper frequencies are limited by the size and phase of the windows. The window sizes of the PSCs are set for 1.3% $\Delta E/E_0$ resolution since the size does not compromise the performance of the instrument at better resolution. The energy ranges for the three windows are only indicative and change slightly according to the resolution setting.

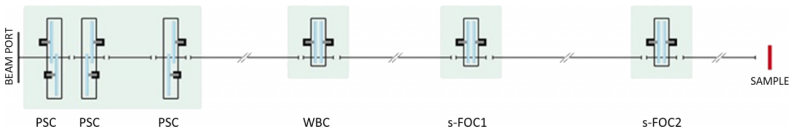

	1		2	3	4	Assembly number
1-2	3-4	5-6	7-8	9-10	11-12	Chopper number
6.5	6.8	7.44	10	19	52	Position (m)
154	154	154	14	28	14	Freq. (Hz)
30 × 60	30 × 60	30 × 60	60 × 80	110 × 100	100 × 90	Beam size (mm^2)
WFM + pulse shaping	WFM + pulse shaping	WFM + pulse shaping	Bandwidth chopper WBC	Sub-frame overlap chopper s-FOC1	Sub-frame overlap chopper s-FOC2	Function
3	3	3	1	3	3	Windows number
						Window openings (deg)
24.31	24.31	24.31		46.89	84.07	503.00-24.02 meV
40.98	40.98	40.98	320.12	45.96	77.95	25.14-8.45 meV
57.32	57.32	57.32		63.58	107.66	8.53-3.56 meV

source and its optimised exploitation, VESPA is well suited to outperform existing instruments in the low-to-middle thermal energy region (E < 150-190 meV depending on the resolution chosen).

To avoid the interference with the prompt pulse of the moderator and the gamma flash that is generated during the high-energy protons collision with the target, the system is designed such that the first frame of neutrons arrives at the detector position only after 6 ms of the 71.429 ms source cycle, which corresponds to avoiding the full initial pulse length including the "tail." A viable solution for shielding these fast neutrons from the prompt pulse implies using a T_0 chopper, which is a relatively large metal block, generally made of NIMONIC [e.g., Nimonic 75: Ni (75%) + Cr (20%) + Fe (5%)] or INCONEL [e.g., Inconel X 750: Ni (74%) + Cr (15%) + Fe (7%) + Nb (1%) + Al (3%)]. Sufficient space to host a T_0 chopper is provided on VESPA at the s-FOC 2 position, should its use be considered essential for improving the performances of the instrument based on detailed background studies or even later based on operational experience.

Although at ESS, the proton beam energy is high and the pulses are very long compared to existing spallation sources, preliminary simulations for instruments within direct line of sight and with similar generic guide geometries imply that a background level of 10^{-5} (noise to signal ratio) or better can be achieved with appropriate shielding and the presence of a T_0 chopper. Currently no evidence is found that the background issue would negatively impact the expected performance in comparison to state-of-the-art instruments at other facilities. It is expected that the performance of VESPA would surpass current day state-of-the-art instruments since VESPA (i) works in a time frame avoiding the prompt pulse, (ii) is nearly 4 times as long as comparable instruments at short pulse sources, (iii) can still adopt a T_0 chopper solution, and (iv) will have (due to its length and expected neighbourhood) space for further improvements in shielding later on.

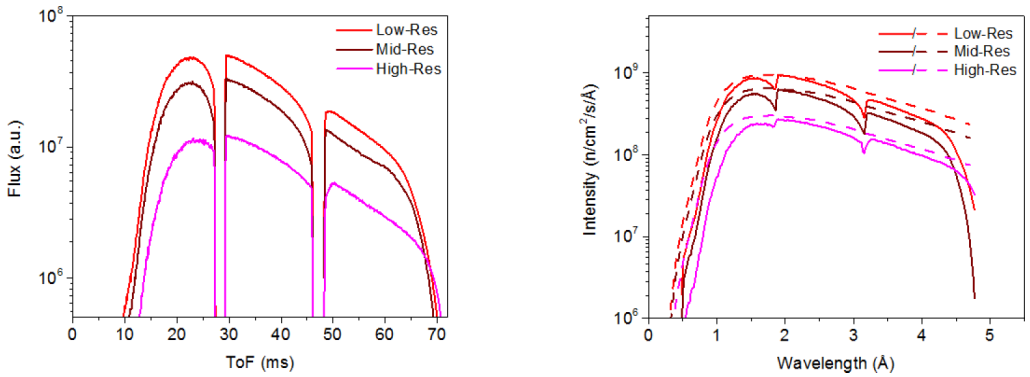

FIG. 6. (Left) Time of flight distribution at the sample position. (Right) Simulated flux at the sample position as a function of wavelength. The clear separation in arrival time of the neutrons only slightly affects the wavelength distribution.

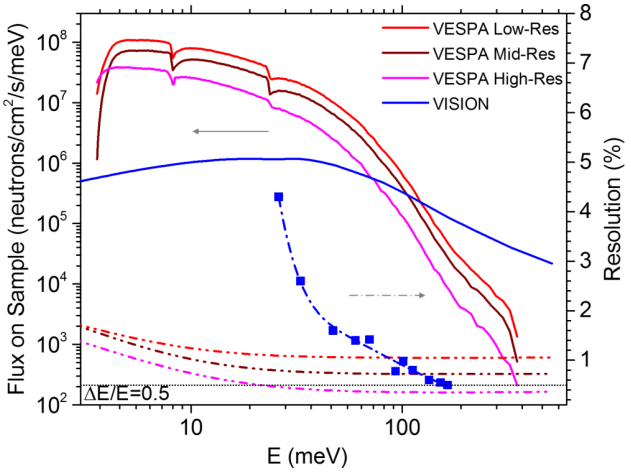

FIG. 7. Energy distribution (McStas simulations: solid lines) and calculated resolution ($\Delta E/E_0$, dashed lines) for all the three resolution settings of VESPA and for VISION (operating at 30 Hz).

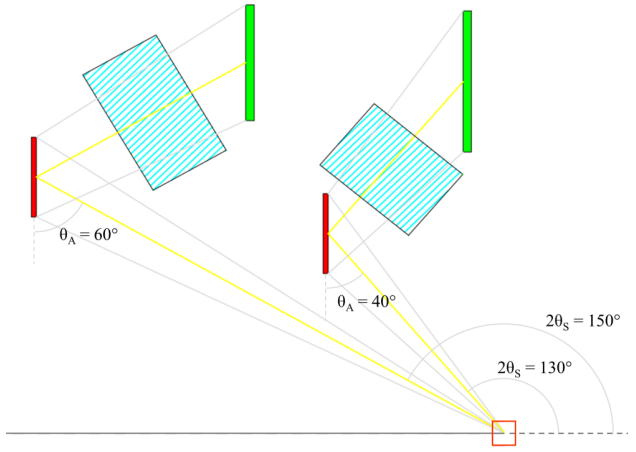

FIG. 8. Backscattering section of the VESPA secondary spectrometer (1/28 of the instrument). The crystal analysers are coloured red, Be-filters light blue, and detector banks green. The sample position is marked by the red square in the bottom-right region of the figure.

V. THE SECONDARY SPECTROMETER

The secondary spectrometer is composed of four different annular sets of crystal analysers, two sets in backscattering ($2\theta_S = 130°$ and $150°$) and two sets in forward scattering ($2\theta_S = 30°$ and $50°$) with respect to the incoming beam (see Fig. 3). The inner sets ($2\theta_S = 50°$ and $130°$) allocate 6 crystal analysers while the external sets ($2\theta_S = 30°$ and $150°$) are able to allocate 8, for a total of 28 analysers each with the approximate dimensions 10×10 cm^2. The crystal analysers use highly oriented pyrolytic graphite (HOPG) crystals (with mosaic spread of 2°) and borated Si supports placed at two distinct Bragg angles ($\theta_A = 40°$ and $60°$) determining two different E_1 values, 4.4 meV and 2.42 meV, respectively. The neutrons of energy E_1 will be elastically scattered from the lattice plane and pass through beryllium filters, cooled down to 30 K. The Be-filters are placed downstream from the crystal analysers and used as a low-bandpass filter to remove the higher order reflections, which also fulfil the Bragg condition. The detector banks will be composed of 20 squashed tubes, 200 mm long, 12.5 mm wide, 2.5 mm thick, charged with pressurized ^{3}He at 20 bars. This reduces the size of the absorption path, thereby increasing resolution while maintaining high detection efficiency.[13,31]

A schematic close-up of a section of the secondary spectrometer is depicted in Figure 8 including the trace of the neutrons from the sample position (red square) to the ^{3}He detector (tall green rectangles). The crystal analysers are represented by the tall rectangles in red. The light blue rectangles are the Be-filters. All three planes, sample, analyser, and detector, are parallel to fulfil the time-focussing condition (see Fig. 9).

The total solid angle collected by the whole system of analysers (back- and forward-scattering graphite banks) amounts to 1.196 ($= 2 \times 0.598$) sr, which roughly corresponds to 1.5 times the present TOSCA-II coverage. In addition, VESPA will operate with a much higher incoming neutron

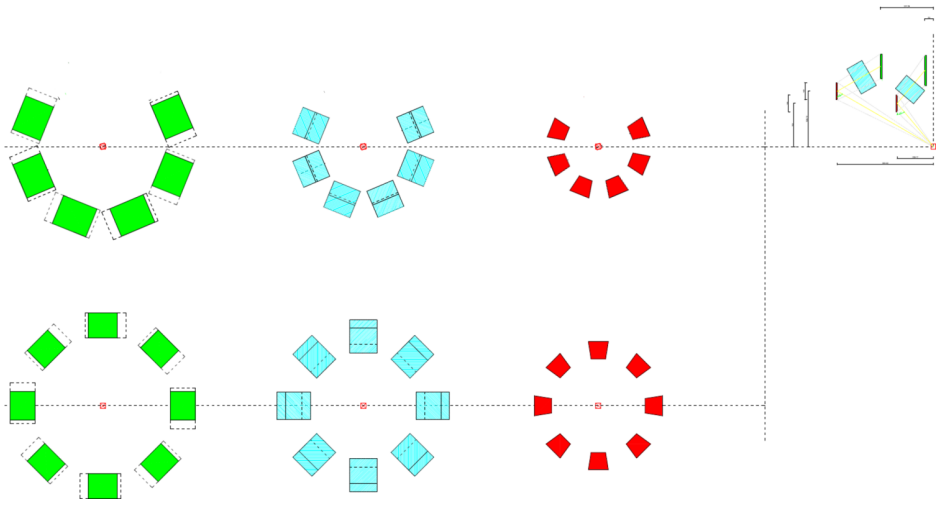

FIG. 9. Projection of the backscattering section of the VESPA secondary spectrometer (in the top right corner, Figure 8 is reported to scale). Only 1/2 of the instrument is shown, the same geometry applies for the forward scattering arms. In the top row, the $2\theta_S$ at 130° is outlined, below the one at 150°. The banks at 130° are lacking of two modules to leave space for sample environment. The crystal analysers are coloured red, Be-filters light blue, and detector banks green.

TABLE III. The characteristics of the four diffraction banks on VESPA.

	Backscattering bank	Equatorial banks
2θ (deg)	152-174	75-105
Q (Å^{-1})	31.37-2.77	24.92-1.74
d (Å)	0.2-2.3	0.25-3.6

beam intensity. As an upgrade, it will be possible to increase the count rate on the secondary spectrometer by adding, downstream of the 30° and 150° scattering angle arms, a third set of HOPG crystal analyser banks in a non-time focussing configuration increasing the solid angle by roughly 28%.

Considering the minimum available energy of the primary beam ($E_{0,\min} \approx 3.6$ meV, cf. Table III), the energy selected by the graphite banks with $\theta_A = 40°$ ($E_1 \approx 4.4$ meV) allows the spectral range to extend below the elastic line with an energy transfer of $E = -0.8$ meV. The corresponding value for the $\theta_A = 60°$ ($E_1 \approx 2.42$ meV) implies that this higher resolution bank can explore spectral shapes down to $E \approx 1.2$ meV only.

A. Auxiliary diffraction detector banks

The instrument will be equipped with four diffraction detector banks: one high resolution backscattering module (covering $2\theta = 152°$-$174°$) and three equatorial detector modules (covering in total $2\theta = 75°$-$105°$) placed in a way to have direct view to the sample. The range of angles will provide a good coverage of Q-space, as reported in Table III. This feature is already available on VISION and proved to be very efficient in providing simultaneous vibrational (information on dynamics) and structural data (information on local and long range order).

The high-resolution detector bank in backscattering geometry will allow for basic neutron pair-distribution function (PDF) measurements, a capability that is of great interest in the materials community. Many modern materials are amorphous and their properties depend on the degree of disorder in their lattice, hence crystallographic structure solutions are often insufficient. PDF opens the possibility to observe changes in the local structure.[32]

The detectors will consist of linear, position-sensitive tubes filled with ^{3}He at 20 bars placed 1 m from the sample. The exact length of the diffraction detector will be determined by the available space.

Despite the backscattering and equatorial banks are covering similar d (and Q) ranges, the detectors' resolution ($\Delta d/d$) of the two banks is different. This is due to the fact that the resolution function depends on a term (cot θ) that dominates at low angles while it becomes very small at high (back-scattering) angles. A simulated diffraction pattern of a $Na_2Ca_3Al_2F_{14}$ calibration sample is reported in Figure 10.

B. Sample environment

The core of VESPA will be a closed cycle, top loading refrigerator (CCR) with helium exchange gas that can be operated between 10 and 600 K. Since it is known from other

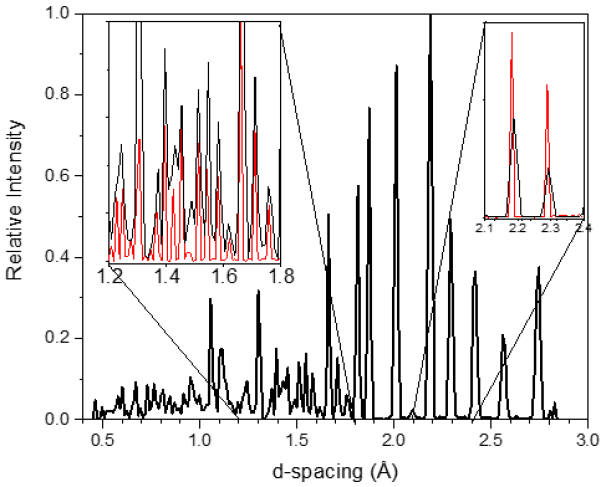

FIG. 10. McStas simulation of $Na_2Ca_3Al_2F_{14}$ powder sample of $3\times3\times0.3$ cm^3. Main figure: the instrument VESPA is set on the low-resolution chopper configuration. The equatorial bank in low resolution (average $2\theta = 102°$) shows the full d-space coverage. Inset: the backscattering bank (red line, average $2\theta = 163°$) is compared to the equatorial bank (black) in the two inserts at different d-spacings to illustrate the much higher resolution of that band.

NVS instruments (VISION and TOSCA) that the choice of sample environment is dictated by the science that will be of interest to the scientific user community at any time, it is our intent to provide the infrastructure necessary to modify the instrumental cryostat for various *in situ* measurements as the demand arises.

The customized CCR will include a setup for a laser light for photoexcitation offering easy access to experiments in the area of photochemistry and solar energy. Build-in, four-point electrode connections for measurements of electric properties of materials are planned for various electrochemical measurements frequently sought after in battery research and catalysis. The build-in electrode connectors are necessary to achieve perfectly shielded, yet easy to use access to *in situ* electrochemistry measurements such as impedance and conductivity. A non-standard, powerful cooling unit for the CCR is needed to remove the heat load emanating from the laser setup inserted in the cryostat and other setups with high heat loads. Several sample sticks equipped with gas-flow cells, electrochemistry cells, photochemistry cells, and a large anvil cell for high-pressure measurements up to 10 GPa as well as a gas cell for pressures up to 100 MPa will be provided. A gas manifold that allows the dosing of gases at a chosen volume (0.01-1 l) at pressures from 10^{-5} bars to 20 bars will be crucial to support catalysis and gas adsorption work on VESPA.

A low temperature sample changer for high-throughput measurements is planned for early operations of VESPA.

VI. CONCLUSIONS

A design study for the vibrational spectrometer VESPA for ESS is presented. The instrument exploits the WFM technique in order to cover a wide range of energy transfers, E = 0-500 meV "*in one shot*." The full spectrum is collected in a single ESS pulse, thus allowing kinetic or parametric

experiments feasible and easy to interpret. The simulation results, using an optimised elliptical neutron guide, show that VESPA will be able to provide an excellent neutron flux up to 150-190 meV (depending on the resolution setting), covering most of the so-called fingerprint region (60-220 meV), which is the crucial interval in neutron vibrational spectroscopy for the scientific community intended to be served. The four bank configuration of the secondary spectrometer provides a rather large solid angle coverage, which could be even increased with further inclusion of extra transmission banks. The instrument resolution was analytically calculated showing that VESPA will be able to outperform corresponding NVS instruments operating at present, achieving a constant relative energy resolution as low as $\Delta E/E_0 = 0.4\%$ over most of its energy transfer range. Moreover, the possibility of improving the resolution at the expenses of the count rate, or on the contrary, sacrificing the resolving power to increase the instrument flux at the sample position, is a feature that makes VESPA unique among all indirect-geometry inelastic instruments worldwide. Thanks to its high energy resolution and the significant increase in flux, VESPA will allow the study of small amounts of materials, making it possible to investigate samples in extreme environments (such as high pressure and *in situ*) and substances that are complex to be manufactured.

ACKNOWLEDGMENTS

The financial support of Elettra-Sincrotrone Trieste S.C.p.A. is gratefully acknowledged.

APPENDIX: ENERGY RESOLUTION

The performance of VESPA has been analytically evaluated with good quantitative accuracy. We follow the calculations in Ref. 8 and assume six independent parameters to contribute to the uncertainty of the measured energy transfer E. These give rise to the following equation for the variance of E:

$$\sigma_E^2 = (2E_0)^2 \left\{ \frac{1}{12}\left(\frac{\Delta_C}{L_{ToF}}\right)^2 + \frac{1}{12}\left(\frac{T_C}{t_0}\right)^2 + \left[\frac{1}{L_{ToF}} + \frac{1}{Z} + \frac{2T}{(L_S + L_D)}\right]^2 \frac{\Delta_S^2}{12} + 4\left[\frac{1}{Z} + \frac{2T}{(L_S + L_D)}\right]^2 \sigma_A^2 + \left[\frac{1}{Z} + \frac{2T}{(L_S + L_D)}\right]^2 \sigma_D^2 \right\} + \frac{E_A^2}{R_D^2}\left(\frac{R_D}{L_S + L_D}\right)^2 \frac{\delta R_D^2}{3}, \tag{A1}$$

where L_S and L_D are the horizontal (i.e., parallel to the incoming neutron beam) sample-to-analyser and analyser-to-detector distance respectively, while L_{ToF} represents the flight path from the mid-point between the pulse shaping choppers to the sample, ${\Delta_C}^2/12$ is variance of the primary path (in this case, it is mainly determined by the uncertainty of the pulse-shaping chopper blade positions, Δ_C). As for the other symbols: $T_C^2/12$ is the time variance of the primary path and corresponds to the opening time of the pulse-shaping choppers T_C; $\Delta_S^2/12$ is the variance due to the longitudinal uncertainty in the scattering point due to finite depth of the sample Δ_S; σ_{A}^2 is the variance due to the longitudinal uncertainty in the secondary path due to the penetration of the secondary neutron in the crystal analyser ($\sigma_A \approx 0.7$ mm in HOPG[8]); σ_D^2 is the variance due to the longitudinal uncertainty in the absorption position within the detector (assumed equal to the spatial detector decay constant: $\sigma_D = l_D$); $\delta R_D^2/12$ is the length variance due to the uncertainty in the height of the collision point of the secondary neutron hitting the detector, δR_D. The last contribution is determined by the combined uncertainty in the radial (along R_D) and transverse (perpendicular to R_D) directions of the collision point of the secondary neutron on the detector. However, to first order approximation, only the radial term contributes.[8]

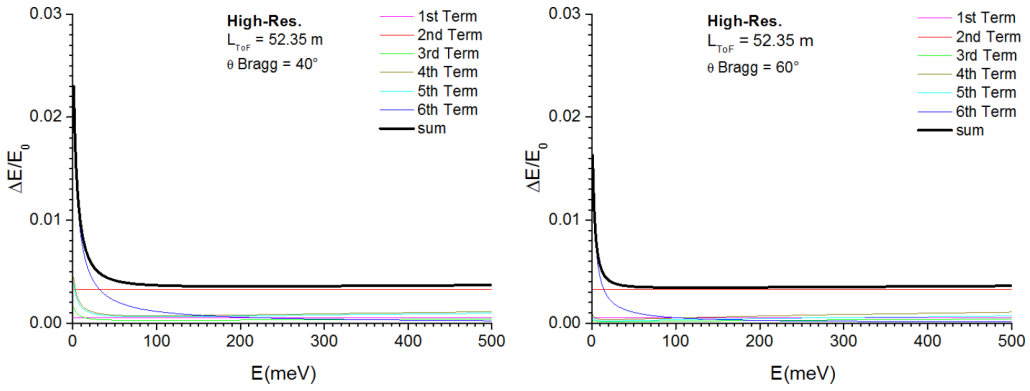

FIG. 11. Calculated relative energy resolution, $\Delta E/E_0$ (with $\Delta E = 2.354\,82\ \sigma_E$), for the two Bragg angles (namely, 40° and 60°) using the high resolution configuration and a full instrument length of 59.0 m. The different contributions have been considered statistically independent and so were summed in quadrature.

The length variable Z is defined as

$$Z = v_A t_0 \tag{A2}$$

while the dimensionless variable T is

$$T = \frac{1}{2}\frac{E_A}{E_0}\frac{1}{\tan^2(\theta_A)}, \tag{A3}$$

where θ_A is the nominal Bragg angle of the analyser, and E_A and v_A are two parameters (energy and a velocity, respectively), which are determined by the fundamental physical constants and the lattice plane spacing, d, of the analyser crystal.[8] For HOPG one finds $d = 3.355$ Å, $v_A = 589.59$ m/s, and $E_A = 1.817$ meV.

The numerical results are summarized in Fig. 11 and confirm that the resolution is largely dominated by the ToF resolution and only in the low energy range in particular also the 6th term of Equation (A1), representing uncertainties due to the detection, also effects the overall instrument resolution.

[1]M. Zoppi, A. Fedrigo, M. Celli, and D. Colognesi, EPJ Web Conf. **83**, 03021 (2015).
[2]B. Stuart, *Infrared Spectroscopy: Fundamentals and Applications* (John Wiley & Sons, Chichester, 2005).
[3]M. O. Jones *et al.*, Appl. Petrochem. Res. **2**, 97 (2012).
[4]D. P. Broom, *Hydrogen Storage Materials* (Springer Verlag, London, 2011).
[5]T. J. Bandosz, M. Seredych, E. Rodriguez-Castellon, Y. Q. Cheng, L. L. Daemen, and A. J. Ramirez-Cuesta, Carbon **96**, 856–863 (2016).
[6]B. S. Hudson, Vib. Spectrosc. **42**, 25 (2006).
[7]N. B. Colthup, L. H. Daly, and S. E. Wiberley, *Introduction to Infrared and Raman Spectroscopy* (Academic Press, San Diego, 1990).
[8]P. A. Seeger, L. L. Daemen, and J. Z. Larese, Nucl. Instrum. Methods Phys. Res., Sect. A **604**, 719–728 (2009).
[9]P. C. H. Mitchell, S. F. Parker, A. J. Ramirez-Cuesta, and J. Tomkinson, *Vibrational Spectroscopy with Neutrons, with Applications in Chemistry, Biology, Materials Science and Catalysis* (World Scientific, Singapore, 2005).
[10]G. J. Kearley and M. R. Johnson, Vib. Spectrosc. **53**, 54 (2010).
[11]See https://www.maxlab.lu.se/balder for information about the BALDER beamline.
[12]C. G. Windsor, *Pulsed Neutron Scattering* (Taylor & Francis, London, 1981).
[13]D. Colognesi, M. Celli, F. Cilloco, R. J. Newport, S. F. Parker, V. Rossi-Albertini, F. Sacchetti, J. Tomkinson, and M. Zoppi, Appl. Phys. A **74**(Suppl. 1), S64–S66 (2002).
[14]S. Ikeda and N. Watanabe, Nucl. Instrum. Methods Phys. Res. **221**, 571–576 (1984).
[15]P. G. Freeman, J. O. Birk, M. Markó, M. Bertelsen, J. Larsen, N. B. Christensen, K. Lefmann, J. Jacobsen, Ch. Niedermayer, F. Juranyi, and H. M. Ronnow, EPJ Web Conf. **83**, 03005 (2015).
[16]K. Lefmann and K. Nielsen, Neutron News **10**(3), 20–23 (1999).
[17]P. K. Willendrup, E. Farhi, and K. Lefmann, Physica B **350**, e735–e737 (2004).
[18]See http://www.mcstas.org for the McStas home page.
[19]K. H. Andersen and M. Bertelsen, Moderator Report 2014.
[20]C. Schanzer, P. Boni, U. Filges, and T. Hils, Nucl. Instrum. Methods Phys. Res., Sect. A **529**, 63 (2004).
[21]K. H. Klenø, K. Lieutenant, K. H. Andersen, and K. Lefmann, Nucl. Instrum. Methods Phys. Res., Sect. A **696**, 75–84 (2012).
[22]M. Bertelsen, H. Jacobsen, U. B. Hansen, H. H. Carlsen, and K. Lefmann, Nucl. Instrum. Methods Phys. Res., Sect. A **729**, 387–398 (2013).
[23]M. Strobl, M. Bulat, and K. Habicht, Nucl. Instrum. Methods Phys. Res., Sect. A **705**, 74–84 (2013).
[24]M. Bertelsen and K. Lefmann, "Constraining neutron guide optimizations with phase-space considerations," Nucl. Instrum. Methods Phys. Res., Sect. A (submitted).
[25]M. Bertelsen, guide_bot, the automatic guide optimizer.
[26]K. Lieutenant and F. Mezei, J. Neutron Res. **14**(2), 177 (2006).
[27]F. Mezei, C. R. - Phys. **8**(7-8), 909 (2007).
[28]K. Lefmann, K. H. Klenø, J. O. Birk, B. R. Hansen, S. L. Holm, E. Knudsen, K. Lieutenant, L. von Moos, M. Sales, P. K. Willendrup, and K. H. Andersen, Rev. Sci. Instrum. **84**, 055106 (2013).
[29]H. Schober, E. Farhi, F. Mezei, P. Allenspach, K. Andersen, P. Bentley, P. Christiansen, B. Cubitt, R. Heenan, J. Kulda, P. Langan, K. Lefmann, K. Lieutenant, M. Monkenbusch, P. Willendrup, J. Saroun, P. Tindemans, and G. Zsigmond, Nucl. Instrum. Methods Phys. Res., Sect. A **589**, 34–46 (2008).
[30]A. Van Well, Physica B **180**, 959–961 (1992).
[31]Z. A. Bowden, M. Celli, F. Cilloco, D. Colognesi, R. J. Newport, S. F. Parker, F. P. Ricci, V. Rossi-Albertini, F. Sacchetti, J. Tomkinson, and M. Zoppi, Physica B **276-278**, 98–99 (2000).
[32]T. Proffen, K. L. Page, S. E. McLain, B. Clausen, T. W. Darling, J. A. TenCate, S. Y. Lee, and E. Ustundag, Z. Kristallogr. **220**, 1002–1008 (2005).

A.10 Neutron guide shielding for the BIFROST spectrometer at ESS

Here the high energy neutron background for a modern guide was calculated using the MCNPX simulation tool. A proof of concept interface between McStas and MCNPX was used, so that thermal neutron transport was calculated by McStas and the lost neutrons were handed over to MCNPX. Such work have since been made simpler by the MCPL standard. The paper was published in the Journal of Physics: Conference Series in connection to ECNS2015.

Abstract

We report on the study of fast-neutron background for the BIFROST spectrometer at ESS. We investigate the effect of background radiation induced by the interaction of fast neutrons from the source with the material of the neutron guide and devise a reasonable fast, thermal/cold neutron shielding solution for the current guide geometry using McStas and MCNPX. We investigate the effectiveness of the steel shielding around the guide by running simulations with three different steel thicknesses. The same approach is used to study the efficiencies of the steel wall a flat cylinder pierced by the guide in the middle and the polyethylene layer. The final model presented here has a 3 cm thick steel shielding around the guide, 30 cm of polyethylene around the shielding, two 5 mm thick B_4C layers and a steel wall at position Z = 38 m, being 1 m thick and 10 m in radius. The final model finally proves that it is sufficient to bring the background level below the cosmic neutron rate, which defines an order of magnitude of the lowest obtainable background in the instruments.

My contribution

Handed over the geometry description of the final BIFROST guide. It was recreated in MCNPX and I validated the accuracy of the recreated geometry. Wrote the section of the manuscript describing McStas, guide optimizations and guide_bot. Commented on the manuscript.

Neutron guide shielding for the BIFROST spectrometer at ESS

K. Mantulnikovs[1], M. Bertelsen[1], C.P. Cooper-Jensen[2,3], K. Lefmann[1] and E.B. Klinkby[3,4]

[1] Nano-Science Center, Niels Bohr Institute, University of Copenhagen, Denmark
[2] Department of Physics and Astronomy, Uppsala University, Uppsala, Sweden
[3] European Spallation Source ESS AB, Lund, Sweden
[4] Center for Nuclear Technologies, Technical University of Denmark, Denmark

E-mail: esbe@dtu.dk

Abstract. We report on the study of fast-neutron background for the BIFROST spectrometer at ESS. We investigate the effect of background radiation induced by the interaction of fast neutrons from the source with the material of the neutron guide and devise a reasonable fast, thermal/cold neutron shielding solution for the current guide geometry using McStas and MCNPX. We investigate the effectiveness of the steel shielding around the guide by running simulations with three different steel thicknesses. The same approach is used to study the efficiencies of the steel wall a flat cylinder pierced by the guide in the middle and the polyethylene layer. The final model presented here has a 3 cm thick steel shielding around the guide, 30 cm of polyethylene around the shielding, two 5 mm thick B_4C layers and a steel wall at position Z = 38 m, being 1 m thick and 10 m in radius. The final model finally proves that it is sufficient to bring the background level below the cosmic neutron rate, which defines an order of magnitude of the lowest obtainable background in the instruments.

1. Introduction

The worlds strongest neutron source for the study of materials and biosystems will be the European Spallation Source (ESS) [1], which is presently under construction in Lund, Sweden. At ESS, neutrons will be produced by a 2 GeV protons impinging on a rotating tungsten target. The beam power will reach 5 MW resulting in unprecedented cold and thermal neutron brightness, but will also give rise to experimental backgrounds to a level beyond what is observed at existing neutron facilities [2].

Prompt neutrons escaping the target monolith have energies reaching up to the energy of the initial proton beam, and thus the task of instrument shielding is completely different compared to the case of reactor sources, based on which most shielding experience relies. At neutron energies exceeding 10 MeV, the scattering cross section of most commonly used shielding materials drops dramatically meaning that the task of instrument shielding at the ESS is even more complex than what the proton beam power dictates.

Having in mind also that ultimately the performance of most instruments mostly depends on the signal-to-noise ratio (S/N), and that shielding is expected to be a significant cost driver of the facility, the shielding design at ESS is as important as it is complex.

The present study focusses on evaluating the shielding options of the BIFROST spectrometer, which will in 2016 enter Phase 1 of its technical design at ESS. The beam optics of BIFROST is designed and optimised using the ray-tracing code McStas [3, 4, 5, 6, 7]. While McStas is well-recognised for its capability to precisely describe neutron scattering instruments in terms of signal distributions, it does lack in the description of backgrounds. To remedy this challenge an exact one-to-one implementation of the instrument is developed MCNPX [8, 9] - which is the standard Monte Carlo tool used for shielding calculations. Below we study the performance of various shielding design options considered for the BIFROST instrument. The aim of such study is to outline the shielding design prior to the instrument construction, hereby allowing to iterate the instrument and shielding design to a common optimum.

2. Methods

MCNP and MCNPX are general purpose Monte Carlo radiation transport codes that have the ability to track many particle types over a broad energy range. These capabilities include but are not limited to tracking protons and electrons. MCNP and MCNPX stands for Monte Carlo N-Particle and Monte Carlo N-Particle Extended. The extended version has been developed to simulate 34 different particle types and more than 2000 heavy ions in a broad range of energies.

McStas is a ray tracing software package for simulating neutron scattering experiments from the moderator to the detector. Such experiments can be described by a series of components, where the ray is propagated through each one without the ability to move back, which enables the code to be relatively simple, fast and modular. For this reason, McStas is well suited to exploration of possibilities, as development times are manageable, and the resulting simulations are fast enough to be used with numerical optimisers.

When designing a neutron guide system, there is a overwhelming amount of possibilities, even when only considering the geometry of the guide system. Writing McStas code for every possibility is unfeasible for a single person designing a neutron instrument, meaning that a small number of possible solutions can be investigated. The program guide_bot [10] is meant to reduce the time spent coding in these initial stages of project design, as it will write McStas guide optimisations tailored to the specific requirements of the instrument from a very limited amount of user input. The optimised guides are then automatically compared with comprehensive performance analysis for each case, making the decision making in neutron guide design more informed.

This project also makes use of the McStas-MCNPX coupling interface [11, 12], which takes advantage of the specific areas of expertise of each software package. More precisely, this coupling is used due to the fact that there are no models in MCNPX that account for reflectivity of the neutron guide – this is the area where one would need to use McStas, which is made to perform ray-tracing simulation of neutron transport in the neutron guides.

Since MCNPX and McStas are both Monte Carlo based software packages one would need significant computer power to run simulations on. In this project the cluster of the ESS Science division based in Data Management and Software Centre (DMSC) in Copenhagen is used. The cluster consists of the following components [13]:

- 42 compute nodes, each consisting of 2 processors (Intel Xeon 2.66 GHz) with 6 cores each and 48 Gb memory;
- 50 Tb of storage;
- Management network, used for maintenance;
- InfiniBand network, connecting the nodes in between each other as well as connecting them with the storage system;
- A batch-system for handling jobs.

3. Model description

The BIFROST spectrometer [14, 15] was accepted for construction in 2014 and is designed to achieve high detection efficiency in the horizontal scattering plane. Apart from the spectrometer

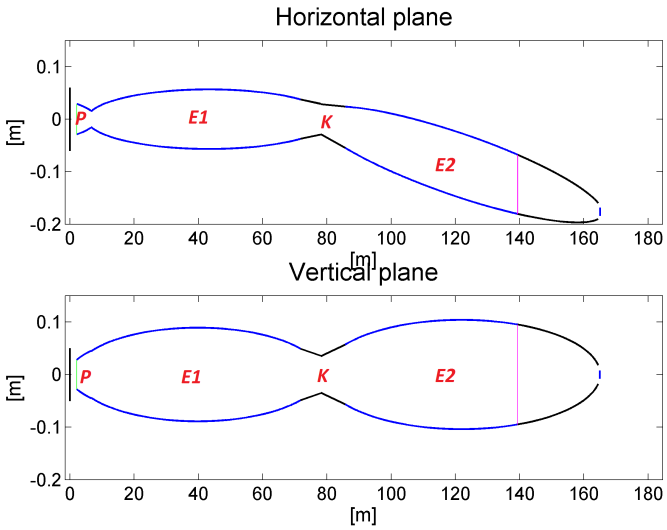

Figure 1. ZX (top) and ZY (bottom) cross sections of the BIFROST neutron guide obtained from McStas. The direction of the guide (the direction of the guide's optical axis) is along the Z axis, the X axis is represented in top image, Y axis – in the bottom one. The guide is composed out of four main sections: P – parabolic feeder, E1 and E2 – two elliptic sections that are connected by the kink – K. Parabolic and elliptic shapes are used to improve neutron intake and transport to the sample, while at the kink the guide's second elliptic section E2 is rotated out of line-of-sight (line-of-sight is broken at the magenta line) to avoid direct beam from the moderator.

itself BIFROST has a neutron guide – a tube that is used to transport cold neutrons to the sample position. The direction of the guide is along the Z axis with the Y axis pointing upwards and X to the right, forming a left-handed coordinate system. The guide, seen in figure 1 utilizes a parabolic feeder to improve neutron intake as well as to decrease the parasitic background [16]. The following neutron guide sections are shaped as a double ellipses to improve neutron transport to the sample position and the optical axis has a kink between the two ellipses to avoid line-of-sight. To take advantage of the time-of-flight measurement technique BIFROST's neutron guide is a long guide with length of 162.24 m and the sample position is situated 164.24 m away from the moderator.

The MCNPX model is based on MIRROTRON's metal-glass sandwich technology [17] with a slight alteration. The world outside the guide is represented by a box, filled with air ($\rho = 1.296 \cdot 10^{-3}$ g/cm^3), spanning $\pm$100 m in the X and Y directions and 164.41 m along Z.

The model used in this study uses the combination of the conventional shielding measures such as steel and polyethylene along with the boron carbide (B_4C) as well as has a steel wall, which mimics the steel end wall of the planned shielding bunker. The modelled wall is basically a flat disk pierced by the guide in the middle. The reasoning for placing a steel wall is that high energy neutrons can get past the initial monolith and guide shielding due to presence of windows (minima) in the cross section. Fast neutrons having energies within windows would then travel

far away from the source and increase the background locally [18]. The steel wall is expected to stop these stray neutrons close to the monolith shielding and prevent their propagation closer to the sample position. The material stack-up in the guide in XY cross section is as follows and can be seen in figure 2:

- 2 μm thick Ni/Ti coating ($\rho = 6.45$ g/cm^3), which serves as a supermirror;
- 1 cm thick substrate of variable material, serving as a structure material;
- 1, 2 or 3 cm thick stainless steel shielding ($\rho = 8.03$ g/cm^3) around the guide;
- 20, 30 or 40 cm thick polyethylene (PE) layer ($\rho = 0.97$ g/cm^3) around the guide to moderate and scatter fast neutrons;
- Two 5 mm thick B_4C layers: one, around the steel shielding (only last 10 m of the guide) and another around the polyethylene to absorb neutrons moderated by the PE layer.

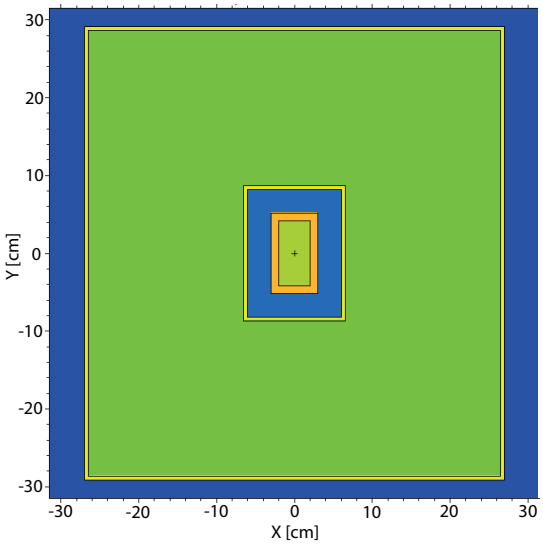

Figure 2. XY cross sections of the final model for BIFROST spectrometer's neutron guide shielding. The inner green is the guide vacuum (low pressure helium atmosphere) inside the Ni/Ti supermirror coating, which is supported by the substrate (yellow frame around the vacuum). The substrate is covered with stainless steel (cyan), serving as initial shielding. The thin yellow frame around steel is the boron carbide layer, which is present only in the last 10 m of the guide. Next layer is the PE layer – a conventional material to moderate fast neutrons and finally the same thin yellow frame of boron carbide to absorb the moderated neutrons. The outside (dark blue) is air.

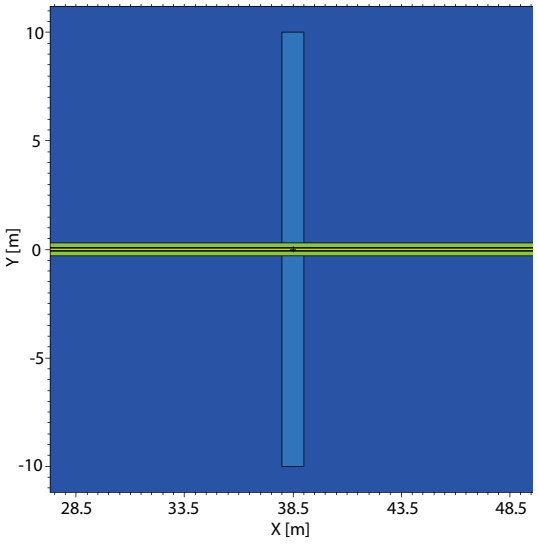

Figure 3. ZX cross sections of the final model for BIFROST spectrometer's neutron guide shielding explicitly showing the steel wall. The outside of the guide (dark blue) is air and the shield is depicted in cyan. It has a 10 m radius and 1 m thickness, being placed at position Z = 38 m.

The variable material of the guide's substrate changes depending on the position along the guide. First 20 m there is a copper substrate ($\rho = 8.96$ g/cm^3), the next 58 m the material is

aluminium ($\rho = 2.73$ g/cm^3) and then until the end of the guide – BORKRON glass ($\rho = 2.39$ g/cm^3). Note that parallel to the work described in this paper it has been shown that the sections made of copper and aluminium are going to be much shorter and the distance previously covered by copper or aluminium sections will be made out of glass. Apart from the lateral stack described above there is a stainless steel wall, seen in figure 3, with radius of 10 m and 0.5, 1 or 2 m thickness for further shielding of fast neutrons placed at position Z = 38 m. This is just before the place where the first elliptic section of the guide is the thickest, thus placing the shield here we expect neutrons to see less material with which they can interact and consequently bring the background level up.

The monolith shielding is made as a steel cylinder with wall thickness of approximately 3.3 m and is centred around the centre of the moderator, which is at Z = 15.54 cm. The choice of the wall thickness is mostly arbitrary but has the idea that even when the construction of the monolith shielding is unknown, we want to study the effect of neutrons entering the guide rather then focusing on the monolith shielding. Thus the walls have been chosen to be thick enough to stop most of the neutrons that come from the source but do not end up in the guide opening.

The MCNPX detectors are placed in two positions. First, just before the kink (Z = 71.8 m), before the guide have turned and the model is symmetric with respect to the origin, so that the data acquired at this position are easy to interpret. This detector is referred to as symmetric plane detector or SPD. Second detector which should give real information about the background, at the sample position just after the end of the guide (Z = 164.4 m). This detector is referred to as endplane detector or EPD. Both of the detectors are planes spanning ±100 m in X and Y directions and utilize the Surface Source Write (SSW) [11, 21] functionality of MCNPX, which allows to obtain energy and position, among other parameters, of every neutron crossing the detector plane.

Note that apart from the statistical error present in the simulation, there is an expected 15 % systematic error associated with nuclear interaction models and nuclear data libraries when running simulations in MCNPX, which has been shown in [1].

4. The source

The neutron source for the simulations in this work has been modelled from running a full MCNPX simulation of the ESS target and moderator [19]. Further details on model of the source in this MCNPX model can be found in [20]. Neutrons that are produced in the process of spallation in the target arrive to the moderator and are slowed down. "The focusing" effect in MCNPX that attracts statistics has been used to boost statistics while sacrificing each particle's weight. To do this a circular area with radius of 12 cm has been specified to attract statistics. The choice of such an area is dictated by the approximate size of a neutron guide entrance, thus giving a boost to statistics of neutrons that enter the guide rather than focusing on monolith shielding, modelling which lies beyond the scope of this paper as mentioned earlier. Neutrons are then tracked back to the plane of the moderator surface and data on each neutron is written into a file for further use.

The ESS source covers a broad range of energies up to 3 GeV, which would mean that to simulate all the energy ranges to the same extent a long simulation is needed. To avoid having very long and complicated simulations we decided to take out some degree of complexity by simplifying the source. The position and angular distributions are left the same, while the energy distribution is changed to a fixed energy of 1 GeV. Check runs have been performed for energies of 1 MeV, 10 MeV, 100 MeV and 1 GeV. Their comparison showed that the simplified simulations preserve the all relevant physical effects and the only difference is the intensity. The reasoning is that the fastest neutrons, although few in number, are hardest to shield. Hence shielding efficiency against this radiation is likely to be even better for the lower energy neutrons. This is in greater detail explained in [20].

Choosing one energy for the emitted neutrons means that the detectors described in the previous section would detect neutrons that have either the energy of the source – 1 GeV or lower energies. The first case can occur when the neutron does not interact with any material and does not loose energy, thus being detected as emitted. In the other case, neutrons interact with matter, for example, via a spallation, neutron capture process or generating a shower [22], which leads to energy loss of the neutron and possibly also re-emission of secondary, lower energy neutrons.

Here we need to make one very important note: only neutrons coming from the moderator are considered. We cannot and are not making any statements considering the overall background, which most definitely needs to be explored in the near future, given the fact that during the time of this study the bunker design has been developing.

5. Runs with different thicknesses of steel shielding

This section describes our study of the thickness of the guide steel shielding. The steel shielding around the guide's substrate should act as shielding and this section presents the study of variations of the thickness of the shielding. Three thicknesses have been tested: 1 cm, 2 cm and 3 cm.

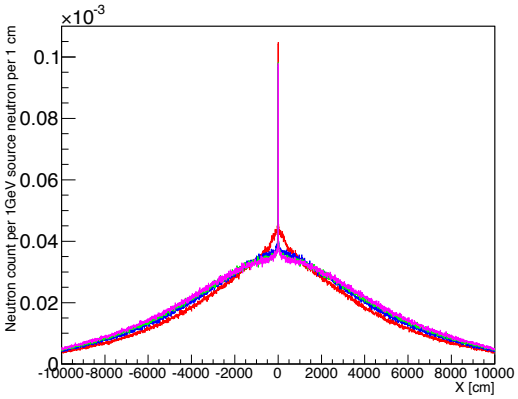

Figure 4. Neutron intensity projections on the X axis at the symmetric detector plane for three different steel shielding thicknesses around the guide. Red curve represents the run without steel shielding, blue – 1 cm of steel around the guide, green – 2 cm, magenta – 3 cm. The runs are made with 1 GeV neutron source.

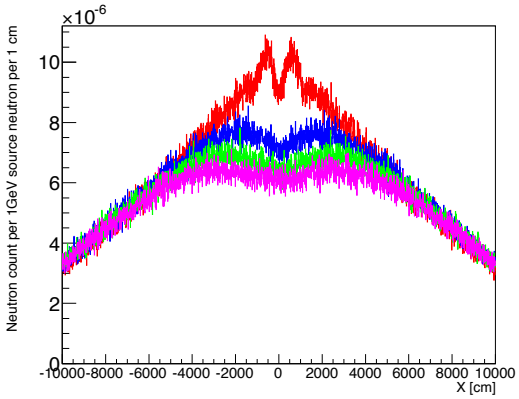

Figure 5. Neutron intensity projections on the X axis at the endplane detector for three different steel shielding thicknesses around the guide. Red curve represents the run without steel shielding, blue – 1 cm of steel around the guide, green – 2 cm, magenta – 3 cm. The runs are made with 1 GeV neutron source.

The results of these runs are presented in the form of intensity projections on the X axis and can be seen in figures 4 and 5. From the SPD plot in figure 4 one can see that the background level actually grows slightly in the region around the guide ($X < \pm 20$ m) with increasing steel thickness and gets even higher than the background solely from the substrate and coating, depicted in red. This can happen due to the presence of spallation in the model – having more material for the fast neutrons from the source to interact with also brings more secondary neutrons coming from spallation. Yet far away from the guide ($X > \pm 20$ m) the guide itself and it's close vicinity the background level falls with increasing thickness of the steel.

The background levels at the sample position (EPD) falls off with increased steel thickness. Two other very important observations are that, firstly, the background spreads in a wide range

and, secondly, the peak from the direct view of the moderator present in the SPD plot is gone at the sample position – EPD plot, which is the effect of going out of line-of-sight.

To get a better quantitative grasp of the situation at the sample position we resort to looking at the integrals under the intensity projections shown in figure 5. Since the integral values are a measure of how much the background level has dropped, this will help to compare the change in the different steel shielding thicknesses efficiencies via calculating a relative change with respect to the run with only substrate and coating, i.e. in the absence of the steel shielding whatsoever. The values are shown in table 1.

Table 1. Intensity integrals under the projection curves and relative change in integral value, calculated with respect to the model with only substrate and coating, for models with different steel thicknesses at the sample position (EPD).

Model	Integral	Relative change
Substrate+coating	0.01303±0.00004	n/a
1 cm steel	0.01213±0.00003	6.9±0.4 %
2 cm steel	0.01147±0.00003	12.0±0.4 %
3 cm steel	0.01095±0.00003	15.9±0.4 %

Judging from table 1 the increase in thickness from 1 cm to 2 cm gives almost a doubled increase in efficiency as compared to the change of solely adding a 1 cm steel shielding around the guide, going from 6.9±0.4 % to 12.0±0.4 %. Further increase of the thickness to 3 cm a slightly smaller increase of 3.9±0.6 %, suggesting that at 2 or 3 cm the effect is starting to decay slowly.

6. Runs with different steel wall thicknesses

Apart from adding a steel wall the rest of the model for these runs is unchanged and a 3 cm thick stainless steel shielding around the guide is used. Once again a simplified run with the source emitting only neutrons with energy of 1 GeV is used.

The results of the effect of the thickness of the stainless steel wall are presented as intensity projection on the X axis in figures 6 and 7. Compared to the plots in figures 4 and 5 we can clearly see that the background levels fall off in the region around the guide when the wall has been introduced into the model. Moreover there is a direct correlation with the walls thickness – the bigger the thickness, the lower the background drop.

A more quantitative representation of the date in the plots are the integrals under the curves, which are presented in table 2. From this, as well as from the plots, we can see that addition of even of a 0.5 m wall introduces a noticeable drop in background, which corresponds to 13.5±0.4 % relative change in background at sample position. Doubling the thickness to 1 m increases the relative change even more but to a smaller extent giving 19.5±0.4 %. Doubling the thickness once more to 2 m gives an increase but only by 1.3±0.6 % increasing the relative change to 20.8±0.4 %. From this we can conclude that a 1 m wall is the one that performs the most efficiently as compared to the additional price for a thicker wall.

7. Runs with different thicknesses of the polyethylene

We cover the guide with a layer of polyethylene (PE). This is a conventional material that is used for shielding purposes to moderate and scatter high energy neutrons, due to its high hydrogen content. The material that absorbs neutrons in this case is boron carbide (B_4C) in form of two 5 mm layers as mentioned above. The runs were performed with three different thicknesses of

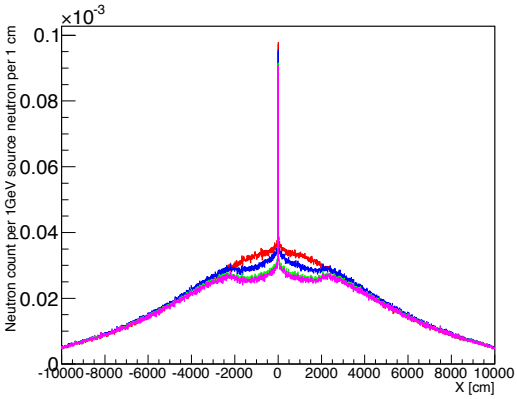

Figure 6. Neutron intensity projections on the X axis at the symmetric detector plane for three different steel wall thicknesses. 3 cm thick stainless steel shielding is used in the model. Red curve represents the run without the steel wall, blue – 0.5 m thick wall, green – 1 m thick, magenta – 2 m thick. The runs are made with 1 GeV neutron source.

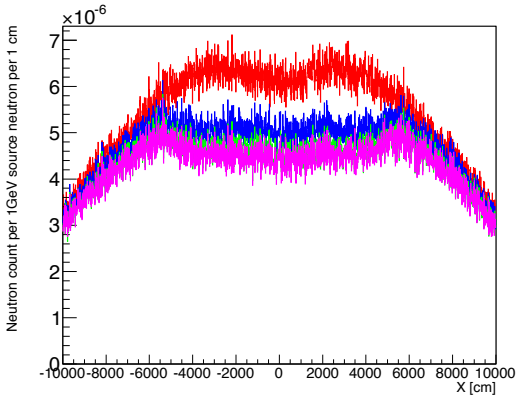

Figure 7. Neutron intensity projections on the X axis at the endplane detector for three different steel wall thicknesses. 3 cm thick stainless steel shielding is used in the model. Red curve represents the run without the steel wall, blue – 0.5 m thick wal, green – 1 m thick, magenta – 2 m thick. The runs are made with 1 GeV neutron source.

Table 2. Intensity integrals under the projection curves and relative change in integral value, calculated in respect to the model with 3 cm of steel shielding around the guide, for models with different wall thicknesses at the sample position (EPD).

Model	Integral	Relative change
3 cm steel	0.01095±0.00003	n/a
0.5 m wall	0.00948±0.00003	13.5±0.4 %
1 m wall	0.00882±0.00003	19.5±0.4 %
2 m wall	0.00867±0.00003	20.8±0.4 %

20 cm, 30 cm and 40 cm. The rest of the model is the same as described above, combining a 3 cm stainless steel shielding around and a 1 m thick, 10 m radius steel wall at position Z = 38 m. The runs are made with a simplified 1 GeV neutron source.

The results of such runs are presented in figures 8 and 9. As compared to the run of the model without any shielding, i.e. only substrate and coating, the background level has dropped significantly. Once again we see that there is a direct correlation between the thickness of the PE layer and the efficiency of the layer – the thicker the layer, the greater the efficiency at both SPD and EPD. From the plots we can also see that a 20 cm thick layer of borated PE (5 wt% B) works almost as efficient as a 20 cm thick PE layer combined with two 5 mm B_4C layers.

A more quantitative picture can be seen by looking at the integral values and relative changes of the integral values underneath the curves and this data is presented in table 3. We can see that the relative change by adding PE layer, 3 cm of shielding around the guide and a 1 m thick stainless steel wall is quite big – 75.9±0.4 %. Increasing the thickness of the PE layer by another 10 cm we get an increase of about 6.2±0.6 %. Another step in increasing the thickness by yet another 10 cm, making the PE layer 40 cm thick, gives only a minor 4.2±0.6 % increase.

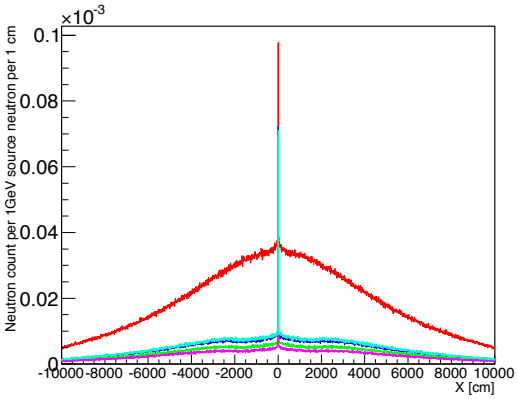

Figure 8. Neutron intensity projections on the X axis at the symmetric detector plane for three different polyethylene layer thicknesses. Red curve represents the run only with 3 cm of steel shielding around the guide, blue – with 3 cm of steel shielding around the guide, 1 m thick wall, 20 cm thick layer of polyethylene and two 5 mm thick layers of B_4C, green – the same as blue but with 30 cm thick layer of polyethylene, magenta – the same as blue but with 40 cm thick layer of polyethylene, cyan – the model which only has 20 cm thick layer of borated polyethylene (5 wt% Boron) around the guide without boron carbide layers. The runs are made with 1 GeV neutron source.

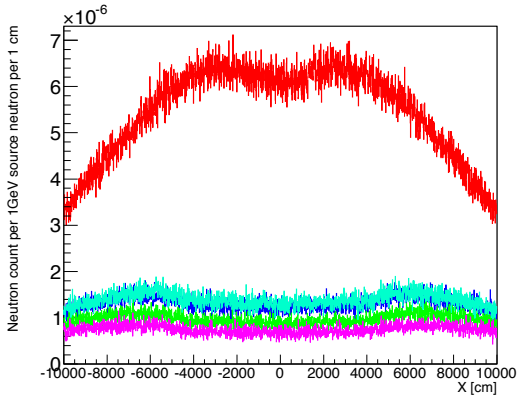

Figure 9. Neutron intensity projections on the X axis at the endplane detector for three different polyethylene layer thicknesses. Red curve represents the run only with 3 cm of steel shielding around the guide, blue – with 3 cm of steel shielding around the guide, 1 m thick wall, 20 cm thick layer of polyethylene and two 5 mm thick layers of B_4C, green – the same as blue but with 30 cm thick layer of polyethylene, magenta – the same as blue but with 40 cm thick layer of polyethylene, cyan – the model which only has 20 cm thick layer of borated polyethylene (5 wt% Boron) around the guide without boron carbide layers. The runs are made with 1 GeV neutron source.

Table 3. Intensity integrals under the projection curves and relative change in integral value, calculated in respect to the model with 3 cm of steel shielding around the guide, for models with 3 cm of steel shielding, 1 m thick steel wall, two B_4C layers and with different PE layer thicknesses at the sample position (EPD).

Model	Integral	Relative change
3 cm steel	0.01095±0.00003	n/a
20 cm PE layer	0.00264±0.00002	75.9±0.4 %
30 cm PE layer	0.00196±0.00001	82.1±0.4 %
40 cm PE layer	0.00150±0.00001	86.3±0.4 %
20 cm borated PE layer	0.00279±0.00002	74.5±0.4 %

From this we can conclude that the most reasonable thicknesses to use range between 20 cm and 30 cm. Using an expensive 20 cm borated polyethylene layer gives the same efficiency as the use of PE layer combined with two boron carbide layers, suggesting it is not the best material of choice.

For the model, described in this paper we decided to use a 20 cm, which reduces the total background level in a 1 GeV run from $(1.3\pm0.1)\cdot10^{-3}$ neutrons per cm^2 per 1 GeV source neutron

in model without the shielding to $(2.6\pm0.5)\cdot10^{-4}$ neutrons per cm^2 per 1 GeV source neutron for the model with full shielding setup as described in this section.

8. Comparison of neutron spectra at sample position.

After having investigated the effectiveness of various shielding parts and their configurations in the simplified 1 GeV runs it is very important to perform the run with a full ESS spectrum. Having obtained the data we want to compare the neutron spectra at the sample position for various setups, namely: the model with only supermirror coating and substrate, model with steel shielding around the guide, the final model with shielding around the guide, PE, B_4C and the wall and some kind of benchmark. The benchmark chosen is the cosmic neutron rate at sea level. The idea behind comparing neutron spectra at the sample position to the spectrum of the cosmic neutrons at sea level is the cosmic neutron background defines an order of magnitude of the lowest obtainable background in the instruments. This cosmic neutron spectra is roughly sketched in figure 10 with a black line and is taken from [23].

As mentioned earlier in the text, only neutrons coming from the moderator are considered and we cannot and are not making any statements considering the overall background, which most definitely needs to be explored in the near future, given the fact that during the time of this study the bunker design has been developing.

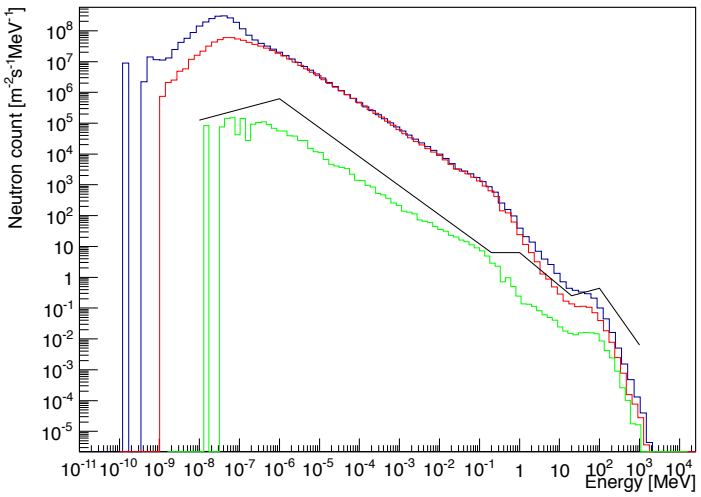

Figure 10. Neutron spectra comparison at the sample position, simulated with the full ESS neutron spectrum. Blue represents the model with only supermirror coating and substrate, red – the model with 3 cm of steel shielding around the guide, green – the final model with 3 cm of steel shielding and 20 cm PE layer around the guide, two 5 mm layers of boron carbide and the steel wall. The black line is a sketch of the cosmic neutron spectra at sea level, taken from [23].

From the plot in figure 10 we can see that the background without any shielding, just with supermirror coating and substrate (blue) is two orders of magnitude above the cosmic neutron rate, which does not satisfy requirements for detector operation. Having added 3 cm of steel shielding around the guide (red) we observe that some part of fast neutron intensities in energy range 10 – 100 MeV are cut down, which also leads to decrease in the amount of neutrons in thermal range ≈10 meV, presumably, due to the fact that there are less fast neutrons to induce secondary neutron emission.

Adding a 1 m thick, 10 m radius steel wall at position Z = 38 m to shield fast neutrons that get through the initial shielding, 20 cm thick layer of polyethylene to moderate fast neutrons and two 5 mm thick layers of boron carbide to absorb slowed down neutrons we move to the green curve. This curve goes below the black one in a broad energy range. Most important being the cold and thermal range – these are the neutrons that get scattered and detected in the experiments. More quantitatively the total background level has dropped from $(4.4\pm0.3)\cdot10^5$ $cm^{-2}s^{-1}$ to $(2.7\pm0.2)\cdot10^3$ $cm^{-2}s^{-1}$, which is a significant two orders of magnitude drop.

9. Conclusion

In this paper a shielding model against fast and thermal/cold neutrons for the 162 m long guide system of the BIFROST spectrometer at ESS has been proposed and tested using MCNPX. Only neutrons coming from the moderator have been considered. The BIFROST neutron guide is modelled using the metal-substrate sandwich technology, which has its roots in MIRROTRON's metal-glass sandwich neutron guide construction technology.

Different parts of the shielding model have been tested for their efficiency in a simplified mode with source neutrons having a fixed energy of 1 GeV, namely: three different thicknesses of steel shielding around the guide, three different thicknesses of the steel wall and three different thicknesses of polyethylene layers surrounding the steel shielding of the guide.

After the simplified runs the model with chosen thicknesses of the above mentioned parts was tested with the full ESS spectrum and the results have shown that the background level drops below the cosmic neutron rate at sea level in a broad range of energies, most importantly in the cold and thermal ranges, since neutrons of these energies are the ones being scattered by the sample and detected by the detectors.

Acknowledgements

We than Stuart Ansell for many illuminating discussions and Jonas Okkels Birk for providing the initial model of the BIFROST guide system.

References

[1] Peggs S *et al* 2013 *ESS Technical Design Report* ESS 2013-001 **10** 20
[2] Cherkashyna N, DiJulio D D, Panzner T, Rantsiou E, Filges U, Ehlers G and Bentley P M 2015 *Phys. Rev.* ST Accel. Beams **18**
[3] Webpage www.mcstas.org
[4] Lefmann K and Nielsen N 1999 *Neutron News* **10** 20
[5] Willendrup P, Farhi E and Lefmann K 2004 *Physica* B **350** 735
[6] Willendrup P K, Knudsen E B, Klinkby E B, Nielsen T, Farhi E, Filges U and Lefmann K 2014 *J. Phys.: Conf. Series* **528**
[7] Willendrup P, Farhi E, Knudsen E B, Filges U and Lefmann K 2014 *Journal of Neutron Research* **17** issue 1 pp 35 - 43
[8] Waters L S *et al* 2007 *The MCNPX Monte Carlo radiation transport code* AIP Conf.Proc. **896** pp 81-90
[9] X-5 Monte Carlo Team 1987 MCNP – A General Monte Carlo N-Particle Transport Code, Version 5, *LA-UR-03-1987*
[10] Bertelsen M 2014 *Optimizing neutron guides using the minimalist principle and guide_bot* University of Copenhagen
[11] Klinkby E B *et al* 2013 Interfacing MCNPX and McStas for simulations of neutron transport *Nuclear Instruments & Methods in Physics Research* A **700**
[12] Klinkby E B, Knudsen E B, Willendrup P K, Lauritzen B, Nobœl E, Bentley P, Filges U 2014 Application of the MCNPX-McStas interface for shielding calculations and guide design at ESS *J. Phys.: Conf. Series* **528**
[13] Webpage http://europeanspallationsource.se/cluster *DMSC*
[14] Freeman P G *et al* 2015 CAMEA ESS - The continuous angle multi-energy analysis indirect geometry spectrometer for the european spallation source *Phys. Web of Conf.* **83**
[15] Birk J O, Marko M, Freeman P G, Jacobsen J, Hansen R L, Christensen N B, Niedermayer C, Månsson M, Rønnow H M, Lefmann K 2014 Prismatic analyser concept for neutron spectrometers *Rev. Sci. Instr.* **85**

[16] Bertelsen M, Jacobsen H, Hansen U B, Carlsen H H, Lefmann K 2013 Prismatic analyzer concept for neutron spectrometers *Nuclear Instruments & Methods in Physics Research* A **85**
[17] Webpage 2006 http://www.mirrotron.hu/media/Brosh/Brosh10.pdf *MIRROTRON*
[18] Cherkashyna N *et al* 2015 *Overcoming High Energy Backgrounds at Pulsed Spallation Sources* Proceedings of ICANS XXI
[19] Batkov K, Takibayev A, Zanini L and Mezei F 2013 Unperturbed moderator brightness in pulsed neutron sources *Nuclear Instr. Meth.* A **729**
[20] Mantulnikovs K 2015 *Neutron guide shielding for the BIFROST spectrometer at ESS* University of Copenhagen
[21] Knudsen E B, Klinkby E B and Willendrup P K 2014 McStas event logger: Definition and applications *Nuclear Instruments and Methods in Physics Research* Section A: Accelerators, Spectrometers, Detectors and Associated Equipment **738** pp 20 - 24
[22] Cherkashyna N *et al* 2014 High energy particle background at neutron spallation sources and possible solutions *J. Phys.: Conf. Series* **528**
[23] Hagmann C, Lange D and Wright D 2012 Monte carlo simulation of proton-induced cosmic-ray cascades in the atmosphere *Lawrence Livermore National Laboratory*

A.11 An optional focusing SELENE extension to conventional neutron guides: A case study for the ESS instrument BIFROST

This paper investigates the feasibility of using a Selene guide as a an optional focusing device at the end of a more traditional ballistic guide. As the Selene guide images the source to sample, problems could have manifested when using the less clean phase-space provided by a ballistic guide. One advantage of this solution is the possibility of using Selene focusing for a long instrument and long wavelengths, which is not usually an option due to the high impact from gravity on long Selene guides. The paper was published in Nuclear Instruments and Methods in Physics Research Section A.

Abstract

The high brilliance at the European Spallation Source (ESS) will allow for performing experiments with much smaller samples than at present neutron facilities and in much more complex sample environments. However the higher flux also results in higher background from unwanted neutrons not originating from scattering of the sample. We here present a new design idea for beam delivery, where a 165 m ballistic guide system with good transport properties is followed by a 4-8 m SELENE guide system similar to Montel optics used for X-ray optics. We have investigated the system by detailed Monte-Carlo simulations using McStas. We show that under certain conditions, this set-up works surprisingly well, with a brilliance transfer of 20-60% for neutrons of wavelength 4 Å and above. We demonstrate that the guide system is able to focus the beam almost perfectly onto samples sizes in the range of 0.1-2 mm. We furthermore show that our SELENE system is insensitive to gravity and to realistic values of guide waviness. We argue that this guide system can be useful as an optional guide insert when small samples are used in the vicinity of bulky sample environment, e.g. for high-field or high-pressure experiments.

My contribution

Participated in some discussion on the topic, but did not contribute to the simulation effort. Provided the software for drawing guide systems. Commented on the manuscript.

Nuclear Instruments and Methods in Physics Research A 852 (2017) 46–56

Contents lists available at ScienceDirect

Nuclear Instruments and Methods in Physics Research A

journal homepage: www.elsevier.com/locate/nima

An optional focusing SELENE extension to conventional neutron guides: A case study for the ESS instrument BIFROST

U.B. Hansen[a,*], M. Bertelsen[a], J. Stahn[b], K. Lefmann[a]

[a] Niels Bohr Institute, University of Copenhagen, Universitetsparken 5, DK-2100 Copenhagen, Denmark
[b] Laboratory for Neutron Scattering and Imaging, Paul Scherrer Institut, CH-5232 Villigen PSI, Switzerland

ARTICLE INFO

Keywords:
Neutron guides
Focusing guides
Monte Carlo simulations
European Spallation Source
Montel Optics

ABSTRACT

The high brilliance at the European Spallation Source (ESS) will allow for performing experiments with much smaller samples than at present neutron facilities and in much more complex sample environments. However the higher flux also results in higher background from unwanted neutrons not originating from scattering of the sample. We here present a new design idea for beam delivery, where a 165 m ballistic guide system with good transport properties is followed by a 4–8 m SELENE guide system similar to Montel optics used for X-ray optics. We have investigated the system by detailed Monte-Carlo simulations using McStas. We show that under certain conditions, this set-up works surprisingly well, with a brilliance transfer of 20–60% for neutrons of wavelength 4 Å and above. We demonstrate that the guide system is able to focus the beam almost perfectly onto samples sizes in the range of 0.1–2 mm. We furthermore show that our SELENE system is insensitive to gravity and to realistic values of guide waviness. We argue that this guide system can be useful as an optional guide insert when small samples are used in the vicinity of bulky sample environment, e.g. for high-field or high-pressure experiments.

1. Introduction

The European Spallation Source (ESS), currently under construction in Lund, Sweden, is expected to have several instruments with neutron guide lengths up to 165 m due to its long pulsed time structure [1–3]. In addition, there is an increased interest in complicated sample environments where it is possible to perform experiments under high pressures, high or low temperatures and large magnetic fields on smaller samples. The combination of these requirements points towards the need for specially designed neutron optics.

Ballistic and elliptic neutron guides were first proposed by Mezei [4] and Schanzer et al. [5] as a way of effectively transporting neutrons over long distances, since the number of reflections within the guide is significantly reduced compared to a straight guide. Simulations have shown that such guides are able to transport the majority of the low-divergent cold/thermal neutrons [6] and also the first physical realisations of such elliptical guides have proven to be of great benefit [7,8]. However these ballistic guides as well as straight guides have the downside that the neutron phase space (area and solid angle) delivered at the sample position often is much larger than required for the experiment, since the guides are designed for the largest needed phase-space and cannot be adjusted to fit the specific requirements of the experiment. This will lead to an increase in the background signal arising from neutrons scattering from the sample environment. The sample illumination will for these guides be controlled by slits 20–50 cm before the sample, which implies that the illuminated sample space is often ≈10 mm larger on each side than needed – depending on the beam divergence. Hence, many of the unwanted neutrons still have a high risk of ending up on the detector as background.

More recently the use of Montel mirrors has gained attention as neutron focusing optics. The Montel mirrors are widely used in the x-ray community as focusing optics and are constructed of two half ellipses arranged perpendicular to each other [9]. The SELENE guide concept [10] has two Montel mirrors in succession, mirrored with respect to each other, in order to correct for the coma aberrations that are intrinsic to the elliptic mirrors due to the extended source size in neutron facilities compared to synchrotrons [11]. With this setup it is possible to tailor the phase space at the sample position already in the beginning of the guide and at the same time to avoid line of sight to the moderator, resulting in an excellent signal-to-noise ratio. This guide setup can be used over the whole instrument length as described by Weischelbaumer et al. [12] and will be used in the reflectometer ESTIA, which will be 40 m long and is accepted for construction at ESS [13], and in a MIEZE type spin echo instrument with a total length of 45 m proposed for the ESS [14].

* Corresponding author.
E-mail address: uhansen@nbi.ku.dk (U.B. Hansen).

http://dx.doi.org/10.1016/j.nima.2017.01.075
Received 24 November 2016; Received in revised form 26 January 2017; Accepted 31 January 2017
Available online 03 February 2017

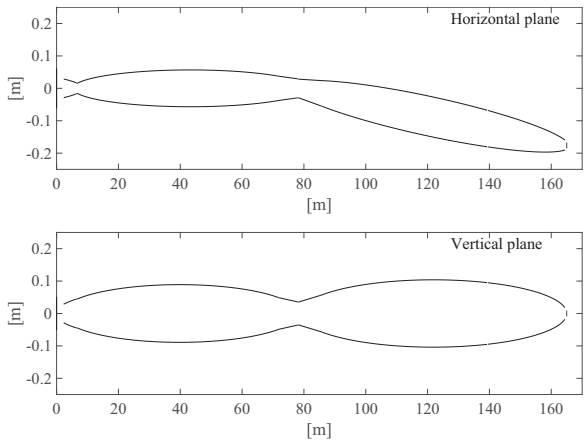

Fig. 1. A sketch of the BIFROST guide design [16]. The upper panel shows the horizontal plane and the lower panel the vertical plane.

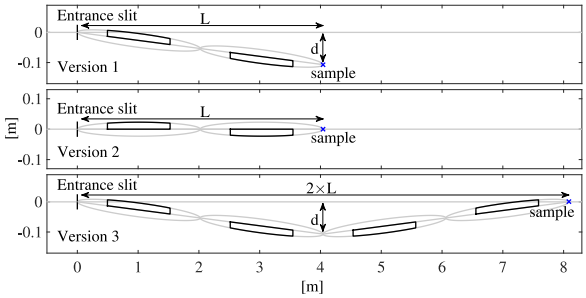

Fig. 2. The three versions of the focusing SELENE guide system. Here the vertical and horizontal planes are the same. The upper panel shows version 1 where the two Montel mirrors are inclined with respect to the incoming beam, the middle panel shows version 2 without the inclination and the lower panel shows version 3 with four Montel mirrors. Note that only the parts of the ellipses shown in black are constructed.

One of the instruments selected for construction at the ESS is the 165 m long BIFROST spectrometer optimised for extreme environment studies using cold neutrons with a wavelength ≥2 Å. Here we have investigated the different possibilities of adding a SELENE focusing guide section to the end of the guide system designed for the BIFROST instrument, hence profiting both from the good neutron transport over the long distances and the low background of the SELENE guide system. The present work is however not part of the accepted BIFROST proposal, but should be seen as a possible add-on, which also could be implemented on other long neutron guide systems.

The concept of adding a small SELENE guide section as a focusing device has in fact already been realised as an add-on to the reflectometer Amor at the Paul Scherrer Institut [15].

2. BIFROST guide and simulations

The preliminary design of the BIFROST guide is described in the BIFROST instrument proposal for the ESS [16,17] and consists of a parabolic guide feeder [18] followed by two elliptic guides in succession with a kink in-between the two to avoid direct line of sight through the guide to the moderator, as shown in Fig. 1. This results in a rather compact phase space close to the focal point of the second ellipse; a good starting point for further optics. We will not try to optimise the BIFROST guide for the combination with the SELENE guide element, but simply add a SELENE guide section to the already simulated BIFROST guide.

The simulations were made using the program McStas v2.0 [19,20]. All simulations were made using a simple 0.12×0.12 m^2 moderator with an equal distribution of wavelengths, so the direct intensity cannot be compared to the expected intensity at the ESS. However, since we use the brilliance transfer (BT) to quantify the performance of the guides, the actual intensity is not relevant. The brilliance or phase space density Ψ is the number of neutrons per unit time, area, solid angle and wavelength interval. The brilliance transfer is then [6]:

$$BT = \frac{\Psi_{SAMPLE}}{\Psi_{ENTRY}}. \quad (1)$$

This quantity can never exceed unity according to Liouville's theorem [21].

3. The SELENE guide

The SELENE guide system consists of two half elliptic guide elements (two Montel mirrors). A virtual source positioned at the first focal point will be imaged at the second focal point by the first mirror, but due to coma aberrations this image will be blurred [11]. In order to correct this, a second mirror identical to the first but reflecting in the opposite transverse direction is placed after the first mirror. This largely corrects for the coma effect and the image at the last focal point will to a great extent be the same as the virtual source [11].

The point-to-point focusing has some key advantages: all unwanted neutrons are filtered away in the beginning of the guide system and moreover it is possible to define exactly the properties of the phase space at the sample position, which greatly reduces the background.

Ideally, the axis of the SELENE guide is inclined with respect to the incoming beam of neutrons. After the SELENE guide, the neutron beam will be parallel to the incoming beam but displaced by the distance d. If the SELENE guide system is not inclined the guide system will use incoming divergence far off-centre where the beam normally is weaker and the neutrons exiting the SELENE guide will be inclined with respect to the axis of the instrument, but the sample position will not be displaced. Another way of circumventing the

Table 1
Parameters for different SELENE guide layouts, where a and b are the major and minor axes of the elliptic guide, respectively, ξ is the fraction of the ellipse that constitutes the guide, m describes the coating of the elliptic guides, L is the length of versions 1 and 2, $2 \times L$ is the length of version 3 and d is the displacement with respect to the incoming beam for version 1, as shown in Fig. 2.

Parameter set number	a (m)	b (m)	b/a	ξ	m	L (m)	$2 \times L$ (m)	d (m)
I	1.011	0.023	0.0224	0.51	5	4.0	8.1	0.10
II	2.022	0.045	0.0224	0.51	5	8.1	16.2	0.21
III	2.066	0.023	0.0113	0.76	5	8.3	16.5	0.14
IV	4.133	0.047	0.0113	0.76	5	16.5	33.1	0.29

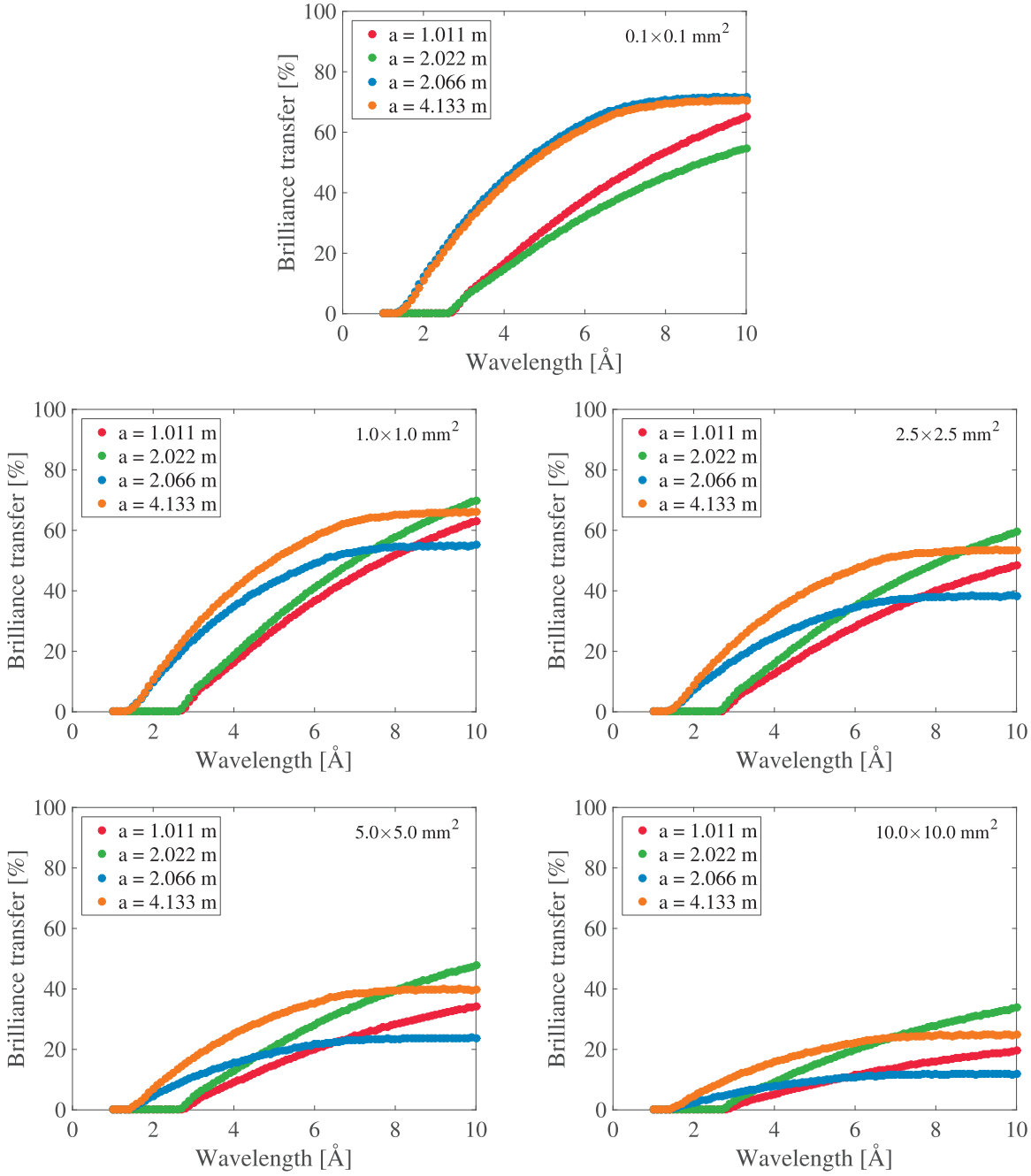

Fig. 3. The brilliance transfer vs. wavelength for versions 1 and 2, for different values of the major axis *a* as given in the legend, corresponding to the different parameter choices listed in Table 1. Aperture sizes 0.1 × 0.1 mm^2, 1×1 mm^2, 2.5 × 2.5 mm^2, 5 × 5 mm^2 and 10×10 mm^2.

displacement problem is to build two times the SELENE guide system (four Montel mirrors), which will bring the sample back on the axis of the incoming beam. These three ways of implementing the SELENE guide system can be seen in Fig. 2 and are in the following denoted versions 1, 2 and 3, respectively.

The BIFROST spectrometer is defined to work in the wavelength range of 1.65–6.40 Å. The guide is designed so that it has a horizontal divergence of 1.5° and a vertical divergence of 2° at the sample position.

In this study we have simplified these requirements to a wavelength range of 2–7 Å and a divergence of 1.5° in both the vertical and horizontal directions. We have chosen 4 different sets of guide parameters for the SELENE guide section, listed in Table 1, that delivers the appropriate divergence and wavelength range at the sample position, while still having at least 0.5 m between the end of the guide and the sample position to allow for bulky sample environment.

First we have simulated only the SELENE guide section in order to evaluate the performance of each of them before combining them with the BIFROST guide. Each of the three versions of the SELENE guide shown in Fig. 2 has been simulated with the 4 different sets of guide

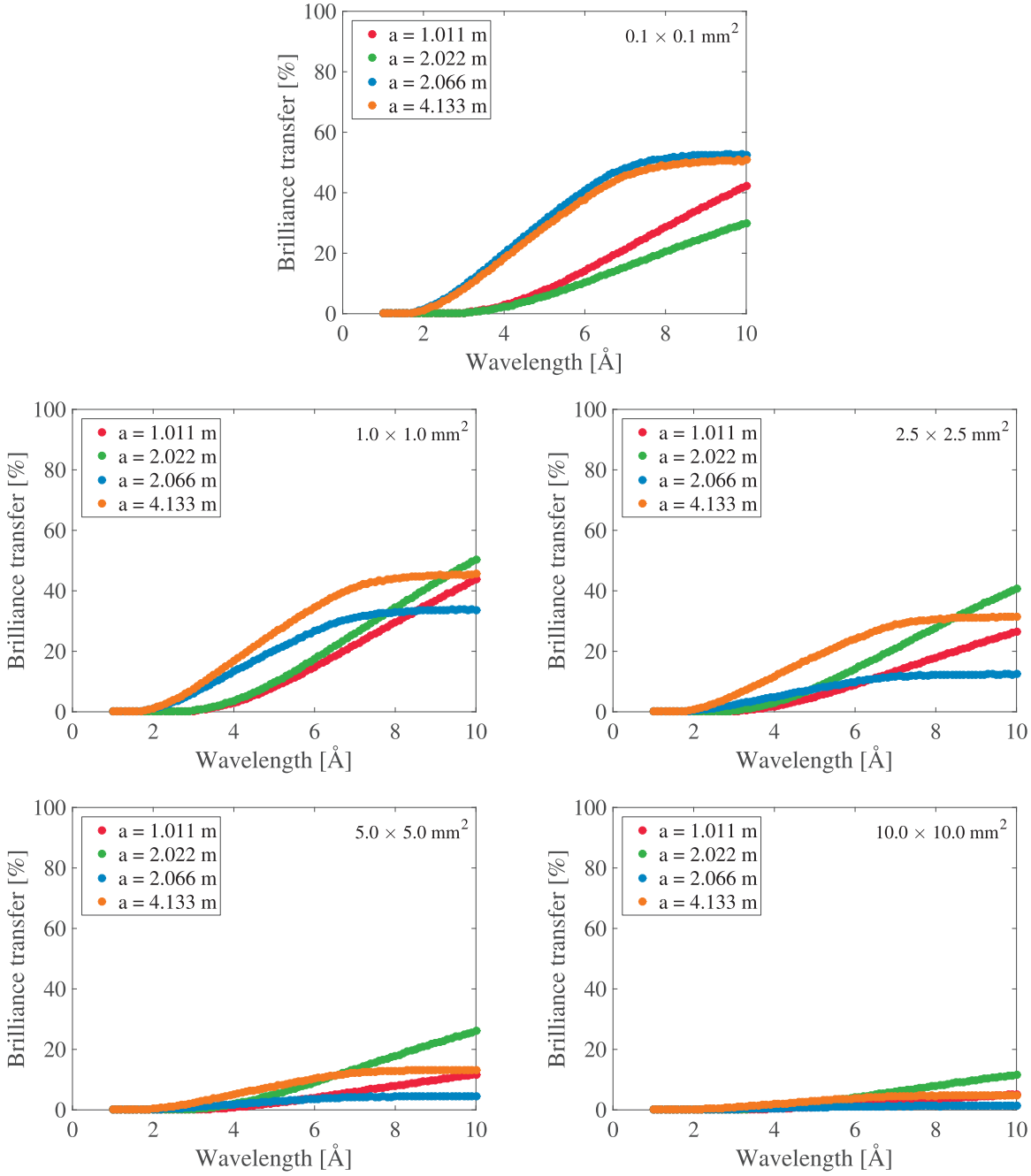

Fig. 4. The brilliance transfer vs. wavelength for version 3 and for different values of the major axis a as given in the legend, corresponding to the different parameter choices listed in Table 1. Aperture sizes 0.1 × 0.1 mm^2, 1×1 mm^2, 2.5 × 2.5 mm^2, 5×5 mm^2 and 10×10 mm^2.

parameters listed in Table 1 for different aperture sizes. Fig. 3 shows the brilliance transfer of version 1 and version 2 as the brilliance transfer is the same for the two guides. As the number of reflections in version 3 is doubled the brilliance transfer is correspondingly lower than the other two layouts, which is shown in Fig. 4.

Depending on the aperture size, different guide parameters will give the optimal sample illumination. A longer guide will in general be better suited for larger aperture sizes compared to a shorter guide with the same b/a-ratio. In this case we are interested in sample sizes around 1×1 mm^2 and a high brilliance transfer at low wavelengths while trying to keep the SELENE section short and limit the m-value for cost reasons. This leads us to focus on the parameter sets I and III with major axis a=1.011 m and a=2.066 m, respectively, listed in Table 1. In Fig. 5 the spatial illumination and divergence at the sample position is shown for these two realisations of version 1. We see that the neutron beam properties to a large extent matches the desired illumination of the sample, both in terms of area and divergence. The point-to-point focusing also allows us to define more advanced aperture shapes than a simple square. As an illustration, in Fig. 6 the aperture opening is shaped as a five pointed star with a radius of

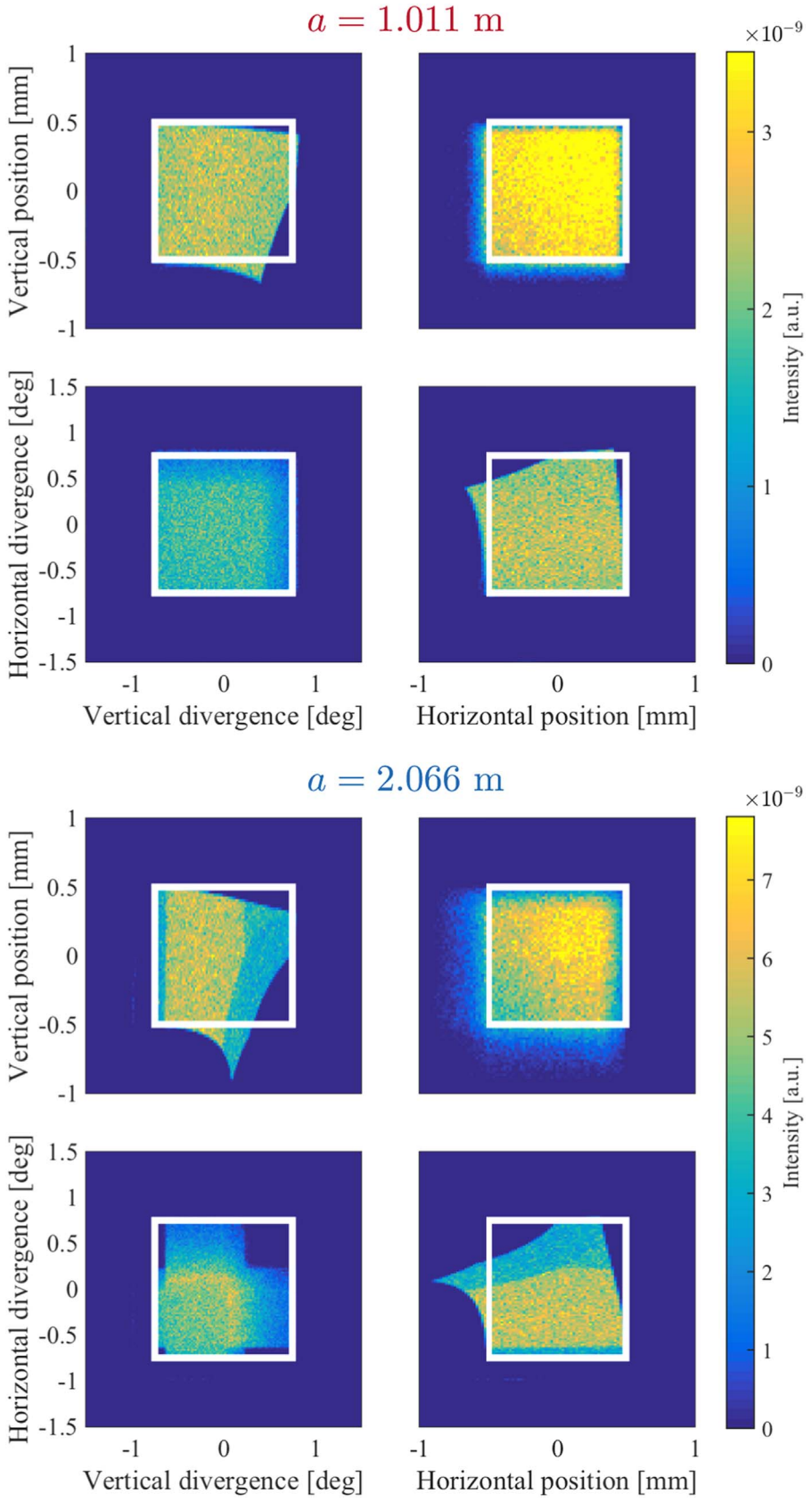

Fig. 5. Simulated acceptance diagrams measured at the sample position. (Top four) The SELENE guide with a=1.011 m. (Bottom four) The SELENE guide with a=2.066 m. The intensity is integrated over a wavelength band of 1–7 Å. Aperture size: 1×1 mm^2 and intended divergence: $\Delta\theta = \pm 0.75° \times \pm 0.75°$. The white box indicates the desired illuminated phase space.

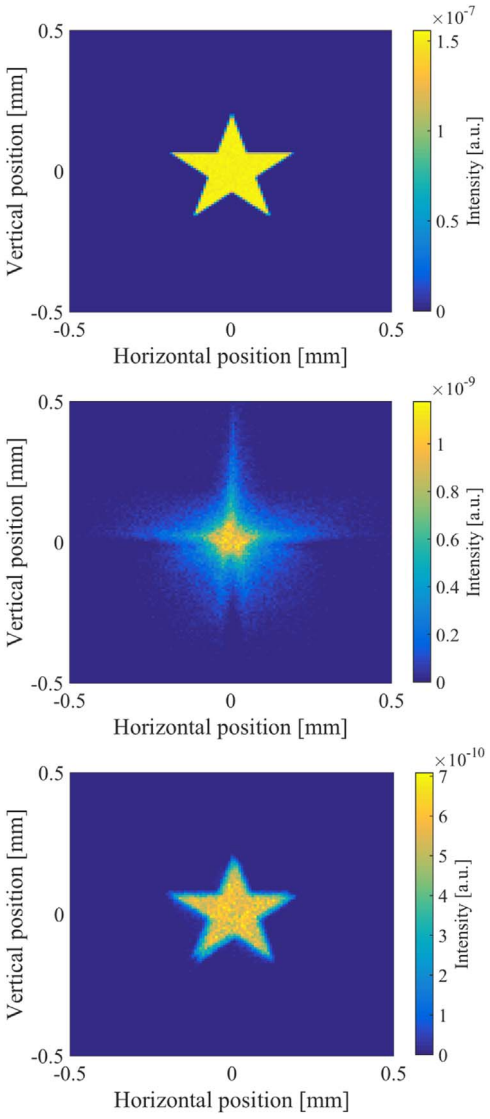

Fig. 6. The spatial illumination just after the five-pointed-star aperture (top panel), at the second focal point in-between the two guides (middle panel) and at the sample position (lower panel).

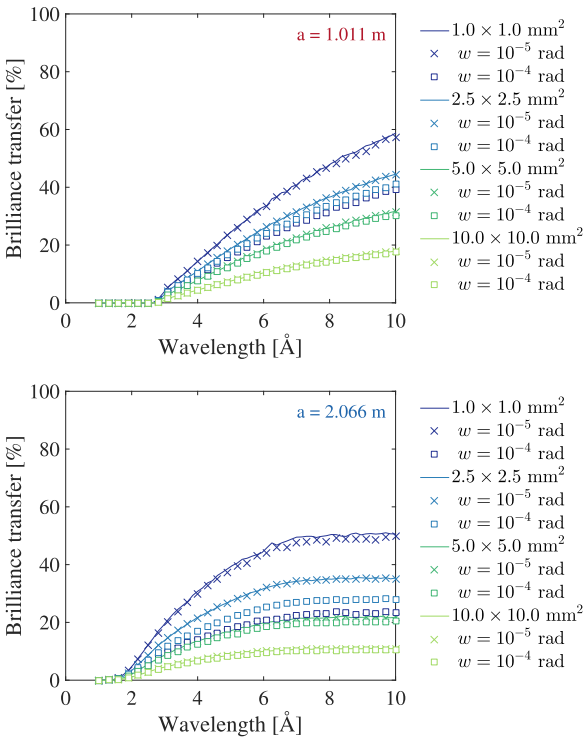

Fig. 8. The brilliance transfer vs. wavelength for different aperture sizes and waviness values as given in the legend. The solid lines correspond to the ideal case without waviness. (Upper panel) The combined BIFROST+SELENE setup with a=1.011 m. (Lower panel) The combined BIFROST+SELENE setup with a=2.066 m.

200 μm and the corresponding sample illumination is then also shaped like a star of the same size. We notice that the edges of the star at the sample position are slightly blurred which is of the order of 10 μm.

4. Performance of the combined guide

For the two parameter combinations I and III in Table 1, we have simulated the combined setup of the BIFROST guide and a SELENE guide element (version 1). The sample illumination is controlled by an aperture positioned right after the BIFROST guide and this constitutes the first focal point of the SELENE ellipses. In Fig. 7 we show the brilliance transfer as a function of wavelength both with and without gravity for the a=1.011 m and a=2.066 m versions of the SELENE guide. In neither of the two setups does gravity have a significant effect,

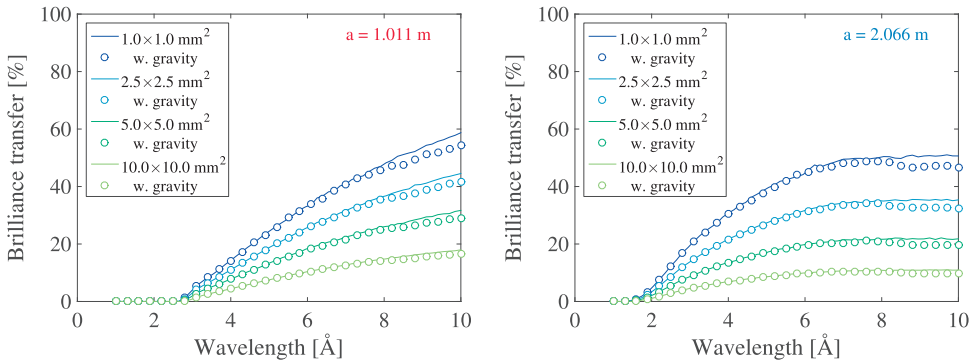

Fig. 7. The brilliance transfer vs. wavelength with (○) and without (–) gravity for different aperture sizes as given in the legend. (Left) The combined BIFROST+SELENE setup with a=1.011 m. (Right) The combined BIFROST+SELENE setup with a=2.066 m.

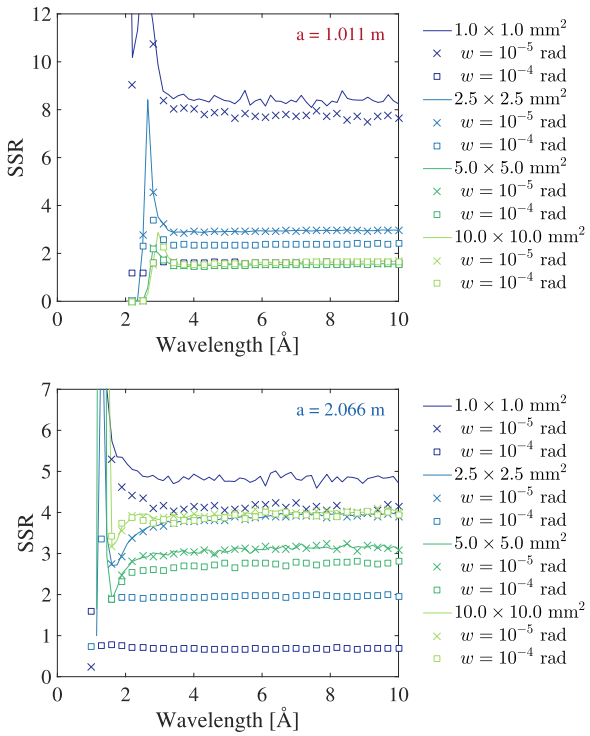

Fig. 9. The Sample-beam to Surrounding-beam Ratio (SSR) vs. wavelength for different aperture sizes and waviness values as given in the legend. The solid lines correspond to the ideal case without waviness. (Upper panel) The combined BIFROST+SELENE setup with a=1.011 m. (Lower panel) The combined BIFROST+SELENE setup with a=2.066 m.

Table 2
The aperture openings for the different sample sizes. The distance between the aperture and the sample was in all cases 0.2 m.

Sample size (mm^2)	Aperture opening (mm^2)
1.0 × 1.0	6.3 × 6.3
2.5 × 2.5	7.8 × 7.8
5.0 × 5.0	10.3 × 10.3
10.0 × 10.0	15.3 × 15.3

except to reduce the brilliance transfer slightly for wavelengths above 8 Å, as seen in Fig. 7.

The effect of waviness has been investigated by using an elliptical guide component with a realistic waviness model [22]. The waviness w is given in terms of the standard deviation of the waviness distribution. The waviness values in the guides for the ESS are expected to be of the order 10^{-4} to 10^{-5} rad [23]. Not surprisingly the waviness primarily affects small samples. This is reflected in the brilliance transfer shown in Fig. 8. The worst effect is seen for small samples, 1 × 1 mm^2, where a divergence of 10^{-4} radians results in brilliance loss of between 1/3 and 1/2 relative to the ideal guide mirrors without waviness. Interestingly, a waviness of 10^{-5} rad does not seem to affect the guide performance, meaning that the SELENE focusing option will need relatively good, but not unrealistic, mirror quality.

The Sample-beam to Surrounding-beam Ratio (SSR), defined as ratio of the integrated intensity on the sample to the intensity of the neutrons transported through the guide but not hitting the sample, is shown in Fig. 9. Note that this definition is different from the one of Weichselbaumer et al. [12] where the signal-to-noise ratio is defined with respect to the total transported intensity. The Sample-beam to Surrounding-beam Ratio is especially good for the 1×1 mm^2 samples, 8.3 for the a=1.011 m guide and 4.8 for the a=2.066 m guide without waviness, as shown in Fig. 9, corresponding to that, respectively, 89.2% and 82.8% of the neutrons will hit the sample. For larger samples, the results are not quite as good, for the 5×5 mm^2 sample the Sample-beam to Surrounding-beam Ratio has fallen to 1.6 and 3.1, again for the a=1.011 m and a=2.066 m guide, respectively. This can be attributed to coma aberrations. On the other hand, the waviness will again affect the smaller samples more severely, but as before we see that a waviness of 10^{-5} rad should be sufficient, since the SSR for the 1×1 mm^2 is only reduced from 4.8 to 4.1 for the a=2.066 m guide.

We notice however that in any case the BT is lower than 30% at 4 Å, so this type of guide should be used only when necessary.

5. Comparison to the BIFROST guide

We now wish to compare the performance of the BIFROST guide to the combination of the BIFROST guide and the SELENE focusing element. When using only the BIFROST guide the sample illumination will be controlled by an aperture placed 0.2 m prior to the sample. The aperture settings were found by calculating the optimal aperture opening for the given divergence of $\Delta\theta = 1.5°$ for each sample size and the optimal settings are listed in Table 2.

In Fig. 10 we compare the phase space of the combined BIFROST +SELENE setup with the BIFROST guide for a 1×1 mm^2 sample. It is apparent how the SELENE guide segment reduces the background at the sample position, since even with an aperture before the sample the transported phase space of the BIFROST guide is much larger than desired at the sample position.

The brilliance transfer, shown in Fig. 11, does however show the

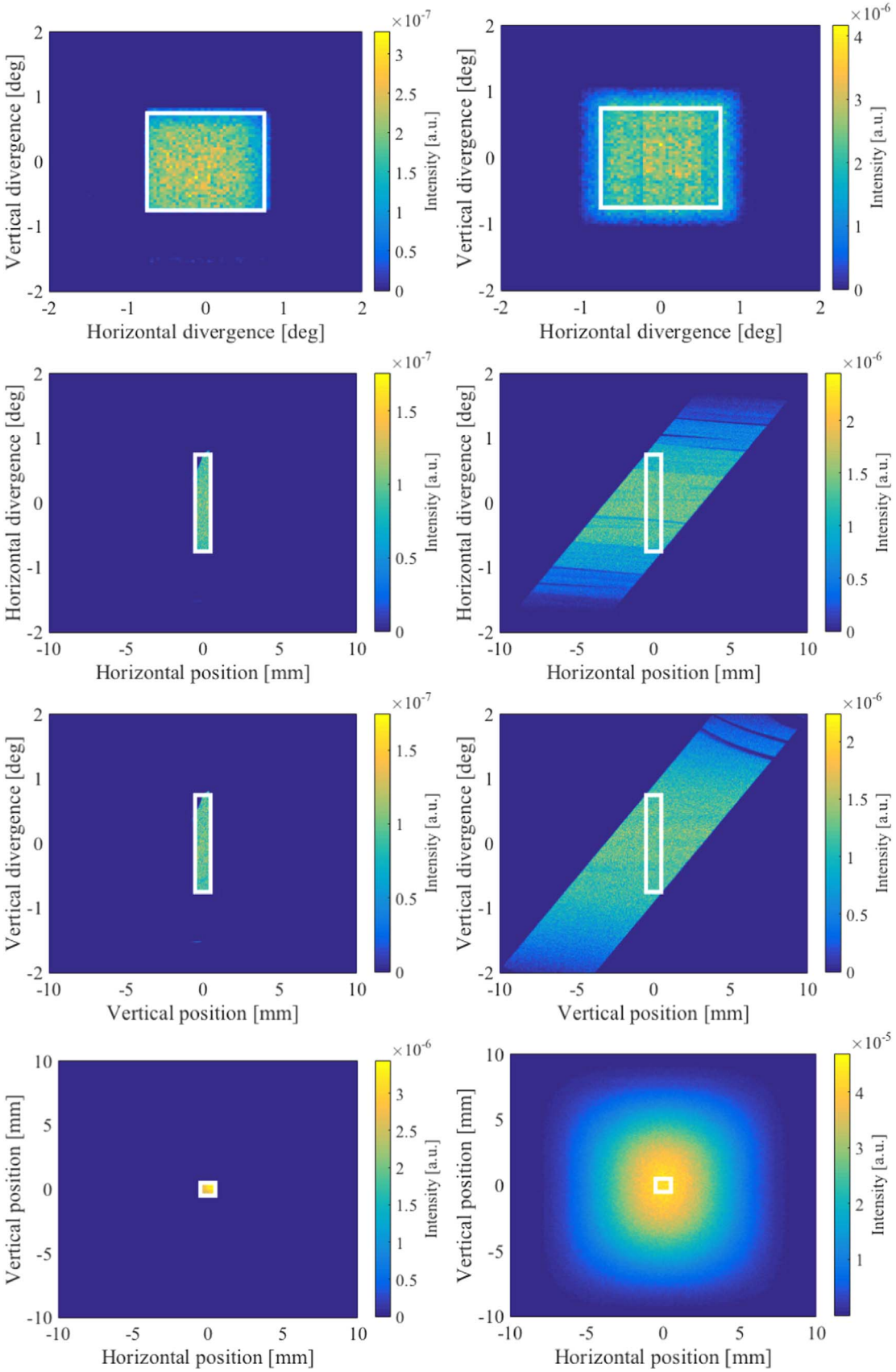

Fig. 10. (Left) The combined BIFROST+SELENE setup with a=1.011 m. (Right) The BIFROST guide. The intensity is integrated over a wavelength band of 1–7 Å. The aperture size for the combined BIFROST+SELENE setup is 1×1 mm^2 while it for the BIFROST guide is 6.3 × 6.3 mm^2 as given in Table 2. The white box indicates the desired illuminated phase space.

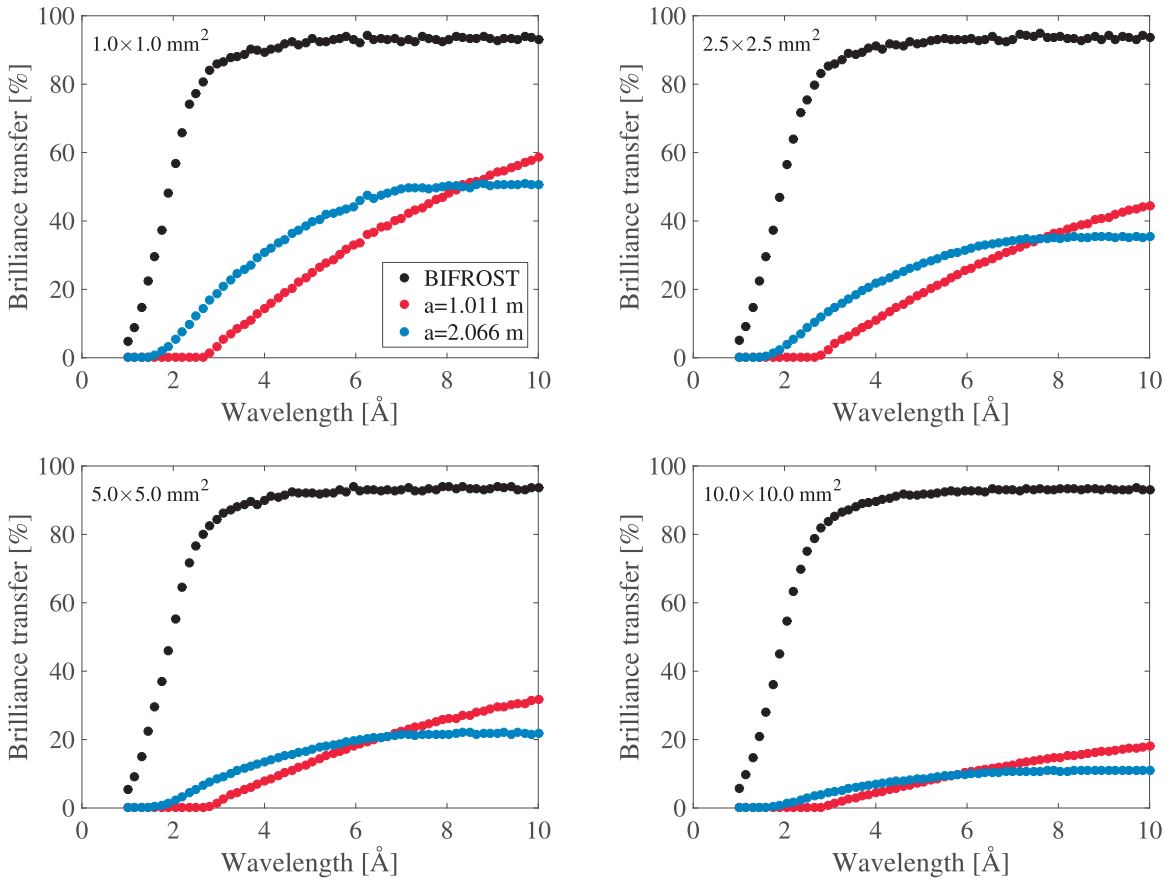

Fig. 11. The brilliance transfer vs. wavelength for different sample sizes 1×1 mm^2, 2.5 × 2.5 mm^2, 5×5 mm^2 and 10×10 mm^2 for the BIFROST guide shown in Fig. 1, the combined instrument with a=1.011 m and the combined instrument with a=2.066 m. The aperture settings of the BIFROST guide are listed in Table 2.

strength of the BIFROST guide since even at 165 m it is capable of transporting the majority of the neutrons with a wavelength above 2 Å all the way to the sample. This cannot be achieved when using the SELENE extension, where the highest brilliance transfer value at 4 Å is 30%.

The high background of the BIFROST guide seen in Fig. 10 does nevertheless mean that the advantage of using the SELENE extension becomes clear when comparing the SSR, as shown in Fig. 12. For small sample sizes the SSR is several hundred times better than compared to the BIFROST guide. A more extensive analysis of a guide very close to the BIFROST guide arrives at similar values for the SSR [24].

6. Discussion and conclusion

We have shown that a short SELENE guide can be used as a focusing extension to a ballistic type guide, e.g. the one for the BIFROST instrument, with a reasonable brilliance transfer for wavelengths above 3–4 Å. It is possible to tailor the beam spot to exactly the need of the experiment with an extremely low background. This implies that in general experiments on small samples in a complex sample environment such as pressure cells or magnets could benefit immensely from a combination of a ballistic guide and a SELENE guide section. We here like to remark that in the simulations, the sample is positioned with absolute accuracy. In actual experiments, the sample is likely to move with some uncertainty, e.g. when the sample rotates in the beam at the end of a sample stick. To employ the focusing scheme presented here, these types of positioning uncertainty need to be addressed.

The brilliance transfer of the combined instrument is nevertheless significantly lower than the BIFROST guide on its own in particular for sample sizes larger than 2.5 × 2.5 mm^2 as seen in Fig. 11. The Sample-beam to Surrounding-beam Ratio (SSR) does however make up for this, in the cases where the background becomes the limiting factor. The combined guide has for the small samples several hundred times better SSR than the BIFROST guide, as shown in Fig. 12. The brilliance transfer is in the low wavelength region best for the SELENE guide version with its major axis a=2.066 m and it also has a better Sample-beam to Surrounding-beam in all cases except for the 1×1 mm^2 sample.

Due to the loss in brilliance transfer, a factor 3.3 at 4 Å – and hence flux on sample – we do not imagine that a permanent installation of the SELENE focusing system would be a viable solution for the BIFROST instrument. Instead, a realistic implementation of the SELENE add-on-guide could in practice be via a two-guide solution, where the full elliptic guide used in these simulations would be replaced by a straight-parabolic guide [6], where the straight part could in effect be shortened when the SELENE setup is in use, as sketched in Fig. 13.

Acknowledgements

This project has been funded by the University of Copenhagen 2016 program through the project CoNeXT. We also thank the Danish

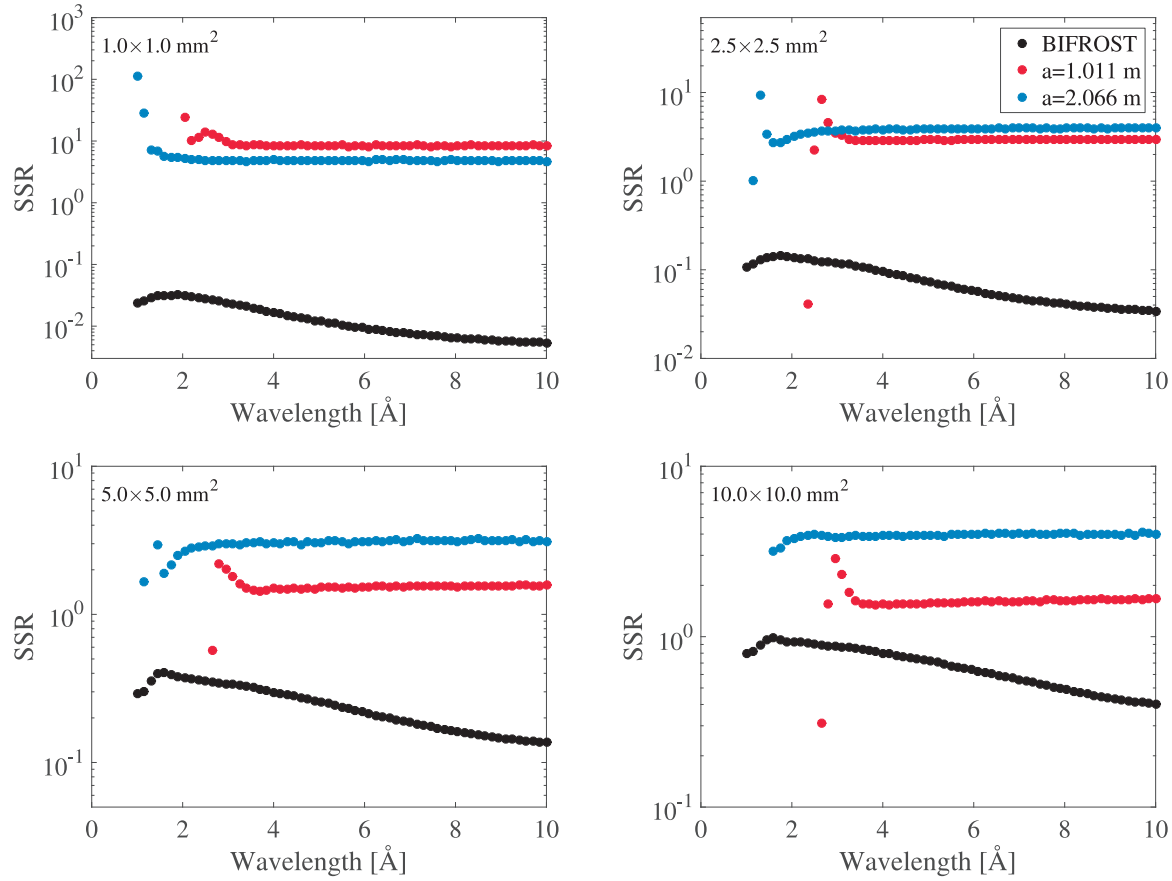

Fig. 12. The Sample-beam to Surrounding-beam (SSR) vs. wavelength for different sample sizes 1×1 mm^2, 2.5 × 2.5 mm^2, 5×5 mm^2 and 10×10 mm^2 for the BIFROST guide shown in Fig. 1, the combined instrument with a=1.011 m and the combined instrument with a=2.066 m. The aperture settings of the BIFROST guide are listed in Table 2.

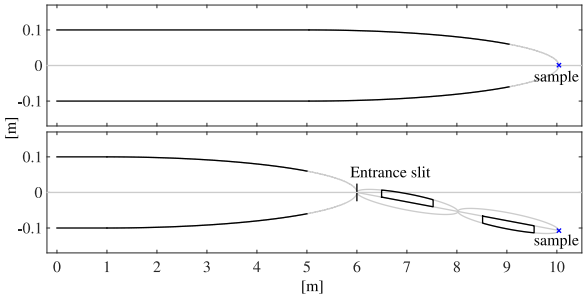

Fig. 13. A sketch of a two-guide implementation of the SELENE guide extension. The top panel shows a straight-parabolic guide where the last 10 m straight-ballistic guide can be exchanged for a shorter ballistic guide end to make room for the SELENE guide, as shown on the lower panel.

Agency for Research and Innovation for their support through the contribution to the ESS design update phase.

References

[1] ESS Technical Design Report, The European Spallation Source, 2013.
[2] H. Schober, E. Farhi, F. Mezei, P. Allenspach, K. Andersen, P. Bentley, P. Christiansen, B. Cubitt, R. Heenan, J. Kulda, P. Langan, K. Lefmann, K. Lieutenant, M. Monkenbusch, P. Willendrup, J. Šaroun, P. Tindemans, G. Zsigmond, Tailored instrumentation for long-pulse neutron spallation sources, Nucl. Instrum. Methods A 589 (1) (2008) 34–46. http://dx.doi.org/10.1016/j.nima.2008.01.102.
[3] K. Lefmann, K.H. Klenø, J.O. Birk, B.R. Hansen, S.L. Holm, E. Knudsen, K. Lieutenant, L. von Moos, M. Sales, P.K. Willendrup, K.H. Andersen, Simulation of a suite of generic long-pulse neutron instruments to optimize the time structure of the European Spallation source, Rev. Sci. Instrum. 84 (5) (2013) 055106. http://dx.doi.org/10.1063/1.4803167.
[4] F. Mezei, The raison d'être of long pulse spallation sources, J. Neutron Res. 6 (1) (1997) 3–32. http://dx.doi.org/10.1080/10238169708200095.
[5] C. Schanzer, P. Böni, U. Filges, T. Hils, Advanced geometries for ballistic neutron guides, Nucl. Instrum. Methods A 529 (13) (2004) 63–68. http://dx.doi.org/10.1016/j.nima.2004.04.178.
[6] K.H. Klenø, K. Lieutenant, K.H. Andersen, K. Lefmann, Systematic performance study of common neutron guide geometries, Nucl. Instrum. Methods A 696 (2012) 75–84. http://dx.doi.org/10.1016/j.nima.2012.08.027.
[7] R.M. Ibberson, Design and performance of the new supermirror guide on HRPD at ISIS, Nucl. Instrum. Methods A 600 (1) (2009) 47–49. http://dx.doi.org/10.1016/j.nima.2008.11.066.
[8] L.C. Chapon, P. Manuel, P.G. Radaelli, C. Benson, L. Perrott, S. Ansell, N.J. Rhodes, D. Raspino, D. Duxbury, E. Spill, J. Norris, Wish: the new powder and single crystal magnetic diffractometer on the second target station, Neutron News 22 (2) (2011) 22–25. http://dx.doi.org/10.1080/10448632.2011.569650.
[9] M. Montel, X-ray Microscopy and Microradiography vol. 177, Academic Press, New York, 1957.
[10] J. Stahn, U. Filges, T. Panzner, Focusing specular neutron reflectometry for small samples, Eur. Phys. J. Appl. Phys. 58 (1) (2012) 11001. http://dx.doi.org/10.1051/epjap/2012110295.
[11] P.M. Bentley, S.J. Kennedy, K.H. Andersen, D. Martin Rodríguez, D.F. Mildner, Correction of optical aberrations in elliptic neutron guides, Nucl. Instrum. Methods A 693 (2012) 268–275. http://dx.doi.org/10.1016/j.nima.2012.07.002.
[12] S. Weichselbaumer, G. Brandl, R. Georgii, J. Stahn, T. Panzner, P. Böni, Tailoring phase-space in neutron beam extraction, Nucl. Instrum. Methods A 793 (2015) 75–80. http://dx.doi.org/10.1016/j.nima.2015.05.003.
[13] J. Stahn, M. Cárdenas, ESS Instrument Construction Proposal Estia Focusing Reflectometer ⟨https://www.psi.ch/lns/estia⟩, 2013.
[14] T. Weber, G. Brandl, R. Georgii, W. Häußler, S. Weichselbaumer, P. Böni, Monte-Carlo simulations for the optimisation of a TOF-MIEZE instrument, Nucl. Instrum. Methods A 713 (2013) 71–75. http://dx.doi.org/10.1016/j.nima.2013.03.010.
[15] J. Stahn, A. Glavic, Focusing neutron reflectometry: implementation and experience on the TOF-reflectometer amor, Nucl. Instrum. Methods A 821 (2016) 44–54.

http://dx.doi.org/10.1016/j.nima.2016.03.007.
[16] H.M. Rønnow, K. Lefmann, N.B. Christensen, C. Niedermayer, F. Jurányi, M. Markó, J.B. Birk, M. Bertelsen, ESS Instrument Construction Proposal CAMEA, The European Spallation Source, 2013, The BIFROST instrument was formerly known as CAMEA.
[17] J.O. Birk, M. Bertelsen, CAMEA: Guide Report, ⟨https://infoscience.epfl.ch/record/190503%20?ln=en⟩, 2014.
[18] M. Bertelsen, H. Jacobsen, U. Bengaard Hansen, H. Hoffmann Carlsen, K. Lefmann, Exploring performance of neutron guide systems using pinhole beam extraction, Nucl. Instrum. Methods A 729 (2013) 387–398.
[19] K. Lefmann, K. Nielsen, McStas, a general software package for neutron ray-tracing simulations, Neutron News 10 (3) (1999) 20–23. http://dx.doi.org/10.1080/10448639908233684.
[20] P. Willendrup, E. Farhi, E. Knudsen, U. Filges, K. Lefmann, McStas: past, present and future, J. Neutron Res. 17 (1) (2014) 35–43. http://dx.doi.org/10.3233/JNR-130004.
[21] L.D. Landau, L.P. Pitaevskii, E.M. Lifshitz, Statistical Physics, Butterworth-Heinemann, Oxford, 1980.
[22] U.B. Hansen, M. Bertelsen, E.B. Knudsen, K. Lefmann, Simulation of waviness in neutron guides, J. Neutron Res. 18 (2–3) (2016) 45–59. http://dx.doi.org/10.3233/JNR-150023.
[23] C. Schanzer, Waviness of Neutron Guides/Mirror Optics, Personal Communication, SwissNeutronics, 2014.
[24] M. Bertelsen, K. Lefmann, Constraining neutron guide optimizations with phase-space considerations, Nucl. Instrum. Methods A 830 (2016) 313–324. http://dx.doi.org/10.1016/j.nima.2016.06.003.

A.12 On the nature of magnetic stripes in cuprate superconductors

A small deviation between the scattering vector for elastic and inelastic peaks relating to stripes in the La_2CuO_{4+y} is reported. Such a discovery would have significant impact for the theoretical studies that have assumed the scattering vector of the elastic and inelastic signal was identical. It was thoroughly determined that the reported effect could not be the result of an instrument effect, but may be caused by crystal twinning. The paper have been submitted to Physcal Review Letters.

Abstract

We present detailed neutron scattering studies of the static and dynamic stripes in an optimally doped high-temperature superconductor, La_2CuO_{4+y}. We find that the dynamic stripes do not disperse towards the static stripes in the limit of vanishing energy transfer. We conclude that the dynamic stripes observed in neutron scattering experiments are not the Goldstone modes associated with the broken symmetry of the simultaneously observed static stripes, but rather that the signals originate from different domains in the sample. These domains may be related by structural twinning, or may be entirely different phases, where the static stripes in one phase are pinned versions of the dynamic stripes in the other. Our results explain earlier observations of unusual dispersions in underdoped $La_{2-x}Ba_xCuO_4$ (x = 0.07) and $La_{2-x}Ba_xCuO_4$ (x = 0.095). Our findings are relevant for all compounds exhibiting magnetic stripes, and may thus be a vital part in unveiling the nature of high temperature superconductivity.

My contribution

The reported effects could have been a instrument effect, and thus a McStas instrument simulation was created to ascertain whether this would be feasible, however no sample component possessed the required features. I wrote the necessary McStas sample component. Read and commented on several iterations of the manuscript.

On the nature of magnetic stripes in cuprate superconductors

H. Jacobsen,[1,2] S.L. Holm,[2,3] M.-E. Lăcătuşu,[4] A. T. Rømer,[2] M. Bertelsen,[2] M. Boehm,[5] R. Toft-Petersen,[6,7] J.-C. Grivel,[4] S. B. Emery,[8,9] L. Udby,[2] B.O. Wells,[8] and K. Lefmann[2]

[1] *Department of Physics, Oxford University, Oxford, OX1 3PU, United Kingdom*
[2] *Nanoscience Center, Niels Bohr Institute, University of Copenhagen, 2100 Copenhagen Ø, Denmark*
[3] *Interdisciplinary Nanoscience Center - INANO-Kemi, Langelandsgade, Aarhus, Denmark*
[4] *Institute of Energy Conversion, Technical University of Denmark, 4000 Roskilde, Denmark*
[5] *Institut Max Von Laue Paul Langevin, F-38042 Grenoble, France*
[6] *Helmholtz-Zentrum Berlin, Hahn-Meitner-Platz 1, 14109 Berlin, Germany*
[7] *Technical University of Denmark, Department of Physics, 2800 Kgs. Lyngby, Denmark*
[8] *Department of Physics and Institute of Materials Science, University of Connecticut, USA*
[9] *Present address: Naval Surface Warfare Center Indian Head EOD Technology Division, Indian Head, MD 20640 USA*

We present detailed neutron scattering studies of the static and dynamic stripes in an optimally doped high-temperature superconductor, La_2CuO_{4+y}. We find that the dynamic stripes do not disperse towards the static stripes in the limit of vanishing energy transfer. We conclude that the dynamic stripes observed in neutron scattering experiments are not the Goldstone modes associated with the broken symmetry of the simultaneously observed static stripes, but rather that the signals originate from different domains in the sample. These domains may be related by structural twinning, or may be entirely different phases, where the static stripes in one phase are pinned versions of the dynamic stripes in the other. Our results explain earlier observations of unusual dispersions in underdoped $La_{2-x}Sr_xCuO_4$ ($x = 0.07$) and $La_{2-x}Ba_xCuO_4$ ($x = 0.095$). Our findings are relevant for all compounds exhibiting magnetic stripes, and may thus be a vital part in unveiling the nature of high temperature superconductivity.

An imperative open question in materials physics is the nature of high-temperature superconductivity. Unlike conventional superconductors, where the Cooper pairing mechanism is well-established [1], the pairing mechanism in high-temperature superconductors (HTS) still sparks controversy [2]. A comprehensive description of the electronic behavior inside HTS is indispensable to push this field of research onward. Hence, the magnetic structures which appear close to as well as inside the superconducting phase are still being studied intensively [3, 4]. In many HTS compounds, experiments indicate a modulated magnetic structure, consistent with superconducting "stripes" of charge separated by magnetic regions as sketched in Fig. 1a [5]. Magnetic excitations, referred to as "dynamic stripes", are found with similar periodicity, and are therefore thought to be related to the Goldstone modes of the static stripes [6].

We present evidence that this model is incomplete for a family of HTS. We find that the dynamic stripes do not disperse towards the static stripes in the limit of vanishing energy transfer, and that the signals therefore have different origins. Either they belong to different twin domains, or the static and dynamic stripes populate different spatial regions of the HTS. This has important consequences for understanding the vast amount of neutron scattering studies on magnetic stripes in *e.g.* the cuprates.

Superconductors based on the La_2CuO_4 family were the first HTS to be discovered [7]. They become superconducting upon doping with electrons or holes, with a maximum critical temperature, $T_c \approx 40$ K, whether the dopant is Sr ($La_{2-x}Sr_xCuO_4$, LSCO), Ba ($La_{2-x}Ba_xCuO_4$, LBCO), or O (La_2CuO_{4+y}, LCO+O). The generic crystal structure of these compounds is illustrated in Fig. 1b. They consist of planes of CuO separated by layers of La/Sr/Ba. Each Cu atom is at the center of an octahedron of oxygen atoms. At elevated temperatures these materials are in the high temperature tetragonal (HTT) phase. Upon lowering the temperature, the crystals enter the low temperature orthorhombic phase (LTO) where the oxygen octahedra tilt around the tetragonal a axes, leading to a change in lattice parameters, $a < b$. Most compounds in the LTO phase are twinned because the oxygen octahedra can tilt around either of the tetragonal a axes, creating different domains with crystallographic axes that are rotated with respect to each other. For details, see Supplementary Material [8].

Since the first discovery, a multitude of HTS have been found in the cuprate family. The amplitude and period of the stripe order modulations vary strongly with the choice and amount of dopant, with static stripes being particularly pronounced in LCO+O [9].

The spin stripes can be measured using magnetic neutron scattering, where they are observed as pairs of intensity peaks at incommensurate (IC) wave vector transfers, *e.g.* at $\mathbf{Q} = (1 + \delta_h, \delta_k, 0)$ and $\mathbf{Q} = (1 - \delta_h, -\delta_k, 0)$ for stripes along the (110) direction, see Fig. 1c. Here, the components of the scattering vector are given in terms of $(2\pi/a, 2\pi/b, 2\pi/c)$, where a, b and c are the orthorhombic lattice constants. The real-space modulation period is $L = 2\pi/\delta$, and we refer to δ as the incommensurability of the stripes. Typically $\delta_h \approx \delta_k$, indicating that the modulation is approximately along the Cu-O-Cu bonds

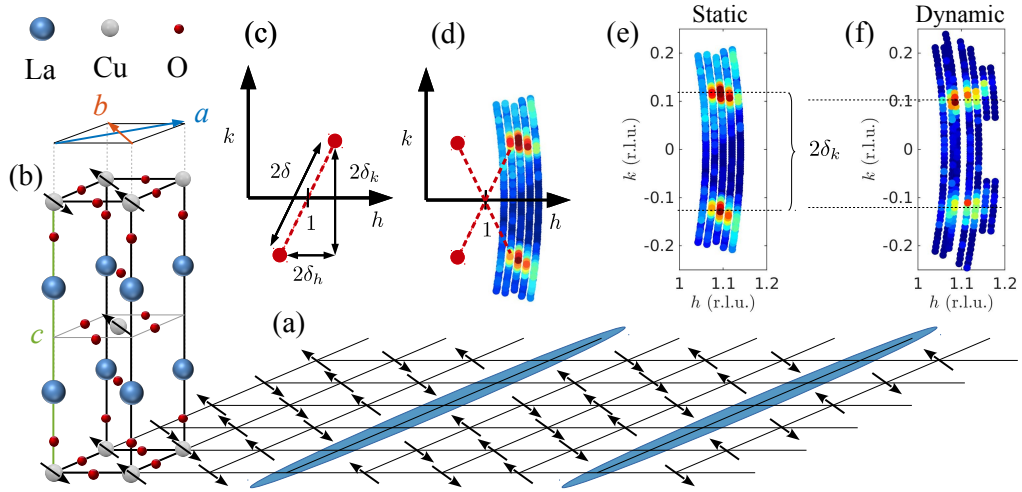

Figure 1. Sketch of magnetic and charge stripes in the cuprate high-temperature superconductor $La_2CuO_{4+\delta}$ (LCO+O). (a) Illustration of magnetic stripes with a period of 8, concurrent with period 4 charge stripes along the Cu-O-Cu bond directions (broad blue lines). Another type of domains exists, where the stripes are rotated 90 degrees, still lying within the plane (not shown). (b) The tetragonal unit cell of LCO+O illustrating the spins on the Cu ions. The spins are aligned along the orthorhombic b-axis, shown above the unit cell. (c) Illustration of reciprocal space (in orthorhombic notation) showing the position of the incommensurate magnetic stripe peaks for stripes approximately along the (110) direction. The difference between δ_h and δ_k is exaggerated for clarity. (d) the quartet of peaks around the (100) position observed when stripes are present along both the (110) and (1$\bar{1}$0) directions. The coloured regions show the regions probed in the present experiment. (e) Example of the static ($E = 0$) and (f) dynamic ($E = 1.5$ meV) stripe signal in LCO+O, measured by neutron scattering.

(the (110) and (1$\bar{1}$0) directions), although variations have been reported, indicating a kink in the stripes after a number of unit cells [9, 10].

Typically, stripes are observed not only at the above mentioned positions, but also at $\mathbf{Q} = (1 - \delta_h, \delta_k, 0)$ and $\mathbf{Q} = (1 + \delta_h, -\delta_k, 0)$, giving rise to a quartet of peaks around the (100) position, as illustrated in Fig. 1d. This indicates that the compound exhibits stripes (approximately) along both the (110) and (1$\bar{1}$0) directions, most likely by the stripes in adjacent layers in each domain alternating between the (110) and (1$\bar{1}$0) directions [11].

Inelastic neutron scattering has shown the presence of dynamic stripes, which at low energies have similar modulation period as the static stripes [12]. The modulation period of the stripes is found to be almost constant up to around 10-15 meV [13, 14]. In the cuprates an hourglass shaped dispersion develops at higher energies [15].

The incommensurability of the stripes has been found to vary with doping. In the LSCO-type cuprates, δ increases linearly with doping and saturates at a maximal value of $\delta = 1/8$ [12]. In some cuprates, similar stripes of charge with half the modulation period have been observed using X-ray diffraction, validating the picture of magnetic and charge stripes in Fig. 1a [16–20]. However, the energy resolution of X-rays does not allow to distinguish between static and dynamic stripes.

The main feature linking the static and dynamic stripes is their common position in reciprocal space in the limit of vanishing energy transfer [12]. In light of the discrepancies mentioned above we therefore investigate the relationship between the static and dynamic stripes.

We have used elastic and inelastic scattering of low energy neutrons to accurately measure the reciprocal space position of the static and dynamic stripes in LCO+O in the LTO phase. The experiments were performed at the cold-neutron triple axis spectrometers FLEXX at HZB, Berlin [21], and ThALES at ILL, Grenoble [22]. For details on the experiments, see the Supplementary Material [8].

Panel (d) of Fig. 1 shows how we probe two of the four IC peaks in our neutron scattering experiments. The actual data for a series of scans are shown in panels (e) and (f) as 2D colorplots. Fig. 2 shows examples of the raw data with 0 and 1.5 meV energy transfer, probing the static and dynamic stripes, respectively. The inset shows the direction of the scans in reciprocal space. We observe that the elastic and inelastic signals unexpectedly are located at different positions.

To eliminate errors from minor misalignments, we determine the incommensurability along k, δ_k, as half the distance between the peak centers. In Fig. 3 we display δ_k for all energy transfers probed in the experiment at two temperatures. As expected, the dynamic stripes in LCO+O appear at the same reciprocal space position in the normal phase (45 K) as in the SC phase (2 K) (within the instrument resolution), whereas the static stripes are only present in the SC phase.

The inelastic dispersion appears continuous and steep,

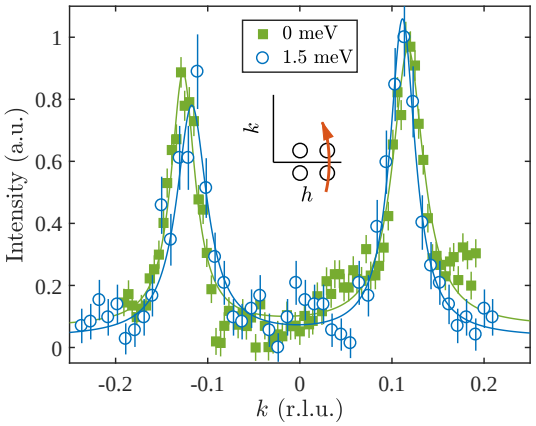

Figure 2. Neutron scattering data for LCO+O scanned along the direction shown in the insets, showing the shift in peak position between the elastic stripes (green) and low-energy inelastic stripes (blue). The data have been rescaled and the background subtracted.

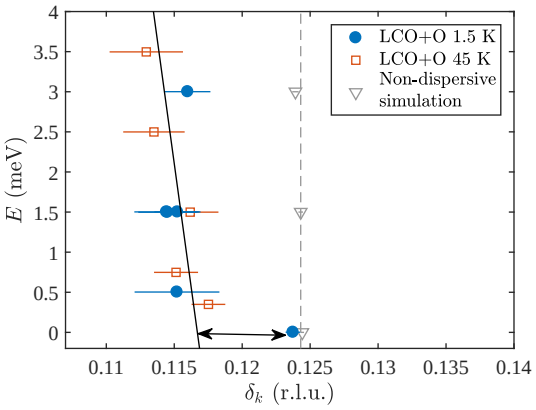

Figure 3. The incommensurability, δ_k at different energy transfers E for LCO+O. A significant shift is seen between the elastic and inelastic data. The solid black line is a linear fit to the dispersion for $E > 0$. Gray triangles represent the dispersion relation obtained from simulated data, where the simulated dispersion relation is vertical.

consistent with earlier cuprate results [13, 14]. However, the elastic signal shows a large and significant difference in δ_k, appearing as a discontinuity in the dispersion relation at vanishing energy transfer. The transverse difference between the observed IC peaks for the static stripes corresponds to a periodicity of $L_s \approx 8.1\,b$ ($\delta_k = 0.124(1)$). In contrast, the dynamic stripes display a periodicity of $L_d \approx 8.7\,b$ ($\delta_k = 0.115(1)$) in the limit of vanishing energy transfer.

To show that this surprising difference in δ_k is not an artifact caused by experimental non-idealities, we have performed a virtual ray-tracing experiment using a close model of our experiment, further detailed in the Supplementary Material [8]. This method is known to accurately reproduce experimental effects like peak broadening and displacement [23]. The virtual experiments show that the experimental resolution can cause a tiny shift in the observed incommensurability, see Fig. 3. The experimentally observed shift in peak position is, however, more than an order of magnitude larger than what can be explained by the resolution, and is therefore a genuine property of the sample. The simulations also exclude misalignment of the instrument as a cause of the effect.

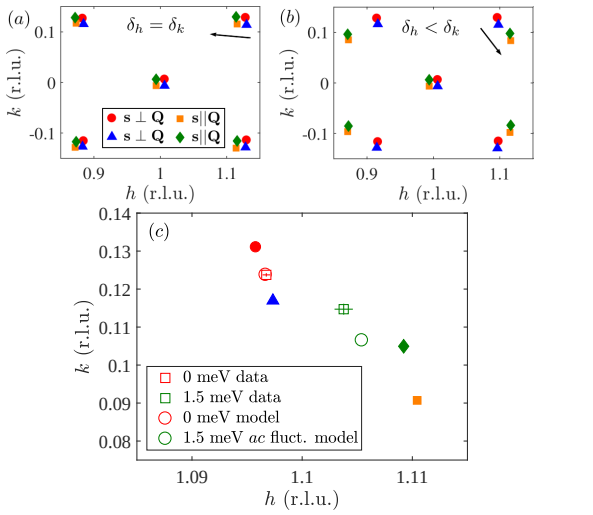

Figure 4. Illustration of reciprocal space for stripe order and twinning. (a) and (b) show the peak positions of the stripes from four twin domains for $\delta_h = \delta_k$ and $\delta_h < \delta_k$, respectively, as well as the center of the peaks for each domain. The arrows indicate the direction the observed peaks would move when going from elastic to inelastic neutron scattering. (c) shows a zoom in comparing the data with a simple model of fluctuations in the ac plane. The filled points correspond to the 4 twin domains as in (a) and (b).

It is generally agreed that the dispersion relation for the stripes in cuprates is very steep down to the lowest energies [13, 14]. Indeed, our data show a steep dispersion, but the data at the lowest probed energy transfer of 0.3 meV show a periodicity deviation of roughly 10% ($\sim$ 0.01 r.l.u.) compared to the static signal. For the dispersion to be continuous, our present data would require the slope of the dispersion to change by almost two orders of magnitude below 0.3 meV. We do not know of an effect that would cause such a dramatic change in dispersion slope [24]. We therefore conclude that the dynamic stripe dispersion does not approach the static stripe signal and therefore that the observed dynamic stripes are not the Goldstone modes associated with the broken symmetry of the observed static stripes.

Hence, the static and dynamic stripes must originate from different phases in the sample. In our view there are two probable ways this can occur:

First, the dynamic stripes could be transverse fluctuations from the static stripe order, resembling ordinary

spin waves. Due to the neutron scattering selection rules, the scattering we observe in the elastic and inelastic channels stem from different twin domains as explained below. Secondly, the static and dynamic stripes may be different but related entities, occupying different microscopic phases of the crystal.

We first consider the effect of twinning on the observed signal. In Fig 4a, the expected position of peaks from each of the four domains are marked, assuming $\delta_h = \delta_k$. Assuming the spins to point along the b axis as found earlier [9], two of the domains giving rise to these peaks have approximately $\mathbf{s} \perp \mathbf{Q}$, while the other two have $\mathbf{s} \parallel \mathbf{Q}$. The static signal from the domains with $\mathbf{s} \parallel \mathbf{Q}$ will be suppressed due the selection rule that neutrons only sense the component of the spins that is perpendicular to $\mathbf{Q}$ [25]. The observed dynamic signal will be a weighted average of the signal from all four domains, with the weight depending on the direction of the fluctuations and the relative sizes of the domains. Due to the finite resolution and peak width the individual peaks will not be resolved. Therefore, this will shift the dynamic signal away from the static signal, causing an apparent discontinuity in the position of the peaks.

For $\delta_h = \delta_k$, however, the shift would be in the opposite direction as the observed shift, see Fig. 4a. This situation changes when considering twinning for $\delta_h < \delta_k$, see Fig. 4b. In this case, the relative positions of the domains with $\mathbf{s} \perp \mathbf{Q}$ and $\mathbf{s} \parallel \mathbf{Q}$ have been reversed. In Fig. 4c we zoom in on one of the peak positions, showing where the expected peaks from the 4 domains will be positioned along with the data. We further show where the expected peak position will be in a simple model where the spins point along b and the fluctuations are perpendicular to this direction, and we assume all four domains are equal in size. Good general agreement is found between the data and this simple model. Perfect agreement can be obtained by assuming the domains to have different sizes. As the domain sizes were not measured in this experiment, due to requirements of a relaxed resolution in the inelastic experiment, we refrain from detailing this further.

Twinning can thus explain the discontinuity in the dispersion, at least qualitatively.

We move on to consider the case of the static and dynamic stripes being located in different microscopic phases of the sample, a view supported by a number of observations. In this model, the static stripes are seen as pinned versions of dynamic stripes, where the pinning forces slightly modify the value of the incommensurability, δ. For example, 12% doped LSCO has been suggested to phase separate into microscopic superconducting regions with gapped dynamic stripes and non-superconducting regions with static stripes [28]. Spontaneous, microscopic phase separation has also been observed in purely oxygen doped LCO+O crystals [29] and in crystals doped with both oxygen and strontium [30]. Furthermore, recent studies of $La_{5/3}Sr_{1/3}CoO_4$ show evidence of microscopic phase separation into components with different local hole concentration [31, 32]. In the latter material the upper and lower parts of the hourglass dispersion are even proposed to originate from different nano-scale structures in the sample [31].

The idea of dynamic and static stripes being different entities are supported by a number of other observations. For example, the static and dynamic stripes exhibit different behaviors as function of temperature. In underdoped LSCO and in LCO+O as evidenced in this experiment, the static stripes vanish above T_c, but the dynamic stripes remain to far higher temperatures [26, 27, 33]. In contrast, in the optimally doped region, the static stripes are altogether absent [14]. When applying a magnetic field, the static stripes are in general strengthened [26, 27, 34–36], with a few exceptions [36, 37]. In many cases this happens with an accompanying change in the dynamic stripe spectrum [26, 27, 34], but in other cases, the dynamic stripe spectrum is unchanged [35]. Hence, the coupling between static and dynamic stripes is not simple and unique.

Based on these consideration, it is plausible that the HTS is indeed phase separated into different spatial regions with pinned static stripes present only in some parts whereas the signal from free dynamic stripes originate in other regions. This spatial phase separation could possibly arise from inhomogeneities in the doping level on the nanoscale. Such variations in the doping value gives rise to different incommensurabilities [12], and might lead to changes in T_c. Phase separation would also explain in broad terms why the static and dynamic stripes display different evolution with temperature and magnetic field.

The observations made here are general and our analysis should be valid for any compound displaying static and dynamic stripes. Indeed, a significant shift in peak position between elastic and inelastic stripes has been observed and briefly remarked upon in underdoped LSCO in the LTO phase [38] and LBCO in the low temperature less orthorhombic phase [11, 24]. Our analysis provides a plausible explanation of the reason for this observed shift also in these other cuprates.

In conclusion we have found that the dynamic stripes do not disperse towards the static stripes in the limit of vanishing energy transfer in a HTSC. The observed static and dynamic stripes thus originate from different regions in the crystal. These regions may either be twin domains with identical properties, or entirely different microscopic phases occupying different spatial regions of the superconductor.

Our observations are relevant for all compounds with magnetic stripes. In particular, we find that this mechanism explains earlier observations of unusual dispersions in underdoped $La_{2-x}Sr_xCuO_4$ ($x = 0.07$) [38] and $La_{2-x}Ba_xCuO_4$ ($x = 0.095$) [24]. Our findings may thus be a vital part in unveiling the nature of high tempera-

ture superconductivity.

[1] J. Bardeen, L.N. Cooper and J.R. Schrieffer, Phys. Rev. **108,** 1175 (1957).

[2] A. J. Leggett, Nature Physics **2,** 134 (2006).

[3] B. Keimer, S. A. Kivelson, M. R. Norman, S. Uchida, and J. Zaanen, Nature **518**, 179 (2015).

[4] E. Fradkin, S. Kivelson and J. M. Tranquada, Rev. Mod. Phys. **87**, 457 (2015).

[5] J. M. Tranquada, B. J. Sternlieb, J. D. Axe, Y. Nakamura, and S. Uchida, Nature **375**, 561 (1995).

[6] M. Vojta, Adv. Phys. **58,** 699 (2009); and references therein.

[7] J. G. Bednorz and K. A. Müller, Z. Phys. B **64,** 189 (1986).

[8] Supplementary material available at the end of the paper.

[9] Y. S. Lee , R. J. Birgeneau, M. A. Kastner, Y. Endoh, S. Wakimoto, K. Yamada, R. W. Erwin, S.-H. Lee, G. Shirane,, Phys. Rev. B **60,** 3643 (1999).

[10] H. Kimura, H. Matsushita, K. Hirota, Y. Endoh, K. Yamada, G. Shirane, Y. S. Lee, M. A. Kastner, R. J. Birgeneau, Phys. Rev. B **61,** 14366 (2000).

[11] M. Hücker, M. V. Zimmermann, G. D. Gu, Z. J. Xu, J. S. Wen, Guangyong Xu, H. J. Kang, A. Zheludev, J. M. Tranquada, , Phys. Rev. B **83,** 104506 (2011).

[12] K. Yamada, C. H. Lee, K. Kurahashi, J. Wada, S. Wakimoto, S. Ueki, H. Kimura, Y. Endoh, S. Hosoya, G. Shirane, R. J. Birgeneau, M. Greven, M. A. Kastner, and Y. J. Kim, Phys. Rev. B **57,** 6165 (1998).

[13] N. B. Christensen, D. F. McMorrow, H. M. Rønnow, B. Lake, S. M. Hayden, G. Aeppli, T. G. Perring, M. Mangkorntong, M. Nohara, and H. Takagi, Phys. Rev. B **83**, 104506 (2011).

[14] B. Lake, G. Aeppli, T. E. Mason, A. Schröder, D. F. McMorrow, K. Lefmann, M. Isshiki, M. Nohara, H. Takagi, and S. M. Hayden, Nature **400,** 43 (2002).

[15] B. Vignolle, S. Hayden, D. McMorrow, H. Rønnow, B. Lake, C. Frost, and T. Perring, Nature Physics **3,** 163 (2007).

[16] J. Chang, E. Blackburn, a. T. Holmes, N. B. Christensen, J. Larsen, J. Mesot, R. Liang, D. a. Bonn, W. N. Hardy, A. Watenphul, M. V. Zimmermann, E. M. Forgan, and S. M. Hayden, Nature Physics **8,** 871 (2012)

[17] E. H. da Silva Neto, P. Aynajian, A Frano, R. Comin, E. Schierle, E. Weschke, A. Gyenis, J. Wen, J. Schneeloch, Z. Xu, S. Ono, G. Gu, M. Le Tacon, A. Yazdani, Science **343**, 393 (2014).

[18] V. Thampy, M. P. M. Dean, N. B. Christensen, L. Steinke, Z. Islam, M. Oda, M. Ido, N. Momono, S. B. Wilkins, and J. P. Hill, Phys. Rev. B **90**, 100510 (2014).

[19] T. P. Croft, C. Lester, M. S. Senn, A. Bombardi, and S. M. Hayden, Phys. Rev. B **89**, 224513 (2014).

[20] X. M. Chen, V. Thampy, C. Mazzoli, A. M. Barbour, H. Miao, G. D. Gu, Y. Cao, J. M. Tranquada, M. P. M. Dean, and S. B. Wilkins, Phys. Rev. Lett. **117**, 167001 (2016)

[21] M. D. Le, D. L. Quintero-Castro, R. Toft-Petersen, F. Groitl, M. Skoulatos, K. C. Rule, and K. Habicht, Nucl. Instr. Meth. Phys. Res. **729,** 220–226 (2013).

[22] K. Lefmann, M. Boehm; S.L. Holm; H. Jacobsen; M.-E. Lacatusu, L. Udby, Institut Laue-Langevin data set, doi:10.5291/ILL-DATA.TEST-2473 (2015).

[23] L. Udby, P. K. Willendrup, E. Knudsen, C. Niedermayer, U. Filges, N. B. Christensen, E. Farhi, B. O. Wells, and K. Lefmann, Nucl. Instr. Meth. A **634,** S138 (2011).

[24] Z. Xu, C. Stock, S. Chi, A. I. Kolesnikov, G. Xu, G. Gu, and J. M. Tranquada, Phys. Rev. Lett. **113,** 177002 (2014).

[25] In this discussion we assume for simplicity that **Q** ∥ (100); the error in the calculated peak position from this assumption is around 1% and thus negligible in this context.

[26] B. Lake, H. M. Rønnow, N. B. Christensen, G. Aeppli, K. Lefmann, D. F. McMorrow, P. Vorderwisch, P. Smeibidl, N. Mangkorntong, T. Sasagawa, M. Nohara, H. Takagi, and T. E. Mason, Nature **415,** 299 (2002).

[27] B. Lake, G. Aeppli, K. N. Clausen, D. F. McMorrow, K. Lefmann, N. E. Hussey, N. Mangkorntong, M. Nohara, H. Takagi, T. E. Mason, and A. Schröder, Science **291,** 1759 (2001).

[28] M. Kofu, S. H. Lee, M. Fujita, H. J. Kang, H. Eisaki, and K. Yamada, Phys. Rev. Lett. **102,** 047001 (2009).

[29] H. E. Mohottala, B. O. Wells, J. I. Budnick, W. a Hines, C. Niedermayer, L. Udby, C. Bernhard, A. R. Moodenbaugh, and F.-C. Chou, Nature Materials **5,** 377 (2006).

[30] L. Udby, J. Larsen, N. B. Christensen, M. Boehm, C. Niedermayer, H. E. Mohottala, T. B. S. Jensen, R. Toft-Petersen, F. C. Chou, N. H. Andersen, K. Lefmann, and B. O. Wells, Phys. Rev. Lett. **111,** 227001 (2013).

[31] Y. Drees, Z. W. Li, A. Ricci, M. Rotter, W. Schmidt, D. Lamago, O. Sobolev, U. Rütt, O. Gutowski, M. Sprung, A. Piovano, J. P. Castellan, and A. C. Komarek, Nature Communications **5,** 5731 (2014).

[32] P. Babkevich, P. G. Freeman, M. Enderle, D. Prabhakaran, and A. T. Boothroyd, Nature Communications **7**, 11632 (2016).

[33] C. Lee, K. Yamada, Y. Endoh, G. Shirane, R. J. Birgeneau, M. A. Kastner, and M. Greven, J. Phys. Soc. Jpn. **69,** 1170-1176 (2000).

[34] J. Chang, N. B. Christensen, C. Niedermayer, K. Lefmann, H. M. Rønnow, D. F. McMorrow, A. Schneidewind, P. Link, A. Hiess, M. Boehm, R. Mottl, S. Pailhés, N. Momono, M. Oda, M. Ido, and J. Mesot, Phys. Rev. Lett. **102,** 177006 (2009).

[35] A. T. Rømer, J. Chang, N. B. Christensen, B. M. Andersen, K. Lefmann, L. Mähler, J. Gavilano, R. Gilardi, C. Niedermayer, H. M. Rønnow, A. Schneidewind, P. Link, M. Oda, M. Ido, N. Momono, and J. Mesot, Phys. Rev. B **87,** 144513 (2013).

[36] J. Chang, C. Niedermayer, R. Gilardi, N. B. Christensen, H. M. Rønnow, D. F. McMorrow, M. Ay, J. Stahn, O. Sobolev, A. Hiess, S. Pailhes, C. Baines, N. Momono, M. Oda, M. Ido, and J. Mesot, Phys. Rev. B **78,** 104525 (2008).

[37] L. Udby, N. H. Andersen, F. C. Chou, N. B. Christensen, S. B. Emery, K. Lefmann, J. W. Lynn, H. E. Mohottala, C. Niedermayer, and B. O. Wells, Phys. Rev. B **80**, 014505 (2009).

[38] H. Jacobsen, I. A. Zaliznyak, A. T. Savici, B. L. Winn, S. Chang, M. Hucker, G. D. Gu, and J. M. Tranquada, *Phys. Rev. B* **92,** 174525 (2015).

[39] . T. Rømer, P. J. Ray, H. Jacobsen, L. Udby, B. M. Andersen, M. Bertelsen, S. L. Holm, N. B. Christensen, R. Toft-Petersen, M. Skoulatos, M. Laver, A. Schneidewind,

P. Link, M. Oda, M. Ido, N. Momono, and K. Lefmann, Phys. Rev. B **91,** 174507 (2015).
[40] K. Lefmann and K. Nielsen Neutron News **10,** 20, (1999).
[41] P. Willendrup, E. Farhi and K. Lefmann Physica B, **350,** e735 (2004). Nucl. Instr. Meth. A **634,** S138 (2011).
[42] E. Farhi, personal communication (2015).
Phys. Rev. B **60,** 3643 (1999).
[43] M. Braden, G. Heger, P. Schweiss, Z. Fisk, K. Gamayunov, I. Tanaka, and H. Kojima, Physica C **191,** 455 (1992).
[44] P. Jensen, M. Sc. thesis, University of Copenhagen (2015).

We thank ILL, Grenoble, France, HZB, Berlin, Germany, and PSI, Villigen, Switzerland for providing us access to their neutron scattering facilities. We are indebted to E. Farhi for providing us with a model of the ILL neutron guide system for use in the Monte Carlo simulations. We thank N. B. Christensen, P. J. Ray, J. M. Tranquada and J.I. Budnick for illuminating discussions. We thank P. J. Ray for help with some of the figures. We thank P.G. Freeman, M. Skoulatos, D. Prabhakaran for illuminating discussions.

Work at University of Connecticut was supported by the USDOE Basic Energy Sciences under contract DE-FG02-00ER45801. The work was supported by the Danish Research Council FNU through the grants DanScatt and Magnetism in Superconductors.

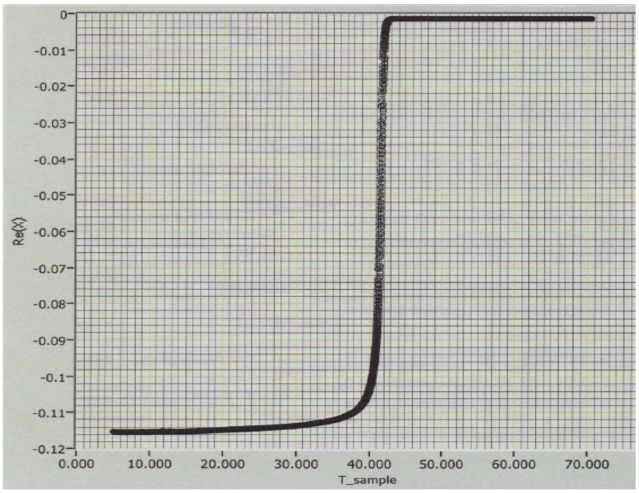

Figure 5. The susceptibility of the LCO+O sample in a weak field, showing the SC transition clearly around $T_C \sim 40$ K.

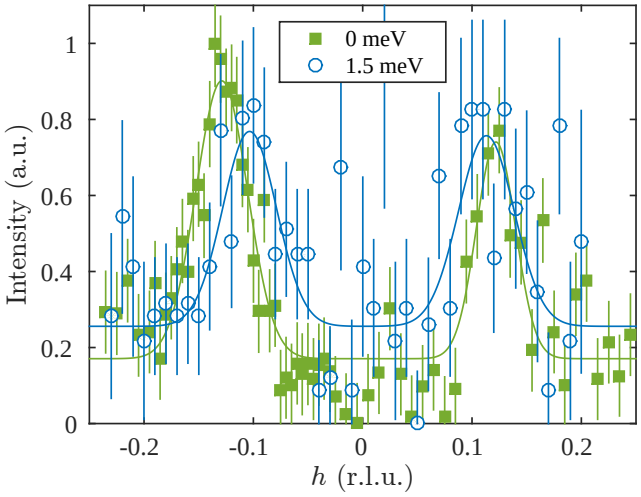

Figure 6. Background subtracted neutron scattering data on LCO+O, measured at FLEXX, HZB. The shift of the peak position between elastic and inelastic data is also seen here.

Sample details

The samples were prepared by growing stoichiometric LCO crystals at the Technical University of Denmark in an optical image furnace using the travelling solvent float zone technique. After annealing and characterization, chosen crystals were super-oxygenated in an aqueous bath at the University of Connecticut. The resulting LCO+O crystals were cut in pieces suitable for neutron scattering experiments and smaller pieces of the sample were characterized by resistivity and susceptibility measurements to find a superconducting transition temperature of 40 ± 1 K, typical for LCO+O .

LCO+O usually has a spontaneous phase separation (miscibility) into a $T_c = 30$ K phase and a $T_c = 40$ K phase [29]. The superconducting transition temperature for our sample was measured by a vibrating sample magnetometer. The data is shown in Fig. 5 and show that our sample clearly has only one superconducting transition near $T = 40$ K, and therefore just one oxygenated phase that is similar to what was obtained by Lee *et al.* [9]. The orthorhombic lattice parameters are $a = 5.33$ Å, $b = 5.40$ Å, $c = 13.2$ Å. The spins align along the b axis in LCO+O, just as for the parent compound [9].

Details on neutron scattering experiments on LCO+O

Neutron scattering experiments were performed at the cold-neutron triple axis spectrometers FLEXX at HZB, Berlin [21], and ThALES at ILL, Grenoble [22]. The spectrometers were configured to run at a constant final energy of 5.0 meV.

At FLEXX the sample was mounted inside a magnet. The results of applying a magnetic field will be reported in a following publication. In both experiments, a velocity selector in the incident beam before the monochromator removed second-order contamination, while a cooled Be-filter between sample and analyzer further reduced background. The sample was aligned in the (a, b) plane. At FLEXX, several cylindrical crystals were co-aligned, resulting in a total sample mass of ~ 9 g. At ThALES, only the largest crystal of mass 3.44 g was used. In both experiments, we used vertically focusing monochromators, leading to relatively loose vertical collimation along the c-direction, where the stripe signal from cuprates is nearly constant [39]. At the ThALES experiment there was a small offset in the A4 angle which was corrected for in the subsequent data analysis.

The effect reported in the main paper was also seen in the experiment at FLEXX. An example of the data is shown in Fig. 6, showing the same difference between elastic and inelastic stripe positions as found at the ThALES experiment. In most of the experiment, however, only a single peak was measured due to time constraints.

We here show additional data from the ThALES experiment. The measurements at 0 meV and 1.5 meV were taken as grid scans in the (h, k) plane around the (100) position. The data were fitted to a pair of two-dimensional Gaussians, as seen in Fig. 7. The fitted peak positions are given in Tab. I

From the fits, the shift in the incommensurability between 0 meV and 1.5 meV is $(-0.0070(15), 0.0090(9), 0)$.

The elastic data around the (010) peak, similar to the data around (100) except for a 90 degree rotation are shown in Fig. 8. The incommensurability is the same within error bars for the two data sets. The static stripes

		Peak 1		Peak 2		Incommensurability	
	Position	h	k	h	k	δ_h	δ_k
Elastic	(100)	1.0965(6)	0.1151(4)	1.0969(7)	-0.1324(5)	0.0967(5)	0.1237(3)
Inelastic	(100)	1.1013(20)	0.1058(11)	1.1063(21)	-0.1236(13)	0.1038(15)	0.1147(8)
Elastic	(010)	0.1249(5)	1.0944(7)	-0.1216(4)	1.0956(7))	0.1233(3)	0.0950(5)

Table I. The fitted positions of the two-dimensional gaussian peaks given in r.l.u.

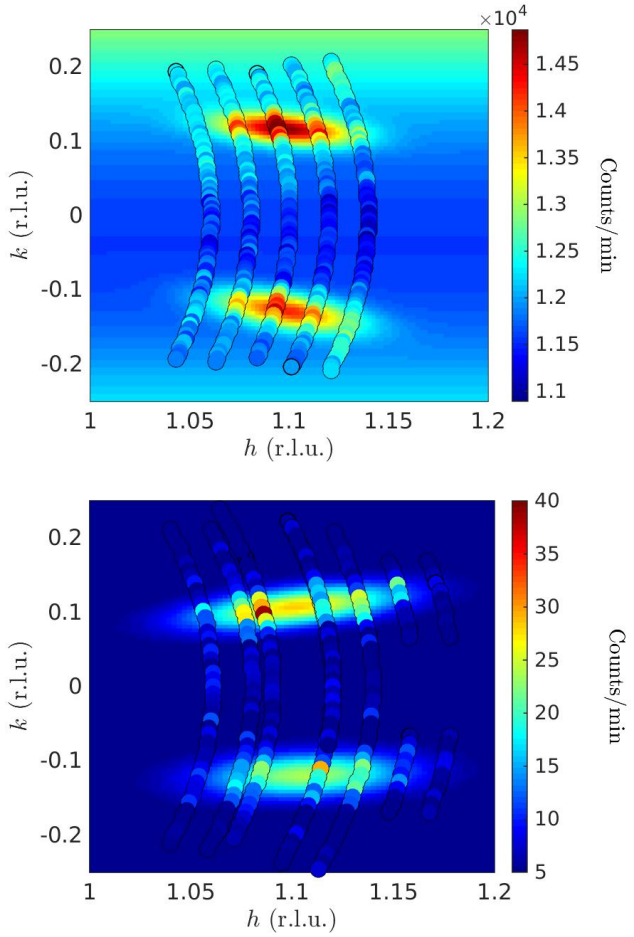

Figure 7. Two-dimensional fits of the LCO+O data at 0 meV (top) and 1.5 meV (bottom). The colored circles show the data, while the area around the circles shows the fit as described in the text.

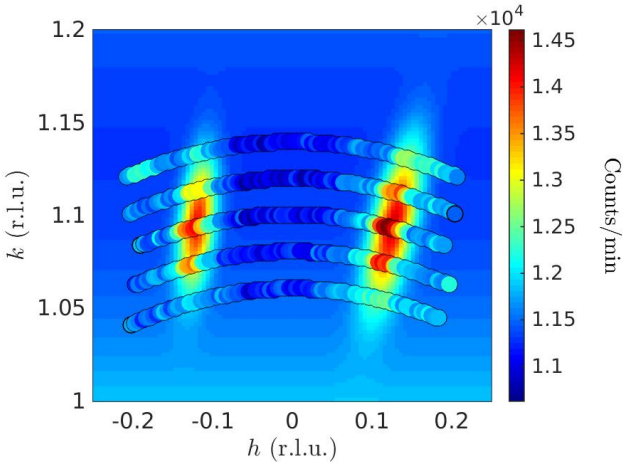

Figure 8. Two-dimensional fit of the LCO+O data at 0 meV near the (010) position. The colored circles show the data, while the area around the circles shows the fit as described in the text.

are rotated by approximately 7° away from the Cu-O-Cu directions; a value that is approximately twice what was found earlier [9].

The peak positions of the fitted two-dimensional Gaussians are shown in Fig. 9. The peak positions from the (010) peak were rotated 90 degrees for comparison. In this figure, it is observed that the inelastic peaks move together in k and to larger h, compared to the elastic peaks.

The data show that the distance between the incommensurate peaks is dependent on where exactly on the peak the measurement is performed. The shape of the resolution function and the peaks implies that the observed value of δ_k increases as function of h. This could lead to systematic errors, if different parts of the peak were probed at different energies. By making the grid scans shown in Figs. 7 and 8, we measured exactly this effect. Each scan in the grid was fitted individually. The resulting value of δ_k, determined as a function of h, is shown in Fig. 10. It is seen that δ_k increases with increasing h, as we move through the peak. However, it is also evident that at any given position in h, a significant shift in δ_k happens between the elastic and inelastic signals.

Virtual experiments

The full neutron scattering experiment at ThALES was simulated using the Monte Carlo (MC) ray tracing program McStas [40, 41], which has previously been shown to produce very accurate results regarding, in particular, instrument resolution [23]. Here follows a more detailed description of the simulation method.

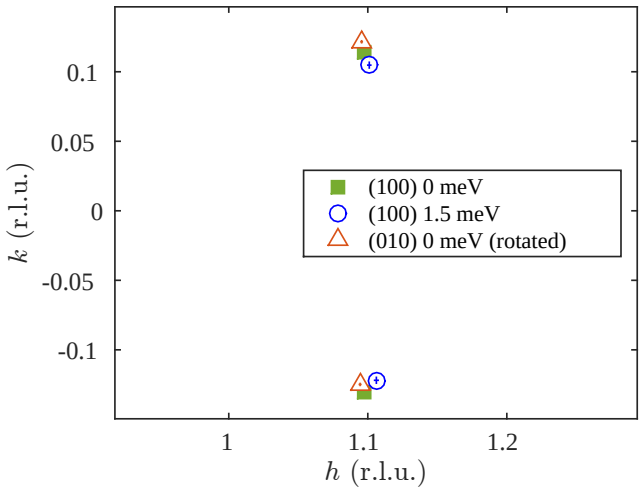

Figure 9. The fitted positions of the two-dimensional gaussian peaks, showing how the inelastic peaks move toward smaller values of $|k|$ in LCO+O.

The guide system at ILL has been simulated by E. Farhi [42], and we adopted his McStas model. The remainder of the instrument was simulated using standard components from McStas: slits, graphite crystals, and a detector. For the purpose of these simulations, a sample model was written, simulating scattering from static and dynamic stripes. This sample scatters elastically at a user-defined position in (h, k)-space (with the scattering being independent of l, as is true to a good approximation near $l = 0$ where the experiment was performed [39]). Furthermore, the sample scatters inelastically at a (possibly different) user-defined position in (h, k)-space. The absolute scattering cross section of the elastic and inelastic scattering can be set individually. For simplicity, and since we are not interested in absolute intensities, the cross section was kept independent of energy transfer, and no incoherent background was simulated. A combination of two such samples, rotated with respect to each other, was used to simulate the two measured peaks at $q = (1 + \delta_h, \pm\delta_k, 0)$.

A small offset in the A4 angle in the experiment caused the lattice parameters to appear slightly larger than their actual values. This was accounted for in the simulations.

Two sets of simulations were made: one with both the elastic and inelastic peaks at $\delta_h = \delta_k = 1/8$, and one with $\delta_h = 0.0973$, $\delta_k = 0.1222$ for the elastic peaks and $\delta_h = 0.1036$, $\delta_k = 0.1133$ for the inelastic peaks, as found in the experiments.

For each set of simulations, similar scans to the ones used in the experiments were simulated. Grid scans, similar to the ones shown in Fig 7 were simulated at $\hbar\omega = 0$ and $\hbar\omega = 1.5$ meV, see Fig. 11, where the simulations are shown on top of fits to two-dimensional Gaussians. The tilt of the peaks in the h, k-plane slightly deviates from the data, although the width of the peaks is reproduced

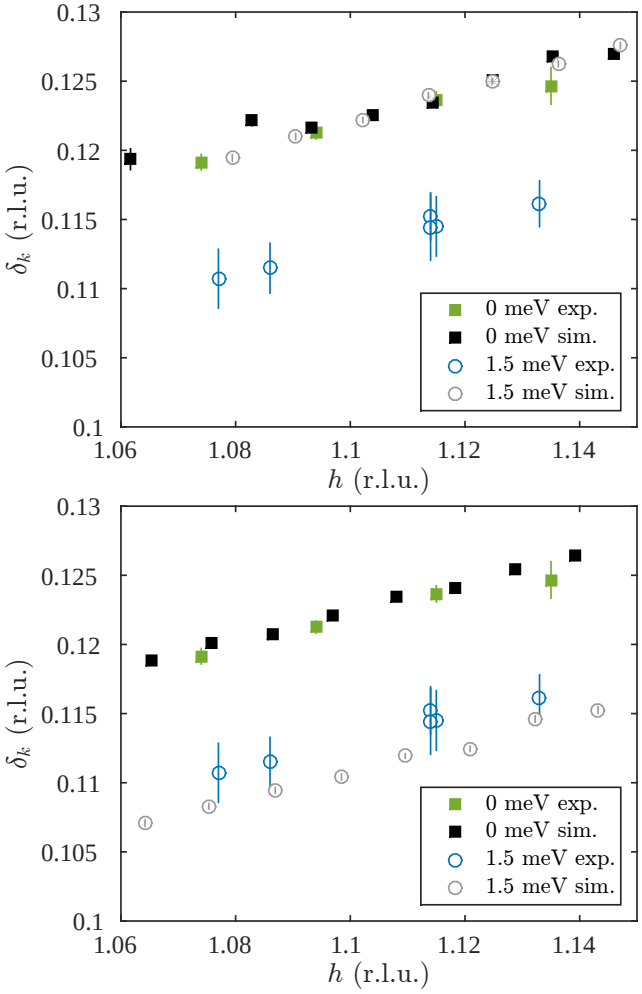

Figure 10. Incommensurability along k as function of h for LCO+O at 0 meV and 1.5 meV, along with simulated data. Top: Measured data compared to simulations where $\delta_h = \delta_k = 1/8$. Bottom: Measured data compared to simulations where δ_h and δ_k are the same as found from the experiments as detailed in the text.

correctly. This deviation is likely caused by small inaccuracies in the description of the ThALES instrument, and does not influence our conclusions.

Single scans are shown in Fig. 12 for the two sets of simulations. It is evident that the resolution of the instrument does not cause a shift in the distance between the incommensurate peaks. In particular, if we assume the traditional model of steeply dispersing stripes, the simulated data do not match the actual data (Fig. 12 a), whereas a model with a significant difference in the peak distance between the elastic and inelastic signals agrees with the data (Fig. 12 b).

In Fig. 10, we show that the experimental observation of δ_k depending on h is reproduced in the simulations. Here it is also clear that a shift in peak position between the elastic and inelastic data is needed to explain the

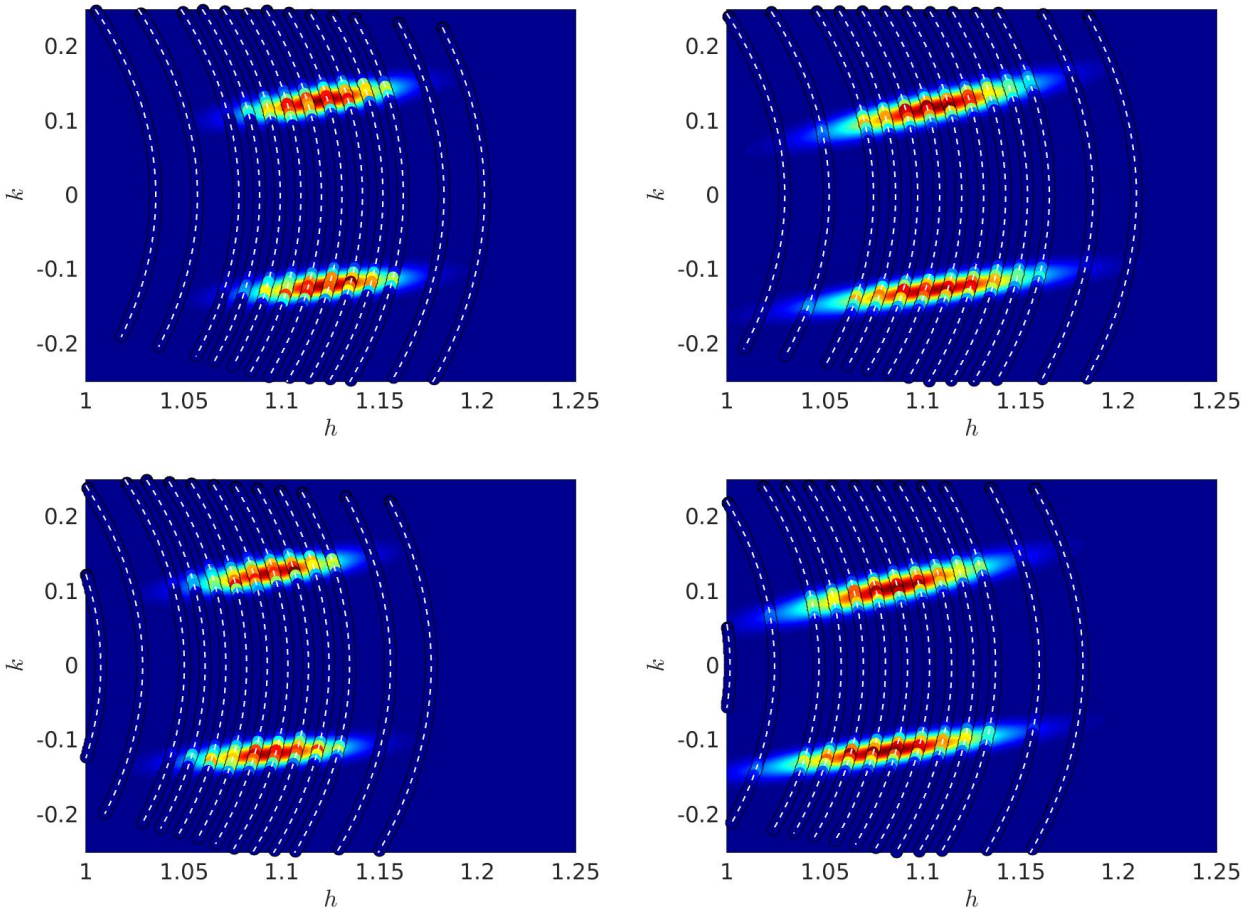

Figure 11. 2d results of virtual experiments on IC peaks from LCO+O at ThALES. The colored circles with white lines through them are simulated data, with the fit shown underneath. Top row: peaks at $(1 + 1/8, 1/8, 0)$. Bottom row: peaks at positions found from experiment. Left: 0 meV. Right: 1.5 meV.

data. There is a small effect of the resolution, causing the peaks to shift slightly towards smaller h and δ_k at higher energies. There is also a small difference between the simulated and measured values of δ_k as function of h for the inelastic data. Both of these effects are too small by at least an order of magnitude to explain the experimental results.

We further checked the effect of the instrument not being perfectly calibrated, so that the actual value of k_f differed slightly from the set value. This was done by increasing/decreasing E_f by 0.05 meV, while keeping all other parameters constant. This did indeed cause a small shift of the peak position in h, but there was no change in δ_k, as expected.

In total, our simulations show that the experimental observations are not caused by instrumental effects such as resolution or misalignment.

Twinning

The stripe modulations in LCO+O are roughly along the Cu-O-Cu bonds [9], 45° to the orthorhombic a (and b) axis, but parallel to the tetragonal a axis as shown in Fig. 1 in the main paper.

Twinning occurs when cooling through the transition from a tetragonal to an orthorhombic unit cell, where $a \neq b$. In LCO+O, $a = 5.33$ Å, $b = 5.40$ Å at low temperature [9]. The twinning is caused by the oxygen octahedra tilting around different axes, which slightly rotates the crystallographic axes of the different domains, see Fig. 13a. The results in reciprocal space is that each peak is split into two as shown in Fig. 13b. Similarly, a domain wall can run along the $(1\bar{1}0)$ direction, creating a second set of twins, giving rise to a total of four close-lying peaks illustrated in Fig. 13c [43].

Two of the peaks originate from domains with the a axis along the experimental "(100)" direction, and two with the b axis along this direction, see Fig. 14 where the

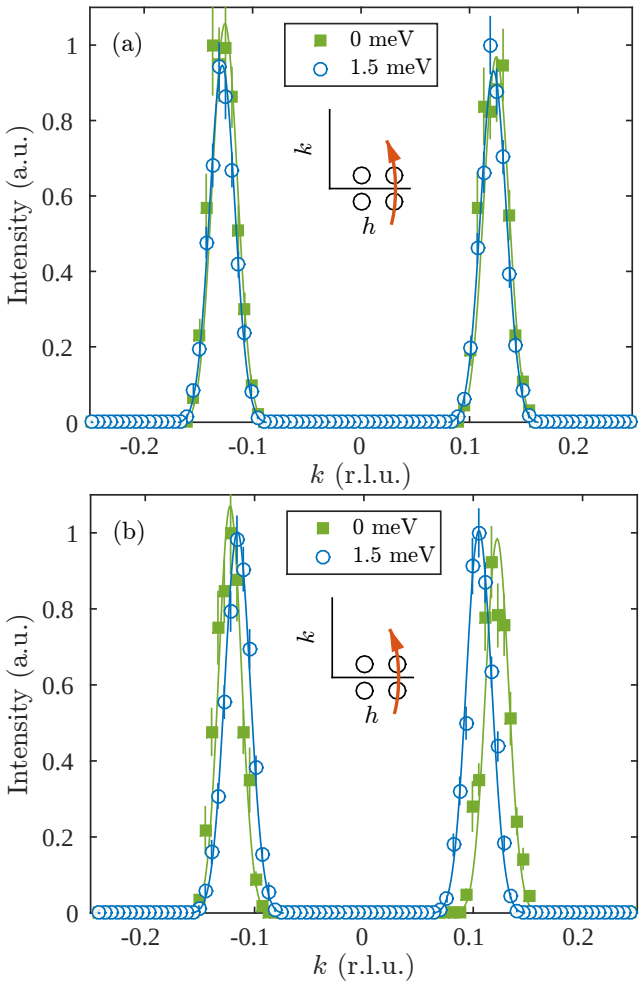

Figure 12. Simulations of transverse scans on ThALES of the two IC peaks in LCO+O at 0 meV and 1.5 meV. (a) simulations with the elastic and inelastic peaks at identical positions. (b) simulations with $\delta_h = 0.0973$, $\delta_k = 0.1222$ for the elastic peaks and $\delta_h = 0.1036$, $\delta_k = 0.1133$ for the inelastic peaks, close to the values found in the experiments.

direction of the spins in each domain is also shown.

Each set of two peaks with similar orientation is split by an angle

$$\Delta = 90^\circ - 2\tan^{-1}\left(\frac{a}{b}\right), \tag{1}$$

which in our case is around 0.7°, or $\sim$ 0.01 r.l.u. at the position of the IC peaks - too small to separate the peaks with our resolution, see Fig. 7. The twinning can, however, easily be observed at *e.g.* the nuclear (200) Bragg peak.

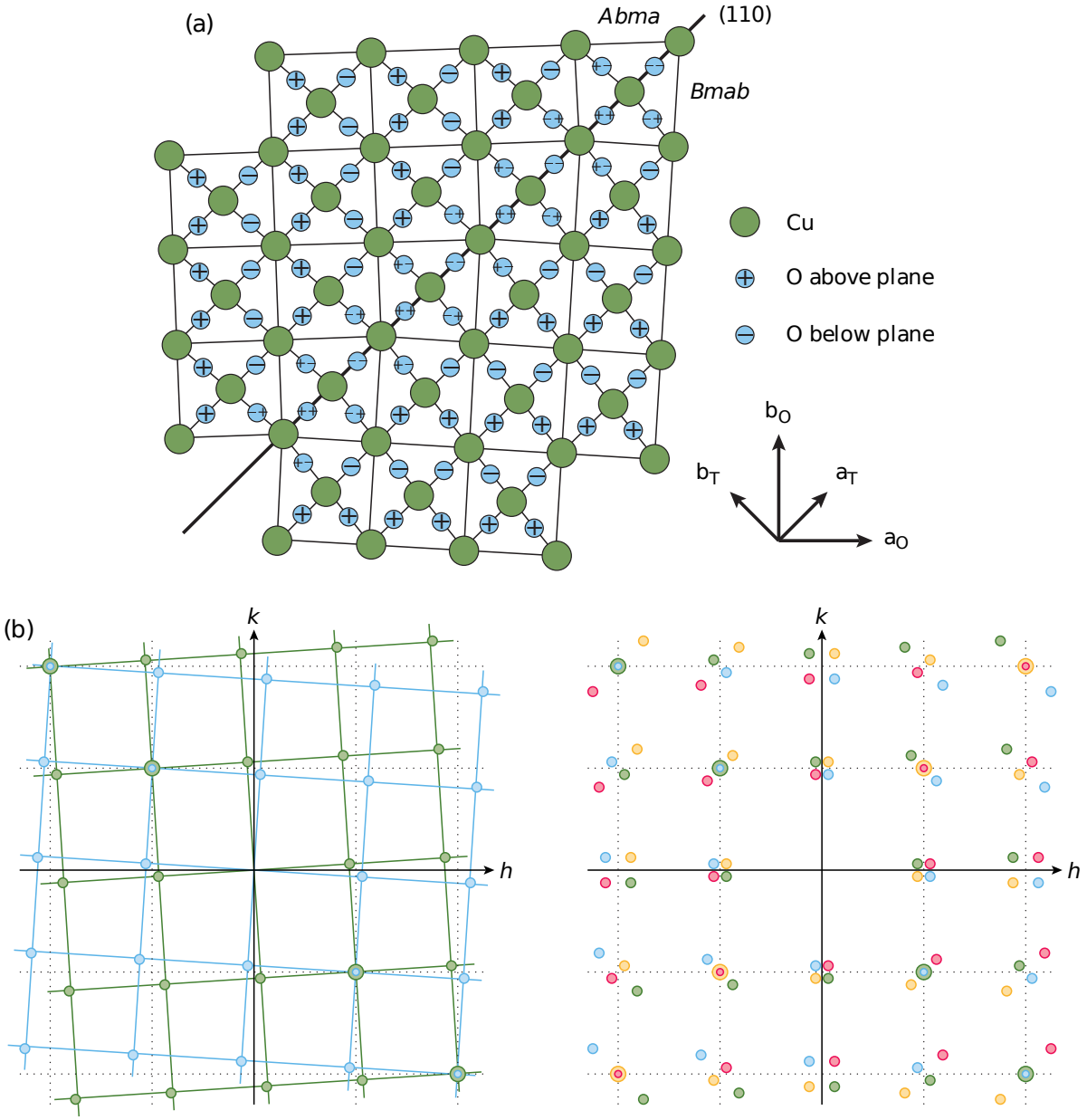

Figure 13. Illustration of twinning. (a) The structure of a crystal around a domain wall along (110). (b) The resulting reciprocal lattice from twinning along (110). (c) The full reciprocal lattice for twinning along (110) and $(1\bar{1}0)$. Adapted from Ref. [44].

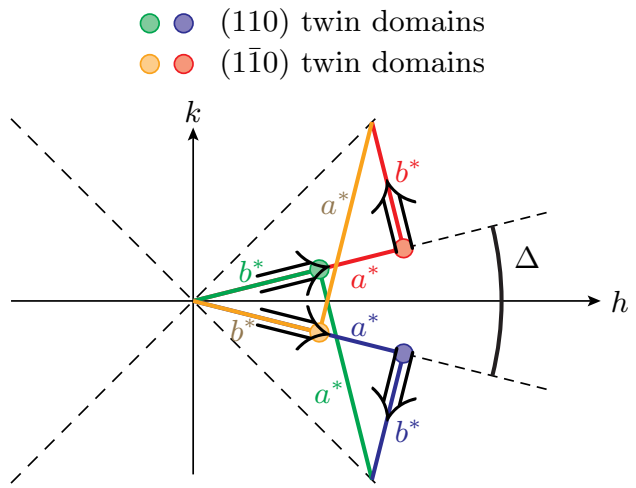

Figure 14. Illustration of the four twin peaks that appear in LCO+O around (100), with the arrows indicating the spin direction for each twin. The difference in the length of a^* and b^* is greatly exaggerated for clarity.

A.13 Field-induced inter-planar correlations in the high-temperature superconductor $La_{1.88}Sr_{0.12}CuO_4$

Investigation of the scattering along the c-axis of $La_{1.88}Sr_{0.12}CuO_4$ with emphasis on planes of CuO_2 in magnetic field. The paper was published in Physical Review B - Condensed Matter and Materials Physics.

Abstract

We present neutron scattering studies of the inter-planar correlations in the high-temperature superconductor $La_{1.88}Sr_{0.12}CuO_4$ (Tc = 27 K). The correlations are studied both in a magnetic field applied perpendicular to the CuO_2 planes, and in zero field under different cooling conditions. We find that the effect of the magnetic field is to increase the magnetic scattering signal at all values of the out-of-plane wave vector L, indicating an overall increase of the magnetic moments. In addition, weak correlations between the copper oxide planes develop in the presence of a magnetic field. This effect is not taken into account in previous reports on the field effect of magnetic scattering, since usually only L $\approx$ 0 is probed. Interestingly, the results of quench-cooling the sample are similar to those obtained by applying a magnetic field. Finally, a small variation of the incommensurate peak position as a function of L provides evidence that the incommensurate signal is twinned with the dominating and sub-dominant twin displaying peaks at even or odd L, respectively.

My contribution

Participated in a neutron scattering experiment at Flexx in Berlin, the result of which was used in the publication. Commented on the manuscript.

Field-induced interplanar magnetic correlations in the high-temperature superconductor $La_{1.88}Sr_{0.12}CuO_4$

A. T. Rømer,[1] P. J. Ray,[1] H. Jacobsen,[1] L. Udby,[1] B. M. Andersen,[1] M. Bertelsen,[1] S. L. Holm,[1] N. B. Christensen,[2] R. Toft-Petersen,[3] M. Skoulatos,[4] M. Laver,[2,4,*] A. Schneidewind,[5] P. Link,[6] M. Oda,[7] M. Ido,[7] N. Momono,[8] and K. Lefmann[1]

[1]*Nanoscience Center, Niels Bohr Institute, University of Copenhagen, DK-2100 Copenhagen, Denmark*

[2]*Department of Physics, Technical University of Denmark, DK-2800 Kongens Lyngby, Denmark*

[3]*Helmholtz Zentrum Berlin für Materialien und Energie, D-14109 Berlin, Germany*

[4]*Laboratory of Neutron Scattering, Paul Scherrer Institute, 5232 Villigen, Switzerland*

[5]*Jülich Centre for Neutron science (JCNS) at MLZ, Forschungszentrum Jülich GmbH, Outstation MLZ, Lichtenbergstrasse 1, 85747 Garching, Germany*

[6]*Heinz Maier-Leibnitz-Zentrum (MLZ), Technische Universität München, Lichtenberstrasse 1, 85747 Garching, Germany*

[7]*Department of Physics, Hokkaido University, Sapporo 060-0810, Japan*

[8]*Department of Applied Sciences, Muroran Institute of Technology, Muroran 050-8585, Japan*

(Received 23 December 2014; revised manuscript received 16 March 2015; published 11 May 2015)

We present neutron-scattering studies of the interplanar magnetic correlations in the high-temperature superconductor $La_{1.88}Sr_{0.12}CuO_4$ ($T_c = 27$ K). The correlations are studied both in a magnetic field applied perpendicular to the CuO_2 planes, and in zero field under different cooling conditions. We find that the effect of the magnetic field is to increase the magnetic scattering signal at all values of the out-of-plane wave vector L, indicating an overall increase of the magnetic moments. In addition, weak correlations between the copper oxide planes develop in the presence of a magnetic field. This effect is not taken into account in previous reports on the field effect of magnetic scattering, since usually only $L \approx 0$ is probed. Interestingly, the results of quench-cooling the sample are similar to those obtained by applying a magnetic field. Finally, a small variation of the incommensurate peak position as a function of L provides evidence that the incommensurate signal is twinned with the magnetic scattering from the dominant and subdominant structural twin displaying peaks at even and odd values of L, respectively, in our crystal.

DOI: 10.1103/PhysRevB.91.174507 PACS number(s): 74.25.Uv, 74.81.−g, 75.30.−m, 75.25.−j

I. INTRODUCTION

The interplay between magnetic ordering and superconductivity remains a topic of intense investigation in both cuprates and iron-based superconductors [1]. In the single-layer cuprate superconductor $La_{2-x}Sr_xCuO_4$ (LSCO), quasi-two-dimensional incommensurate (IC) magnetic order and fluctuations have been observed at a quartet of IC positions around the magnetic ordering vector in the parent compound La_2CuO_4 (LCO); i.e., $\mathbf{Q}_{IC} = (1 \pm \delta_H, \pm \delta_K, L)$ in orthorhombic notation [2–6]. In the doping range $0.06 \leqslant x \leqslant 0.13$ it was shown by Yamada *et al.* [7] that the incommensurability δ scales linearly with the doping, $\delta \approx x$. For doping levels close to $x = 0.125$, the superconducting critical transition temperature is somewhat suppressed [8], which is known as the 1/8 anomaly and presumably caused by stripe ordering [9–15]. The static magnetism in LSCO near $x = 0.125$, as well as its momentum space characteristics, has been previously studied in great detail [4,8,16].

Several experiments have shown that application of a magnetic field perpendicular to the CuO_2 planes leads to an enhancement of the elastic response from the magnetic IC order at $\mathbf{Q}_{IC}$ for doping values in a range around the 1/8 anomaly: $0.10 \leqslant x \leqslant 0.135$ [17–19]. In LSCO of higher doping no static order is present, but it has been shown that magnetic order can be induced by application of a magnetic field [20,21].

Previously, some of us studied the interplanar magnetic correlations in a crystal with doping value of $x = 0.11$ [22,23]. We observed that only the magnetic field component perpendicular to the CuO_2 plane, commonly referred to as the (a,b) plane, gives rise to an enhanced IC scattering, whereas the field component in the plane does not affect the magnetic IC signal. Further, the field-induced intensity was modulated along the c axis, indicating that interplanar spin correlations develop in the presence of a magnetic field perpendicular to the CuO_2 planes.

The observation of enhanced c-axis correlations raises a concern: Parts of, or in principle all of, the field-induced signal observed in measurements using the more common (a,b) plane crystal orientation may be due to the induced correlations, and not to an increase of magnetic volume fraction or ordered magnetic moments in the superconductor, as commonly believed. In the present work, we perform a comprehensive study of the field-induced signal of a LSCO crystal of a slightly larger doping level, $x = 0.12$. Our results confirm the earlier findings of both field-induced magnetism and field-induced c-axis correlations in this system. In particular, we find that much of the observed IC signal in our experiments arises from an actual increase of the magnetic moments in the system. In addition, short-range c-axis correlations develop. We present estimates for corrections of the values of field-induced signal arising due to c-axis correlations. Surprisingly, we also find that fast cooling of the crystal to base temperature induces short-range c-axis correlations similar to what is found when applying a strong magnetic field. In combination with observations by Lee *et al.* [24] on oxygen-doped La_2CuO_{4+y}, these observations

*Present address: School of Metallurgy and Materials, University of Birmingham, Edgbaston, Birmingham, United Kingdom.

suggest that fast cooling and application of a magnetic field have similar effects on the IC order.

II. EXPERIMENTAL METHOD

The $La_{1.88}Sr_{0.12}CuO_4$ sample studied in this work consisted of a single crystal grown by the traveling solvent floating zone method [25]. It exhibits a superconducting transition temperature of $T_c = 27 \pm 1.5$ K and a magnetic ordering temperature of $T_N = 30$ K [18]. In earlier work on the same crystal [18,26], the Sr content $x = 0.120 \pm 0.005$ was determined from the structural transition temperature separating the high-temperature tetragonal (HTT) from the low-temperature orthorhombic (LTO) phase. A neutron-diffraction scan of the structural (200) reflection shows that the crystal displays twinning into primarily two domains.[1] We have checked that the twin pattern is reproducible under slow-cooling conditions.

High-resolution elastic neutron-scattering experiments were carried out on three different cold-neutron triple-axis spectrometers: RITA-II [27] at the SINQ neutron source at PSI, Switzerland; FLEXX [28] at the BER2 research reactor at HZB Berlin, Germany; and PANDA at the FRM II research reactor source in Munich, Germany. Preliminary data were taken at BT-7 [29], NIST Center for Neutron Research (NCNR). We performed measurements with the sample oriented with the c axis in the scattering plane. To obtain scattering from an IC position we therefore tilted the (a,b) plane $\sim 7.8^\circ$ out of the scattering plane as illustrated in Fig. 1. Thereby we get access to wave vectors of the form $\mathbf{Q} = (H\ 0.14H\ L)$ in orthorhombic notation, where $a = 5.312$ Å, $b = 5.356$ Å, and $c = 13.229$ Å. We find an IC signal at the position $\mathbf{Q}_{IC} = (0.887(2), 0.124(1), L)$.

In triple-axis spectrometers, the resolution ellipsoid is elongated out of the scattering plane. This means that in common experiments, where the (a,b) plane is in the scattering plane, the intensity is enhanced by resolution integration along the c axis, along which the IC signal is broad. In the present crystal alignment with the c axis in the scattering plane we do not gain intensity by these resolution effects, and optimization of the experimental setup is required. Sample rotation scans are optimal in this situation since this limits distinct background contributions from, e.g., powder lines. All experiments were therefore carried out by sample rotation scans with the exception of a few scans close to $L = 0$ in the zero-field experiment at PANDA; see the open circles and solid black lines of Fig. 1(b) for an illustration of sample rotation scans.

The PANDA experiment was performed in zero field after a quench cooling of the crystal by 4 K/min. The experimental setup was $E_i = E_f = 5.0$ meV and we used 60′ collimation before and after the sample. A Be filter was placed between the monochromator and the sample.

In the experiments at FLEXX and RITA-II horizontal field magnets were used. The experimental setup on RITA-II was $E_i = E_f = 4.6$ meV and the nine-blade analyzer was arranged in the monochromatic **q**-dispersive mode [30]. We used an 80′ collimation before the sample and a Be filter with radial collimation after the sample. The sample was mounted in a

[1] We note that structural twinning is sample dependent.

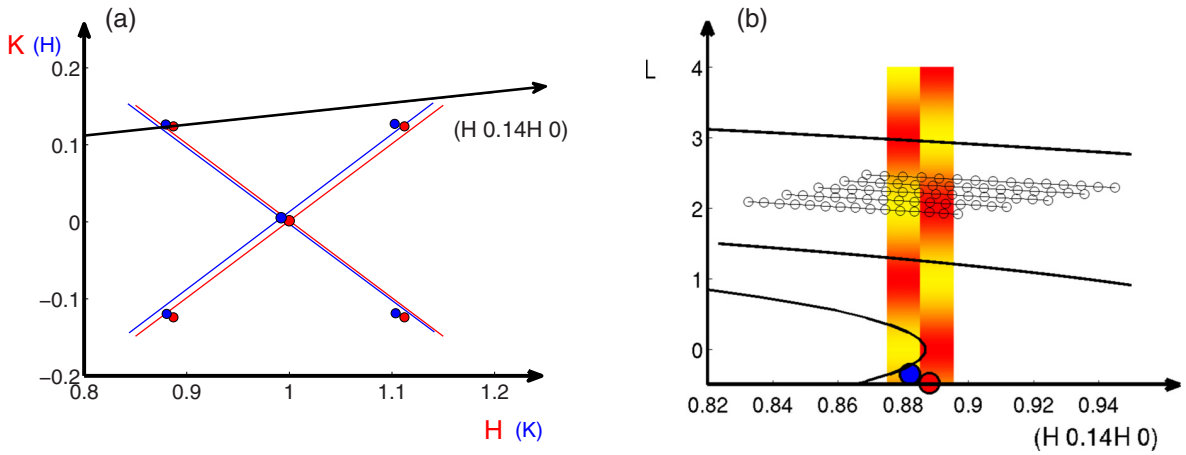

FIG. 1. (Color online) (a) Illustration of the quartet of IC peaks around (100) in orthorhombic notation. The scattering signal from the (100) structural second-order peak belonging to the dominant domain is shown by the red circle. The crystal shows twinning into two subdominant domains of which we show the strongest by the blue circles. The red and blue lines show the Cu-O-Cu axes. Note that the IC peaks are shifted off these high-symmetry axes in agreement with earlier reports [4]. The black arrow shows the axis $(H\ 0.14H\ 0)$, which we probe in the scattering plane. (b) Illustration of the scattering plane spanned by $(H\ 0.14H\ 0)$ and $(0\ 0\ L)$. We show examples of a sample rotation scan through a signal rod with a proposed weak L dependence of the signal shown for the two twins of the IC signal, with maximum signal visualized by red and minimum signal shown in yellow. The width of the signals along $(H\ 0.14H\ 0)$ is exaggerated for clarity. Note that one twin (red circle) displays peaks at even L values and the twin shown by the blue circle exhibits peaks at odd L values. The white points visualize how the nine analyzer blades of the monochromatic **q**-dispersive mode (imaging mode) on RITA-II enable measurements at distinct values of L for one sample rotation scan. For clarity, only every second analyzer blade has been shown. The solid lines show the trajectory of the reciprocal lattice vectors in a sample rotation scan. From the scan line centered at $L = 0$, it is clear that a sample rotation scan is not applicable for small L values. With increasing L, the change in L during one sample rotation scan through the signal rod becomes smaller.

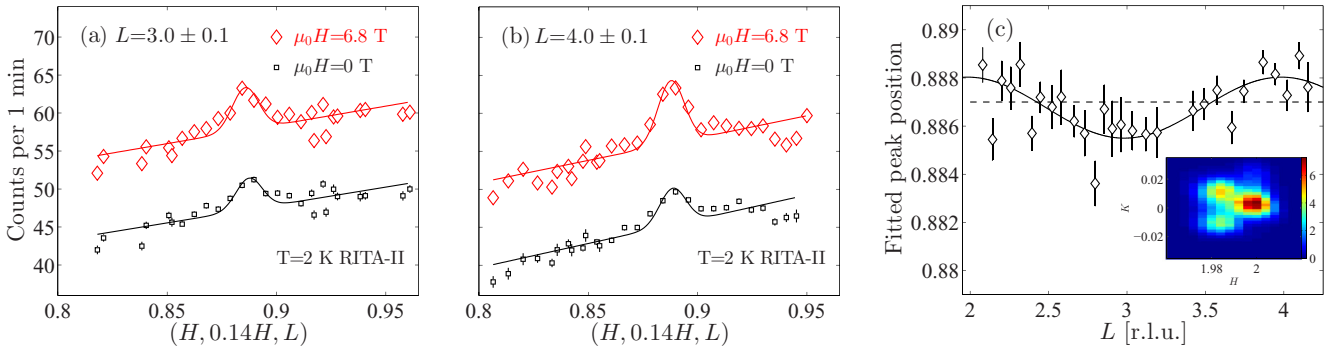

FIG. 2. (Color online) (a, b) Raw data for sample rotation scans through the IC position (H 0.14H L) for $L = 3.0$ and $L = 4.0$ in $H = 6.8$ T (red data points) and zero (black data points) applied field along the c direction, taken at $T = 2$ K. These data were taken at RITA-II, PSI. For each scan the data of five blades were combined, leading to an uncertainty in L of 0.1 r.l.u. Error bars are smaller than the marker size. The field data are shifted upwards by a constant offset for clarity. The solid curves display fits to Gaussian functions on a sloping background. (c) The fitted peak position H_{IC} for 6.8 T field data as a function of L. The dashed black line shows a fit to a straight line and the solid black line displays a fit to a sine function, which provides a better fit to the data. The color inset shows the intensity of the structural scattering signal around (200).

6.8-T horizontal field cryomagnet and data were taken in 6.8 T field applied along the c axis as well as in zero field. To improve data statistics, we performed a similar experiment at FLEXX with the sample placed in a 6-T horizontal magnet with the same orientation as in the RITA-II experiment. The FLEXX experiment was performed with energies $E_i = E_f = 5.0$ meV and we used 60′ collimation between monochromator and sample as well as between sample and analyzer. Second-order contamination from the monochromator was eliminated by a velocity selector. In both the RITA-II and FLEXX experiments the same slow sample cooling of 1 K/min was performed from $T = 190$ K down to $T = 50$ K. We studied the magnetic order by scanning through the magnetic ordering vector $\mathbf{Q}_{IC}$ at $T = 2$ K by rotating both the sample and the magnet, keeping the magnetic field along the c axis. In some of the scans the background contribution was estimated by performing similar scans at $T = 40$ K, where the magnetic order is absent.

III. RESULTS

Figures 2(a) and 2(b) show the raw data taken on RITA-II through the IC position $\mathbf{Q}_{IC}$ at different magnetic fields for $L = 3$ and $L = 4$, respectively. It is seen that for the zero-field data the peak intensity is roughly the same at $L = 3$ and $L = 4$, whereas the measurements in an applied field show a higher intensity at $L = 4$ than at $L = 3$. We fit the raw data to a single Gaussian on a sloping background keeping the width of the peak constant. The peak width is resolution limited and corresponds to a large in-plane correlation of $\xi_{\text{in-plane}} \geqslant 120$ Å , consistent with earlier measurements finding resolution-limited correlations in the (a,b) plane [18,31]. Due to the use of the monochromatic $\mathbf{q}$-dispersive mode, the RITA-II experiment amounts to almost 80 individual scans. In Figs. 2(a) and 2(b), the data of five blades are combined for an integration range of $\Delta L = 0.1$ reciprocal lattice units (r.l.u.). For the individual scans the fitted center position of the peaks varies within ≈0.002 r.l.u. around the mean value of $H_{IC} = 0.887$. Further inspection of the fitted peak center shows a clear modulation as a function of L as shown in Fig. 2(c) with $H_{IC} = 0.888$ for even L and $H_{IC} = 0.886$ for odd L. Although significant, the variation in the fitted peak center is smaller than the resolution-limited width of 0.006 r.l.u. and we cannot resolve the signal into two separate peaks. We later see that the clear modulation of the peak center provides evidence that the IC signal is twinned. In the inset of Fig. 2(c) the twinning of the structural peak at (200) is depicted, showing that three distinct structural domains are visible.

In Fig. 3 we show scans at $L = 2$ from the independent experiment on FLEXX. In this experiment we carefully measured the background intensity by sample rotation scans above the magnetic ordering temperature at $T = 40$ K and performed a pointwise background subtraction of the incommensurate magnetic signal. The figure clearly shows the effect of a 6-T magnetic field; the IC magnetic signal is roughly doubled. This is in agreement with the enhancement of the $L = 0$ signal in 7 T, observed in Ref. [31].

Now we turn to the main purpose of the study, which is to map out the full L dependence of the IC signal in field and in zero field. We did several scans similar to those shown

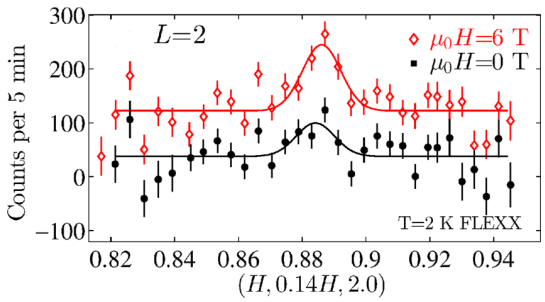

FIG. 3. (Color online) Measured peak intensity at $T = 2$ K for the IC position (H 0.14H 2.0) in 6 T field (red data points) and zero field (black data points). Pointwise background subtraction has been performed, using 40-K data as background. The solid curves are Gaussian fits to the data. These data were taken at FLEXX, HZB. The field data are shifted upwards by a constant offset for clarity.

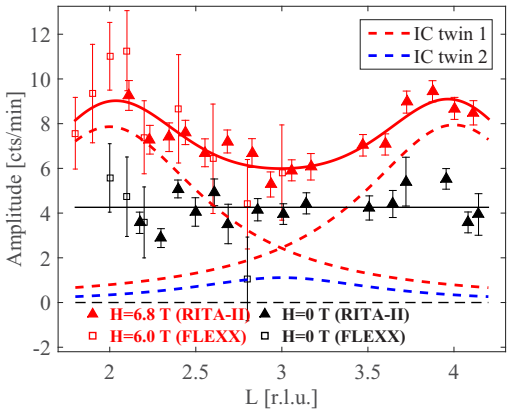

FIG. 4. (Color online) Background-subtracted elastic response at the IC position (0.887(2),0.124(1),L) versus L in zero field, a 6.0-T field (FLEXX data), and a 6.8-T field (RITA-II data). The y-axis label corresponds to the counting rate at the RITA-II experiment. To compare the two data sets, the FLEXX data have been scaled by a constant factor determined by the fraction of the signal intensities at the common data point $L = 2.2$. The red solid line corresponds to a fit to three Lorentzian functions with the same width and fixed centers at $L = 2$, 3, and 4. The three Lorentzian functions are shown separately by the red and blue dashed lines, belonging to the first and second IC twins, respectively. The color code is the same as in the cartoon drawing in Fig. 1(b).

in Figs. 2(a), 2(b), and 3 for L in the range 1.8–4.15. This span in L is significantly broader than in the previous field study in Ref. [22]. The results are summarized in Fig. 4 for both the RITA-II and FLEXX experiments. In zero field the measured IC signal is flat as a function of L; i.e., there is no observable interplanar correlations when the sample has been cooled down slowly. The effect of applying a magnetic field perpendicular to the copper oxide planes is twofold. First, weak correlations between the CuO_2 planes develop. In zero field there is no intensity modulation as a function of L, whereas a clear modulation builds up upon application of field. This is in agreement with the observations of Lake *et al.* in LSCO $x = 0.11$ [22]. Second, and more pronounced, an overall enhancement of the magnetic signal takes place for all values of L. A fit of the field data to three Lorentzian functions with same width and fixed centers at 2, 3, and 4 gives a broad modulation with half width at half maximum (HWHM) = 0.7(1) r.l.u. This corresponds to a very short correlation length of 3 Å, smaller than the distance between neighboring CuO_2 planes. Thus, the spins in neighboring planes are only very weakly correlated.

As a measure of the true enhanced intensity we integrate the signal measured in field along L and compare to the L-integrated zero-field signal. From Fig. 4 we get an L-integrated enhanced intensity of 77(8)%. For a comparison we calculate the enhancement effect at $L = 2$ from Fig. 4 and get 109(9)%. The latter corresponds to the effect which would be estimated from a measurement with the current crystal aligned in the (a,b) plane.

Finally, in Fig. 5 we show the results of the PANDA experiment, which was done at zero field, but under different experimental conditions since the crystal was quench cooled by 4 K/min. We observe a small correlation between the CuO_2 planes even when no magnetic field is applied. In this case a fit to two Lorentzian functions centered at even L, which gives a width of HWHM = 0.58(8) r.l.u., similar to the broad modulation observed in field. This leaves us with the interesting observation that quench cooling has the same qualitative effect of enhancing interplanar correlations as the application of an external magnetic field in the c direction.

IV. DISCUSSION

In the previous section we reported that c-axis correlations are absent when the system is cooled slowly from $T = 190$ K to 50 K. Further, we observed that a magnetic field as well as quench cooling can lead to the development of clear, but short-range, c-axis correlations. Now we turn to a thorough

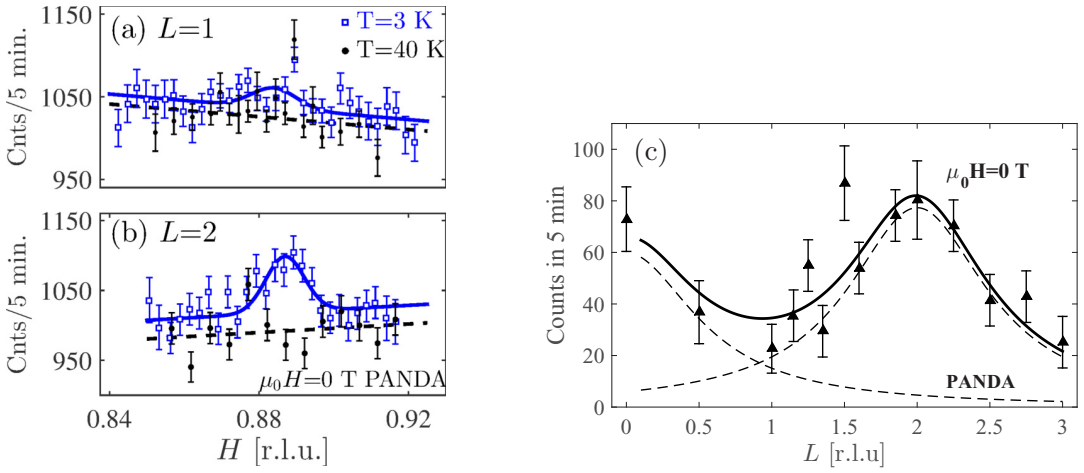

FIG. 5. (Color online) Scans through (H 0.14H L) at $T = 3$ K (blue open squares) and $T = 40$ K (black points) in zero field for (a) $L = 1$ and (b) $L = 2$. In both panels, the solid blue line shows a fit to a Gaussian function on a sloping background. (c) L dependence of the incommensurate magnetic signal above background in zero field measured at PANDA. The solid black line shows the fit to two Lorentzian functions with fixed centers at $L = 0$ and $L = 2$. The dashed lines show each of the Lorentzian functions separately.

discussion of the magnetic signal and how it is affected by an applied magnetic field and quench cooling the system. Finally, we discuss our experimental findings in the framework of theoretical microscopic models.

A. Peak position of the magnetic signal

We observe an IC signal at all values of L in field as well as in zero field. In field the position is at $H = 0.887(2)$ with a weak L dependence as shown in Fig. 2(c). Under the assumption that this IC signal belongs to the dominating structural twin, the mean IC position corresponds to a displacement angle of $\theta = 2.7^\circ$ away from the high-symmetry axis of the underlying CuO_2 plane. This is consistent with the findings of Kimura *et al.* [4] on a crystal of similar doping. In zero field the mean peak position is the same as in field with a slightly larger uncertainty due to the very weak signal. In zero field there is no discernible variation in peak position along L.

The signal structure along the L direction for different twin components of the IC order in LSCO has not been measured previously. Our expectations stem from the parent compound La_2CuO_4 [32,33] and superoxygenated La_2CuO_{4+y} [34]. The parent compound La_2CuO_4 displays long-range three-dimensional antiferromagnetic order with spins aligned mainly along the orthorhombic b axis [32,33]. With this spin structure the magnetic signal is peaked at *even* L for scattering at $(1\,0\,L)$ and at *odd* L for scattering at $(0\,1\,L)$. In the work by Lee *et al.* [34] the three-dimensionality of the IC signal in superoxygenated La_2CuO_{4+y} was investigated. A clear splitting of the incommensurate signal allowed measurements of IC signals centered at $(1\,0\,L)$ and $(0\,1\,L)$ simultaneously. Lee and co-workers reported the presence of incommensurate peaks, which are broad along L; for the IC signal centered at $(1\,0\,L)$ the peak is at even L while it occurs for odd L for the IC signal centered at $(0\,1\,L)$. Thus, in La_2CuO_{4+y} the arrangement of the spins in the interplanar direction bears resemblance to the spin arrangement in the parent compound with the spins being correlated across two to three CuO_2 planes [34].

In our case the orthorhombicity of the crystal is much smaller than in La_2CuO_{4+y} which makes it harder to identify a possible twinning of the IC signal. Twinning of the crystal can result in development of four different structural domains [35]. From scans through the structural peaks, three structural domains are visible as shown in the inset of Fig. 2(c). The subdominant second-order peak close to $(1\,0\,0)$ is displaced from the dominant peak by 0.8% in both directions. This corresponds to a rotation of 0.22° between the two twins. In Ref. [4] the twin splitting was reported to be $\sim 0.3^\circ$.

By a rotation of 0.22° and a rescaling of the vector length, the structural peak of the dominant twin is brought to the same position as the structural peak of the subdominant twin. Performing the same transformation on the IC peak at (0.888,0.124,0) we might expect an IC twin at the position (0.879,0.126,0). This predicts a larger deviation in peak center than expected from the lower value of the fitted peak center shown in Fig. 2(c) for $L = 3$, which is $H = 0.886$. Note, however, that the expected difference in peak position of the two IC twin signals is of the order of the resolution limitation of 0.006 r.l.u. Due to this resolution limitation along the $(H\,0.14H\,0)$ axis and due to the broadness of the signals along the $(0\,0\,L)$ axis, both IC twin signals will contribute for all values of L. Since we measure the IC signal centered at $(1\,0\,L)$ defined with respect to the dominant structural domain we expect interplanar correlations from the dominant twin to be peaked at even L. The subdominant twin signal is centered at $(0\,1\,L)$ and will therefore be peaked at odd L. Thus, the IC twin centered at (0.888,0.124,0) will dominate at even L and the other twin appears with weak intensity at odd L. The individual contributions to the field intensity are visualized by the dashed lines in Fig. 4. Since the twin which shows correlations peaked at even L is more pronounced than the twin with correlations peaked at odd L, the total signal displays peaks at even $L = 2$ and 4, whereas the peak at $L = 3$ is masked by the tails of the other two. Due to the broadness of the signals, the peak position is an average over both twins at all values of L. This is why we observe only a very small shift in the fitted peak center as a function of L shown in Fig. 2(c). Our observations are consistent with this picture.

B. Field-induced *c*-axis correlations

From the two independent field experiments done at RITA-II and FLEXX we find that the IC signal at $(0.887,0.124,L)$ is enhanced by a magnetic field at all values of L, but in particular for even L. The results of both experiments agree on the magnitude of the magnetic field enhancement at even L which is close to a factor of 2 in both cases.

Although the FLEXX experiment provided fewer data points, it is clear from Fig. 4 that both experiments agree on the development of weak interplanar correlations in a field as reflected in the L dependence of the amplitude of the IC intensities. The peaks which are centered at even values of L are very broad and the correlation length is smaller than the interplanar distance of 6.5 Å. This deviates from the correlation length of more than 10 Å as found in Ref. [22] for LSCO $x = 0.11$. We note that the correlation length determined in Ref. [22] is likely uncertain due to the sparse data. However, we cannot rule out a real difference in the field-induced interplanar correlation length between these two crystals of different doping levels. Since our crystal displays enhanced magnetic order in zero field compared to smaller doping values [18], it might be harder to induce the interplanar correlations by a field.

The primary effect of an applied magnetic field is to enhance the magnetic signal by enlarging either the magnetic volume fraction or the ordered magnetic moments. In principle, rotation of the spins could give rise to an enhancement of the magnetic signal at $L = 0$, but this was ruled out by the study by Lake *et al.* [22]. Our neutron-scattering experiment does not allow for a distinction between an enlarged magnetic volume fraction or increased ordered magnetic moments. Muon spin-rotation studies on the same crystal show that magnetic order is present throughout the entire volume of the sample with a resolution of 20 Å given by the effective range over which a muon is sensitive to the presence of static electronic moments [18,36], and we conclude that the

main effect arises from enlargening of the ordered magnetic moments.

In addition, development of weak interplanar correlations occurs as a response to the applied magnetic field. As a consequence, the field effect reported in the literature on magnetism in the cuprates that has been measured in the usual configuration $L = 0$ must be requantified, since it is either over- or underestimated, depending on whether the dominant IC peak belongs to a "(100)" or "(010)" IC quartet. For our crystal, measuring at the IC peak at (0.887,0.124,0) with $L = 0$ would cause an overestimation of the field effect. At even L the amplitude enhancement is roughly 109%, whereas the real increase of magnetic order measured from the L-averaged intensity is only 77%. Thus, the field effect is overestimated by 40%.

C. Cooling-induced *c*-axis correlations

Another new finding in this work is the fact that interplanar correlations are also found in zero field under different experimental conditions where the crystal is quench cooled from room temperature down to base temperature below 4 K. In contrast to the experiments on RITA-II and FLEXX, where the temperature regime for ordering of possible excess oxygen was traversed slowly, this was passed extremely fast in the PANDA zero-field experiment. This is likely to have resulted in finite interplanar correlations as evident from Fig. 5, qualitatively similar to the result of an applied magnetic field.

To understand this behavior, we first compare our sample to superoxygenated crystals where the excess oxygen ions order in a three-dimensional structure upon slow cooling. Lee *et al.* [24] showed that fast cooling leads to an oxygen-disordered state displaying enhanced spin-density-wave (SDW) order compared to the oxygen-ordered state. In fact, in this work it was observed that disordering the excess oxygen has the same enhancement effect of the SDW signal as the application of a 7.5-T field. However, it remains unknown how disordered oxygen ions or applied magnetic field affect the magnetic correlations between the CuO_2 planes.

In this paper we show that the cooling history can be important for the interplanar correlations and thereby also affect the strength of the IC signal when measured in the $L = 0$ configuration. We put forward a possible explanation for our observations. The sample might have a small amount of excess oxygen since this is not easily avoided during crystal growth. Fast cooling through the temperature regime where ordering of possible excess oxygen takes place, which occurs down to $\sim$180 K, might cause random positions of the excess oxygen ions. Such impurities could act as pinning centers enhancing the magnetic correlations between the planes.

D. Theoretical scenario

Theoretically, the slowing down and subsequent pinning of static magnetic order by disorder sites and twin boundaries [37–46] and vortices [47–53] has been previously discussed extensively in the literature. From the microscopic studies, it is clear that the modulations of charge density and/or electron hopping amplitudes induced by impurities and twin boundaries can lead to local magnetic instabilities which nucleate magnetic order in the vicinity of the perturbing sites. The vortices, on the other hand, typically induce local magnetic order due to the suppressed superconducting gap and an associated enhanced local density of states near the Fermi level in the cores. It has been shown that even in strongly disordered situations vortices enhance the in-plane magnetic moments [53,54]. To the best of our knowledge, the out-of-plane induced magnetic order by disorder or by vortices has not been described by microscopic models, and constitutes an interesting future study. For the pure superconducting system, flux lines along the c axis should lead to substantially enhanced spin correlations along L [22]. The weak coupling between the CuO_2 planes will lead to short-ranged vortex-induced magnetic order, but the extremely short c-axis correlations found here point to additional effects. Certainly, the full magnetic volume fraction already in zero field indicates that there is hardly any "room" for vortices to induce coherent spin correlations along the c axis. Instead, the vortices lead to local enhancements of the magnetic moments and presumably adapt to the many preexisting pinning centers and strongly meander along c, leading to only very weak c-axis field-induced correlations in qualitative agreement with our observations. Within this scenario, samples with less static magnetic order in zero field should lead to longer-ranged and more pronounced c-axis correlations in the presence of a magnetic field.

V. CONCLUSIONS

We have studied the field dependence of the interplanar magnetic correlations in $La_{1.88}Sr_{0.12}CuO_4$. The primary effect of an applied magnetic field is an enhancement of the magnetic moments. Further, there is an effect of increased interplanar correlations in the presence of an applied field. The interplanar correlation length is very small and implies correlations only between neighboring planes. This indicates that the magnetic order is already strongly pinned by impurities in the sample and that vortices tend to bend rather than go perpendicular to the CuO_2 planes on the way through the sample. We observe that a fast-cooling procedure results in the same feature as application of a magnetic field, namely development of weak interplanar correlations. One possible scenario caused by excess oxygen could lead to pinning of the magnetic order between the CuO_2 planes thereby explaining why a quench-cooled system behaves similarly as a system subjected to an external field.

ACKNOWLEDGMENTS

We are grateful for the access to neutron beam time at the neutron facilities at NCNR, BER-2 at Helmholtz-Zentrum Berlin, FRM II at MLZ Garching, and SINQ at the Paul Scherrer Institute. This project was supported by the Danish Council for Independent Research through DANSCATT and by Grant No. 0602-01982B. B.M.A. acknowledges support from the Lundbeckfond (Fellowship Grant No. A9318).

[1] M. Vojta, Adv. Phys. **58**, 699 (2009); D. C. Johnston, *ibid.* **59**, 803 (2010).

[2] R. J. Birgeneau, D. R. Gabbe, H. P. Jenssen, M. A. Kastner, P. J. Picone, T. R. Thurston, G. Shirane, Y. Endoh, M. Sato, K. Yamada, Y. Hidaka, M. Oda, Y. Enomoto, M. Suzuki, and T. Murakami, Phys. Rev. B **38**, 6614 (1988).

[3] R. J. Birgeneau, Y. Endoh, K. Kakurai, Y. Hidaka, T. Murakami, M. A. Kastner, T. R. Thurston, G. Shirane, and K. Yamada, Phys. Rev. B **39**, 2868 (1989).

[4] H. Kimura, H. Matsushita, K. Hirota, Y. Endoh, K. Yamada, G. Shirane, Y. S. Lee, M. A. Kastner, and R. J. Birgeneau, Phys. Rev. B **61**, 14366 (2000).

[5] J. M. Tranquada, in *Handbook of High-Temperature Superconductivity Theory and Experiment*, edited by J. R. Schrieffer (Springer, New York, 2007).

[6] R. J. Birgeneau, C. Stock, J. M. Tranquada, and K. Yamada, J. Phys. Soc. Jpn. **75**, 111003 (2006).

[7] K. Yamada, C. H. Lee, K. Kurahashi, J. Wada, S. Wakimoto, S. Ueki, H. Kimura, Y. Endoh, S. Hosoya, G. Shirane, R. J. Birgeneau, M. Greven, M. A. Kastner, and Y. J. Kim, Phys. Rev. B **57**, 6165 (1998).

[8] S. Katano, M. Sato, K. Yamada, T. Suzuki, and T. Fukase, Phys. Rev. B **62**, R14677 (2000).

[9] Q. Li, M. Hücker, G. D. Gu, A. M. Tsvelik, and J. M. Tranquada, Phys. Rev. Lett. **99**, 067001 (2007).

[10] J. M. Tranquada, G. D. Gu, M. Hücker, Q. Jie, H.-J. Kang, R. Klingeler, Q. Li, N. Tristan, J. S. Wen, G. Y. Xu, Z. J. Xu, J. Zhou, and M. V. Zimmermann, Phys. Rev. B **78**, 174529 (2008).

[11] M. Hücker, M. V. Zimmermann, G. D. Gu, Z. J. Xu, J. S. Wen, G. Xu, H. J. Kang, A. Zheludev, and J. M. Tranquada, Phys. Rev. B **83**, 104506 (2011).

[12] H.-H. Wu, M. Buchholz, C. Trabant, C. F. Chang, A. C. Komarek, F. Heigl, M. v. Zimmermann, M. Cwik, F. Nakamura, M. Braden, and C. Schüßler-Langeheine, Nat. Comm. **3**, 1023 (2012).

[13] N. B. Christensen, J. Chang, J. Larsen, M. Fujita, M. Oda, M. Ido, N. Momono, E. M. Forgan, A. T. Holmes, J. Mesot, M. Huecker, and M. v. Zimmermann, arXiv:1404.3192.

[14] V. Thampy, M. P. M. Dean, N. B. Christensen, L. Steinke, Z. Islam, M. Oda, M. Ido, N. Momono, S. B. Wilkins, and J. P. Hill, Phys. Rev. B **90**, 100510(R) (2014).

[15] T. P. Croft, C. Lester, M. S. Senn, A. Bombardi, and S. M. Hayden, Phys. Rev. B **89**, 224513 (2014).

[16] T. Suzuki, T. Goto, K. Chiba, T. Shinoda, T. Fukase, H. Kimura, K. Yamada, M. Ohashi, and Y. Yamaguchi, Phys. Rev. B **57**, R3229 (1998).

[17] B. Lake, H. M. Rønnow, N. B. Christensen, G. Aeppli, K. Lefmann, D. F. McMorrow, P. Vorderwisch, P. Smeibidl, N. Mangkorntong, T. Sasagawa, M. Nohara, H. Takagi, and T. E. Mason, Nature (London) **415**, 299 (2002).

[18] J. Chang, Ch. Niedermayer, R. Gilardi, N. B. Christensen, H. M. Rønnow, D. F. McMorrow, M. Ay, J. Stahn, O. Sobolev, A. Hiess, S. Pailhés, C. Baines, N. Momono, M. Oda, M. Ido, and J. Mesot, Phys. Rev. B **78**, 104525 (2008).

[19] M. Kofu, S.-H. Lee, M. Fujita, H.-J. Kang, H. Eisaki, and K. Yamada, Phys. Rev. Lett. **102**, 047001 (2009).

[20] J. Chang, N. B. Christensen, Ch. Niedermayer, K. Lefmann, H. M. Rønnow, D. F. McMorrow, A. Schneidewind, P. Link, A. Hiess, M. Boehm, R. Mottl, S. Pailhés, N. Momono, M. Oda, M. Ido, and J. Mesot, Phys. Rev. Lett. **102**, 177006 (2009).

[21] B. Khaykovich, S. Wakimoto, R. J. Birgeneau, M. A. Kastner, Y. S. Lee, P. Smeibidl, P. Vorderwisch, and K. Yamada, Phys. Rev. B **71**, 220508(R) (2005).

[22] B. Lake, K. Lefmann, N. B. Christensen, G. Aeppli, D. F. McMorrow, H. M. Rønnow, P. Vorderwisch, P. Smeibidl, N. Mangkorntong, T. Sasagawa, M. Nohara, and H. Takagi, Nat. Mater. **4**, 658 (2005).

[23] The doping of the crystal in Ref. [22] was later shown to be closer to $x = 0.11$ rather than $x = 0.10$ from a measurement of the transition temperature from HTT to LTO [26].

[24] Y. S. Lee, F. C. Chou, A. Tewary, M. A. Kastner, S. H. Lee, and R. J. Birgeneau, Phys. Rev. B **69**, 020502(R) (2004).

[25] T. Nakano, N. Momono, M. Oda, and M. Ido, J. Phys. Soc. Jpn. **67**, 2622 (1998).

[26] R. Gilardi, Ph.D. dissertation no. 15780, ETH Zürich, 2004.

[27] C. R. H. Bahl, P. Andersen, S. N. Klausen, and K. Lefmann, Nucl. Instrum. Methods Phys. Res., Sect. A **226**, 667 (2004).

[28] M. D. Le, D. L. Quintero-Castro, R. Toft-Petersen, F. Groitl, M. Skoulatos, K. C. Rule, and K. Habicht, Nucl. Instrum. Methods Phys. Res., Sect. A **729**, 220 (2013).

[29] J. W. Lynn, Y. Chen, S. Chang, Y. Zhao, S. Chi, W. Ratcliff II, B. G. Ueland, and R. W. Erwin, J. Res. Natl. Inst. Stand. Technol. **117**, 61 (2012).

[30] C. R. H. Bahl, K. Lefmann, A. B. Abrahamsen, H. M. Rønnow, F. Saxild, T. B. S. Jensen, L. Udby, N. H. Andersen, N. B. Christensen, H. S. Jacobsen, T. Larsen, P. S. Häfliger, S. Streule, and Ch. Niedermayer, Nucl. Instrum. Methods Phys. Res., Sect. B **246**, 452 (2006); K. Lefmann, Ch. Niedermayer, A. B. Abrahamsen, C. R. H. Bahl, N. B. Christensen, H. S. Jacobsen, T. L. Larsen, P. Häfliger, U. Filges, and H. M. Rønnow, Phys. B (Amsterdam, Neth.) **385-386**, 1083 (2006).

[31] A. T. Rømer, J. Chang, N. B. Christensen, B. M. Andersen, K. Lefmann, L. Mähler, J. Gavilano, R. Gilardi, Ch. Niedermayer, H. M. Rønnow, A. Schneidewind, P. Link, M. Oda, M. Ido, N. Momono, and J. Mesot, Phys. Rev. B **87**, 144513 (2013).

[32] D. Vaknin, S. K. Sinha, D. E. Moncton, D. C. Johnston, J. M. Newsam, C. R. Safinya, and H. E. King, Jr., Phys. Rev. Lett. **58**, 2802 (1987).

[33] Y. Endoh, K. Yamada, R. J. Birgeneau, D. R. Gabbe, H. P. Jenssen, M. A. Kastner, C. J. Peters, P. J. Picone, T. R. Thurston, J. M. Tranquada, G. Shirane, Y. Hidaka, M. Oda, Y. Enomoto, M. Suzuki, and T. Murakami, Phys. Rev. B **37**, 7443 (1988).

[34] Y. S. Lee, R. J. Birgeneau, M. A. Kastner, Y. Endoh, S. Wakimoto, K. Yamada, R. W. Erwin, S.-H. Lee, and G. Shirane, Phys. Rev. B **60**, 3643 (1999).

[35] M. Braden, G. Heger, P. Schweiss, Z. Fisk, K. Gamayunov, I. Tanaka, and H. Kojima, Phys. C (Amsterdam, Neth.) **191**, 455 (1992).

[36] J. Larsen, Ph.D. dissertation, Technical University of Denmark, 2013.

[37] H. Tsuchiura, Y. Tanaka, M. Ogata, and S. Kashiwaya, Phys. Rev. B **64**, 140501(R) (2001).

[38] Z. Wang and P. A. Lee, Phys. Rev. Lett. **89**, 217002 (2002).

[39] J.-X. Zhu, I. Martin, and A. R. Bishop, Phys. Rev. Lett. **89**, 067003 (2002).

[40] Y. Chen and C. S. Ting, Phys. Rev. Lett. **92**, 077203 (2004).

[41] H. Kontani and M. Ohno, Phys. Rev. B **74**, 014406 (2006).

[42] J. W. Harter, B. M. Andersen, J. Bobroff, M. Gabay, and P. J. Hirschfeld, Phys. Rev. B **75**, 054520 (2007).

[43] B. M. Andersen, P. J. Hirschfeld, A. P. Kampf, and M. Schmid, Phys. Rev. Lett. **99**, 147002 (2007).
[44] B. M. Andersen, S. Graser, and P. J. Hirschfeld, Phys. Rev. Lett. **105**, 147002 (2010).
[45] R. B. Christensen, P. J. Hirschfeld, and B. M. Andersen, Phys. Rev. B **84**, 184511 (2011).
[46] U. Tricoli and B. M. Andersen, J. Supercond. Novel Magn. **25**, 1329 (2012).
[47] D. P. Arovas, A. J. Berlinsky, C. Kallin, and S.-C. Zhang, Phys. Rev. Lett. **79**, 2871 (1997).
[48] B. M. Andersen, H. Bruus, and P. Hedegård, Phys. Rev. B **61**, 6298 (2000).
[49] E. Demler, S. Sachdev, and Y. Zhang, Phys. Rev. Lett. **87**, 067202 (2001).
[50] Y. Chen and C. S. Ting, Phys. Rev. B **65**, 180513(R) (2002).
[51] M. Takigawa, M. Ichioka, and K. Machida, Phys. Rev. Lett. **90**, 047001 (2003).
[52] B. M. Andersen, O. F. Syljuåsen, and P. Hedegard, Phys. Rev. B **80**, 052509 (2009).
[53] B. M. Andersen, S. Graser, M. Schmid, A. P. Kampf, and P. J. Hirschfeld, J. Phys. Chem. Solids **72**, 358 (2011).
[54] M. Schmid, B. M. Andersen, A. P. Kampf, and P. J. Hirschfeld, New J. Phys. **12**, 053043 (2010).